UNIVERSITY OF CALIFORNIA

Los Angeles

Polymethine fluorophores for *in vivo* shortwave infrared imaging

A dissertation submitted in partial satisfaction of the

requirements for the degree Doctor of Philosophy

in Chemistry

by

Emily Donovan Cosco

2020

ABSTRACT OF THE DISSERTATION

Polymethine fluorophores for *in vivo* shortwave infrared imaging

by

Emily Donovan Cosco

Doctor of Philosophy in Chemistry

University of California, Los Angeles, 2020

Professor Ellen May Sletten, Chair

Optical detection of biological function in living cells, model organisms, and humans is a powerful approach for studying physiology and disease. The amount of information that can be gained noninvasively, however, is limited in penetration depth and resolution by unfavorable interactions between light and tissue. Optical imaging with detection in the shortwave infrared (SWIR, 1,000–2,000 nm) region enables the observation of structure and function in deep tissue. With low scattering coefficients and few naturally occurring molecules with SWIR absorption or emission, SWIR light has minimal competing optical phenomena within biology. While rapid development of contrast agents has followed the decade-old discovery of SWIR detection as a noninvasive imaging technique, improved bright and biocompatible contrast agents are vital for imaging with minimal biological perturbation. In this dissertation, long wavelength absorbing and

emitting polymethine dyes are established, optimized, and applied, in combination with imaging methodology, to advance SWIR imaging in mice.

Chapter One is a perspective on the growth and application of polymethine dyes as shortwave infrared contrast agents. Chapter Two describes the initial development and *in vivo* SWIR imaging application of 7-dimethylamino flavylium polymethine dyes.

Chapters Three and Four establish excitation multiplexing with shortwave infrared detection as an effective method to obtain real-time multicolor images *in vivo*, noninvasively. In Chapter Three, flavylium heptamethine dyes with absorption wavelengths matched to excitation lasers enable two- and three-color imaging in anesthetized and awake animals. Chromenylium penta- and heptamethine dyes which display increased brightness are offered in Chapter Four as improved labels for fast and multicolor SWIR imaging using near infrared excitation wavelengths.

Chapter Five details strategies taken to facilitate delivery of polymethine dyes to biological systems. The approaches include encapsulation in phospholipid, organic polymer-based, and perfluorocarbon nanomaterials, as well as appending lipophilic, fluorophilic, and hydrophilic solubilizing tags to the chromophores. Chapter Six explores the use of hollow mesoporous silica nanoparticles (HSMNs) to stabilize J-aggregates for SWIR imaging. Chapter Seven is a study of the photophysical properties of indocyanine green (ICG) relevant to benchmarking SWIR imaging experiments.

The dissertation of Emily Donovan Cosco is approved.

Miguel A. Garcia-Garibay

Kendall N. Houk

Alexander Michael Spokoyny

Anna Wu Work

Ellen May Sletten, Committee Chair

University of California, Los Angeles

2020

This dissertation is dedicated to my parents, Sally and Peter

and to my brother, Stephen

TABLE OF CONTENTS

LIST OF FIGURES

CHAPTER ONE

CHAPTER TWO

CHAPTER FIVE

CHAPTER SIX

LIST OF SCHEMES

CHAPTER TWO

CHAPTER THREE

CHAPTER FOUR

CHAPTER FIVE

LIST OF TABLES

CHAPTER THREE

CHAPTER FOUR

CHAPTER FIVE

CHAPTER SIX

CHAPTER SEVEN

LIST OF CHARTS

CHAPTER TWO

CHAPTER FOUR

ACKNOWLEDGEMENTS

Graduate school was an experience like no other. Looking back, I really had little idea what I was signing up for. I knew I enjoyed doing experiments, solving problems and thinking about chemistry, so I thought it was worth a shot. It turns out, it was. There were highs and lows, but throughout all of these experiences there was an incredible network of people that offered their support, insight, expertise, mentorship, and friendship.

Foremost, I owe colossal thanks to my advisor Ellen Sletten. Ellen started at UCLA shortly after I began the program, and from our first discussion, I knew I wanted to learn from her. I was initially inspired by her lofty ideas and big picture goals, but soon came to realize the extent of Ellen's excellence as a scientist and educator. To her lab, she has ensured wholistic training in all aspects important to being a successful scientist and communicator. Some of my favorite memories that were instrumental to my scientific growth include learning how to write a manuscript by doing the first one in her office together, and the many practice talks we had, in preparing for the first talk I would give to the department, on cycloparaphenylenes. While providing keen guidance, Ellen consistently encouraged me to follow the science. Because of that freedom, I was able to yield to my scientific curiosity and explore so many areas I never could have conceived at the outset. Equally important to my growth were the times she kept me on track by encouraging me to focus on the end game instead of starting yet another project, the times she pushed me to solve problems on my own, and the times when she told me I could do something I didn't realize I was ready for. Ellen, from the first reaction you helped me set up in a hood at its cleanest state, to brainstorming sessions at the large whiteboard in your office, to letting me run with the crazy idea of going to Germany for experiments- I am so grateful for everything you have done to help me

become the scientist that I am today. There were so many other mountains, valleys, sunny days, and rainstorms on the roadmap to this PhD. Throughout all of it, Ellen, thank you for the tissues and the champagne. I needed them both. It was an incredible honor to help you set up your lab and watch it grow to the vibrant, inquisitive, and creative group of scientists that it is today. I am so excited to watch your career blossom.

I also have a huge amount of thanks for my second mentor in grad school, Oliver Bruns. Oliver was just starting his lab at the Helmholtz Pioneer Campus in 2018, when he recruited me to perform imaging experiments in Munich. Those first three months I spent in Germany were some of the most challenging I experienced in grad school, yet they resulted in a huge amount of learning. Oliver was dedicated to teaching me just about everything I needed to know to be successful in SWIR imaging in a short time frame, while we were troubleshooting the experimental set up and while I was learning how to do animal work at the same time. Since that time, Oliver has never ceased to offer his advice and support and has been an incredible scientist to learn from whether I am in Germany or the US. I am so inspired by Oliver's ability to envision how the scientific findings we observe on a daily basis could be transformed into real life applications. Along with his extraordinary ability to communicate science to a broad audience, he is also so in tune with the smallest experimental details and never missed an opportunity to get his hands wet by coming into lab to help with tough experiments. Oliver, I am incredibly grateful for all of the experiences I had in Germany, none of which could have been possible without you. Thank you for the impeccable scientific training and for your continued support of my personal growth.

I am also so grateful for the support of my committee members. It was an enlightening experience to TA Physical Organic Chemistry for Ken Houk in my second year. I appreciate all of the effort he put in make those courses the most fun I've ever had teaching. When early on, I

thought I wanted to pursue computational chemistry, Ken generously set me up with a mentor in his lab and made sure I had all the resources I could possibly need. I enjoyed all of the conversations that we had at department receptions, his elaborate birthday parties, and appreciate his insights on physical organic data from my own research. Unfortunately, my Houk number is still at 2, but there's still time to collaborate on a paper! Miguel Garcia-Garibay has always had his door open and was more than happy to talk about whatever—from the unexpected photophysical phenomena I was observing in the chemistry I was working on, to checking in about how grad school was going. I am inspired by his passion for photochemistry and dedication to being a wonderful educator. I am lucky to have experienced his mentorship in action by attending a few of his group meetings as well as in the photochemistry journal club we put together. Finally, I am happy I was able to use his lab as a second home in the Molecular Sciences Building. I appreciate the support from Alex Spokoyny throughout grad school, some of which was behind the scenes. I enjoyed all of our discussions about science, and life as a scientist, which was usually over drinks. He was always willing to lend a hand, offering use of instruments, along with his own and his trainees' expertise. Anna Wu was kind enough to offer her insights on my scientific goals as well as sharing her own, after a cold email. I admire her approach to science and hope that future work can combine some of her expertise with that of the Sletten Lab. Finally, an "unofficial committee member," Justin Caram, taught me more than I could have hoped for much about photophysics. I enjoyed all of the whiteboard discussions, emails, slack threads, soldering sessions, and more. I could always count on his enthusiasm to break down a concept I was struggling to understand or help in troubleshooting experiments. It was so fun working on projects together, starting before he even began at UCLA, to the present. A few additional mentors outside of UCLA

whose support throughout graduate school has been so meaningful are Martin Schnermann at the NCI, Luke Lavis at Janelia, and Tulio Valdez at Stanford.

There are so many other professors and staff in the Chemistry and Biochemistry Department that have helped me successfully navigate to the end of my PhD. The department was such a nurturing home to have for five years—I am still in awe of how much support is given and received between members of this department. To name a few, Janette Kropat, Nati Alcaraz, Ricky Ruiz, Jose Gonzalez and Julio Gonzalez always went above and beyond whenever there were unusual things I needed. I owe Saeed Khan, Ignacio Martini and Laurent Bentolila thanks for their scientific expertise. Bill Gelbart was so kind in my first year and struggling with the difficulties of grad school before I had a lab or mentor. I am thankful that Heather Maynard convinced me to come to UCLA for my graduate studies. I enjoyed all of my interactions with Jeffrey Zink, who shared his love of mesoporous silica nanoparticles, brainstormed experimental set ups, and taught me a bit about navigating the publishing world. I am grateful to Hosea Nelson, Yves Rubin, and Patrick Harran, for pushing me to be a better organic chemist through their challenging and empowering courses. I will continue to have such positive memories from this department, and this is due to the tremendous group of supportive and kind people that work there.

I now arrive at the people that I had the pleasure of doing science with day to day. Getting the lab up and running in our first year was a rollercoaster. I could not have made it through without the support of Wendell Scott and Grace Tang. I am so grateful to have had them by my side, writing 100s of SOPs and unpacking boxes taller than myself. Wendell, thank you for being such a rock in that first year. I am glad you found your right fit and celebrate in all your successes. Broader, the entire group of Organic students in the 2015 cohort provided a network of support that was vital to surviving our first year together. Additionally, I am so grateful to all of the advanced

graduate students and postdocs in other labs that took me under their wing: Jeong Hoon Ko (JK), Cyndi He, Jon Axtell, and Evan Darzi. The fourth floor in MSB was never the same after JK left, it was such a joy to have conversations with him about science and life when taking breaks between experiments. Cyndi was so patient with offering her mentorship when I was trying to learn some computation. Jon knew how to give me some tough love when I needed it, always offered out of the box ideas for experiments, and was always eager to help in any situation. I will always share a love of conjugated systems with Evan. I enjoyed all of our discussions, on campus and on bus rides from Culver City.

Crucially, the Sletten Lab was a wonderful place to grow into a trained scientist. I am incredibly grateful to everyone who contributed to the creative, supportive, and lighthearted lab environment. To you all, it was an absolute honor to learn alongside you and I am so humbled by the incredible scientist you have become. Monica Pengshung was a terrific bay-mate to have for the first couple years. I am jealous of her musical taste and knowledge, and enjoyed the various concerts we were able to experience together. No one introduced me to more great food than Gina Lee, including the best places for boba tea, $2 street tacos, as well as her own baking. Talking with Margeaux Miller never failed to brighten my day. I am grateful that she shared her synthetic prowess and was always willing to help. Joe Jaye added great humor to time in lab. I could always count on his real takes that really put everything in perspective. I learned from Anna Kataki-Anastasakou that nothing helps a tough week in lab like some meditative time at the beach. Because of Dan Estabrook, I can't watch a football game without screaming "Lets GOOO," and I will never forget his creative take on "cheesy potatoes." Rachael Day was an essential source of conceptual and experimental biological expertise. I enjoyed all of our discussions and knew I could always count on her help. It was a blast doing the first *in vivo* imaging experiments in the Sletten

Lab with Irene Lim, I wish we could have started much sooner! I cannot listen to The Weeknd without thinking about Anthony Spearman. It was a rewarding experience teaching him all of the dye synthesis tricks I knew and then watching him figure out his own. It was awesome sharing a bay with Cesar Garcia for the latter half of my time in the lab, we had so much fun jamming out while running dye columns together. I am so happy that I could see Kelly Wong, Erika Ramirez, and Joseph Garcia get their bearings and succeed in a new environment despite such a challenging year. The postdocs Wei Cao, Heidi van de Wouw, Shang Jia, and Jon were also a source of inspiration and I am grateful for all of their insights they added to discussions. I am happy to have come to know Dom Larubina, "unofficial lab member," as well as experience his amazing cooking and taste in beer. Finally, I had the privilege of mentoring undergraduate students Ryan McLaughlin, Olivia Leland, and Zhumin Zhang, who were fantastic and taught me so much about mentorship. I am excited to watch where their careers go.

I was also able to collaborate with some other incredible scientists at UCLA. Wei Chen and Annie Cheng were a wonderful team to work with on a project that started out with a shot in the dark and ended with bright particles in mice. They were so dedicated to getting the project to work, long after many would have already given up. I appreciate how they jumped at every opportunity to add more experiments and controls to make our results stronger. Erik Farr offered essential expertise when I was just getting my bearings in grad school. It's been invigorating learning from Tim Atallah and Hannah Friedman while working on projects together. Tim has helped with so many optics and photophysics question I have had beyond our explicit work together and I am grateful for his mentorship. It's been a delight seeing Hannah's scientific progress and talking with her about all of the insights she has been able to uncover. I also want to thank Daniel Franke, who was happy to spend the afternoon giving me a tour of MIT when I showed up with a day's notice,

as well as Moungi Bawendi, and Vasilis Ntziachristos for their important contributions to the science contained within this dissertation.

I had the pleasure of working with another group of talented and supportive scientists at the Helmholtz Pioneer Campus in Munich. I am so grateful to everyone at the HPC for inviting me into their labs with open arms. The Bruns lab was an incredibly joyful and supportive environment. I had never before experienced a work setting where everyone in the lab tried to join each other to share lunch or a coffee almost every day. This was a great opportunity to get broad advice on anything you were struggling with, and to keep up with relevant news and German culture, which the Germans were so excited to share. There were so many there that were generous with their time and knowledge; I can only name a few here. Jakob Lingg was down for anything, whether it was offering advice on data work up, or summiting a mountain together in the German Alps. Sarah Glasl patiently taught me how to successfully perform experiments with mice and added so much spirit to our imaging sessions. Shyam Ramakrishnan was always just a phone call away from the imaging suite, ready to offer technical help. Martin Warmer never failed to find a more convenient solution to a logistical question, and went out of his way help you solve it. Talking though experiment plans and results or going out of her way to research mouse models and provide advice, Mara Saccomano was always there to help. Thomas Bischof introduced me to the best restaurants and beer in Munich, and the most affordable place to play golf. Doing experiments with Bernardo Arús and making such rapid progress was one of the most exhilarating experiences I have had in the lab. I will always be grateful for those moments and the conversations we had over “shrimps.” Jian Cui, while leading his own group, has been a consistent source of life advice and encouragement. The experiences I had in Munich were formative and I appreciate everyone who made that possible.

Before graduate school, my research experiences in the Fantini lab at Dension University and with Eric Wall at Cincinnati Children's Hospital Medical Center were so formative for inspiring my scientific career. So many of my Denison professors, classmates and labmates supported me in my educational journey to grad school, to name a few, Joe Reczek, Alex Sterdjevich, Casey Cempre, Ian Delahunty, Riley Secrest, Ariana Gray Bé and Kyle Vesper. Kyle, you were such a wise, joyful, and supportive friend and colleague. I miss you so much and I will never forget the light you shone in this world. I couldn't imagine going through life without the incredible friendships I gained from my time at Denison with Luchen Peng, Abby Chua, Megan Worden, Emily Marguerite, Sarah Hunter, Ankita Henry and Emily Dean. Emily Dean, you are a constant source of encouragement and inspiration, thank you for sharing so much of your life with me.

I am forever grateful for the people turned LA into my home over the past five years. I was so lucky to come home every day for the first half of grad school to a wonderful roommate, Khalela Hatchett. I appreciate her encouragement to sleep more as well as showing me all the best dessert places in LA. Jordan Dotson was my first friend at UCLA. I doubt I would have lasted through this program without his support. I can't count the amount of times we discussed a mechanism or unexpected synthetic observation at his hood while he was in the middle of running a column. Jordan's intellectual curiosity and is unmatched and I am so lucky to have him in my life. Marcus Jellen never ceased to be a source of adventure. From dragging me into the craziest art exhibits to searching for non-existent hiking trails in the middle of the desert, grad school certainly wouldn't have been the same without his friendship. Together with Jordan, Vince Hipwell, and Trevor Chang, we had many game nights that were rife with all of their antics. I thank Marcus for introducing me to Shima Gholizadeh, the person I didn't know I needed in my life. Shima has

added so much excitement and humor to my time in LA. I also had so many wonderful memories over the years with Alethia Shih and David Gonzalez, it was incredible to be able to cheer each other on in each of our academic pursuits. I was lucky be able to welcome two great friends to LA in the last year, Ariana, and Ellie Geiger. I owe an additional strange and apocalyptic thank you to all of the people that have made 2020 bearable. Ariana, Ellie, Marcus, Shima, and David, thanks for riding out COVID with me.

Finally, last but certainly not least, I never could have dreamed of finishing graduate school without the support of my family throughout my entire education. I am delighted to share a love of imaging, albeit using different wavelengths, with my brother Stephen. I have watched him overcome so many challenges in pursuit of his dream career and am constantly in awe of his creativity and ambition. I have always admired the intelligence and success of my brother Joe and used it as a motivator for my own career. My aunts and uncles and cousins happily dealt with me showing off my latest imaging video, and offered curiosity and support. I owe so much of my success in life thus far to my parents who ensured I had the best education possible, even if that meant teaching me yourselves at some points. From my mom, I learned to think about a problem from all angles and that there are always creative solutions. This thinking has shaped how I tackle challenges in science and something I will keep building on throughout life. From my dad, I learned how to focus on developing a skill and how to push through challenges. The dedication that I discovered early on from him has been essential for my educational success. To both of my parents, thank you for coming around after I told you I was moving across the country for grad school, even though you hoped I wouldn't move so far away. Your support has been a lifeline, I love you. I hope I have not left anyone out in this narrative. For all who have aided me in this endeavor, I am and will be forever grateful.

Chapter One is an unpublished perspective written by Cosco.

Chapter Two is a version of Cosco, E. D.; Caram, J. R.; Bruns, O. T.; Franke, D.; Day, R. A.; Farr, E. P.; Bawendi, M. G.; Sletten, E. M. Flavylium Polymethine Fluorophores for Near- and Shortwave Infrared Imaging. *Angew. Chem. Int. Ed.* **2017**, *56*, 13126–13129. Cosco, Caram, Bruns, Franke, Day, and Farr contributed to experimental work. Sletten and Cosco contributed to writing.

Chapter Three is a version of Cosco, E. D.; Spearman, A. L.; Ramakrishnan, S.; Lingg, J. G. P.; Saccomano, M.; Pengshung, M.; Arús, B. A.; Wong, K. C. Y.; Glasl, S.; Ntziachristos, V.; Warmer, M. McLaughlin, R. R.; Bruns, O. T.; Sletten, E. M. Shortwave Infrared Polymethine Fluorophores Matched to Excitation Lasers Enable Non-Invasive, Multicolour in Vivo Imaging in Real Time. *Nat. Chem.* **2020**, *12*, 1123–1130. Cosco, Spearman, Ramakrishnan, Lingg, Saccomano, Pengshung, Arús, Wong, Glasl, Warmer and McLaughlin contributed to experimental work. Cosco, Sletten and Bruns contributed to writing.

Chatper Four is a version of a submitted manuscript, Cosco, E. D.; Arús, B. A.; Spearman, A. L.; Atallah, T. L.; Leland, O. S.; Caram, J. R.; Bischof, T. S.; Bruns, O. T.; Sletten, E. M. Bright chromenylium polymethine dyes enable fast, four-color in vivo imaging with shortwave infrared detection. Cosco, Arús, Spearman, Atallah, Leland, Caram, and Bischof contributed to experimental work. Cosco, Sletten, Bruns, Arús, and Bischof contributed to writing.

Chapter Five is unpublished studies with authors Cosco, E. D.; Leland, O. S.; Zhang, Z. All authors contributed to experimental work. Cosco is responsible for writing.

Chapter Six is a version of Chen, W.#; Cheng, C. -A.#; Cosco, E. D.#; Ramakrishnan, S.; Lingg, J. G. P.; Bruns, O. T.; Zink, J. I.; Sletten, E. M. Shortwave infrared imaging with J-aggregates stabilized in hollow mesoporous silica nanoparticles. *J. Am. Chem. Soc.* **2019**, *141*,

12475–12480. Chen, Cheng, Cosco, Ramakrishnan, and Lingg contributed to experimental work. Sletten, Cosco and Zink contributed to writing.

Chapter Seven is a version of an unpublished manuscript, Cosco, E. D.; Lim, I.; Sletten, E. M. Photophysical properties of indocyanine green in the shortwave infrared region. Cosco and Lim contributed to experimental work. Cosco, Sletten and Lim contributed to writing.

Throughout these studies, I was supported by the NSF GRFP and the Christopher S. Foote Fellowship. Additional funding sources for the work described herein include UCLA, Helmholtz Pioneer Campus Institute for Biomedical Engineering, Emmy-Noether- Programm of DFG, Sloan Research Award, NIH NIBIB, MIT- Harvard Center for Excitonics EFRC, Laser Biomedical Research Center, NSF MRI, Boehringer Ingelheim Fonds, Zink student research fund, and instrumentation grants from the NSF and the NIH

BIOGRAPHICAL SKETCH

Education:
University of California, Los Angeles, Los Angeles, CA
MS in Chemistry, 2017

Denison University, Granville, Ohio
BS in Chemistry with Honors, *magna cum laude*, 2015
Thesis title: 2,2'-Linked sulfonated dicalix[4]arene as a component in a supramolecular species
Thesis advisor: Jordan L. Fantini

Professional and Academic Experience:
Graduate Research Assistant
University of California, Los Angeles, Department of Chemistry and Biochemistry, 2015–2020
Advisor: Prof. Ellen M. Sletten
- Design and synthesis of polymethine fluorophores for *in vivo* shortwave infrared imaging.
- Investigation of structure-property relationships by photophysical characterization.

Visiting Scientist
Helmholtz Pioneer Campus, Helmholtz Zentrum München, 5 months over Fall 2018–Winter 2020
Advisor: Dr. Oliver T. Bruns
- Multiplexed shortwave infrared imaging in mice with polymethine fluorophores.

Undergraduate Research Assistant
Denison University, Department of Chemistry and Biochemistry, 2013–2015
Advisor: Prof. Jordan L. Fantini
- Synthesis of a p-sulfonatodicalix[4]arene and investigation of its host-guest interactions.

Research Assistant
Cincinnati Children's Hospital Medical Center, Division of Orthopaedic Surgery, 2012
Advisor: Dr. Eric J. Wall
- Conducted a retrospective case-controlled radiographic study of nursemaid's elbows.

Honors and Awards:
Theodore A. Geissman Dissertation Award, 2020
Dafni Amirsakis Fellowship Award, 2019
Greater Los Angeles "GALA" of Chemical Biology Poster Award, 2019
Senior Foote Graduate Fellowship, 2018
Excellence in Second Year Academics and Research Award, 2018
NSF Graduate Research Fellowship, 2017
UCLA ACS Research Showcase Fellowship Award, 2017, 2019
UCLA Seaborg Symposium Poster Award, 2016
UCLA Alumni Association Fellowship, 2015
ACS Organic Division Undergraduate Award, 2015
Anderson Summer Research Fellowship, 2014

Publications:

7. Cosco, E. D.; Lim, I.; Sletten, E. M. Photophysical properties of indocyanine green in the shortwave infrared region. *(In preparation)*

6. Friedman, H. C.; Cosco, E. D.; Atallah, T. L.; Sletten, E. M.; Caram, J. R. Design principles for brightly emissive organic SWIR emitters. *(Submitted)*

5. Cosco, E. D.; Arús, B. A.; Spearman, A. L.; Atallah, T. L.; Leland, O. S.; Caram, J. R.; Bischof, T. S.; Bruns, O. T.; Sletten, E. M. Bright chromenylium polymethine dyes enable fast, four-color in vivo imaging with shortwave infrared detection. *(Submitted)*

4. Cosco, E. D.; Spearman, A. L.; Ramakrishnan, S.; Lingg, J. G. P.; Saccomano, M.; Pengshung, M.; Arús, B. A.; Wong, K. C. Y.; Glasl, S.; Ntziachristos, V.; Warmer, M. McLaughlin, R. R.; Bruns, O. T.; Sletten, E. M. Shortwave Infrared Polymethine Fluorophores Matched to Excitation Lasers Enable Non-Invasive, Multicolour in Vivo Imaging in Real Time. *Nat. Chem.* **2020**, *12*, 1123–1130.

3. Chen, W.#; Cheng, C. -A.#; Cosco, E. D.#; Ramakrishnan, S.; Lingg, J. G. P.; Bruns, O. T.; Zink, J. I.; Sletten, E. M. Shortwave infrared imaging with J-aggregates stabilized in hollow mesoporous silica nanoparticles. *J. Am. Chem. Soc.* **2019**, *141*, 12475–12480.

2. Cosco, E. D.; Caram, J. R.; Bruns, O. T.; Franke, D.; Day, R. A.; Farr, E. P.; Bawendi, M. G.; Sletten, E. M. Flavylium Polymethine Fluorophores for Near- and Shortwave Infrared Imaging. *Angew. Chem. Int. Ed.* **2017**, *56*, 13126–13129.

1. Eismann E. A.; Cosco E. D.; Wall E. J. Absence of Radiographic Abnormalities in Nursemaid's Elbows. *J. Pediatr. Orthop*. **2014**, *34,* 426–431.

CHAPTER ONE

Polymethine Dyes in Shortwave Infrared Optical Imaging, from the Flask to the Clinic

1.1 Perspective

Optical imaging is a sensitive, low cost, non-invasive, and safe imaging modality that is widely used for clinical diagnosis and for studying physiology and pathophysiology.[1] Currently, optical detection in these contexts has been constrained to the narrow range of wavelengths compatible with imaging in living tissue, as well as the limited depth penetration and resolution that is available using visible (350–700 nm) and near-infrared (NIR, 700–1,000 nm) light. Deep tissue optical imaging techniques, including multiphoton methods,[2] which use long wavelength excitation sources, and shortwave infrared (SWIR, 1,000–2,000 nm, also called NIR-II) imaging,[3] which relies on a long wavelength detection region, advertise improvement in depth penetration, resolution, contrast, and reduction in background autofluorescence compared to traditional visible or NIR optical imaging. A combination of properties governs the interaction between tissue and different wavelengths of light. In the case of SWIR detection, the improved contrast and resolution observed is a result of decreased scattering coefficients,[4–6] fewer endogenous chromophores which can absorb and emit light at these wavelengths,[7–8] and increased water absorption that preferentially attenuates scattered light.[9] Additionally, adding the wavelengths at which current InGaAs detectors[10] are sensitive (~950–1,700 nm) to those in the NIR, accessed using silicon-based detectors,[11] more than triples the wavelength region that can be utilized for deep tissue imaging, facilitating multiplexed experiments. These combined properties manifest in an optical imaging technique which could render improvement in the

amount, quality and specificity of optical information available to clinicians in diagnosing and treating disease, including in resection and preservation of tissues during planning, procedures, and post-operative assessments. Likewise, non-invasive longitudinal experiments become readily accessible to scientists studying disease in model organisms, greatly increasing the amount of information that can be gained from a single animal. For these aims to be realized, suitable label-free or contrast-based fluorescence tools, and appropriate imaging technologies are needed.

Initiated by the first report of *in vivo* SWIR imaging using carbon nanotubes,[12] there has been a great deal of effort devoted to developing and optimizing contrast agents that can be used for SWIR experiments. For the first several years, these studies were focused primarily on carbon nanotubes,[13] quantum dots,[8,14], and rare-earth metal-based materials.[15–16] More recently, organic molecules and materials have taken up some of the spotlight in the field on the platform of biocompatibility, relatively small sizes, and simple bioconjugation approaches. Beginning in 2016, benzo-bis-thiadiazole acceptor-based donor-acceptor-donor (DAD) dyes[17] have been optimized for brightness[18–19] solubility, nanomaterial encapsulation[20–21] and protein binding,[22] and used in a variety of SWIR imaging applications as bioconjugates for imaging ovarian,[23–24] brain,[25] and tumor tissues.[20,26–27] Concurrently, polymethine dyes, charged fluorophores composed of two terminal group heterocycles linked by a polymethine backbone, were introduced to shortwave infrared imaging with the laser dye, IR-1061, as a component of layer-by-layer assemblies[28] or in lipid based micelles.[29–30] In 2017, we reported a polymethine dye designed for SWIR imaging (named Flav7) which demonstrated improved brightness compared to classical long wavelength laser dyes like IR-1061 and IR-26.[31] Since this time, there has been increased focus in the optimization of polymethine fluorophores for SWIR imaging applications.

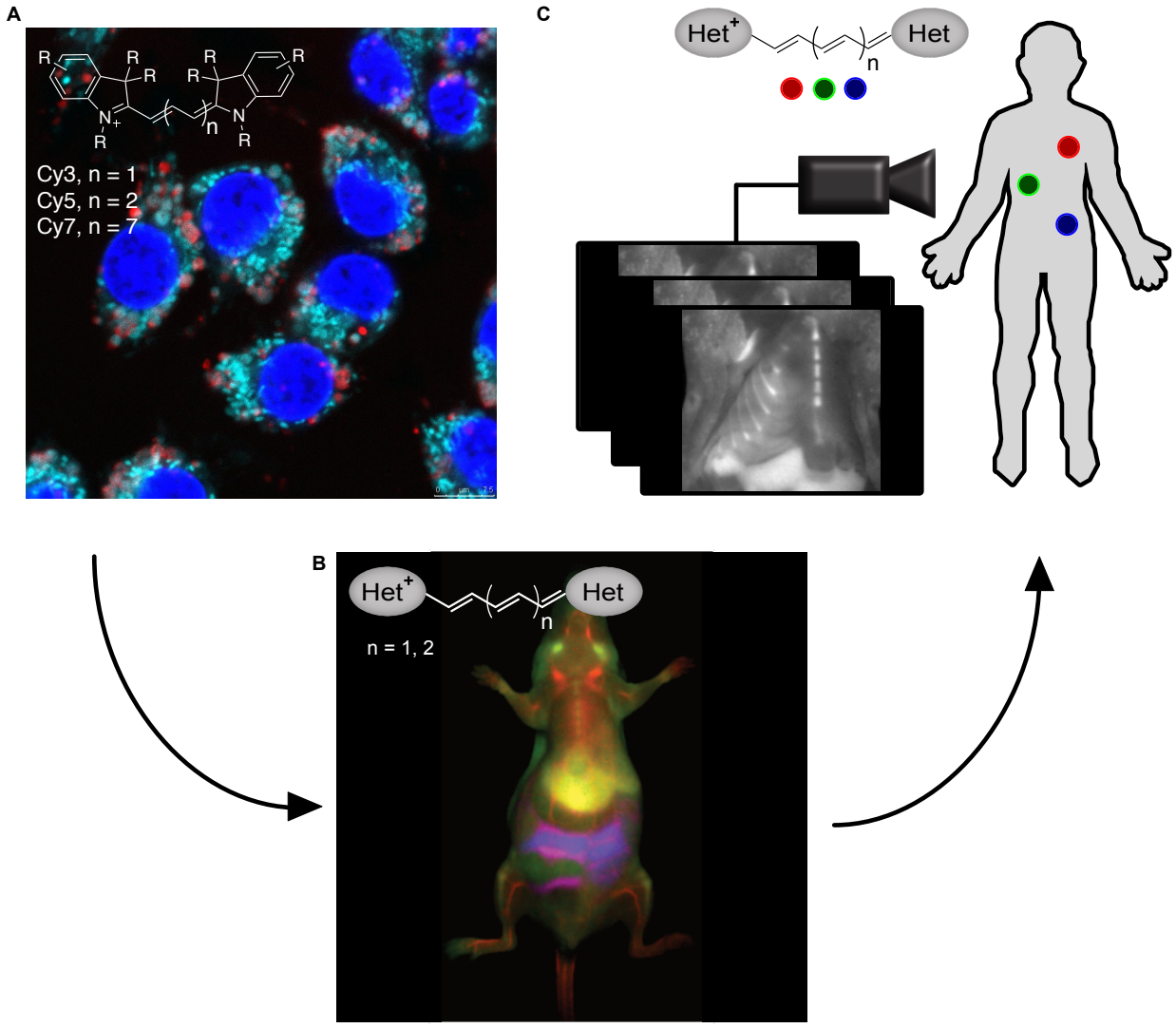

Figure 1.1 Polymethine dyes applied as contrast agents in mammalian cells (A), in mice (B), and in humans (C). Microscopy image in (A) of RAW264.7 cells by Rachael Day. SWIR image in 4-colors of a living mouse in (B), with Bernardo Arús. SWIR image of the thorax in a mouse necropsy in (C), with Irene Lim.

Polymethine dyes encompass a diverse class of chromophores, widely studied since their initial discovery in 1857.[32] Early applications as photographic sensitizers[33] fueled development of the molecule class and preceded use in lasing,[34] all optical switching,[35] and in dye sensitized solar cells[36]. In biology, polymethine dyes have been a staple in optical microscopy, flow cytometry, and microarray[37] experiments. Most classically, applications are

with the nitrogen-containing indoleninium heterocycle-based "Cy" dyes, developed for biological use in the 1990s (Figure 1.1A).[38] Electronically symmetric polymethine dyes are characterized by their high absorption coefficients (ε), narrow absorption and emission bands, and small Stokes shifts, and typically display moderate fluorescence quantum yields (Φ_F).[39] While all of these qualities are favorable for experiments relying on fluorescence detection, the early success of polymethine dyes in cell biology, proteomics, immunological studies, and nucleotide labelling was largely due to the wide and facile photophysical tunability of the scaffold.[40] Course tuning of the $\lambda_{max,abs}$ can be achieved by adjusting the number of methine units in the polymethine chain, i.e. Cy3, Cy5, Cy7, which represent dyes with 3, 5, and 7 methine units, respectively, and result in ~100 nm red shift per two methine extension. Congruently, the heterocycle identity and functional group substitution allowed for a finer tuning of the $\lambda_{max,abs}$. These properties were ideal for obtaining probes with orthogonal excitation and emission wavelengths for multicolor experiments. Thus, along with optimization of solubility and bioconjugation handles, probes which were closely matched to laser wavelengths and filter sets in commercial microscopes and flow cytometers were developed and became widely available.[40] The tunability of the polymethine scaffold also provides an ideal platform for chemosensors based on non-covalent or covalent chemistries which can alter the absorption and emission wavelengths and/or brightness of the chromophore. Probes based on the cyanine scaffold have afforded a wide array of responsive probes for ions, pH, biological signaling molecules, and enzyme activity.[41]

Polymethine dyes have also been a workhorse of *in vivo* optical imaging in humans and in preclinical model organisms (Figure 1.1B-C). Indocyanine green (ICG), a benzo[e]indoleninium based polymethine dye with absorption and emission in the NIR, has been FDA approved since 1956.[42] With clinical and pre-clinical uses including angiography,[43] lymphatic,[44]

biliary[45] and intestinal[46] imaging, ICG is one of two contrast agents for optical imaging used in the clinic (the other being methylene blue). In addition to clinical trials for a multitude of expanded uses of ICG, related conjugatable probes including IRDye800 and ZW800-1[47] conjugates are in trials for oncological image guided surgery.[48] The translation of responsive probes which can increase sensitivity is also imminent.[49] These advances in molecular targeted probes are complemented by the development of advanced optical and robotic devices to further assist clinicians in identifying healthy vs diseased tissue.[50]

While there is substantial momentum centered around intraoperative guidance using fluorescence based molecular imaging, some of the key advantages of polymethine dyes which are highlighted in optical microscopy experiments, particularly their ability to provide opportunities for multiplexing, lag further behind in their applications *in vivo*. In comes the SWIR, and with it, the broadened region of the electromagnetic spectrum which is compatible with deep tissue imaging. In parallel to the use of Cy dyes in multicolor experiments in the visible and NIR regions, long wavelength polymethine dyes can now enable advanced multicolor experiments with NIR and SWIR excitation wavelengths.[51] Further, with longer wavelength detection, advantages in resolution and imaging depth can also be capitalized on. For many of the same reasons that the Cy dyes are successful in the visible and NIR regions, we envision that long wavelength polymethine dyes will thrive in SWIR applications. High absorption coefficients, narrow absorption profiles, and structural tunability conferred on the visible and NIR cyanine dyes are also present in their long-wavelength counterparts. A few additional challenges apply to longer wavelength dyes, including arriving at molecules which are chemically stable, photostable, and bright enough for real-time detection, as all three of these properties trend downward with more red-shifted dyes.[52] Further obstacles for SWIR dyes include obtaining fully aqueous soluble or non-aggregating

species on a large and hydrophobic chromophore scaffold. In only few years, a range of polymethine chromophores, including those with flavylium,[31,51,53] thioflavylium,[54] pyrylium,[55] thiopyrylium,[55] benzo[c,d]indoleninium[56–58] bis-indole,[59] and chromenylium,[60] heterocycles have been explored for use in SWIR imaging (Figure 1.2). Within these studies, substantial progress has already been made towards improving essential properties for imaging, namely, (1) tuning photophysics to increase Φ_F values and to obtain excitation wavelengths of interests and (2) enabling efficient delivery in aqueous environments, targeting to locations of interest, and selective responses to particular biological molecules, cells, or tissues.

One of the initial challenges of using small molecule chromophores for SWIR imaging is obtaining dyes with high brightness such that images can be detected with high signal to noise ratios (SNR) with exposure times in a macroscopic biological time scale. The Φ_F of fluorophores decreases drastically for fluorophores with $\lambda_{max,abs}$ past ~900 nm, due to decreased radiative rates related to the small singlet energy gaps, and increased nonradiative decay correlated with high frequency vibrations.[61] These energy gap laws provide a substantial challenge in obtaining molecular structures with absorption maxima >1,000 nm with quantum yields higher than ~3%. Progress on this goal began with the development of Flav7 (Φ_F ~0.6% (DCM)) with conceptual modifications from the laser dye IR-26 (Φ_F ~0.05% (DCM)). Further quantum yield improvements include those obtained using chromenylium dyes (Chrom7, Φ_F ~1.7%(DCM)) and bis-indole dyes, (LZ-1105, Φ_F ~3% (EtOH)), such that video-rate imaging (~25-30 fps) imaging is attainable and experiments can even be performed at up to 300 fps.[60] Quantum yield numbers, however, only tell part of the story. Due to the drastic impacts of energy gap laws, a more relevant comparison of chromophores from a physical chemistry perspective takes these effects into account, and compares quantum yield values in a wavelength independent manor, with an energy-gap

independent improvement factor (ξ).[61] Additionally, as brightness is reliant on both emissive properties in the relevant detection region and absorptive properties at the wavelength of excitation (λ) (brightness = $\varepsilon_\lambda \times \Phi_F \times \alpha$), absorption coefficients and the % emission within the SWIR region (α = % emission within the SWIR) are also essential parameters that have been relatively less explored.

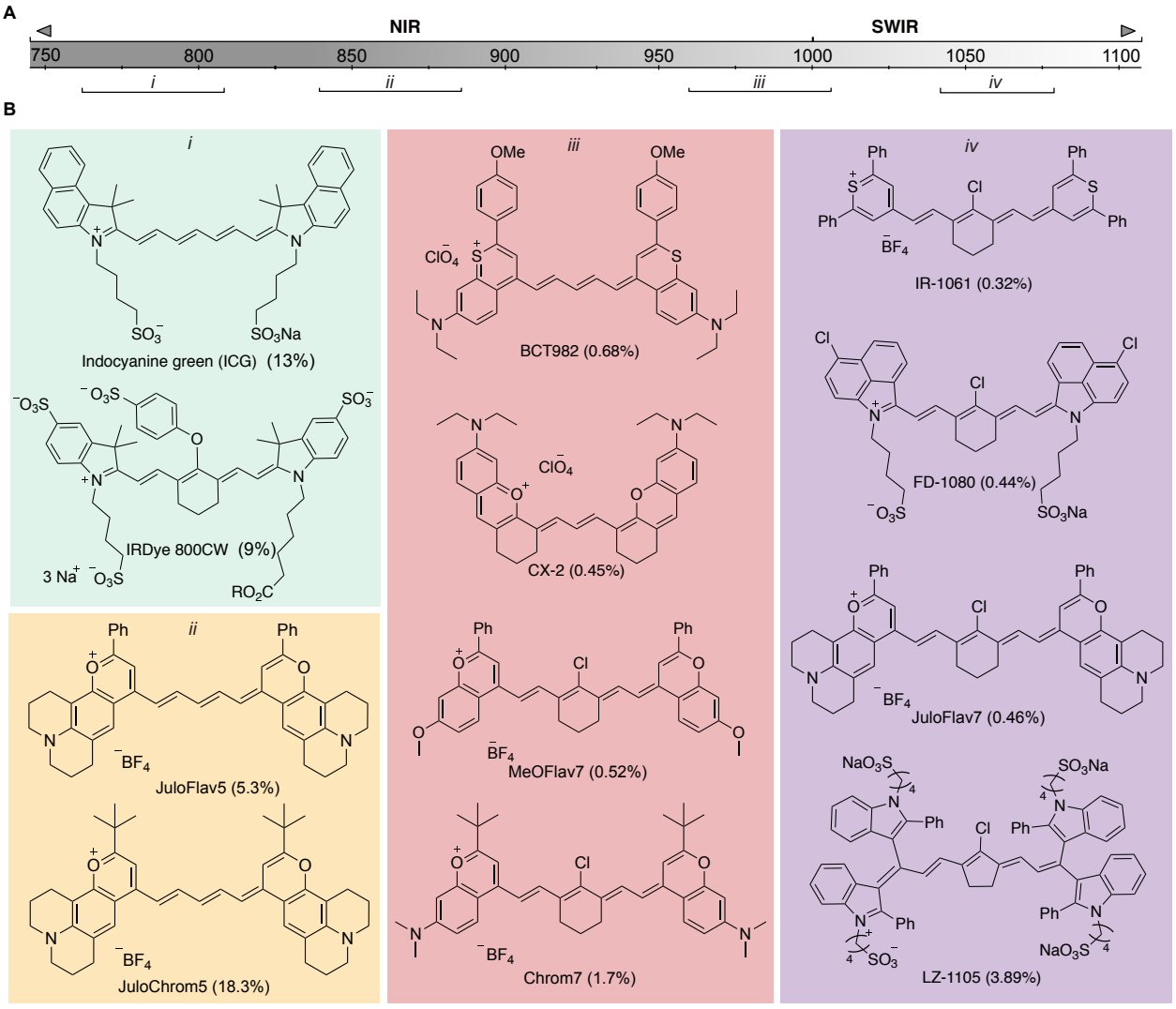

Figure 1.2 Electromagnetic (EM) spectrum (A) and selected polymethine chromophores (B) used for SWIR imaging experiments and excitable in regions of the EM spectrum *i–iv*. Quantum yield values are provided in parenthesis.

Fortunately, the relationship between brightness of chromophores and the percent of emission lying within the SWIR region is aligned well with the energy gap laws, allowing for more blue shifted chromophores to have similar or brighter SWIR emission than their long wavelength counterparts. Indeed, ICG, and other NIR polymethine dyes can be visualized as bright contrast agents using SWIR detection, due to a long wavelength emissive tail extending past 1,000 nm.[62–64] These properties allow for relatively brightness-matched chromophores in multiplexed experiments, and suggest a classification in which chromophores can be categorized. Similar to filter cubes used in optical microscopes, where the fluorescent labels used in an experiment are chosen and optimized around the cubes available, SWIR emissive chromophores can be classified according to the closest available excitation wavelength, and their properties can be optimized comparing to others corresponding to the same excitation laser. Thus, the ability to finely tune $\lambda_{max,abs}$ wavelengths to maximize brightness as well as minimize cross-talk between channels becomes increasingly crucial. Again, this is a strength of polymethine dyes, and can be obtained by relying on complementary modifications to the heterocycle,[51] and polymethine chain.[65] Further, dyes with suitably overlapping absorption and emission wavelengths can be used to develop more complex energy transfer tools, such as in Förster resonance energy transfer (FRET)[53] and bioluminescence energy transfer (BRET)[66] experiments. With the tools of physical chemistry,[61] physical organic chemistry,[51] and theory and computation,[67–68] the relationships between structure and photophysical properties can be deciphered and used to create predictive metrics for the design of chromophores with improved properties tailored to their application.

Complementary to tuning the monomer photophysical properties of polymethine dyes, there are also promising J-aggregation properties of polymethine dyes which could be leveraged

to reach longer excitation wavelengths.[69–71] J-aggregation, first describe by Jelley[72] and Sheibe[73] in the 1930s, is the coherent coupling of excited state transition dipoles, induced by a slip-stacked alignment of monomer units.[74] While the properties of J-aggregates, namely increased absorption coefficients, increased radiative rates, and red-shifted absorption properties are promising for imaging applications, a more thorough understanding of these properties in relationship with dye structure are needed. Additionally, J-aggregates have been only minimally applied to biological imaging experiments due to their high reliance on their immediate solvent environment to remain in an aggregated form.[74] Thus, robust methods to stabilize J-aggregates in complex environments are necessary for more widespread use and exploration in imaging experiments.

Long wavelength polymethine dyes, many of which are derived from structures developed for use in laser dyes, typically have a large, planar, and hydrophobic core, making their use in aqueous environments challenging. Thus, many studies have relied on nanoparticles encapsulation to deliver the hydrophobic molecules to biology. While an effective strategy that benefits from the protection of nanomaterials to reactive biomolecules and increased avidity of targeting groups, many dyes also display H-aggregation in lipophilic environments, which hinders the optimal photophysical properties from being transferred from the flask.[31] Further, the large nanoparticle size limits the biomolecules which could be labelled without compromising their function. The strategic placement of water solubilizing groups has shown success in enabling the delivery of free-small molecule dyes.[60] An alternate strategy leverages non-covalent protein binding properties to complex and deliver the fluorophores *in vivo*.[57] Conjugation to targeting agents including, peptides,[55,75] small-molecules, and antibodies,[77–78] or to synthetic polymers[79] or polymeric biomolecules[80] can also assist in the solubilization and delivery of these probes.

Regardless, it's likely that further optimization of the solubilizing groups will be necessary to obtain optimal photophysical properties.[81] Additionally, polymethines have already begun to be developed for responsive probes, for pH,[54,82] signaling molecules such as hydrogensulfide,[83] and peroxynitrite,[53,84] glutathione,[80] and ATP,[66,83] and enzyme activity, such as for nitroreductatse[85–86] Further improvements on these aims to increase sensitivity and selectivity, as well as expansion to other disease-relevant triggers position the strategies to have increasing impact in the non-invasive and longitudinal monitoring of disease state and progression.

The extent in which SWIR imaging will impact clinical practice will be seen in the coming years. Key questions are whether the improvement in contrast and penetration depth can appreciably improve the clinical results that can be achieved, and which clinical applications are the most suitable for SWIR detection. For these questions to be answered, imaging tools and methods that are optimized to study a specific application are needed. In some applications, contrast-free methods show a great deal of promise, and offer a relatively straightforward path to clinical use, without the need for approval of a contrast agent.[87–88] However, these techniques are limited to the inherent absorption and/or fluorescence of naturally occurring molecules and tissues. Exogenous tags, or contrast agents, offer the opportunity to label a healthy or diseased tissue, cell type, or biomolecule of choice such that theoretically any target of interest can be visualized selectively. Investigating SWIR applications of ICG and other NIR dyes which are currently in clinical trials is also a lower barrier entry point to clinical impact.[89] With only these tools, however, experiments in which multiple cell types or tissues can be orthogonally labelled is more challenging. The exploration of structurally distinct polymethine fluorophores with longer wavelength absorption offers increasing flexibility in producing orthogonal, multicolor signals using well-separated excitation sources, as well as in complex experiments using energy transfer

and responsive probes. Research aims that prioritize a greater understanding of structure property relationships, through the combination of experiment and theory/computation across fluorophore scaffolds will enable predictive measures and accelerate improvement in the desired properties for imaging. Further, investigation of the molecular interactions with biomolecules, cells and tissues will drive the discovery of highly specific probes for selective biological labelling. Altogether, along with the development of relevant imaging tools, including advanced microscopes and endoscopes, polymethine dyes in the SWIR will offer scientists and clinicians a wide range of selective and sensitive orthogonal labels for studying disease longitudinally and non-invasively in model organisms and for safe and low-cost diagnostic and intraoperative tools useful in clinical practice.

1.2 References and Notes

[1] Frangioni, J. V. In Vivo Near-Infrared Fluorescence Imaging. *Curr. Opin. Chem. Biol.* **2003**, *7*, 626–634.

[2] Helmchen, F.; Denk, W. Deep Tissue Two-Photon Microscopy. *Nat. Methods* **2005**, *2*, 932–940.

[3] Smith, A. M.; Mancini, M. C.; Nie, S.; Smith, M.; Mancini, M. C. Bioimaging: Second Window for in Vivo Imaging. *Nat. Nanotechnol.* **2009**, *4*, 710–711.

[4] Lim, Y. T.; Kim, S.; Nakayama, A.; Stott, N. E.; Bawendi, M. G.; Frangioni, J. V. Selection of Quantum Dot Wavelengths for Biomedical Assays and Imaging. *Mol. Imaging* **2003**, *2*, 50–64.

[5] Bashkatov, A. N.; Genina, E. A.; Kochubey, V. I.; Tuchin, V. V. Optical Properties of Human Skin, Subcutaneous and Mucous Tissues in the Wavelength Range from 400 to 2000 nm. *J. Phys. D. Appl. Phys.* **2005**, *38*, 2543–2555.

[6] Zhang, H.; Salo, D.; Kim, D. M.; Komarov, S.; Tai, Y.; Berezin, M. Y. Penetration Depth of Photons in Biological Tissues from Hyperspectral Imaging in Shortwave Infrared in Transmission and Reflection Geometries. *J. Biomed. Opt.* **2016**, *21*, 126006.

[7] Diao, S.; Hong, G.; Antaris, A. L.; Blackburn, J. L.; Cheng, K.; Cheng, Z.; Dai, H. Biological Imaging without Autofluorescence in the Second Near-Infrared Region. *Nano Res.* **2015**, *8*, 3027–3034.

[8] Del Rosal, B.; Villa, I.; Jaque, D.; Sanz-Rodríguez, F. In Vivo Autofluorescence in the Biological Windows: The Role of Pigmentation. *J. Biophotonics* **2016**, *9* (10), 1059–1067.

[9] Bruns, O. T.; Bischof, T. S.; Harris, D. K.; Franke, D.; Shi, Y.; Riedemann, L.; Bartelt, A.; Jaworski, F. B.; Carr, J. A.; Rowlands, C. J.; et al. Next-Generation in Vivo Optical Imaging with Short-Wave Infrared Quantum Dots. *Nat. Biomed. Eng.* **2017**, *1*, 0056.

[10] Hansen, M. P.; Malchow, D. S. Overview of SWIR Detectors, Cameras, and Applications. In *Thermosense XXX*; Vavilov, V. P., Burleigh, D. D., Eds.; 2008; Vol. 6939, p 69390I.

[11] Mangold, K.; Shaw, J. A.; Vollmer, M. The Physics of Near-Infrared Photography. *Eur. J. Phys.* **2013**, *34*, S51–S71.

[12] Welsher, K.; Liu, Z.; Sherlock, S. P.; Robinson, J. T.; Chen, Z.; Daranciang, D.; Dai, H. A Route to Brightly Fluorescent Carbon Nanotubes for Near-Infrared Imaging in Mice. *Nat. Nanotechnol.* **2009**, *4*, 773–780.

[13] Diao, S.; Blackburn, J. L.; Hong, G.; Antaris, A. L.; Chang, J.; Wu, J. Z.; Zhang, B.; Cheng, K.; Kuo, C. J.; Dai, H. Fluorescence Imaging In Vivo at Wavelengths beyond 1500 nm. *Angew. Chem. Int. Ed.* **2015**, *54*, 14758–14762.

[14] Hong, G.; Robinson, J. T.; Zhang, Y.; Diao, S.; Antaris, A. L.; Wang, Q.; Dai, H. In Vivo Fluorescence Imaging with Ag2S Quantum Dots in the Second Near-Infrared Region. *Angew. Chem. Int. Ed.* **2012**, *51*, 9818–9821.

[15] Chen, G.; Ohulchanskyy, T. Y.; Liu, S.; Law, W. C.; Wu, F.; Swihart, M. T.; Ågren, H.; Prasad, P. N. Core/Shell NaGdF 4:Nd 3+/NaGdF 4 Nanocrystals with Efficient near-Infrared to near-Infrared Downconversion Photoluminescence for Bioimaging Applications. *ACS Nano* **2012**, *6*, 2969–2977.

[16] Naczynski, D. J.; Tan, M. C.; Zevon, M.; Wall, B.; Kohl, J.; Kulesa, A.; Chen, S.; Roth, C. M.; Riman, R. E.; Moghe, P. V. Rare-earth-doped biological composites as *in vivo* shortwave infrared reporters. *Nat. Commun.* **2013**, *4*, 2199.

[17] Antaris, A. L.; Chen, H.; Cheng, K.; Sun, Y.; Hong, G.; Qu, C.; Diao, S.; Deng, Z.; Hu, X.; Zhang, B.; et al. A Small-Molecule Dye for NIR-II Imaging. *Nat. Mater.* **2016**, *15*, 235–242.

[18] Yang, Q.; Ma, Z.; Wang, H.; Zhou, B.; Zhu, S.; Zhong, Y.; Wang, J.; Wan, H.; Antaris, A.; Ma, R.; et al. Rational Design of Molecular Fluorophores for Biological Imaging in the NIR-II Window. *Adv. Mater.* **2017**, *29*, 1605497.

[19] Yang, Q.; Hu, Z.; Zhu, S.; Ma, R.; Ma, H.; Ma, Z.; Wan, H.; Zhu, T.; Jiang, Z.; Liu, W.; et al. Donor Engineering for NIR-II Molecular Fluorophores with Enhanced Fluorescent Performance. *J. Am. Chem. Soc.* **2018**, *140*, 1715–1724.

[20] Wan, H.; Yue, J.; Zhu, S.; Uno, T.; Zhang, X.; Yang, Q.; Yu, K.; Hong, G.; Wang, J.; Li, L.; et al. A Bright Organic NIR-II Nanofluorophore for Three-Dimensional Imaging into Biological Tissues. *Nat. Commun.* **2018**, *9*, 1171.

[21] Xiao, F.; Lin, L.; Chao, Z.; Shao, C.; Chen, Z.; Wei, Z.; Lu, J.; Huang, Y.; Li, L.; Liu, Q.; et al. Organic Spherical Nucleic Acids Facilitate NIR-II Emitting Dye to Cross Blood-Brain Barrier. *Angew. Chem. Int. Ed.* **2020**, *518055*, 2–11.

[22] Antaris, A. L.; Chen, H.; Diao, S.; Ma, Z.; Zhang, Z.; Zhu, S.; Wang, J.; Lozano, A. X.; Fan, Q.; Chew, L.; et al. A High Quantum Yield Molecule-Protein Complex Fluorophore for near-Infrared II Imaging. *Nat. Commun.* **2017**, *8*, 15269.

[23] Feng, Y.; Zhu, S.; Antaris, A. L.; Chen, H.; Xiao, Y.; Lu, X.; Jiang, L.; Diao, S.; Yu, K.; Wang, Y.; et al. Live Imaging of Follicle Stimulating Hormone Receptors in Gonads and Bones Using near Infrared II Fluorophore. *Chem. Sci.* **2017**, *8*, 3703–3711.

[24] Zhu, S.; Herraiz, S.; Yue, J.; Zhang, M.; Wan, H.; Yang, Q.; Ma, Z.; Wang, Y.; He, J.; Antaris, A. L.; et al. 3D NIR-II Molecular Imaging Distinguishes Targeted Organs with High-Performance NIR-II Bioconjugates. *Adv. Mater.* **2018**, *30*, 1705799.

[25] Zhu, S.; Yang, Q.; Antaris, A. L.; Yue, J.; Ma, Z.; Wang, H.; Huang, W.; Wan, H.; Wang, J.; Diao, S.; et al. Molecular Imaging of Biological Systems with a Clickable Dye in the Broad 800- to 1,700-nm near-Infrared Window. *Proc. Natl. Acad. Sci.* **2017**, *114* (5), 962–967.

[26] Tian, R.; Ma, H.; Yang, Q.; Wan, H.; Zhu, S.; Chandra, S.; Sun, H.; Kiesewetter, D. O.; Niu, G.; Liang, Y.; et al. Rational Design of a Super-Contrast NIR-II Fluorophore Affords High-Performance NIR-II Molecular Imaging Guided Microsurgery. *Chem. Sci.* **2019**, *10*, 326–332.

[27] Wang, W.; Ma, Z.; Zhu, S.; Wan, H.; Yue, J.; Ma, H.; Ma, R.; Yang, Q.; Wang, Z.; Li, Q.; et al. Molecular Cancer Imaging in the Second Near-Infrared Window Using a Renal-Excreted NIR-II Fluorophore-Peptide Probe. *Adv. Mater.* **2018**, *30*, 1800106.

[28] Dang, X.; Gu, L.; Qi, J.; Correa, S.; Zhang, G.; Belcher, A. M.; Hammond, P. T. Layer-by-Layer Assembled Fluorescent Probes in the Second near-Infrared Window for Systemic Delivery and Detection of Ovarian Cancer. *Proc. Natl. Acad. Sci.* **2016**, *113* (19), 5179–5184.

[29] Tao, Z.; Hong, G.; Shinji, C.; Chen, C.; Diao, S.; Antaris, A. L.; Zhang, B.; Zou, Y.; Dai, H. Biological Imaging Using Nanoparticles of Small Organic Molecules with Fluorescence Emission at Wavelengths Longer than 1000 nm. *Angew. Chemie Int. Ed.* **2013**, *52*, 13002–13006.

[30] Kamimura, M.; Takahiro, S.; Yoshida, M.; Hashimoto, Y.; Fukushima, R.; Soga, K. Over-1000 nm near-Infrared Fluorescent Biodegradable Polymer Nanoparticles for Deep Tissue in Vivo Imaging in the Second Biological Window. *Polym. J.* **2017**, 799–803.

[31] Cosco, E. D.; Caram, J. R.; Bruns, O. T.; Franke, D.; Day, R. A.; Farr, E. P.; Bawendi, M. G.; Sletten, E. M. Flavylium Polymethine Fluorophores for Near- and Shortwave Infrared Imaging. *Angew. Chemie Int. Ed.* **2017**, *56*, 13126–13129.

[32] Williams, C. G. XXVI. Researches on Chinoline and Its Homologues. *Trans. - R. Soc. Edinburgh* **1857**, *21*, 377–01.

[33] Hamer, F. M. The Cyanine Dyes. *Q. Rev. Chem. Soc.* **1950**, *4*, 327–355.

[34] Miyazoe, Y.; Maeda, M. Polymethine Dye Lasers. *Opto-electronics* **1970**, *2*, 227–233.

[35] Hales, J. M.; Matichak, J.; Barlow, S.; Ohira, S.; Yesudas, K.; Brédas, J. L.; Perry, J. W.; Marder, S. R. Design of Polymethine Dyes with Large Third-Order Optical Nonlinearities and Loss Figures of Merit. *Science.* **2010**, *327*, 1485–1488.

[36] Mishra, A.; Fischer, M. K. R.; Büuerle, P. Metal-Free Organic Dyes for Dye-Sensitized Solar Cells: From Structure: Property Relationships to Design Rules. *Angew. Chem. Int. Ed.* **2009**, *48*, 2474–2499.

[37] Waggoner, A. Fluorescent Labels for Proteomics and Genomics. *Curr. Opin. Chem. Biol.* **2006**, *10*, 62–66.

[38] Mujumdar, R. B.; Ernst, L. A.; Mujumdar, S. R.; Lewis, C. J. Cyanine Dye Labeling Reagents: Sulfoindocyanine Succinimidyl Esters. *Bioconjug. Chem.* **1993**, *4*, 105–111.

[39] Bricks, J. L.; Kachkovskii, A. D.; Slominskii, Y. L.; Gerasov, A. O.; Popov, S. V. Molecular Design of near Infrared Polymethine Dyes: A Review. *Dye. Pigment.* **2015**, *121*, 238–255.

[40] Waggoner, A. Fluorescent Labels for Proteomics and Genomics. *Curr. Opin. Chem. Biol.* **2006**, *10*, 62–66.

[41] Sun, W.; Guo, S.; Hu, C.; Fan, J.; Peng, X. Recent Development of Chemosensors Based on Cyanine Platforms. *Chem. Rev.* **2016**, *116*, 7768–7817.

[42] Alander, J. T.; Kaartinen, I.; Laakso, A.; Pätilä, T.; Spillmann, T.; Tuchin, V. V.; Venermo, M.; Välisuo, P. A Review of Indocyanine Green Fluorescent Imaging in Surgery. *Int. J. Biomed. Imaging* **2012**, *2012*, 940585.

[43] Tozzi, M.; Boni, L.; Soldini, G.; Franchin, M.; Piffaretti, G. Vascular Fluorescence Imaging Control for Complex Renal Artery Aneurysm Repair Using Laparoscopic Nephrectomy and Autotransplantation. *Case Rep. Transplant.* **2014**, *2014*, 563408.

[44] Rasmussen, J. C.; Fife, C. E.; Sevick-Muraca, E. M. Near-Infrared Fluorescence Lymphatic Imaging in Lymphangiomatosis. *Lymphat. Res. Biol.* **2015**, *13*, 195–201.

[45] Schwarz, C.; Plass, I.; Fitschek, F.; Punzengruber, A.; Mittlböck, M.; Kampf, S.; Asenbaum, U.; Starlinger, P.; Stremitzer, S.; Bodingbauer, M.; et al. The Value of Indocyanine Green Clearance Assessment to Predict Postoperative Liver Dysfunction in Patients Undergoing Liver Resection. *Sci. Rep.* **2019**, *9*, 8421.

[46] Kwon, S.; Sevick-Muraca, E. M. Non-Invasive, Dynamic Imaging of Murine Intestinal Motility. *Neurogastroenterol Motil.* **2011**, *23*, 881-e344.

[47] de Valk, K. S.; Deken, M. M.; Handgraaf, H. J. M.; Bhairosingh, S. S.; Bijlstra, O. D.; van Esdonk, M. J.; Terwisscha van Scheltinga, A. G. T.; Valentijn, A. R. P. M.; March, T. L.; Vuijk, J.; et al. First-in-Human Assessment of CRGD-ZW800-1, a Zwitterionic, Integrin-Targeted, Near-Infrared Fluorescent Peptide in Colon Carcinoma. *Clin. Cancer Res.* **2020**, *26*, 3990–3998.

[48] Information about current clinical trials can be found at: Clinicaltrials.gov

[49] Widen, J. C.; Tholen, M.; Yim, J. J.; Antaris, A.; Casey, K. M.; Rogalla, S.; Klaassen, A.; Sorger, J.; Bogyo, M. AND-Gate Contrast Agents for Enhanced Fluorescence-Guided Surgery. *Nat. Biomed. Eng.* **2020**. https://doi.org/10.1038/s41551-020-00616-6.

[50] Koch, M.; Ntziachristos, V. Advancing Surgical Vision with Fluorescence Imaging. *Annu. Rev. Med.* **2016**, *67*, 153–164.

[51] Cosco, E. D.; Spearman, A. L.; Ramakrishnan, S.; Lingg, J. G. P.; Saccomano, M.; Pengshung, M.; Arús, B. A.; Wong, K. C. Y.; Glasl, S.; Ntziachristos, V.; et al. Shortwave Infrared Polymethine Fluorophores Matched to Excitation Lasers Enable Non-Invasive, Multicolour in Vivo Imaging in Real Time. *Nat. Chem.* **2020**, *12*, 1123–1130.

[52] Thimsen, E.; Sadtler, B.; Berezin, M. Y. Shortwave-Infrared (SWIR) Emitters for Biological Imaging : A Review of Challenges and Opportunities. *Nanophotonics* **2017**, *6*, 1043–1054.

[53] Lei, Z.; Sun, C.; Pei, P.; Wang, S.; Li, D.; Zhang, X.; Zhang, F. Stable, Wavelength-Tunable Fluorescent Dyes in the NIR-II Region for In Vivo High-Contrast Bioimaging and Multiplexed Biosensing. *Angew. Chem. Int. Ed.* **2019**, *58*, 8166–8171.

[54] Wang, S.; Fan, Y.; Li, D.; Sun, C.; Lei, Z.; Lu, L.; Wang, T.; Zhang, F. Anti-Quenching NIR-II Molecular Fluorophores for in Vivo High-Contrast Imaging and pH Sensing. *Nat. Commun.* **2019**, *10*, 1058.

[55] Ding, B.; Xiao, Y.; Zhou, H.; Zhang, X.; Qu, C.; Xu, F.; Deng, Z.; Cheng, Z.; Hong, X. Polymethine Thiopyrylium Fluorophores with Absorption beyond 1000 nm for Biological Imaging in the Second Near-Infrared Subwindow. *J. Med. Chem.* **2019**, *62*, 2049–2059.

[56] Henary, M.; Mojzych, M.; Say, M.; Strekowski, L. Functionalization of Benzo[c,d]Indole System for the Synthesis of Visible and Near-Infrared Dyes. *J. Heterocycl. Chem.* **2009**, *46*, 84–87.

[57] Li, B.; Lu, L.; Zhao, M.; Lei, Z.; Zhang, F. An Efficient 1064 Nm NIR-II Excitation Fluorescent Molecular Dye for Deep-Tissue High-Resolution Dynamic Bioimaging. *Angew. Chem. Int. Ed.* **2018**, *57*, 7483–7487.

[58] Meng, X.; Zhang, J.; Sun, Z.; Zhou, L.; Deng, G.; Li, S.; Li, W.; Gong, P.; Cai, L. Hypoxia-Triggered Single Molecule Probe for High-Contrast NIR II/PA Tumor Imaging and Robust Photothermal Therapy. *Theranostics* **2018**, *8*, 6025–6034.

[59] Li, B.; Zhao, M.; Feng, L.; Dou, C.; Ding, S.; Zhou, G.; Lu, L.; Zhang, H.; Chen, F.; Li, X.; et al. Organic NIR-II Molecule with Long Blood Half-Life for in Vivo Dynamic Vascular Imaging. *Nat. Commun.* **2020**, *11*, 3102.

[60] Cosco, E. D.; Arús, B. A.; Spearman, A. L.; Atallah, T. L.; Leland, O. S.; Caram, J. R.; Bischof, T. S.; Bruns, O. T.; Sletten. E. M. Bright chromenylium polymethine dyes enable fast, four-color in vivo imaging with shortwave infrared detection. *(Submitted)*

[61] Friedman, H.C.; Cosco, E. D.; Atallah, T. L.; Sletten, E. M., Caram, J. R. Design principles for brightly emissive organic SWIR emitters. *(Submitted)*

[62] Carr, J. A.; Franke, D.; Caram, J. R.; Perkinson, C. F.; Saif, M.; Askoxylakis, V.; Datta, M.; Fukumura, D.; Jain, R. K.; Bawendi, M. G.; et al. Shortwave Infrared Fluorescence Imaging with the Clinically Approved Near-Infrared Dye Indocyanine Green. *Proc. Natl. Acad. Sci.* **2018**, *115*, 4465–4470.

[63] Starosolski, Z.; Bhavane, R.; Ghaghada, K. B.; Vasudevan, S. A.; Kaay, A.; Annapragada, A. Indocyanine Green Fluorescence in Second Near-Infrared (NIR-II) Window. *PLoS One* **2017**, *12*, e0187563.

[64] Bhavane, R.; Starosolski, Z.; Stupin, I.; Ghaghada, K. B.; Annapragada, A. NIR-II Fluorescence Imaging Using Indocyanine Green Nanoparticles. *Sci. Rep.* **2018**, *8*, 14455.

[65] Bandi, V. G.; Schmermann, M. J. Water Soluble Novel Cyanine Fluorophore with Tunable Properties between Near IR and SWIR Region for in vivo Imaging. WO 2020/041743, 2020.

[66] Lu, L.; Li, B.; Ding, S.; Fan, Y.; Wang, S.; Sun, C.; Zhao, M.; Zhao, C. X.; Zhang, F. NIR-II Bioluminescence for in Vivo High Contrast Imaging and in Situ ATP-Mediated Metastases Tracing. *Nat. Commun.* **2020**, *11*, 4192.

[67] Pengshung, M.; Li, J.; Mukadum, F.; Lopez, S. A.; Sletten, E. M. Photophysical Tuning of Shortwave Infrared Flavylium Heptamethine Dyes via Substituent Placement. *Org. Lett.* **2020**, *22*, 6150–6154.

[68] Uranga-Barandiaran, O.; Casanova, D.; Castet, F. Flavylium Fluorophores as Near-Infrared Emitters. *ChemPhysChem* **2020**, *21*, 2243–2248.

[69] Sun, P.; Wu, Q.; Sun, X.; Miao, H.; Deng, W.; Zhang, W.; Fan, Q.; Huang, W. J-Aggregate Squaraine Nanoparticles with Bright NIR-II Fluorescence for Imaging Guided Photothermal Therapy. *Chem. Commun.* **2018**, *54*, 13395–13398.

[70] Chen, W.; Cheng, C.-A.; Cosco, E. D.; Ramakrishnan, S.; Lingg, J. G. P.; Bruns, O. T.; Zink, J. I.; Sletten, E. M. Shortwave Infrared Imaging with J-Aggregates Stabilized in Hollow Mesoporous Silica Nanoparticles. *J. Am. Chem. Soc.* **2019**, *141*, 12475–12480.

[71] Sun, C.; Li, B.; Zhao, M.; Wang, S.; Lei, Z.; Lu, L.; Zhang, H.; Feng, L.; Dou, C.; Yin, D.; et al. J -Aggregates of Cyanine Dye for NIR-II in Vivo Dynamic Vascular Imaging beyond 1500 nm. *J. Am. Chem. Soc.* **2019**, *141*, 19221–19225.

[72] Jelley, E. E. Spectral absorption and fluorescence of dyes in the molecular state. *Nature* **1936**, *138*, 1009−1010.

[73] Scheibe, G. Uber die veranderlichkeit der absorptionsspektren in losungen und die nebenvalenzen als ihre ursache. *Angew. Chem.* **1937**, *50*, 212−219.

[74] Bricks, J. L.; Slominskii, Y. L.; Panas, I. D.; Demchenko, A. P. Fluorescent J-Aggregates of Cyanine Dyes: Basic Research and Applications Review. *Methods Appl. Fluoresc.* **2017**, *6*, 012001.

[75] Li, T.; Li, C.; Ruan, Z.; Xu, P.; Yang, X.; Yuan, P.; Wang, Q.; Yan, L. Polypeptide-Conjugated Second Near-Infrared Organic Fluorophore for Image-Guided Photothermal Therapy. *ACS Nano* **2019**, *13*, 3691–3702.

[76] Zhu, S.; Hu, Z.; Tian, R.; Yung, B. C.; Yang, Q.; Zhao, S.; Kiesewetter, D. O.; Niu, G.; Sun, H.; Antaris, A. L.; et al. Repurposing Cyanine NIR-I Dyes Accelerates Clinical Translation of Near-Infrared-II (NIR-II) Bioimaging. *Adv. Mater.* **2018**, *30*, 1802546.

[77] Suo, Y.; Wu, F.; Xu, P.; Shi, H.; Wang, T.; Liu, H.; Cheng, Z. NIR-II Fluorescence Endoscopy for Targeted Imaging of Colorectal Cancer. *Adv. Healthc. Mater.* **2019**, *8*, 1900974.

[78] Tsuboi, S.; Jin, T. Shortwave-Infrared (SWIR) Fluorescence Molecular Imaging Using Indocyanine Green-Antibody Conjugates for the Optical Diagnostics of Cancerous Tumours. *RSC Adv.* **2020**, *10*, 28171–28179.

[79] Liu, M.-H.; Zhang, Z.; Yang, Y.-C.; Chan, Y.-H. Polymethine-Based Semiconducting Polymer Dots with Narrow-Band Emission and Absorption/Emission Maxima at NIR-II for Bioimaging. *Angew. Chem. Int. Ed.* **2020**, *59*, 2–9.

[80] Tang, Y.; Li, Y.; Hu, X.; Zhao, H.; Ji, Y.; Chen, L.; Hu, W.; Zhang, W.; Li, X.; Lu, X.; et al. "Dual Lock-and-Key"-Controlled Nanoprobes for Ultrahigh Specific Fluorescence Imaging in the Second Near-Infrared Window. *Adv. Mater.* **2018**, *30*, 1801140.

[81] Luciano, M. P.; Crooke, S. N.; Nourian, S.; Dingle, I.; Nani, R. R.; Kline, G.; Patel, N. L.; Robinson, C. M.; Difilippantonio, S.; Kalen, J. D.; et al. A Nonaggregating Heptamethine Cyanine for Building Brighter Labeled Biomolecules. *ACS Chem. Biol.* **2019**, *14*, 934–940.

[82] Zhang, X.-B.; Ren, T.-B.; Wang, Z.-Y.; Xiang, Z.; Lu, P.; Lai, H.-H.; Yuan, L.; Tan, W. General Strategy for Development of Activatable NIR-II Fluorescent Probes for in Vivo High-Contrast Bioimaging. *Angew. Chem. Int. Ed.* **2020**, 2–8.

[83] Xu, G.; Yan, Q.; Lv, X.; Zhu, Y.; Xin, K.; Shi, B.; Wang, R.; Chen, J.; Gao, W.; Shi, P.; et al. Imaging of Colorectal Cancers Using Activatable Nanoprobes with Second Near-Infrared Window Emission. *Angew. Chem. Int. Ed.* **2018**, *57*, 3626–3630.

[84] Zhao, M.; Li, B.; Wu, Y.; He, H.; Zhu, X.; Zhang, H.; Dou, C.; Feng, L.; Fan, Y.; Zhang, F. A Tumor-Microenvironment-Responsive Lanthanide–Cyanine FRET Sensor for NIR-II Luminescence-Lifetime In Situ Imaging of Hepatocellular Carcinoma. *Adv. Mater.* **2020**, *32*, 2001172.

[85] Meng, X.; Zhang, J.; Sun, Z.; Zhou, L.; Deng, G.; Li, S.; Li, W.; Gong, P.; Cai, L. Hypoxia-Triggered Single Molecule Probe for High-Contrast NIR II/PA Tumor Imaging and Robust Photothermal Therapy. *Theranostics* **2018**, *8*, 6025–6034.

[86] Ouyang, J.; Sun, L.; Zeng, Z.; Zeng, C.; Zeng, F.; Wu, S. Nanoaggregate Probe for Breast Cancer Metastasis through Multispectral Optoacoustic Tomography and Aggregation-Induced NIR-I/II Fluorescence Imaging. *Angew. Chem. Int. Ed.* **2020**, *59*, 10111–10121.

[87] Carr, J. A.; Valdez, T. A.; Bruns, O. T.; Bawendi, M. G. Using the Shortwave Infrared to Image Middle Ear Pathologies. *Proc. Natl. Acad. Sci.* **2016**, *113*, 9989–9994. =

[88] Saif, M.; Kwanten, W. J.; Carr, J. A.; Chen, I. X.; Posada, J. M.; Srivastava, A.; Zhang, J.; Zheng, Y.; Pinter, M.; Chatterjee, S.; et al. Non-Invasive Monitoring of Chronic Liver Disease via near-Infrared and Shortwave-Infrared Imaging of Endogenous Lipofuscin. *Nat. Biomed. Eng.* **2020**. *4*, 801–813.

[89] Hu, Z.; Fang, C.; Li, B.; Zhang, Z.; Cao, C.; Cai, M.; Su, S.; Sun, X.; Shi, X.; Li, C.; et al. First-in-Human Liver-Tumour Surgery Guided by Multispectral Fluorescence Imaging in the Visible and near-Infrared-I/II Windows. *Nat. Biomed. Eng.* **2020**, *4*, 259–271.

CHAPTER TWO

Flavylium Polymethine Dyes as Contrast Agents for Shortwave Infrared Imaging

Adapted from: Emily D. Cosco, Justin. R. Caram, Oliver T. Bruns, Daniel Franke, Rachael A. Day, Erik P. Farr, Moungi G. Bawendi, and Ellen M. Sletten.* Flavylium Polymethine Fluorophores for Near- and Shortwave Infrared Imaging. *Angew. Chemie Int. Ed.* **2017**, *56*, 13126–13129. DOI: 10.1002/anie.201706974

2.1 Abstract

Bright fluorophores in the near-infrared and short- wave infrared (SWIR) regions of the electromagnetic spectrum are essential for optical imaging in vivo. In this work, we utilized a 7-dimethylamino flavylium heterocycle to construct a panel of novel red-shifted polymethine dyes, with emission wavelengths from 680 to 1045 nm. Photophysical characterization revealed that the 1- and 3-methine dyes display enhanced photostability and the 5- and 7-methine dyes exhibit exceptional brightness for their respective spectral regions. A micelle formulation of the 7-methine facilitated SWIR imaging in mice. This report presents the first polymethine dye designed and synthesized for SWIR *in vivo* imaging.

2.2 Introduction

Fluorophores emitting at near-infrared (NIR, λ = 700–1000 nm, Figure 2.1) wavelengths have been critical to the success of optical imaging in mammals.[1] Compared to visible light, NIR irradiation allows non-invasive, real-time analysis of biological processes due to decreased

autofluorescence and scattering.[2] Optical imaging has the potential to become a cost-effective leading tool for clinical diagnoses and surgical guidance if bright, biocompatible, red-shifted fluorophores are developed.[3] Clinical NIR imaging has been championed by indocyanine green (ICG), [4] whose success is linked to low toxicity and favorable photophysical properties. These properties include the absorption coefficient (ε) and fluorescence quantum yield (Φ_F), which can be combined into a single brightness value (brightness = $\varepsilon \times \Phi_F$).[5] ICG has a brightness of 1350 $M^{-1}cm^{-1}$, providing a brightness benchmark for new NIR contrast agents.[6] Moving beyond the traditional NIR portion of the electromagnetic spectrum to the shortwave infrared (SWIR, λ = 1,000–2,000 nm) region has emerged as a complementary strategy to enhance optical imaging.[7] The superior resolution and depth penetration attained with SWIR imaging were originally validated with carbon nanotubes,[8] rare-earth materials,[9] and quantum dots.[10] However, to translate the advantages of this region to the clinic, non-toxic SWIR fluorophores are necessary. Initial progress toward this goal entailed formulations of the SWIR polymethine dye IR-1061.[11] Dai and co-workers have explored donor-acceptor-donor (D-A-D) benzobisthiadiazole chromophores as SWIR emissive contrast agents.[12] Their work has shown that structural and formulation changes can enhance emission.[13] Despite impressive Φ_F values, the brightness of the D-A-D chromophores are limited by their low absorption coefficients. Recently, the effect of high ε values has been highlighted by off-peak SWIR detection of ICG fluorescence surpassing the brightness of early-generation benzobisthiadiazoles.[14]

The high absorption coefficient of ICG is mirrored in other members of its chromophore class, the polymethine dyes. These dyes are charged molecules composed of heterocycles linked by a methine chain (Figure 2.1). Nitrogen-containing polymethines (cyanine dyes) with 1–5 methine units span the visible region, while 7-methines, such as ICG, reach NIR wavelengths.[15]

Cyanine dyes are widely used in microarrays and live-cell microscopy, [16] while further engineering for sensing and photoinitiated drug delivery demonstrates the versatility of the polymethine scaffold.[17] Despite their promise as bright, tunable fluorophores, polymethines have yet to be optimized as SWIR contrast agents. Lengthening the polymethine chain, a classic method to red-shift cyanine dyes, can compromise Φ_F, decrease stability, and lead to the loss of symmetric electron delocalization.[18] Heterocycle modification is an alternate approach and represents a promising avenue toward stable, SWIR-emissive polymethines.[19] Extending heterocycle conjugation or adding electron-donating groups has been shown to bathochromically shift polymethine dyes.[18, 20]

Varying the heteroatom from oxygen to other chalcogens results in red- shifted absorption, although increased intersystem crossing due to the heavy-atom effect can compromise Φ_F.[21]

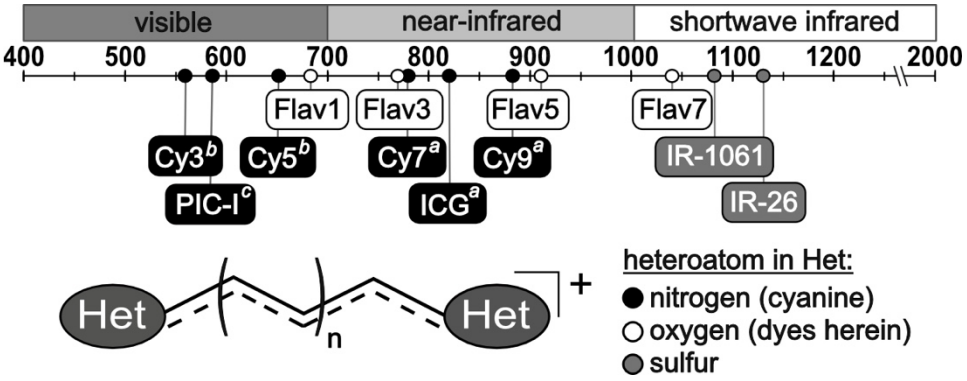

Figure 2.1 Regions of the electromagnetic spectrum and selected polymethine dyes, positioned by $\lambda_{max,em}$. The numbers in the Cy (structures in Section 2.6.1) and Flav (dyes presented herein) nomenclature indicate the number of methine units in the chain.

Collectively, these fundamental studies give insight into fluorophore design, which we looked to apply to the benchmark SWIR polymethine, thiaflavylium dye IR-26.[22] We hypothesized that exchange of the sulfur atom for oxygen would enhance the Φ_F, although it would blue-shift the absorbance. To compensate for this shift, we proposed the addition of an electron-donating dimethylamino group. Thus, we directed our attention to dimethylamino flavylium polymethine fluorophores.

2.3 Results and Discussion

Polymethine dyes are prepared through the introduction of an activated heterocycle to an aldehyde or bis(aldehyde) equivalent. We prepared the requisite 7-*N*,*N*-dimethylamino- 4-methyl-flavylium (**2.1**; Scheme 2.1)[23] and explored the photophysical scope of the polymethine dyes that can be accessed with this heterocycle. Combining **2.1** with bis(phenylimine) **2.2**, malonaldehyde bis(phenylimine), or paraformaldehyde under basic conditions yielded the series of flavylium dyes **2.3**, **2.4**, and **2.5**, respectively (Scheme 2.2). The synthesis of **2.3** originally yielded a mixture of highly colored products, which included **2.5** and **2.6**. Further investigation revealed that treatment of **2.1** with only base in ethanol gave a mixture of **2.5** and **2.6**. We determined this transformation to be oxygen-dependent (Figure 2.2) and hypothesize that radical addition of O_2 to the flavylium generates a peroxide that combines with deprotonated **2.1** to yield **2.6** and an equivalent of formaldehyde (Scheme 2.3). This provides unique access to less common monomethine dyes through a single heterocycle.

Scheme 2.1 Synthesis of 7-*N,N*-dimethylamino-4-methyl-flavylium perchlorate **2.1**.[23]

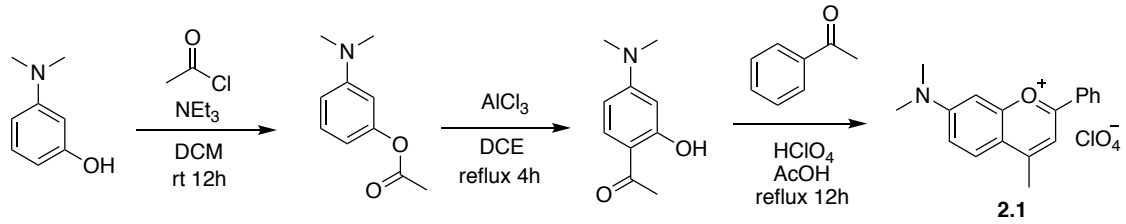

Scheme 2.2 Synthesis of dimethylamino flavylium polymethine dyes **2.3**–**2.6**.

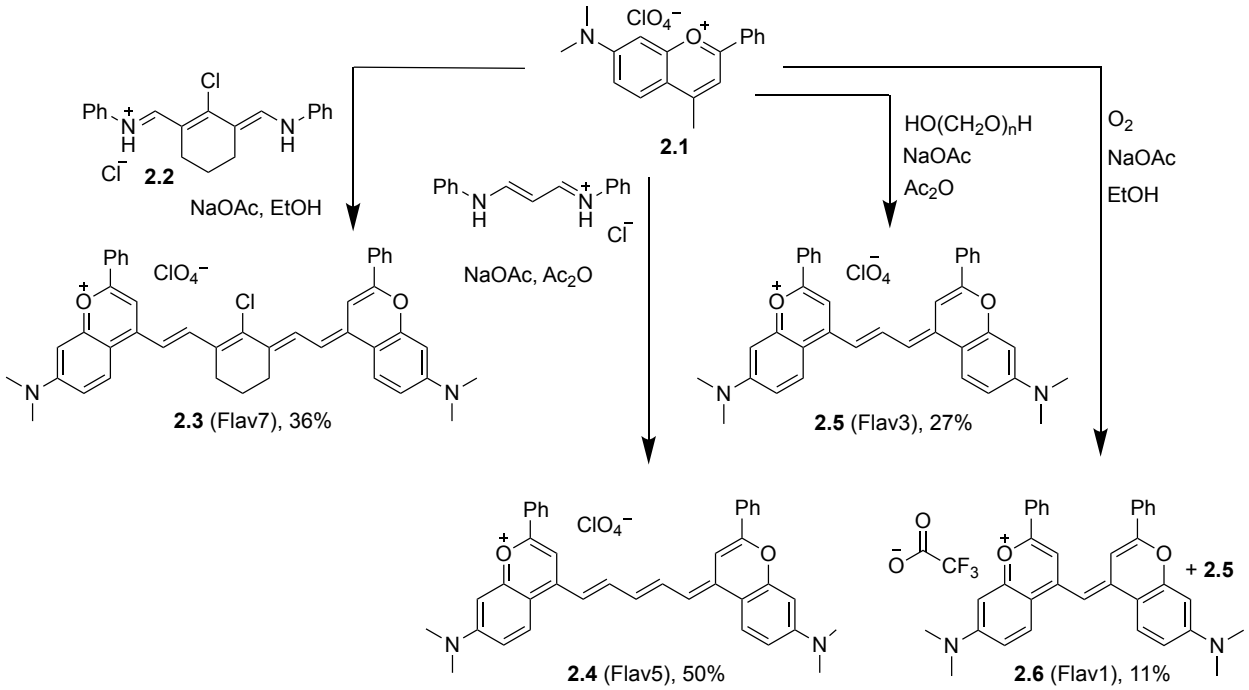

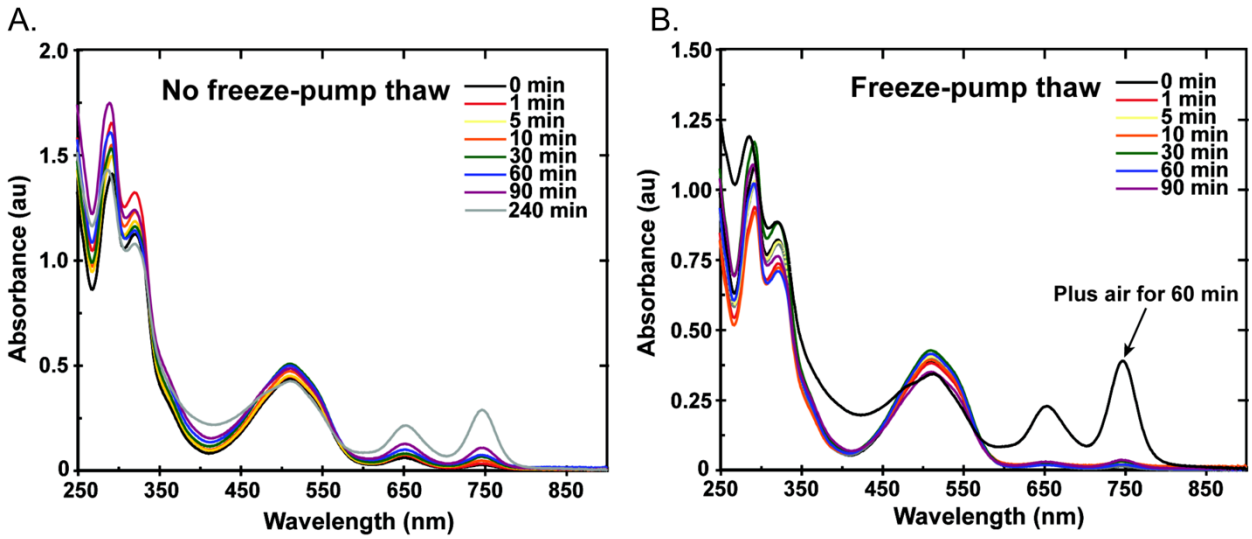

Figure 2.2 Absorbance traces (in dichloromethane) monitoring the reaction of flavylium (**2.1**) with excess sodium acetate in ethanol (B) with and (A) without freeze-pump thawing. The absorbance peaks at 650 nm and 740 nm indicate that **2.6** and **2.5** are produced in (A) when oxygen is present, but minimal reaction is observed in (B), until the addition of air, at which point both dye species are detected.

Scheme 2.3 Mechanistic hypothesis for the formation of **2.6**.

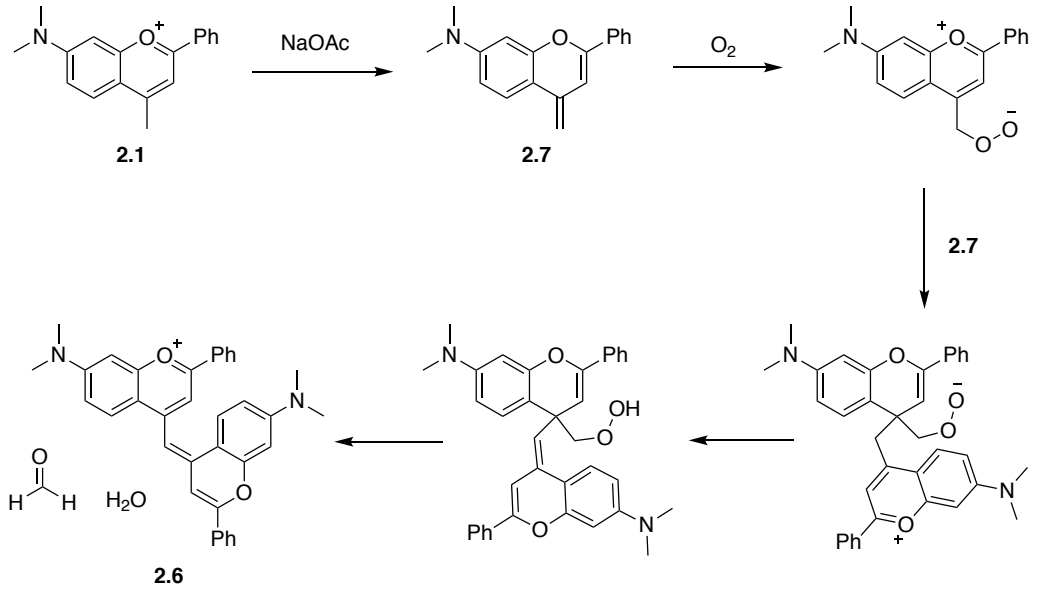

The dimethylamino flavylium heterocycle resulted in stable polymethine dyes spanning the electromagnetic spectrum from far-red to SWIR wavelengths (Figure 2.3, Table 2.1). The flavylium dyes are bathochromically shifted from classic cyanine dyes by approximately 200 nm

(Figure 2.1). The photostability of dyes **2.3**–**2.6** were measured under irradiation at 532 nm (530 $mWcm^{-2}$) and the results indicate that all of the fluorophores display moderate to excellent photostability (Table 2.2, Figure 2.4). Dye **2.6** absorbs at 650 nm, similar to a 5-cyanine, but has lower ε and Φ_F values, which are consistent with the short polymethine chain.[19] Compound **2.5** has similar absorption properties to the standard 7-cyanine HITCI. While HITCI has an approximately 10-fold higher Φ_F than **2.5**,[24] it is 4-fold less photostable (Figure 2.5 and Table 2.3). The most intriguing dyes of this series are **2.4** and **2.3** due to their far-NIR and SWIR fluorescence. Dye **2.4** emits at 908 nm, a relatively unique wavelength for existing polymethine dyes, with high brightness (10,000 $M^{-1}cm^{-1}$) and photostability. Finally, **2.3** is a true SWIR fluorophore with emission at 1045 nm, an impressive SWIR brightness of 1200 $M^{-1}cm^{-1}$, and a 10^3 slower per-photon photobleaching rate when irradiated at 1050 nm (16 $mWcm^{-2}$) compared to 532 nm (Table 2.4, Figure 2.6). As a result of its advantageous SWIR photophysical properties, **2.3** was named Flav7 and further investigated as a contrast agent.

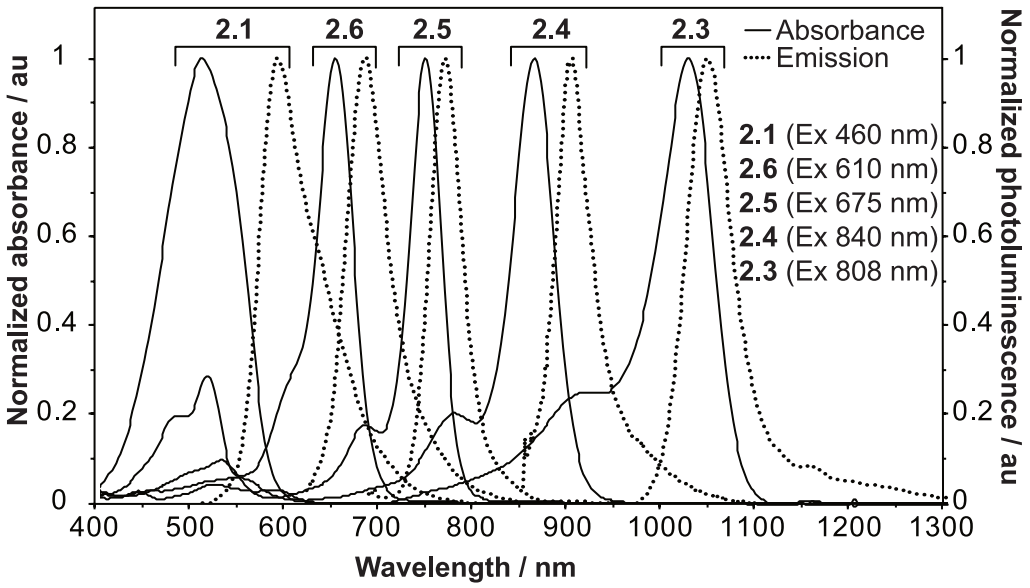

Figure 2.3 Normalized absorbance (solid) and photoluminescence (dotted) of **2.1**, **2.3**–**2.6** in dichloromethane.[25]

Table 2.1 Photophysical characterization of **2.1**, **2.3**–**2.6** in dichloromethane.

Compd	$\lambda_{max,abs}$ (nm)	$\varepsilon(\lambda_{max})$ ($M^{-1}cm^{-1}$)	$\lambda_{max,em}$ (nm)	Φ_F (%)	Brightness[6] ($M^{-1}cm^{-1}$)
2.1	510	17 000 ± 2 000	587	–	–
2.6	650	16 000 ± 5 000	684	0.7 ± 0.5	100 ± 90
2.5	746	220 000 ± 10 000	766	2.9 ± 0.5	6 600 ± 500
2.4	862	240 000 ± 20 000	908	5 ± 2	10 000 ± 3 000
2.3	1026	236 000 ± 2 000	1045	0.53 ± 0.03	1 200 ± 100

Table 2.2 Photobleaching rates of **2.3**–**2.6** as observed with irradiation at 532 nm with 0.53 ± 0.05 Wcm^{-2} fluence.

Compound	raw rate, k (s^{-1} x 10^{-3})	ε at 532 nm ($M^{-1}cm^{-1}$ x 10^4)	relative rate, k_{rel} (s^{-1} x 10^{-3})	relative stability
2.3	0.43 ± 0.01	0.23 ± 0.08	4 ± 1	0.27 ± 0.09
2.4	1.00 ± 0.06	2.0 ± 0.1	1.00 ± 0.06	1.0 ± 0.6
2.5	2.7 ± 0.2	1.29 ± 0.08	4.1 ± 0.3	0.24 ± 0.02
2.6	28. ± 3.	1.4 ± 0.2	40. ± 6.	0.025 ± 0.004

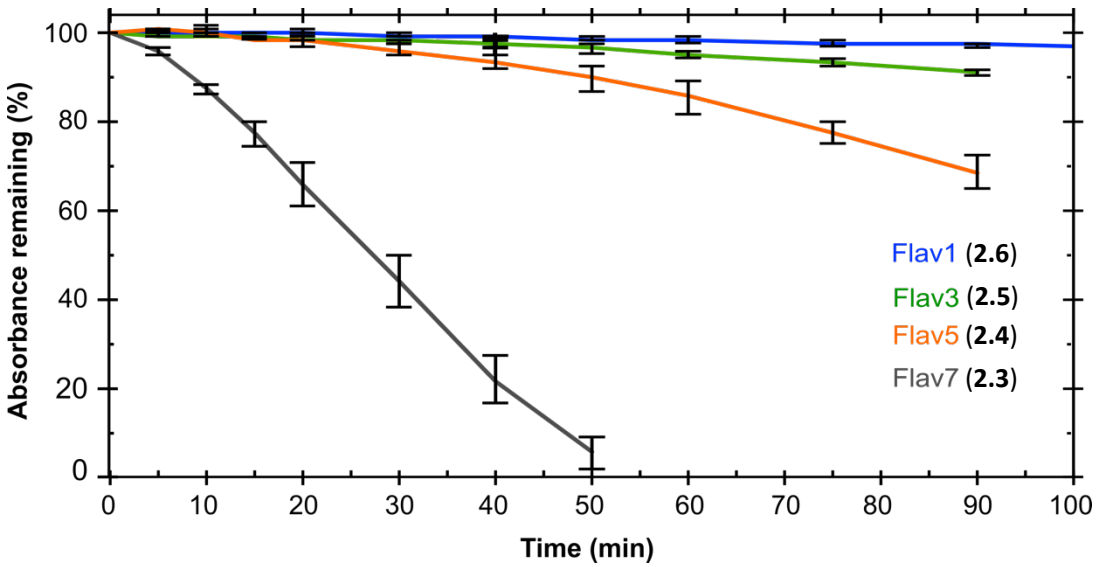

Figure 2.4 Photobleaching of **2.3**–**2.6**. Dyes in dichloromethane were subjected to continuous-wave irradiation at 532 nm with a fluence of 0.53 ± 0.05 Wcm^{-2} and monitored by decreasing absorbance at $\lambda_{max,abs}$.

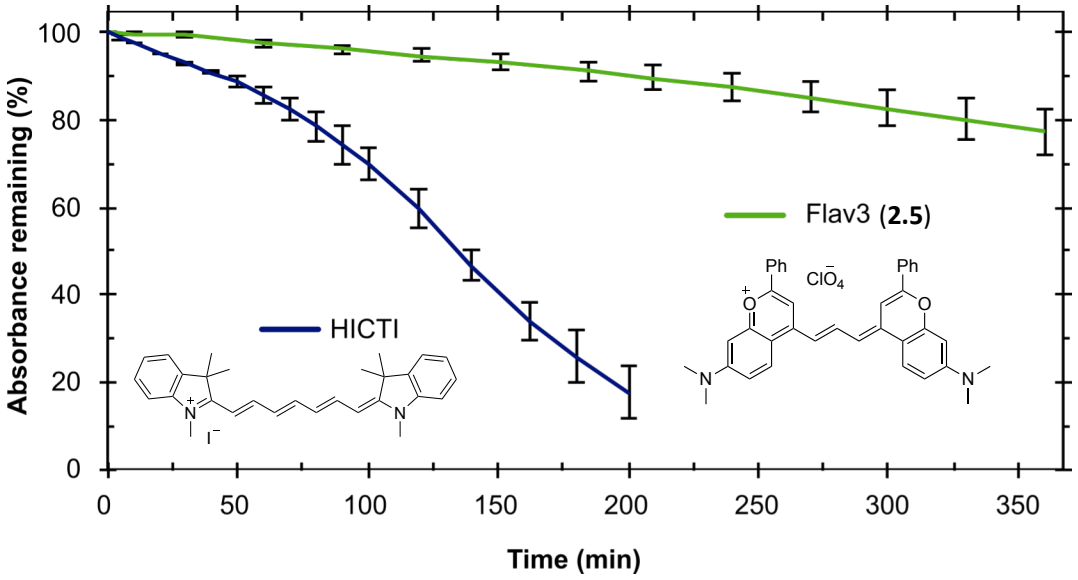

Figure 2.5 Photobleaching of **2.5** and 1,1',3,3,3',3'-hexamethyl-indotricarbocyanine iodide (HITCI) (Sigma Aldrich). Dye solutions in dichloromethane were irradiated with a 730 nm LED with 140 ± 10 mWcm^{-2} fluence and monitored by decreasing absorbance at $\lambda_{max,abs}$.

Table 2.3 Photobleaching rates of **2.5** and HITCI measured with a 730 nm LED at 140 ± 10 mWcm^{-2} fluence.

Compd	raw rate, k (s^{-1} x 10^{-4})	relative rate, k_{rel} (s^{-1} x 10^{-4})
2.5	6.9 ± 0.3	7.9 ± 0.6
HITCI	34 ± 2	34 ± 2

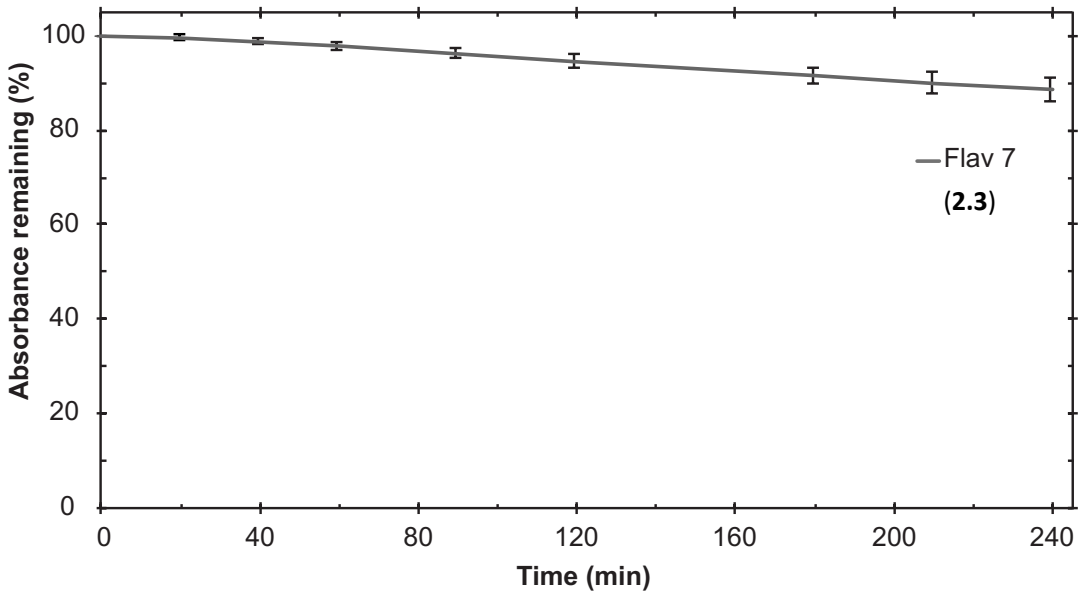

Figure 2.6 Photobleaching of Flav7 (**2.3**) in dichloromethane observed under continuous irradiation with a 1050 nm LED at 16.3 ± 0.4 mWcm^{-2}.

Table 2.4 Photobleaching rate of Flav7 (**2.3**) at 1050 nm vs. 532 nm.

Light source	Fluence (mWcm^{-2})	raw rate, k (s^{-1})	relative rate, k_{rel} (s^{-1})
1050 nm LED	16.3 ± 0.4	8.8 ± 0.2 x 10^{-6}	1.7 ± 0.1 x 10^{-5}
532 nm laser	530 ± 0.05	2.8 ± 0.3 x 10^{-2}	2.8 ± 0.3 x 10^{-2}

First, we evaluated the emission of Flav7 (**2.3**) against the SWIR dyes IR-26 and IR-1061. The reported Φ_F values for IR-26 have been inconsistent,[24,26] and the Φ_F of IR-1061 has yet to be thoroughly characterized.[11,27] To establish that Flav7 is more emissive than existing SWIR polymethine dyes, we directly compared the photoluminescence of each dye with a SWIR camera. Solutions of Flav7, IR-26, and IR-1061 in dichloromethane with identical absorbance at 808 nm (Figure 2.7) were excited and imaged over 1000–1600 nm (Figure 2.8A). The average intensity

was quantified (Figure 2.8B) and revealed that Flav7 has the highest Φ_F of the three dyes. These data correlate with absolute Φ_F values determined using an integrating sphere (Figure 2.8C).

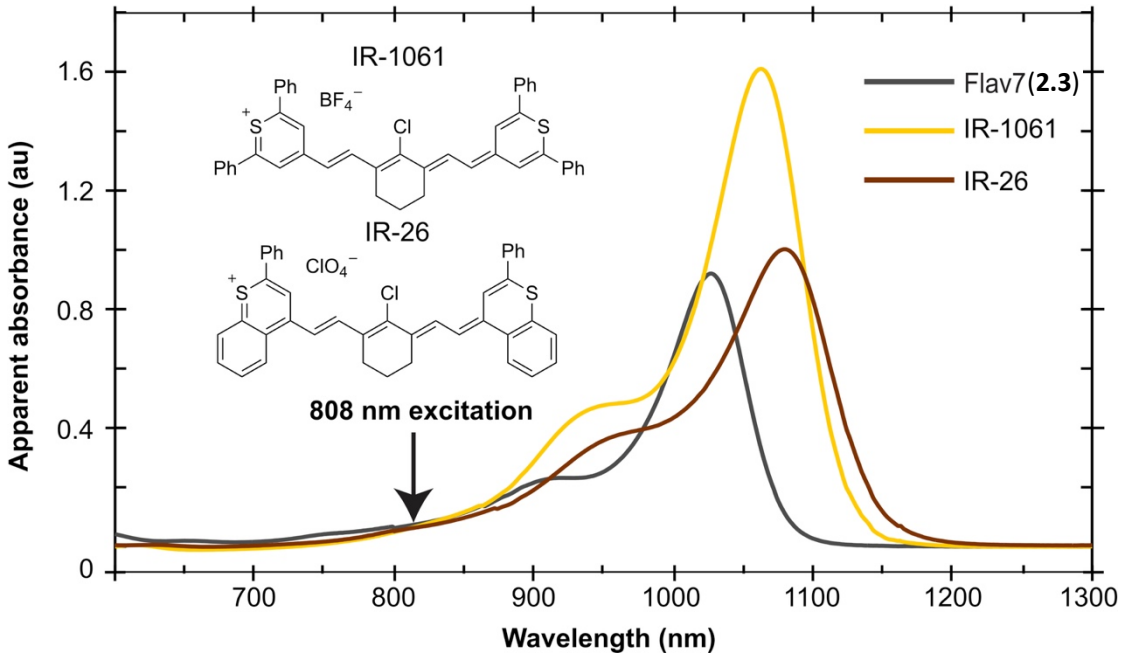

Figure 2.7 Absorbance spectra of the solutions of IR-26, IR-1061, Flav7 (**2.3**) dissolved in dichloromethane that were employed in Figure 2.8A. Note that the absorbance of all three solutions was matched at 808 nm.

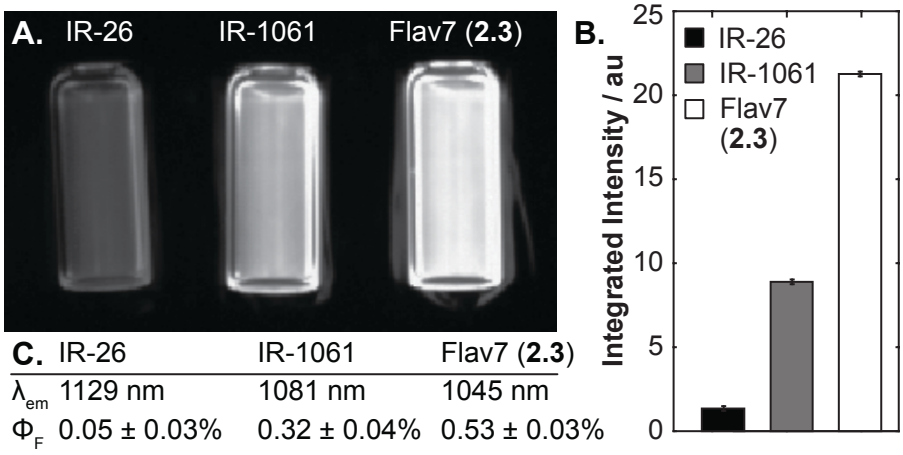

C.	IR-26	IR-1061	Flav7 (**2.3**)
λ_{em}	1129 nm	1081 nm	1045 nm
Φ_F	0.05 ± 0.03%	0.32 ± 0.04%	0.53 ± 0.03%

Figure 2.8 Brightness of polymethine dyes in a SWIR imaging configuration. A) Image of vials of IR-26, IR-1061, and **2.3** with matched optical density at 808 nm in dichloromethane, excited at 808 nm and collected using an InGaAs camera (λ = 1,000–1,600 nm). B) Average background-subtracted intensity for 10 frames normalized to exposure. C) Absolute Φ_F of the three dyes.

To employ Flav7 for in vivo imaging, a formulation in phosphate buffered saline (PBS) was necessary. We first assayed the stability of Flav7 in water/acetonitrile mixtures. These studies indicated that in the presence of water, Flav7 undergoes aggregation, but the monomer appears stable (Figures 2.9–2.12),[28] which suggests that Flav7 is suitable for micelle encapsulation.

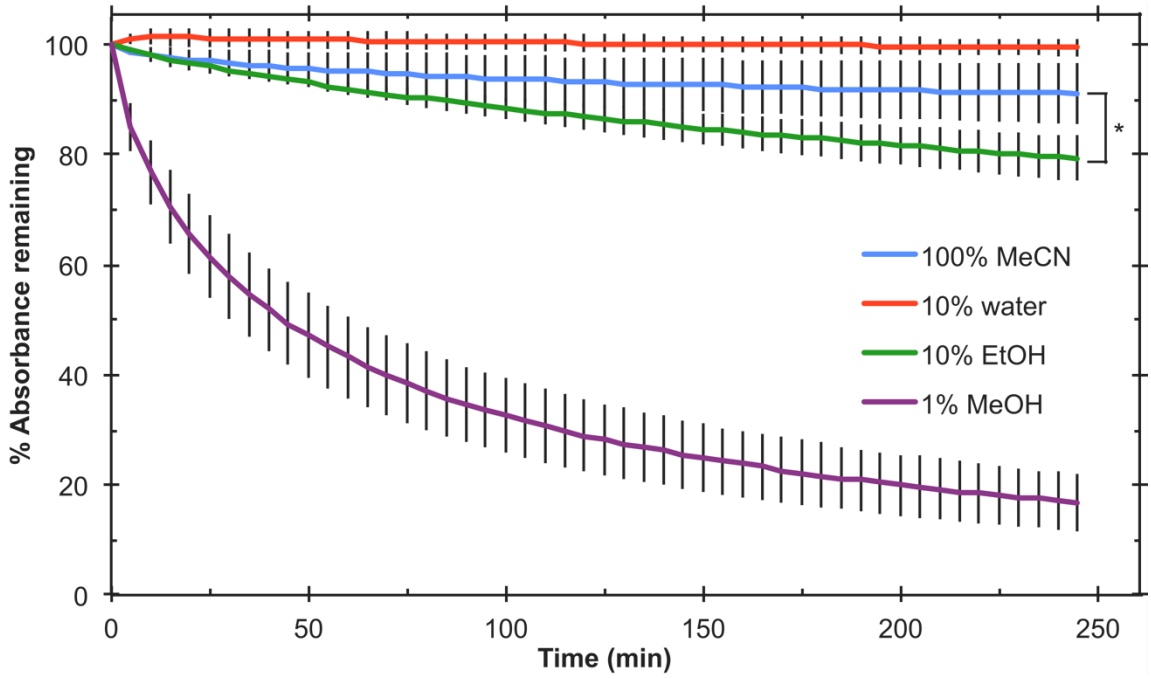

Figure 2.9 Stability of Flav 7 (**2.3**) in 100% MeCN (blue), and MeCN with 10% water (red), 10% EtOH (green), and 1% MeOH (purple), as measured by loss of absorbance at $\lambda_{max,abs}$. Error represents standard deviation. *denotes $p \leq 0.015$.

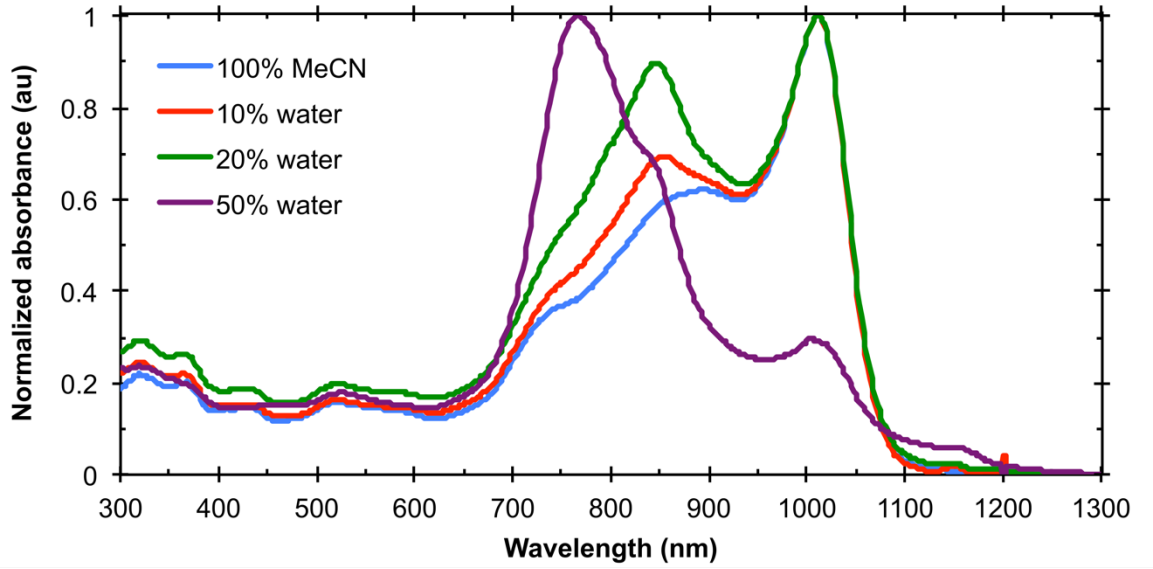

Figure 2.10 Normalized absorption of Flav7 (**2.3**) in acetonitrile (blue) and acetonitrile containing 10-50% water (red, green, purple). These data indicate that aggregation increases dose-dependently with water content in acetonitrile.

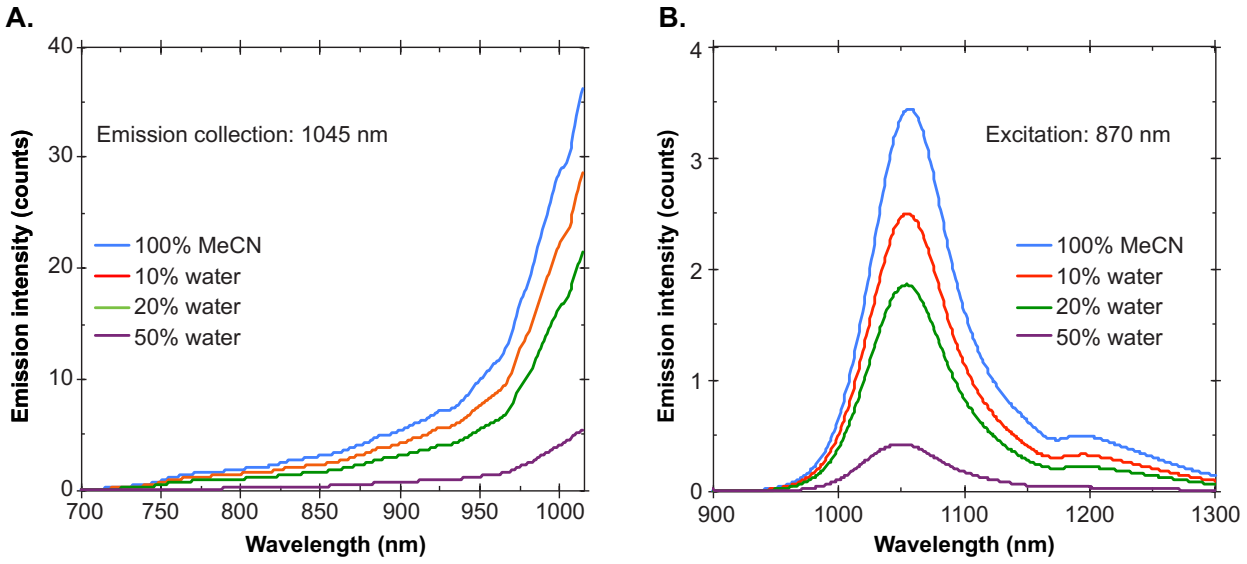

Figure 2.11 Photophysical characterization of Flav7 (**2.3**) in mixtures of acetonitrile and water. (A) Excitation spectra (collection at 1045 nm) and (B) emission spectra (excitation at 870 nm) of Flav7 (**2.3**) in acetonitrile (blue) and acetonitrile with 10–50% water (red, green, purple). Both excitation and emission intensities scale inversely with the increase in aggregation observed in Figure 2.10, suggesting that the monomer is the only emissive species present.

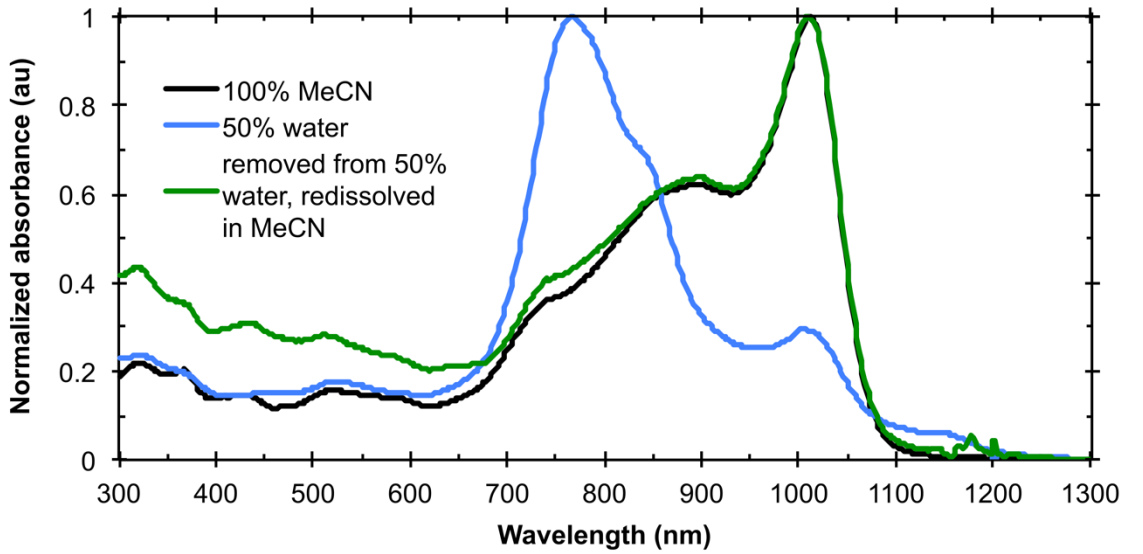

Figure 2.12 Normalized absorbance of Flav7 (**2.3**) in 100% acetonitrile (black). The sample was then diluted by the addition of water to reach 50% water in acetonitrile (blue). After 1.5 hours, the solvent mixture was evaporated and the sample, re-dissolved in 100% acetonitrile (green), exhibited recovery of the $\lambda_{max,abs}$ at 1013 nm, demonstrating that aggregate formation is reversible.

Building upon prior work with mPEG- DSPE lipids,[11] we prepared micelles containing Flav7 in PBS. The formulations displayed broad absorption from 700–1100 nm, yet sharp emission at 1075 nm from monomeric Flav7 (Figure 2.13). We assayed the biocompatibility of the formulations in mammalian cell culture and found no significant difference between empty and Flav7-loaded micelles (Figure 2.14). SWIR imaging in mice was performed with the fluorescent formulation of Flav7. Nude mice were intravenously injected with Flav7 micelles and immediately imaged with 808 nm excitation and 1000–1600 nm detection (Figure 2.15A–B; 2.16A–B, Figures 2.17–2.19, Supplementary Videos 2.1–2.4). The characteristic high spatial and temporal resolution of the SWIR region[8–11] is evident in the vasculature of the hind limb and the ability to quantify the heart rate of the anesthetized mouse (Figure 2.15C–D; 2.16C–D). These results illustrate that the flavylium scaffold is a promising new addition to SWIR contrast agents.

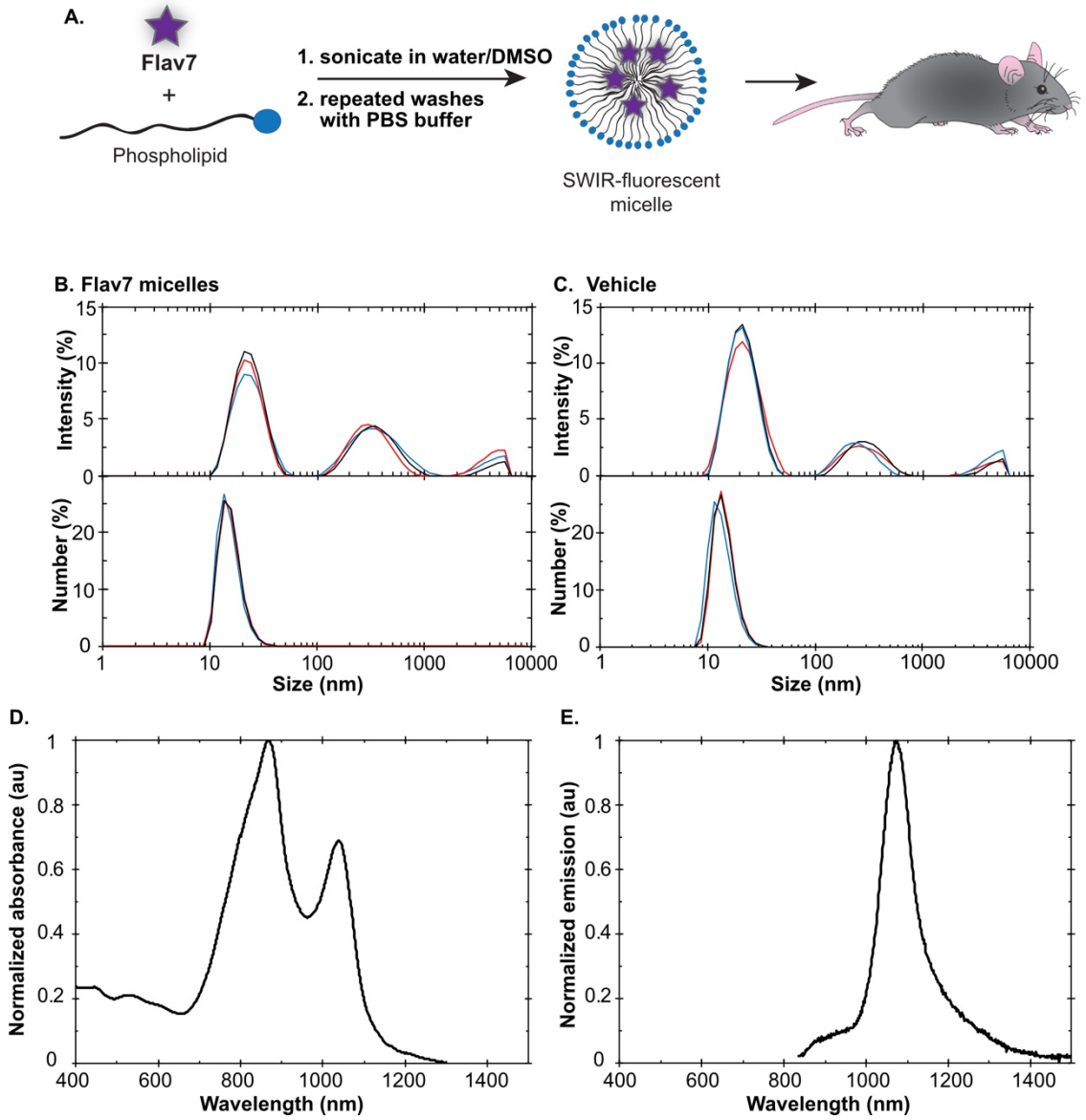

Figure 2.13 Characterization of Flav7 (**2.3**) micelles. (A) Schematic of micelle formation and use *in vivo*. Hydroscopic diameter by intensity and number as determined by dynamic light scattering (DLS) for (B) Flav7 (**3**) micelles and (C) vehicle micelles. The hydroscopic diameter for the Flav7 (**3**) was 24 ± 7 nm and for the vehicle micelles the diameter was 22 ± 7 nm. (D) Absorbance and (E) photoluminescence (Ex. 808 nm) of the Flav7 (**2.3**) micelles. All data was obtained at pH 7.4.

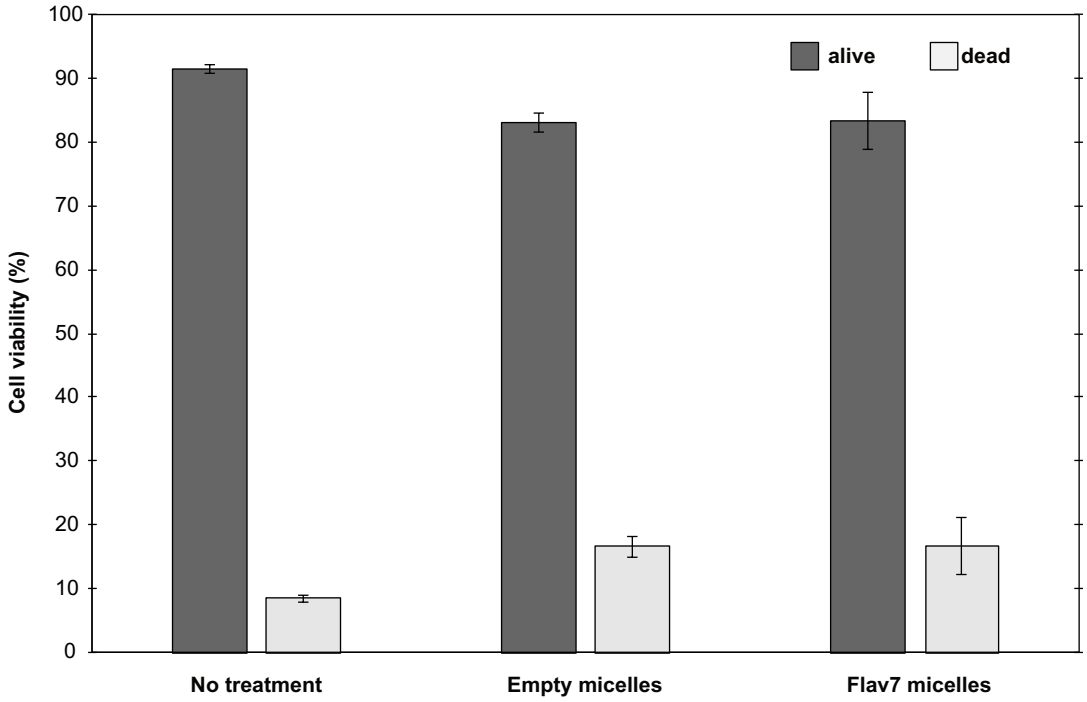

Figure 2.14[1] Flav7 (**2.3**) micelles do not display significant toxicity. Cell viability of HEK 293 cells upon treatment for 3 hours with Flav7 (**2.3**) and vehicle micelles was measured by flow cytometry with a propidium iodide stain. The empty micelles and Flav7 (**2.3**) micelles do not show statistical significance ($p > 0.05$). Error bars represent standard deviation.

[1] Cell culture work by Rachael Day

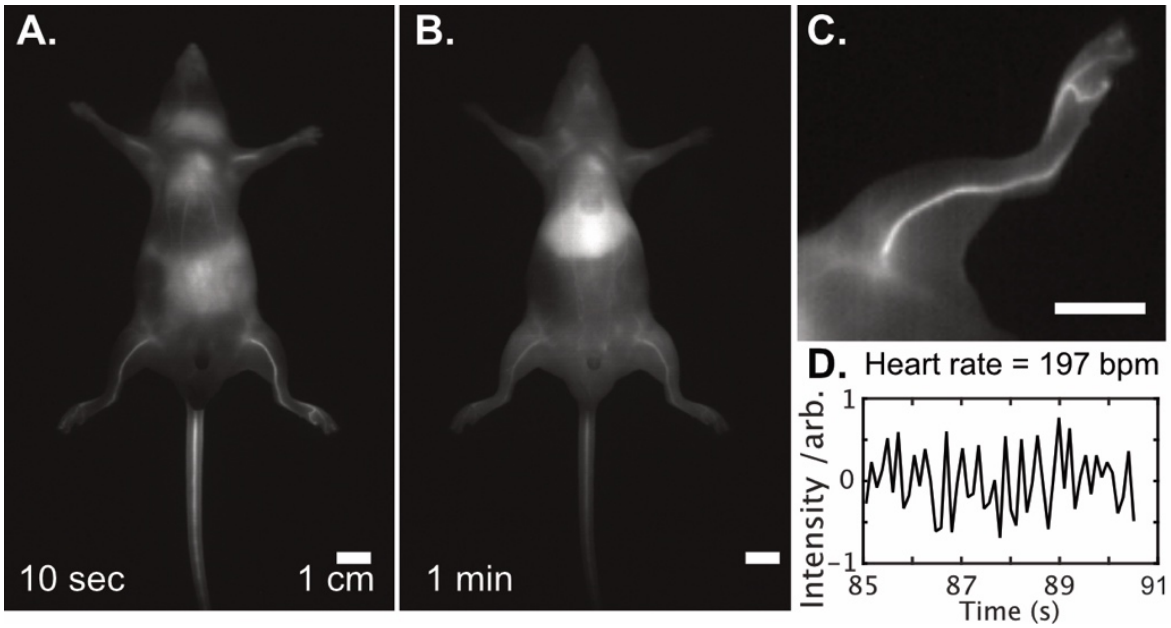

Figure 2.15[2] Images of nude mouse following tail-vein injection of Flav7 (**2.3**) micelles with diffuse 808 nm excitation and collection on an InGaAs camera (1,000–1,600 nm) at 9.17 frames s^{-1}. Average background-subtracted images were taken for 10 frames at 10 s (A) and 1 min (B) after injection. C) Close-up image of the hindlimb from (A). D) Intensity versus time plot of signal from the heart region. mPEG-DSPE = methoxy-poly(ethylene glycol)-1,2-di- stearoyl-sn-glycero-3-phosphoethanolamine-N. See Supplementary Videos 2.1–2.4 for imaging at 9.17 frames s^{-1}.

[2] All imaging work in this chapter by Oliver Bruns and Daniel Franke

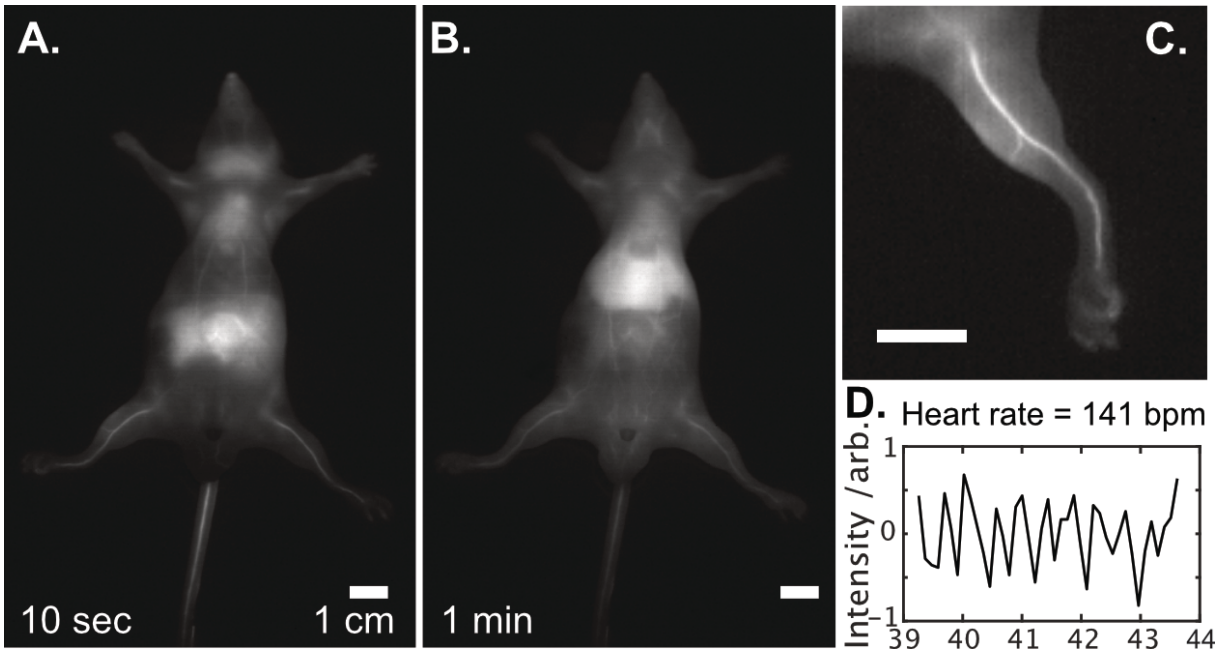

Figure 2.16 Replicate of experiment in Figure 2.14. Images of nude mouse with tail vein injection of Flav7 (**2.3**) micelles with diffuse 808 nm excitation and collection on an InGaAs camera (1000–1600 nm). Average background subtracted images taken for 10 frames at (A) 10 seconds and (B) 1 min after injection. (C) Close-up image of the hind limb. (D) Intensity vs time plot of signal from the heart region. See Supplementary Videos 2.1–2.4 for imaging at 9.17 frames s^{-1}.

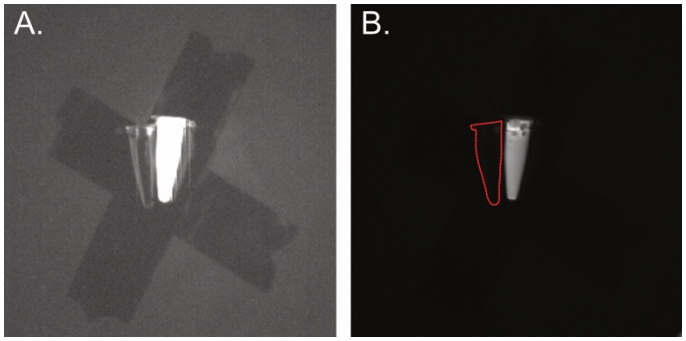

Figure 2.17 The formulations are only SWIR fluorescent when Flav7 (**2.3**) is incorporated. Images of the Flav7 (**2.3**) micelle (right) and vehicle micelle (left) in 1.5 mL centrifuge tubes with diffuse excitation at 808 nm and emission collected on an InGaAs camera (1000–1600 nm). (A) A contrast-adjusted photo showing the presence of both samples (the Flav7 (**2.3**) vial appears oversaturated at these settings). (B) At more representative contrast settings, the image depicts emission from the Flav7 (**2.3**) micelle solution and no emission from the vehicle.

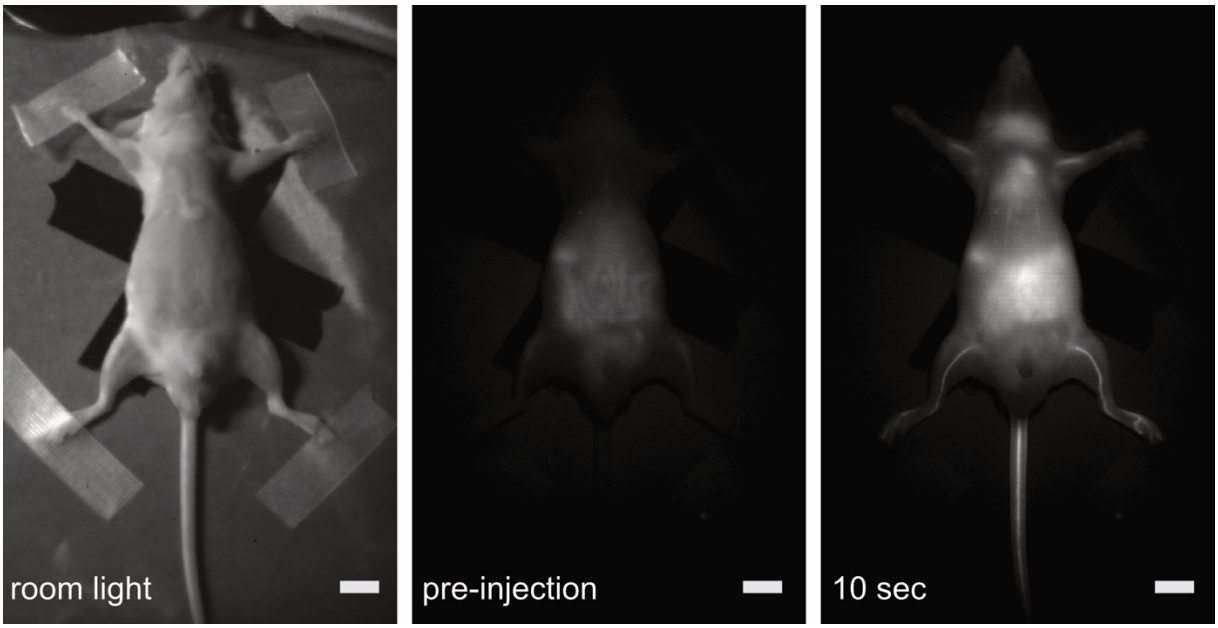

Figure 2.18 Nude mouse under diffuse 808 nm excitation and emission collected by an InGaAs detector between 1,000–1,600 nm, with no background autofluorescence subtracted. (A) Image from the average intensity over 5 frames in room light. (B) Image acquired before Flav7 (**2.3**) micelle injection, displays SWIR autofluorescence (averaged intensity over 10 frames). (C) Image of mouse 10 seconds after Flav7 (**2.3**) micelle injection (averaged intensity over 10 frames). Scale bar set to 1 cm.

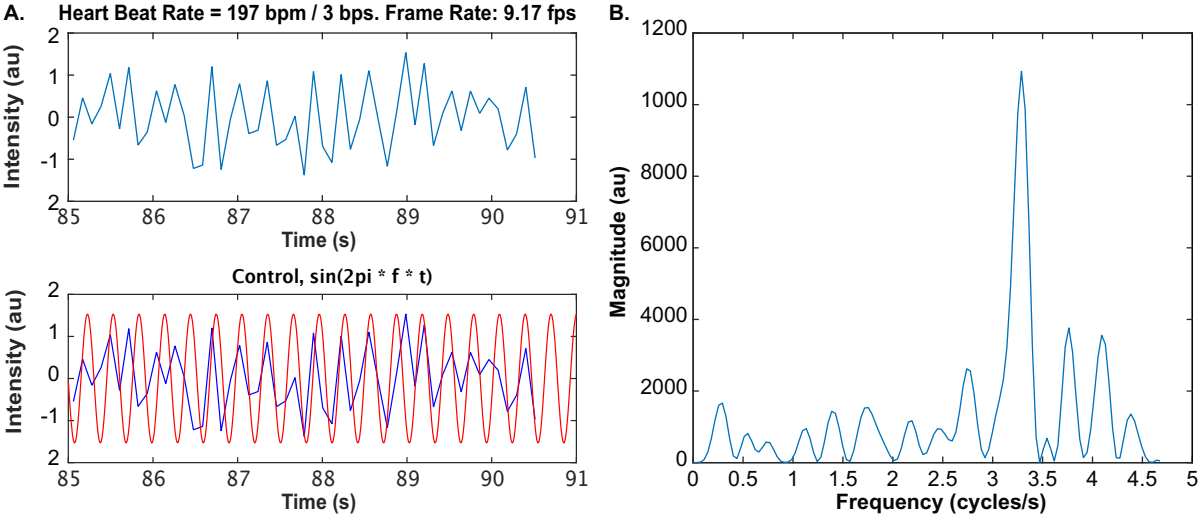

Figure 2.19 Anesthetized heartbeat determination. The temporal resolution was sufficient to determine the heartbeat of the anesthetized mouse. The intensity fluctuations (A) were measured on the mouse heart to be 197 beats per minute. For control, the obtained heart rate was entered into a sine function and overlaid with the measured intensity. The Fourier transform (B) gives the dominant frequency corresponding with heart rate.

2.4 Conclusion

In summary, we have designed a new class of polymethine dyes with dimethylamino flavylium heterocycles. These dyes are notably red-shifted compared to prevalent cyanine dyes, and expand the opportunities for imaging and detection at NIR and SWIR wavelengths. The hallmark fluorophore is the 7-methine (Flav7) which is 13 times brighter than IR-26, the current SWIR benchmark. The *in vivo* performance of this new contrast agent was assessed through the detection of dye-containing micelles. With these studies, we have achieved the brightest SWIR polymethine employed for imaging to date. As a class, polymethine dyes show distinct advantages as organic SWIR contrast agents due to their high absorption coefficients, which lead to high brightness. Furthermore, small Stokes shifts provide potential for both SWIR excitation and detection. These qualities, coupled with the clinical success of ICG and the results herein, suggest that polymethine fluorophores are poised to translate SWIR diagnostics into the clinic.

2.5 Experimental Procedures

2.5.1 General Experimental Procedures

Materials and Instruments Chemical reagents were purchased from Sigma-Aldrich or Acros Organics and used without purification unless noted otherwise. Anhydrous DMSO was obtained from a Sure-Seal^{TM} bottle (Aldrich). Anhydrous and deoxygenated solvents DCM, MeCN, MeOH, THF were dispensed from a Grubb's-type Phoenix Solvent Drying System. Anhydrous but oxygenated DCM and EtOH were prepared by drying over 4 Å molecular sieves for at least 3 days. Thin layer chromatography was performed using Silica Gel 60 F_{254} (EMD Millipore) plates. Flash chromatography was executed with technical grade silica gel with 60 Å pores and 40 – 63 μm mesh particle size (Sorbtech Technologies). High performance liquid

chromatography was performed using a semi-prep reverse phase (C_{18}) column with a Waters HPLC system equipped with a UV-Vis detector set at 254 nm. Solvent was removed under reduced pressure with a Büchi Rotovapor with a Welch self-cleaning dry vacuum pump and further dried with a Welch DuoSeal pump. Bath sonication was performed using a Branson 3800 ultrasonic cleaner. Nuclear magnetic resonance (^{1}H NMR, ^{13}C NMR, and ^{19}F NMR) spectra were taken on Bruker Avance 500 (^{1}H NMR and ^{13}C NMR) or AV-300 (^{19}F NMR) instruments and processed with MestReNova software. All ^{1}H NMR and ^{13}C NMR peaks are reported in reference to DMSO-d_6 at 2.50 ppm and 39.52 ppm, respectively. ^{19}F NMR is in respect to α,α,α-trifluorotoluene at -63.90 ppm as an external standard.[29] HRMS data were obtained from the MIT Department of Chemistry Instrument Facility. Masses for analytical measurements were taken on a Sartorius MSE6.6S-000-DM Cubis Micro Balance. Absorbance spectra were collected on a JASCO V-770 UV-Visible/NIR spectrophotometer with a 4000 nm/min or 2000 nm/min scan rate after blanking with the appropriate solvent or on a Cary 5000 UV-VIS-NIR spectrometer. Photoluminescence spectra were obtained on a Horiba Instruments PTI QuantaMaster Series fluorometer or a Fluoromax-3 spectrofluorometer or home-built InGaAs array detector (Princeton Instruments). Quartz cuvettes (1 cm or 0.33 cm) were used for absorbance and photoluminescence measurements. Absorption coefficients were calculated with serial dilutions in dichloromethane in volumetric glassware. Error was taken as the standard deviation of the triplicate measurement. Absolute quantum yields were determined in DCM with an integrating sphere as described in absolute quantum yield experimental procedure. Analysis by X-ray photoelectron spectroscopy (XPS) was performed on a Kratos Axis Ultra DLD spectrometer with a monochromatic (Al-K_α) radiation source. For assessment of the statistical significance of differences, one-tailed Student's t-tests assuming unequal sample variance were

employed. Results were considered significantly different if $p < 0.05$. Abbriviations: DCM = dichloromethane; DMSO = dimethylsulfoxide; EtOH = ethanol; MeCN = acetonitrile; MeOH = methanol; THF = tetrahydrofuran

SWIR imaging configuration The *in vivo* imaging set-up employs excitation from a 10 W 808 nm laser (Opto Engine; MLL-N-808) coupled into a 910 μm-core metal-cladded multimode fiber (Thorlabs; MHP910L02) and diffused through a ground-glass plate (Thorlabs; DG10-220-MD). This yielded an excitation power density of 50 mW/cm^2. The InGaAs camera (Princeton Instruments, NIRvana 640) was cooled to -80 °C, the analog to digital (AD) conversion rate set to 10 MHz, the gain set to high, and exposure time was set to 100 ms, yielding an effective frame rate of 9.17 fps. The emitted light was directed from the imaging stage to the camera using a four inch square first-surface silver mirror (Edmund Optics, Part No. 84448), then filtered through two colored glass 1,000 nm longpass filters (Thorlabs FGL1000S) and focused onto the SWIR camera with a C-mount objective (Navitar SWIR-35). All images were background- and blemish-corrected within the LightField imaging software. ImageJ was used to average 10 frames for the displayed images, unless noted otherwise. Frame averaging was not used in videos unless otherwise noted. ImageJ was also used for all image measurements (pixel intensity average, standard deviation, etc.). Matlab (Mathworks) was employed to fit heart intensity fluctuations. Noninvasive SWIR imaging was performed in two NCRNU mice (32.5 g and 29 g, male, 22 weeks old, Taconic) and reproduced with a second batch of Flav7 (**2.3**) formulation in three additional NCRNU mice. Mice were anaesthetized and were placed in the imaging set-up, and one 200 μL bolus of Flav7 (**2.3**) in 1x phosphate buffered saline were injected via the tail vein while imaging the emission.

2.5.2 Experimental procedures

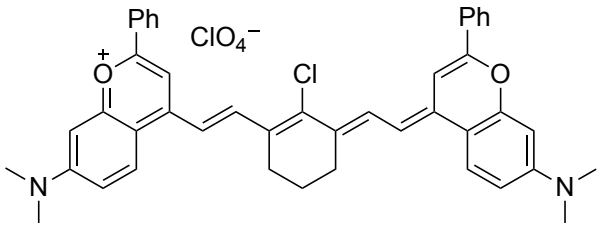

7-Dimethylamino flavylium heptamethine dye (**2.3, Flav7**); **4-((*E*)-2-((*E*)-2-chloro-3-(2-((*E*)-7-(dimethylamino)-2-phenyl-4*H*-chromen-4-ylidene)ethylidene)cyclohex-1-en-1-yl)vinyl)-7-(dimethylamino)-2-phenylchromenylium perchlorate** 7-*N*,*N*-dimethylamino-4-methyl-flavylium perchlorate (**2.1**) (31.1 mg, 0.0855 mmol, 2.4 equiv.), *N*-[(3-(anilinomethylene)-2-chloro-1-cyclohexen-1-yl)methylene]aniline hydrochloride **2.6** (13.0 mg, 0.0362 mmol, 1.0 equiv.) and anhydrous sodium acetate (9 mg, 0.1 mmol, 3 equiv.) were dissolved in EtOH (0.78 mL, anhydrous,) and heated to 90 °C for 6 hours. The solution was cooled to rt and evaporated onto silica gel. Dye **2.3** was purified via silica gel chromatography, eluting with a DCM/MeOH solvent gradient of 200:1, 150:1, 100:1, 80:1, 67:1 and 50:1. This procedure gave pure **2.3** (11.1 mg, 0.0145 mmol, 40%). ^{1}H NMR (500 MHz, DMSO-d_6): δ 8.21 (d, J = 10 Hz, 2H), 8.14 – 8.10 (m, 6H), 7.70 – 7.53 (m, 8H), 7.06 (d, J = 15 Hz, 2H), 6.96 (dd, J = 10 Hz, 2.5 Hz, 2H), 6.81 (d, J = 2.5, 2H), 3.14 (s, 12H), 2.87 – 2.81 (m, 4H), 1.91 (t, J = 6.3 Hz, 2H). ^{13}C NMR (126 MHz, DMSO-d_6): δ 156.9, 155.9, 154.6, 145.0, 144.5, 138.5, 132.0, 131.6, 131.3, 129.6, 126.7, 126.5, 113.9, 113.8, 112.4, 102.3, 97.9, 27.2, 21.3, {peak at 38.9-40.1 beneath DMSO-d$_6$ solvent peak}. HRMS (ESI$^+$): Calculated for $C_{44}H_{40}ClN_2O_2^+$ [M]$^+$: 663.2773; found: 663.2784. Absorbance (DCM): 522 nm (ε = 1.5 ± 0.2 x 10^4 $M^{-1}cm^{-1}$), 916 nm (ε = 6.3 ± 0.1 x 10^4 $M^{-1}cm^{-1}$), 1026 nm (ε = 2.4 ± 0.2 x 10^5 $M^{-1}cm^{-1}$). Emission (DCM, Ex. 730 nm): 1045 nm, Φ_F = 0.53 ± 0.03 %.

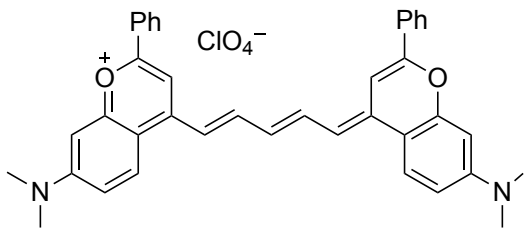

7-Dimethylamino flavylium pentamethine dye (2.4, Flav5); 7-(dimethylamino)-4-((1*E*,3*E*)-5-((*E*)-7-(dimethylamino)-2-phenyl-4*H*-chromen-4-ylidene)penta-1,3-dien-1-yl)-2 phenylchromenylium perchlorate 7-*N*,*N*-dimethylamino-4-methyl-flavylium perchlorate (**2.1**) (29.8 mg, 0.0819 mmol, 2.1 equiv), malonaldehyde bis(phenylimine) (10.2 mg, 0.0394 mmol, 1.0 equiv.), and anhydrous sodium acetate (9 mg, 0.1 mmol, 2.7 equiv.) were combined in acetic anhydride (0.66 mL). The solution was freeze-pump-thawed x3 and subsequently heated at 110 °C for 2.5h. The solution was let cool to rt and evaporated onto silica gel. Dye **2.4** was purified via silica gel chromatography, eluting with a DCM/MeOH solvent gradient of 200:1, 167:1, 143:1, 125:1, 111:1, 100:1, 67:1. The procedure yielded pure **2.4** (13.1 mg, 0.0198 mmol, 50%). ^{1}H NMR (500 MHz, DMSO-d_6): δ 8.2 (t, J = 12.8 Hz, 2H), 8.11 – 8.03 (m, 4H), 7.98 (d, J = 9.4 Hz, 2H), 7.66 (s, 2H), 7.61 – 7.52 (m, 6H), 7.07 (d, J = 13.2 Hz, 2H), 6.94 – 6.86 (dd, J = 9.2, 1.5 Hz, 2H), 6.82 (t, J = 12.3 Hz, 1H), 6.77 (s, 2H), 3.13 (s, 12H). ^{13}C NMR (126 MHz, DMSO-d_6): δ 156.3, 155.4, 154.2, 149.1, 145.7, 131.6, 131.2, 129.1, 126.1, 125.9, 115.3, 113.2, 110.9, 101.6, 97.4, {peak at 38.9-40.1 beneath DMSO-d$_6$ solvent peak}. HRMS (ESI$^+$): Calculated for $C_{39}H_{35}N_2O_2^+$ $[M]^+$: 563.2693; found: 563.2702. Absorbance (DCM): 546 nm (ε = 1.4 ± 0.1 x 10^4 $M^{-1}cm^{-1}$), 776 nm (ε = 4.8 ± 0.4 x 10^4 $M^{-1}cm^{-1}$), 862 nm (ε = 2.4 ± 0.2 x 10^5 $M^{-1}cm^{-1}$). Emission (DCM, Ex. 840 nm): 908 nm, Φ_F = 5 ± 2 %.

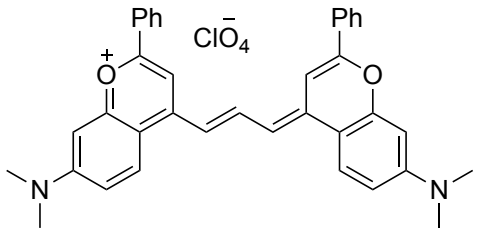

7-Dimethylamino flavylium monomethine dye (2.5, Flav3); **7-(dimethylamino)-4-((*E*)-3-((*E*)-7-(dimethylamino)-2-phenyl-4*H*-chromen-4-ylidene)prop-1-en-1-yl)-2-phenylchromenylium perchlorate** 7-*N*,*N*-dimethylamino-4-methyl-flavylium perchlorate (**2.1**) (49.8 mg, 0.137 mmol, 1.5 equiv.), paraformaldehyde (2.7 mg, 0.090 mmol, 1.0 equiv.), and anhydrous sodium acetate (15 mg, .18 mmol, 2.0 equiv) were combined in acetic anhydride (1.0 mL). The solution was freeze-pump-thawed x3 and heated at 70 °C for 30 m. The solution was cooled to rt and evaporated onto silica gel. Dye **2.5** was purified via silica gel chromatography, eluting with a DCM/EtOH solvent gradient of 200:1, 167:1, 143:1, 125:1, 111:1, 100:1. The most pure fractions, as determined by UV-Vis/IR spectroscopy were loaded onto a second silica gel column and run as before. The impure fractions from both columns were combined and run on another silica gel column with the same solvent system and gradient. This procedure yielded pure **2.5** (15.5 mg, 0.0243 mmol, 27%). ^{1}H NMR (500 MHz, DMSO-d_6): δ 8.81 (t, J = 12.9 Hz, 1H), 8.18 – 8.10 (m, 4H), 7.99 (s, 2H), 7.89 (d, J = 9.6 Hz, 2H), 7.67 – 7.57 (m, 6H), 7.16 (d, J = 13.0 Hz, 2H), 6.91 (dd, J = 9.3, 2.5 Hz, 2H), 6.72 (d, J = 2.5 Hz, 2H), 3.12 (s, 12H). ^{13}C NMR (126 MHz, DMSO-d_6) δ 156.7, 155.4, 154.2, 147.2, 145.5, 131.6, 131.1, 129.0, 126.4, 125.5, 115.9, 113.2, 110.6, 102.0, 97.1, {peak at 38.9-40.1 beneath DMSO-d$_6$ solvent peak}. HRMS (ESI$^+$): Calculated for $C_{37}H_{33}N_2O_2^+$ [M]$^+$: 537.2537; found: 537.2525. Absorbance (DCM): 530 nm (ε = 2.0 ± 0.1 x 10^4 $M^{-1}cm^{-1}$), 682 nm (ε = 3.9 ± 0.2 x 10^4 $M^{-1}cm^{-1}$), 746 (ε = 2.2 ± 0.1 x 10^5 $M^{-1}cm^{-1}$). Emission (DCM, Ex. 675 nm): 766 nm, Φ_F = 2.9 ± 0.5 %.

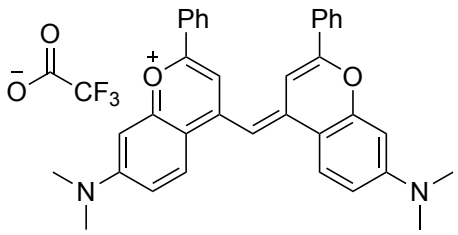

7-Dimethylamino flavyliym trimethine dye (**6, Flav1**); **(*E*)-7-(dimethylamino)-4-((7-(dimethylamino)-2-phenyl-4*H*-chromen-4-ylidene)methyl)-2-phenylchromenylium 2,2,2-trifluoroacetate** (**2.6**) 7-*N*,*N*-dimethylamino-4-methyl-flavylium *perchlorate* (**2.1**) (49.7 mg, .137 mmol, 1 equiv.) and anhydrous sodium acetate (25 mg, 0.31 mmol, 2.2 equiv) were dissolved in 10 mL EtOH and refluxed at 90 °C under air for 3.3 h. The mixture was cooled to rt and evaporated onto silica gel. Dye **2.6** was purified via silica gel chromatography and reverse-phase HPLC. Via silica gel chromatography, dye **2.6** was eluted with a DCM/MeOH solvent gradient of 400:1, 200:1, 167:1, 143:1, 125:1, 111:1, 67:1, and 33:1. The most pure fractions were further purified in aliquots by HPLC in a water/MeCN with 0.1% TFA solvent mixture. The method used is as follows: 70:30 for 2 min, gradient to 30:70 over 60 min, gradient to 5:90 over 20 min, followed by a hold for 5 min and subsequent re-equilibration to 70:30 for 10 min. The procedure yielded pure **2.6** (9.5 mg, 0.016, 11%). ^{1}H NMR (500 MHz, DMSO-d_6): δ 8.40 (d, J = 10.5 Hz, 2H), 8.17 (dd, J = 8.0, 1.7 Hz, 4H), 7.98 (s, 2H), 7.66 – 7.59 (m, 6H), 7.47 (s, 1H), 7.10 (dd, J = 9.4, 2.6 Hz, 2H), 6.99 (d, J = 2.6 Hz, 2H), 3.21 (s, 12H). ^{13}C NMR (126 MHz, DMSO-d_6) δ 158.96, 158.63, 158.39, 158.15, 157.90, 156.31, 155.19, 150.61, 132.60, 131.54, 129.76, 127.63, 126.97, 121.43, 119.03, 116.64, 115.01, 114.06, 112.09, 105.40, 103.64, 97.71 {peak at 38.9-40.1 beneath DMSO-d$_6$ solvent peak}. ^{19}F NMR (282 MHz, DMSO-d_6) δ -73.16. HRMS (ESI$^+$): Calculated for $C_{35}H_{31}N_2O_2^+$ [M]$^+$: 511.2380; found: 511.2366. Absorbance (DCM): 324 nm (ε = 3. ± 1. x 10^3 $M^{-1}cm^{-1}$), 484 nm (ε = 3. ± 1. x 10^3 $M^{-1}cm^{-1}$), 514 nm (ε = 4. ± 1. x 10^3 $M^{-1}cm^{-1}$), 650 nm (ε = 1.6 ± 0.5 x 10^4 $M^{-1}cm^{-1}$). Emission (DCM, Ex. 610 nm): 684 nm, Φ_F = 0.7 ± 0.5 %.

2.5.3 Table experimental procedures

Table 2.1 The $\lambda_{max,abs}$ values were obtained in DCM on a JASCO V-770 UV-Visible/NIR spectrophotometer with a 2,000 nm/min scan rate. Absorption coefficient values were obtained from serial dilutions using 10 mL and 5 mL volumetric flasks and 1 mL Hamilton glass syringes. All masses were determined on a Sartorius MSE6.6S-000-DM Cubis Micro Balance. Error reported in the SI reflects the standard deviation of the triplicate measurement. $\lambda_{max,em}$ values were obtained as described in the Figure 2.3 experimental procedure, below. The quantum yield values were collected as described in Figure 2.8C experimental procedures and further elaborated in Section 2.6.2, below.

Table 2.2 The raw photobleaching rate, k, was obtained by treating the reaction as pseudo first order [30] and taking the – slope of the linear region ($R^2 > 0.95$). To incorporate the respective absorption coefficients at 532 nm, the relative rate, k_{rel}, was calculated by dividing k by the relative absorption coefficient compared to dye **2.5**. These data were compared to **2.5** as it has the highest absorption coefficient at that wavelength. All error reported represents the propagated error from standard deviation of three replicates.

Table 2.3 In a similar fashion to the normalization of photobleaching rate for the number of incident 532 nm photons absorbed (Table 2.2 experimental procedures), photobleaching rates for **2.5** and HITCI at 730 nm excitation must be corrected before direct comparison. The raw values for the rates were determined as described in Table S1. The 730 nm LED source (ThorLabs) is non-monochromatic, with a Gaussian profile and FWHM bandwidth of 55 nm and the absorption coefficients for the two dye molecules change appreciably over this range. This, a slightly altered procedure must be used because of the non-monochromatic source and absorption. The convolution of the excitation source and the wavelength dependent cross-sections are calculated

for each dye, and these areas are used as the scalar factor correction to normalize the rates by the actual number of photons absorbed. The magnitude of this correction only altered the relative photobleaching rates by about 14% in favor of a faster decay for **2.5**. With this correction, **2.5** decays at a rate 4x slower than HITCI. The error reported represents propagated error from standard deviation of three replicates.

Table 2.4 The raw rates were determined as described in Table 2.2 experimental procedures. To compare the photobleaching rates taken at 532 nm monochromatic irradiation with the 1,050 nm non-monochromatic light source necessitates comparing the rates on a per-photon-absorbed basis. The convolution of the 1050 LED (Thor Labs) emission spectrum and the dye cross-section between 800 and 1200 nm was calculated to obtain an effective cross-section. This effective cross-section can then be scaled by the number of photons per second from the measured fluence. The ratio obtained (0.53) represents the relative number of photons absorbed per second between the two experiments, allowing for a quantitative comparison of how the rate behaves while varying excitation wavelength. Dividing the photobleaching rate at 1050 nm by this factor yields the relative rate values listed. The error represents the standard deviation of three experiments. The results indicate that **2.3** bleaches 1.7×10^3 times faster with a 532 nm photon than with a 1050 nm photon, suggesting that the photobleaching mechanisms with high and low energy photons are distinct.

2.5.4 Figure experimental procedures

Figure 2.2 Flavylium **2.1** at 2.5 mM in EtOH, with excess sodium acetate was heated to 85 °C after (A) no removal of oxygen and (B) freeze-pump-thaw x3. Aliquots were taken via syringe and

further diluted in DCM for analysis by UV-Vis-IR (Cary 4000 UV/Vis spectrophotometer, Agilent Technologies) with a scan rate of 2,000 nm/min.

Figure 2.3 Absorbance spectra were obtained in DCM on a JASCO V-770 UV-Visible/NIR spectrophotometer with a 4,000 nm/min scan rate. Plotted are the baseline corrected and normalized data. Emission spectra were taken in DCM on either a Horiba Instruments PTI QuantaMaster Series fluorometer (**2.6**), a Fluoromax-3 spectrofluorometer (**2.1**, **2.3**–**2.5**), or home-built InGaAs array detector (Princeton Instruments). For **2.6**, the following parameters were used: ex. 610 nm, emission collected from 620 – 900 nm, slits 5nm, step size 1 nm, integration time 1 s. Plotted is the DCM corrected, baseline corrected, normalized data. For **2.1**, and **2.3**–**2.5**, the following parameters were used: slits 5 nm, step size 1 nm, integration time, 0.25 s. Excitation values and emission collection were as follows: **2.1** (ex. 460, collection 470–800 nm), **2.5** (ex. 675 nm, collection 685–950 nm), **2.4** (ex. 840 nm, emission 850–1100 nm), **2.3** (ex. 730 nm, emission 950–1400). Plotted are the baseline corrected, normalized data.

Figure 2.4 Each dye was dissolved in dichloromethane (anhydrous, not degassed), until Abs ~1. Solution (1.4 mL) was then transferred to a 1.5 mL cuvette with a sealed screw-top lid to minimize evaporation. The cuvette was irradiated with a 532 nm laser at 0.53 ± 0.05 Wcm^{-2} fluence. The fluence was taken as the average over 1/*e* of the Gaussian profile (FieldMate Laser Power Meter). The absorbance was monitored at distinct time points (JASCO V-770 UV-Visible/NIR spectrophotometer or a PerkinElmer Lambda25 spectrophotometer). From baseline corrected data, the percent absorbance at $\lambda_{max,abs}$ was plotted. The error represents standard deviation of the triplicate measurement.

Figure 2.5 Solutions of dye in dichloromethane (anhydrous, not degassed, 1.4 mL, Abs ~ 1) were irradiated with a 750 nm LED (ThorLabs mounted LED and collimation adaptor) and monitored

by UV-Vis-NIR spectroscopy. The power density (140 ± 10 $mWcm^{-2}$) was measured with a FieldMate Laser Power Meter. Percent absorbance remaining was taken with respect to $\lambda_{max,abs}$ at t = 0 min.

Figure 2.6 Solutions of dye in dichlormethane (anhydrous, not degassed, 1.4 mL, Abs ~1) were irradiated with a 1050 nm LED (ThorLabs mounted LED and collimation adaptor) and monitored by UV-Vis-NIR spectroscopy. The intensity (16.3 ± 0.4 $mWcm^{-2}$) was measured with a FieldMate Laser Power Meter. Percent absorbance remaining was taken with respect to $\lambda_{max,abs}$ at t = 0 min.

Figure 2.7 Flav 7 (**2.3**), IR-26 and IR-1061 were dissolved in DCM and their concentrations were adjusted until matched absorbance values were reached at 808 nm, as observed by UV-Vis-NIR spectroscopy (Cary 5000 UV-VIS-NIR spectrometer).

Figure 2.8A–B Flav 7 (**2.3**), IR-26 (Exciton) and IR-1061 (Sigma Aldrich) were diluted in DCM until matching absorbance was achieved at 808 nm (Figure 2.7). Spatially dispersed 808 nm illumination was used to image 1 mL samples in 2.5 mL cuvettes of the SWIR dyes alongside a DCM blank. Each dye was compared at the same position to ensure consistent camera illumination. SWIR images were collected on an InGaAs camera (Princeton Instruments, NIRvana 640) with a 1000 nm long-pass filter. The camera was cooled to -80 ^{o}C, the analog to digital (AD) conversion rate set to 2 MHz, the gain set to high, and different exposure times used to achieve sufficient signal and/or frame rates. All images were background- and blemish-corrected within the LightField imaging software. All analysis was performed using ImageJ and Matlab (Mathworks). Bar graph intensities were taken as the average camera intensity for 10 frames, background corrected to the DCM blank, with the error corresponding to standard deviation.

Figure 2.8C IR-26 and IR-1061 were diluted in DCM to 0.5 maximum absorbance for quantum yield measurements. Absorption spectra were measured using Cary 5000 UV-VIS-NIR

spectrometer, and emission spectra were recorded using a Fluoromax-3 spectrofluorometer, or a home-built InGaAs array detector (Princeton Instruments). Quantum yield was performed using a Labsphere integrating sphere and a 5 mW 405/780 nm laser, with optical chopping at 210 Hz. The output was collected using either a calibrated silicon or InGAs detector connected to a Lock-In amplifier (Stanford Research Instruments). Colored Glass Filters were used to spectrally separate the fluorescence, and the final quantum yield was corrected for reflectance and leakage of the filter.

Figure 2.9 Solutions of **2.3** were prepared in DCM with an Abs ~ 2.3. Aliquots of 2.5–3 mL were evaporated, dissolved in MeCN, sonicated for ~1 min, and additive solvent was added (if applicable) to reach the appropriate volume. Absorbance was monitored over time by UV-Vis-NIR spectroscopy, and absorbance remaining was taken with respect to $\lambda_{max,abs}$ at t = 0 min.

Figure 2.10 A stock solution of Flav7 (**2.3**) in acetonitrile was prepared with Abs ~ 1.4. Aliquots were diluted to 2x the volume to achieve 0%, 10%, 20% and 50% water in acetonitrile. Plotted are the baseline corrected and normalized data.

Figure 2.11 A stock solution of Flav7 (**2.3**) in acetonitrile was prepared with Abs ~0.7. Aliquots were diluted to 2x volume to reach 0%, 10%, 20% and 50% water in acetonitrile, such that the concentration of Flav7 (**2.3**) is constant in each sample. (A) Excitation data were collected between 700-1,015 nm with detection at 1,045 nm using the following parameters: 15 nm excitation slit width, 20 nm emission slit width, 1 nm step size, 0.1 sec integration time. The default excitation correction was used with the bias set at -1.047, and background values manually input. (B) Emission data were collected between 900-1300 nm with excitation at 870 nm using the following parameters: 15 nm excitation slit width, 30 nm excitation slit width, 1 nm step size, 0.1 sec integration time. No emission correction was used, and the background was automatically acquired. Plotted are the baseline corrected data for both excitation and emission.

Figure 2.12 A stock solution of Flav7 (**2.3**) in acetonitrile was prepared with Abs ~ 1.4. An aliquot (1mL) was diluted with 1mL water and the absorbance was measured. After 1.5h, solvent was evaporated, **2.3** was re-dissolved in 2 mL acetonitrile, sonicated, and absorbance was measured. Plotted are the baseline corrected and normalized data.

Figure 2.13 The lipid, mPEG-DSPE (20 mg) (Laysan Bio, Inc, 5,000 average MW) was dissolved in 2.0 mL MilliQ water and sonicated in a bath sonicator until the lipid was fully dissolved. Flav7 (**2.3**) (0.1 mg) was dissolved in DMSO (1.0 mL anhydrous, Sigma Aldrich). The aqueous lipid solution and the DMSO/Flav7 (**2.3**) solution were combined at 0 °C. The resulting solution was sonicated with a probe sonicator at 35% power for 5 min at 0 °C. The solution was then transferred to a 4 mL centrifuge filter (10kDa, EMD Millipore Amicon Ultra) and a series of washes with 1x PBS buffer were performed. Each wash consisted of centrifugation (4000 xg for 5-10 min, Sorvall ST 16 centrifuge - Thermo Scientific), removing the filtered solvent and replacing it with the same volume of 1x PBS. The filter was inverted several times after buffer addition. This was performed 6x or until the amount of DMSO left is <1%. The formulations were then concentrated by centrifugation to 5x concentration for use *in vivo* and 2x for use *in celluo*. For the vehicle, the exact same procedure was followed but without the addition of dye. The size of the micelle formulations were characterized by dynamic light scattering (DLS) on a Zetasizer NanoSampler (Malvern). A dilution of 20 µL in 2 mL MilliQ water was taken for the DLS measurements. The size and error values (standard deviation) were taken from the intensity trace, peak one, as the average of 3 experiments (15 scans each). The pH was measured on a SympHony B40PCID benchtop Multi Parameter Meter (VWR). UV/Vis/NIR spectroscopy and fluorescence spectroscopy were performed as described in the general experimental procedures.

Figure 2.14 HEK293 cells were donated by the lab of Professor Jorge Torres. Propidium iodide was purchased from VWR and used without purification. 96-well v-bottom plate was plated with a cell density of 100,000 cells per well with a final volume of 150 μL in DMEM supplemented with FBS and Pen/Strep. Micelles were concentrated to 2x and 50 μL of the final dilution were added to each well of cells to reach a final volume of 200 μL. The concentration utilized was equivalent to the micelle concentration in mouse serum for the *in vivo* experiments. Cells were incubated for 1 hour at 37 ˚C and 5% CO_2. Following incubation, cells were washed three times by centrifugation (3,000 rpm, 3 min, 4 ˚C). PI solution (2μL of 1 mg/ml in PBS) were added to each well. Cells/PI were transferred to FACS tubes with a final volume of 300 μl FACS buffer (PBS + 1% FBS). Cells were incubated on ice for 15 minutes prior to flow cytometry measurement. Flow cytometry was performed on a 2-laser BD FACSCalibur Flow Cytometer. PI fluorescence was measured on FL2 channel. Data was analyzed on FlowJo by mean FL2 fluorescence, and splitting the population at 10^2 as a live/dead line.

Figure 2.15–2.19 All animal experiments were conducted in accordance with approved institutional protocols of the MIT Committee on Animal Care. No blinding or randomization was required for the animal studies.

2.6 Notes relevant to Chapter Two

2.6.1 Dye structures and emission maxima for Figure 2.1.[3]

Chart 2.1 Dye structures and emission maxima for Figure 2.1

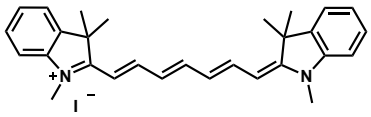

Cy7: HITCI
(1,1',3,3,3',3'-hexamethylindotricarbocyanine iodide)
$\lambda_{max,em}$ = 773 nm (EtOH)[a]

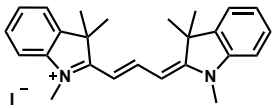

Cy3: HICI
(1,1',3,3,3',3'-Hexamethylindocarbocyanine iodide)
$\lambda_{max,em}$ = 556 nm (acetonitrile)[b]

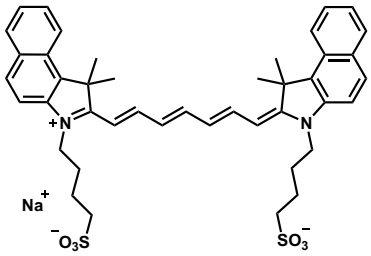

ICG (indocyanine green), IR-125
$\lambda_{max,em}$ = 818 nm (EtOH)[a]

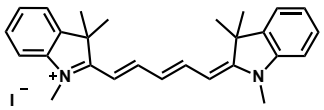

Cy5: HIDCI
(1,1',3,3,3',3'-hexamethylindoledicarbocyanine iodide)
$\lambda_{max,em}$ = 650 nm (acetonitrile)[b]

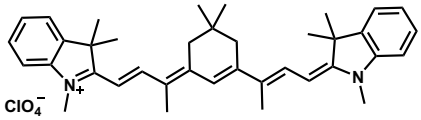

Cy9: ONITCP
(1,1',3,3,3',3'(3,3')-octamethyl-3,5-neopentylene-2,2'-indotetracarbocyanine perchlorate)
$\lambda_{max,em}$ = 888 nm (EtOH)[a]

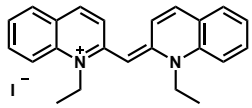

1,1'-diethyl-2,2'-cyanine iodide (PIC-I)
$\lambda_{max,em}$ = 570 nm (EtOH)[c]

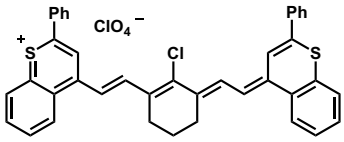

IR-26
$\lambda_{max,em}$ = 1129 nm (dichloromethane)

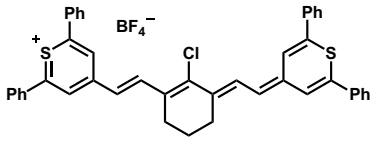

IR-1061
$\lambda_{max,em}$ = 1081 nm (dichloromethane)

[3] (a) ref [31]. (b) ref [32]. (c) ref [33].

2.6.2 Solvent study on Flav7

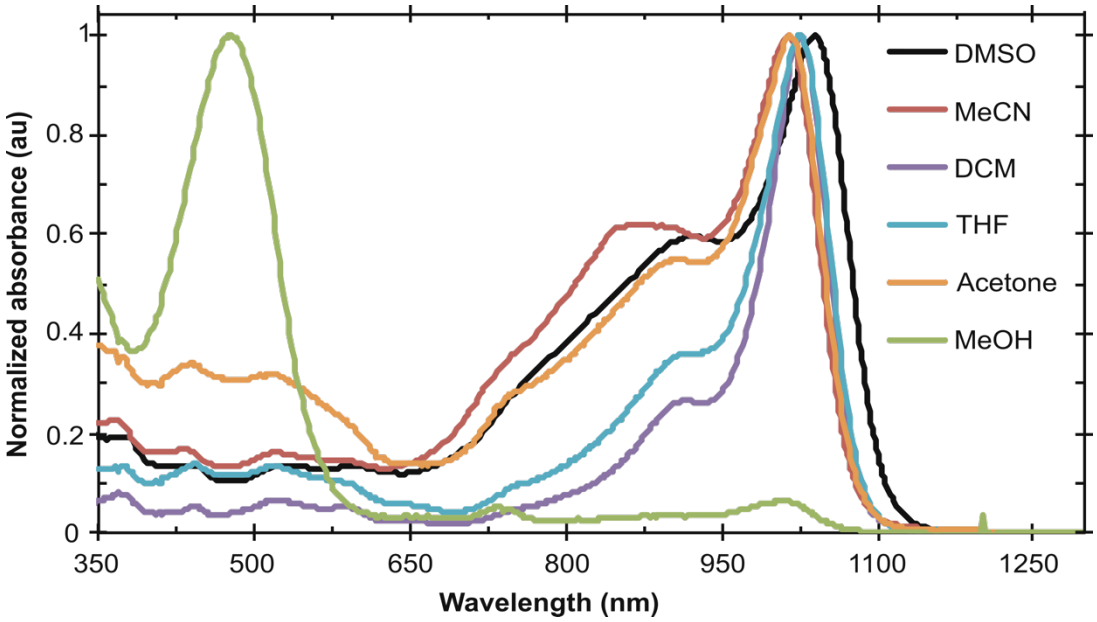

Figure 2.20 Normalized absorption spectra of Flav7 (**2.3**) in several solvents. The concentrations used were 2–10 x 10^{-5} M. While there is minimal variation in $\lambda_{max,abs}$, spectral broadening in polar solvent is indicative of the stabilization of an asymmetric electronic structure.[18]

Experimental: Flav7 (**2.3**) was dissolved in anhydrous solvents DMSO, MeCN, DCM, THF, MeOH, and acetone (not anhydrous). All samples were sonicated before taking an absorbance spectrum (see general experimental procedure for instrument and settings), with a baseline in the appropriate solvent. The concentrations were as follows: 2 x 10^{-6} M for acetone, THF, and MeOH, 5 x 10^{-5} M for DCM and 1 x 10^{-5} M for DMSO and MeCN. These data were baseline corrected to 1,300 nm and normalized.

Table 2.5 $\lambda_{max,abs}$ (nm) in organic solvents.

compound	THF	DCM	Acetone	MeCN	DMSO	MeOH
2.3	1026	1026	1016	1013	1039	476
2.4	848	862	854	848	868	845

Experimental: Dyes were dissolved in the appropriate solvents and UV-Vis-NIR spectrometry was performed as described in the experimental procedure for Figure 2.20. From the baseline corrected and normalized data, the $\lambda_{max,abs}$ values were obtained.

Table 2.6 Solubility limits of Flav7 (**2.3**) in organic solvents.

compound	THF	DCM	Acetone	MeCN	DMSO	MeOH
Solubility	M	Y	Y	M	Y	S

Solubility key: Y (yes) = more than 0.1 mg/mL, M (moderate) = between 0.05 and 0.1 mg/mL, S (sparingly) = less than 0.05 mg/mL. Solubilities determined by visual inspection.

Experimental: The mass of **2.3** (between 0.040 mg and 0.160 mg) was determined on a micro balance, and solvent was added using Hamilton microliter syringes (100 µl and 250 µl) until no precipitate was visible to the eye. Brief sonication (<30 seconds) in a bath sonicator was used. Solubilities were determined from the triplicate measurement.

2.6.3 Fluorescence Quantum Yields[4]

The photoluminescence quantum yield of a dye or material is defined as follows

$$QY = P_E/P_A \quad (1)$$

Where $P_{E,A}$ are the number of photons absorbed and emitted respectively. To determine absolute quantum yield, we either use a known standard (relative method), or measure the number of photons absorbed and emitted independently (absolute method). Due to the lack of a bright consistent standard in the SWIR range (1,000–2,000 nm), the absolute method is preferable. Here, we describe our procedure for measuring quantum yields in the shortwave infrared, and compare several SWIR emissive dyes.

Absolute measures of quantum yield

To perform an absolute quantum yield measurement, we use an integrating sphere, where a standard cuvette is illuminated on all sides by scattering a laser against white Teflon. The direct scatter is obfuscated by a baffle, and a side port is used with a large-area detector (E.G. 818VIS/IR from Newport). We modulate the laser using an optical chopper, and the photogenerated current is measured on a lock-in amplifier. In this way, pA signals can be measured against large constant backgrounds. We record the current at the chopping frequency using both a solvent filled blank, and the fluorophore. A filter is placed in front of the detector that only allows the fluorescence to pass through, and the procedure is repeated. The simplest calculation of quantum yield is therefore,

$$\frac{P_E}{P_A} = \frac{I_{SF} - I_{NSF}}{I_{NSNF} - I_{SNF}}, \quad (2)$$

Where (N)S(N)F denotes (no) sample and (no) filter respectively. This approach neglects the impact of detector quantum efficiency at the wavelength of excitation, and the emitted wavelength.

[4] Work by Justin Caram

In Figure 2.6.1 we plot the relative external quantum efficiency (EQE = $\eta = I_{rel}/P_A$) of the detector (Newport, 818IR Germanium). We calculate the average response over the emitted wavelength range as follows,

$$\eta_{em} = \frac{\int_{\lambda_{min}}^{\lambda_{max}} d\lambda \eta(\lambda) S(\lambda)}{\int_{\lambda_{min}}^{\lambda_{max}} d\lambda S(\lambda)}, \quad (3)$$

where S(λ) is the measured PL spectrum. For excitation, we evaluate the EQE at λ_{exc}. These correction terms go into equation 2.

$$\frac{P_E}{P_A} = \frac{(I_{SF} - I_{NSF})/\eta_{em}}{(I_{NSNF} - I_{SNF})/\eta_{exc}} \quad (4)$$

For excitation at 780, and emission in the 1100-1200 range, η can range over a factor of 2, making this correction crucial to accurate QY determination. To further refine our estimate, we consider the light emitted by the sample (the fluorescence) and detected in I_{SNF}. We adjust equation 5 by subtracting the emitted photons from the denominator.

$$\frac{P_E}{P_A} = \frac{(I_{SF} - I_{NSF})/\eta_{em}}{(I_{NSNF} - I_{SNF})/\eta_{exc} - (I_{SF} - I_{NSF})/\eta_{em}} \quad (5)$$

This tends to lower the observed quantum yield. The last step is considering reflection and loss due to the filter. Filter transmission can be measured and divided to give the final estimate = $\Phi_{F(eq.5)}/T_f$.

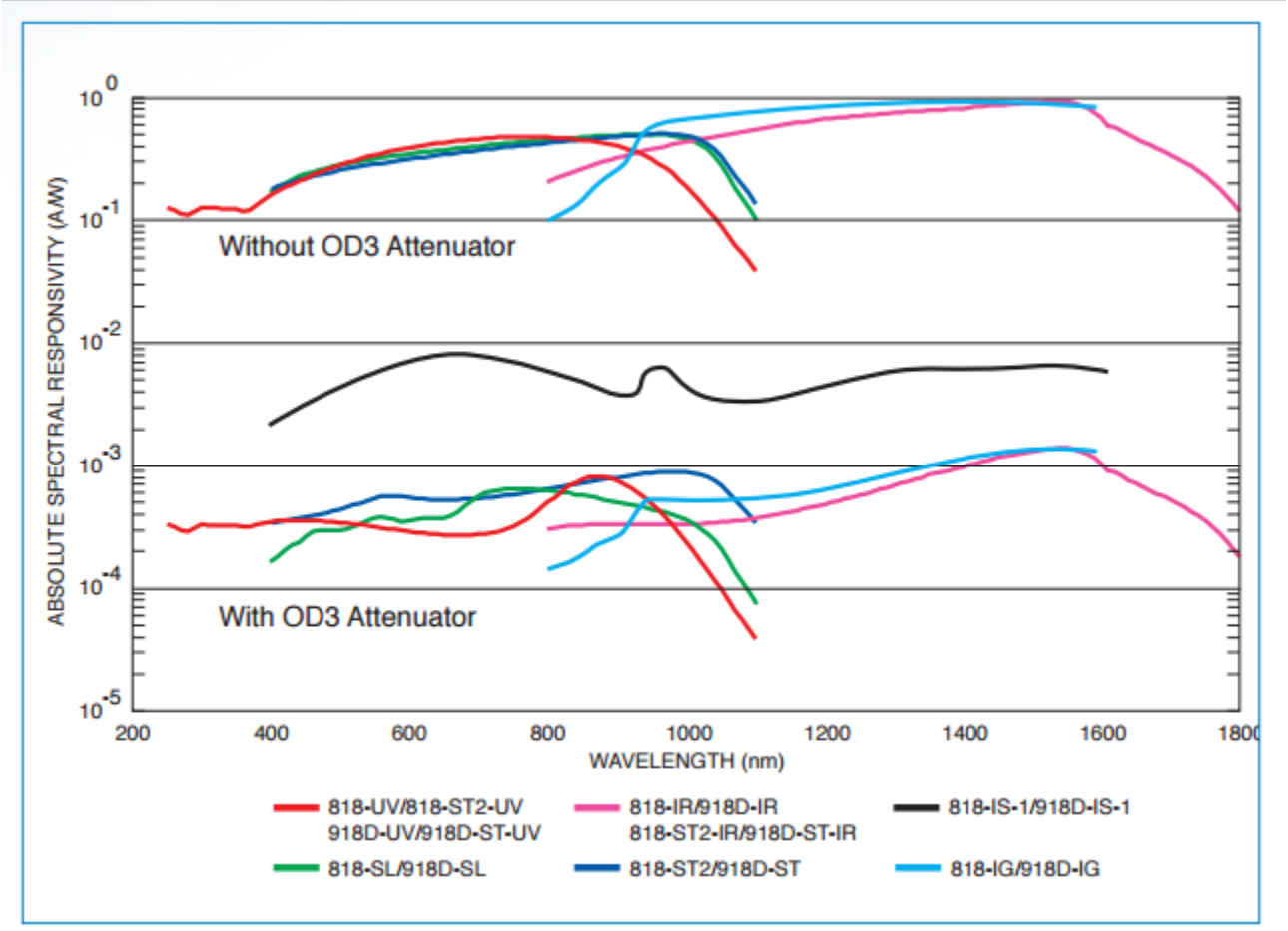

Figure 2.21 Detector response taken from Newport instruments. We use the 818IR calibrated photodiode (germanium).

Reabsorption Correction: Including sample/solvent reabsorption is typically done using a dilution series. However, in the case of IR dyes, there are significant solvent absorption in the spectra. Therefore, and alternative approach is necessary. As a first step, we will use the absorption and emission spectrum collected at the same angle (0 or 180 degrees). We will use this geometry to calculate the effect of absorption on the emission. We will calculate the effect of sample penetration and reabsorption on the "real emission spectrum" f(λ). We derive a correction factor R(λ), such that R(λ)f*(λ) = f(λ), the measured experimental emission spectrum.

$$R(\lambda) = \frac{1}{L}\int_0^L dx 10^{-x/L(A_{exc}+A(\lambda))} = \frac{1-10^{-(A_{exc}+A(\lambda))}}{(A_{exc}+A(\lambda))ln(10)} \quad (6)$$

The results are shown in Figure 2.22. Using this, we then derive a correction factor associated with reabsorption in the integrating sphere. For simplicity, we assume normalize the spectrum at 1,300 nm, where no reabsorption occurs, and integrate the ratio of the "real spectra" to the reabsorption corrected measure. Our final quantum yield is multiplied by this correction factor.

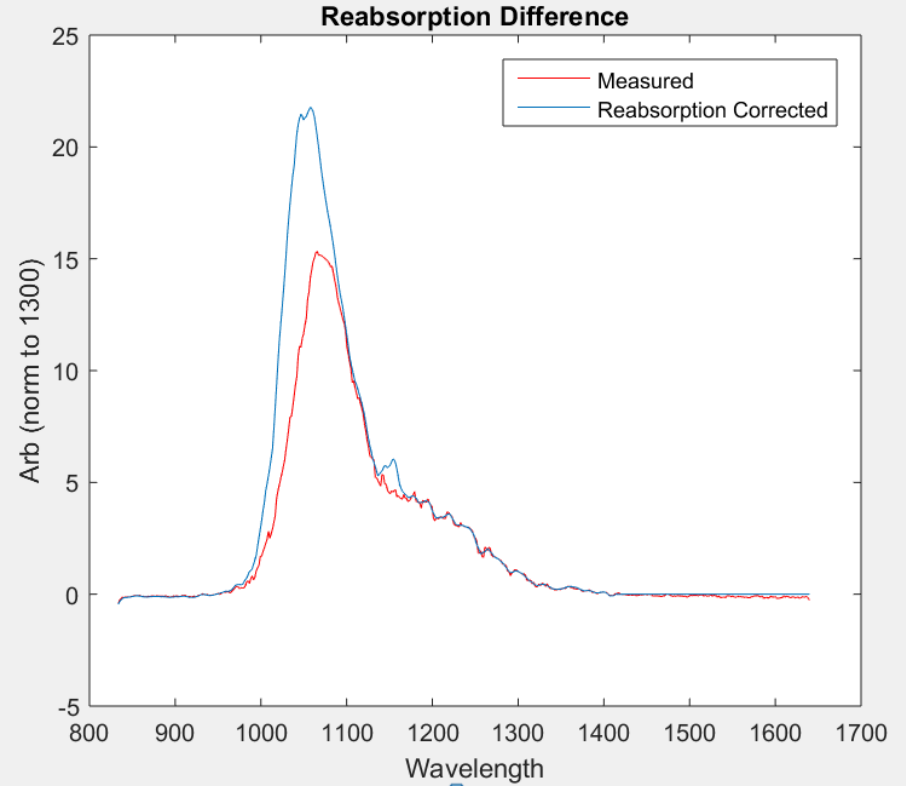

Figure 2.22 Reabsorption corrected spectroscopy.

Comments on overall approach: Our approach enables the rapid determination and comparison of quantum yield, and allows us to obtain results comparable to those described in the literature for IR26 (0.05% from Beard and Nozick, 0.09% from Resch-Genger in DCE). Unlike prior methods, this approach does not spectrally resolve emission, and can be completed in under 1

minute, enabling rapid quantification and comparison among different samples. The use of single detector also enables lock-in detection, decreasing background. However, our approach does not allow us to fully consider reabsorption, as we do not account for the geometry of emission and reabsorption within the integrating sphere. While equation 2.6 partially accounts for reabsorption (and is consistent with the approach provided in Beard and Nozick), it may account for the ~2 difference between our measurement and the measurement of Resch-Genger. Reabsorption is particularly important in the SWIR, as overtone solvent vibrational modes contribute to absorption (and cannot be eliminated using conventional dilution.

In Table 2.6.1, we provide a list of SWIR dyes whose QY have been measured using these methods.

Table 2.7 Φ_F values (reported as %) for SWIR fluorophores, analyzed as describe above.

Dye	**Eq. (2.2)**	**Eq. (2.4)**	**Eq. (2.5)**	**Φ_F**	**Error (±)**
Flav7 (**2.3**)	0.79	0.4	0.39	0.53	0.03
IR1061	0.51	0.26	0.26	0.32	0.04
IR26	0.06	0.028	0.028	0.05	0.03

All QY are corrected for filter transmission. The values in Eq. 2.2 are derived from equation 2, Eq. 4.2 from equation 4, and Eq. 5.5 from equation 5, listed above. The final, reabsorption corrected quantum yield values are Φ_F, as described in the text. Error is propagated from uncertainty in photodiode current, and repeat measurements with different sample concentrations.

2.6.4 Formulation optimization

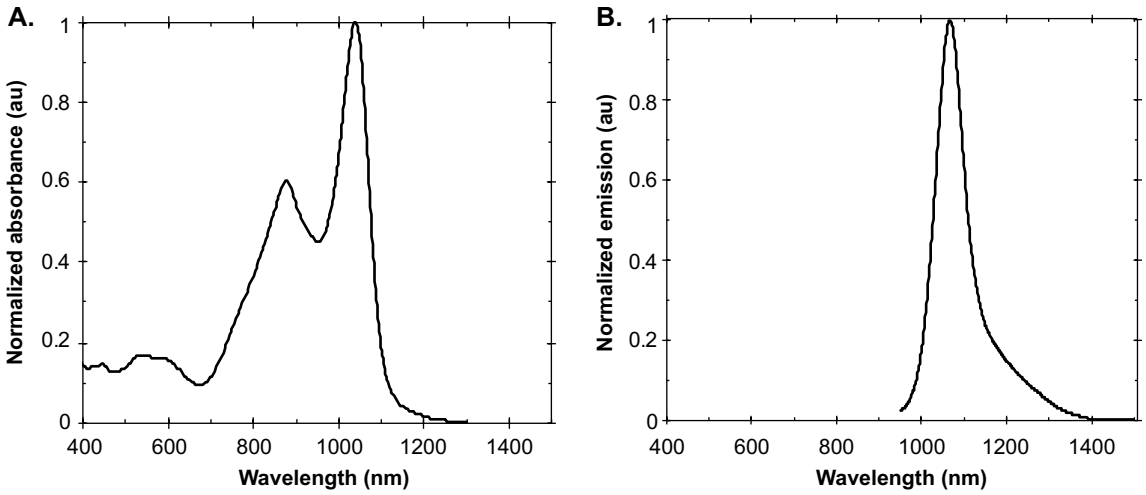

Figure 2.23 (A) Absorbance and (B) photoluminescence spectra (ex. 808 nm) of Flav7 (**2.3**) encapsulated in mPEG-DSPE/poly(acrylic acid) micelles. The spectra display minimal aggregation in an acidic environment (pH ~3).

Experimental: Flav 7 (**2.3**) (0.1 mg) and poly(acrylic acid) (2.2 mg) (Sigma-Aldrich, 1,800 average MW) were dissolved in 1.2 mL anhydrous DMSO (Sigma Aldrich) and sonicated briefly in a bath sonicator. 20 mg mPEG-DSPE (Laysan Bio, Inc, 5000 average MW) was dissolved in 2.0 mL water (MilliQ water) and sonicated in bath sonicator. 1.0 mL of the DMSO solution was transferred into the 2.0 mL aqueous solution, placed in an ice bath, and sonicated for 5 min in a probe sonicator (35% power was used). The solution was transferred to a 4 mL centrifuge filter (10kDa, EMD Millipore Amicon Ultra). Six repeated washes were performed by centrifugation at 4,000 xg (Sorvall ST 16 centrifuge - Thermo Scientific). Wash 1 was for 15 mins, wash 2 for 10 mins, and washes 3-6 for 5 min each. After each wash the filtered solvent was removed and replaced with the same volume of MilliQ water. The filtrations were monitored by UV-Vis and the disappearance of a DMSO absorbance peak at ~1160 could be seen.

Notes: This formulation is analogous to that previously employed for SWIR imaging of IR-1061 (Ref. 11). When buffer exchanged above pH 4, considerable aggregation was observed (analogous to that observed in Figure 2.13, thus we did not move forward with this formulation.

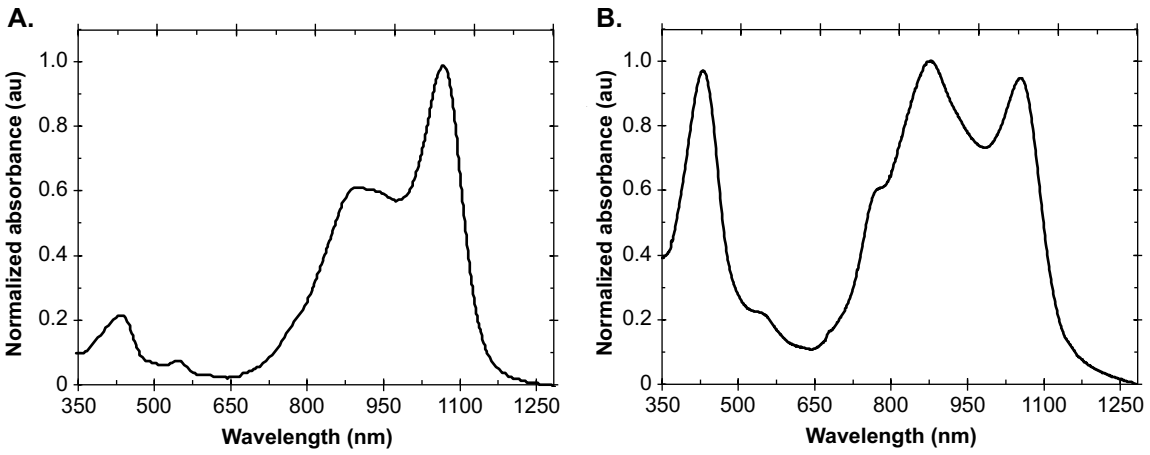

Figure 2.24 (A) Absorbance of IR-1061 encapsulated in mPEG-DSPE/poly(acrylic acid) micelles displaying minimal aggregation in an acidic environment (pH ~3). (B) Absorbance of IR-1061 encapsulated in mPEG-DSPE micelles in PBS buffer.

Experimental: For (A), 0.1 mg of IR-1061 and poly(acrylic acid) (2.2 mg) (Sigma-Aldrich, 1,800 average MW) were dissolved in 1.2 mL anhydrous DMSO (Sigma Aldrich) and sonicated briefly in a bath sonicator. 20 mg mPEG-DSPE (Laysan Bio, Inc, 5000 average MW) was dissolved in 2.0 mL water (MilliQ water) and sonicated in bath sonicator. 1.0 mL of the DMSO solution was transferred into the 2.0 mL aqueous solution, placed in an ice bath, and sonicated for 5 min in a probe sonicator (35% power was used). The solution was transferred to a 4 mL centrifuge filter (10kDa, EMD Millipore Amicon Ultra). Six repeated 5 min washes with water were performed by centrifugation at 4000 xg (Sorvall ST 16 centrifuge - Thermo Scientific). After each wash the filtered solvent was removed and replaced with the same volume of MilliQ water. The filtrations were monitored by UV-Vis and the disappearance of a DMSO absorbance peak at ~1160 could

be seen. For (B), 0.1 mg of IR-1061 was dissolved in DMSO, sonicated briefly and immersed in an mPEG-DSPE water solution at pH = 3.9, and sonicated for 5 min at 35%. The solution was then washed in a centrifuge filter 6x with MilliQ water and 1 time with 1x PBS, to bring the micelles to pH = 7.4.

Notes: When formulations were prepared with IR-1061 both aggregation (by the appearance of an absorbance peak at ~880 nm) and decomposition (by appearance of an absorbance peak at ~ 430 nm) were observed upon buffer exchange with PBS. This decomposition was not observed with Flav7 (**3**) indicating **3** not only has superior Φ_F but also enhanced stability at biologically relevant pH.

2.6.5 Determination of perchlorate counterion by X-ray photoelectron spectroscopy[5]

Samples were prepared by dissolving in DCM, drop-casting repeatedly onto a copper sample holder, and drying *in vacuo*. Survey and high-resolution scans were acquired at 160 and 20 eV pass energy respectively, with step sizes of 1 and 0.1 eV. As the samples were not conductive, the charge neutralizer filament was used. Data analysis and quantification was performed with Casa-XPS software. The atomic relative sensitivity factors used were from the Kratos library within the Casa software.

High-resolution X-ray photoelectron scan of the binding energies from 193 – 210 eV, showing distinct peaks for ClO_4^- and Cl^- at three locations on the sample of **2.4**. The presence of Cl^- is rationalized by the coexistence of Na^+. The relative increase in area % of Cl^- in position 3 is accompanied by an increase in Na^+ content at position 3 (above, 0.37 atomic% Na^+ in position 3

[5] XPS Experiments performed by Ignacio Martini

vs 0.23 atomic% Na^+ in positions 1 and 2). These data support that ClO_4^- is retained as the counterion throughout the synthesis.

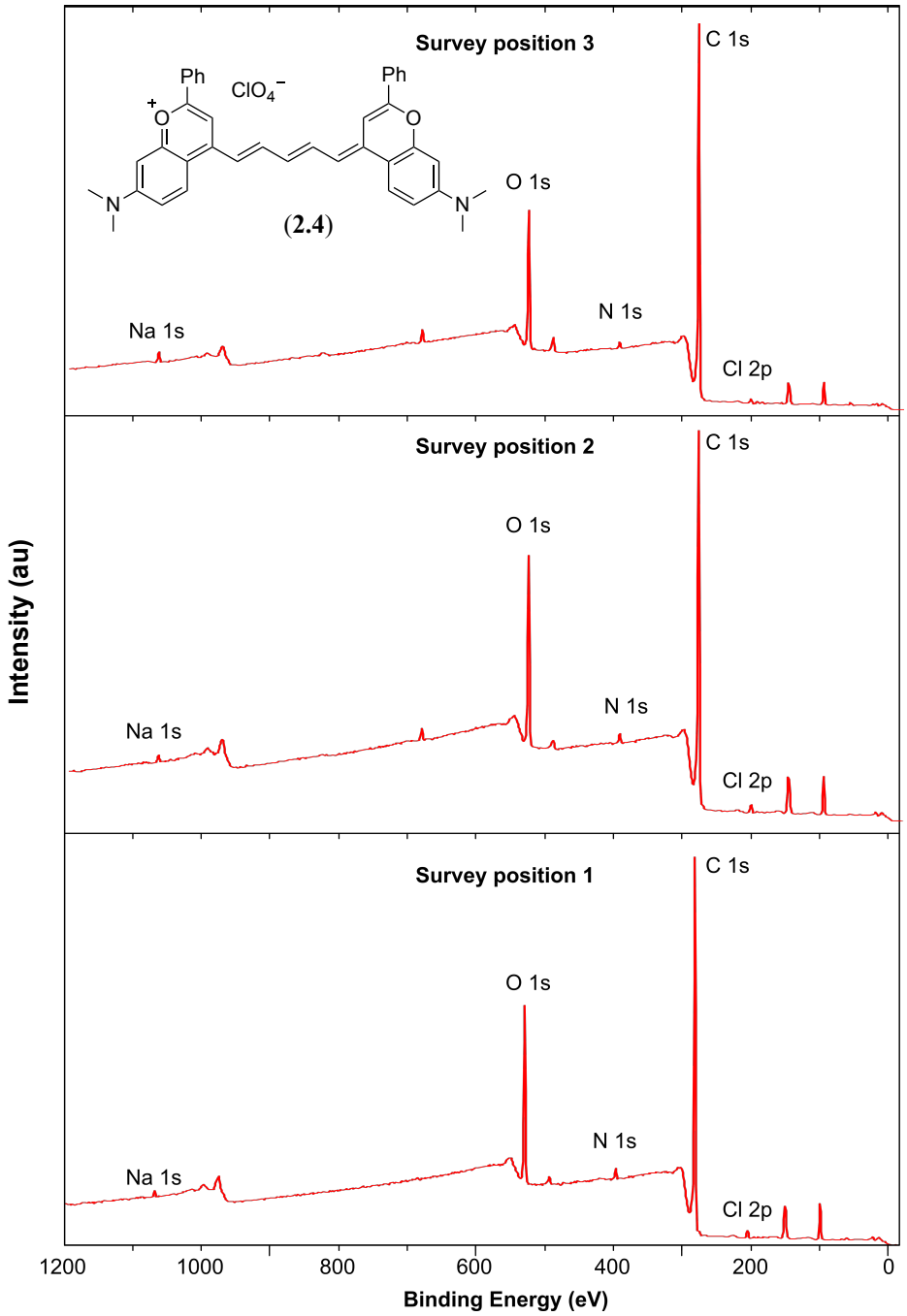

Figure 2.25 X-ray photoelectron scan of the binding energies from 0 – 1,200 eV, showing peaks for Na, O, N, C, and Cl at three locations on the sample of **2.4**.

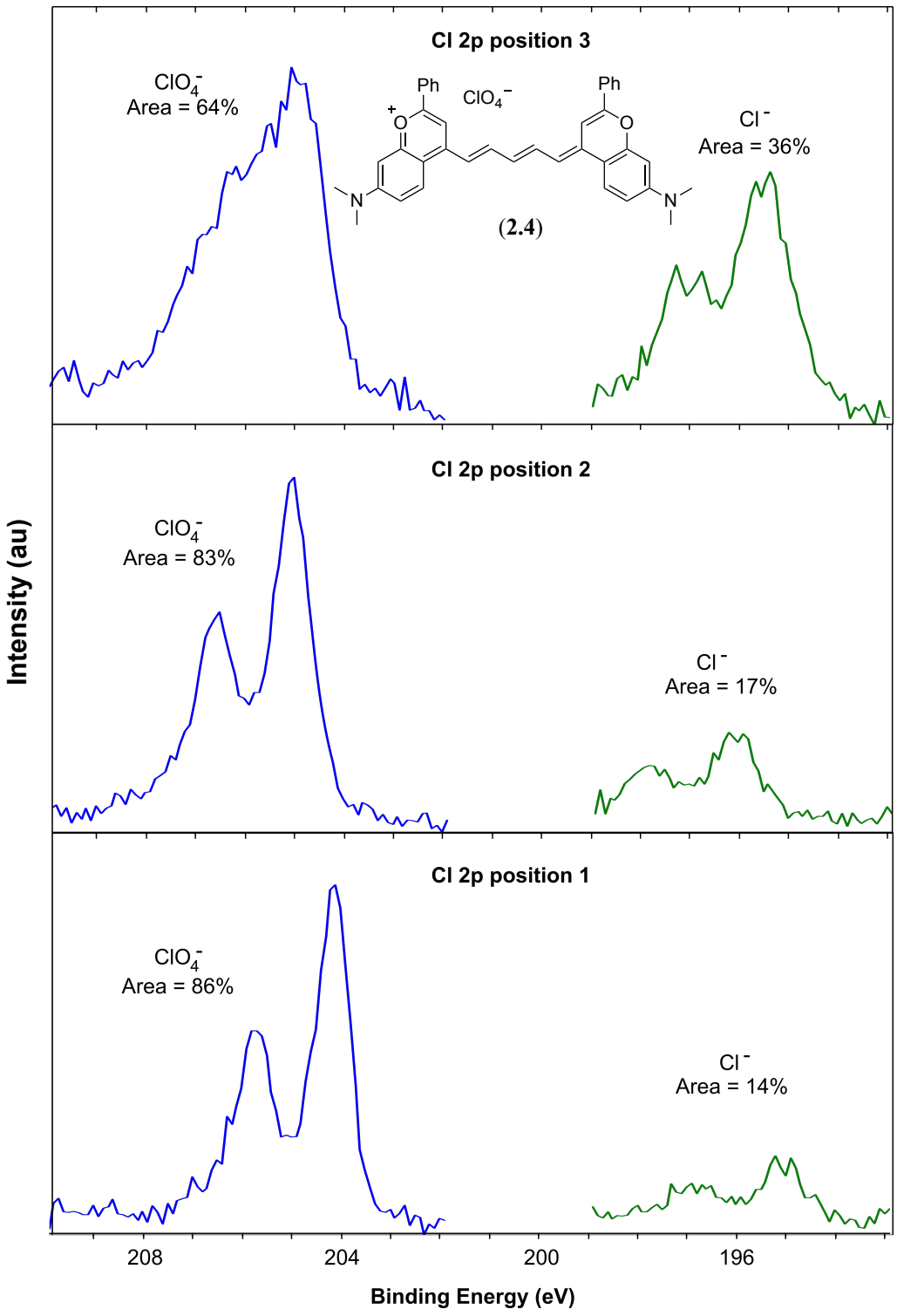

Figure 2.26 High-resolution X-ray photoelectron scan of the binding energies from 193–210 eV, showing distinct peaks for ClO_4^- and Cl^- at three locations on the sample of **2.4**.

2.7 Spectra relevant to Chapter Two

2.7.1 ^{1}H NMR Spectra

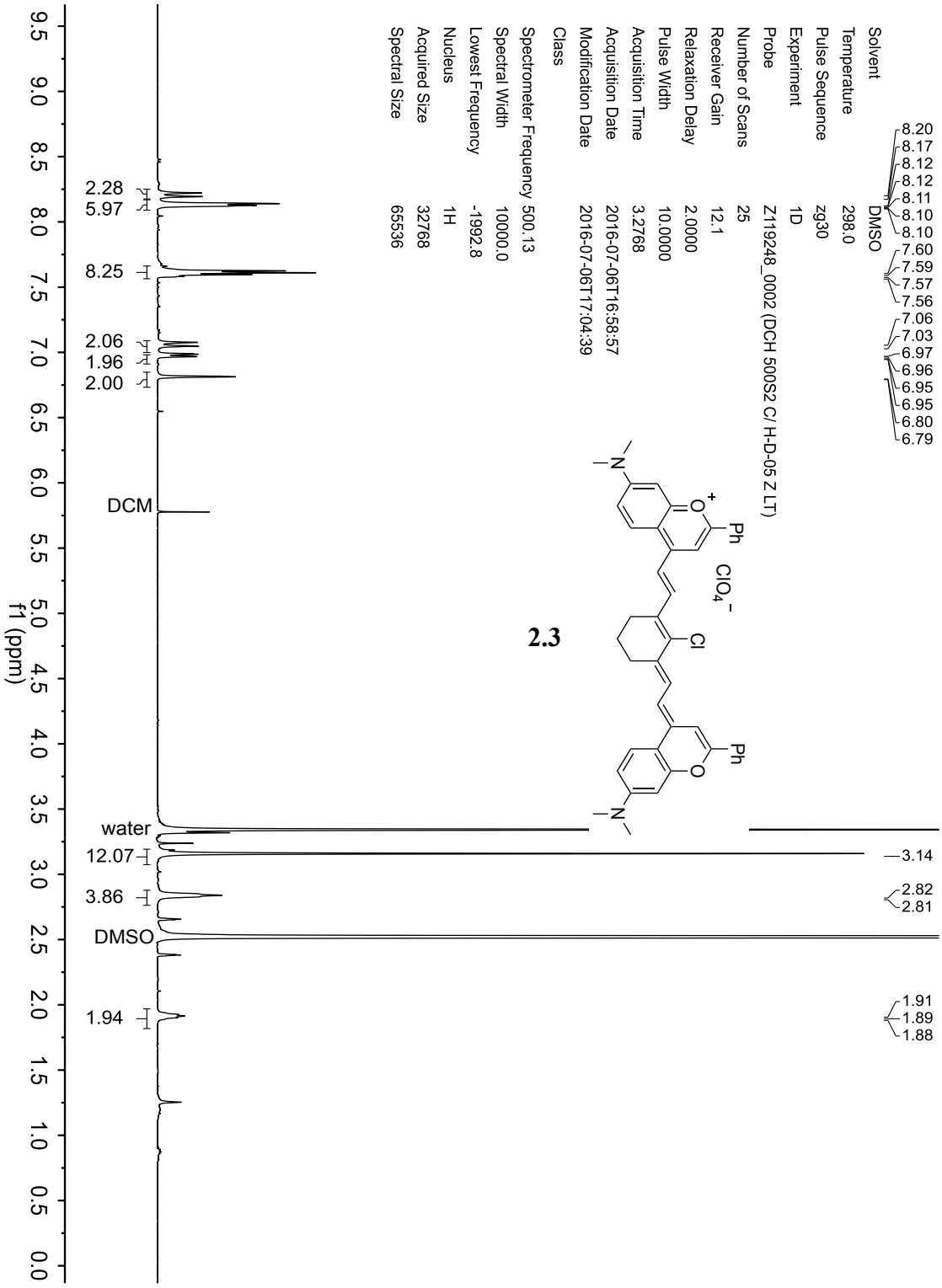

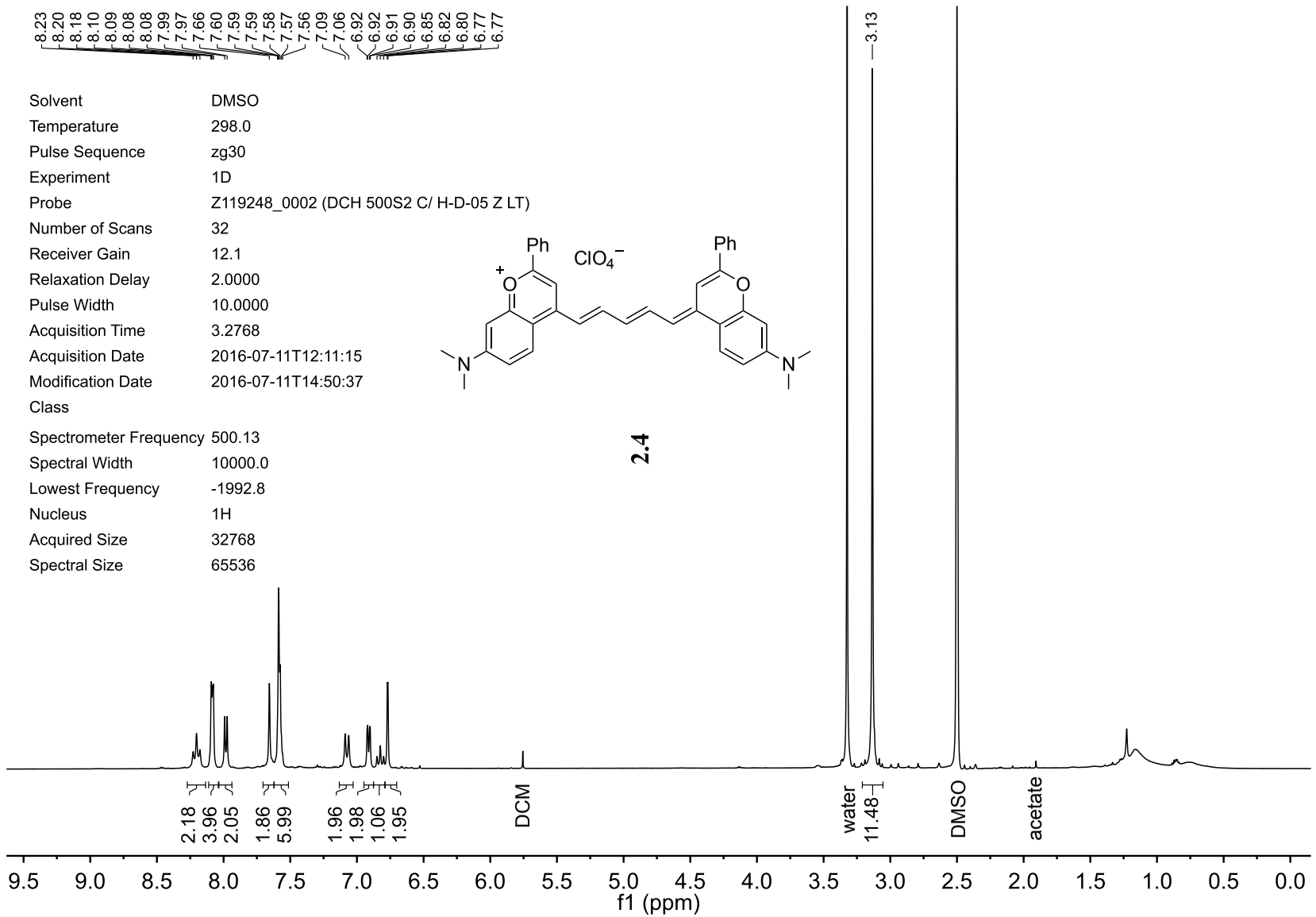
8.23
8.20
8.18
8.10
8.09
8.08
8.08
7.99
7.97
7.66
7.60
7.59
7.59
7.58
7.57
7.56
7.09
7.06
6.92
6.92
6.91
6.90
6.85
6.82
6.80
6.77
6.77
3.13
Solvent DMSO
Temperature 298.0
Pulse Sequence zg30
Experiment 1D
Probe Z119248_0002 (DCH 500S2 C/ H-D-05 Z LT)
Number of Scans 32
Receiver Gain 12.1
Relaxation Delay 2.0000
Pulse Width 10.0000
Acquisition Time 3.2768
Acquisition Date 2016-07-11T12:11:15
Modification Date 2016-07-11T14:50:37
Class
Spectrometer Frequency 500.13
Spectral Width 10000.0
Lowest Frequency -1992.8
Nucleus 1H
Acquired Size 32768
Spectral Size 65536
Ph
ClO4−
Ph
O
O
N
N
2.4
2.18
3.96
2.05
1.86
5.99
1.96
1.98
1.06
1.95
DCM
water
11.48
DMSO
acetate
9.5 9.0 8.5 8.0 7.5 7.0 6.5 6.0 5.5 5.0 4.5 4.0 3.5 3.0 2.5 2.0 1.5 1.0 0.5 0.0
f1 (ppm)

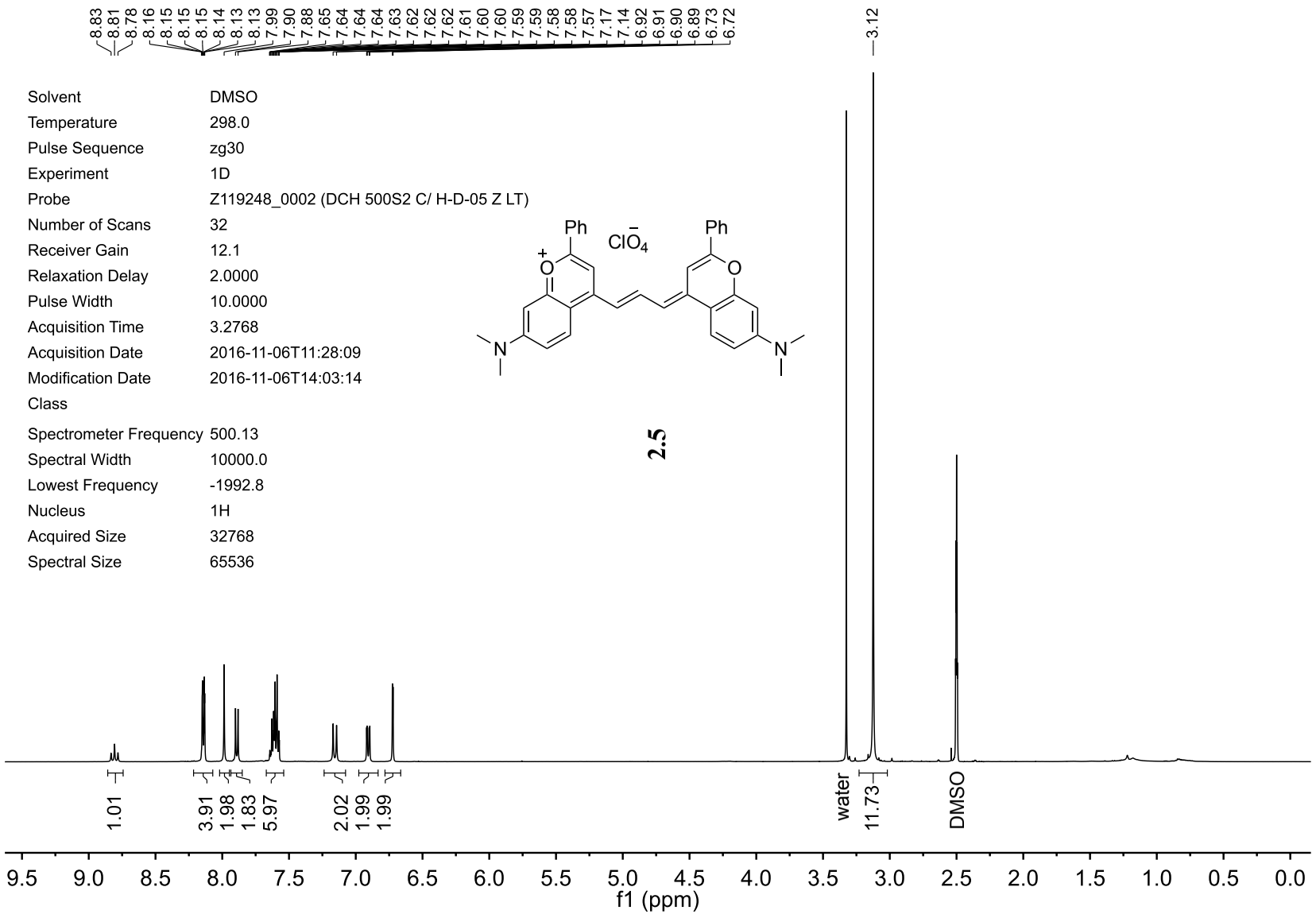
8.83 8.81 8.78 8.16 8.15 8.15 8.15 8.14 8.13 8.13 7.99 7.90 7.88 7.65 7.64 7.64 7.64 7.63 7.62 7.62 7.62 7.61 7.60 7.60 7.59 7.59 7.58 7.58 7.57 7.17 7.14 6.92 6.91 6.90 6.89 6.73 6.72
3.12
Solvent DMSO
Temperature 298.0
Pulse Sequence zg30
Experiment 1D
Probe Z119248_0002 (DCH 500S2 C/ H-D-05 Z LT)
Number of Scans 32
Receiver Gain 12.1
Relaxation Delay 2.0000
Pulse Width 10.0000
Acquisition Time 3.2768
Acquisition Date 2016-11-06T11:28:09
Modification Date 2016-11-06T14:03:14
Class
Spectrometer Frequency 500.13
Spectral Width 10000.0
Lowest Frequency -1992.8
Nucleus 1H
Acquired Size 32768
Spectral Size 65536
Ph
ClO4
Ph
O
O
N
N
2.5
1.01
3.91
1.98
1.83
5.97
2.02
1.99
1.99
water
11.73
DMSO
9.5 9.0 8.5 8.0 7.5 7.0 6.5 6.0 5.5 5.0 4.5 4.0 3.5 3.0 2.5 2.0 1.5 1.0 0.5 0.0
f1 (ppm)

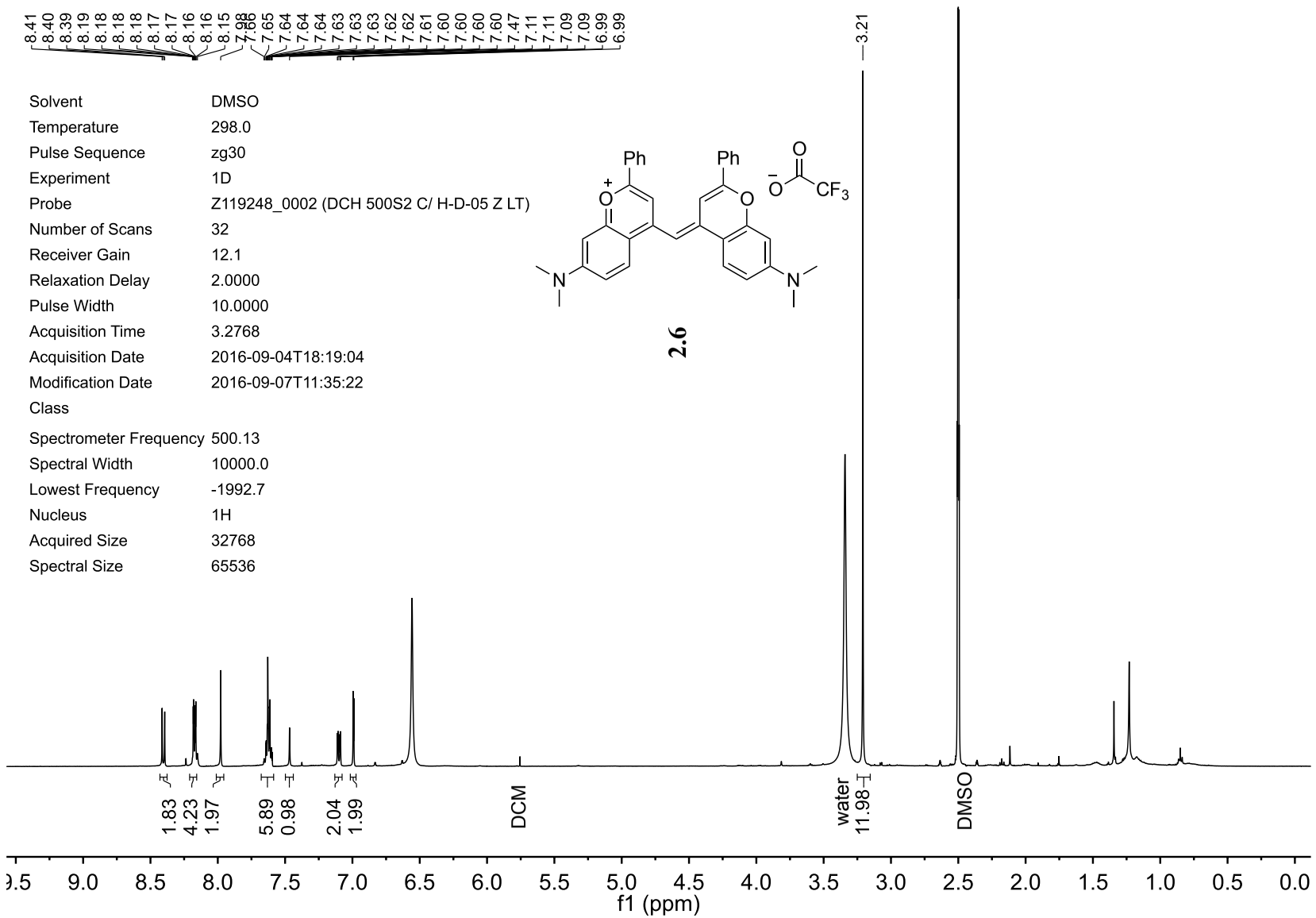
8.41 8.40 8.39 8.19 8.18 8.18 8.18 8.17 8.17 8.16 8.16 8.15 7.66 7.65 7.64 7.64 7.64 7.63 7.63 7.63 7.62 7.62 7.61 7.60 7.60 7.60 7.60 7.47 7.11 7.11 7.09 7.09 6.99 6.99
3.21
Solvent DMSO
Temperature 298.0
Pulse Sequence zg30
Experiment 1D
Probe Z119248_0002 (DCH 500S2 C/ H-D-05 Z LT)
Number of Scans 32
Receiver Gain 12.1
Relaxation Delay 2.0000
Pulse Width 10.0000
Acquisition Time 3.2768
Acquisition Date 2016-09-04T18:19:04
Modification Date 2016-09-07T11:35:22
Class
Spectrometer Frequency 500.13
Spectral Width 10000.0
Lowest Frequency -1992.7
Nucleus 1H
Acquired Size 32768
Spectral Size 65536
Ph
Ph
O
O
CF3
N
N
2.6
1.83
4.23
1.97
5.89
0.98
2.04
1.99
DCM
water
11.98
DMSO
9.5 9.0 8.5 8.0 7.5 7.0 6.5 6.0 5.5 5.0 4.5 4.0 3.5 3.0 2.5 2.0 1.5 1.0 0.5 0.0
f1 (ppm)

2.7.2 ^{13}C NMR Spectra

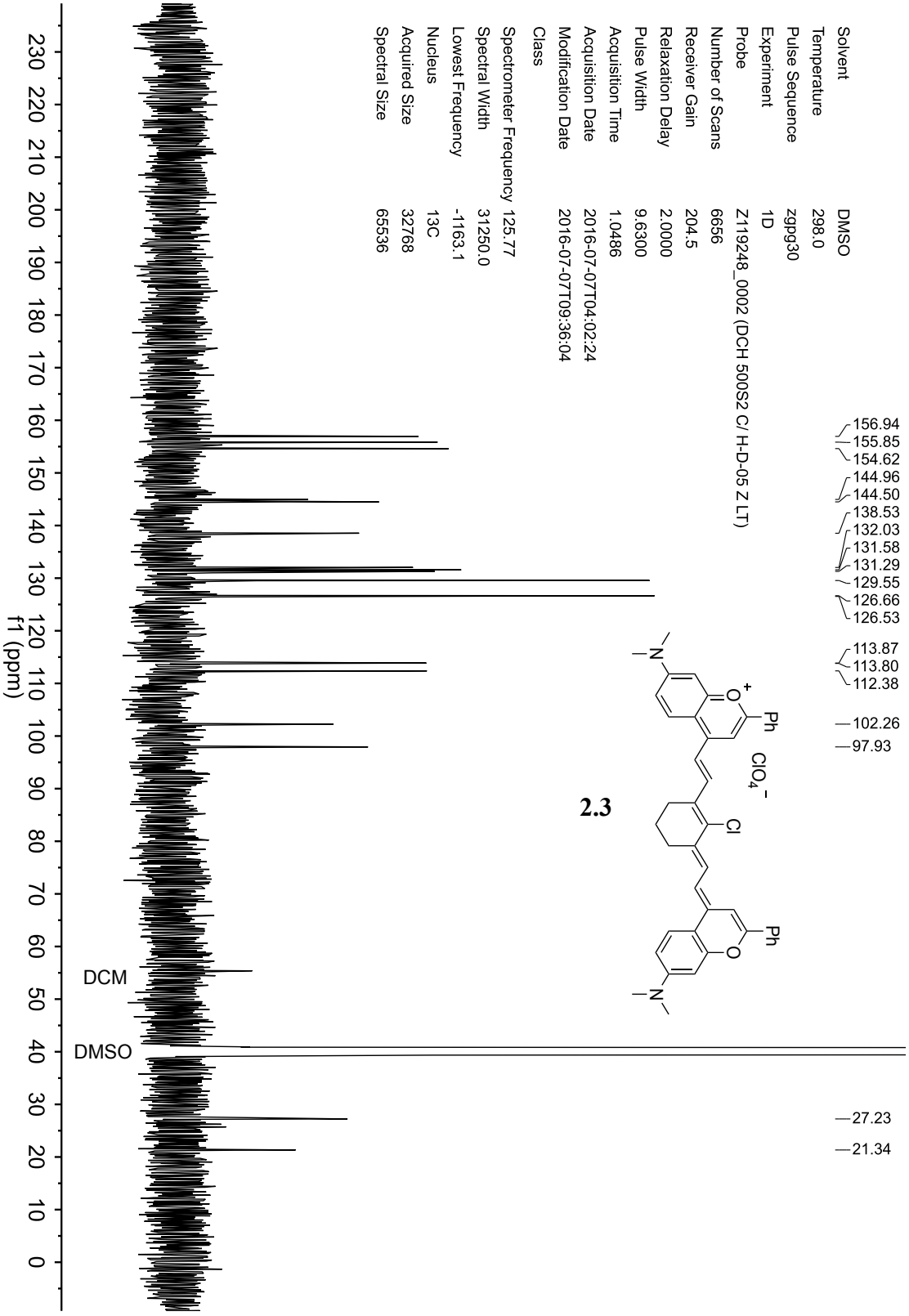

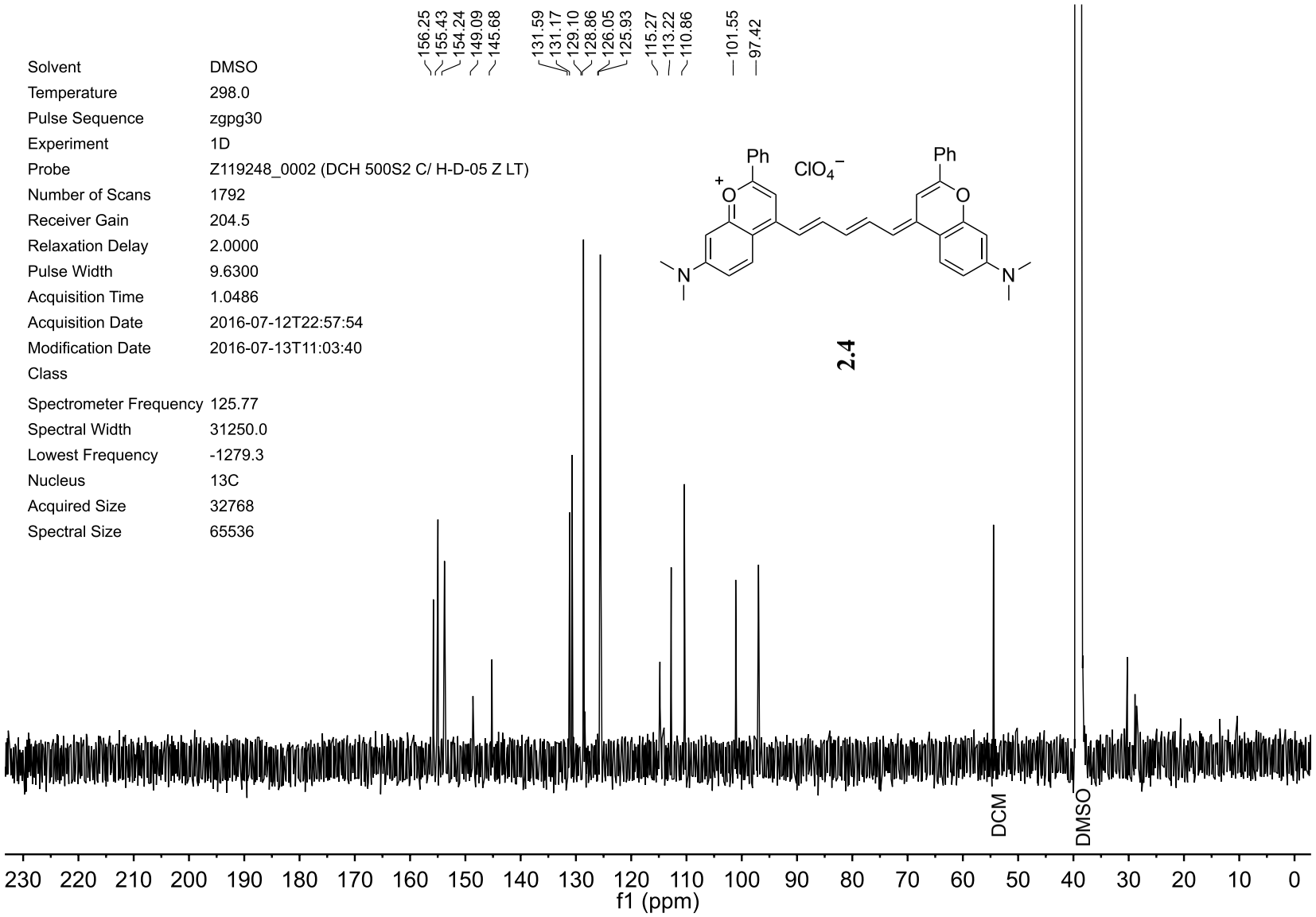
156.25
155.43
154.24
149.09
145.68
131.59
131.17
129.10
128.86
126.05
125.93
115.27
113.22
110.86
101.55
97.42
Solvent DMSO
Temperature 298.0
Pulse Sequence zgpg30
Experiment 1D
Probe Z119248_0002 (DCH 500S2 C/ H-D-05 Z LT)
Number of Scans 1792
Receiver Gain 204.5
Relaxation Delay 2.0000
Pulse Width 9.6300
Acquisition Time 1.0486
Acquisition Date 2016-07-12T22:57:54
Modification Date 2016-07-13T11:03:40
Class
Spectrometer Frequency 125.77
Spectral Width 31250.0
Lowest Frequency -1279.3
Nucleus 13C
Acquired Size 32768
Spectral Size 65536
Ph
ClO4−
Ph
O
O
N
N
2.4
DCM
DMSO
230 220 210 200 190 180 170 160 150 140 130 120 110 100 90 80 70 60 50 40 30 20 10 0
f1 (ppm)

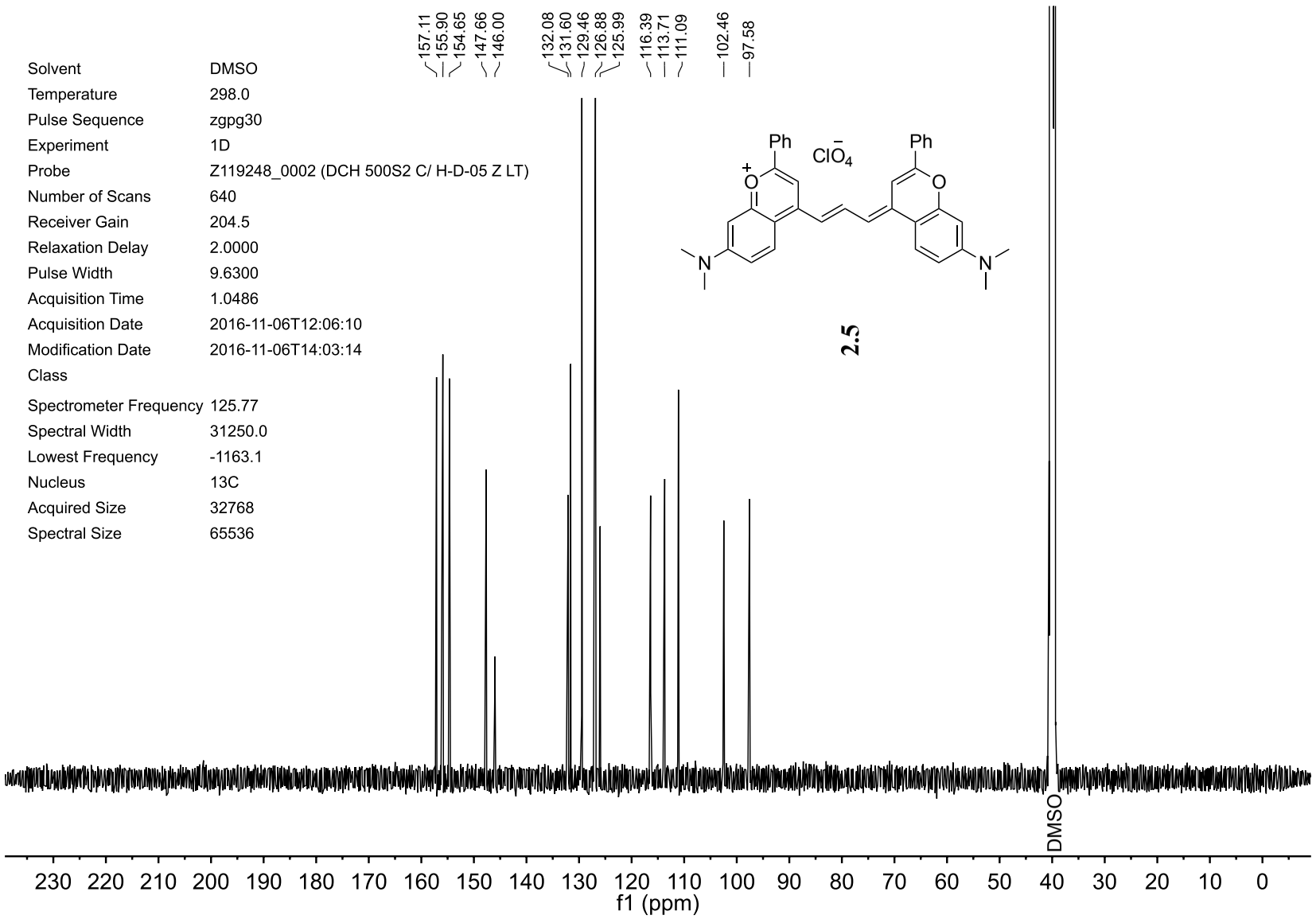
157.11
155.90
154.65
147.66
146.00
132.08
131.60
129.46
126.88
125.99
116.39
113.71
111.09
102.46
97.58
Solvent DMSO
Temperature 298.0
Pulse Sequence zgpg30
Experiment 1D
Probe Z119248_0002 (DCH 500S2 C/ H-D-05 Z LT)
Number of Scans 640
Receiver Gain 204.5
Relaxation Delay 2.0000
Pulse Width 9.6300
Acquisition Time 1.0486
Acquisition Date 2016-11-06T12:06:10
Modification Date 2016-11-06T14:03:14
Class
Spectrometer Frequency 125.77
Spectral Width 31250.0
Lowest Frequency -1163.1
Nucleus 13C
Acquired Size 32768
Spectral Size 65536
Ph
ClO4
Ph
O
O
N
N
2.5
DMSO
230 220 210 200 190 180 170 160 150 140 130 120 110 100 90 80 70 60 50 40 30 20 10 0
f1 (ppm)

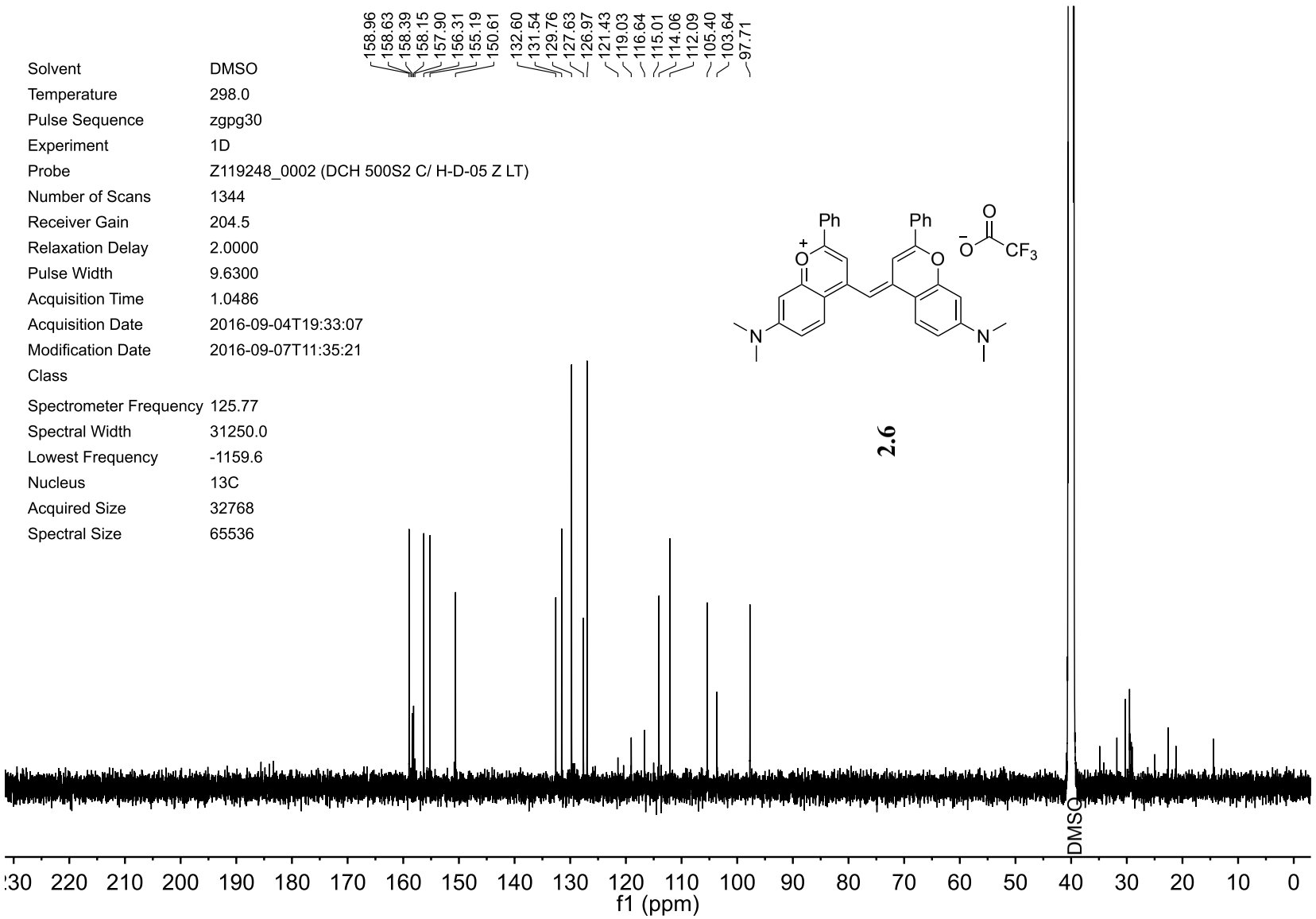
158.96
158.63
158.39
158.15
157.90
156.31
155.19
150.61
132.60
131.54
129.76
127.63
126.97
121.43
119.03
116.64
115.01
114.06
112.09
105.40
103.64
97.71
Solvent DMSO
Temperature 298.0
Pulse Sequence zgpg30
Experiment 1D
Probe Z119248_0002 (DCH 500S2 C/ H-D-05 Z LT)
Number of Scans 1344
Receiver Gain 204.5
Relaxation Delay 2.0000
Pulse Width 9.6300
Acquisition Time 1.0486
Acquisition Date 2016-09-04T19:33:07
Modification Date 2016-09-07T11:35:21
Class
Spectrometer Frequency 125.77
Spectral Width 31250.0
Lowest Frequency -1159.6
Nucleus 13C
Acquired Size 32768
Spectral Size 65536
Ph
Ph
O
O
CF3
N
N
2.6
DMSO
f1 (ppm)

2.7.3 ^{19}F NMR Spectrum

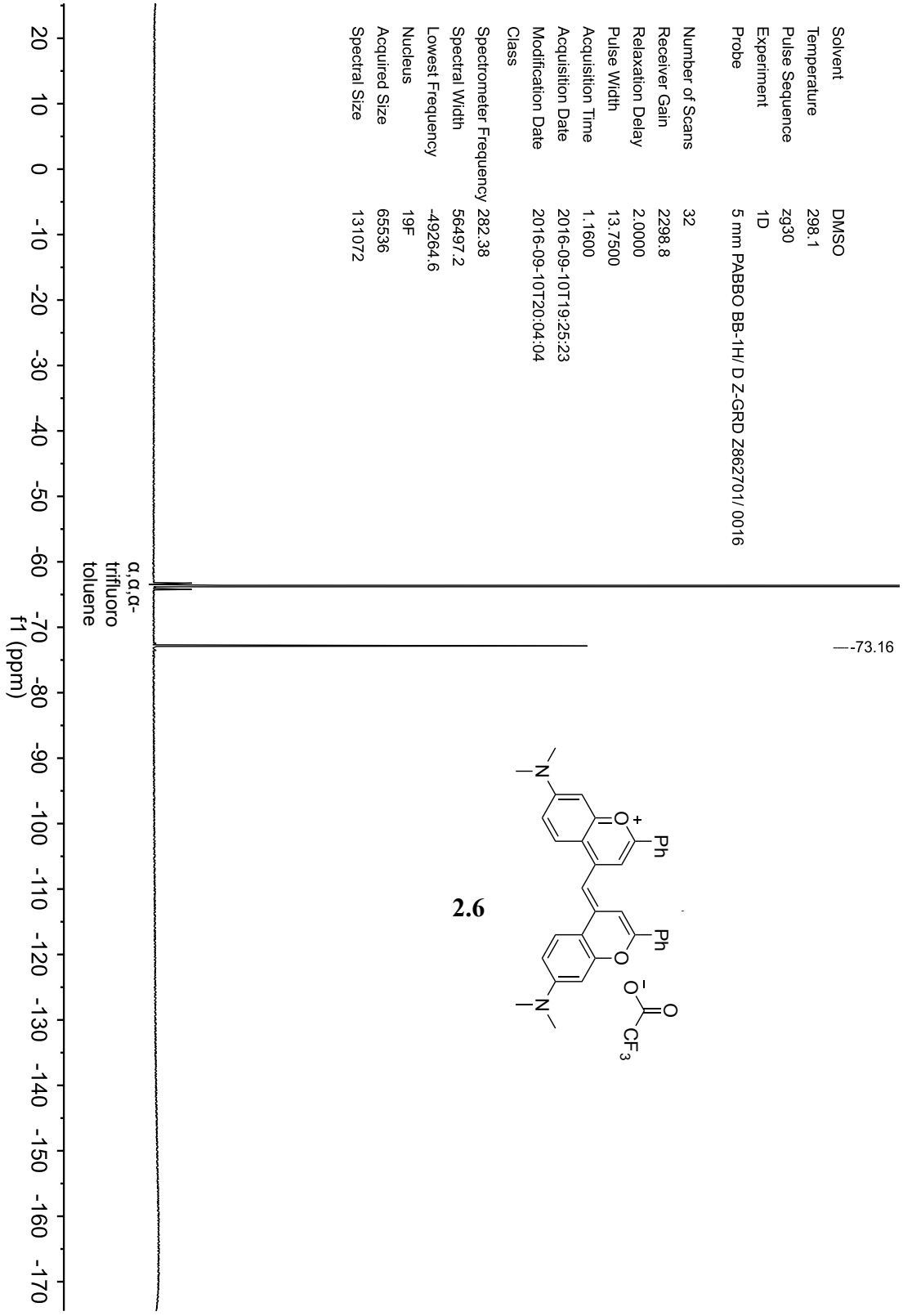

2.6

2.7.4 Absorbance and emission spectra

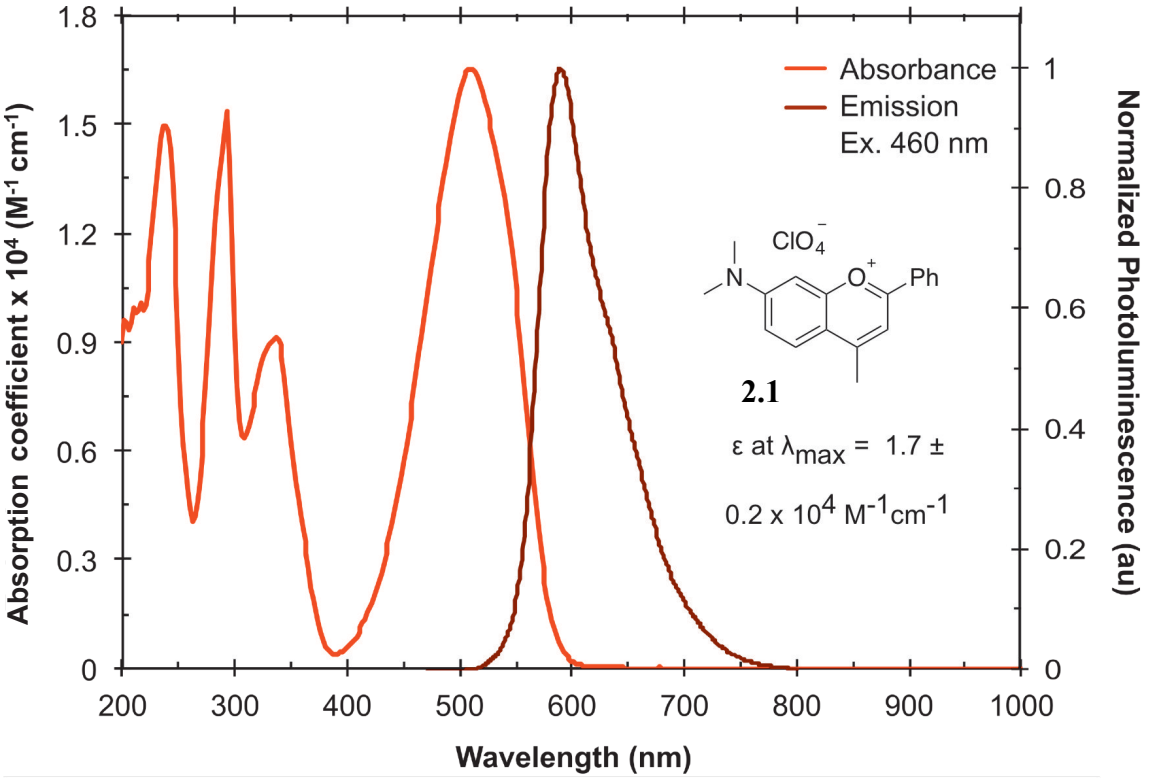

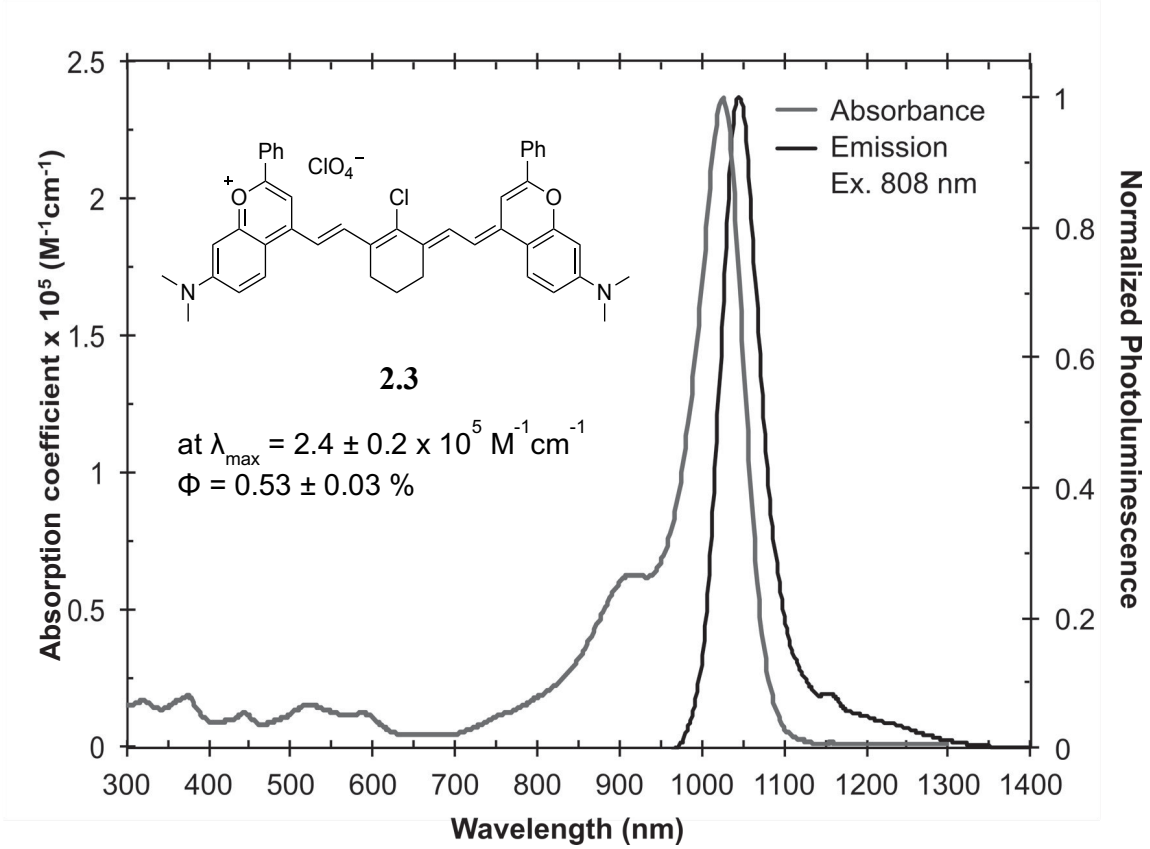

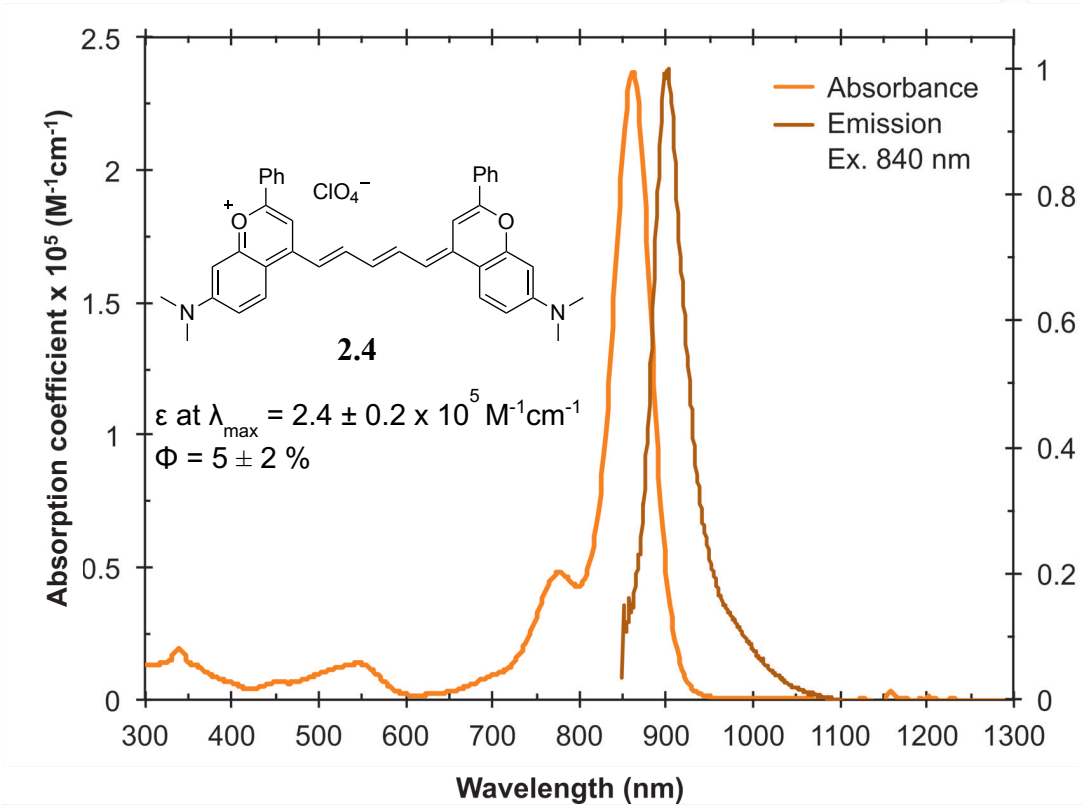
Absorbance
Emission
Ex. 840 nm
Ph
ClO4−
Ph
O
O
N
N
2.4
ε at λmax = 2.4 ± 0.2 x 10^5 M-1cm-1
Φ = 5 ± 2 %
Absorption coefficient x 10^5 (M-1cm-1)
Normalized Photoluminescence (au)
Wavelength (nm)

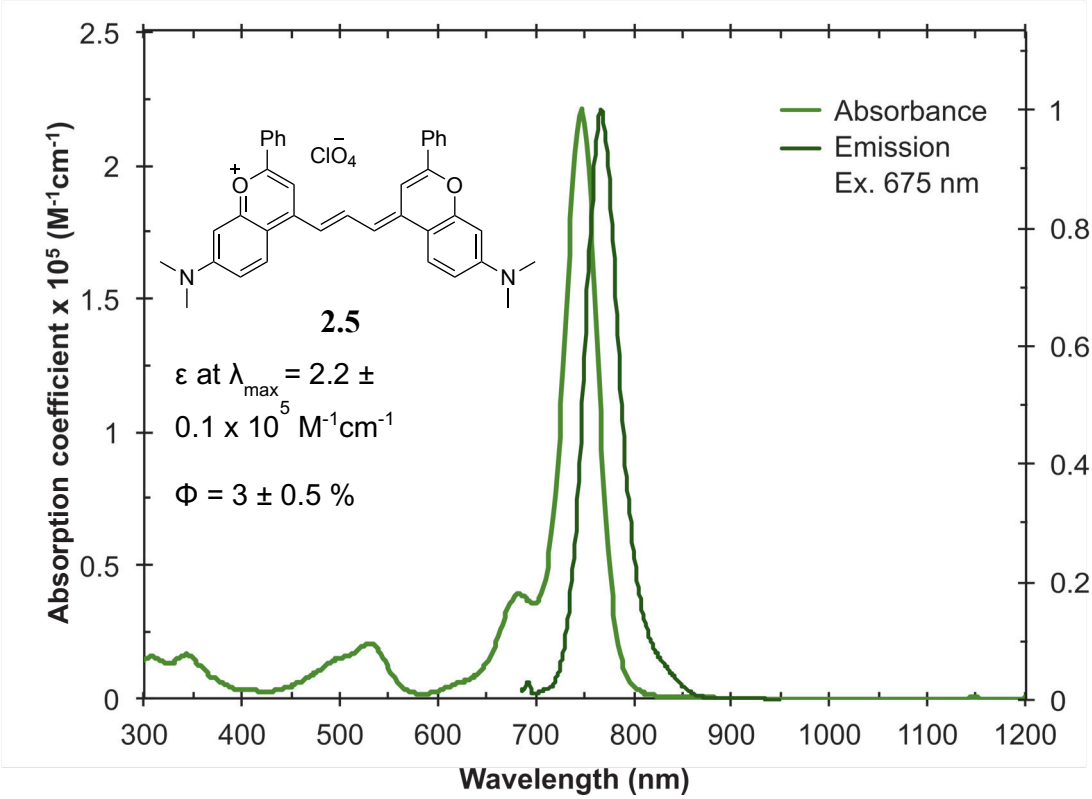
Absorbance
Emission
Ex. 675 nm
Ph
ClO4−
Ph
O
O
N
N
2.5
ε at λmax = 2.2 ±
0.1 x 10^5 M-1cm-1
Φ = 3 ± 0.5 %
Absorption coefficient x 10^5 (M-1cm-1)
Normalized Photoluminescence (au)
Wavelength (nm)

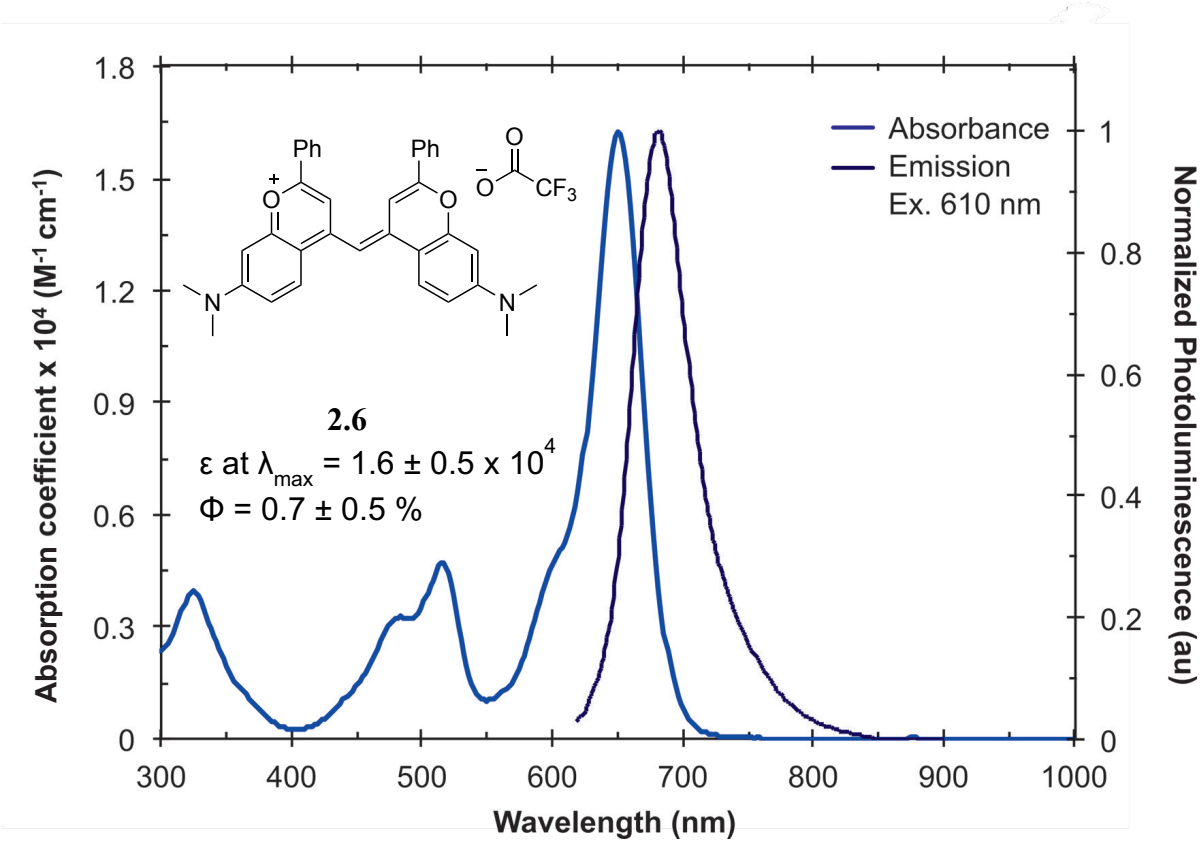

2.8 List of Supplementary Information Relevant to Chapter Two

Supplementary Video 2.1 Background corrected imaging of the injection of Flav7 (**2.3**) micelles in a mouse with diffuse 808 nm excitation and collection on an InGaAs Camera (1,000–1,600 nm) at 9.17 frames/sec.

Supplementary Video 2.2 Replicate of Supplementary Video 2.1

Supplementary Video 2.3 Raw imaging of the injection of Flav7 (**2.3**) micelles in a mouse with diffuse 808 nm excitation and collection on an InGaAs Camera (1,000–1,600 nm) at 9.17 frames/sec.

Supplementary Video 2.4 Replicate of Supplementary Video 2.3

2.9 References and Notes

[1] Hilderbrand, S. A.; Weissleder, R. Near-Infrared Fluorescence: Application to in Vivo Molecular Imaging. *Curr. Opin. Chem. Biol.* **2010**, *14*, 71–79.

[2] Lim, Y. T.; Kim, S.; Nakayama, A.; Stott, N. E.; Bawendi, M. G.; Frangioni, J. V. Selection of Quantum Dot Wavelengths for Biomedical Assays and Imaging. *Mol. Imaging* **2003**, *2*, 50–64.

[3] Garland, M.; Yim, J. J.; Bogyo, M. A Bright Future for Precision Medicine: Advances in Fluorescent Chemical Probe Design and Their Clinical Application. *Cell Chem. Biol.* **2016**, *23*, 122–136.

[4] Marshall, M. V; Rasmussen, J. C.; Tan, I.; Aldrich, M. B.; Adams, K. E.; Wang, X.; Fife, C. E.; Maus, E. A.; Smith, L. A.; Sevick-Muraca, E. M. Near-Infrared Fluorescence Imaging in Humans with Indocyanine Green: A Review and Update. *Open Surg. Oncol. J.* **2010**, *2*, 12–25.

[5] Goswami, P. P.; Syed, A.; Beck, C. L.; Albright, T. R.; Mahoney, K. M.; Unash, R.; Smith, E. A.; Winter, A. H. BODIPY-Derived Photoremovable Protecting Groups Unmasked with Green Light. *J. Am. Chem. Soc.* **2015**, *137*, 3783–3786.

[6] Brightness is taken as the product of the ε at $\lambda_{max,abs}$ and Φ_F. Values for ICG taken from Ref. [14].

[7] Thimsen, E.; Sadtler, B.; Berezin, M. Y. Shortwave-Infrared (SWIR) Emitters for Biological Imaging : A Review of Challenges and Opportunities. *Nanophotonics* **2017**, *6*, 1043–1054.

[8] a) Welsher, K.; Liu, Z.; Sherlock, S. P.; Robinson, J. T.; Chen, Z.; Daranciang, D.; Dai, H. A Route to Brightly Fluorescent Carbon Nanotubes for Near-Infrared Imaging in Mice. *Nat. Nanotechnol.* **2009**, *4*, 773–780. b) Hong, G.; Lee, J. C.; Robinson, J. T.; Raaz, U.; Xie, L.; Huang, N. F.; Cooke, J. P.; Dai, H. Multifunctional in Vivo Vascular Imaging Using Near-Infrared II Fluorescence. *Nat. Med.* **2012**, *18*, 1841–1846.

[9] a) Chen, G.; Ohulchanskyy, T. Y.; Liu, S.; Law, W. C.; Wu, F.; Swihart, M. T.; Ågren, H.; Prasad, P. N. Core/Shell NaGdF 4:Nd 3+/NaGdF 4 Nanocrystals with Efficient near-Infrared to near-Infrared Downconversion Photoluminescence for Bioimaging Applications. *ACS Nano* **2012**, *6*, 2969–2977. b) Naczynski, D. J.; Tan, M. C.; Zevon, M.; Wall, B.; Kohl, J.; Kulesa, A.; Chen, S.; Roth, C. M.; Riman, R. E.; Moghe, P. V. Rare-Earth-Doped Biological Composites as in Vivo Shortwave Infrared Reporters. *Nat. Commun.* **2013**, *4*, 2199.

[10] a) Hong, G.; Robinson, J. T.; Zhang, Y.; Diao, S.; Antaris, A. L.; Wang, Q.; Dai, H. In Vivo Fluorescence Imaging with Ag2S Quantum Dots in the Second Near-Infrared Region. *Angew. Chemie Int. Ed.* **2012**, *51*, 9818–9821. b) Bruns, O. T.; Bischof, T. S.; Harris, D. K.; Franke, D.; Shi, Y.; Riedemann, L.; Bartelt, A.; Jaworski, F. B.; Carr, J. A.; Rowlands,

C. J.; et al. Next-Generation in Vivo Optical Imaging with Short-Wave Infrared Quantum Dots. *Nat. Biomed. Eng.* **2017**, *1*, 0056.

[11] a) Tao, Z.; Hong, G.; Shinji, C.; Chen, C.; Diao, S.; Antaris, A. L.; Zhang, B.; Zou, Y.; Dai, H. Biological Imaging Using Nanoparticles of Small Organic Molecules with Fluorescence Emission at Wavelengths Longer than 1000 nm. *Angew. Chemie Int. Ed.* **2013**, *52*, 13002–13006. b) Dang, X.; Gu, L.; Qi, J.; Correa, S.; Zhang, G.; Belcher, A. M.; Hammond, P. T. Layer-by-Layer Assembled Fluorescent Probes in the Second Near-Infrared Window for Systemic Delivery and Detection of Ovarian Cancer. *Proc. Natl. Acad. Sci.* **2016**, *113*, 5179–5184.

[12] Antaris, A. L.; Chen, H.; Cheng, K.; Sun, Y.; Hong, G.; Qu, C.; Diao, S.; Deng, Z.; Hu, X.; Zhang, B.; et al. A Small-Molecule Dye for NIR-II Imaging. *Nat. Mater.* **2016**, *15*, 235–242.

[13] a) Yang, Q.; Ma, Z.; Wang, H.; Zhou, B.; Zhu, S.; Zhong, Y.; Wang, J.; Wan, H.; Antaris, A.; Ma, R.; et al. Rational Design of Molecular Fluorophores for Biological Imaging in the NIR-II Window. *Adv. Mater.* **2017**, *29*, 1605497. b) Antaris, A. L.; Chen, H.; Diao, S.; Ma, Z.; Zhang, Z.; Zhu, S.; Wang, J.; Lozano, A. X.; Fan, Q.; Chew, L.; et al. A High Quantum Yield Molecule-Protein Complex Fluorophore for near-Infrared II Imaging. *Nat. Commun.* **2017**, *8*, 15269.

[14] Carr, J. A.; Franke, D.; Caram, J. R.; Perkinson, C. F.; Saif, M.; Askoxylakis, V.; Datta, M.; Fukumura, D.; Jain, R. K.; Bawendi, M. G.; et al. Shortwave Infrared Fluorescence Imaging with the Clinically Approved Near-Infrared Dye Indocyanine Green. *Proc. Natl. Acad. Sci.* **2018**, *115*, 4465–4470.

[15] Lavis, L. D.; Raines, R. T. Bright Ideas for Chemical Biology. *ACS Chem. Biol.* **2008**, *3*, 142–155.

[16] Waggoner, A. Fluorescent Labels for Proteomics and Genomics. *Curr. Opin. Chem. Biol.* **2006**, *10*, 62–66.

[17] Gorka, A. P.; Nani, R. R.; Schnermann, M. J. Cyanine Polyene Reactivity: Scope and Biomedical Applications. *Org. Biomol. Chem.* **2015**, *13*, 7584–7598.

[18] Bricks, J. L.; Kachkovskii, A. D.; Slominskii, Y. L.; Gerasov, A. O.; Popov, S. V. Molecular Design of near Infrared Polymethine Dyes: A Review. *Dye. Pigment.* **2015**, *121*, 238–255.

[19] Ishchenko, A. A. Structure and Spectral-Luminescent Properties of Polymethine Dyes. *Russ. Chem. Rev.* **1991**, *60*, 865–884.

[20] Narayanan, N.; Patonay, G. A New Method for the Synthesis of Heptamethine Cyanine Dyes: Synthesis of New Near-Infrared Fluorescent Labels. *J. Org. Chem.* **1995**, *60*, 2391–2395.

[21] Detty, M. R.; Murray, B. J. Telluropyrylium Dyes. 1. 2,6-Diphenyltelluropyrylium Dyes. *J. Org. Chem.* **1982**, *47*, 5235–5239.

[22] Kopainsky, B.; Qiu, P.; Kaiser, W.; Sens, B.; Drexhage, K. H. Lifetime, Photostability, and Chemical Structure of IR Heptamethine Cyanine Dyes Absorbing beyond 1 μm. *Appl. Phys. B* **1982**, *29*, 15–18.

[23] Chen, J.-R.; Wong, J.-B.; Kuo, P.-Y.; Yang, D.-Y. Synthesis and Characterization of Coumarin-Based Spiropyran Photochromic Colorants. *Org. Lett.* **2008**, *10*, 4823–4826.

[24] Hatami, S.; Würth, C.; Kaiser, M.; Leubner, S.; Gabriel, S.; Bahrig, L.; Lesnyak, V.; Pauli, J.; Gaponik, N.; Eychmüller, A.; et al. Absolute Photoluminescence Quantum Yields of IR26 and IR-Emissive Cd1−xHgxTe and PbS Quantum Dots – Method- and Material-Inherent Challenges. *Nanoscale* **2015**, *7*, 133–143.

[25] Dyes **2.3** and **2.4** are soluble in a variety of organic solvents and display minimal solvatochromism (*Section 2.7.1*).

[26] a) Semonin, O. E.; Johnson, J. C.; Luther, J. M.; Midgett, A. G.; Nozik, A. J.; Beard, M. C. Absolute Photoluminescence Quantum Yields of IR-26 Dye, PbS, and PbSe Quantum Dots. *J. Phys. Chem. Lett.* **2010**, *1*, 2445–2450. b) Kranitzky, W.; Kopainsky, B.; Kaiser, W.; Drexhage, K. H.; Reynolds, G. A. A New Infrared Laser Dye of Superior Photostability Tunable to 1.24 μm with Picosecond Excitation. *Opt. Commun.* **1981**, *36*, 149–152.

[27] Casalboni, M.; De Matteis, F.; Prosposito, P.; Quatela, A.; Sarcinelli, F. Fluorescence Efficiency of Four Infrared Polymethine Dyes. *Chem. Phys. Lett.* **2003**, *373*, 372–378.

[28] We performed similar stability studies with mixtures of acetonitrile and alcohols, which suggested covalent modification (Figure 2.9).

[29] Bexrud, J. A.; Eisenberger, P.; Leitch, D. C.; Payne, P. R.; Schafer, L. L. Selective C-H Activation α to Primary Amines. Bridging Metallaaziridines for Catalytic, Intramolecular α-Alkylation. *J. Am. Chem. Soc.* **2009**, *131*, 2116–2118.

[30] a) A. Toutchkine, D. V. Nguyen, K. M. Hahn, *Org. Lett.* **2007**, *9*, 2775; b) B. Song, Q. Zhang, W. H. Ma, X. J. Peng, X. M. Fu, B. S. Wang, *Dyes Pigments* **2009**, *82*, 396; c) X. Chen, X. Peng, A.; Cui, B. Wang, L. Wang, R. *J.* Zhang, *Photochem. Photobiology. A Chem.* **2006**, *181*, 79.

[31] Rurack, K.; Spieles, M. Fluorescence Quantum Yields of a Series of Red and Near-Infrared Dyes Emitting at 600−1000 nm. *Anal. Chem.* **2011**, *83*, 1232–1242.

[32] Sato, S.; Tsunoda, M.; Suzuki, M.; Kutsuna, M.; Takido-uchi, K.; Shindo, M.; Mizuguchi, H.; Obara, H.; Ohya, H. Synthesis and Spectral Properties of Polymethine-Cyanine Dye-Nitroxide Radical Hybrid Compounds for Use as Fluorescence Probes to Monitor Reducing Species and Radicals. *Spectrochim. Acta - Part A Mol. Biomol. Spectrosc.* **2009**, *71*, 2030–2039.

[33] Guarin, C. A.; Villabona-Monsalve, J. P.; López-Arteaga, R.; Peon, J. Dynamics of the Higher Lying Excited States of Cyanine Dyes. An Ultrafast Fluorescence Study. *J. Phys. Chem. B* **2013**, *117*, 7352–7362.

CHAPTER THREE

Multicolor in vivo Imaging in Real Time using Excitation-Multiplexing with Shortwave Infrared Polymethine Fluorophores

Adapted from: Emily D. Cosco, Anthony L. Spearman, Shyam Ramakrishnan, Jakob G. P. Lingg, Mara Saccomano, Sarah Glasl, Monica Pengshung, Bernardo A. Arús, Kelly C. Y. Wong, Vasilis Ntziachristos, Martin Warmer, Ryan R. McLaughlin, Oliver T. Bruns,* and Ellen M. Sletten* Shortwave infrared polymethine fluorophores matched to excitation lasers enable non-invasive, multicolor in vivo imaging in real time. *Nat. Chem.* **2020**, *12*, 1123–1130. DOI: 10.1038/s41557-020-00554-5

3.1 Abstract

High-resolution, multiplexed experiments are a staple in cellular imaging. Analogous experiments in animals are challenging, however, due to substantial scattering and autofluorescence in tissue at visible (350–700 nm) and near-infrared (700–1,000 nm) wavelengths. Here, we enable real-time, non-invasive multicolor imaging experiments in animals through the design of optical contrast agents for the shortwave infrared (SWIR, 1,000–2,000 nm) region and complementary advances in imaging technologies. We developed tunable, SWIR-emissive flavylium polymethine dyes and established relationships between structure and photophysical properties for this class of bright SWIR contrast agents. In parallel, we designed an imaging system with variable near-infrared/SWIR excitation and single-channel detection, facilitating video-rate multicolor SWIR imaging for optically guided surgery and imaging of awake and moving mice

with multiplexed detection. Optimized dyes matched to 980 nm and 1,064 nm lasers, combined with the clinically approved indocyanine green, enabled real-time, three-color imaging with high temporal and spatial resolutions.

3.2 Introduction

Improvements in imaging technologies and optical probes have combined to revolutionize our ability to study cells and small organisms using fluorescence microscopy[1,2]. The tools developed for fluorescent imaging in cells can be readily applied to small model organisms such as *Caenorhabditis elegans*, *Danio rerio* (zebrafish) and *Drosophila melanogaster*. Translating these tools to mammals is challenging, however, as most fluorophores used in cellular imaging are excited by light in the visible (VIS, 350–700 nm) region of the electromagnetic spectrum, which exhibits low photon penetration and high background autofluorescence. For these reasons, imaging in mammals has been primarily focused on the near-infrared (NIR, 700–1,000 nm) region, where there are fewer endogenous chromophores, but where light scattering remains a limitation[3]. Further, the limited wavelength range of the NIR makes multiplexed experiments challenging. Notable approaches to multicolor fluorescence imaging experiments in mice that are compatible with VIS and NIR fluorophores include two-photon intravital microscopy methods, requiring body windows[4–7], or endoscopy[8]. Efforts towards non-invasive, multiplexed imaging in mice have been explored with quantum dots[9], fluorescently labelled silica particles[10], fluorescent proteins[11] and surface-enhanced Raman scattering nanoparticles[12]. While critical advances, these approaches suffer from low spatial and temporal resolution, limiting the biological information that can be obtained.

To enable robust, real-time, multiplexed imaging in animals it is necessary to (1) detect in a region of the electromagnetic spectrum that provides high spatial resolution; (2) establish efficient, orthogonal excitation and/or detection of bright fluorophores; and (3) rapidly detect each channel on the millisecond timescale. Here, we present a method that meets these requirements and enables whole-animal, three-color imaging with high spatial and temporal resolutions. Key to this technique is the implementation of excitation multiplexing and 'color-blind' single-channel detection of low-energy shortwave infrared (SWIR, 1,000–2,000 nm) light emitted by bright, 'excitation-matched' polymethine fluorophores (Figure 3.1A).

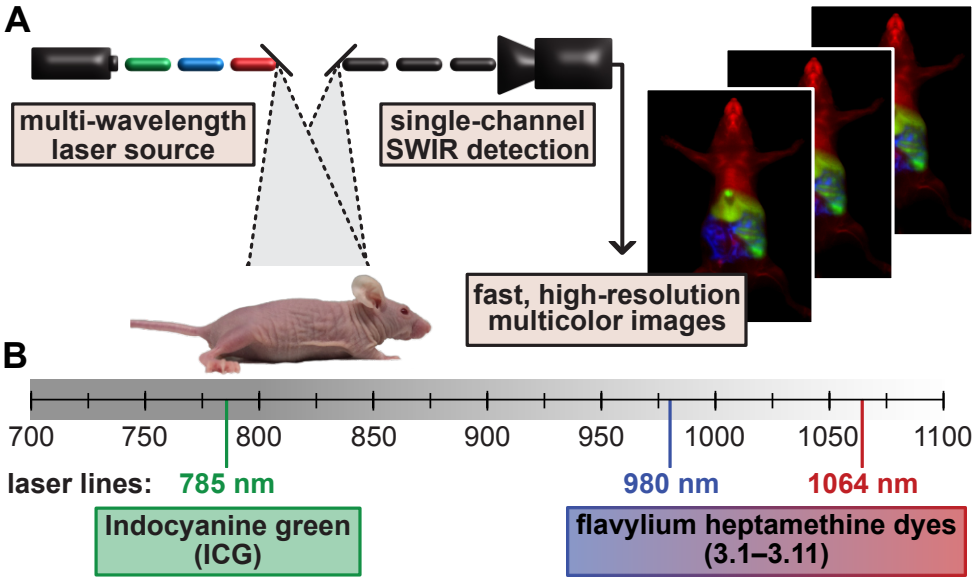

Flav7 (**3.1**): R_1 = $N(Me)_2$; R_2 = H, ***prior work***

3.2–3.11: R_1 = alkyl & aromatic amines, methoxy, H; R_2 = H, alkyl, ***this work***

Figure 3.1 Real-time excitation-multiplexed SWIR imaging design. A) Multiple laser sources are pulsed and delivered to the biological sample. Single-channel SWIR detection (InGaAs, 1,100–1,700 nm) acquires frames that are temporally separated by color on the millisecond timescale.

Fast frame rates produce real-time multicolor *in vivo* images at up to 50 fps. B) Relevant portions of the NIR and SWIR regions of the electromagnetic spectrum, lasers used for excitation and dyes used and/or presented in this study that are excited by the distinct laser lines. C) Flavylium polymethine scaffold explored here to match bright SWIR dyes to appropriate lasers.

The SWIR region is essential for multiplexed *in vivo* fluorescence imaging, as it provides superior resolution and greater tissue penetration than the NIR region[13,14], in addition to an expanded range of wavelengths allowing for multiple channels[15] separated by at least 80 nm. The optimal properties of the SWIR for *in vivo* imaging were first demonstrated with carbon nanotubes[16] and further validated with quantum dots[17,18], rare-earth nanomaterials[15] and small molecules[19,20]. Combinations of these materials have been utilized to obtain multiplexed images in mice[18,21–23] and tissues[24] at higher spatial resolutions than NIR images. The approach of excitation multiplexing with single-channel SWIR detection reported herein addresses multicolor SWIR imaging with high temporal resolution, facilitating real-time analysis (>27 frames per second (fps)) of biological processes at sub-millimetre resolutions.

To facilitate rapid multicolor imaging in the SWIR region, we diverged from traditional multiplexing approaches employing a common excitation wavelength and different detection windows[15,21–25] or spectral unmixing[18]. These classic approaches can result in different resolutions for each channel due to dramatic changes in the contrast and resolution that occur throughout wavelength bands of the NIR and SWIR[14,26,27]. Furthermore, fast imaging speeds can be impeded by low photon throughput in sectioned regions of the electromagnetic spectrum or by mechanical components, such as filter wheels. Instead of these approaches, we differentiate the contrast agents via excitation wavelength and employ a single SWIR detection channel. This method, referred to as excitation multiplexing, is advantageous due to the consistent resolution achieved in all channels, high photon efficiency and ease of rapid collection of each frame on a single detector[28,29]. Excitation multiplexing was initially applied to single-molecule

spectroscopy methods, microscopy and low-concentration DNA sequencing[30]. Subsequent variations on these methods have been explored[31,32], but excitation-multiplexed methods have yet to be adapted for animals. The implementation of excitation multiplexing in the SWIR is particularly beneficial as excitation can be optimized for each fluorophore and photons can be detected over a wide range of wavelengths. These properties combine to maximize the signal obtained from SWIR contrast agents, which have inherently low quantum yields when compared to those in the VIS and NIR[33].

To perform real-time excitation multiplexing in animals, bright SWIR-emissive contrast agents with absorption spectra compatible with common and cost-efficient laser lines are required (Figure 3.1B). Polymethine dyes are opportune contrast agents for excitation multiplexing as they have characteristically narrow absorption bands with high absorption coefficients[34]. A preeminent member of the polymethine dye family is indocyanine green (ICG), an FDA-approved contrast agent[35,36]. While ICG has been extensively used in NIR optical imaging, in 2017, we reported that the dye can be detected readily in a SWIR imaging configuration due to the long tail of the emission spectrum[37,38]. Concurrently, we reported a polymethine dye designed for SWIR optical imaging[39]. This dye, Flav7 (**3.1**, Figure 3.1C), has both SWIR absorption and high brightness for the SWIR region. Notably, since the introduction of Flav7, similar strategies have been employed to utilize or design polymethine dyes for SWIR imaging[40–44]. Due to the ability to image both bright NIR-excitable dyes, such as ICG, as well as red-shifted SWIR-excitable polymethine dyes, such as Flav7, using an identical SWIR detection window, we envisioned that polymethine dyes with both well-separated and laser-line-compatible absorption could enable efficient multicolor SWIR imaging via excitation multiplexing. To realize this multiplexing strategy, structural modifications to Flav7 were necessary to tune the wavelength of maximum

absorption ($\lambda_{max,abs}$) to match the accessible laser wavelengths used for SWIR imaging. Towards this goal, we set out to fine-tune the absorption properties of flavylium polymethine dyes through heterocycle modification. This work ultimately allowed access to a set of dyes that were optimal for real-time, multicolor SWIR imaging (see Figure 3.2A).

3.3 Results and Discussion

3.3.1 Design and Synthesis of Flavylium Heptamethine Dyes[1]

To tune the absorption properties of flavylium polymethine dyes for excitation multiplexing, robust synthetic approaches towards flavylium heterocycles were necessary. The original report of Flav7 used a previously published[45], low-yielding, electronically sensitive and potentially explosive route. We developed an alternate approach relying on a key 7-substituted flavone intermediate that could be converted to the desired heterocycles by treatment with a methyl nucleophile and dehydration (Scheme 3.1)[46]. Using three general routes to flavones, (1) Mentzer pyrone synthesis[47], (2) functionalization of 7-hydroxyflavone by Buchwald–Hartwig coupling of the corresponding triflate[48] and (3) acylation of the commercial 7-aminoflavone, we accessed a diverse set of 7-aminoflavylium heterocycles (Tables 3.1–3.3). The heptamethine dyes **3.1**–**3.11** (Figure 3.2A) were then obtained through the base-promoted reaction of each flavylium heterocycle with the relevant bis(phenylimine) polymethine chain (Table 3.4; see Section 3.6.1 for further discussion)

[1] Anthony Spearman, Monica Pengshung and Ryan McLaughlin contributed in this section.

Scheme 3.1 Retrosynthesis of 7-aminoflavylium heterocycles.

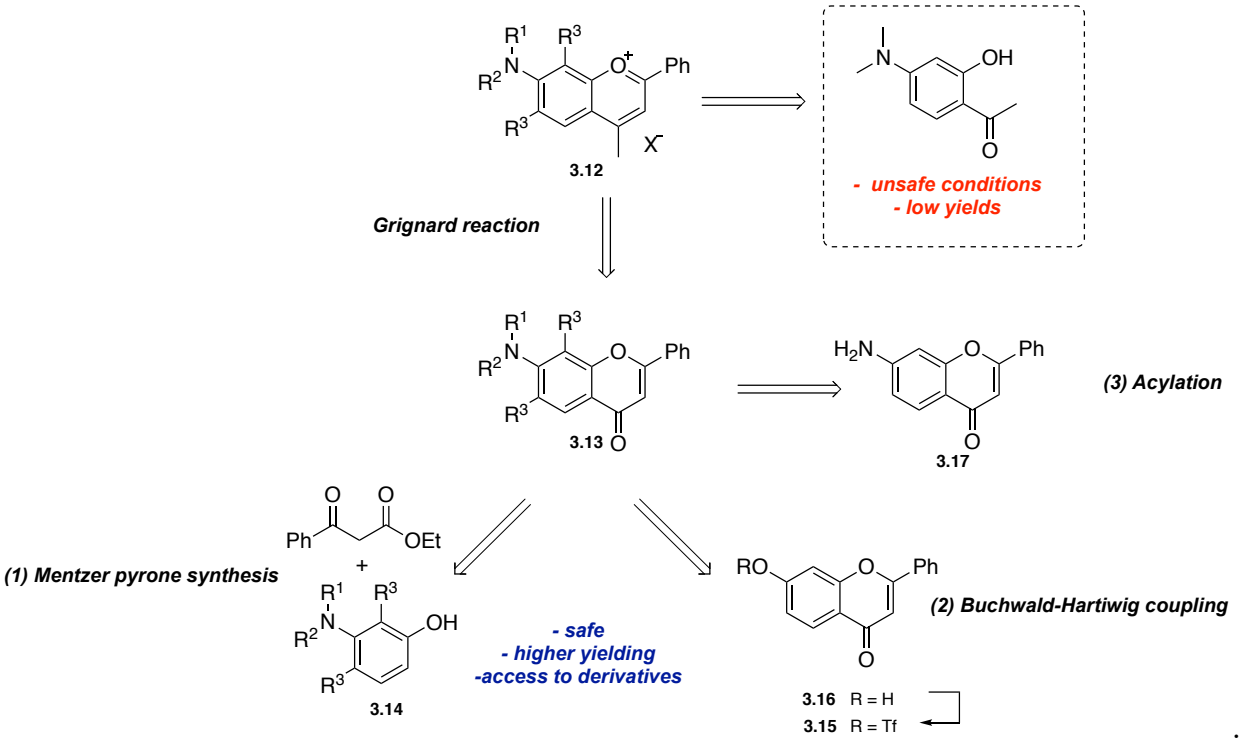

Table 3.1 Synthesis of flavones **3.13a**–**c**.

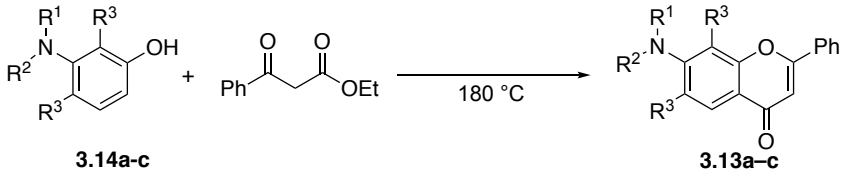

3-aminophenol 3.14		*7-aminoflavone 3.13*			
number	*structure*	*number*	*structure*	*time (h)*	*yield (%)*
3.14a	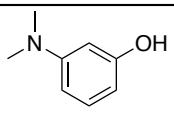	**3.13a**	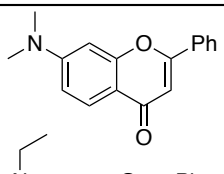	24	51
3.14b	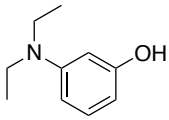	**3.13b**	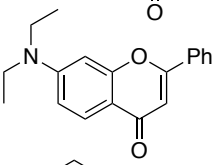	20	51
3.14c	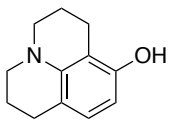	**3.13c**	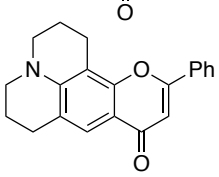	48	55

Table 3.2 Synthesis of flavones **3.13d**–**h**.

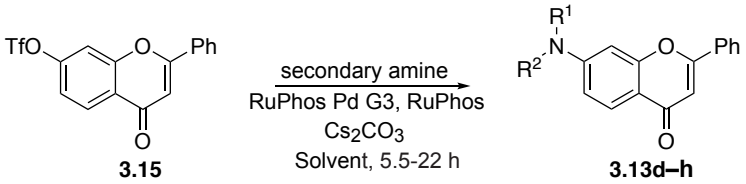

secondary amine	*7-aminoflavone 3.13*	*solvent*	*temp (°C)*	*yield (%)*
	**3.13d**	THF	50	63
	**3.13e**	Toluene	100	74
	**3.13f**	Toluene	100	71
	**3.13g**	THF	50	79
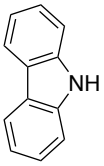	**3.13h**	Toluene	110	83

Table 3.3 Synthesis of flavyliums **3.12a**–**i**.

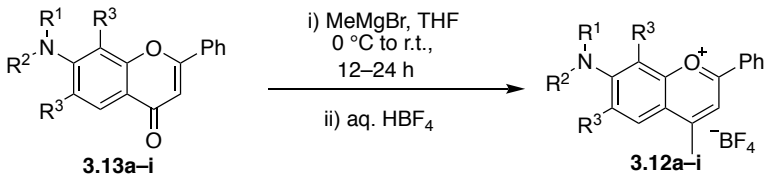

3.13a–i — ***7-aminoflavone 3.13***

3.12a–i — ***7-aminoflavylium 3.12***

number	*structure*	*number*	*structure*	
3.13a	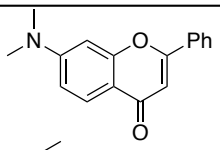	**3.12a**	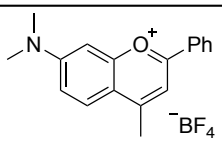	73
3.13b	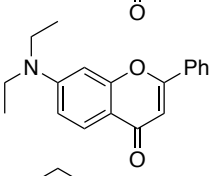	**3.12b**	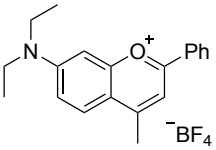	81
3.13c	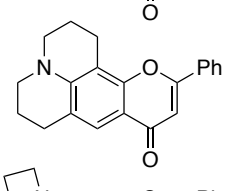	**3.12c**	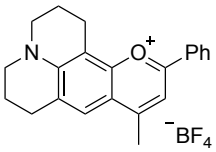	74
3.13d	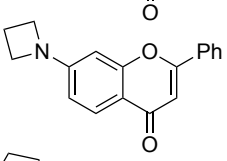	**3.12d**	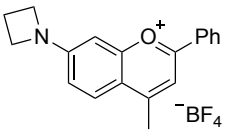	39
3.13e	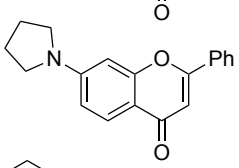	**3.12e**	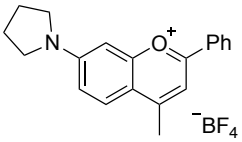	65
3.13f	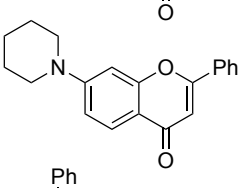	**3.12f**	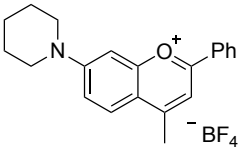	86
3.13g	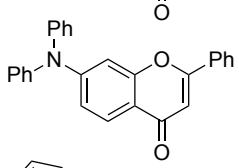	**3.12g**	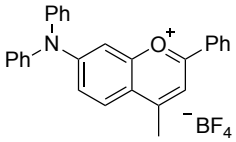	71
3.13h	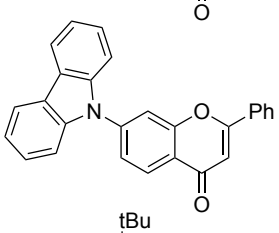	**3.12h**	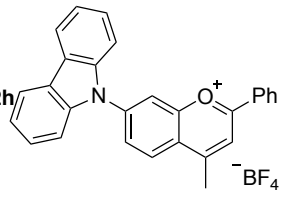	62
3.13i	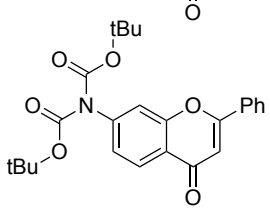	**3.12i**	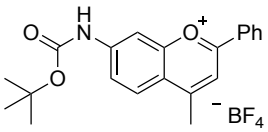	—[a]

[a]not isolated

Table 3.4 Synthesis of flavylium heptamethine dyes **3.1**–**3.11**.

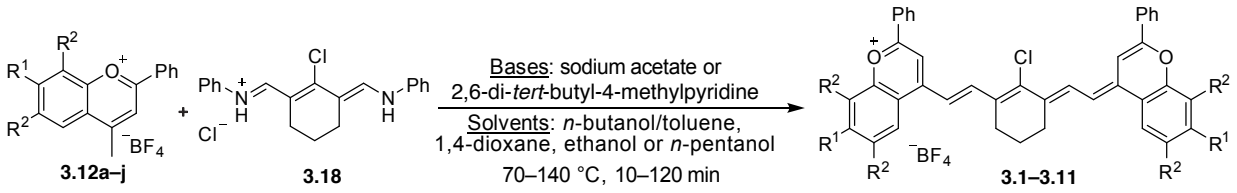

3.12a–j **3.18** **3.1–3.11**

Flavylium 12	*R^1*	*R^2*	*base*[a]	*solvent*	*temp (°C)*	*time (min)*	*yield # (%)*	*dye*
3.12a		H	A	*n*-butanol/toluene	100	15	51	**3.1**
3.12b		H	A	*n*-butanol/toluene	100	10	40	**3.2**
3.12c	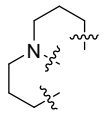		A	ethanol	70	120	37	**3.3**
3.12d		H	A	*n*-butanol/toluene	100	10	37	**3.4**
3.12e		H	B	*n*-pentanol	140	50	8	**3.5**
3.12f		H	B	*n*-butanol/toluene	100	120	26	**3.6**
3.12g		H	B	1,4-dioxane	100	15	11	**3.7**
3.12h	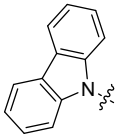	H	B	1,4-dioxane	90	15	13	**3.8**
3.12i	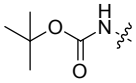	H	B	1,4-dioxane	95	15	33[b]	**3.9**
3.12j [c]		H	B	*n*-butanol/toluene	100	15	33	**3.10**
–		H	B	*n*-butanol/toluene	90	45	5	**3.11**

[a]base: A = sodium acetate; B = 2,6-di-*tert*-butyl-4-methylpyridine
[b]yield over two steps, flavylium **12**i not isolated.
[c]counterion is Cl^-

3.3.2 Photophysical Characterization of Flavylium Heptamethine dyes

Differences in $\lambda_{max,abs}$ are essential for excitation multiplexing. We characterized the photophysical properties of **3.1**–**3.11** in dichloromethane (DCM), finding that the flavylium heptamethine dyes have absorption/emission spanning the NIR to SWIR regions of the

electromagnetic spectrum (Figure 3.2A–C, Table 3.5). Compared to Flav7 (**3.1**), with $\lambda_{max,abs}$ = 1,027 nm, **3.9** and **3.10** underwent hypsochromic shifts. The 7-methoxy-substituted dye **3.10** is ~43 nm blue-shifted from Flav7 ($\lambda_{max,abs}$ = 984 nm), similar to the unsubstituted flavylium dye **3.11** (IR-27)[49]. Conversely, dyes **3.3** and **3.7** displayed substantial bathochromic shifts compared to Flav7. The diphenylamino-substituted **3.7** is ~23 nm red-shifted, while julolidine derivative **3.3** is red-shifted by ~35 nm ($\lambda_{max,abs}$ = 1,061 nm). Linear and cyclic aliphatic amine-substituted dyes **3.2** and **3.4**–**3.6** exhibit minor red-shifts. Plotting absorption/emission wavelengths of nine dyes in the series against Hammett σ_m values[50] resulted in a strong correlation (R^2 = 0.96; Figure 3.2D and Section 3.6.2). This increased understanding of the relationship between structure and absorption/emission wavelengths sets up opportunities for predicting fluorophore structures to match any desired excitation wavelength. Further characterization of the panel of flavylium polymethine dyes was necessary to determine their maximum brightness (brightness(ε_λ) = $\varepsilon_\lambda \times \Phi_F$). We found that the absorption coefficients (ε) vary from ~110,000 to ~240,000 $M^{-1}cm^{-1}$, in line with the high-absorption cross-sections characteristic for polymethine fluorophores.[34] The fluorescence quantum yields (Φ_F; relative measurements to dye IR-26 = 0.05% (refs. [51,52]); see Section 3.6.3) remain rather constant, in the ~0.4–0.6% range. The combined high and relatively consistent ε and Φ_F values result in a series of bright dyes spanning from 984–1,061 nm (Figure 3.2B; Table 3.5), primed for real-time excitation multiplexing in the SWIR.

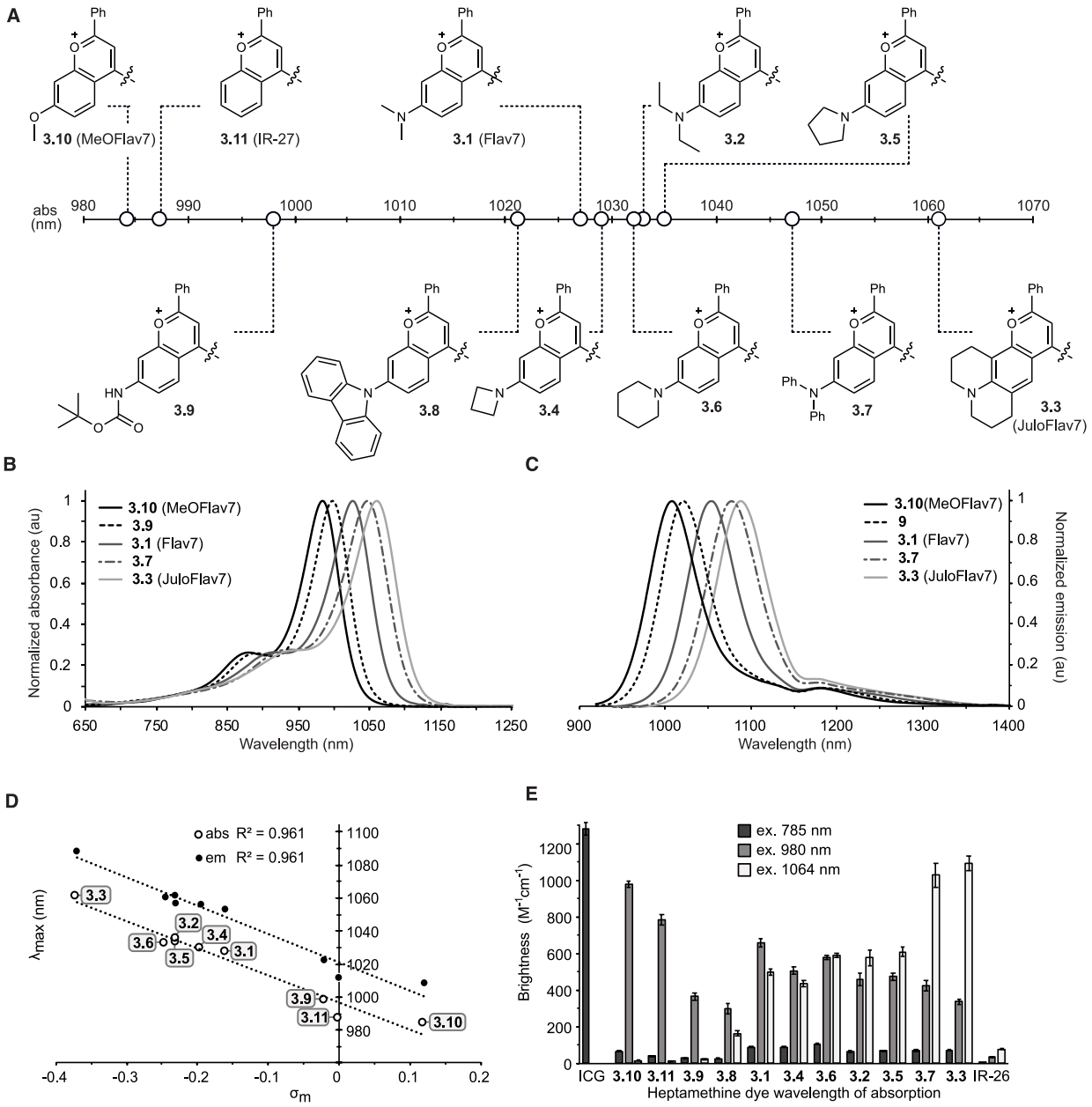

Figure 3.2 Panel of flavylium heptamethine dyes and their photophysical properties. A) Heterocycle structures and absorption wavelength maxima visualized graphically on the electromagnetic spectrum. B–C) Absorption (B) and emission (C) profiles (excitation wavelength, 885 nm) of selected polymethine dyes. D) Hammett plot relating σ_m substituent constants[50] to absorption and emission wavelengths of dyes **3.1**–**3.6** and **3.9**–**3.11**. E) Brightness (defined as $\varepsilon_\lambda \times \Phi_F$) of the heptamethine derivatives at relevant excitation wavelengths (λ = 785 nm (dark grey), λ = 980 nm (light grey) and λ = 1,064 nm (white)). Error bars represent the propagated error from standard deviations in ε and Φ_F measurements.

Table 3.5 Photophysical properties of flavylium heptamethine dyes

dye	$\lambda_{max,abs}$ (nm)	ε_{max} ($M^{-1}cm^{-1}$)	$\lambda_{max,em}$ (nm)	Φ_F (%)	Brightness(ε_{max}) ($M^{-1}cm^{-1}$)
3.1 (Flav7)	1027	241,000 ± 1,000	1053	0.61 ± 0.02	1470 ± 50
3.2	1033	190,000 ± 10,000	1057	0.62 ± 0.02	1180 ± 70
3.3 (JuloFlav7)	1061	238,000 ± 7,000	1088	0.46 ± 0.01	1090 ± 40
3.4	1029	207,000 ± 1,000	1056	0.51 ± 0.02	1060 ± 40
3.5	1034	247,000 ± 1,000	1061	0.48 ± 0.02	1190 ± 50
3.6	1032	110,000 ± 10,000	1060	0.54 ± 0.01	590 ± 60
3.7	1047	210,000 ± 10,000	1078	0.58 ± 0.02	1220 ± 70
3.8	1021	140,000 ± 10,000	1048	0.45 ± 0.01	630 ± 40
3.9	998	108,000 ± 4,000	1022	0.42 ± 0.02	450 ± 30
3.10 (MeOFlav7)	984	190,000 ± 1,000	1008	0.52 ± 0.01	990 ± 20
3.11 (IR-27)	987	231,000 ± 6,000	1011	0.35 ± 0.01	810 ± 30
ICG	787[a]	194,000[a] ± 5,000	818[a]	0.66[a,b] ± 0.01	1,280 ± 30[b]
IR-26	1080	171,000 ± 5,000	1114	0.05[c]	86 ± 3

[a]data taken from Rurack, K. & Spieles, M. *Anal. Chem.* **83**, 1232–1242 (2011). (measured in EtOH)
[b]value includes only the % emission between 1000–1300 nm (5%), from Carr, J. A. *et al. Proc. Natl. Acad. Sci. USA* **115**, 4465–4470 (2018).
[c]value from Semonin, O. E. et al. *J. Phys. Chem. Lett.* 1, 2445–2450 (2010). and treated as a constant for relative Φ_F measurements.

3.3.3 Excitation Multiplexing with Flavylium SWIR Dyes

For excitation multiplexing, we are most interested in properties of the series of polymethine fluorophores when excited at 980 and 1,064 nm, as these wavelengths correspond to readily available, low-cost and high-power (≥25 W) continuous-wave lasers and allow for multiplexing with established dyes like ICG and IRDye 800CW at 785 or 808 nm. Thus, we calculated brightness(ε_λ) values for each dye using the absorption coefficient at the relevant wavelengths. The variation in brightness when excited at the wavelength of interest versus all other wavelengths used determines the amount of cross-talk between channels. Cross-talk reduces the contrast between channels, limiting the dynamic range. From Figure 3.2E and Figure 3.3 we observe that Flav7 (**3.1**) has similar brightness when excited with 980 or 1,064 nm light, and thus

is poorly suited for excitation multiplexing with these lasers. Examining Figure 3.2E and Figure 3.3, candidates emerge for excitation-multiplexed imaging, with **3.3** (named JuloFlav7) being superior for imaging at 1,064 nm (brightness(ε_{1064}) = 1,090 ± 40 M^{-1} cm^{-1}) and **3.10** (named MeOFlav7) having the advantage at 980 nm (brightness(ε_{980}) = 980 ± 20 $M^{-1}cm^{-1}$). We further analyzed the photophysical properties of JuloFlav7 (**3.3**) for multiplexing using the percent difference of brightness at λ = 1,064 versus λ = 980 nm as a numerical metric to predict multiplexing performance and found that JuloFlav7 (**3.3**) is predicted to have the lowest levels of cross-talk compared to existing polymethine dyes (Figure 3.4)[19,41]. This 'excitation-matching' concept can be further visualized by observing the absorption profiles and excitation wavelengths on the same plot (Figure 3.5A). Employing ICG, which is well matched to the common 785 nm laser, adds a third color.

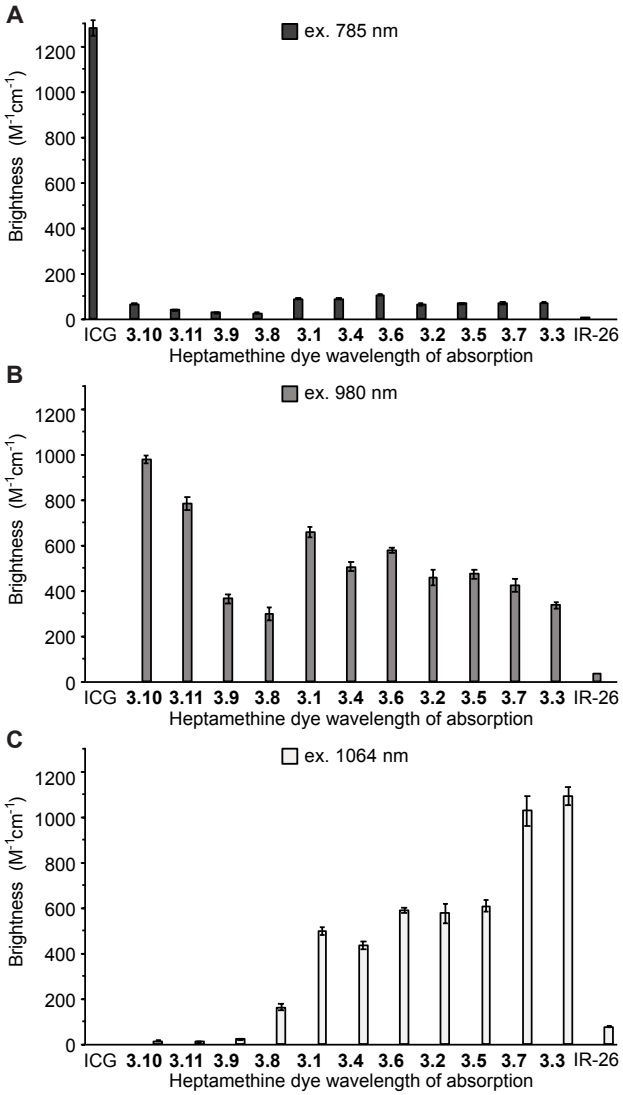

Figure 3.3 Brightness (defined as $\varepsilon_\lambda \times \Phi_F$) of the heptamethine dyes at relevant excitation wavelengths A) λ = 785 nm, B) λ = 980 nm, and C) λ = 1,064 nm. Error bars represent the propagated error from standard deviations in ε and Φ_F measurements. Data here are identical to those in Figure 3.2E and are displayed here in separate plots for increased visibility.

A

dye	$\lambda_{max,abs}$ (nm)	ε_{980} ($M^{-1}cm^{-1}$)	ε_{1064} ($M^{-1}cm^{-1}$)	Φ_F (%)	Brightness (ε_{980}) ($M^{-1}cm^{-1}$)	Brightness (ε_{1064}) ($M^{-1}cm^{-1}$)	Percent difference[c] (%)	exposure time (ms)	frame rate (s^{-1})	delivery vehicle	citation
Flav7 (3.1)	1027	108,000	81,200	0.61	660	495	-28	100	9.1	micelles	d
IR-1061	1063	98,100	296,000	0.32	310	947	102	100	8.4	micelles	e
FD-1080	1043[a]	29,300[a,b]	36,200[a,b]	0.44[a]	130	159	21	100	7.2	FBS complex	f
BCT1070	1014	81,100[b]	37,300[b]	0.09	70	34	-80	200	n.d.	micelles	g
JuloFlav7 (3.3)	1061	73,000	236,000	0.46	340	1087	105	10	100	micelles	this work

All photophysics are in DCM, except when stated otherwise
[a]Measured in DMSO
[b]Data extracted from absorption trace and reported ε value
[c]Percent difference = $\frac{\text{Brightness}(\varepsilon_{1064}) - \text{Brightness}(\varepsilon_{980})}{[\text{Brightness}(\varepsilon_{1064}) + \text{Brightness}(\varepsilon_{980})]\ /2} * 100$

[d]Cosco, E. D. *et al. Angew. Chem. Int. Ed.* **56**, 13126–13129 (2017).
[e]Tao, Z. *et al. Angew. Chemie Int. Ed.* **52**, 13002–13006 (2013).
[f]Li, B., Lu, L., Zhao, M., Lei, Z. & Zhang, F. *Angew. Chemie Int. Ed.* **57**, 7483–7487 (2018).
[g]Wang, S. *et al. Nat. Commun.* **10**, 1058 (2019).

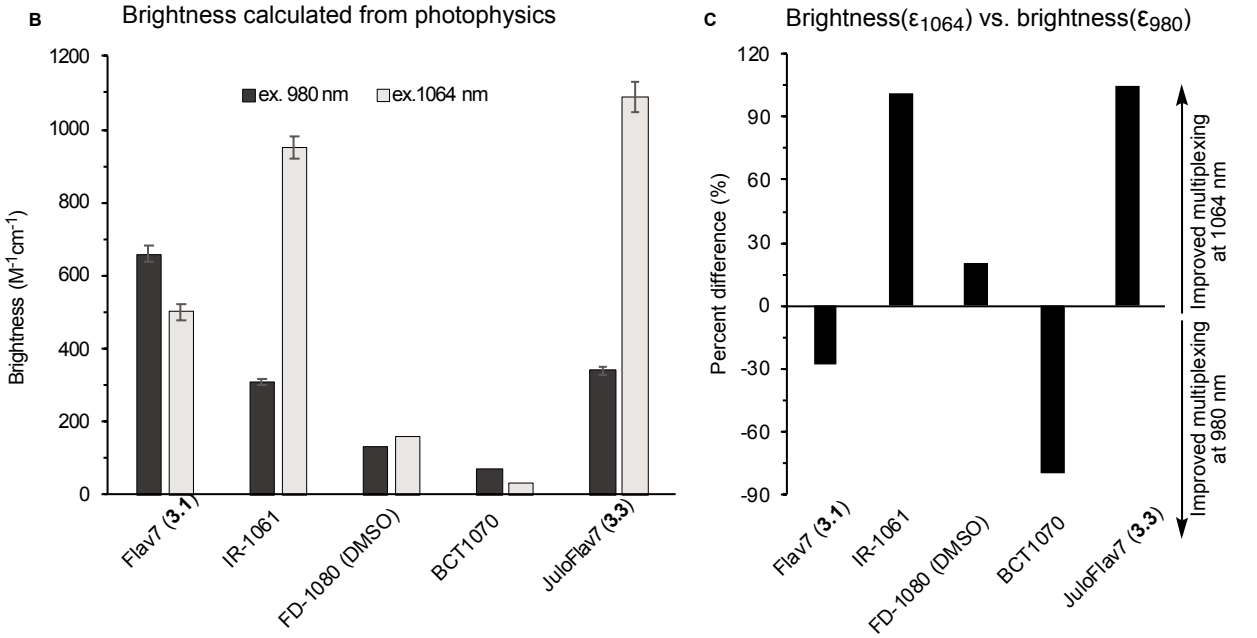

Figure 3.4[2,3] Comparison of photophysical properties related to multiplexing between 980 and 1,064 nm of JuloFlav7 (**3.3**) to initial dyes used for SWIR imaging with >1,000 nm. A) Table comparing photophysical properties of dyes upon 980 or 1,064 nm excitation, exposure times and frame rates of imaging obtained, and delivery vehicles used in the original report. (Imaging speeds are dependent on camera gain, read noise, dark current, pixel size, read time, optical throughput, and irradiation wavelength/intensity, in addition to probe concentrations and deliverable dose. Aiming for a qualitative comparison, we assume each report chose suitable or optimal parameters to obtain the reported results.) B) Brightness values upon 980 or 1,064 nm excitation plotted for each dye. Error bars

[2] While IR-1061 looks to be a close second to JuloFlav7, in both brightness and relative signal at 1,064 nm, these results are not translated *in vivo*, likely due to instability in physiological environments, as we have characterized previously (Ref. [39]).

[3] Donor-acceptor-donor (DAD) dyes[20–22, 24 and others] have broad NIR absorption bands ~750 nm which precludes them from the longer wavelength excitation (980 nm, 1,064 nm) that are needed for the presented excitation-multiplexed imaging.

represent propagated error from the standard deviation of the ε and Φ_F (if available). C) Percent difference of brightness at 1,064 vs. 980 nm plotted for each dye.

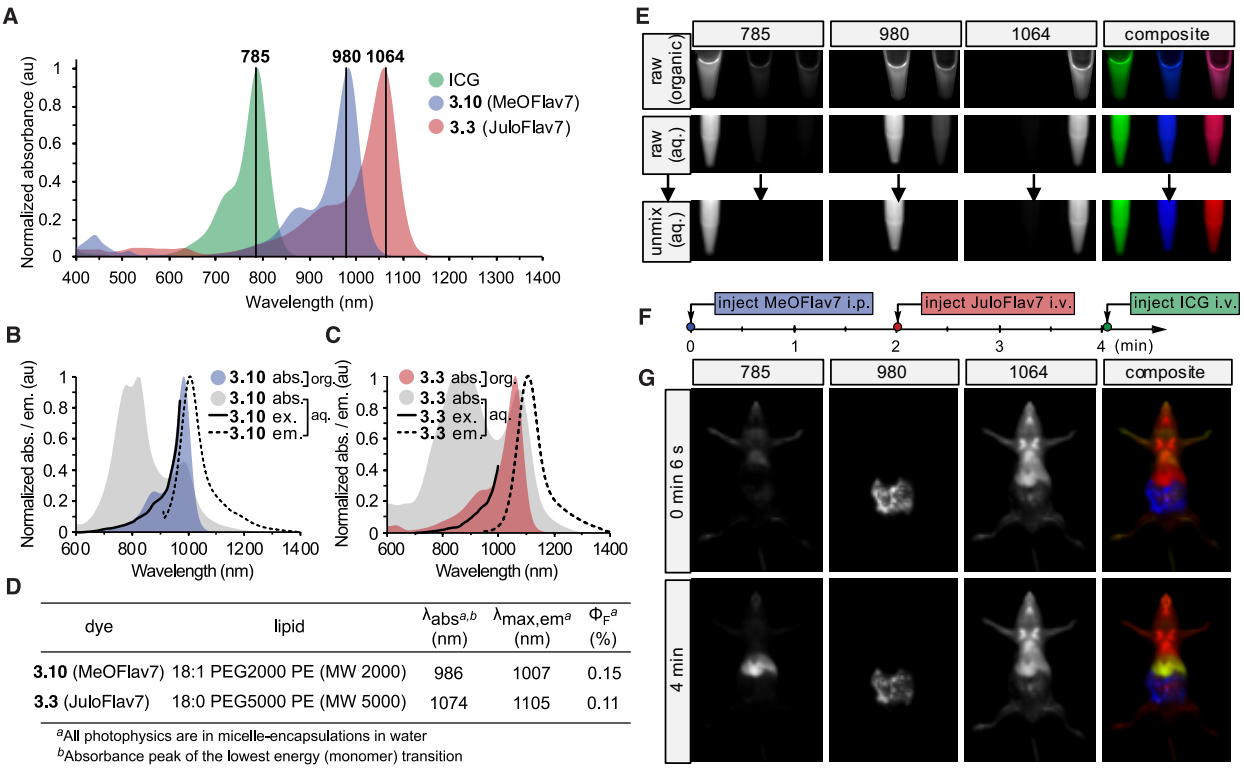

Figure 3.5[4] Excitation-multiplexed SWIR imaging. A) Absorption profiles of dyes used in imaging experiments plotted against excitation wavelengths employed. B-C) Absorption spectra (grey); emission spectra (excitation at 880 nm (B) and 900 nm (C), black dotted line); and excitation spectra (emission monitored at 1,008 nm (B) and 1,088 nm (C), black solid line) of micelle-encapsulated **3.10** (B) and **3.3** (C) overlaid with absorption traces of dyes in DCM (colored). D) Photophysics of the micelle-encapsulated dyes in water. E) Raw and unmixed images of successive frames and merged three-color images of vials containing ICG (left), **3.10** (center) and **3.3** (right) in ethanol or DCM (top) and in micelles in water (middle and bottom). Arrows indicate linear unmixing procedure. F) Experimental timeline of administration of the three probes used in (G). G) Multiplexed *in vivo* images using 785, 980 and 1,064 nm excitation wavelengths (average power density = 78 mW cm^{-2}) and 1,150–1,700 nm collection (10 ms exposure time; 27.8 fps). Displayed images are averaged over five frames. Abs, absorption; em, emission; ex, excitation; org, organic; aq, aqueous; PEG, polyethylene glycol; PE, phosphoethanolamine; MW, molecular weight; λ_{abs}, wavelength of absorption maximum for the lowest energy (monomer) species; $\lambda_{max,em}$, wavelength of maximum emission.

To perform excitation multiplexing with single-channel SWIR detection using the new, bright SWIR-emissive dyes, a custom SWIR imaging configuration with three lasers and a fast

[4] Imaging data in this chapter with Mara Saccomano, Bernardo Arús, and Sarah Glasl.

InGaAs camera was constructed (Figure 3.6). With 785, 980 and 1,064 nm lasers, tailored excitation could preferentially excite three fluorophores. Emission is detected in a color-blind fashion using identical filters and settings for all channels. This approach provides high-resolution images without optical aberrations arising from detection at different wavelengths (Figures 3.7–3.8 and Section 3.6.4 for multiplexing resolution effects). In addition, this method enables fast acquisition of all channels in each imaging frame by using rapidly modulated excitation sources and identical acquisition settings in a single detector. To accomplish real-time imaging, triggers on the millisecond timescale are sent independently to each continuous-wave laser, and the detector is programmed to collect a single frame for each sequential excitation pulse (Section 3.6.5). While the effective frame rate of collection is slowed by a factor equal to the number of channels, video-rate acquisition was still achievable due to the well-matched, bright fluorophores.

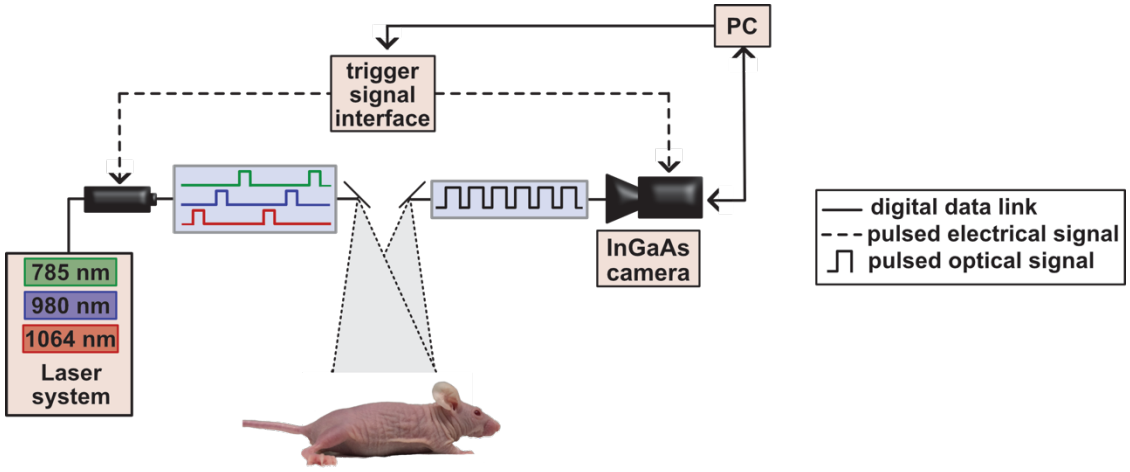

Figure 3.6 Electronic trigger-controlled excitation-multiplexed shortwave infrared imaging system.

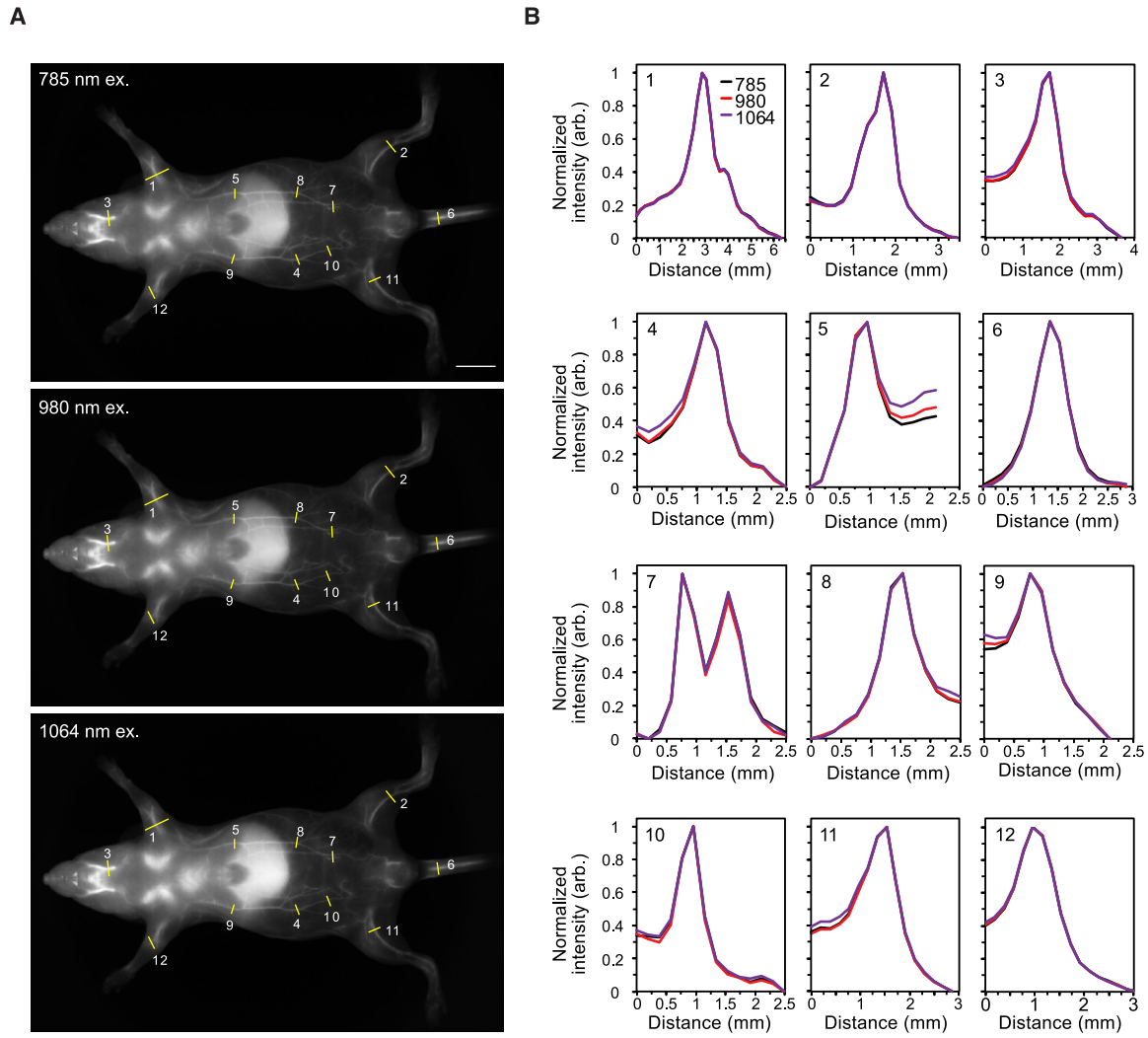

Figure 3.7 Resolution effects upon excitation multiplexing and single-channel detection in the SWIR. A) Images of a mouse phantom acquired after injection of JuloFlav7 (**3.3**) (94 nmol) and immediate euthanasia. Images were acquired with 785 nm excitation (93 mW cm^{-2}), 980 nm (30 mW cm^{-2}), and 1,064 nm (11 mW cm^{-2}) and collection 1,150–1,700 nm (48 ms, 20 fps). Displayed images are averaged over 200 frames. B) To observe resolution, 12 cross-sections were drawn over different vessels (labelled in (A)) and the baseline subtracted and normalized cross-sections are overlaid. ex. = excitation; LP = longpass.

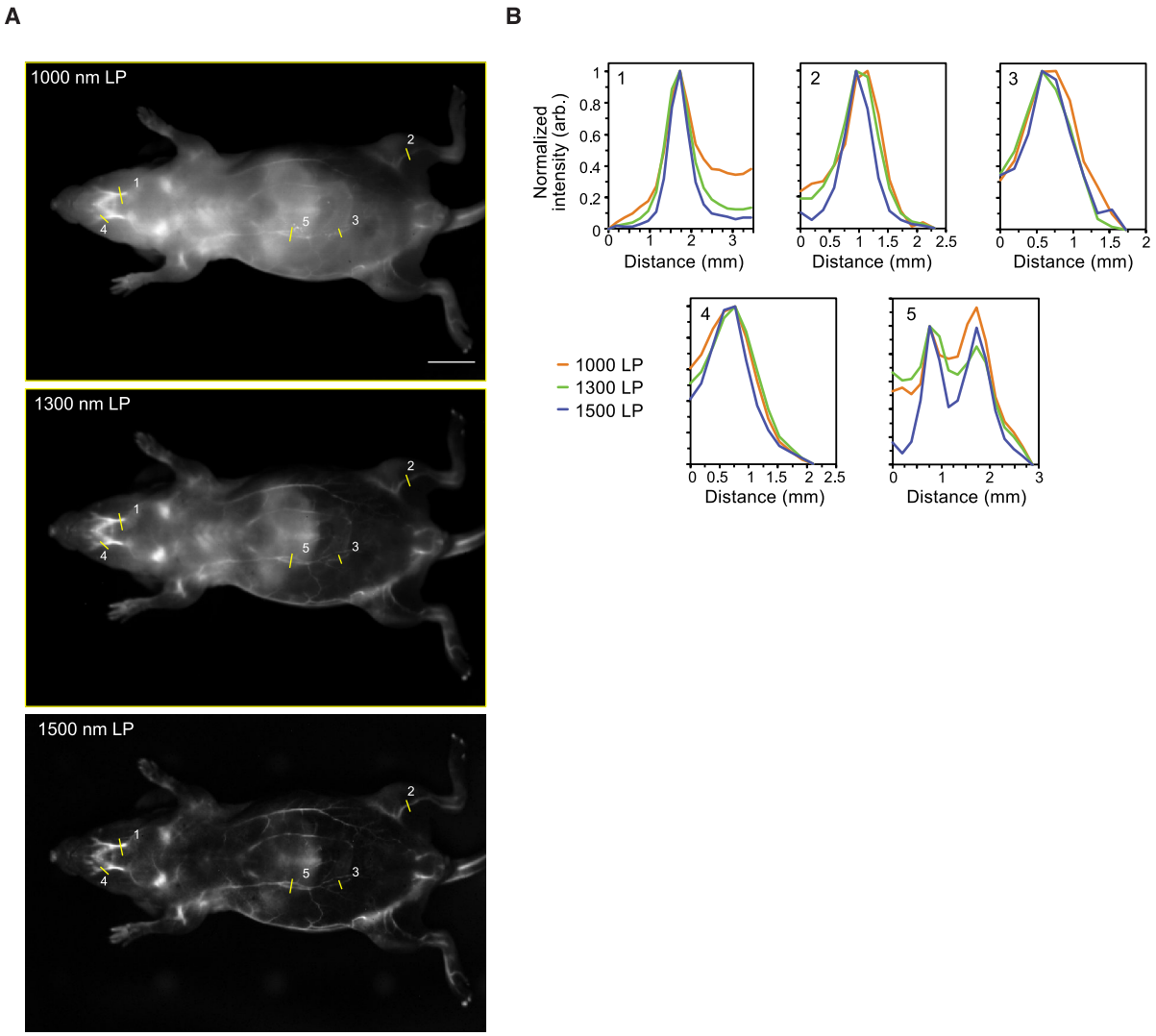

Figure 3.8 Resolution effects observed upon emission multiplexing with a single excitation wavelength in the SWIR. A) Images of a mouse phantom acquired after injection of JuloFlav7 (**3.3**) (94 nmol) and immediate euthanasia, after one freeze-thaw cycle. Images were acquired with 980 nm excitation. Laser powers and exposure time are as follows (1) 1,000 nm LP = 8.1 mW cm^{-2}, 30 ms; 1,300 nm LP = 24 mW cm^{-2}, 500 ms; 1,500 nm LP = 177 mW cm^{-2}, 500 ms. Displayed images are averaged over 200 frames. B) To observe resolution, 5 cross-sections were drawn over different vessels (labelled in (A)) and the baseline subtracted and normalized cross-sections are overlaid. LP = longpass.

In preparation for *in vivo* delivery of SWIR dyes, JuloFlav7 (**3.3**) and MeOFlav7 (**3.10**) were encapsulated in polyethylene glycol-coated micelles to impart water solubility (Figures 3.9–3.10). The micelle-encapsulated dyes demonstrate low toxicities to mammalian cells (Figure 3.11). The aqueous-soluble formulations of **3.3** and **3.10** display aggregation, which decreases the

concentration of emissive species present in the aqueous environment, but does not substantially alter their excitation or emission profiles (Figure 3.5B–D and Figure 3.12). We verified that excitation multiplexing proceeded in both organic and aqueous environments by imaging tubes containing ICG (Figure 3.5E, left), MeOFlav7 (**3.10**; center) and JuloFlav7 (**3.3**; right) in organic solvent (top), and micelle encapsulations in water (middle). In each case, three successive frames collected with 785, 980 and 1,064 nm lasers show high intensities in the left, center and right samples, respectively. Merging the three frames together yields a three-color image representing one effective multiplexed frame. Because molecules absorb minimal light at energies lower than their S_0 to S_1 transition, cross-talk occurs primarily in one direction. Linear unmixing can correct for minor signal overlaps between channels as seen in Figure 3.5E (bottom) and further discussed in the figure experimental procedures in Section 3.5.3.

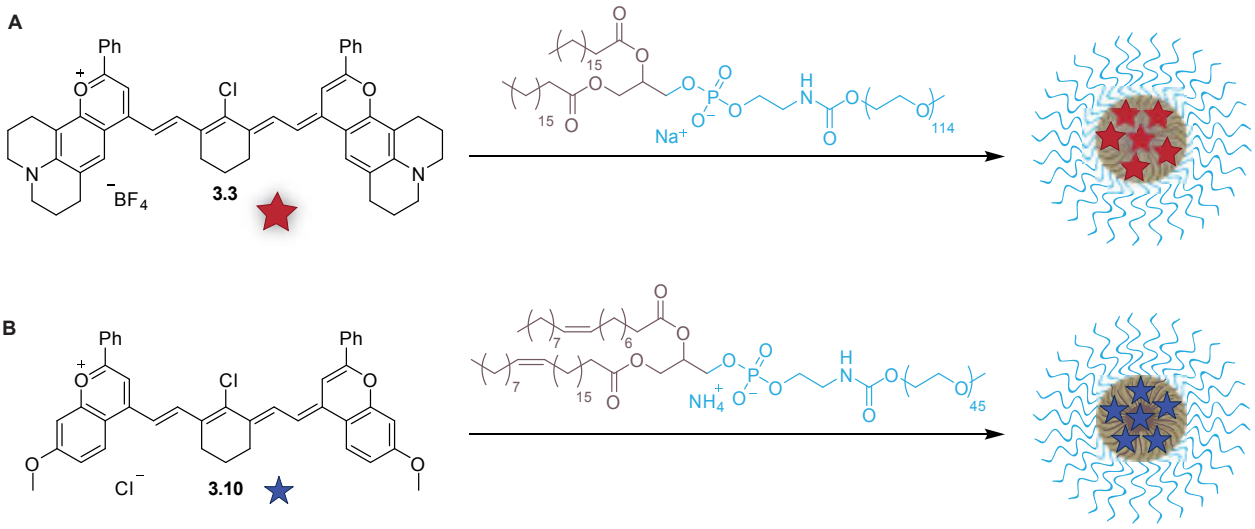

Figure 3.9 Assembly of PEG-phospholipid micelles. A) Encapsulation of JuloFlav7 (**3.3**) in 1,2-distearoyl-*sn*-glycero-3-phosphoethanolamine-*N*-[methoxy(polyethylene glycol)-5000] (sodium salt) lipid (abbreviated 18:0 PEG5000 PE) micelles. B) Encapsulation of MeOFlav7 (**3.10**) in 1,2-dioleoyl-*sn*-glycero-3-phosphoethanolamine-*N*-[methoxy(polyethylene glycol)-2000] (ammonium salt) lipid (abbreviated 18:1 PEG2000 PE) micelles.

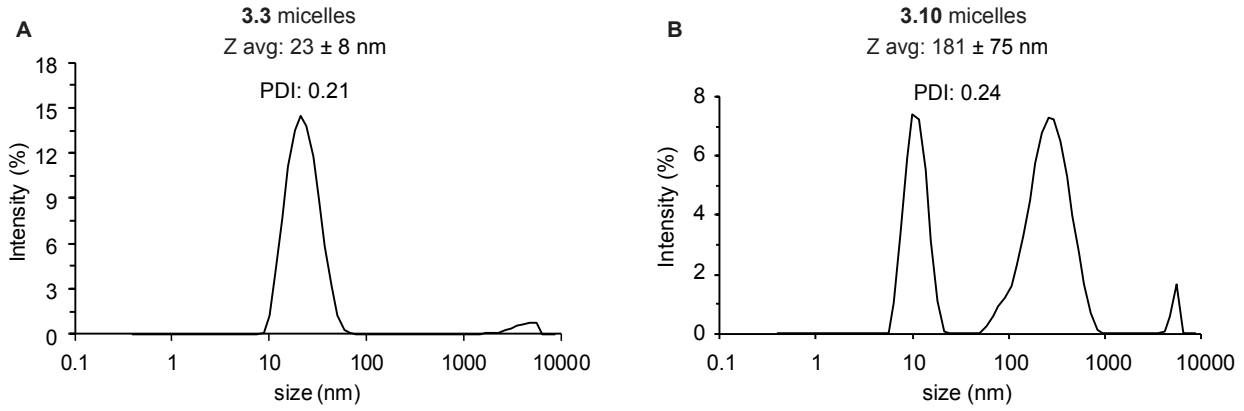

Figure 3.10 Dynamic light scattering (DLS) characterization of PEG-phospholipid micelles of A) JuloFlav7 (**3.3**) in 18:0 PEG5000 PE and B) MeOFlav7 (**3.10**) in 18:1 PEG2000 PE. Data are the average of three measurements, error represents the standard deviation. Note: in B) the peak at ~3 μm is 3% intensity by area but constitutes minimal aggregation as intensity measurements are proportional to diameter to the sixth power.

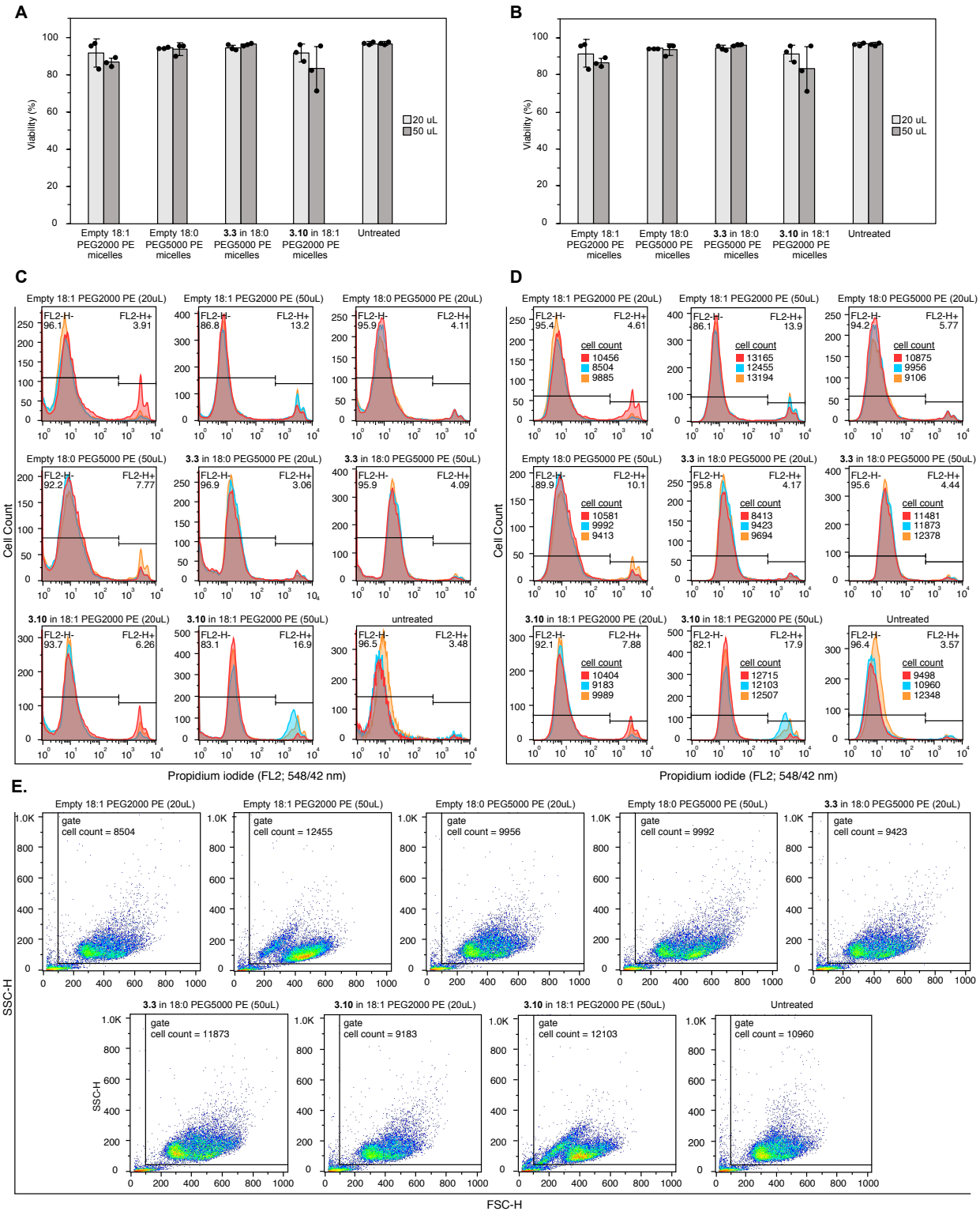

Figure 3.11[5] Viability of HEK293 cells upon incubation with empty (vehicle) and dye-filled micelles of **3.3** or **3.10** (light grey = 20 uL treatment; dark grey = 50 uL treatment) for 3 hours. A–B) Bar graphs displaying percent viability of ungated (A) and gated (B) populations. Data represent

[5] Data by Kelly Wong

the mean ± SD, n = 3 biological replicates. C–D) Histograms of ungated (C) and gated (D) populations. Number of cells for all ungated samples is 15000. E) Forward side scatter plots, with gates overlaid. One-tailed Student's t-test assuming unequal sample variance for each treatment with dye containing micelles compared to empty micelles do not show statistical significance (results were considered ns if $P > 0.05$). Ungated analysis: $P = 0.21$, **3.3** in 18:0 PEG5000 PE (20 uL); $P = 0.19$, **3.3** in 18:0 PEG5000 PE (50 uL); $P = 0.49$, **3.10** in 18:1 PEG2000 PE (20 uL); $P = 0.33$, **3.10** in 18:1 PEG2000 PE (50 uL). Gated analysis: $P = 0.42$, **3.3** in 18:0 PEG5000 PE (20 uL); $P = 0.15$, **3.3** in 18:0 PEG5000 PE (50 uL); $P = 0.50$, **3.10** in 18:1 PEG2000 PE (20 uL); $P = 0.34$, **3.10** in 18:1 PEG2000 PE (50 uL). Data are representative of two replicate experiments.

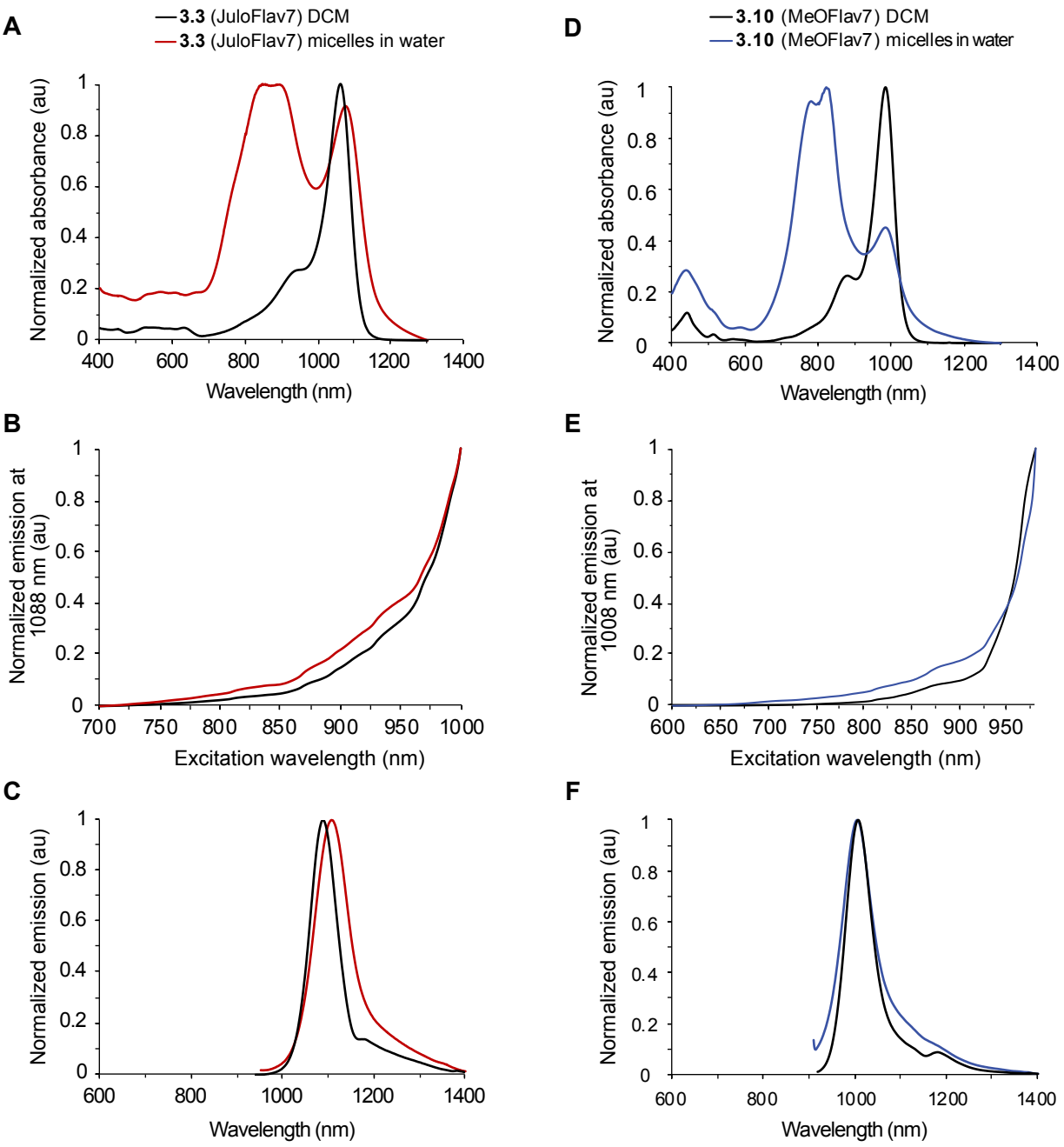

Figure 3.12 Absorption, excitation, and emission spectra of monomer dyes dissolved in DCM (black traces) and micelle-encapsulated dyes dispersed in water (colored traces) of A–C) JuloFlav7 (**3.3**, red), [excitation spectra: em. 1088 nm; emission spectra: ex. 885 nm (DCM) and ex. 900 nm (water)] and D-F) MeOFlav7 (**3.10,** blue), [excitation spectra: em. 1008 nm; emission spectra: ex. 885 nm (DCM) and ex. 880 nm (water)]. Consistency between excitation and emission spectra in organic solvent and micelles in aqueous solvent indicates that aggregation effects are not contributing to the emissive properties of the dye.

3.3.4 In vivo Demonstration of Multicolor SWIR imaging

Using single-channel imaging, we validated that micelles containing JuloFlav7 (**3.3**) could be imaged with 8–9 ms exposure time after intravenous (i.v.) injection through a tail vein catheter in anaesthetized mice, under 1,064 nm excitation and 1,150–1,700 nm detection (Supplementary Video 3.1 and Figure 3.13). The high signal-to-noise ratio obtained at 100 fps was encouraging and suggested that video-rate speeds would be attainable upon addition of multiple channels. Further, the excitation-matching strategy was validated by an approximately ten-fold improvement in speed compared to previously reported polymethine chromophores for imaging with 1,064 nm excitation (Figure 3.4). We performed three-color imaging *in vivo* by first performing an intraperitoneal (i.p.) injection of MeOFlav7 (**3.10**), followed by i.v. injections of JuloFlav7 (**3.3**) and finally ICG (Figure 3.5F and Supplementary Videos 3.2 and 3.3). Representative time points of the three-color video are displayed in Fig. 3.5G and Figure 3.14. The (bio)distribution of each dye over any position can be determined from the relative contributions of the three channels, as visualized in the single-channel images. After establishing both the technology and the molecular tools for multiplexed real-time observation of function in mice, the next goal was to enhance applications of SWIR imaging.

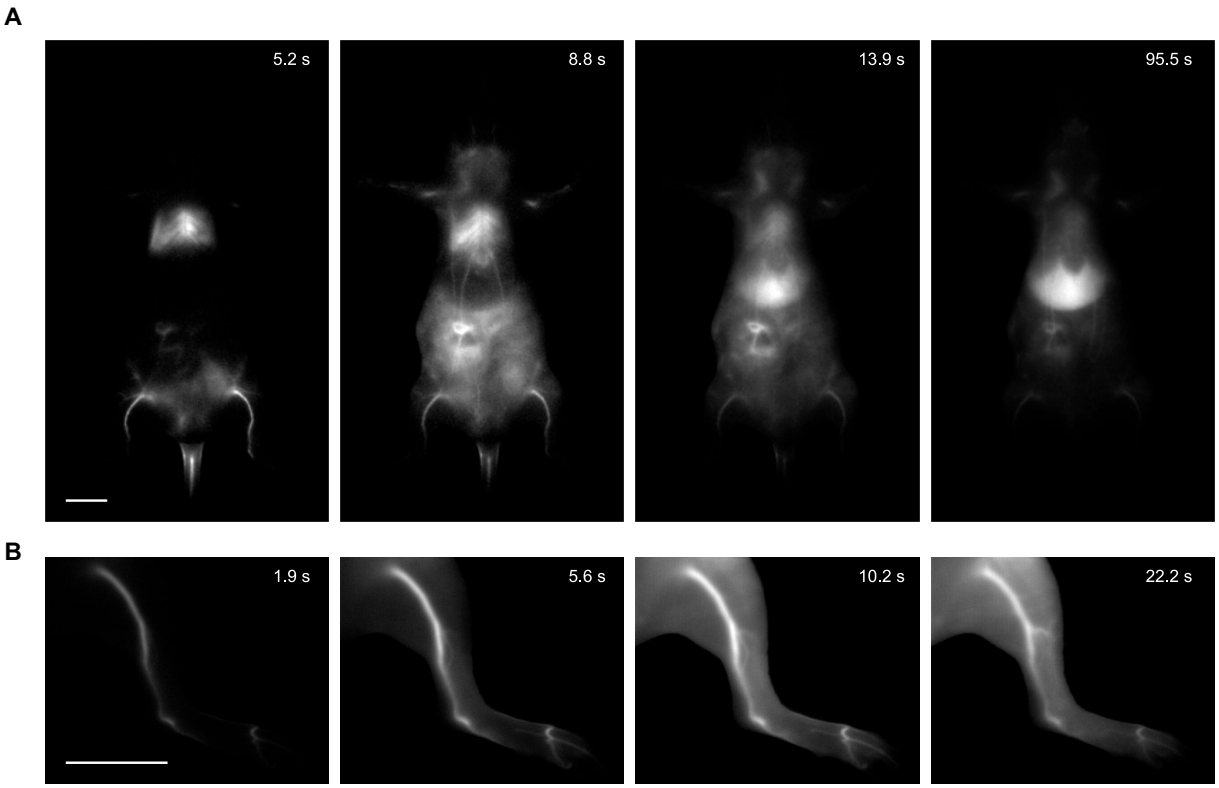

Figure 3.13 Imaging with 1,064 nm excitation after injection of JuloFlav7 (**3.3**) micelles. A) Whole mouse imaging at selected time-points after i.v. injection of JuloFlav7 (**3.3**) micelles (44 nmol) in PBS buffer with excitation at 1,064 nm (103 mW cm^{-1}) and 1,150–1,700 nm collection (8 ms exposure time, 100 fps). B) Imaging of the mouse hind-limb at selected time points after i.v. injection of JuloFlav7 (**3.3**) micelles (55 nmol) with excitation at 1,064 nm (95 mW cm^{-1}) with 1,100–17,00 nm collection (9 ms exposure time, 100 fps). Displayed images are averaged over 5 frames. Scale bars represent 1 cm. Data are representative of two replicate experiments.

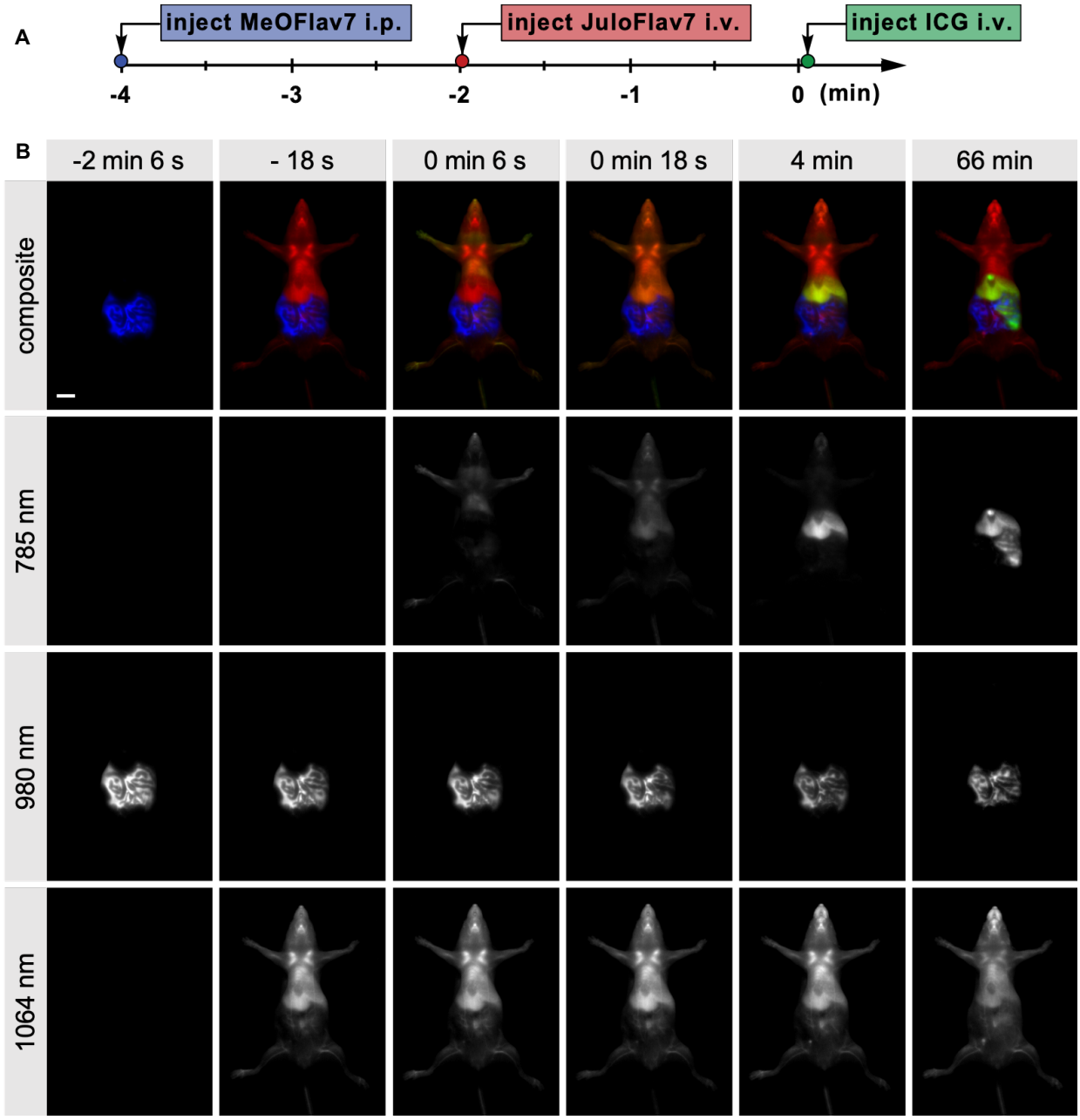

Figure 3.14 Video-rate multiplexed imaging *in vivo*. Imaging occurred after delivery of probes **3.10** (i.p, 211 nmol in micelles), **3.3** (i.v. 50 nmol in micelles) and ICG (i.v., 6.5 nmol). Acquisition parameters were excitation for three channels at 785 nm (78 $mWcm^{-1}$), 980 nm (77 $mWcm^{-1}$), and 1,064 nm (79 $mWcm^{-1}$) and 1150–1700 nm collection (10 ms exposure time, 27.8 fps). Displayed images are averaged over 5 frames. Data are representative of two replicate experiments. Scale bar represents 1 cm.

3.3.5 Applications of Multicolor Real-Time SWIR Imaging

Physiological properties such as heart rate, respiratory rate, thermoregulation, metabolism and central nervous system function are highly impacted by anaesthesia[53]. Methods to observe animals in their natural state are necessary to study physiology, but are currently limited to telemetric sensors and electrocardiography, involving surgical implantation[54] or external contact[55], respectively. Recently, high-speed SWIR imaging has enabled contact-free monitoring of physiology in awake mice[18]. Due to frame rates that are faster than macroscopic movements in animals, the heart rate and respiratory rate in awake animals can be quantified. In this study, we expanded this technique by observing awake, unperturbed mice in three colors. In Figure 3.15A, Figure 3.16 and Supplementary Video 3.4, awake mouse imaging was performed 80 min after i.p. administration of MeOFlav7 (**3.10**) and consecutive i.v. administration of JuloFlav7 (**3.3**) and ICG. From the top view of the moving mouse, ICG could be visualized exclusively in the liver and MeOFlav7 (**3.10**) in the abdomen, while JuloFlav7 (**3.3**) remained systemically distributed throughout the mouse. In addition to the ability to assess natural physiology, such as the awake breathing rate (Figure 3.15B, quantified here at 247 breaths per minute), contact free, these tools foreshadow more complex experiments in which the location of multiple probes could be monitored longitudinally, non-invasively and without anaesthesia.

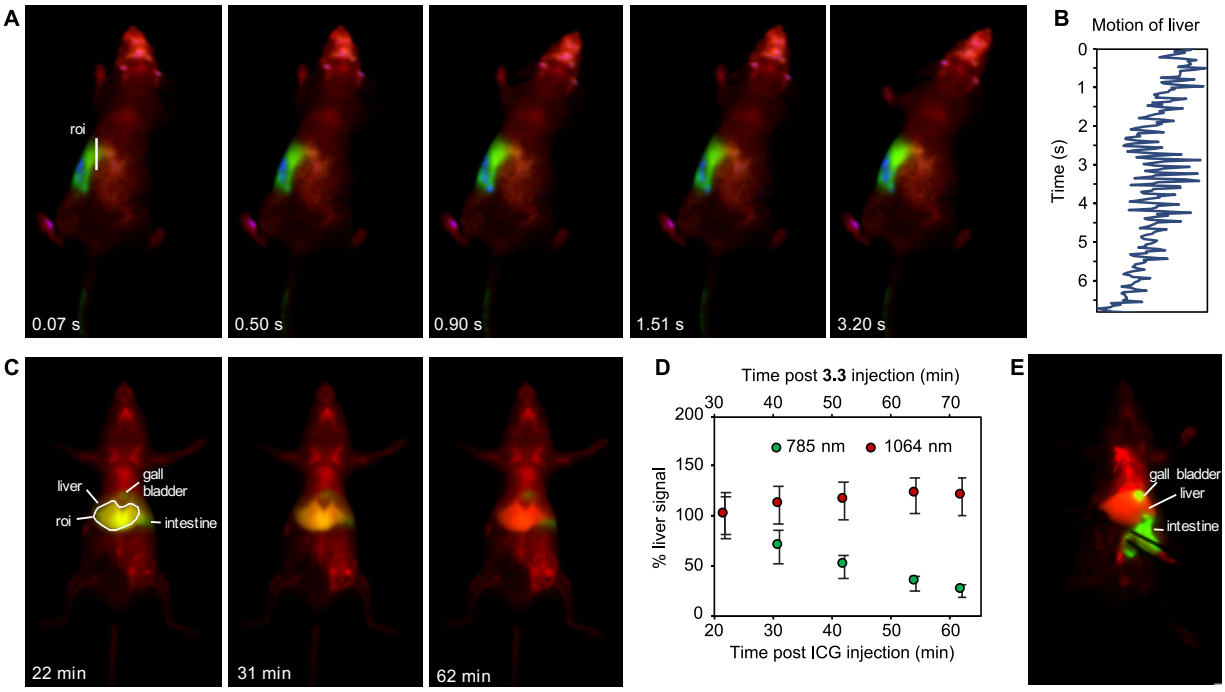

Figure 3.15 Applications enhanced by SWIR multiplexed imaging. A) Multiplexed imaging of an awake mouse showing one continuous movement of the head with 785, 980 and 1,064 nm excitation wavelengths (average power density = 78 mW cm^{-2}) and 1,150–1,700 nm collection (10 ms exposure time; 27.8 fps). Displayed images are a single frame. B) Awake breathing rate (247 breaths per minute), analyzed by quantifying the liver motion (by the center of mass) over the region of interest (r.o.i.) in (A). C) Imaging of ICG clearance with systemic labelling by JuloFlav7 (**3.3**) micelles. Multiplexed *in vivo* images using 785 and 1,064 nm excitation (100 mW cm^{-2}) and 1,150–1,700 nm collection (5 ms exposure time; 50 fps). Displayed images are averaged over five frames. D) Percent signal in the liver of ICG and micelles of JuloFlav7 (**3.3**) over one hour. Data are displayed as the mean intensity over the r.o.i. (in c) ± standard deviation, n = 805 pixels within the r.o.i. E) Two-color necropsy procedure, captured in real time in Supplementary Video 3.5. Acquisition settings are as in (C).

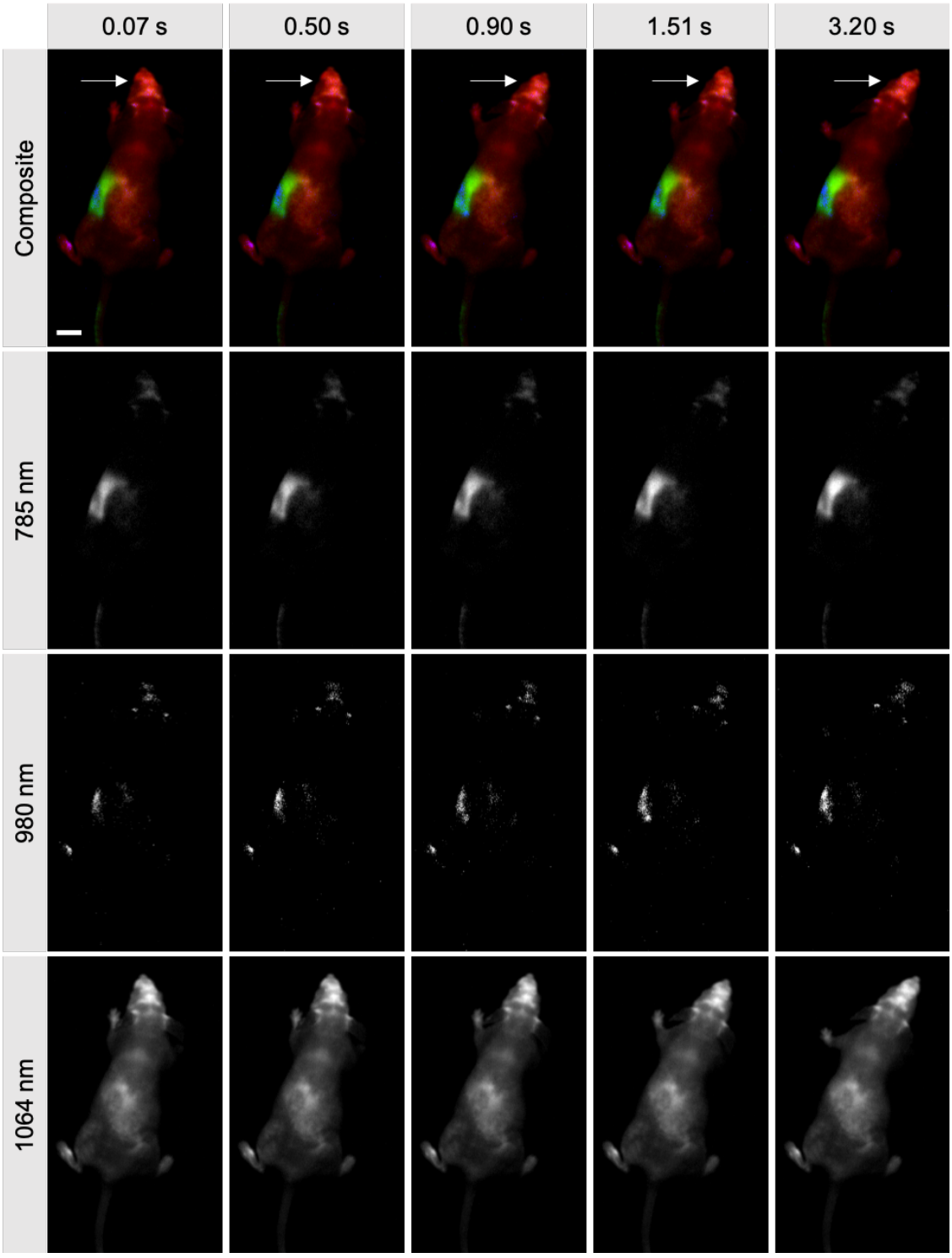

Figure 3.16 Imaging of an awake mouse in three colors. Imaging occurred ~80 min after delivery of probes **3.10** (i.p, 211 nmol in micelles), **3.3** (i.v. 50 nmol in micelles) and ICG (i.v., 6.5 nmol). The acquisition parameters were excitation for three channels at 785 nm (78 $mWcm^{-1}$), 980 nm (77 $mWcm^{-1}$), and 1,064 nm (79 $mWcm^{-1}$) and 1150–1700 nm collection (10 ms exposure time, 27.8 fps). Displayed images are single frames. Scale bar represents 1 cm.

In addition, biodistribution of two species can be monitored in the same organs. For example, the accumulation and clearance from the liver of each probe can be observed and decoupled. We injected JuloFlav7 (**3.3**) and ICG consecutively through the tail vein and imaged the whole mouse at several time points over a one-hour period (Figure 3.15C). In the duration of the experiment, the liver signal from the 1,064 channel remained constant, in contrast to the 785 channel, which shows depletion over time. (Figure 3.15D and Figure 3.17). The fast acquisition speeds obtained via excitation multiplexing enable real-time (50 fps in two colors) feedback during necropsies and surgeries (Figure 3.15E and Supplementary Video 3.5). The methods reported herein are applicable not only to non-invasive imaging but also in aiding surgeons in identifying essential and/or diseased structures during intraoperative procedures[56,57].

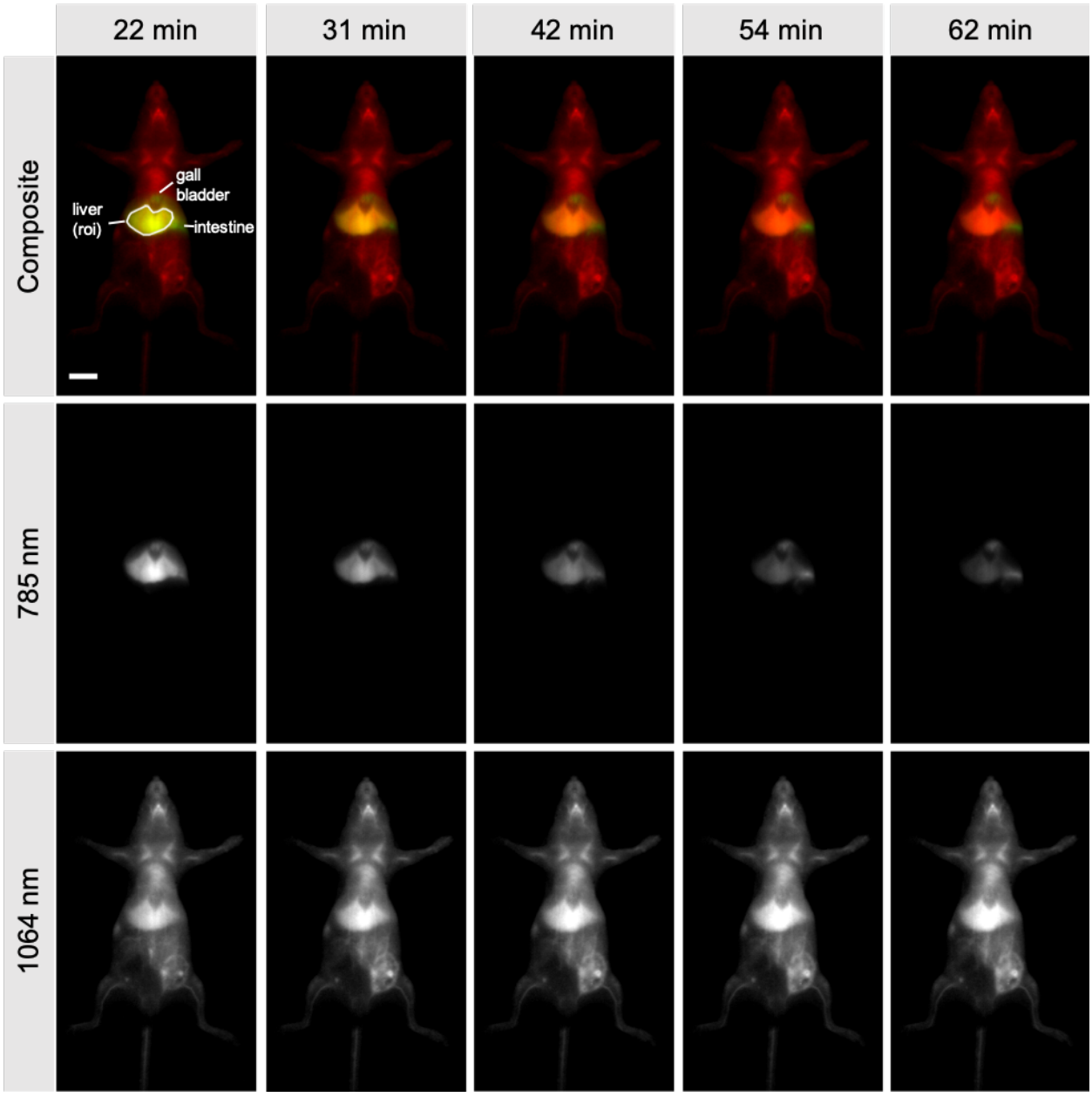

Figure 3.17 Liver clearance monitored over time in two colors. Probes **3.3** (50 nmol in micelles) and ICG (6.5 nmol) were delivered by i.v. injection. Acquisition parameters were excitation for two channels at 785 nm (100 $mWcm^{-1}$), and 1,064 nm (100 $mWcm^{-1}$) and 1150–1700 nm collection (5 ms exposure time, 50 fps). Displayed images are averaged over 5 frames. Scale bar represents 1 cm.

A widely investigated use of fluorescence-guided surgery is for the lymphatic system, both to identify sentinel lymph nodes implicated in cancer[58] and to assess the structure/function of

lymphatic networks in lymphovascular disorders[59]. A complementary clinical need is to safely and quickly assess vascular function[60]. With administration of ICG and JuloFlav7 (**3.3**) in the lymphatic and circulatory systems, respectively, both essential functions can be observed simultaneously. ICG was injected intradermally into the footpads and the tail. After 40 min, ICG had accumulated in the lymph system, and the pulsating motion of the collecting lymphatic vessels could be observed (Supplementary Video 3.6). Subsequently, JuloFlav7 (**3.3**) was injected intravenously, immediately filling the vasculature (Figure 3.18A–C, Figure 3.19 and Supplementary Video 3.6). Image collection at 21 fps in two channels gave high spatially and temporally resolved images with separate visualization of lymph vessels from veins and arteries (Figure 3.18D–E and Figure 3.20). Notably, the function of each vessel, modelled by the signal across a linear cross-section, can be observed in real time (Figure 3.18F). The ability to differentiate lymph and circulatory structures and simultaneously monitor their function has implications in non-invasive diagnostics as well as in expanding technologies for fluorescence-guided surgery.

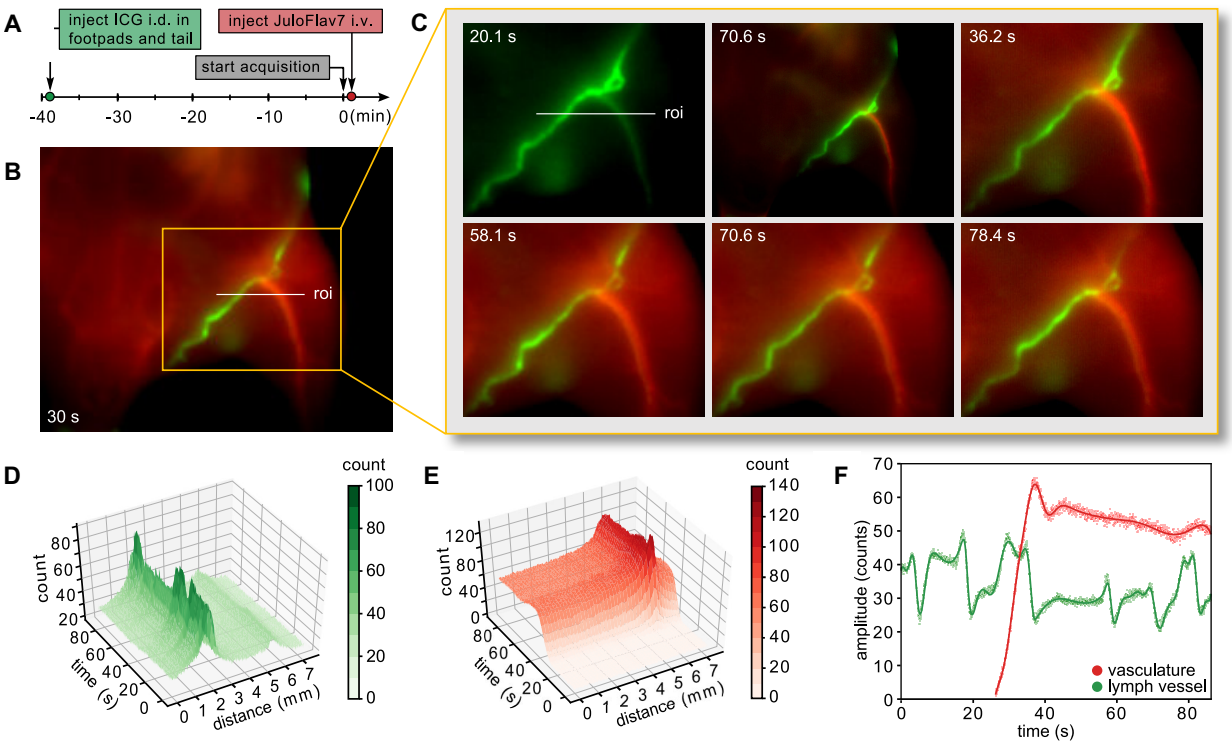

Figure 3.18 Orthogonal lymphatic and circulatory imaging with high spatiotemporal resolution after intradermal (i.d.) injection of ICG and i.v. injection of JuloFlav7 (**3.3**) micelles. A) Experimental timeline. B) Representative image acquired 30 s after injection of JuloFlav7 (**3.3**) micelles. C) Time points over the relevant time period analyzed in D–F. D–E) Three-dimensional plots of the 785 nm channel (D) and 1,064 nm channel (E) demonstrating simultaneous intensity information in two colors over the r.o.i. indicated in (B) and (C), and highlighting the spatial and temporal resolution captured. Contour plots are shown in Figure 3.19. F) The signal in each vessel over time can be quantified by plotting the amplitude of the vessel, fit as a Gaussian curve at each frame (points). The data is interpolated using a smoothing spline fit (solid lines). Acquisition, 785 and 1,064 nm excitation wavelengths (96 mW cm^{-2}) and 1,100–1,700 nm collection (20 ms exposure time; 21.7 fps). Displayed images are averaged over five frames.

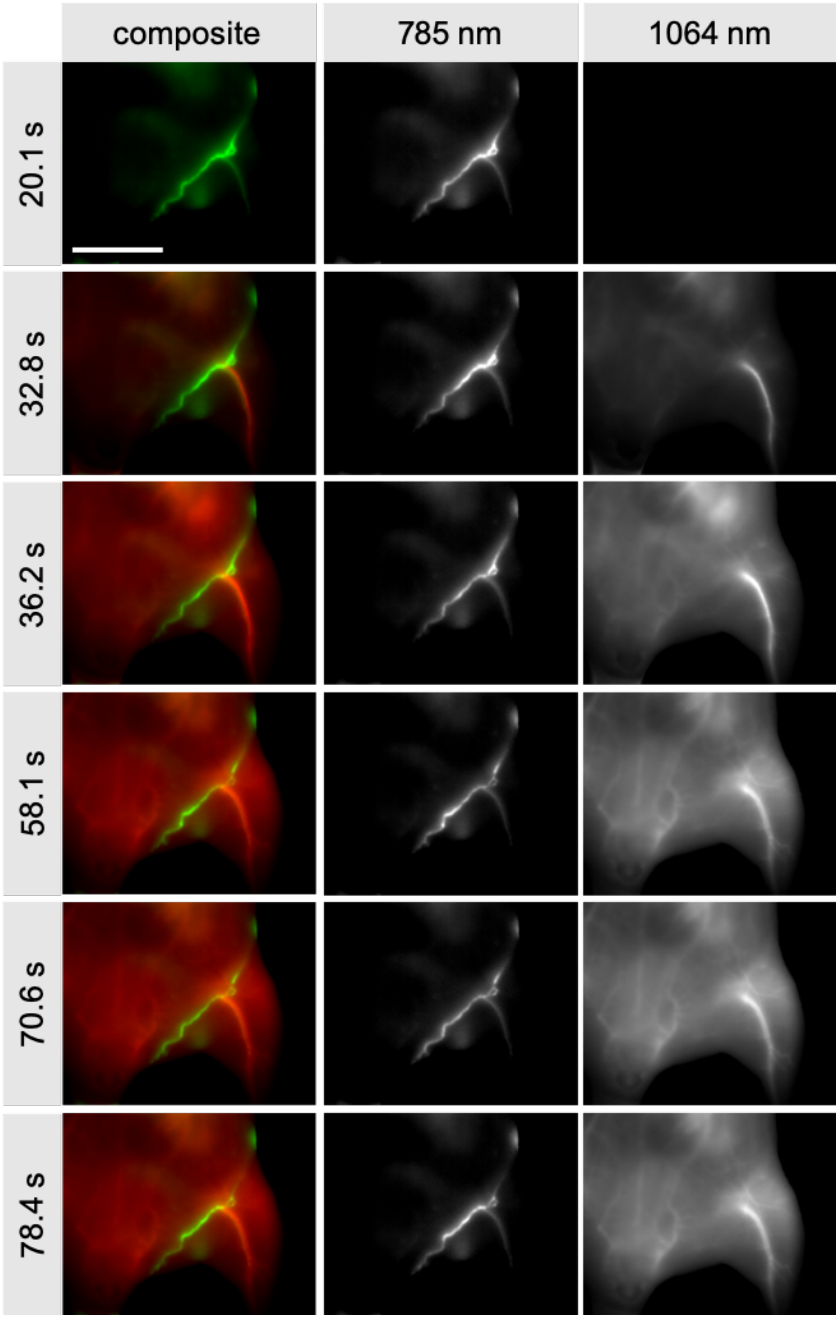

Figure 3.19 Imaging of blood and lymphatic circulation in two colors. Imaging occurred after delivery of probes ICG (i.d., 323 nmol) and **3.3** (i.v., 55 nmol in micelles). The excitation for two channels was 785 nm (96 $mWcm^{-1}$), and 1,064 nm (96 $mWcm^{-1}$). Collection 1150–1700 nm, 20 ms exposure time, 21.7 fps. Displayed images are averaged over 5 frames. Data are representative of two replicate experiments. Scale bar represents 1 cm.

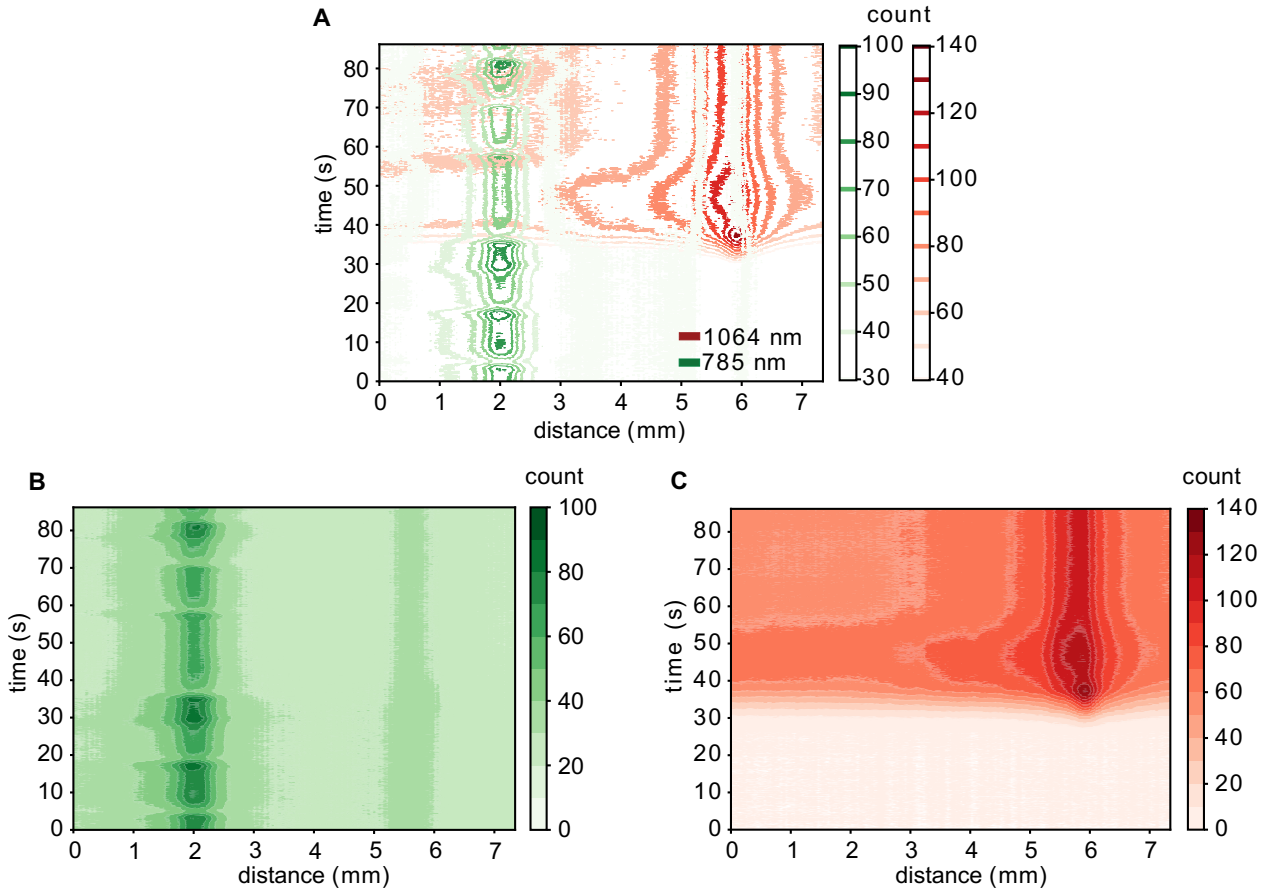

Figure 3.20[6] Contour plots of orthogonal circulatory and lymphatic imaging, corresponding to Figure 3.17D–E. A) Combined 785 nm and 1,064 channels. B) 785 nm channel and C) 1,064 channel.

3.4 Conclusion

Despite the large set of optical tools developed for the VIS and NIR regions of the electromagnetic spectrum, which enable fast, multiplexed detection in small model organisms, non-invasive, multicolor imaging in mammals with high resolution is still a considerable challenge. By developing predictably tunable SWIR polymethine fluorophores, along with a triggered multi-excitation SWIR optical configuration, we demonstrated multicolor whole-animal imaging at video-rate speeds and sub-millimetre resolution. The approach of excitation

[6] Figure by Jakob Lingg

multiplexing with single-channel SWIR detection presented here minimizes challenges due to the low quantum yields of SWIR fluorophores by using efficient excitation and detection, and also expands the wavelengths of the electromagnetic spectrum compatible with multicolor deep-tissue imaging.

Several key advances were necessary to successfully translate excitation-multiplexed imaging methods to whole animals. The ability to fine-tune the spectral properties of the fluorophores to excitation-match relevant lasers was accomplished by systematic functional group manipulation on a bright SWIR dye scaffold. These studies revealed predictive metrics for SWIR fluorophore absorption/emission using physical organic chemistry and produced MeOFlav7 (**3.10**), well matched to 980 nm, and JuloFlav7 (**3.3**), well matched to 1,064 nm. These dyes, along with FDA-approved ICG, enable single-channel imaging at 100 fps and two- or three-color imaging at video-rate speeds (≥27 fps). Ultimately, we envision that excitation-matching will be an essential design principle for the future optimization and utility of fluorophores and other light-activated probes. The technologies open a new realm in monitoring orthogonal function in mammals, even in awake animals without restraint or implantation. Furthermore, the rapid acquisition speeds combined with the high spatial resolution at which multiplexed imaging can be performed will enable real-time information regarding the localization of tagged biomolecules, labelled structures (for example, a tumour) and anatomical reference structures such as tissues (for example, liver or bones) and blood and lymphatic vessels. These tools, as well as further exploration of polymethine-based probes and the development of clinical imaging systems, will enable superior surgical, diagnostic and biomedical studies.

3.5 Experimental Procedures

3.5.1 General Experimental Procedures

Materials. Chemical reagents were purchased from Accela, Acros Organics, Alfa Aesar, Carl Roth, Fisher Scientific, Sigma-Aldrich or TCI and used without purification unless noted otherwise. Lipids were purchased from Laysan Bio and Avanti Polar Lipids. Anhydrous and deoxygenated solvents (toluene, THF) were dispensed from a Grubb's-type Phoenix Solvent Drying System constructed by J. C. Meyer. Anhydrous solvents were prepared by drying over 4 Å molecular sieves for at least three days (1,4-dioxane, ethanol, n-butanol, n-pentanol) or dried with $CaCl_2$, followed by $MgSO_4$ and distilled (EtOAc). Oxygen was removed by three consecutive freeze–pump–thaw cycles in air-free glassware directly before use.

Instrumentation. Thin layer chromatography was performed using Silica Gel 60 F254 (EMD Millipore) plates. Flash chromatography was executed with technical grade silica gel with 60 Å pores and 40–63 μm mesh particle size (Sorbtech Technologies). Solvent was removed under reduced pressure with a Büchi Rotavapor with a Welch self-cleaning dry vacuum pump and further dried with a Welch DuoSeal pump. Bath sonication was performed using a Branson 3800 ultrasonic cleaner or an Elma S15Elmasonic. Nuclear magnetic resonance (^{1}H NMR, ^{13}C NMR and ^{19}F NMR) spectra were taken on a Bruker Avance 300, AV-400, AV-500 or AV-600 instrument and processed with MestReNova or TopSpin software. All ^{1}H NMR and ^{13}C NMR peaks are reported in ppm in reference to their respective solvent signals. The ^{19}F NMR spectra are reported in ppm in reference to α,α,α-trifluorotoluene at −63.90 ppm as an external standard[61]. High-resolution mass spectra (electrospray ionization) were obtained on a Thermo Scientific Q Exactive Plus Hybrid Quadrupole-Orbitrap M with Dionex UltiMate 3000 RSLCnano System. Infrared spectra were obtained on a PerkinElmer UATR Two FT-IR spectrometer and are

reported in terms of frequency of absorption (cm^{-1}). Nanomaterial size was analyzed with a Malvern Zetasizer Nano dynamic light scattering instrument in plastic 1 cm cuvettes. Absorption spectra were collected on a JASCO V-770 UV–visible/NIR spectrophotometer with a 2,000 nm min^{-1} scan rate after blanking with the appropriate solvent. Photoluminescence spectra were obtained on a Horiba Instruments PTI QuantaMaster Series fluorometer. Quartz cuvettes (10 mm × 10 mm, 2 mm × 10 mm or 3 mm × 3 mm; Starna Cells or Thorlabs) were used for absorption and photoluminescence measurements. All spectra were obtained at ambient temperature. Normalized spectra are displayed for clarity. Absorption coefficient (ε_{max}) values in DCM were calculated using serial dilutions with Hamilton syringes in volumetric glassware and are displayed as the mean ± standard deviation (n = 3 measurements). Relative quantum yields were determined in DCM relative to IR-26 in DCM. See Section 3.6.3 for a detailed discussion of quantum yield measurements.

General synthetic procedures. Flavones **3.13a–c** were synthesized by subjecting the corresponding 3-aminophenol (150–750 mg scale, 1.0 equiv.) to ethyl benzoylacetate (1.75–2.0 equiv.) and heating at 180 °C for 15–48 h. Compounds were purified by column chromatography with a hexanes/EtOAc solvent gradient (51–55% yield). Flavone **3.15** was synthesized following a known procedure[62]from 7-hydroxyflavone **3.16**. Flavones **3.13d–h** were synthesized by subjecting flavone **3.15** (50–180 mg scale, 1.0 equiv.) to the corresponding secondary amine (1.5–2.8 equiv.), RuPhos Pd G3 (0.1 equiv.), RuPhos (0.1 equiv.) and caesium carbonate (1.5 equiv.), in either toluene (at 100–110 °C; 0.1–0.3 M) or THF (at 50 °C; 0.1–0.3 M) for 5.5–22 h. Compounds were purified by column chromatography with a hexanes/EtOAc solvent gradient (63–83% yield). Flavone **3.13i** was synthesized by subjecting 7-aminoflavone (**3.17**) (180 mg scale, 1.0 equiv.) to di-*tert*-butyl dicarbonate (3.2 equiv.), triethylamine (2.5 equiv.) and

dimethylamino pyridine (0.3 equiv.) in THF (0.2 M), and heating to reflux for 48 h. The compound was purified by column chromatography with a hexanes/EtOAc solvent gradient (66% yield).

Flavyliums **3.12a–i** were synthesized by subjecting the corresponding flavone (**3.13a–i**) (20–770 mg scale, 1.0 equiv.) to methyl magnesium bromide (1.5–3.2 equiv.) in THF (0.05–0.1 M) at 0 °C, warming to room temperature and stirring for 12–24 h. The reaction was quenched with aqueous fluoroboric acid, extracted with DCM and aqueous fluoroboric acid, dried and filtered. The compounds were purified by trituration with EtOAc or with diethyl ether and toluene (39–86% yield, **3.12i** not isolated for yield). Flavylium **3.12j** was synthesized following a literature procedure[45].

Heptamethine dyes **3.1**–**3.11** were synthesized by subjecting the corresponding flavylium (**3.12a**–**j**) (10–150 mg scale, 1.0 equiv.) to *N*-((3-(anilinomethylene)-2-chloro-1-cyclohexen-1-yl)methylene)aniline hydrochloride (**3.18**) (0.40–0.49 equiv.) with either sodium acetate or 2,6-di-*tert*-butyl-4-methylpyridine (1.5–5.6 equiv.) in either *n*-butanol/toluene, 1,4-dioxane, ethanol or *n*-pentanol (0.05–0.1 M) at 70–140 °C for 10–120 min. Compounds were purified by a mixture of column chromatography (with a gradient of either DCM/EtOH, DCM/acetone, DCM/MeCN or DCM/toluene/EtOH), trituration (in toluene and THF) and Soxhlet extraction (compound **3.10**, in toluene). Compounds were isolated in 5–51% yield. See the specific experimental procedures in *Section 3.5.2* for individual procedures used to obtain each flavone, flavylium and heptamethine dye and the full characterization of all new compounds.

Animal procedures. Animal experiments were conducted in conformity with the institutional guidelines. Non-invasive whole mouse imaging was performed on athymic nude female mice (6–16 weeks old, weight between 20–25 g), purchased from Envigo. Mice were anaesthetized with an i.p. injection of a ketamine/xylazine mixture. Tail vein injections were performed with a catheter

assembled from a 30-gauge needle connected through plastic tubing to a syringe prefilled with isotonic saline solution. The bevel of the needle was then inserted into the tail vein and secured using tissue adhesive. The plastic tubing was then connected to a syringe (30-gauge needle) prefilled with the probe of interest. All probes were filtered through a 0.22 μm syringe filter prior to i.v. injection.

SWIR imaging apparatus. For whole mouse imaging, a custom-built set-up was used. Lumics laser units (LU1064DLD350-S70AN03 (35 W), 1,064 nm; LU0980D350-D30AN (35 W), 980 nm; and LU0785DLU250-S70AN03 (25 W), 785 nm) were used for excitation. Laser modules are specced to ±10 nm. Laser outputs were coupled in a 4 × 1 fan-out fibre-optic bundle (Thorlabs BF46LS01) of 600 μm core diameter for each optical path. The output from the fibre was fixed in an excitation cube (Thorlabs KCB1EC/M), reflected off of a mirror (Thorlabs BBE1-E03) and passed through a positive achromat (Thorlabs AC254-050-B), SP filter (if necessary) and ground glass diffuser (Thorlabs DG10-120-MD) or an engineered diffuser (Thorlabs ED1-S20-MD) to provide uniform illumination over the working area. In a typical experiment, the excitation flux at the object was adjusted to be close to 100 mW cm^{-2} with an error of ±3% (the power density used is defined separately in each experiment). The working area was covered by a heating mat coated with blackout fabric (Thorlabs BK5). Emitted light was directed onto an Allied Vision Goldeye G-032 Cool TEC2 camera with a sensor temperature set point of −20 °C. Two lens systems were used, as follows:

Lens system A: emitted light was directed through a four-inch square first-surface silver mirror (Edmund Optics, 84448) with a custom filter set (defined for each experiment) and a C-mount camera lens (Navitar, SWIR-35).

Lens system B: the custom lens system consists of a 4f configuration with three

lenses with focal length (f) = 500.0 mm (Thorlabs LB1909-C) and two f = 200.0 mm lenses (Thorlabs LB1199-C) with a custom filter set (defined for each experiment). For ergonomic reasons, a 2-inch protected silver-coated elliptical mirror (PFE20-P01) mounted to a kinematic mount (Thorlabs KCB2EC/M) was used.

The assembly was partially enclosed to avoid excess light while enabling manipulation of the field of view during operation. The image acquisition toolbox of the MATLAB programming environment was used in combination with a custom MATLAB script to preview and collect the required image data in 8-bit or 12-bit format. The prepared MATLAB script allows users to access basic functionalities of the image acquisition device by establishing the necessary communication layer and a stable streaming link between the host computer and the imaging device.

Multiplexed imaging acquisition. To facilitate real-time multiplexed imaging, a programmable trigger controller was implemented using an Arduino Nano Rev 3 (A000005) microcontroller unit. Predetermined triggering sequences written in C language were compiled using the Arduino Integrated Development Environment in the host computer and uploaded via USB interface to the microcontroller unit. The pre-programmed trigger controller was then used to deliver the sequential electrical voltage signals of 5 V to the laser driver units and InGaAs camera to perform multiplexed image acquisition. A semi-automatic imaging algorithm adopted in MATLAB (see above, SWIR imaging apparatus), in combination with manual control of laser parameters via the individual laser modules, and the programmed microcontroller unit facilitate excitation-synchronized imaging. Excitation-synchronized frames are collected by the camera and transferred to the personal computer via the GigE interface. Further information and illustrative figures can be found in Section 3.6.5.

Image processing procedures. Images were processed using the Fiji distribution[63] of ImageJ[64]. All images were background corrected with a ten-frame averaged background file to correct for non-linearities in the detector and/or excitation. Raw images underwent no further processing. Unmixed images were image subtracted according to the relative contribution of each channel, determined separately for each experiment, and detailed in the figure experimental procedures, Section 3.5.3. All still images were averaged over five frames and converted to 8-bit PNG files for display, unless stated otherwise. Videos were frame averaged to reduce file size, if necessary, before compression with FFmpeg to a .mov file.

3.5.2 Experimental Procedures

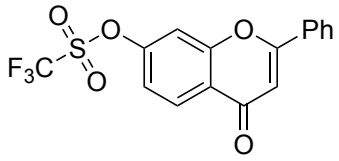

7-(trifluoromethanesulfonate)-2-phenyl-*4H*-chromen-4-one(3.15): The preparation was adapted from Kövér and Antus[62]. In a 150 mL flask, 7-hydroxyflavone (**3.16**) (902 mg, 3.79 mmol, 1.0 equiv.) and pyridine (15.0 mL, 186 mmol, 49 equiv.) were combined and placed in an ice bath. Trifluormethanesulfonic anhydride (1.30 mL, 7.73 mmol, 2.0 equiv.) was added dropwise. After 2 h, the reaction was quenched with sodium bicarbonate, extracted into EtOAc, washed with brine, and evaporated. The crude product was purified via column chromatography in an 8:1 hexanes/EtOAc mixture to yield a white solid (934 mg, 2.52 mmol, 67%. ^{1}H NMR (400 MHz, Chloroform-*d*) δ 8.34 (d, *J* = 8.8 Hz, 1H), 7.96 – 7.86 (m, 2H), 7.63 – 7.50 (m, 4H), 7.34 (dd, *J* = 8.8, 2.3 Hz, 1H), 6.85 (s, 1H). ^{1}H NMR agrees with the literature.

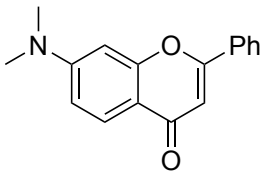

7-(dimethylamino)-2-phenyl-4*H*-chromen-4-one (3.13a): 3-dimethylaminophenol (**3.14a**) (500 mg, 3.64 mmol, 1 equiv.) and ethyl benzoylacetate (1.10 mL, 6.37 mmol, 1.75 equiv.) were combined in a 10 mL flask and heated at 180 °C for 24 h. The solution was cooled to room temperature, evaporated onto silica gel and purified via column chromatography with a 50:1 to 1:4, followed by a second column in 6:1 to 1:1 hexanes/EtOAc gradient. The procedure gave a beige solid (493 mg, 1.86 mmol, 51%). R_f = 0.4 in 1:1 hexanes/EtOAc ^{1}H NMR (500 MHz, Chloroform-*d*) δ 8.01 (d, *J* = 9.0 Hz, 1H), 7.91 – 7.84 (m, 2H), 7.54 – 7.44 (m, 3H), 6.73 (dd, *J* = 9.0, 2.4 Hz, 1H), 6.67 (s, 1H), 6.55 (d, *J* = 2.4 Hz, 1H), 3.07 (s, 6H). ^{13}C NMR (126 MHz, Chloroform-*d*) δ 177.9, 162.3, 158.4, 154.2, 132.3, 131.1, 129.0, 126.6, 126.1, 113.7, 110.9, 107.3, 97.2, 40.3. HRMS (ESI$^+$) calcd for $C_{17}H_{16}NO_2^+$ $[M+H]^+$: 266.1176; found: 266.1178. Absorbance (CH_2Cl_2): 229, 274, 358 nm.

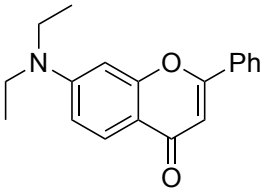

7-(diethylamino)-2-phenyl-4*H*-chromen-4-one (3.13b): 3-diethylamino phenol (**3.14b**) (151 mg, 0.911 mmol, 1.0 equiv.) and ethyl benzoyl acetate (0.314 mL, 1.81 mmol, 2.0 equiv.) were added to a flame-dried 1-dram vial and heated to 100 ºC for 5 h, followed by 180 °C for 15 h. The crude mixture was evaporated onto silica gel and purified by column chromatography in a 9:1, 6:1, and 3:1 hexanes/EtOAc gradient. The product was collected as a beige solid (136 mg, 0.463 mmol, 51%). R_f = 0.5 in 1:1 hexanes/EtOAc. ^{1}H NMR (500 MHz, Chloroform-*d*) δ 7.96 (d, *J* = 9.0 Hz, 1H), 7.87 – 7.75 (m, 2H), 7.5 – 7.37 (m, 3H), 6.66 (dd, *J* = 9.1, 2.5 Hz, 1H), 6.62 (s, 1H), 6.49 (d, *J* = 2.5 Hz, 1H), 3.38 (q, *J* = 7.1 Hz, 4H), 1.18 (t, *J* = 7.1 Hz, 6H). ^{13}C NMR (126 MHz, Chloroform-*d*) δ 177.5, 161.9, 158.7, 151.9, 132.2, 130.9, 128.8, 126.6, 125.9, 113.1, 110.4, 107.1, 96.3, 44.7, 12.5. HRMS

(ESI$^+$) calcd for $C_{19}H_{20}NO_2^+$ [M+H]$^+$: 294.1489; found: 294.1491. Absorbance (CH_2Cl_2): 233, 275, 365 nm.

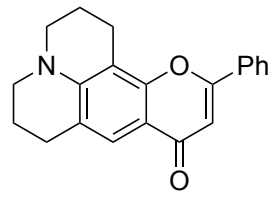

11-phenyl-2,3,6,7-tetrahydro-1*H*,5*H*,9*H*-pyrano[2,3-*f*]pyrido[3,2,1-*ij*]quinolin-9-one (3.13c): 8-hydroxyjulolidine (**3.14c)** (749 mg, 3.96 mmol,1.0 equiv.) and ethyl benzoyl acetate (1.20 mL, 6.93 mmol, 1.75 equiv.) were combined in a flame-dried 20 mL vial and heated at 180 °C for 48 h. The crude mixture was evaporated onto silica gel and purified by column chromatography with a 9:1 to 4:1 hexanes/EtOAc gradient, followed by chromatography with a 6:1 to 1:2 with 1% ethanol gradient. A beige solid (687 mg, 2.16 mmol, 55%) resulted. R_f = 0.5 in 1:1 hexanes/EtOAc. ^{1}H NMR (500 MHz, Chloroform-*d*) δ 7.75 (dd, *J* = 6.7, 3.0 Hz, 2H), 7.52 (s, 1H), 7.46 – 7.25 (m, 3H), 6.57 (s, 1H), 3.17 (dt, *J* = 7.9, 5.5 Hz, 4H), 2.86 (t, *J* = 6.5 Hz, 2H), 2.69 (t, *J* = 6.3 Hz, 2H), 1.95 (p, *J* = 6.3 Hz, 2H), 1.86 (p, *J* = 6.2 Hz, 2H). ^{13}C NMR (126 MHz, Chloroform-*d*) δ 177.6, 161.0, 153.6, 147.0, 132.4, 130.7, 128.7, 125.6, 122.1, 120.1, 112.7, 106.5, 105.5, 49.8, 49.3, 27.5, 21.3, 20.50, 20.48. HRMS (ESI$^+$) calcd for $C_{21}H_{20}NO_2^+$ [M+H]$^+$: 318.1489; found: 318.1495. Absorbance (CH_2Cl_2): 283, 381 nm.

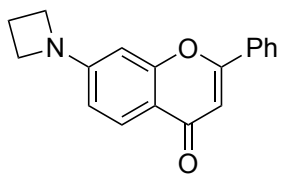

7-(azetidin-1-yl)-2-phenyl-4*H*-chromen-4-one (3.13d): Triflate **3.15** (58.5 mg, 0.158 mmol, 1.0 equiv.), RuPhos-Pd-G3 (12.8 mg, 0.0153 mmol, 0.1 equiv), RuPhos (7.2 mg, 0.015 mmol, 0.1 equiv.), and cesium carbonate (72.6 mg, 0.223 mmol, 1.4 equiv,) were added to a 15 mL flame-dried 2-neck flask, dissolved in THF (0.80 mL), and stirred at 50 °C under N_2 atmosphere for 5.5 h. Azetidine (0.034 mL, 0.50 mmol, 2.8 equiv.) was added by two 0.017 mL portions, initially and after 2.5 h. The reaction mixture was extracted with dichloromethane/water, dried with $MgSO_4$, filtered, and

evaporated. The crude product was purified with a 10:1 to 2:1 hexanes/EtOAc solvent gradient to yield a yellow solid (26.7 mg, 0.100 mmol, 63%). R_f = 0.5 in 1:1 hexanes/EtOAc. ^{1}H NMR (500 MHz, Chloroform-*d*) δ 8.03 (d, *J* = 8.7 Hz, 1H), 7.94 – 7.87 (m, 2H), 7.50 (m, 3H), 6.76 (s, 1H), 6.46 (dd, *J* = 8.7, 2.2 Hz, 1H), 6.32 (d, *J* = 2.2 Hz, 1H), 4.06 (t, *J* = 7.4 Hz, 4H), 2.48 (p, *J* = 7.3 Hz, 2H). ^{13}C NMR (126 MHz, Chloroform-*d*) δ 177.9, 162.4, 158.5, 155.3, 132.3, 131.3, 129.1, 126.9, 126.3, 114.3, 109.9, 107.3, 96.0, 51.8, 16.6. HRMS (ESI$^+$) calcd for $C_{18}H_{16}NO_2^+$ [M+H]$^+$: 278.1176; found: 278.1175. Absorbance (CH_2Cl_2): 227, 272, 307, 355 nm.

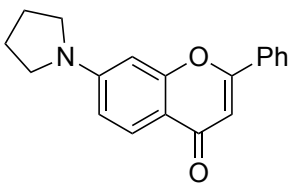

7-(pyrrolidin-1-yl)-2-phenyl-*4H*-chromen-4-one (3.13e): Triflate **3.15** (103 mg, 0.278 mmol, 1.0 equiv.), pyrrolidine (0.042 mL, 0.50 mmol, 1.5 equiv.), RuPhos-Pd-G3 (24.2 mg, 0.0289 mmol, 0.1 equiv.) RuPhos (12.9 mg, 0.0276 mmol, 0.1 equiv.), and cesium carbonate (136 mg, 0.418 mmol, 1.5 equiv.) were dissolved in toluene (2.6 mL) in a 20 mL scintillation vial and heated to 100 °C for 24 h under an N_2 atmosphere. The solution was cooled to rt and evaporated onto silica gel. The crude product was purified via column chromatography, eluting with a 9:1, 7:1 and 5:1 hexanes/EtOAc solvent gradient. This procedure gave an amber solid (59.8 mg, 0.205 mmol, 74%). R_f = 0.5 in 1:1 hexanes/EtOAc. ^{1}H NMR (400 MHz, Chloroform-*d*) δ 8.05 (d, *J* = 8.9 Hz, 1H), 7.95 – 7.90 (m, 2H), 7.55 – 7.48 (m, 3H), 6.87 (s, 1H), 6.68 (dd, *J* = 9.0, 2.3 Hz, 1H), 6.49 (d, *J* = 2.3 Hz, 1H), 3.48 – 3.38 (m, 4H), 2.15 – 2.05 (m, 4H). ^{13}C NMR (126 MHz, Chloroform-*d*) δ 178.0, 162.6, 158.8, 152.1, 132.6, 131.4, 129.2, 127.0, 126.4, 113.4, 111.7, 107.3, 97.1, 48.1, 25.8. HRMS (ESI$^+$) calcd for $C_{19}H_{18}NO_2$ [M+H]$^+$: 292.1332; found: 292.1326. Absorbance (CH_2Cl_2): 233, 275, 307, 364 nm.

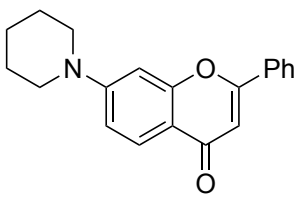

7-(piperidin-1-yl)-2-phenyl-*4H*-chromen-4-one (3.13f): Triflate **3.15** (183 mg, 0.495 mmol, 1.0 equiv.), piperidine (0.072 mL, 0.73 mmol, 1.5 equiv.), RuPhos (21.2 mg, 0.0455 mmol, 0.1 equiv.), RuPhos-Pd-G3 (42.5 mg, 0.0508 mmol, 0.1 equiv.) and cesium carbonate (243 mg, 0.747 mmol, 1.5 equiv.) were dissolved in toluene (4.5 mL) in a 20 mL scintillation vial and heated to 100 °C for 24 h under an N_2 atmosphere. The solution was cooled to rt and evaporated onto silica gel. The crude product was purified via column chromatography, eluting with a 9:1, 7:1 and 5:1 gradient of hexanes/EtOAc to yield an amber solid (106 mg, 348 mmol, 71%). R_f = 0.6 in 1:1 hexanes/EtOAc. ^{1}H NMR (400 MHz, Chloroform-*d*) δ 8.03 (d, *J* = 9.0 Hz, 1H), 7.89 (s, 2H), 7.50 (s, 3H), 7.04 – 6.88 (m, 1H), 6.80 (d, *J* = 2.4 Hz, 1H), 6.70 (s, 1H), 3.41 (s, 4H), 1.69 (s, 6H). ^{13}C NMR (126 MHz, Chloroform-*d*) δ 177.9, 162.6, 158.6, 155.1, 132.4, 131.2, 129.1, 126.7, 126.2, 115.1, 113.5, 107.5, 100.3, 49.1, 25.4, 24.4. HRMS (ESI$^+$) calcd for $C_{20}H_{20}NO_2$ $[M+H]^+$: 306.1489; found: 306.1486. Absorbance (CH_2Cl_2): 275, 308, 356 nm.

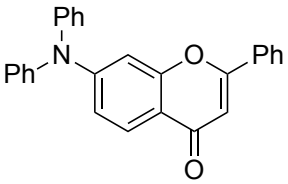

7-(diphenylamino)-2-phenyl-4*H*-chromen-4-one (3.13g): Triflate **3.15** (151 mg, 0.407 mmol, 1.0 equiv.), RuPhos (18.8 mg, 0.0403 mmol, 0.1 equiv.), RuPhos-Pd-G3 (33.7 mg, 0.0403 mmol, 0.1 equiv.), cesium carbonate (200 mg, 0.164 mmol, 1.5 equiv.) and diphenylamine (103 mg, 0.609 mmol, 1.5 equiv.) were added to a flame-dried 2-dram vial under a N_2 atmosphere and dissolved in THF (1.4 mL). The solution was heated at 50 °C for 21 h. The crude mixture was purified by column chromatography with a 20:1, 15:1, 10:1, and 8:1 hexanes/EtOAc gradient to yield a light-yellow solid (126 mg, 0.324 mmol, 80%). R_f = 0.7 in 1:1 hexanes/EtOAc. ^{1}H NMR (400 MHz, Chloroform-*d*) δ 8.01 (d, *J* = 8.9 Hz, 1H), 7.85 (dd, *J* = 7.7, 1.9 Hz, 2H), 7.51 – 7.42 (m, 3H), 7.40 – 7.34 (m, 4H), 7.24 – 7.17 (m, 6H), 7.01 (dd, *J* = 8.8, 2.3 Hz, 1H), 6.97 (d, *J* = 2.2 Hz, 1H), 6.74

(s, 1H). ^{13}C NMR (151 MHz, Chloroform-*d*) δ 177.7, 162.8, 157.8, 153.1, 146.2, 132.0, 131.4, 129.9, 129.0, 126.5, 126.4, 126.2, 125.3, 118.1, 117.5, 107.6, 106.5. HRMS (ESI$^+$) calcd for $C_{27}H_{20}NO_2^+$ $[M+H]^+$: 390.1489, found: 390.1490. Absorbance (CH_2Cl_2): 228, 285, 371 nm.

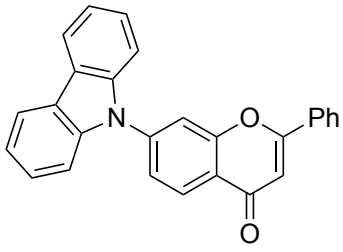

7-(9H-carbazol-9-yl)-2-phenyl-*4H*-chromen-4-one (3.13h): Triflate **3.15** (60.1 mg, 0.162 mmol, 1.0 equiv.), RuPhos (7.6 mg, 0.016 mmol, 0.1 equiv.), RuPhos-Pd-G3 (14.1 mg, 0.0169 mmol, 0.1 equiv.), cesium carbonate (81.6 mg, 0.250 mmol, 1.5 equiv.), and carbazole (40.1 mg, 0.240 mmol, 1.5 equiv.) were added to a flame-dried 2-dram vial under a N_2 atmosphere and dissolved in toluene (1 mL). The solution was heated at 100 °C for 22 h. The crude mixture was purified by column chromatography with a 20:1, 15:1, 10:1, and 8:1, 5:1, 4:1 hexanes/EtOAc gradient to isolate a beige solid (51.6 mg, 0.133 mmol, 82%). R_f = 0.8 in 1:1 hexanes/EtOAc. ^{1}H NMR (600 MHz, Chloroform-*d*) δ 8.47 (d, *J* = 8.4 Hz, 1H), 8.16 (dd, *J* = 7.7, 1.1 Hz, 2H), 7.99 – 7.94 (m, 2H), 7.84 (d, *J* = 1.9 Hz, 1H), 7.70 (dd, *J* = 8.4, 1.9 Hz, 1H), 7.60 – 7.53 (m, 5H), 7.47 (ddd, *J* = 8.2, 7.2, 1.2 Hz, 2H), 7.35 (t, *J* = 7.4 Hz, 2H), 6.91 (s, 1H). ^{13}C NMR (126 MHz, Chloroform-*d*) δ 177.7, 163.8, 157.2, 143.0, 140.1, 131.9, 131.6, 129.2, 127.7, 126.5, 126.4, 124.1, 123.7, 122.6, 121.1, 120.7, 115.5, 109.9, 108.0. HRMS (ESI$^+$) calcd for $C_{27}H_{18}NO_2^+$ $[M+H]^+$: 388.1332, found: 388.1336. Absorbance (CH_2Cl_2): 239, 289, 311, 339 nm.

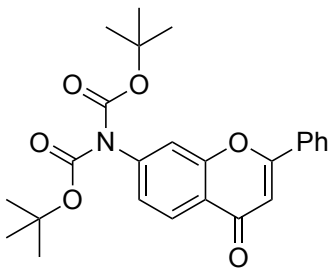

7-(di-(*tert*-butoxycarbonyl))-2-phenyl-4*H*-chromen-4-one (3.13i): 7-aminoflavone **3.17** (180 mg, 0.760 mmol, 1.0 equiv.), di-*tert*-butyl dicarbonate (529 mg, 2.42 mmol, 3.2 equiv.), triethylamine (0.26 mL, 1.9 mmol, 2.5 equiv.), dimethylamino pyridine (27.0 mg, 0.220 mmol, 0.3 equiv.), and THF (4.5 mL) were added to an oven-dried 20 mL vial and refluxed for 48 h. The

resulting mixture was evaporated onto silica gel and purified by column chromatography with a 10:1, 8:1, 5:1 hexanes/EtOAc gradient to yield a white solid (218 mg, 0.498 mmol, 66%). R_f = 0.9 in 1:1 hexanes/EtOAc. ^{1}H NMR (600 MHz, Chloroform-*d*) δ 8.19 (d, *J*= 8.5 Hz, 1H), 7.90 – 7.86 (m, 2H), 7.49 (dt, *J*= 5.8, 2.9 Hz, 3H), 7.40 (d, *J*= 1.9 Hz, 1H), 7.19 (dd, *J*= 8.4, 1.9 Hz, 1H), 6.80 (d, *J*= 1.3 Hz, 1H), 1.42 (s, 18H). ^{13}C NMR (126 MHz, Chloroform-*d*) δ 177.8, 163.7, 156.2, 151.2, 144.1, 131.8, 131.5, 129.1, 126.3, 126.1, 125.3, 122.9, 117.4, 107.7, 83.7, 27.9. HRMS (ESI$^+$) calcd for $C_{25}H_{28}NO_6^+$ [M+H]$^+$: 438.1911, found: 438.1915. Absorbance (CH_2Cl_2): 252, 296 nm.

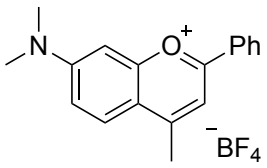

7-(dimethylamino)-4-methyl-2-phenylchromenylium tetrafluoroborate (3.12a): Flavone **3.7a** (769 mg, 2.90 mmol, 1.0 equiv.) was dissolved in THF (25 mL) in a 100 mL flame dried 3-neck flask and cooled to 0 °C. Dropwise addition of methylmagnesium bromide (1.0 M in THF, 4.35 mL, 1.5 equiv.) was followed by stirring at room temperature overnight under a N_2 atmosphere. The resulting solution was quenched with several drops of fluoroboric acid (50%, aqueous), extracted into DCM with the addition of 5% HBF_4, dried with Na_2SO_4, filtered, and evaporated. The crude product was purified by trituration in EtOAc to yield a dark red solid (740 mg, 2.11 mmol, 73%). ^{1}H NMR (500 MHz, Acetone-d_6) δ 8.42 – 8.35 (m, 2H), 8.29 (d, *J*= 9.6 Hz, 1H), 8.18 (s, 1H), 7.82 – 7.76 (m, 1H), 7.75 – 7.66 (m, 2H), 7.60 (dd, *J*= 9.6, 2.5 Hz, 1H), 7.40 (d, *J*= 2.5 Hz, 1H), 3.48 (s, 6H), 3.04 – 2.94 (m, 3H) {peak at 3.04 – 2.94 appears as a multiplet and as < 3H due to proton-deuterium exchange with Acetone-d_6}. ^{13}C NMR (126 MHz, Acetone-d_6) δ 166.2, 165.2, 159.9, 159.1, 135.1, 130.7, 130.6, 129.7, 128.7, 119.2, 119.0, 113.0, 97.1, 41.3, 20.0. ^{19}F NMR (376 MHz, DMSO-d_6) δ -148.0. HRMS (ESI$^+$) calcd for $C_{18}H_{18}NO^+$ [M]$^+$: 264.1383; found: 264.1379. Absorbance (CH_2Cl_2): 238, 294, 338, 510 nm. Emission (CH_2Cl_2, ex. 500 nm): 589 nm.

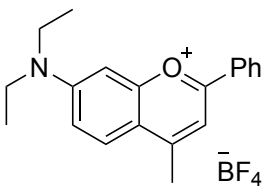

7-(diethylamino)-4-methyl-2-phenylchromenylium tetrafluoroborate (3.12b): Flavone **3.7b** (100 mg, 0.342 mmol, 1.0 equiv.) was dissolved in THF (3.3 mL) in

a flame-dried 20 mL vial in an N_2 atmosphere. The solution was cooled to 0 °C and methylmagnesium bromide (1.0 M in THF, 0.821 mL, 2.4 equiv.) was added dropwise. The reaction was warmed to room temperature and stirred for 26 h. The reaction mixture was quenched with fluoroboric acid (5%, aqueous, ~1.5 mL), extracted with dichloromethane/water, dried with Na_2SO_4, filtered, and evaporated. The crude product was purified by trituration in EtOAc to yield a dark red solid (104 mg, 0.275 mmol, 81%). ^{1}H NMR (300 MHz, Acetone-d_6) δ 8.40 – 8.34 (m, 2H), 8.28 (d, J = 9.6 Hz, 1H), 8.13 (s, 1H), 7.81 – 7.66 (m, 3H), 7.64 – 7.57 (m, 1H), 7.43 (d, J = 2.6 Hz, 1H), 3.86 (q, J = 7.1 Hz, 4H), 2.98 (s, 3H), 1.38 (t, J = 7.1 Hz, 6H).^{13}C NMR (126 MHz, Acetone-d_6) δ 165.8, 164.6, 160.1, 157.4, 134.9, 130.6, 130.6, 130.03, 128.7, 119.2, 119.0, 112.7, 96.8, 46.8, 19.9, 12.8. HRMS (ESI$^+$) calcd for $C_{20}H_{22}NO^+$ [M]$^+$: 292.1696; found: 292.1689. Absorbance (CH_2Cl_2): 239, 295, 338, 514 nm. Emission (CH_2Cl_2, ex. 500 nm): 592 nm.

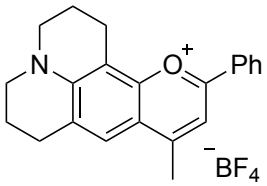

9-methyl-11-phenyl-2,3,6,7-tetrahydro-1*H*,5*H*-pyrano[2,3-*f*]pyrido[3,2,1-*ij*]quinolin-12-ium tetrafluoroborate (3.12c): Flavone **3.7c** (149 mg, 0.469 mmol, 1.0 equiv.) was dissolved in THF (3.5 mL) in a 10 mL flame dried flask under N_2 atmosphere. The solution was cooled to 0 °C and methylmagnesium bromide (1.1 M in THF, 1.12 mL, 2.5 equiv.) was added dropwise. The reaction was warmed to rt and stirred overnight. The reaction mixture was quenched with several drops of fluoroboric acid (5%, aqueous), extracted with dichloromethane after adding more 5% HBF_4, quickly washed with brine, dried with Na_2SO_4, filtered, and evaporated. The crude product was purified by trituration and filtration from cold EtOAc, yielding a dark purple solid (140 mg, 0.347 mmol, 74%). ^{1}H NMR (500 MHz, DMSO-d_6) δ 8.26 – 8.21 (m, 2H), 8.04 (s, 1H), 7.85 (s, 1H), 7.74 – 7.66 (m, 3H), 3.59 (t, J= 5.9 Hz, 4H), 3.04 (t, J= 6.4 Hz, 2H), 2.93 (t, J= 6.2 Hz, 2H), 2.78 (s, 3H), 2.04 – 1.93 (m, 4H). ^{13}C NMR (126 MHz, DMSO-d_6) δ 161.9, 159.7, 152.9, 152.2, 133.4, 129.9, 129.7, 128.5, 127.1, 124.1, 117.7, 111.0, 104.3, 50.6, 50.0, 27.2, 19.8, 19.2, 19.1, 18.8. HRMS (ESI$^+$) calcd for $C_{22}H_{22}NO^+$ [M]$^+$: 316.1696; found: 316.1694. Absorbance (CH_2Cl_2): 250, 301, 341, 533 nm. Emission (CH_2Cl_2, ex. 530 nm): 617 nm.

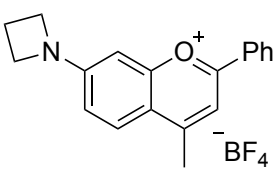

7-(azetidin-1-yl)-4-methyl-2-phenylchromenylium tetrafluoroborate) (3.12d): Flavone **3.7d** (25 mg, 0.089 mmol, 1.0 equiv.) was dissolved in THF (1.4 mL) in a flame-dried 15 mL 2-neck flask and cooled to 0 °C. Methylmagnesium bromide (1.0 M in THF/toluene, 0.238 mL, 2.8 equiv.) was added dropwise and the resulting solution was let warm to rt and stirred overnight under an atmosphere of N_2. The reaction was quenched with a few drops of fluoroboric acid (5%, aqueous), and with additional water, extracted with dichloromethane, dried with $MgSO_4$, filtered, and evaporated. The crude product was purified by trituration in EtOAc and filtration to yield a red solid (13 mg, 0.036 mmol, 39%). ^{1}H NMR (400 MHz, Acetone-d_6) δ 8.40 – 8.30 (m, 2H), 8.24 (d, J = 9.3 Hz, 1H), 8.08 (s, 1H), 7.81 – 7.64 (m, 3H), 7.14 (dd, J = 9.3, 2.2 Hz, 1H), 6.94 (d, J = 2.2 Hz, 1H), 4.65 – 4.42 (m, 4H), 2.95 (s, 3H), 2.64 (p, J = 7.7 Hz, 2H). ^{13}C NMR (126 MHz, Acetonitrile-d_3) δ 165.4, 164.1, 159.8, 158.0, 134.9, 130.71, 130.70, 129.8, 128.4, 119.2, 117.4, 112.5, 94.4, 53.1, 52.9, 20.1, 16.6. HRMS (ESI$^+$) calcd for $C_{19}H_{18}NO^+$ $[M]^+$: 276.1383; found: 276.1376. Absorbance (CH_2Cl_2): 242, 293, 336, 511 nm. Emission (CH_2Cl_2, ex. 500 nm): 590 nm.

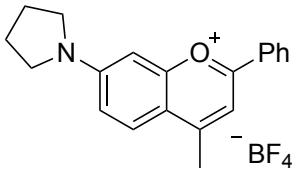

7-(pyrrolidin-1-yl)-4-methyl-2-phenylchromenylium tetrafluoroborate (3.12e): Flavone **3.7e** (62.0 mg, 0.213 mmol, 1.0 equiv.) was dissolved in THF (2.2 mL) in a 15 mL 2-neck round bottom flask and cooled to 0 °C. Methylmagnesium bromide was added dropwise (1.0 M in THF, 0.508 mL, 2.5 equiv.) and the solution was warmed to rt and stirred for 24 h. The reaction was quenched by dropwise addition of fluoroboric acid (5%, aqueous, ~30 mL) on ice, extracted with dichloromethane after the addition of more 5% HBF_4, dried with Na_2SO_4, filtered, and evaporated. The crude product was triturated with ice cold EtOAc and vacuum filtered to produce a red solid (52.1 mg, 0.138 mmol, 65%). ^{1}H NMR (400 MHz, Acetonitrile-d_3) δ 8.25 – 8.18 (m, 2H), 8.06 (d, J = 9.5 Hz, 1H), 7.76 (d, J = 0.5 Hz, 1H), 7.75 – 7.71 (m, 1H), 7.70 – 7.64 (m, 2H), 7.26 (dd, J = 9.5, 2.3 Hz, 1H), 6.98 (d, J = 2.4 Hz, 1H), 3.69 (t, J = 6.2 Hz, 2H), 3.60 (t, J = 6.1 Hz, 2H), 2.83 (s, 3H), 2.12 – 2.08 (m, 4H). ^{13}C NMR (126 MHz, Acetonitrile-d_3) δ 165.7, 164.3, 159.8, 156.4, 135.0, 130.8, 130.7, 129.7, 128.5, 120.2 119.2, 112.6, 97.2, 50.4, 50.1, 26.0, 25.7, 20.1. HRMS (ESI$^+$) calcd for

$C_{20}H_{20}NO^+$ $[M]^+$: 290.1539; found: 290.1542. Absorbance (CH_2Cl_2): 238, 296, 339, 516 nm. Emission (CH_2Cl_2, ex. 500 nm): 595 nm.

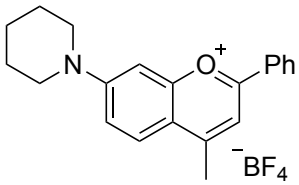

7-(piperidin-1-yl)-4-methyl-2-phenylchromenylium (3.12f): Flavone **3.7f** (90.4 mg, 0.296 mmol, 1.0 equiv.) was dissolved in THF (2.3 mL) in a 15 mL double-neck round bottom flask and cooled to 0 °C. Methylmagnesium bromide was added dropwise on ice (1.0 M in THF, 0.702 mL, 2.5 equiv.). The solution was warmed to rt and left stir under a N_2 atmosphere for 24 h. The reaction was quenched by dropwise addition of fluoroboric acid (5%, aqueous, ~30 mL) on ice, extracted with dichloromethane the addition of more 5% HBF_4, dried with Na_2SO_4, filtered, and evaporated. The crude product was triturated with ice cold EtOAc and vacuum filtered to yield a dark red solid (99.8 mg, 0.255 mmol, 86%). ^{1}H NMR (600 MHz, Acetonitrile-d_3) δ 8.19 – 8.12 (m, 2H), 7.99 (d, *J*= 9.7 Hz, 1H), 7.73 – 7.66 (m, 2H), 7.66 – 7.59 (m, 2H), 7.44 (dd, *J*= 9.7, 2.6 Hz, 1H), 7.17 (d, *J*= 2.6 Hz, 1H), 3.82 – 3.67 (m, 4H), 2.77 (s, 3H), 1.80 – 1.75 (m, 2H), 1.77 – 1.71 (m, 4H). ^{13}C NMR (126 MHz, Acetonitrile-d_3) δ 164.9, 163.2, 159.4, 157.0, 134.1, 129.8, 129.6, 128.9, 127.5, 118.4, 118.0, 111.9, 96.4, 48.9, 25.8, 23.8, 19.1. HRMS (ESI^+) calcd for $C_{21}H_{22}NO^+$ $[M]^+$: 304.1696; found: 304.1696. Absorbance (CH_2Cl_2): 243, 297, 338, 520 nm. Emission (CH_2Cl_2, ex. 500 nm): 608 nm.

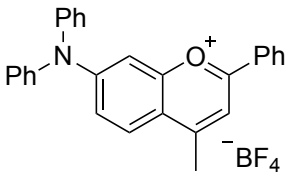

7-(diphenylamino)-4-methyl-2-phenylchromenylium tetrafluoroborate (3.12g): Flavone **3.7g** (63.2 mg, 0.162 mmol, 1.0 equiv.) was added to a flame-dried 15 mL under a N_2 atmosphere, dissolved in THF (1.5 mL), and cooled to 0 °C. Methylmagnesium bromide (1.0 M in THF, 0.500 mL, 3.1 equiv.) was added dropwise, and the solution was warmed to rt and stirred for 14 h. The solution was quenched with fluoroboric acid (50%, aqueous, 5 drops), and with the addition of 50% fluoroboric acid, extracted with dichloromethane, dried with Na_2SO_4, filtered, and evaporated. The crude product was purified by trituration in a mixture of diethyl ether and toluene, filtered, and dried to yield a dark purple solid (54.8 mg, 0.115 mmol, 71%). ^{1}H NMR (600 MHz, Chloroform-*d*) δ 8.24 (dt, *J*= 7.3, 1.3 Hz, 2H), 8.19 (s, 1H), 8.06 (d, *J*= 9.5 Hz, 1H), 7.69 – 7.64

(m, 1H), 7.59 (td, *J*= 8.0, 7.4, 1.8 Hz, 2H), 7.52 (ddt, *J*= 8.2, 5.7, 1.8 Hz, 4H), 7.42 (td, *J*= 7.3, 1.2 Hz, 2H), 7.36 – 7.30 (m, 5H), 7.05 (d, *J*= 2.3 Hz, 1H), 3.02 (s, 3H). ^{13}C NMR (126 MHz, Chloroform-*d*) δ 168.0, 167.5, 158.6, 157.6, 143.4, 135.2, 130.8, 130.0, 129.0, 128.9, 128.8, 128.4, 127.2, 121.7, 119.8, 114.7, 101.5, 20.5. HRMS (ESI$^+$) calcd for $C_{28}H_{22}NO^+$ [M]$^+$: 388.1696, found: 388.1690. IR (film): 2929, 1634, 1566, 1490, 1386, 1277, 1057 cm^{-1}. Absorbance (CH_2Cl_2): 234, 248, 288, 350, 529 nm.

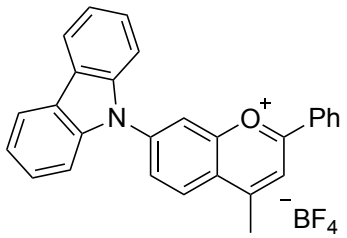

7-(9H-carbazol-9-yl)-4-methyl-2-phenylchromenylium tetrafluoroborate (3.12h): Flavone **3.7h** (128 mg, 0.331 mmol, 1.0 equiv.) was placed in a 50 mL flame-dried flask, dissolved in THF (3.2 mL), and cooled to 0 °C. Methylmagnesium bromide (1.0 M in THF, 0.800 mL, 2.4 equiv.) was added dropwise. The reaction was warmed to rt and stirred for 17 h before quenching with a few drops of fluoroboric acid (50%, aqueous, ~0.1 mL). After the addition of 50% fluoroboric acid, the product was extracted into dichloromethane, dried with Na_2SO_4, filtered, and evaporated. The crude product was purified by trituration in cold EtOAc, filtered and dried to yield a maroon solid (96.5 mg, 0.204 mmol, 62%). ^{1}H NMR (600 MHz, Acetonitrile-d_3) δ 8.64 (d, *J*= 8.9 Hz, 1H), 8.62 – 8.55 (m, 2H), 8.55 – 8.49 (m, 2H), 8.38 (dd, *J*= 8.9, 2.1 Hz, 1H), 8.25 (dd, *J*= 7.8, 1.1 Hz, 2H), 7.93 (d, *J*= 7.4 Hz, 1H), 7.85 – 7.78 (m, 4H), 7.56 (ddd, *J*= 8.3, 7.2, 1.3 Hz, 2H), 7.47 – 7.42 (m, 2H), 3.18 (s, 3H). ^{13}C NMR (126 MHz, Acetonitrile-d_3) δ 173.3, 172.7, 157.9, 148.4, 140.1, 138.1, 131.3, 130.9, 130.0, 129.6, 128.6, 128.0, 125.7, 124.0, 123.6, 121.8, 119.0, 115.4, 111.4, 21.7. HRMS (ESI$^+$) calcd for $C_{28}H_{22}NO^+$ [M]$^+$: 386.1539, found: 388.1545. IR (film): 2923, 1576, 1521, 1445, 1378, 1335, 1191, 1057, 752, 689 cm^{-1}. Absorbance (CH_2Cl_2): 236, 284, 382, 564 nm.

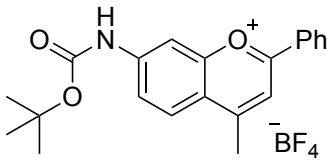

7-methoxy-4-methyl-2-phenylchromenylium chloride (3.12i): Flavone **3.12i** (20.5 mg, 0.0469 mmol, 1.0 equiv.) was dissolved in THF (0.300 mL) in a flame-dried 1.5 mL vial and cooled to 0 °C. Methylmagnesium bromide (1 M in THF, 0.100 mL, 3.2 equiv.) was added dropwise and the resulting solution was let warm to rt and stirred for 19 h under an atmosphere of N_2. Fluoroboric acid (50%, 0.016 mL) was added dropwise over ice and the crude reaction mixture was transferred directly to the following reaction. Note: Intermediate **3.12i** was isolated in low yield by subjecting the reaction mixture to several drops of 50% fluoroboric acid, extracting with dichloromethane/water, drying with Na_2SO_4, and filtering. After evaporating and triturating in EtOAc, a light green product resulted. ^{1}H NMR (600 MHz, Acetone-d_6) δ 9.90 (s, 1H), 8.81 (d, J= 2.1 Hz, 1H), 8.78 (s, 1H), 8.67 – 8.62 (m, 2H), 8.57 (d, J= 9.1 Hz, 1H), 7.98 (dd, J= 9.1, 2.1 Hz, 1H), 7.95 – 7.89 (m, 1H), 7.84 – 7.77 (m, 2H), 3.22 - 320 (m, 3H) {peak at 3.22 – 3.20 appears as a multiplet and as < 3H due to proton-deuterium exchange with Acetone-d_6}, 1.58 (s, 9H). HRMS (ESI$^+$) calcd for $C_{21}H_{22}NO_3^+$ $[M]^+$: 336.1594, found: 336.1598. Absorbance (CH_2Cl_2): 236, 272, 312, 356, 445 nm. Emission (CH_2Cl_2, ex. 390 nm): 497 nm.

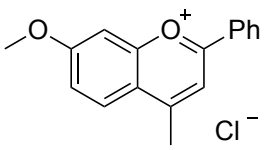

7-methoxy-4-methyl-2-phenylchromenylium chloride (3.12j): The preparation of flavylium **3.12j** was adapted from Yang and coworkers.[Error! Bookmark not defined.] 3-methoxy flavone (1.00 g, 8.06 mmol, 1.0 equiv.), benzoyl acetone (1.31 g, 8.06 mmol, 1.0 equiv.), were dissolved in EtOAc (40 mL) and placed in a 100 mL 3-neck flask. After bubbling HCl(*g*) for 3 h, the reaction was stirred at rt for an additional 24 h under a N_2 atmosphere. The reaction mixture was filtered and rinsed with additional EtOAc to yield a bright yellow solid (814 mg, 2.84 mmol, 35%). ^{1}H NMR (500 MHz, Acetonitrile-d_3) δ 8.45 – 8.39 (m, 3H), 8.35 (d, J= 9.3 Hz, 1H), 7.90 – 7.84 (m, 1H), 7.79 – 7.75 (m, 3H), 7.57 (dd, J= 9.3, 2.4 Hz, 1H), 4.14 (s, 3H), 3.07 (s, 3H). ^{13}C NMR (126 MHz, Acetonitrile-d_3) δ 172.1, 171.5, 170.5, 160.1, 137.1, 131.2, 130.1, 130.0, 129.8, 122.9, 121.2, 117.1, 101.7, 58.5, 21.4. HRMS (ESI$^+$) calcd for $C_{17}H_{15}O_2^+$ $[M]^+$: 251.1067, found: 251.1061. Absorbance (CH_2Cl_2): 228, 265, 303, 428 nm. Emission (CH_2Cl_2, ex. 390 nm): 460 nm.

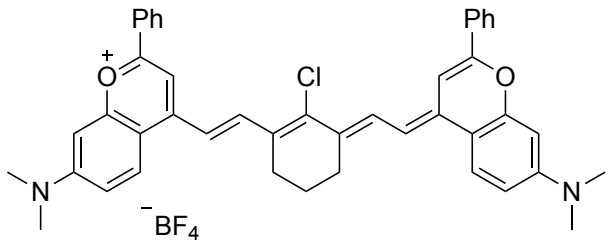

4-((*E*)-2-((*E*)-2-chloro-3-(2-((*E*)-7-(dimethylamino)-2-phenyl-4*H*-chromen-4-ylidene)ethylidene)cyclohex-1-en-1-yl)vinyl)-7-(dimethylamino)-2-phenylchromenylium tetrafluoroborate (3.1, Flav7): Flavylium **3.12a** (131 mg, 0.374 mmol, 1.0 equiv.), *N*-[(3-(anilinomethylene)-2-chloro-1-cyclohexen-1-yl)methylene]aniline hydrochloride (**3.13**) (64.5 mg, 0.180 mmol, 0.48 equiv.), and sodium acetate (90.0 mg, 1.10 mmol, 2.9 equiv.) were dissolved in *n*-butanol (2.1 mL) and toluene (0.9 mL) in a flame dried Schleck flask under N_2 atmosphere. The solution was freeze–pumped–thawed x3 and heated to 100 °C for 15 min. The crude mixture was evaporated, loaded onto silica gel, and purified by column chromatography, with a gradient of dichloromethane plus 0.5 to 10% ethanol. The procedure yielded a dark purple solid (68.2 mg, 0.0909 mmol, 51%). R_f = 0.5 in 9:1 DCM/EtOH. ^{1}H NMR (500 MHz, DMSO-d_6) δ 8.23 (d, J = 13.6 Hz, 2H), 8.22 – 8.11 (m, 6H), 7.69 (s, 2H), 7.63 – 7.54 (m, 6H), 7.11 (d, J = 13.8 Hz, 2H), 7.01 (dd, J = 9.3, 2.4 Hz, 2H), 6.87 (d, J = 2.6 Hz, 2H), 3.17 (s, 12H), 2.94 – 2.79 (m, 4H), 1.88 (p, J = 6.5 Hz, 2H). ^{19}F NMR (376 MHz, DMSO-d_6) δ -148.0. HRMS (ESI$^+$) calcd for $C_{44}H_{40}ClN_2O_2^+$ $[M]^+$: 663.2773; found: 663.2764. Absorbance (CH_2Cl_2): 522, 916, 1027 nm. Emission (CH_2Cl_2, ex. 885 nm): 1053 nm.

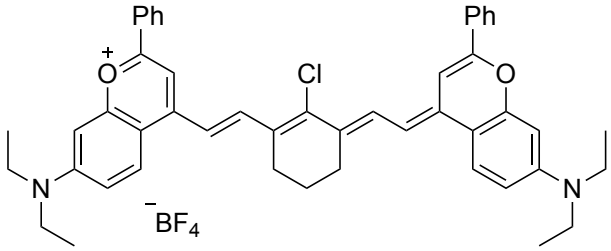

4-((*E*)-2-((*E*)-2-chloro-3-(2-((*E*)-7-(diethylamino)-2-phenyl-4*H*-chromen-4-ylidene)ethylidene)cyclohex-1-en-1-yl)vinyl)-7-(diethylamino)-2-phenylchromenyliumtetrafluoroborate (3.2): Flavylium **3.12b** (10.6 mg, 0.0280 mmol, 1.0 equiv.), *N*-[(3-(anilinomethylene)-2-chloro-1-cyclohexen-1-yl)methylene]aniline hydrochloride (**3.13**) (4.5 mg, 0.013 mmol, 0.45 equiv.), and sodium acetate (6.9 mg, 0.084 mmol, 3.0 equiv.)

were added to a flame–dried 1 mL vial and dissolved in *n*-butanol (0.17 mL) and toluene (0.08 mL). The mixture was freeze–pump–thawed x3 and heated to 100 °C for 10 min. The crude product was purified by column chromatography in a gradient of DCM with 0.5 to 6% ethanol to yield a purple solid (4.0 mg, 0.0054 mmol, 40%). R_f = 0.5 in 9:1 DCM/EtOH. ^{1}H NMR (500 MHz, Acetonitrile-d_3) δ 8.04 (d, *J* = 13.8 Hz, 2H), 7.86 (d, *J* = 7.5 Hz, 4H), 7.62 (dd, *J* = 9.8, 3.7 Hz, 2H), 7.58 – 7.50 (m, 6H), 7.18 (d, *J* = 3.6 Hz, 2H), 6.70 (d, *J* = 13.8, 2H), 6.62 (dd, *J* = 9.2, 2.9 Hz, 2H), 6.40 (m, 2H), 3.38 (q, *J* = 6.6 Hz, 8H), 2.74 (t, *J* = 6.0 Hz, 4H), {peak at 2.0-1.9 ppm, beneath CD_3CN solvent peak, (m, 2H)}, 1.18 (t, *J* = 6.9 Hz, 12H). HRMS (ESI$^+$) calcd for $C_{48}H_{48}ClN_2O_2^+$ $[M]^+$: 719.3399, found: 719.3385. Absorbance (CH_2Cl_2): 526, 922, 1033 nm. Emission (CH_2Cl_2, ex. 885 nm): 1057 nm.

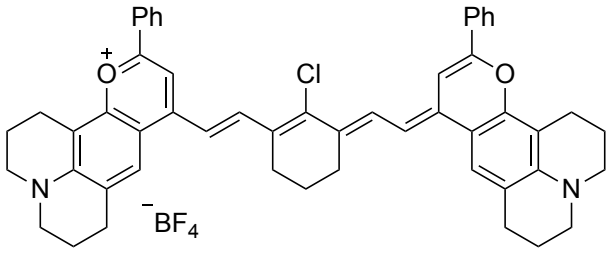

9-((*E*)-2-((*E*)-2-chloro-3-((*E*)-2-(11-phenyl-2,3,6,7-tetrahydro-1*H*,5*H*,9*H*-pyrano[2,3-*f*]pyrido[3,2,1-*ij*]quinolin-9-ylidene)ethylidene)cyclohex-1-en-1-yl)vinyl)-11-phenyl-2,3,6,7-tetrahydro-1*H*,5*H*-pyrano[2,3-*f*]pyrido[3,2,1-*ij*]quinolin-12-ium tetrafluoroborate (3.3, JuloFlav7): Flavylium **3.12c** (40.1 mg, 0.0995 mmol, 1.0 equiv.), *N*-[(3-(anilinomethylene)-2-chloro-1-cyclohexen-1-yl)methylene]aniline hydrochloride (**3.13**) (17.5 mg, 0.0487 mmol, 0.49 equiv.) and sodium acetate (12.4 mg, 0.151 mmol, 1.5 equiv.) were added to an oven-dried 20 mL vial, dissolved in ethanol (1 mL), freeze–pump–thawed x3, and heated at 70 °C for 2 h. The crude product was dry loaded onto silica gel, and purified by column chromatography with a 9:1 DCM/acetone solvent mixture. The product was collected as a dark purple solid (15.4 mg, 0.018 mmol, 37%). R_f = 0.5 in 9:1 DCM/EtOH. ^{1}H NMR (500 MHz, DMSO-d_6) δ 8.21 – 8.03 (m, 6H), 7.75 (s, 2H), 7.66 – 7.58 (m, 6H), 7.55 (s, 2H), 7.01 (d, *J* = 13.9 Hz, 2H), 3.43 – 3.36 (m, 8H), 2.89 (t, *J* = 6.4 Hz, 4H), 2.83 (t, *J* = 6.0 Hz, 4H), 2.79 (t, *J* = 6.3 Hz,

4H), 2.01 – 1.94 (m, 4H), 1.91 (m, 6H). HRMS (ESI$^+$) calculated for $C_{52}H_{48}ClN_2O_2^+$ [M]$^+$: 767.3399, found: 767.3386. Absorbance (CH_2Cl_2): 527, 949, 1061 nm. Emission (CH_2Cl_2, ex. 885 nm): 1088 nm.

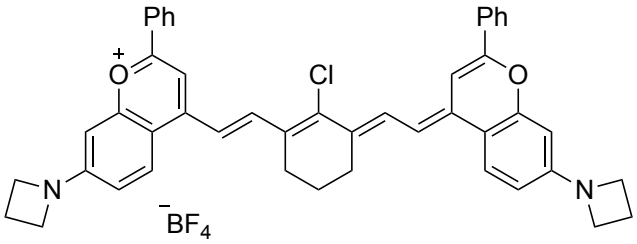

7-(azetidin-1-yl)-4-((*E*)-2-((*E*)-3-(2-((*E*)-7-(azetidin-1-yl)-2-phenyl-4*H*-chromen-4-ylidene)ethylidene)-2-chlorocyclohex-1-en-1-yl)vinyl)-2-phenylchromenylium tetrafluoroborate (3.4): Flavylium **3.12d** (12 mg, 0.034 mmol, 1.0 equiv.), *N*-[(3-(anilinomethylene)-2-chloro-1-cyclohexen-1-yl)methylene]aniline hydrochloride (**3.13**) (5.8 mg, 0.016 mmol, 0.47 equiv.), and sodium acetate (9.3 mg, 0.11 mmol, 3.3 equiv.) were added to a flame dried 1 mL vial and dissolved in *n*-butanol (0.2 mL) and toluene (0.09 mL) under an N_2 atmosphere. The reaction mixture was freeze–pump–thawed x3, and heated to 100 °C for 10 min. The crude mixture was evaporated onto silica gel and purified via column chromatography with a gradient of DCM plus 0.5–6% ethanol, followed by chromatography with dichloromethane plus 1–2% ethanol. The procedure yielded an iridescent maroon solid (4.6 mg, 0.0059 mmol, 37%). R_f = 0.5 in 9:1 DCM/EtOH. ^{1}H NMR (500 MHz, DMSO-d_6) δ 8.16 – 8.01 (m, 8H), 7.67 – 7.54 (m, 8H), 7.03 (d, J = 13.8 Hz, 2H), 6.59 (dd, J = 8.9, 2.3 Hz, 2H), 6.47 (d, J = 2.2 Hz, 2H), 4.10 (t, J = 7.5 Hz, 8H), 2.80 (t, J = 5.5 Hz, 4H), 2.43 (p, J = 7.2 Hz, 4H), 1.88 (p, J = 6.5 Hz, 2H). HRMS (ESI$^+$) calcd for $C_{46}H_{40}ClN_2O_2^+$ [M]$^+$: 687.2773; found: 687.2757. Absorbance (CH_2Cl_2): 523 nm, 920 nm, 1029 nm. Emission (CH_2Cl_2, ex. 885 nm): 1056 nm.

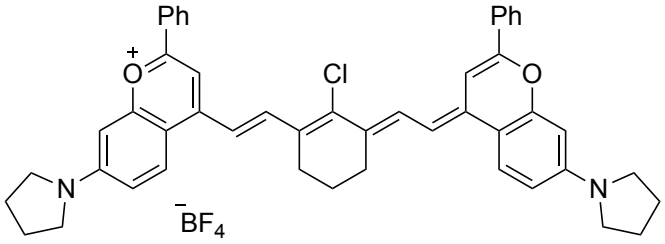

4-((E)-2-((E)-2-chloro-3-(2-((E)-2-phenyl-7-(pyrrolidin-1-yl)-4H-chromen-4-ylidene)ethylidene)cyclohex-1-en-1-yl)vinyl)-2-phenyl-7-(pyrrolidin-1-yl)chromenylium tetrafluoroborate (3.5): Flavylium **3.12e** (75.3 mg, 0.199 mmol, 1.0 equiv.)

N-[(3-(anilinomethylene)-2-chloro-1-cyclohexen-1-yl)methylene]aniline hydrochloride (**3.13**) (29.6 mg, 0.0825 mmol, 0.45 equiv.) and 2,6-di-tert-butyl-4-methyl pyridine (137 mg, 0.667 mmol, 3.0 equiv.) were dissolved in *n*-pentanol (1.9 mL) in a 25 mL Schlenk flask, freeze–pump–thawed x3, and heated to 140 °C for 1.5 h. The solution was cooled to rt and evaporated onto silica gel. The crude product was purified via silica gel chromatography, eluting with a 7:3 DCM/toluene solvent mixture plus 0.2 to 10% EtOH, followed by a trituration with ice cold THF. The procedure gave a dark purple solid. (10.3 mg, 0.0128 mmol, 8%). R_f = 0.5 in 9:1 DCM/EtOH. ^{1}H NMR (500 MHz, Methylene Chloride-d_2) δ 8.35 (d, *J* = 13.8 Hz, 2H), 8.09 – 8.00 (m, 4H), 7.94 (d, *J* = 9.3 Hz, 2H), 7.64 – 7.55 (m, 6H), 7.48 (s, 2H), 6.99 (d, *J* = 13.9 Hz, 2H), 6.83 (dd, *J* = 9.2, 2.5 Hz, 2H), 6.59 (d, *J* = 2.3 Hz, 2H), 3.56 – 3.46 (m, 8H), 2.84 (t, *J* = 6.2 Hz, 4H), 2.15 – 2.09 (m, 8H), 2.01 (p, *J* = 5.6 Hz, 2H). HRMS (ESI$^+$) calcd for $C_{48}H_{44}ClN_2O_2^+$ [M]$^+$: 715.3086; found: 715.3070. Absorbance (CH_2Cl_2): 525 nm, 924 nm, 1034 nm. Emission (CH_2Cl_2, ex. 885 nm): 1061 nm.

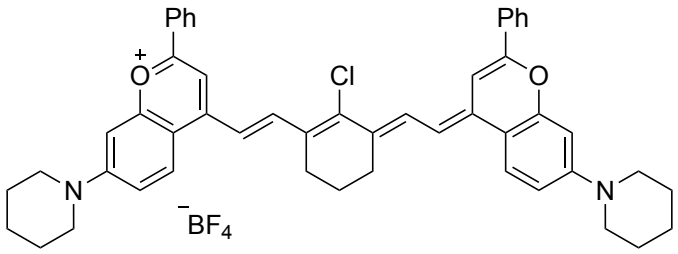

4-((E)-2-((E)-2-chloro-3-(2-((E)-2-phenyl-7-(piperidin-1-yl)-4H-chromen-4-ylidene)ethylidene)cyclohex-1-en-1-yl)vinyl)-2-phenyl-7-(piperidin-1-yl)chromenylium tetrafluoroborate (3.6) Flavylium **3.12f** (30.3 mg, 0.0775 mmol, 1.0 equiv.), *N*-[(3-(anilinomethylene)-2-chloro-1-cyclohexen-1-yl)methylene]aniline hydrochloride (**3.13**) (47.5 mg, 0.132 mmol, 0.45 equiv.), and 2,6-di-tert-butyl-4-methyl pyridine (15.2 mg, 0.740 mmol, 3.0 equiv.) were dissolved in a mixture of *n*-butanol (0.46 mL) and toluene (0.20 mL) in a 25 mL Schlenk flask, freeze–pump–thawed x3, and heated to 100 °C for 2 h. The solution was cooled to rt and evaporated onto silica gel. The crude product was purified via silica gel

chromatography, eluting with a 7:3 DCM/Toluene solvent mixture plus 0.2–10% EtOH, followed by a trituration with ice cold THF. The procedure gave a dark purple solid (17.1 mg, 0.0205 mmol, 26%). R_f = 0.5 in 9:1 DCM/EtOH. ^{1}H NMR (500 MHz, Methylene Chloride-d_2) δ 8.25 (d, *J*= 13.8 Hz, 2H), 7.97 – 7.95 (m, 4H), 7.87 (d, *J*= 9.3 Hz, 2H), 7.61 – 7.53 (m, 6H), 7.38 (s, 2H), 7.04 (dd, *J*= 9.4, 2.6 Hz, 2H), 6.91 (d, *J*= 13.8 Hz, 2H), 6.76 (d, *J*= 2.5 Hz, 2H), 3.50 (m, 8H), 2.82 – 2.78 (m, 4H), 2.00 (p, *J*= 6.2 Hz, 2H), 1.73 (m, 12H). HRMS (ESI$^+$) Calculated for $C_{50}H_{48}ClN_2O_2^+$ $[M]^+$: 743.3399; found: 743.3386. Absorbance (CH_2Cl_2): 523 nm, 922 nm, 1034 nm. Emission (CH_2Cl_2, ex. 885 nm): 1060 nm.

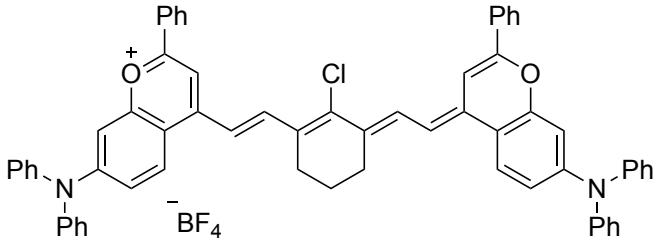

4-((E)-2-((E)-2-chloro-3-(2-((E)-7-(diphenylamino)-2-phenyl-4H-chromen-4-ylidene)ethylidene)cyclohex-1-en-1-yl)vinyl)-7-(diphenylamino)-2-phenylchromenylium tetrafluoroborate (3.7): Flavylium **3.12g** (23.9 mg, 0.0503 mmol, 1.0 equiv.), *N*-[(3-(anilinomethylene)-2-chloro-1-cyclohexen-1-yl)methylene]aniline hydrochloride (**3.13**) (8.0 mg, 0.22 mmol, 0.44 equiv.) and 2,6-di-tert-butyl-4-methyl pyridine (30.8 mg, 0.150 mmol, 3.0 equiv.) were dissolved in 1,4-dioxane (0.80 mL), freeze–pump–thawed x3, and heated to 100 °C for 15 min. The crude product was purified by column chromatography with a gradient of 60:40 DCM/toluene plus 0.2% EtOH to DCM plus 0.6% EtOH, producing a copper colored solid (5.6 mg 0.0056 mmol, 11%). R_f = 0.3 in 9:1 DCM/EtOH. ^{1}H NMR (500 MHz, Methylene Chloride-d_2) δ 8.41 (d, *J*= 13.7 Hz, 2H), 8.02 – 7.94 (m, 4H), 7.90 (d, *J*= 9.2 Hz, 2H), 7.61 – 7.52 (m, 8H), 7.48 – 7.42 (m, 8H), 7.38 – 7.19 (m, 12H), 7.09 (dd, *J*= 9.2, 2.5 Hz, 2H), 7.03 (d, *J*= 13.8 Hz, 2H), 6.95 (d, *J*= 2.4 Hz, 2H), 2.82 (t, *J*= 6.3 Hz, 4H), 2.00 (p, *J*= 6.4 Hz, 2H). HRMS (ESI$^+$)

Calculated for $C_{64}H_{48}ClNO_2^+$ $[M]^+$: 911.3399; found: 911.3379. Absorbance (CH_2Cl_2): 526 nm, 936 nm, 1047 nm Emission (CH_2Cl_2, ex. 885 nm): 1078 nm.

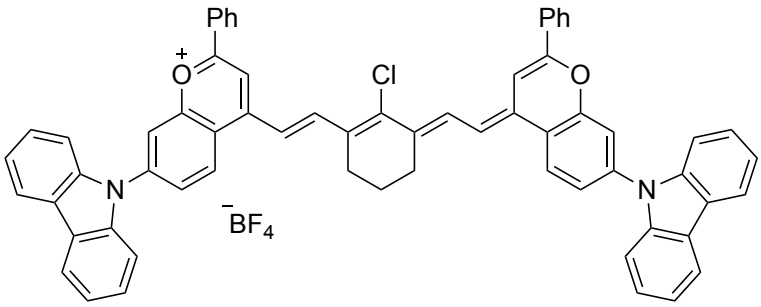

4-((E)-2-((E)-3-(2-((E)-7-(9H-carbazol-9-yl)-2-phenyl-4H-chromen-4-ylidene)ethylidene)-2-chlorocyclohex-1-en-1-yl)vinyl)-7-(9H-carbazol-9-yl)-2-phenylchromenylium tetrafluoroborate (3.8): Flavylium **3.12h** (29.9 mg, 0.0632 mmol, 1.0 equiv.), *N*-[(3-(anilinomethylene)-2-chloro-1-cyclohexen-1-yl)methylene]aniline hydrochloride (**3.13**) (10.3 mg, 0.287 mmol, 0.45 equiv.), .and 2,6-di-tert-butyl-4-methyl pyridine (42.5 mg, 0.207 mmol, 3.3 equiv.) were added to a 25 mL flame-dried Schlenk flask and dissolved in *n*-butanol (0.70 mL) and toluene (0.50 mL), freeze–pump–thawed x3, and heated to 90 °C for 17 min. The crude product was purified by column chromatography with a gradient of DCM plus 1 – 7% MeCN and subsequently washed with cold toluene to produce a dark purple solid (3.6 mg, 0.0036 mmol, 13%). R_f = 0.5 in 9:1 DCM/EtOH. ^{1}H NMR (500 MHz, Methylene Chloride-d_2) δ 8.69 (d, *J*= 13.0 Hz, 2H), 8.42 (d, *J*= 8.4 Hz, 2H), 8.21 – 8.14 (m, 8H), 7.98 (s, 2H), 7.92 (d, *J*= 7.7 Hz, 2H), 7.83 (s, 2H), 7.72 -7.64 (m, 10H), 7.52 (t, *J*= 7.3 Hz, 4H), 7.41 (t, *J*= 7.3 Hz, 4H), 7.35 (d, *J*= 13.7 Hz, 2H), 3.02 – 2.95 (m, 4H), 2.16 – 2.08 (m, 2H). HRMS (ESI$^+$) Calculated for $C_{64}H_{44}ClNO_2^+$ $[M]^+$: 907.3086; found: 911.3107. Absorbance (CH_2Cl_2): 452 nm, 910 nm, 1021 nm. Emission (CH_2Cl_2, ex. 885 nm): 1048 nm.

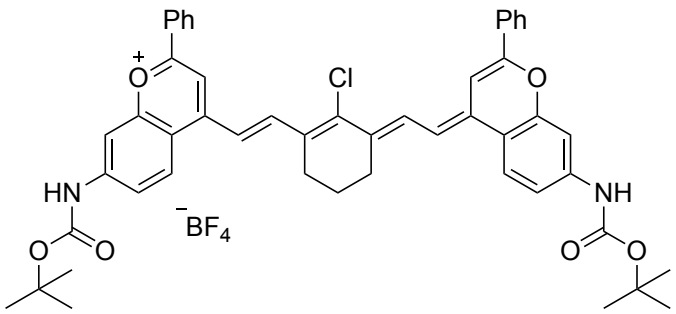

7-((tert-butoxycarbonyl)amino)-4-((E)-2-((E)-3-(2-((E)-7-((tert-butoxycarbonyl)amino)-2-phenyl-4H-chromen-4-ylidene)ethylidene)-2-chlorocyclohex-1-en-1-yl)vinyl)-2-phenylchromenylium tetrafluoroborate (3.9): The crude reaction mixture containing flavylium **3.12i** was transferred to a flame-dried 1.5 mL vial charged with *N*-[(3-(anilinomethylene)-2-chloro-1-cyclohexen-1-yl)methylene]aniline hydrochloride (**3.13**) (6.7 mg, 0.019 mmol, 0.40 equiv.), and 2,6-di-tert-butyl-4-methyl pyridine (53.5 mg, 0.261 mmol, 5.6 equiv.) and sodium sulfate (44 mg). Dioxane (0.250 mL) was added, the mixture was freeze–pump–thawed x3, and it was heated to 95 °C for 14 min. The crude mixture was evaporated directly onto silica gel and purified via column chromatography in a DCM/acetone solvent mixture with a gradient of 20:1 to 1:1, yielding a brick red solid (13.9 mg, 0.0155 mmol, 33%, over 2 steps). R_f = 0.4 in 9:1 DCM/EtOH. ^{1}H NMR (500 MHz, DMSO-d_6) δ 10.28 (s, 2H), 8.50 – 8.36 (m, 4H), 8.32 – 8.24 (m, 4H), 8.06 – 7.97 (m, 4H), 7.71 – 7.59 (m, 6H), 7.52 (dd, *J*= 9.1, 2.2 Hz, 2H), 7.29 (d, *J*= 13.7 Hz, 2H), 2.90 (t, *J*= 5.0 Hz, 4H), 1.92 (p, *J*= 7.7, 7.3 Hz, 2H), 1.54 (s, 18H). HRMS (ESI$^+$) Calculated for $C_{50}H_{48}ClNO_6^+$ [M]$^+$: 807.3195; found: 807.3187. Absorbance (CH_2Cl_2): 445 nm, 891 nm, 998 nm. Emission (CH_2Cl_2, ex. 885 nm): 1022 nm.

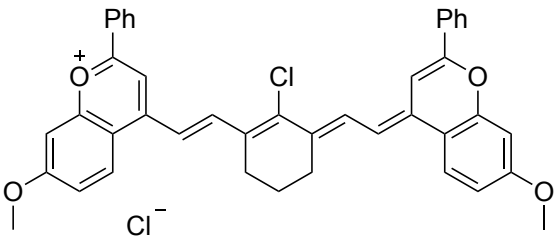

4-((E)-2-((E)-2-chloro-3-(2-((E)-7-methoxy-2-phenyl-4H-chromen-4-ylidene)ethylidene)cyclohex-1-en-1-yl)vinyl)-7-methoxy-2-phenylchromenylium chloride (3.10, MeOFlav7): Flavylium **13.2j** (150 mg, 0.523 mmol, 1.0 equiv.), *N*-[(3-(anilinomethylene)-2-chloro-1-cyclohexen-1-yl)methylene]aniline hydrochloride

(**3.13**) (75 mg, 0.21 mmol, 0.40 equiv.) and 2,6-di-tert-butyl-4-methylpyridine (327 mg, 1.59 mmol, 3.0 equiv.) were dissolved in toluene (4.05 mL) and *n*-butanol (1.25 mL) and heated to 100 °C for 15 min. The solution was cooled to rt then cooled with ice. Toluene (10 mL) was added and a reddish brown solid precipitated and was collected through filtration and washed with an additional 25 mL of toluene. The crude product was purified through Soxhlet extraction with toluene for 4 hours at 130 °C to give a brick red solid. (47 mg, 0.070 mmol, 33%). R_f = 0.4 in 9:1 DCM/EtOH. ^{1}H NMR (400 MHz, Methylene Chloride-d_2) δ 8.55 (d, J = 13.6 Hz, 2H), 8.14 – 8.02 (m, 4H), 7.69 (s, 2H), 7.65 (t, J = 6.8 Hz, 4H), 7.40 – 7.23 (m, 6H), 7.25 – 7.09 (m, 4H), 4.01 (s, 3H), 2.93 – 2.84 (m, 4H), 2.08 – 1.96 (m, 2H). HRMS (ESI$^+$) Calculated for $C_{42}H_{34}ClNO_4^+$ [M]$^+$: 637.2140; found: 637.2124. Absorbance (CH_2Cl_2): 441 nm, 880 nm, 984 nm. Emission (CH_2Cl_2, ex. 885 nm): 1008 nm.

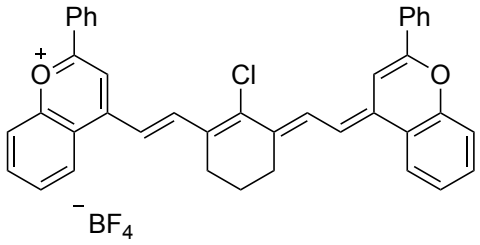

4-((E)-2-((E)-2-chloro-3-(2-((E)-2-phenyl-4H-chromen-4-ylidene)ethylidene)cyclohex-1-en-1-yl)vinyl)-2-phenylchromenylium tetrafluoroborate (3.11, IR-27): 4-methyl-2-phenylchromenylium tetrafluoroborate (Santa Cruz Biotechnology) (50.0 mg, 0.162 mmol, 1.0 equiv.), *N*-[(3-(anilinomethylene)-2-chloro-1- cyclohexen-1-yl)methylene]aniline hydrochloride (**3.13**) (27.5 mg, 0.0765 mmol, 0.47 equiv.) and 2,6-di-tert-butyl-4-methylpyridnie (67 mg, 0.33 mmol, 2.0 equiv.) were dissolved in toluene (0.40 mL) and *n*-butanol (0.90 mL) and freeze–pump–thawed x3. The reaction was heated to 90 °C for 45 min before cooling and evaporating. The crude product was purified by column chromatography in DCM with 1 to 12 % MeCN, followed by column chromatography in DCM with 0.2 to 0.4 % EtOH, followed by column chromatography in DCM with 0.5 to 1.5 % acetone to produce a light orange solid (2.3 mg 0.035 mmol, 5 %). R_f = 0.4 in 10% EtOH/DCM. ^{1}H NMR (500 MHz, Acetonitrile-d_3) δ 8.52 (m, 2H), 8.17 (m, 2H), 8.11 (d, J=

7.4 Hz, 4H), 7.78 (m, 4H), 7.60 (m, *J*= 7.5 Hz, 8H), 7.49 (t, *J*= 7.6 Hz, 2H), 7.19 (m, 2H), 3.05 – 2.71 (m, 4H) {peak under CD3CN solvent peak at ~1.96, m, 2H}. HRMS (ESI^+) Calculated for $C_{40}H_{30}ClNO_2^+$ $[M]^+$: 577.1929; found: 577.1924. Absorbance (CH_2Cl_2): 449 nm, 884 nm, 987 nm. Emission (CH_2Cl_2, ex. 885 nm): 1011 nm.

3.5.3 Figure Experimental Procedures

Figure 3.2B Absorbance traces were obtained on samples in a 1 cm quartz cuvette, in dichloromethane with OD $\leq$ 1.0 and $\geq$ 0.1 with a 1.0 nm step size and 2,000 nm/min scanning rate. Plotted are the baseline corrected (to 1,300 nm) and normalized data.

Figure 3.2C Emission traces were obtained on samples in a 1 cm quartz cuvette, in dichloromethane with OD $\leq$ 0.1. Excitation was at 885 nm, with 15 nm (5.76 mm) excitation slit widths, 30 nm (11.52 mm) emission slit widths, with a 900 nm SP filter (FES 900, Thorlabs) placed between the excitation source and the sample. Data were acquired with 1 nm step size and 0.1 sec integration time, automatic background correction, and using a correction file which accounts for non-linearity of the detector. Plotted are the baseline corrected (to 1500 nm) and normalized data. Note: the raw emission spectra contain an artifact from absorption of the solvent, dichloromethane, at 1,154 nm.

Figure 3.2D The absorbance emission λ_{max} values were obtained from traces acquired as described in **Figure 3.2B** and **Figure 3.2C** experimental procedures. Absorption coefficients are taken as the average of the triplicate measurement. See Section 3.6.3 for a discussion of photoluminescence quantum yields. The brightness(ε_{max}) was calculated for each dye, according to the following equation:

$$\text{brightness}(\varepsilon_{max}) = \varepsilon_{\lambda\text{max}} * \Phi_F \qquad \text{(Eq. 3.1)}$$

Error values for all absorption coefficients, photoluminescence quantum yields, and brightness values are reported in **Table 3.5** and are taken as the standard deviations and propagated error from the standard deviations, respectively.

Figure 3.2E The Hammett σ_m values were obtained as described in Section 3.6.2. The λ_{max} values for absorbance and emission were taken as the max wavelength from traces obtained as described in **Figure 3.2B** and **Figure 3.2C** experimental procedures. The points were subjected to a linear fit and the closeness of fit is qualified by the listed R^2 value.

Figure 3.2F The brightness(ε_λ) was calculated for λ = 785 nm, λ = 980 nm and λ = 1,064 nm by the following equations:

$$\text{brightness}(\varepsilon_{785}) = \varepsilon_{785} * \Phi_F \quad \text{(Eq. 3.2)}$$

$$\text{brightness}(\varepsilon_{980}) = \varepsilon_{980} * \Phi_F \quad \text{(Eq. 3.3)}$$

$$\text{brightness}(\varepsilon_{1064}) = \varepsilon_{1064} * \Phi_F \quad \text{(Eq. 3.4)}$$

Error is taken as the propagated values from the standard deviation of the absorption coefficient at the relevant wavelengths and the error in fluorescence quantum yield measurements. Brightness values of each dye are plotted in order of $\lambda_{max,abs}$.

Figure 3.3 See experimental procedures for **Figure 3.2F**.

Figure 3.5A Absorbance trances of dyes **3.3** and **3.10** in organic solvent (acquisition parameters as described in **Figure 3.2B** experimental procedure) are compared to ICG in organic solvent. The ICG absorbance trace was acquired in EtOH at OD $\leq$ 1.0 and $\geq$ 0.1 with a 1.0 nm step size and 2000 nm/min scanning rate. Plotted are the baseline corrected (to 1,000 nm) and normalized data. Laser excitation wavelengths are denoted by black lines.

Figure 3.5B The absorbance trace in organic solvent was obtained as described in **Figure 3.2B** experimental procedure. The absorbance trace in water was obtained on a sample in a 3 mm quartz

cuvette, with a 2.0 nm step size and 2,000 nm/min scanning rate. The raw OD $= 1.61$; plotted are the baseline corrected (to 1,300 nm) and normalized data. Emission data were obtained on a sample in water in a 3 mm quartz cuvette with OD ≤ 0.1. Excitation was at 880 nm, with 15 nm excitation slit widths and 30 nm emission slit widths, with a 900 nm SP filter placed between the excitation source and the detector. The plotted data are baseline corrected (to 1,400 nm) and normalized. Excitation data were collected on a sample in water in a 1 cm cuvette with OD ≤ 0.1. Emission collection was at 1,008 nm, with 15 nm excitation slit widths, 30 nm emission slit widths, and a 1,200 nm SP filter placed between the excitation source and the sample. The plotted data are baseline corrected (to 600 nm) and scaled arbitrarily to match monomer signal in the organic solvent absorbance trace.

Figure 3.5C The absorbance trace in organic solvent was obtained as described in **Figure 3.2B** experimental procedure. The absorbance trace in water was obtained on a sample in a 1 cm quartz cuvette, with a 1.0 nm step size and 2,000 nm/min scanning rate. The raw OD $= 0.63$; plotted are the baseline corrected (to 1,300 nm) and normalized data. Emission data were obtained on a sample in water in a 2 mm x 10 mm quartz cuvette (10 mm path length aligned with the excitation source) with OD ≤ 0.1 (for a 10 mm path length). Excitation was at 900 nm, with 15 nm excitation slit widths and 30 nm emission slit widths. The plotted data are baseline corrected (to 1,500 nm) and normalized. Excitation data were collected on a sample in water in a 1 cm cuvette with OD ≤ 0.1. Emission collection was at 1,088 nm, with 15 nm excitation slit widths, 30 nm emission slit widths, and a 1,200 nm SP filter placed between the excitation source and the sample. The plotted data are baseline corrected (to 700 nm) and scaled arbitrarily to match monomer signal in the organic solvent absorbance trace.

Figure 3.5D. Absorbance emission λ_{max} values were obtained from the traces in **Figure 3.5B** and **Figure 3.5C**. See Section 3.6.3 for a discussion of photoluminescence quantum yields.

Figure 3.5 E *(top)* Dyes were dissolved at 0.004 mg/mL in DCM (**3.3** and **3.10**) or EtOH (ICG) in 0.3 mL Eppendorf tubes. Excitation was at 785 nm (29 $mWcm^{-2}$), 980 nm (10 $mWcm^{-2}$), and 1,064 nm (6.4 $mWcm^{-2}$), with an 1,100 nm SP filter (Edmund Optics #64-339). Dyes were imaged on Lens System B, with an 1,100 nm LP filter (Edmund Optics #84-768). The acquisition parameters were exposure time 5 ms, 100 fps, with a 10 ms trigger pulse width and 60% duty cycle, and 8-bit format. Displayed images are averaged over 5 frames. *(middle and bottom)* Micelles of JuloFlav7 (**3.3**) and MeOFlav7 (**3.10**) were prepared as described in the experimental procedures for **Figure 3.9**, and diluted to a final volume of 12 mL. MeOFlav7 micelles were diluted 1:5 (0.007 mg/mL; 9.9 μM) and JuloFlav7 micelles were diluted 1:15 (0.002 mg/mL; 2.6 μM). ICG was prepared as a 0.1 mg/mL solution and diluted 1:20 (0.005 mg/mL; 6.5 μM). Samples were added to 0.5 mL Eppendorf tubes and imaged using continuous acquisition with manually modulated excitation at 785 nm (61 $mWcm^{-2}$), 980 nm (100 $mWcm^{-2}$), and 1,064 nm (100 $mWcm^{-2}$), with 2 x 1,100 SP filters (Edmund Optics #64-339). Dyes were imaged in Lens System B, with 1 x 1,100 LP filter Thorlabs FELH1100) and 3 x 1,100 nm LP filters (Edmund Optics #84-768). The acquisition parameters were exposure time 20 ms, 50 fps, continuous acquisition, 14-bit format. Displayed images are averaged over 200 frames.

Images were unmixed according to the following equations:

$$1064_f = 1064_r$$

$$980_f = 980_r - (0.44 * 1064_r)$$

$$785_f = 785_r - \left(0.17 * 980_f\right) - (0.13 * 1064_f)$$

where the subscripts r and f represent “raw” and “final” images, respectively, and 785, 980 and 1,064 represent the images from the wavelength channels.

Figure 3.5G The probes were delivered to the anesthetized animal as follows: 1) i.p. injection of **3.10** (MeOFlav7) micelles (0.250 mL, 0.57 mg/mL, 211 nmol) in PBS buffer; 2) i.v. injection of **3.3** (JuloFlav7) micelles (0.150 mL, 0.26 mg/ml, 50 nmol) in PBS buffer; 3) i.v. injection of ICG in cell culture water (0.050 mL, 0.1 mg/mL, 6.5 nmol). Excitation for three channels: 785 nm (78 $mWcm^{-1}$), 980 nm (77 $mWcm^{-1}$), and 1,064 nm (79 $mWcm^{-1}$), with an 1,100 nm SP filter (Edmund Optics #64-339). Imaging was performed on Lens System A, with an 1,100 nm LP filter (Edmund Optics #84-768), and an 1,150 nm LP filter (FELH 1150, Thorlabs). The acquisition parameters were 10 ms exposure time, 27.8 fps, 12 ms trigger pulse width and 83% duty cycle, and 8-bit format. Displayed images are averaged over 5 frames.

Images were unmixed according to the following equations:

$$1064_f = 1064_r - (0.15 * 980_f)$$

$$980_f = 980_r - (0.40 * 1064_r)$$

$$785_f = 785_r - \left(0.35 * 980_f\right) - (0.20 * 1064_f)$$

where the subscripts r and f represent “raw” and “final” images, respectively, and 785, 980 and 1,064 represent the images from the wavelength channels.

Figure 3.7–3.8 See Section 3.6.4.

Figure 3.9 *Assembly of PEG-phospholipid micelles*. *A) Encapsulation of JuloFlav7 (**3.3**) in micelles*. General assembly procedure: JuloFlav7 (**3.3**, 0.40 mg) was dissolved in DMSO (4.0 mL) and added to 8.0 mL of a 10 mg/mL solution of 1,2-distearoyl-*sn*-glycero-3-phosphoethanolamine-*N*-[methoxy(polyethylene glycol)-5000] (sodium salt) lipid (abbreviated 18:0 PEG5000 PE) (Laysan Bio) on ice. The mixture was divided into 3 mL aliquots and sonicated in a probe sonicator

(5 min, 35%) on ice. The resulting micelles were combined in a 10 kDa MW cutoff filter (Amicon Ultra-15) and centrifuged at 4000 rpm. Sequential washes with 1x PBS were performed, until the remaining DMSO consisted of < 1%. The micelles were then concentrated by centrifugation (4000 rpm) to 1.7–2.0 mL. *B) Encapsulation of MeOFlav7 (**3.10**) in micelles*. General assembly procedure: MeOFlav7 (**3.10**, 0.426 mg) was dissolved in DCM (2.0 mL) and added to a vessel containing 1,2-dioleoyl-*sn*-glycero-3-phosphoethanolamine-*N*-[methoxy(polyethylene glycol)-2000] (ammonium salt) lipid (abbreviated 18:1 PEG2000 PE) (Avanti Polar lipids, 48 mg). The solution was sonicated briefly in a bath sonicator and divided into four 0.50 mL aliquots before the solvent was evaporated by gently flushing with N_2. Sodium chloride (0.9 % in water, 3.0 mL) was added and the solution was sonicated on a probe sonicator (35%, 90 s). The aliquots were then combined in a 10 kDa MW cutoff filter (Amicon Ultra-15) and centrifuged at 4000 rpm to a final volume of 0.75 mL.

Figure 3.10 *Dynamic light scattering characterization of PEG-phospholipid micelles***.** Size data by DLS were acquired after a 1:100 (20 μL to 2 mL) dilution in MilliQ water. SOP parameters were as follows: sample refractive index 1.4, 3 measurements, no delay between measurements, 25 °C with 120 second equilibration time.

Figure 3.11 *Viability of HEK293 cells treated with micelles containing **3.3** and **3.10***. Dye containing micelles were prepared as described in experimental procedures for **Figure 3.9**, on 25% scale. Empty micelles were prepared analogously, without the addition of dye. JuloFlav7 (**3.3**) micelles and the analogous empty micelles were diluted to a final volume of 2 mL. MeOFlav7 (**3.10**) and the analogous empty micelles were diluted to a final volume of 3 mL. HEK293 cells were added to a 96-well v-bottom plate with a cell density of 200,000 cells per well in MEM supplemented with fetal bovine serum (FBS), Pen/Strep, and sodium pyruvate. Micelles (20 μL

and 50 µL treatments) were added without dilution to a final volume of 200 µL in each well. Cells were incubated for 3 hours at 37 °C and 5% CO_2. The incubated cells were washed three times by centrifugation (3,000 rpm, 3 min, 4 °C) with FACS buffer (PBS + 1% FBS). Cells were resuspended in 200 µL FACS buffer and transferred to FACS tubes. Propidium iodide solution (1.5 µL of 1 mg/mL in PBS) was added to each tube and incubated on ice for 15 min. An additional 200 µL of FACS buffer was added to each tube. PI fluorescence was measured on a 2-laser BD FACSCalibur Flow Cytometer on the FL2 channel and collected using CellQuest (version 3.3). A preliminary FSC/SSC gate was implemented on the starting cell population to omit debris. PI staining and laser power were adjusted such that there was at least an order of magnitude difference between stained and unstained samples, verified by healthy cells and heat-kill control. Data was analyzed on FlowJo (v10) by mean FL2 fluorescence with the population split at $10^{2.5}$ to distinguish live and dead cells.

Figure 3.12 *Absorption, excitation, and emission spectra of monomer dyes and micelle-encapsulated dyes in water A) Absorption spectra* were acquired as described in **Figure 3.5 C** experimental procedures. *B) Excitation spectrum* of JuloFlav7 (**3.3**) in micelles in water was acquired as described in experimental procedures for **Figure 3.5C**. Displayed is the baseline corrected (to 700 nm) and normalized trace (to 1.0 at 1,000 nm). Excitation spectrum of JuloFlav7 (**3.3**) in DCM was acquired on a sample in a 1 cm cuvette with OD ≤ 0.1. Emission collection was at 1,088 nm, with 15 nm excitation slit widths, 20 nm emission slit widths, and a 1,200 nm SP filter placed between the excitation source and the sample. The plotted data are baseline corrected (to 700 nm) and normalized (to 1.0 at 1,000 nm). *C) Emission spectrum* of **3.3** in dichloromethane was acquired as described in **Figure 3.2C** experimental procedures. Emission spectrum of **3.3** micelles in water was acquired as described in **Figure 3.5C** experimental procedures. *D)*

Absorption spectra were acquired as described in **Figure 3.5B** experimental procedures. *E) Excitation spectrum* of MeOFlav7 (**3.10**) in micelles in water was acquired as described in experimental procedures for **Figure 3.5C**. Displayed is the baseline corrected (to 600 nm) and normalized (to 1.0 at 980 nm) trace. Excitation spectrum of MeOFlav7 (**3.10**) in DCM was acquired on a sample in a 1 cm cuvette with OD $\leq$ 0.1. Emission collection was at 1,008 nm, with 15 nm excitation slit widths, 10 nm emission slit widths, and a 1,200 nm SP filter placed between the excitation source and the sample. The plotted data are baseline corrected (to 600 nm) and normalized (to 1.0 at 980 nm). *F) Emission spectrum* of **3.10** in dichloromethane was acquired as described in **Figure 2C** experimental procedures. Emission spectrum of **3.10** micelles in water was acquired as described in **Figure 3.5B** experimental procedures.

Figure 3.13 *Imaging with 1064 nm excitation after injection of JuloFlav7 micelles*. A) *Whole mouse imaging with 1064 nm excitation after injection of JuloFlav7 micelles.* The probe (**3.3,** JuloFlav7 micelles in PBS buffer) was delivered to the anesthetized animal by i.v. injection (0.170 mL, 0.22 mg/mL, 44 nmol); Excitation: 1,064 nm (103 $mWcm^{-1}$). Imaging was performed on Lens System A, with 2x 1,150 nm LP filters (FELH 1150, Thorlabs). The acquisition parameters were 8 ms exposure time, 100 fps, and 8-bit format. Displayed images are averaged over 5 frames. Data were transformed by 40° on ImageJ using bicubic interpolation. *B) Hind-limb imaging with 1064 nm excitation after injection of JuloFlav7 micelles.* The probe (**3.3**, JuloFlav7 micelles) was delivered to the anesthetized animal by i.v. injection (0.200 mL, 0.24 mg/mL, 55 nmol); Excitation: 1,064 nm (95 $mWcm^{-1}$), with a 1,050 ± 50 nm BP filter (Edmund Optics #85-893). Imaging was performed on Lens System B with an 1,100 nm LP filter (Edmund Optics #84-768). The acquisition parameters were 9 ms exposure time, 100 fps, and 12-bit format. Displayed images are averaged over 5 frames.

Figure 3.14 See experimental procedures for **Figure 3.5G**.

Figure 3.15A The probes were delivered to the anesthetized animal, and the optics and image processing are as described in **Figure 3.5G** experimental procedure. Displayed images are one frame. Imaging occurred 80 minutes after probe administration.

Fig. 3.15B Using ImageJ, a vertical, rectangular roi was assigned over the liver to measure motion due to breathing. At each time point in the 785 nm channel, the center of mass was calculated. Spatial variation in the center of mass is used to represent breathing rate.

Fig. 3.15C The probes were delivered to the anesthetized animal as follows: 1) i.v. injection of **3.3** (JuloFlav7) micelles (0.150 mL, 0.26 mg/mL, 50 nmol) in PBS buffer; 2) i.v. injection of ICG in cell culture water (0.050 mL, 0.1 mg/mL, 6.5 nmol). Excitation for two channels: 785 nm (100 $mWcm^{-1}$) and 1,064 nm (100 $mWcm^{-1}$), with an 1,100 nm SP filter (Edmund Optics #64-339). Imaging was performed on Lens System A, with an 1,100 nm LP filter (Edmund Optics #84-768), and an 1,150 nm LP filter (FELH 1150, Thorlabs). The acquisition parameters were 5 ms exposure time, 50 fps, 10 ms trigger pulse width and 60% duty cycle, and 8-bit format. Displayed images are averaged over 5 frames.

Images were unmixed according to the following equations:

$$1064_f = 1064_r$$

$$785_f = 785_r - (0.15 * 1064_f)$$

where the subscripts r and f represent “raw” and “final” images, respectively, and 785, and 1,064 represent the images from the wavelength channels. Data are representative of two biological replicates.

Figure 3.15D Using ImageJ, a roi was assigned at the location of the liver for the images displayed in **Figure 3.15C** and **Figure 3.17**. The mean intensity and standard deviation were recorded for each time point and plotted versus injection time of each probe.

Fig. 3.15E Approximately 2 h after probe administration, the mouse was euthanized and subsequently, necropsy was performed under real-time fluorescence guidance. Fluorescence from ICG provided precise localization of the gall bladder as well as the upper intestinal tract, due to its biliary excretion. In parallel, perfusion of organs such as the lungs and liver is visualized by the long circulating JuloFlav7 (**3.3**) micelles. Acquisition parameters and image processing were identical to **Figure 3.15C**.

Figure 3.16 See experimental procedures for **Figure 3.15A**.

Figure 3.17 See experimental procedures for **Figure 3.15C**.

Figure 3.18B–C The probes were delivered to the anesthetized animal as follows: 1) i.d. injection of ICG in water (0.050 mL, 5 mg/mL, 323 nmol) over four injection sites (left and right hindfoot pads and left and right sides of the base of the tail); 2) i.v. injection of **3.3** (JuloFlav7) micelles (0.200 mL, 0.24 mg/mL, 55 nmol); Excitation for two channels: 785 nm (96 $mWcm^{-1}$) and 1,064 nm (96 $mWcm^{-1}$). Imaging was performed on Lens System B, with an 1,100 nm LP filter (Edmund Optics #84-768). The acquisition parameters were 20 ms exposure time, 21.7 fps, 23 ms trigger pulse width and 91% duty cycle, and 8-bit format. Displayed images are averaged over 5 frames. Images were unmixed according to the following equations:

$$1064_f = 1064_r$$

$$785_f = 785_r - (0.08 * 1064_f)$$

where the subscripts r and f represent “raw” and “final” images, respectively, and 785, and 1,064 represent the images from the wavelength channels. Data are representative of two replicate experiments.

Figure 3.18D–F Images were processed with Python, using the libraries scikit-image for image processing, NumPy for array manipulations, and Matplotlib for plotting. In **Figure 3.15F**, the line profiles of the raw data have been fit using a gaussian model and a constant model, the lmfit library

has been used. The interpolation was done using the scipy library, a one-dimensional smoothing spline fit of degree k=4 has been fit to the amplitude data.

Figure 3.19 See experimental procedures for **Figure 3.18B–C**.

Figure 3.20 See experimental procedures for **Figure 3.18D–F**.

3.6 Notes Relevant to Chapter Three

3.6.1 Synthetic Discussion

Using three general routes to flavones: 1) Mentzer pyrone synthesis,[47] a thermally induced condensation between a beta-keto-ester and a phenol; 2) functionalization of a commercial 7-hydroxy flavone by Buchwald-Hartwig coupling of the corresponding triflate[48] and; 3) acylation of the commercial 7-amino flavone, we were able to access a diverse set of 7-amino flavylium heterocycles. By route 1), the alkylated amino flavones **3.13a**–**c** were obtained in moderate yields, 51-55%, by subjecting a substituted 3-aminophenol **(3.14a–c)** to ethylbenzoylacetate and heating neat for 20–48 h (see **Table 3.1**). In route 2) aliphatic and aromatic aminoflavones **3.13d**–**h** were acquired by palladium catalyzed C–N coupling reactions of triflate **3.15** with a variety of secondary amines in 63-83% yield (see **Table 3.2**). Finally, by route 3), a BOC substituted 7-aminoflavone was synthesized by treatment of 7-aminoflavone **3.17** with BOC-anhydride in base with catalytic dimethylaminopyridine to obtain the doubly BOC protected product **3.13i** in 75% yield. Each flavone was subsequently converted to the corresponding 4-methyl flavylium **3.12a–i** in moderate to good yields (39-86%) by treatment with methyl Grignard and quenching with fluoroboric acid[65] (see **Table 3.3**). The fluoroboric acid gives rise to a tetrafluoroborate counterion that is retained in the final dye species, as confirmed by ^{19}F NMR (see synthetic procedures). The 7-methoxy substituted 4-methyl flavylium **3.12j** was synthesized according to a known route[45].

The heptamethine dyes were synthesized by the base-promoted reaction of 4-methyl flavylium heterocycles with bis(phenylimine) **3.13** (see **Table 3.4**). The conditions required for successful dye formation proved to be dependent on the heterocycle used. Thus, the solvent and base used were tailored to each heterocycle. Notably, the non-nucleophilic base 2,6-di-*tert*-butyl-4-methylpyridine facilitated efficient polymethine formation with few signs of degradation of the dye, as monitored by UV-Vis-NIR spectrophotometry. For most heterocycles (**3.12a**–**d**; **3.12g**–**j**), 90-100 °C was sufficient to achieve fast (10-15 min) conversion to the heptamethine. The cyclic alkyl amine heterocycles **3.12e** and **3.12f** required either extended time (up to 120 min), or higher temperatures (up to 140 °C) for efficient reaction conversion. Note that the reported isolated yields are lower than conversions due to similar retention times by normal-phase column chromatography between heptamethine dyes and other dye species obtained in small amounts including monomethine, trimethine, and half-dye species.

3.6.2 Hammett Plot Calculations and Approximations

To relate absorption and emission values of the heptamethine dyes to Hammett σ_m values, a few approximations must be made. First, some substituents lacked reported constants[50]. In these cases, the σ_m value from an approximate group, or an appropriate linear combination of σ_m was used. Pyrrolidine was taken to be equivalent to dimethylamino. NHCOOtBu (BOC) was approximated by the similar functional group NHCOOMe. Azetidine was approximated with the average of diethylamino and dimethylamino substituent constants. Piperidine was taken as the average of diethylamino and dibutylamino substituent constants. Finally, julolidine was approximated by the addition of σ_m values for diethylamino and 2x methyl. The aromatic derivatives **3.7** and **3.8** were omitted from the analysis due to being an outlier (**3.7**), or

unavailability of a published Hammett value (**3.8**), respectively. The relationship of negative σ_m values to longer absorption wavelengths suggests that the electron donating ability of the substituent is responsible for the red-shifted photophysical behavior, aligning with the initial design hypothesis.

3.6.3 Photoluminescence Quantum Yield Measurements

The photoluminescence quantum yield (Φ_F) of a molecule or material is defined as follows,

$$\Phi_F = \frac{P_E}{P_A} \qquad \text{(Eq. 3.5)}$$

where P_E and P_A are the number of photons absorbed and emitted, respectively. To determine the quantum yield, we either use a relative method with a known standard in the same region of the electromagnetic spectrum, or an absolute method, in which the number of photons absorbed and emitted are measured independently. Here, due to the limits of our petite integrating sphere (Horiba KSPHERE-Petite with InGaAs detector Horiba Edison DSS IGA 020L), we use a relative method, with IR-26 as the known standard. To compare an unknown to a reference with a known quantum yield, the following relationship was used:

$$\Phi_{F,x} = \Phi_{F,r}(m_x/m_f)(\eta_x{}^2/\eta_r{}^2) \qquad \text{(Eq. 3.6)}$$

where m represents the slope of the line (y = mx + b) obtained from graphing integrated fluorescence intensity versus optical density across a series of samples, η is the refractive index of the solvent, and the subscripts x and r represent values of the unknown and reference, respectively. The ($\Phi_{F,r}$) of IR-26 was taken to be a constant, 0.05%, as we have previously measured[39], and which agrees with several recent measurements.[51,52] Here, we measured relative fluorescence quantum yields of (1) each dye in dichloromethane and (2) the relevant dyes used for imaging JuloFlav7 (**3.3**) and MeOFlav7 (**3.10**) encapsulated in micelles in water.

(1) Fluorescence quantum yields of molecules in dichloromethane.

To obtain a plot of integrated fluorescence intensity versus absorbance for the reference and unknown, five solutions and a solvent blank were prepared and their absorbance and emission spectra (with an excitation wavelength of 885 nm) were acquired. IR-26 and the unknown dyes were diluted in dichloromethane to concentrations with optical densities less than 0.1 to minimize effects of reabsorption. The baseline corrected (to 1,500 nm) fluorescence traces were integrated, and the raw integrals were corrected by subtracting the integral over an identical range from fluorescence traces of the blank solvent. The integrated fluorescence intensities were then plotted against the baseline corrected absorbance values at the relevant wavelength (885 nm), and the slope and error in slope were obtained ($R^2 > 0.99$ for all traces) (**Figure 3.21**).

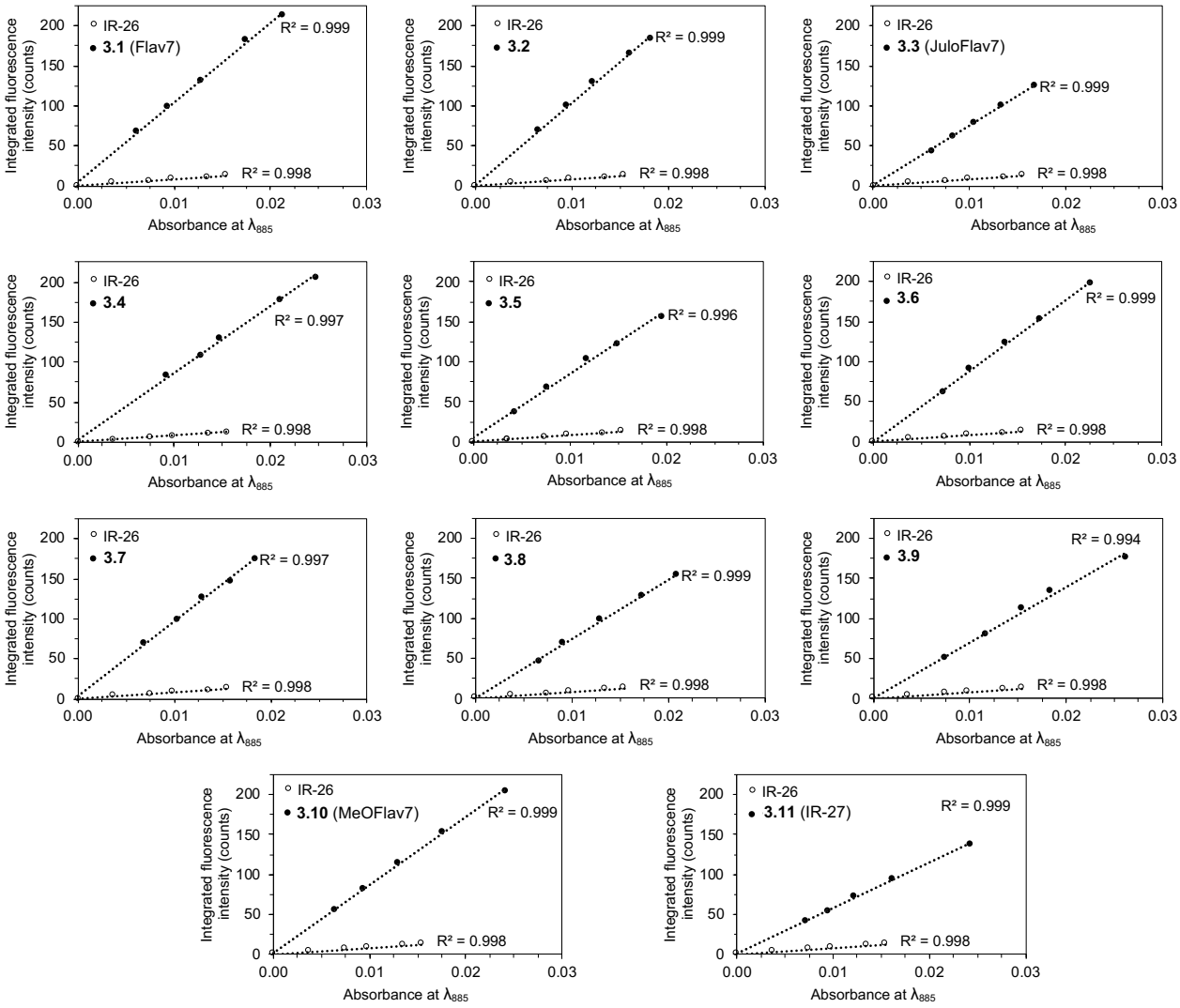

Figure 3.21 Integrated fluorescence intensity vs. absorbance at 885 nm plots for IR-26 vs. each unknown dye sample in DCM.

The refractive indices were omitted from the calculation as all samples were measured in the same solvent (dichloromethane). The fluorescence quantum yields were then calculated using **Eq. 3.6** and are reported in **Table 3.5**. Error measurements were propagated from the error in slope of the reference and the unknown. The methods employed here were validated with comparison of IR-26 to IR-1061, giving a Φ_F value of 0.32 ± 0.01 %, which agrees with our prior absolute quantum yield measurement[39].

(2) Fluorescence quantum yields of micelle encapsulations in water

A similar procedure was followed to obtain quantum yields of micelle encapsulations of JuloFav7 (**3.3**) and MeOFlav7 (**3.10**) in water. The slope and error in slope of the integrated fluorescence intensity vs. absorbance plots for five concentrations and one blank sample were obtained (**Figure 3.22**).

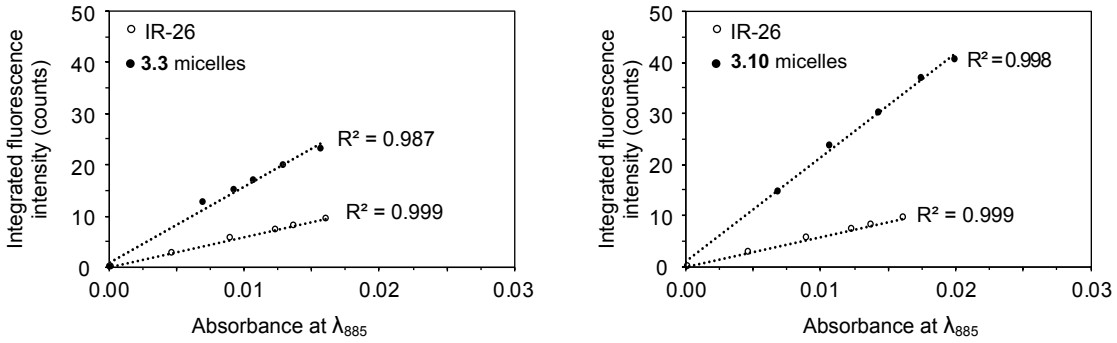

Figure 3.22 Integrated fluorescence intensity vs. absorbance at 885 nm plots for IR-26 vs each unknown micelle encapsulation sample in water.

For these measurements, as a different solvent is used for the reference and unknown samples, refractive indices are accounted for in the quantum yield equation. The refractive indices used were dichloromethane = 1.424 and water = 1.333. Each was designated to have a precision of 0.001. The fluorescence quantum yields were then calculated according to **Eq. 3.6** and are reported in **Figure 3.5D**.

Acquisition settings for fluorescence quantum yield measurements: For quantum yield measurements, fluorescence traces were acquired with ex. 885 nm with a 900 nm SP filter (Thorlabs FES 900) and collection from 920–, 940–, or 950–1,500 nm. The slits were 5.76 mm for excitation and 11.52 mm for emission. The step size used was 1.0 nm, integration time 0.1 s, and traces were acquired after an automatic detector background subtraction, and with the default excitation correction. A correction file was used to account for the non-linearity of the detector. All absorbance and fluorescence traces were taken in a 10 mm x 10 mm path length cuvette, with emission detection occurring at 90° from excitation.

3.6.4 Resolution Effects Observed with Excitation-Multiplexed SWIR Imaging

Resolution and contrast of optical imaging have been shown to vary greatly over different detection regions in the NIR and SWIR.[14,26,27] Here, we characterize resolution effects in SWIR imaging when using multiple excitation wavelengths and a single detection channel (representing an "excitation-multiplexed, single-channel detection" SWIR imaging configuration), as is described in this manuscript. We compare the results to resolutions effects when using a single excitation wavelength and multiple detection regions (representing an "emission-multiplexed" SWIR imaging configuration). To compare resolutions between imaging channels, we created a mouse phantom that could be analyzed without concern for movement of biological structures, by performing an i.v. injection of JuloFlav7 (**3.3**) in a living mouse and then immediately sacrificing it. The mouse phantom was then imaged in an excitation-multiplexed, single channel detection configuration, and after one freeze-thaw cycle, in an emission-multiplexed configuration.

The imaging results from an "excitation-multiplexed, single-channel detection configuration" are displayed in **Figure 3.7**. Varied irradiation powers of 785, 980, and 1,064 nm lasers were used such that approximately equal signal in each channel was obtained. From the images obtained in each channel (**Figure 3.7A**), linear cross-sections across various vasculature structures in the mouse were drawn and the baseline subtracted and normalized cross-sections are overlaid on each other in (**Figure 3.7B**). From these data, it is clear that the shape and width of each structure varies only slightly, and we can conclude that spatial resolutions are nearly identical

in each excitation channel.[7] The imaging results from an "emission-multiplexing" configuration, with a single excitation wavelength and differing emission windows, are displayed in **Figure 3.8**. Using a common 980 nm laser, we observed emission in three different SWIR emission windows: 1,000–1,700 nm, 1,300–1,700 nm, and 1,500–1,700 nm, by placing the corresponding LP filters in the optical path to the camera. Laser powers and exposure times were adjusted in each channel to produce approximately equal signal in each channel. From the images obtained in each channel (**Figure 3.8A**), linear cross-sections across various vasculature structures in the mouse were drawn and the baseline subtracted and normalized cross-sections are overlaid on each other in **Figure 3.8B**. From these data, it is clear that in different emission windows, the shape and width of each structure, and thus the resolution, varies considerably, in accordance with prior reports.

3.6.5 Multicolor SWIR Imaging with Triggered Excitation[8]

Imaging System Description – Programmable Trigger Controller: The programmable trigger controller receives user instructions from a desktop PC and executes predefined triggering sequence autonomously. The interface and the architecture of trigger controller is shown in **Figure 3.23.** The programmable, general purpose Input/output (I/O) pins of an Atmel Atmega328 micro-controller unit (MCU) is used for pulse generation. An Arduino Nano Rev 3 MCU (A000005) is used for the implementation of trigger controller unit. The trigger controller can be programmatically accessed by desktop personal computer (PC) via universal serial bus (USB)

[7]While resolution remains constant, there are some minor changes in the penetration depth of imaging with varied excitation wavelengths due to changes in the attenuation amounts of light at different wavelengths. The longer excitation wavelengths show slightly deeper photon penetration, resulting in deeper structures, such as the liver to have higher brightness in the order of 1,064 nm > 980 nm > 785 nm. This effect can be seen in cross sections 4, 5, and 9, where increased signal is present from deeper organs that are underneath the vasculature structures.

[8]Contributions by Shyam Ramakrishnan

interface to upload predetermined triggering sequence. The sequential trigger pulses of 5V TTL (5V Transistor–Transistor Logic) are delivered to the specific driver units of each laser units and the InGaAs SWIR camera. The driver units then control the switching of their respective laser diodes to illuminate an object of interest. The excitation-synchronized camera then acquires required image data. Upon completion of acquisition, image data is transferred to the desktop PC via a Gigabit Ethernet (GigE) interface.

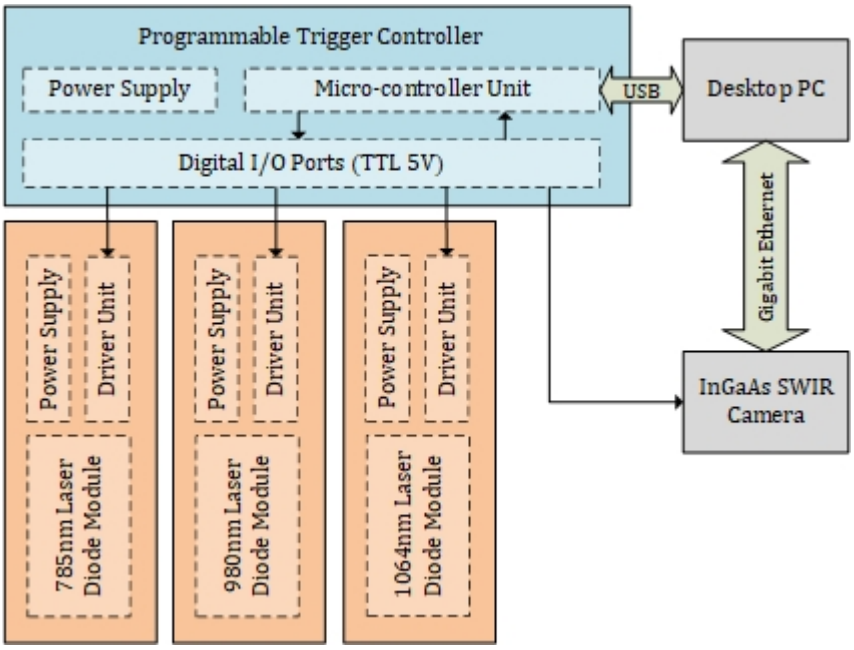

Figure 3.23 System Architecture for Programmable Trigger Controller

Imaging algorithm for operating trigger controller: For operating the developed SWIR imaging system, a semi-automatic imaging algorithm was adopted by means of MATLAB programming environment and Arduino Integrated Development Environment (IDE). **Figure 3.24** describes the flowchart for excitation-synchronized imaging algorithm using developed SWIR imaging system. User may assign the camera parameters such as exposure time, trigger mode, analog gain and post-image processing attributes via a custom MATLAB script. Next, laser parameters such as per pulse power and modulation mode are manually fed to the driver units. The pin assignment for sequential

triggering is done in the Arduino IDE and the user may program the MCU via USB interface. Once the object of interest is ready for imaging, the user may switch ON the trigger controller to acquire the image data. The MATLAB image acquisition script will display a live feedback of SWIR camera acquisition and directly import the image data to the memory of desktop PC. Image data post-processing attributes are applied to the image data at the end of acquisition cycle.

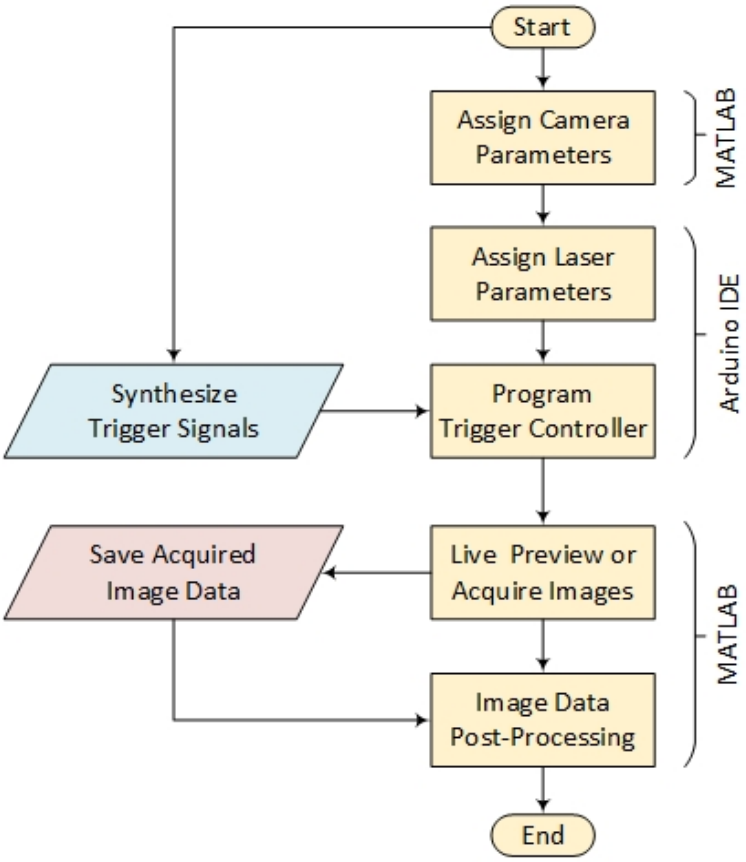

Figure 3.24 Flowchart for Excitation-Synchronized Imaging Algorithm.

Pulse generation for synchronized imaging algorithm: As described earlier, the trigger controller requires a predetermined trigger sequence to be programmed in the MCU for autonomous acquisition of image data, such that the light sources (laser diode modules) are switched ON sequentially and their synchronized camera triggers are sent to the camera trigger unit. A sample timing diagram illustrating a three-color image data acquisition is given in **Figure 3.25**. Upon receiving a rising edge of a trigger pulse, the SWIR camera exposes the InGaAs sensor

for a period set by the MATLAB acquisition script. This event will be followed by a camera readout event, where the acquired image data is passed to the GigE data link to transmit the images. For a three-color imaging, each cycle would consist of three imaging sequence where the camera sensor exposure time is encapsulated by the laser light illumination. The laser module duty-cycle is maintained to not exceed the imaging sequence time. Each imaging sequence time consists of the camera exposure time (ET) duration and a compound time delay (CD). The minimum achievable camera expose-readout time is constrained by the camera framerate. The compound time delay allows the camera to complete the readout of current imaging sequence and absorbs any associated laser diode switch OFF transients (which are higher than the switch ON transients). Hence, a programmed trigger controller repeats the trigger sequence in each cycle achieving three-color image data in real-time.

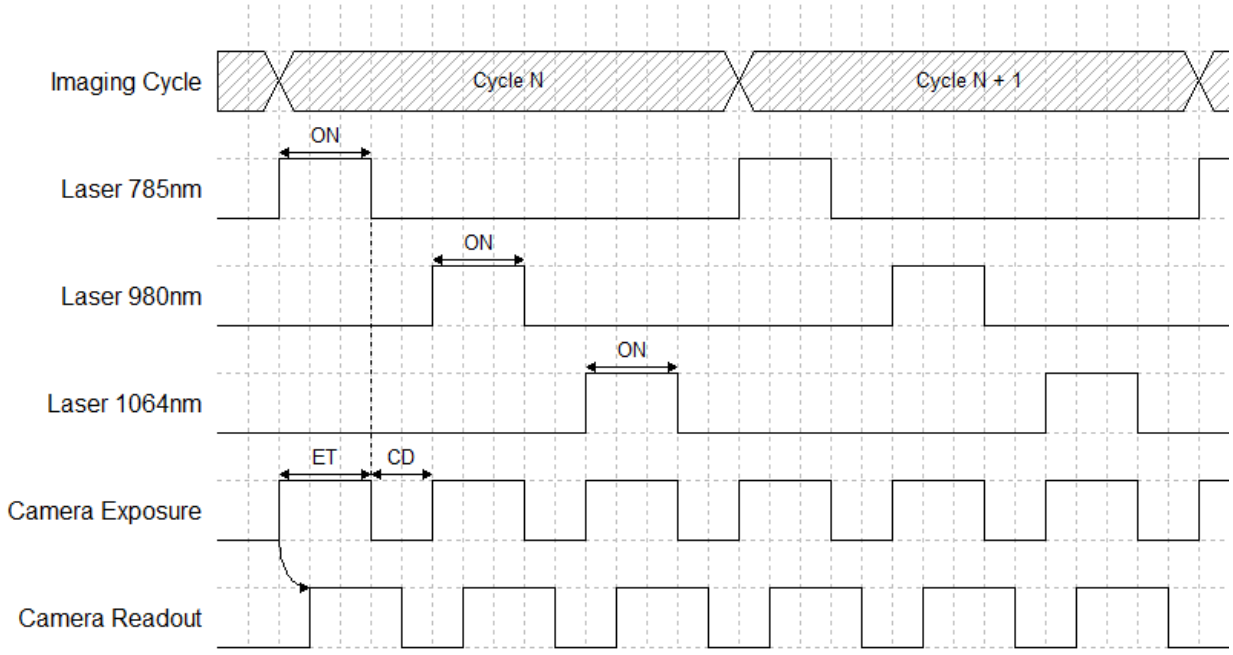

Figure 3.25 Timing Diagram Illustrating a Three-color Image Acquisition. ET = exposure time; CD = compound delay time

3.7 Spectra Relevant to Chapter Three

3.7.1 ^{1}H NMR Spectra

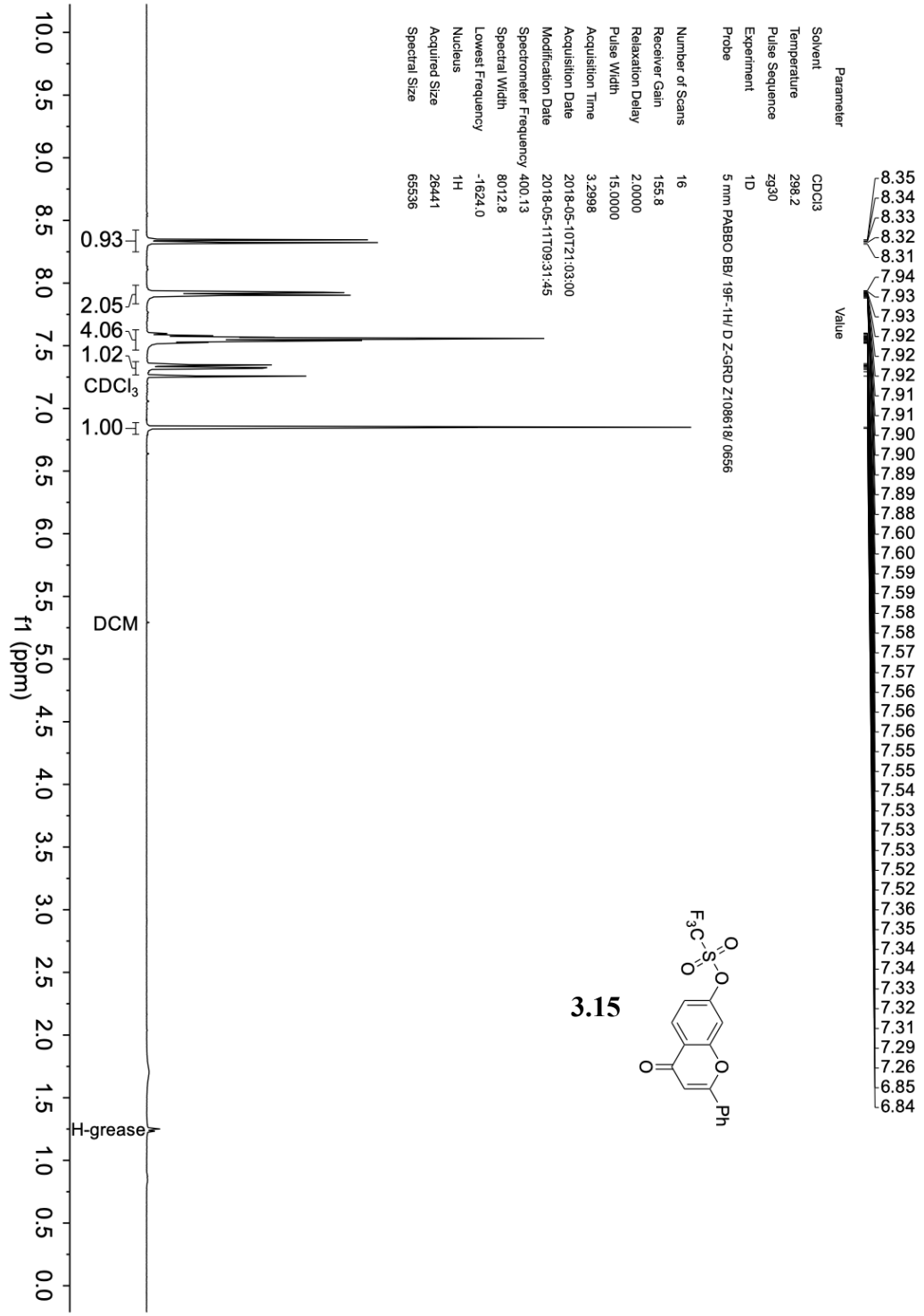

3.15

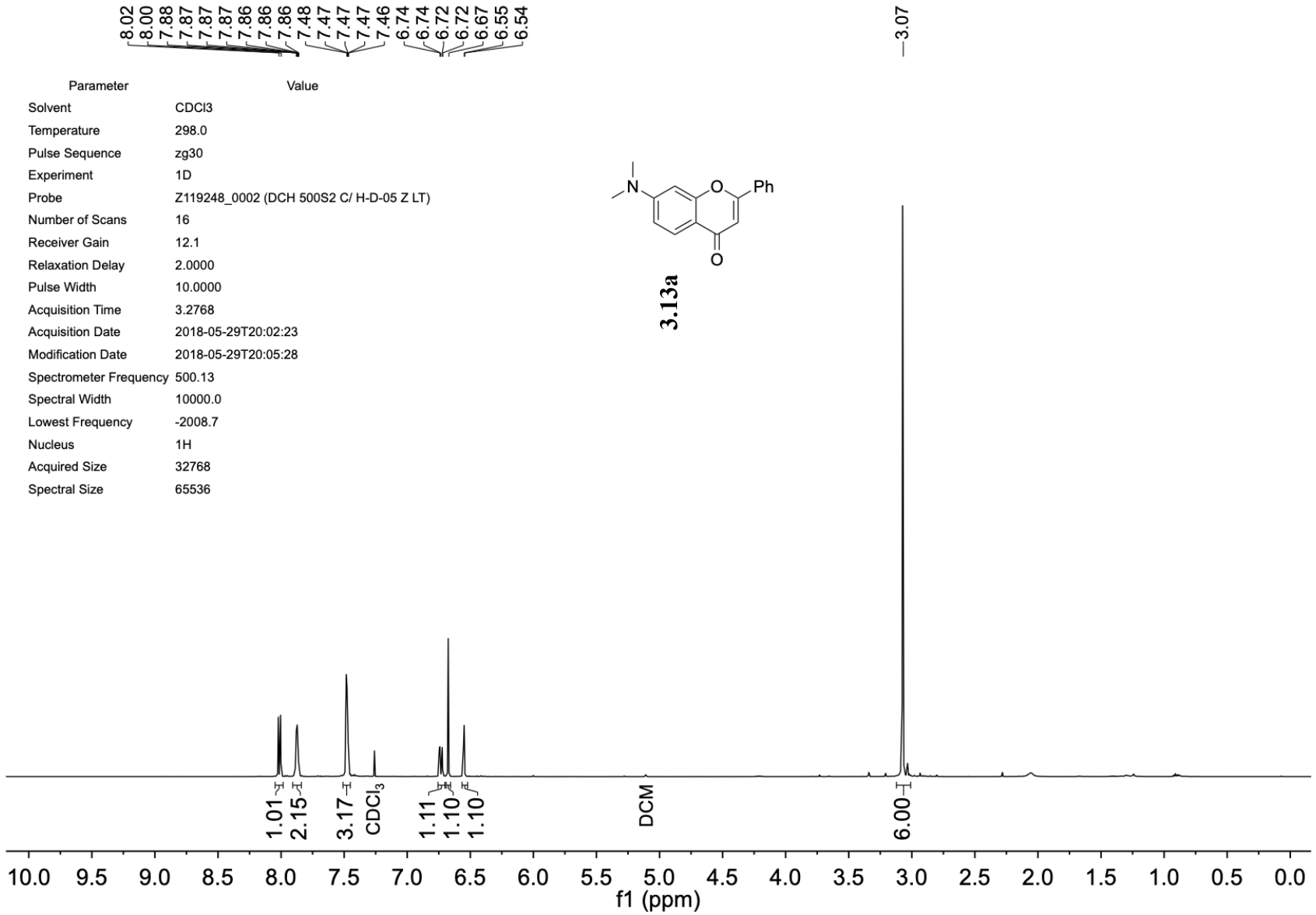
8.02
8.00
7.88
7.87
7.87
7.87
7.86
7.86
7.86
7.48
7.47
7.47
7.47
7.46
6.74
6.74
6.72
6.72
6.67
6.55
6.54
3.07
Parameter
Value
Solvent
CDCl3
Temperature
298.0
Pulse Sequence
zg30
Experiment
1D
Probe
Z119248_0002 (DCH 500S2 C/ H-D-05 Z LT)
Number of Scans
16
Receiver Gain
12.1
Relaxation Delay
2.0000
Pulse Width
10.0000
Acquisition Time
3.2768
Acquisition Date
2018-05-29T20:02:23
Modification Date
2018-05-29T20:05:28
Spectrometer Frequency
500.13
Spectral Width
10000.0
Lowest Frequency
-2008.7
Nucleus
1H
Acquired Size
32768
Spectral Size
65536
N
O
Ph
O
3.13a
1.01
2.15
3.17
CDCl3
1.11
1.10
1.10
DCM
6.00
10.0 9.5 9.0 8.5 8.0 7.5 7.0 6.5 6.0 5.5 5.0 4.5 4.0 3.5 3.0 2.5 2.0 1.5 1.0 0.5 0.0
f1 (ppm)

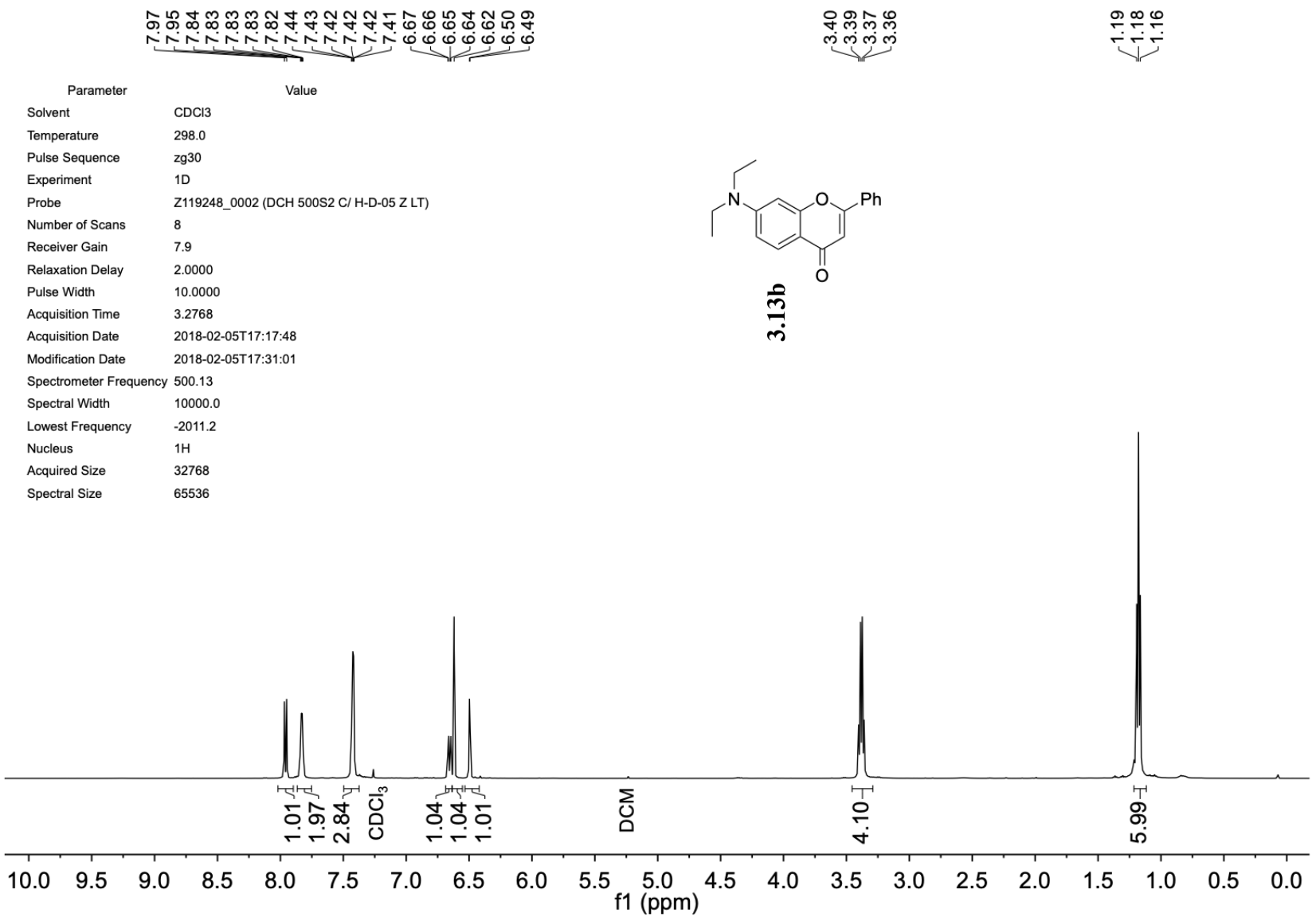
7.97
7.95
7.84
7.83
7.83
7.83
7.82
7.44
7.43
7.42
7.42
7.42
7.41
6.67
6.66
6.65
6.64
6.62
6.50
6.49
3.40
3.39
3.37
3.36
1.19
1.18
1.16
Parameter Value
Solvent CDCl3
Temperature 298.0
Pulse Sequence zg30
Experiment 1D
Probe Z119248_0002 (DCH 500S2 C/ H-D-05 Z LT)
Number of Scans 8
Receiver Gain 7.9
Relaxation Delay 2.0000
Pulse Width 10.0000
Acquisition Time 3.2768
Acquisition Date 2018-02-05T17:17:48
Modification Date 2018-02-05T17:31:01
Spectrometer Frequency 500.13
Spectral Width 10000.0
Lowest Frequency -2011.2
Nucleus 1H
Acquired Size 32768
Spectral Size 65536
N
O
Ph
O
3.13b
1.01
1.97
2.84
CDCl3
1.04
1.04
1.01
DCM
4.10
5.99
10.0 9.5 9.0 8.5 8.0 7.5 7.0 6.5 6.0 5.5 5.0 4.5 4.0 3.5 3.0 2.5 2.0 1.5 1.0 0.5 0.0
f1 (ppm)

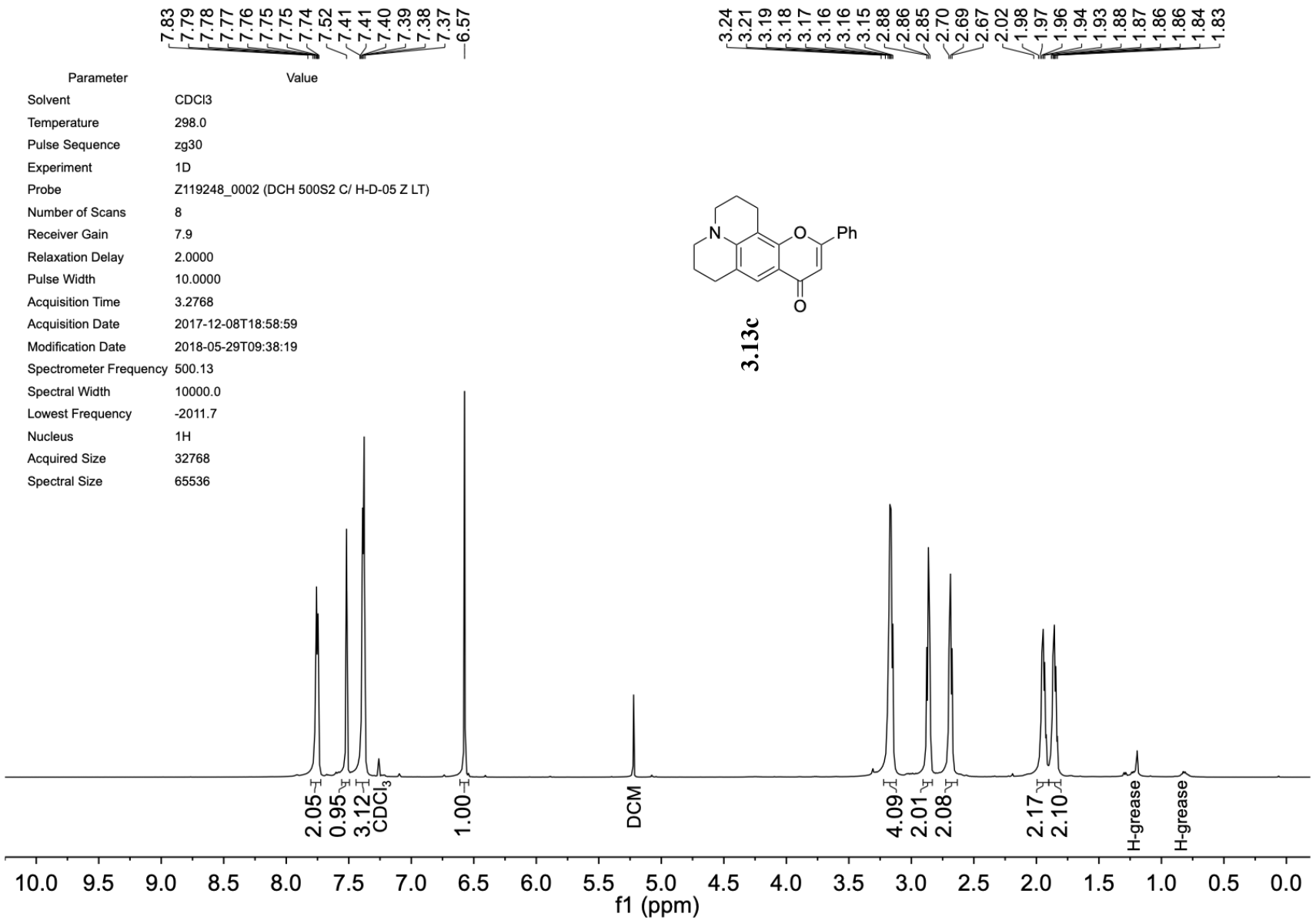
7.83
7.79
7.78
7.77
7.76
7.75
7.75
7.74
7.52
7.41
7.41
7.40
7.39
7.38
7.37
6.57
3.24
3.21
3.19
3.18
3.17
3.16
3.16
3.15
2.88
2.86
2.85
2.70
2.69
2.67
2.02
1.98
1.97
1.96
1.94
1.93
1.88
1.87
1.86
1.86
1.84
1.83
Parameter Value
Solvent CDCl3
Temperature 298.0
Pulse Sequence zg30
Experiment 1D
Probe Z119248_0002 (DCH 500S2 C/ H-D-05 Z LT)
Number of Scans 8
Receiver Gain 7.9
Relaxation Delay 2.0000
Pulse Width 10.0000
Acquisition Time 3.2768
Acquisition Date 2017-12-08T18:58:59
Modification Date 2018-05-29T09:38:19
Spectrometer Frequency 500.13
Spectral Width 10000.0
Lowest Frequency -2011.7
Nucleus 1H
Acquired Size 32768
Spectral Size 65536
N
O
Ph
O
3.13c
2.05
0.95
3.12
CDCl3
1.00
DCM
4.09
2.01
2.08
2.17
2.10
H-grease
H-grease
10.0 9.5 9.0 8.5 8.0 7.5 7.0 6.5 6.0 5.5 5.0 4.5 4.0 3.5 3.0 2.5 2.0 1.5 1.0 0.5 0.0
f1 (ppm)

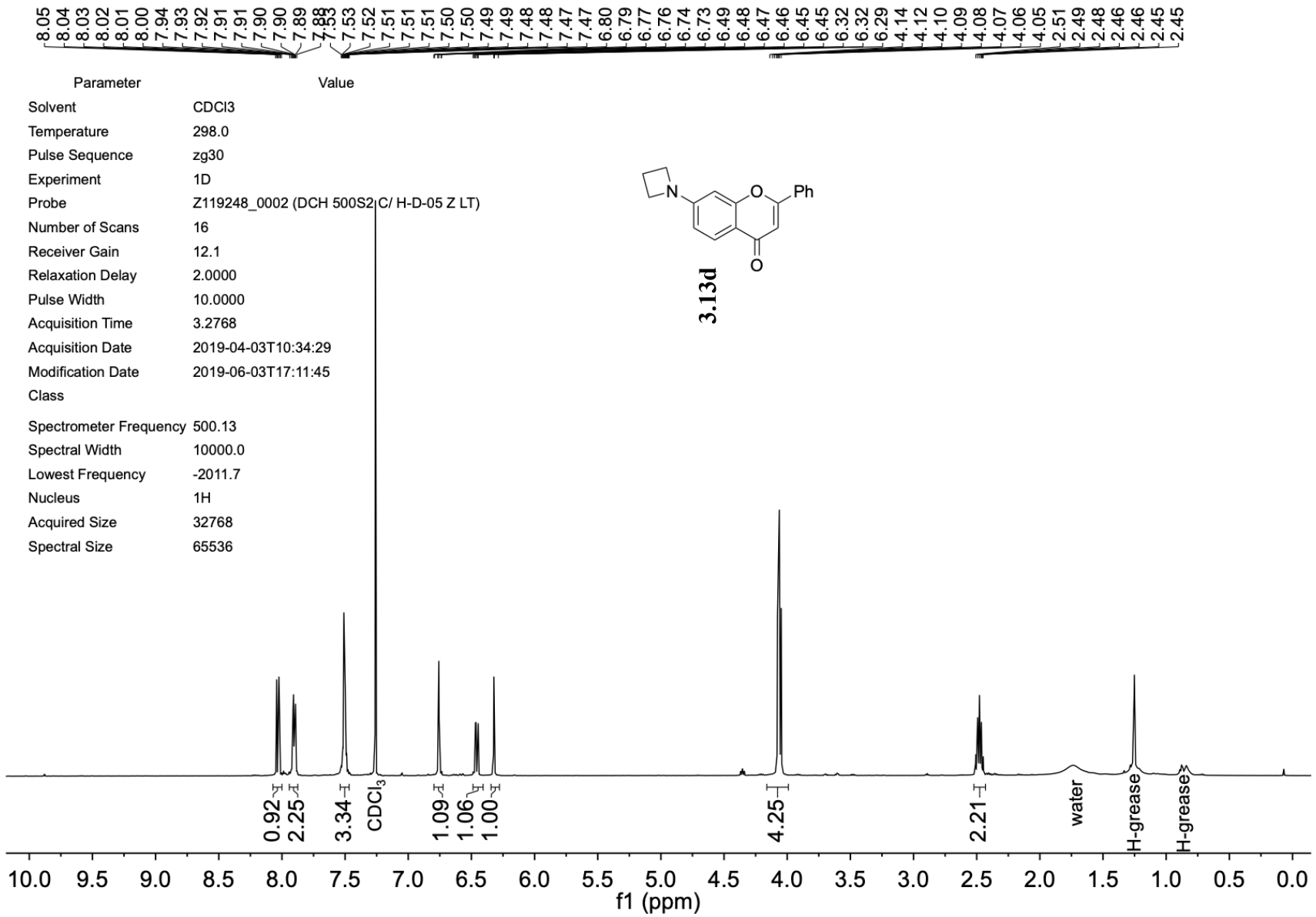
8.05 8.04 8.03 8.02 8.01 8.00 7.94 7.93 7.92 7.91 7.91 7.90 7.90 7.89 7.88 7.53 7.52 7.51 7.51 7.51 7.50 7.50 7.49 7.49 7.48 7.48 7.47 7.47 6.80 6.79 6.77 6.76 6.74 6.73 6.49 6.48 6.47 6.46 6.45 6.45 6.32 6.32 6.29 4.14 4.12 4.10 4.09 4.08 4.07 4.06 4.05 2.51 2.49 2.48 2.46 2.46 2.45 2.45
Parameter Value
Solvent CDCl3
Temperature 298.0
Pulse Sequence zg30
Experiment 1D
Probe Z119248_0002 (DCH 500S2 C/ H-D-05 Z LT)
Number of Scans 16
Receiver Gain 12.1
Relaxation Delay 2.0000
Pulse Width 10.0000
Acquisition Time 3.2768
Acquisition Date 2019-04-03T10:34:29
Modification Date 2019-06-03T17:11:45
Class
Spectrometer Frequency 500.13
Spectral Width 10000.0
Lowest Frequency -2011.7
Nucleus 1H
Acquired Size 32768
Spectral Size 65536
N
O
Ph
O
3.13d
0.92
2.25
3.34
CDCl3
1.09
1.06
1.00
4.25
2.21
water
H-grease
H-grease
10.0 9.5 9.0 8.5 8.0 7.5 7.0 6.5 6.0 5.5 5.0 4.5 4.0 3.5 3.0 2.5 2.0 1.5 1.0 0.5 0.0
f1 (ppm)

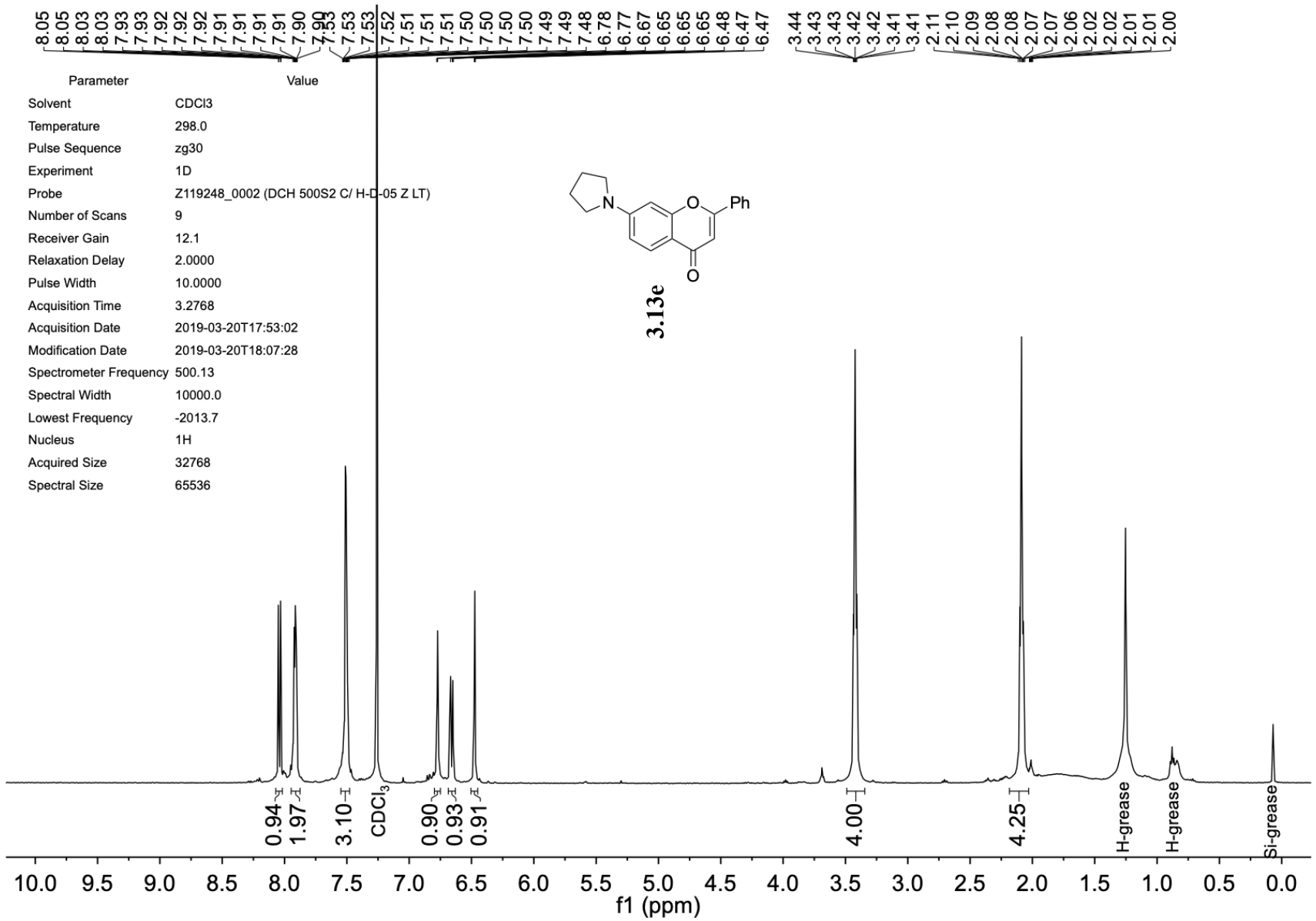
8.05 8.05 8.03 8.03 7.93 7.93 7.92 7.92 7.92 7.91 7.91 7.91 7.91 7.90 7.90 7.53 7.53 7.53 7.52 7.51 7.51 7.51 7.50 7.50 7.50 7.50 7.49 7.49 7.48 6.78 6.77 6.67 6.65 6.65 6.65 6.48 6.47 6.47 3.44 3.43 3.43 3.42 3.42 3.41 3.41 2.11 2.10 2.09 2.08 2.08 2.07 2.07 2.06 2.02 2.02 2.01 2.01 2.00
Parameter Value
Solvent CDCl3
Temperature 298.0
Pulse Sequence zg30
Experiment 1D
Probe Z119248_0002 (DCH 500S2 C/ H-D-05 Z LT)
Number of Scans 9
Receiver Gain 12.1
Relaxation Delay 2.0000
Pulse Width 10.0000
Acquisition Time 3.2768
Acquisition Date 2019-03-20T17:53:02
Modification Date 2019-03-20T18:07:28
Spectrometer Frequency 500.13
Spectral Width 10000.0
Lowest Frequency -2013.7
Nucleus 1H
Acquired Size 32768
Spectral Size 65536
N
O
Ph
O
3.13e
0.94
1.97
3.10
CDCl3
0.90
0.93
0.91
4.00
4.25
H-grease
H-grease
Si-grease
10.0 9.5 9.0 8.5 8.0 7.5 7.0 6.5 6.0 5.5 5.0 4.5 4.0 3.5 3.0 2.5 2.0 1.5 1.0 0.5 0.0
f1 (ppm)

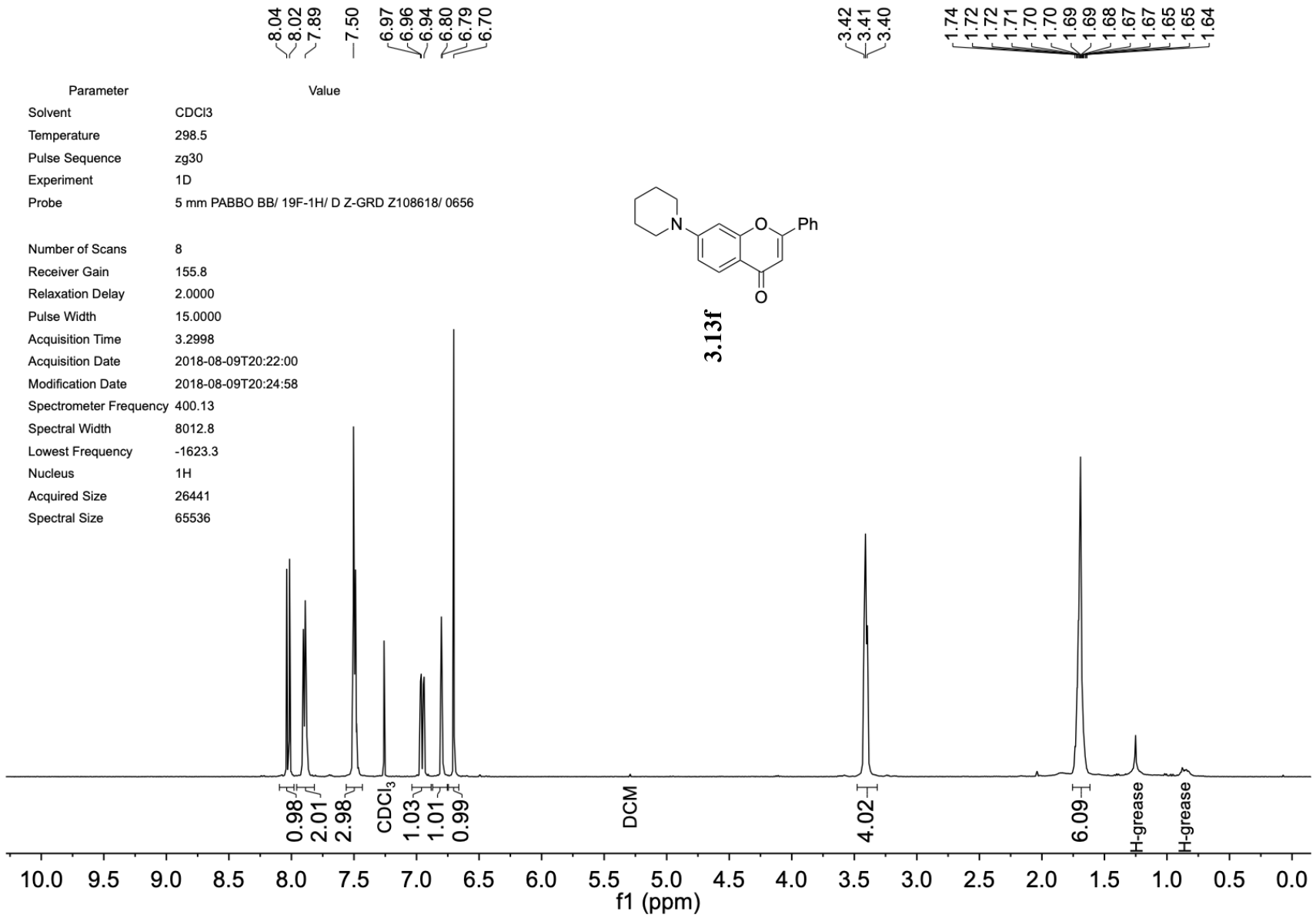
8.04
8.02
7.89
7.50
6.97
6.96
6.94
6.80
6.79
6.70
3.42
3.41
3.40
1.74
1.72
1.72
1.71
1.70
1.70
1.69
1.69
1.68
1.67
1.67
1.65
1.65
1.64
Parameter Value
Solvent CDCl3
Temperature 298.5
Pulse Sequence zg30
Experiment 1D
Probe 5 mm PABBO BB/ 19F-1H/ D Z-GRD Z108618/ 0656
Number of Scans 8
Receiver Gain 155.8
Relaxation Delay 2.0000
Pulse Width 15.0000
Acquisition Time 3.2998
Acquisition Date 2018-08-09T20:22:00
Modification Date 2018-08-09T20:24:58
Spectrometer Frequency 400.13
Spectral Width 8012.8
Lowest Frequency -1623.3
Nucleus 1H
Acquired Size 26441
Spectral Size 65536
N
O
Ph
O
3.13f
0.98
2.01
2.98
CDCl3
1.03
1.01
0.99
DCM
4.02
6.09
H-grease
H-grease
10.0 9.5 9.0 8.5 8.0 7.5 7.0 6.5 6.0 5.5 5.0 4.5 4.0 3.5 3.0 2.5 2.0 1.5 1.0 0.5 0.0
f1 (ppm)

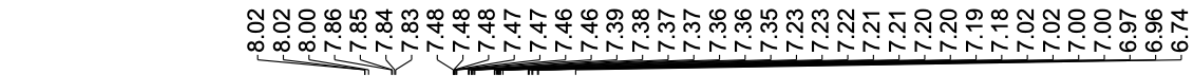

Parameter	Value
Solvent	CDCl3
Temperature	298.3
Pulse Sequence	zg30
Experiment	1D
Probe	5 mm PABBO BB/ 19F-1H/ D Z-GRD Z108618/ 0656
Number of Scans	16
Receiver Gain	73.9
Relaxation Delay	2.0000
Pulse Width	15.0000
Acquisition Time	3.2998
Acquisition Date	2018-05-10T16:58:00
Modification Date	2018-05-10T17:46:27
Spectrometer Frequency	400.13
Spectral Width	8012.8
Lowest Frequency	-1623.2
Nucleus	1H
Acquired Size	26441
Spectral Size	65536

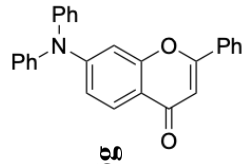

3.13g

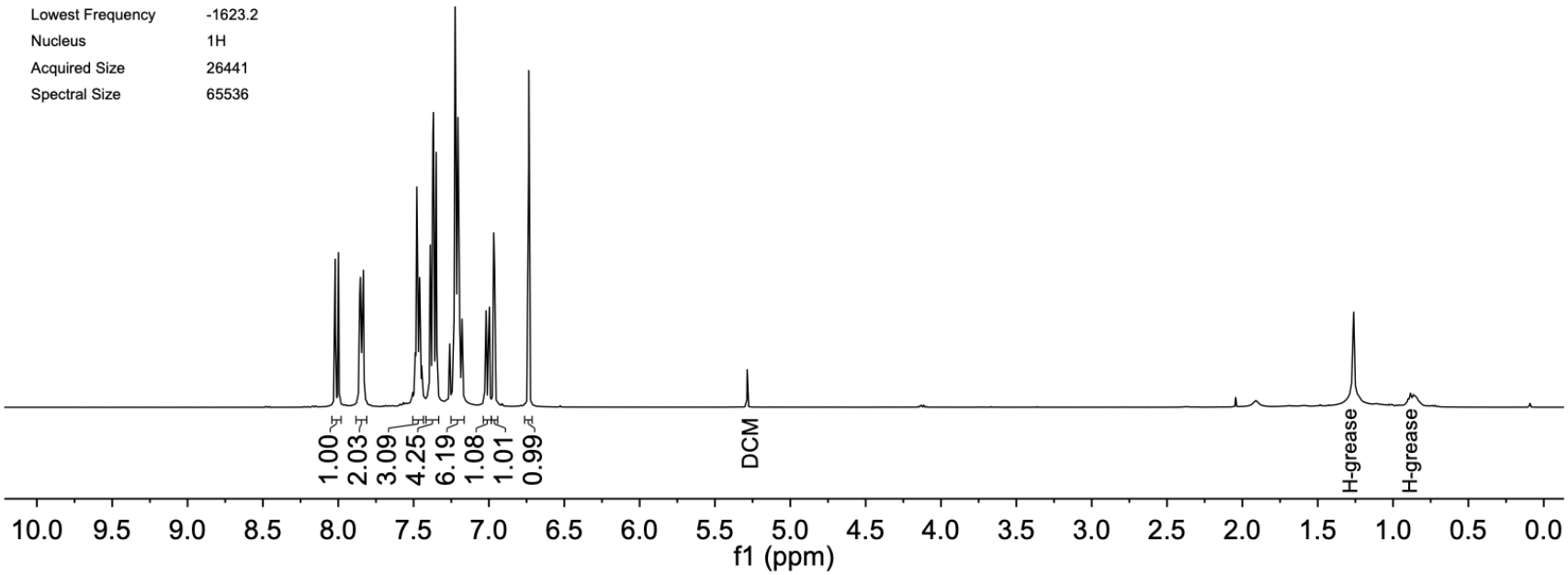

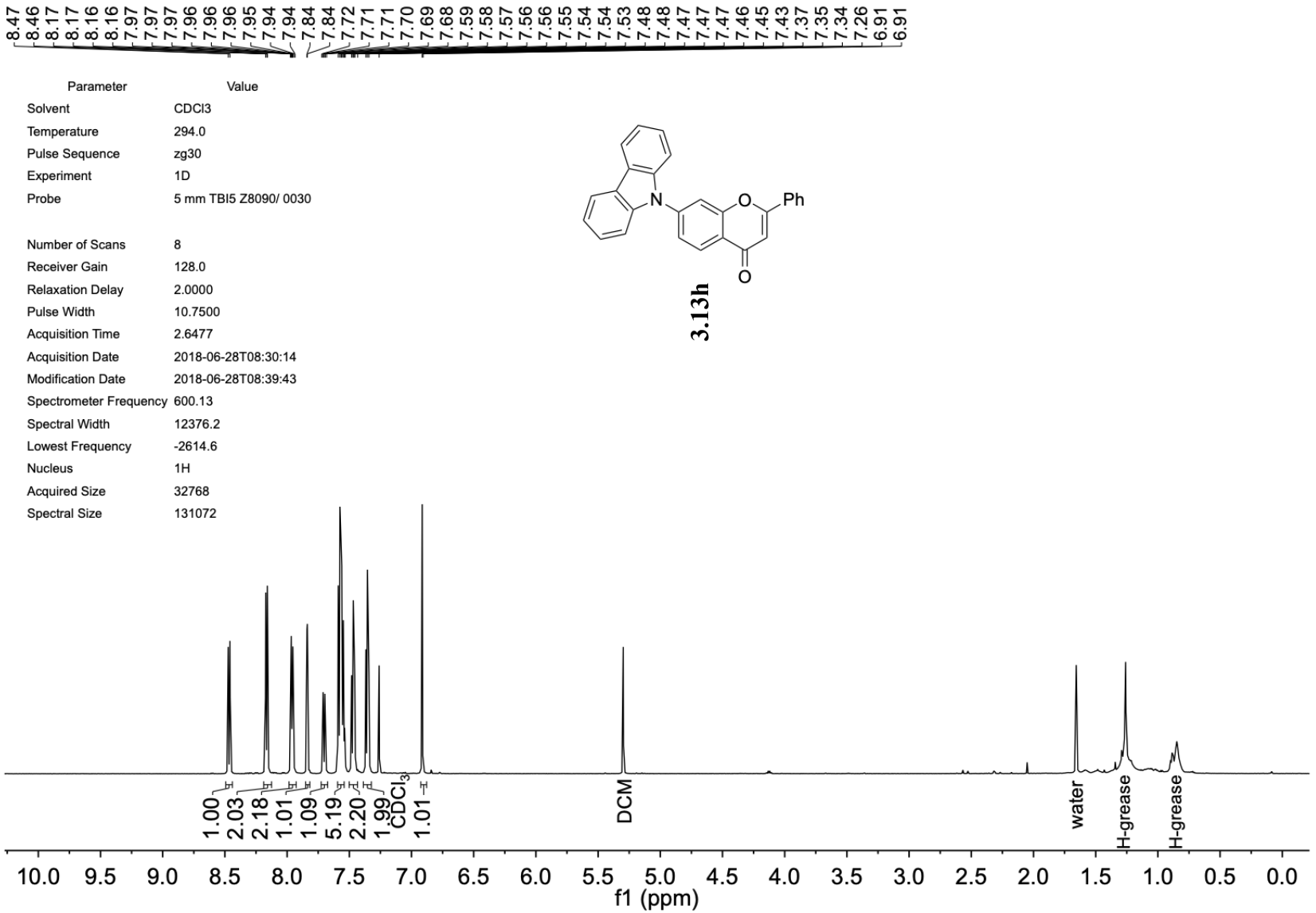
8.47 8.46 8.17 8.17 8.16 8.16 7.97 7.97 7.97 7.96 7.96 7.96 7.95 7.94 7.94 7.84 7.84 7.72 7.71 7.71 7.70 7.69 7.68 7.59 7.58 7.57 7.56 7.56 7.55 7.54 7.54 7.53 7.48 7.48 7.47 7.47 7.47 7.46 7.45 7.43 7.37 7.35 7.34 7.26 6.91 6.91
Parameter Value
Solvent CDCl3
Temperature 294.0
Pulse Sequence zg30
Experiment 1D
Probe 5 mm TBI5 Z8090/ 0030
Number of Scans 8
Receiver Gain 128.0
Relaxation Delay 2.0000
Pulse Width 10.7500
Acquisition Time 2.6477
Acquisition Date 2018-06-28T08:30:14
Modification Date 2018-06-28T08:39:43
Spectrometer Frequency 600.13
Spectral Width 12376.2
Lowest Frequency -2614.6
Nucleus 1H
Acquired Size 32768
Spectral Size 131072
N
O
Ph
O
3.13h
1.00 2.03 2.18 1.01 1.09 5.19 2.20 1.99 CDCl3 1.01
DCM
water
H-grease
H-grease
10.0 9.5 9.0 8.5 8.0 7.5 7.0 6.5 6.0 5.5 5.0 4.5 4.0 3.5 3.0 2.5 2.0 1.5 1.0 0.5 0.0
f1 (ppm)

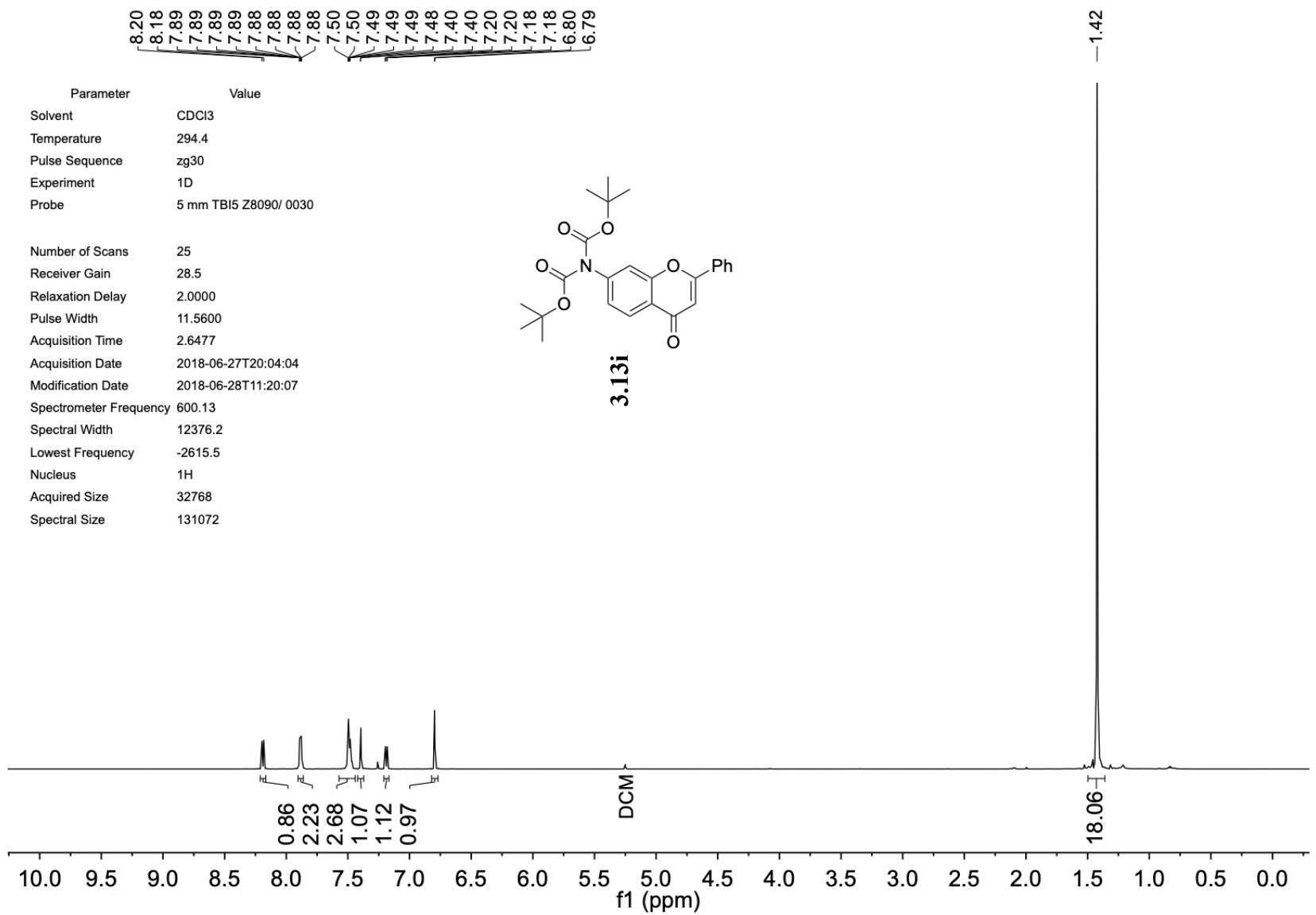
8.20
8.18
7.89
7.89
7.89
7.88
7.88
7.88
7.88
7.50
7.50
7.49
7.49
7.49
7.48
7.40
7.40
7.20
7.20
7.18
7.18
6.80
6.79
1.42
Parameter Value
Solvent CDCl3
Temperature 294.4
Pulse Sequence zg30
Experiment 1D
Probe 5 mm TBI5 Z8090/ 0030
Number of Scans 25
Receiver Gain 28.5
Relaxation Delay 2.0000
Pulse Width 11.5600
Acquisition Time 2.6477
Acquisition Date 2018-06-27T20:04:04
Modification Date 2018-06-28T11:20:07
Spectrometer Frequency 600.13
Spectral Width 12376.2
Lowest Frequency -2615.5
Nucleus 1H
Acquired Size 32768
Spectral Size 131072
O
O
O
N
O
Ph
O
O
O
3.13i
0.86
2.23
2.68
1.07
1.12
0.97
DCM
18.06
10.0 9.5 9.0 8.5 8.0 7.5 7.0 6.5 6.0 5.5 5.0 4.5 4.0 3.5 3.0 2.5 2.0 1.5 1.0 0.5 0.0
f1 (ppm)

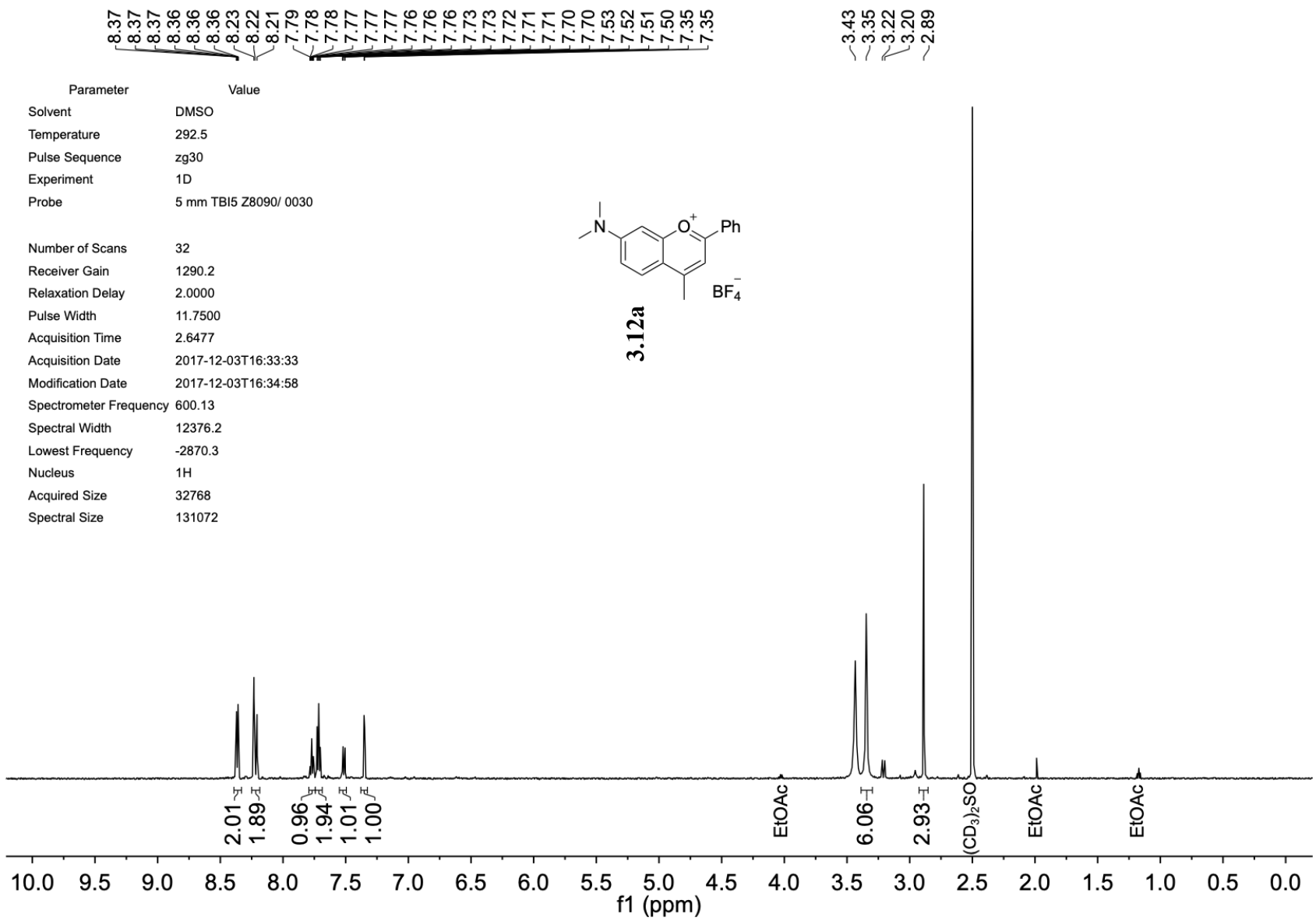
8.37 8.37 8.37 8.36 8.36 8.36 8.23 8.22 8.21 7.79 7.78 7.78 7.77 7.77 7.77 7.76 7.76 7.76 7.73 7.73 7.72 7.71 7.71 7.70 7.70 7.53 7.52 7.51 7.50 7.35 7.35
3.43 3.35 3.22 3.20 2.89
Parameter Value
Solvent DMSO
Temperature 292.5
Pulse Sequence zg30
Experiment 1D
Probe 5 mm TBI5 Z8090/ 0030
Number of Scans 32
Receiver Gain 1290.2
Relaxation Delay 2.0000
Pulse Width 11.7500
Acquisition Time 2.6477
Acquisition Date 2017-12-03T16:33:33
Modification Date 2017-12-03T16:34:58
Spectrometer Frequency 600.13
Spectral Width 12376.2
Lowest Frequency -2870.3
Nucleus 1H
Acquired Size 32768
Spectral Size 131072
N
O+
Ph
BF4−
3.12a
2.01 1.89 0.96 1.94 1.01 1.00
EtOAc
6.06
2.93
(CD3)2SO
EtOAc
EtOAc
10.0 9.5 9.0 8.5 8.0 7.5 7.0 6.5 6.0 5.5 5.0 4.5 4.0 3.5 3.0 2.5 2.0 1.5 1.0 0.5 0.0
f1 (ppm)

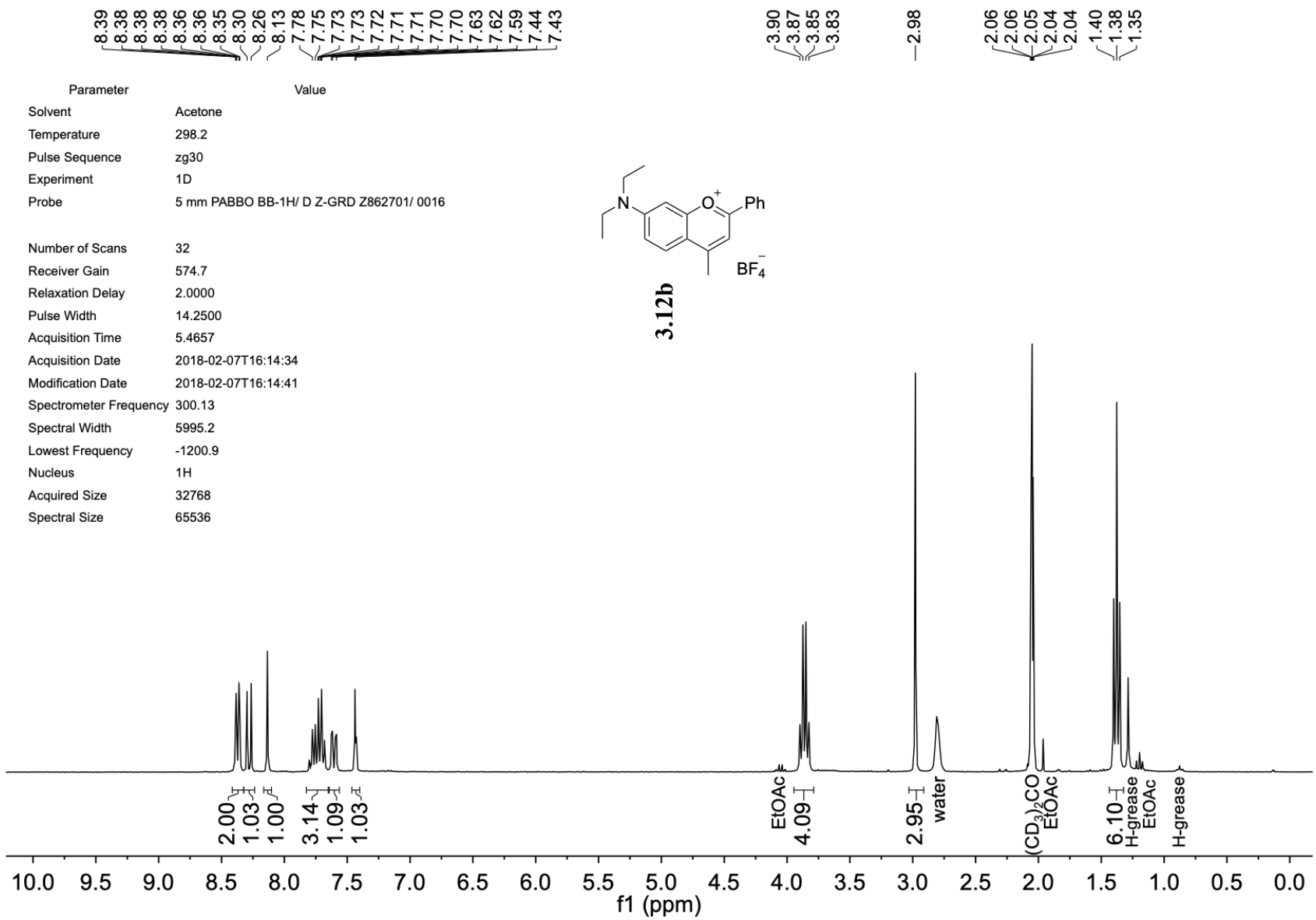
8.39 8.38 8.38 8.38 8.36 8.36 8.35 8.30 8.26 8.13 7.78 7.75 7.73 7.73 7.72 7.71 7.71 7.70 7.70 7.63 7.62 7.59 7.44 7.43
3.90 3.87 3.85 3.83
2.98
2.06 2.06 2.05 2.04 2.04
1.40 1.38 1.35
Parameter Value
Solvent Acetone
Temperature 298.2
Pulse Sequence zg30
Experiment 1D
Probe 5 mm PABBO BB-1H/ D Z-GRD Z862701/ 0016
Number of Scans 32
Receiver Gain 574.7
Relaxation Delay 2.0000
Pulse Width 14.2500
Acquisition Time 5.4657
Acquisition Date 2018-02-07T16:14:34
Modification Date 2018-02-07T16:14:41
Spectrometer Frequency 300.13
Spectral Width 5995.2
Lowest Frequency -1200.9
Nucleus 1H
Acquired Size 32768
Spectral Size 65536
N
O+
Ph
BF4−
3.12b
2.00 1.03 1.00 3.14 1.09 1.03
EtOAc 4.09
2.95 water
(CD3)2CO EtOAc
6.10 H-grease EtOAc H-grease
10.0 9.5 9.0 8.5 8.0 7.5 7.0 6.5 6.0 5.5 5.0 4.5 4.0 3.5 3.0 2.5 2.0 1.5 1.0 0.5 0.0
f1 (ppm)

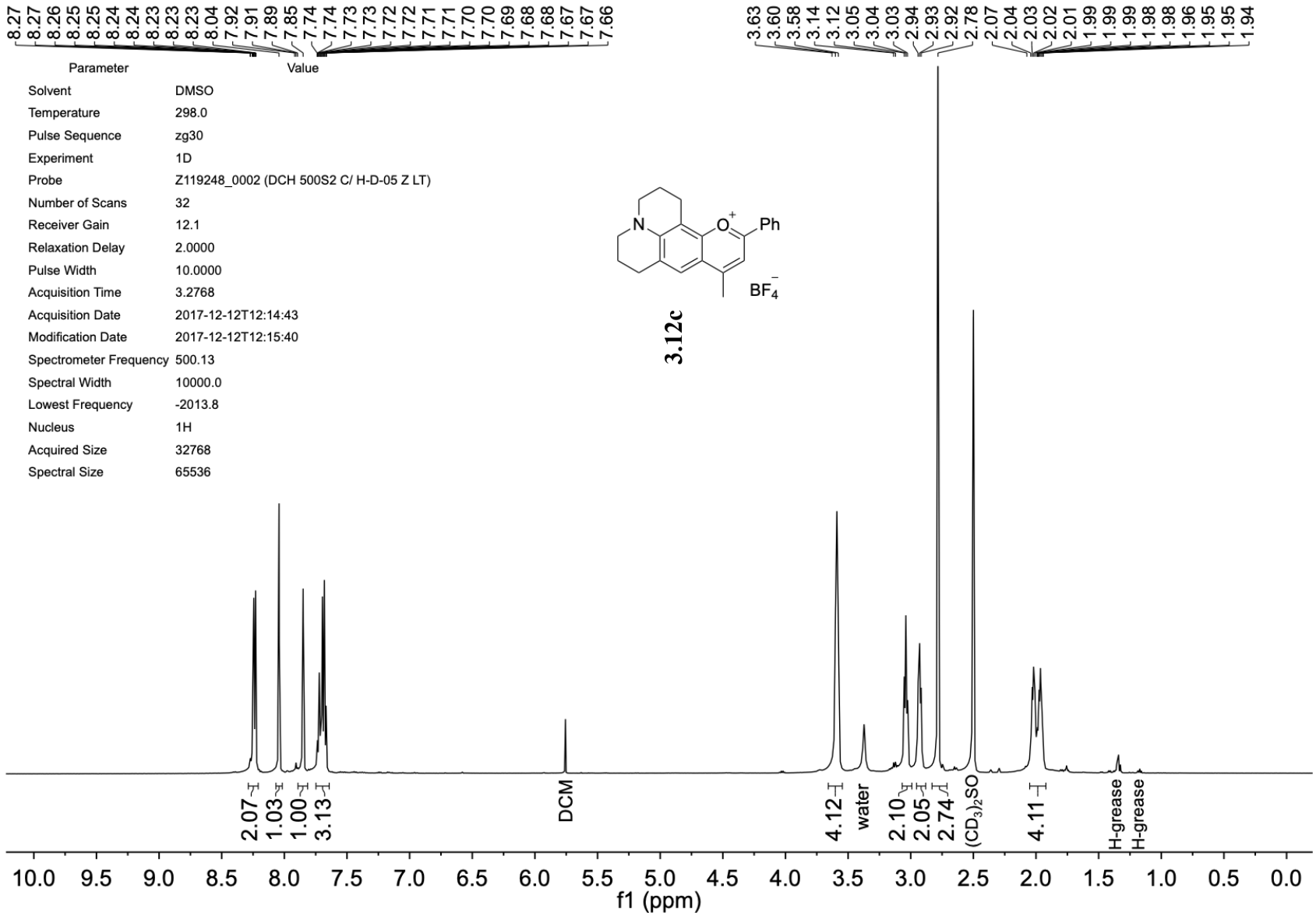
8.27 8.27 8.26 8.25 8.25 8.24 8.24 8.23 8.23 8.23 8.04 7.92 7.91 7.89 7.85 7.74 7.74 7.73 7.73 7.72 7.72 7.71 7.71 7.70 7.70 7.69 7.68 7.68 7.67 7.67 7.66
3.63 3.60 3.58 3.14 3.12 3.05 3.04 3.03 2.94 2.93 2.92 2.78 2.07 2.04 2.03 2.02 2.01 1.99 1.99 1.99 1.98 1.98 1.96 1.95 1.95 1.94
Parameter Value
Solvent DMSO
Temperature 298.0
Pulse Sequence zg30
Experiment 1D
Probe Z119248_0002 (DCH 500S2 C/ H-D-05 Z LT)
Number of Scans 32
Receiver Gain 12.1
Relaxation Delay 2.0000
Pulse Width 10.0000
Acquisition Time 3.2768
Acquisition Date 2017-12-12T12:14:43
Modification Date 2017-12-12T12:15:40
Spectrometer Frequency 500.13
Spectral Width 10000.0
Lowest Frequency -2013.8
Nucleus 1H
Acquired Size 32768
Spectral Size 65536
N
O+
Ph
BF4−
3.12c
2.07
1.03
1.00
3.13
DCM
4.12
water
2.10
2.05
2.74
(CD3)2SO
4.11
H-grease
H-grease
10.0 9.5 9.0 8.5 8.0 7.5 7.0 6.5 6.0 5.5 5.0 4.5 4.0 3.5 3.0 2.5 2.0 1.5 1.0 0.5 0.0
f1 (ppm)

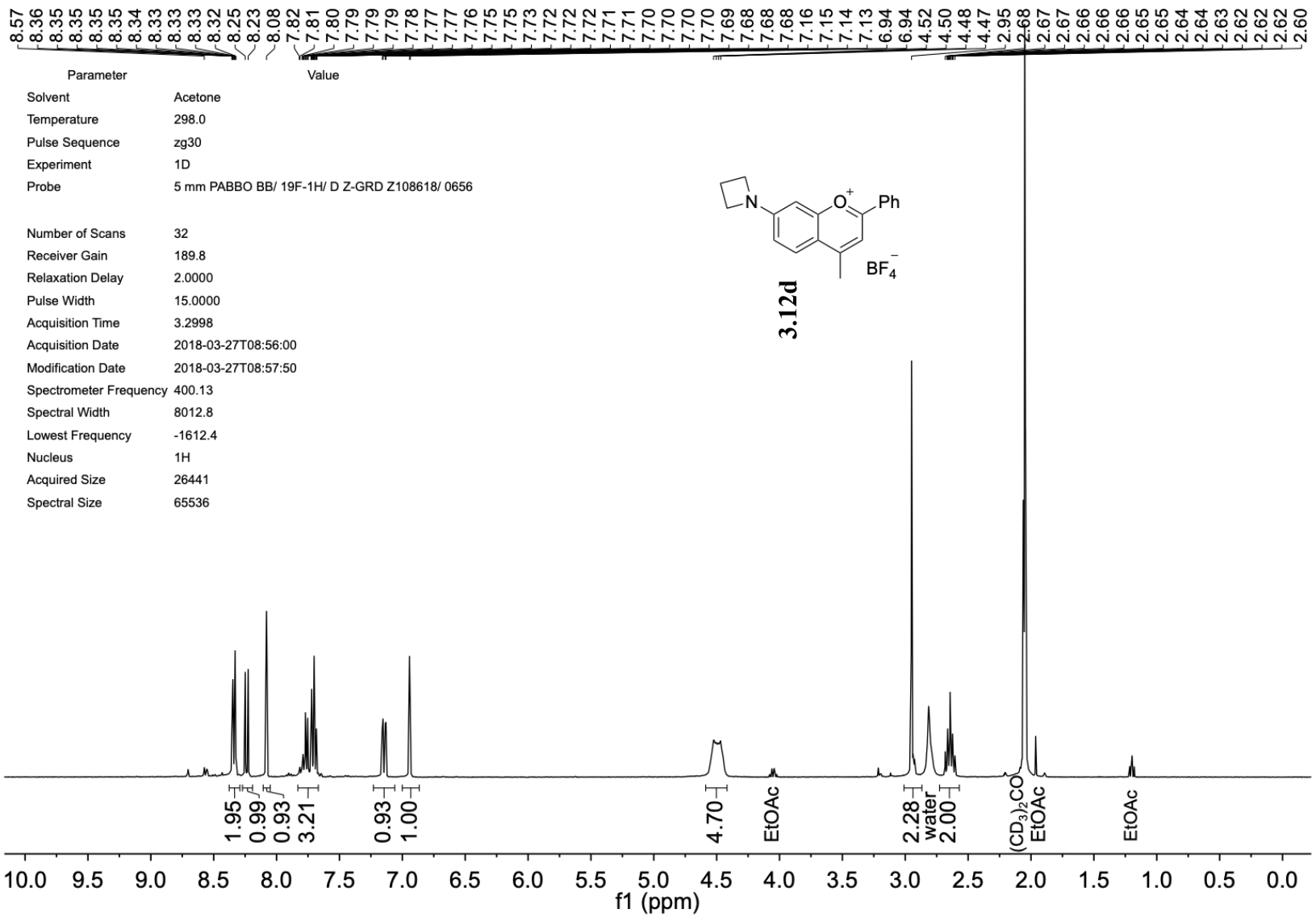
8.57 8.36 8.35 8.35 8.35 8.35 8.34 8.33 8.33 8.33 8.32 8.25 8.23 8.08 7.82 7.81 7.80 7.79 7.79 7.79 7.78 7.77 7.77 7.76 7.75 7.75 7.73 7.72 7.72 7.72 7.71 7.71 7.70 7.70 7.70 7.70 7.69 7.68 7.68 7.68 7.16 7.15 7.14 7.13 6.94 6.94 4.52 4.50 4.48 4.47 2.95 2.68 2.67 2.67 2.66 2.66 2.66 2.65 2.65 2.64 2.64 2.63 2.62 2.62 2.62 2.60
Parameter Value
Solvent Acetone
Temperature 298.0
Pulse Sequence zg30
Experiment 1D
Probe 5 mm PABBO BB/ 19F-1H/ D Z-GRD Z108618/ 0656
Number of Scans 32
Receiver Gain 189.8
Relaxation Delay 2.0000
Pulse Width 15.0000
Acquisition Time 3.2998
Acquisition Date 2018-03-27T08:56:00
Modification Date 2018-03-27T08:57:50
Spectrometer Frequency 400.13
Spectral Width 8012.8
Lowest Frequency -1612.4
Nucleus 1H
Acquired Size 26441
Spectral Size 65536
N
O+
Ph
BF4−
3.12d
1.95 0.99 0.93 3.21 0.93 1.00 4.70 EtOAc 2.28 water 2.00 (CD3)2CO EtOAc EtOAc
10.0 9.5 9.0 8.5 8.0 7.5 7.0 6.5 6.0 5.5 5.0 4.5 4.0 3.5 3.0 2.5 2.0 1.5 1.0 0.5 0.0
f1 (ppm)

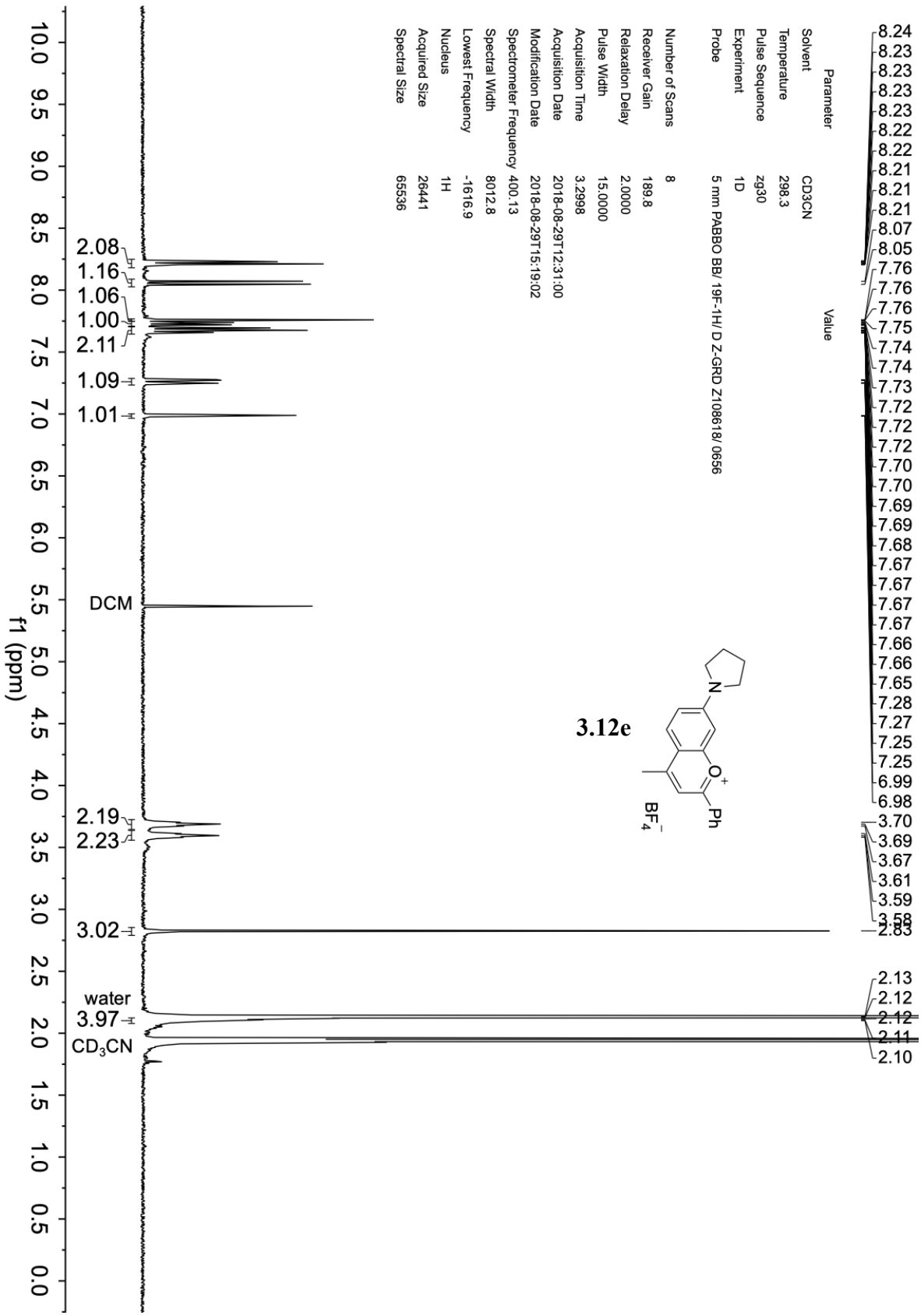
Parameter Value
Solvent CD3CN
Temperature 298.3
Pulse Sequence zg30
Experiment 1D
Probe 5 mm PABBO BB/ 19F-1H/ D Z-GRD Z108618/ 0656
Number of Scans 8
Receiver Gain 189.8
Relaxation Delay 2.0000
Pulse Width 15.0000
Acquisition Time 3.2998
Acquisition Date 2018-08-29T12:31:00
Modification Date 2018-08-29T15:19:02
Spectrometer Frequency 400.13
Spectral Width 8012.8
Lowest Frequency -1616.9
Nucleus 1H
Acquired Size 26441
Spectral Size 65536
3.12e
BF4−
Ph
DCM
water
CD3CN
f1 (ppm)

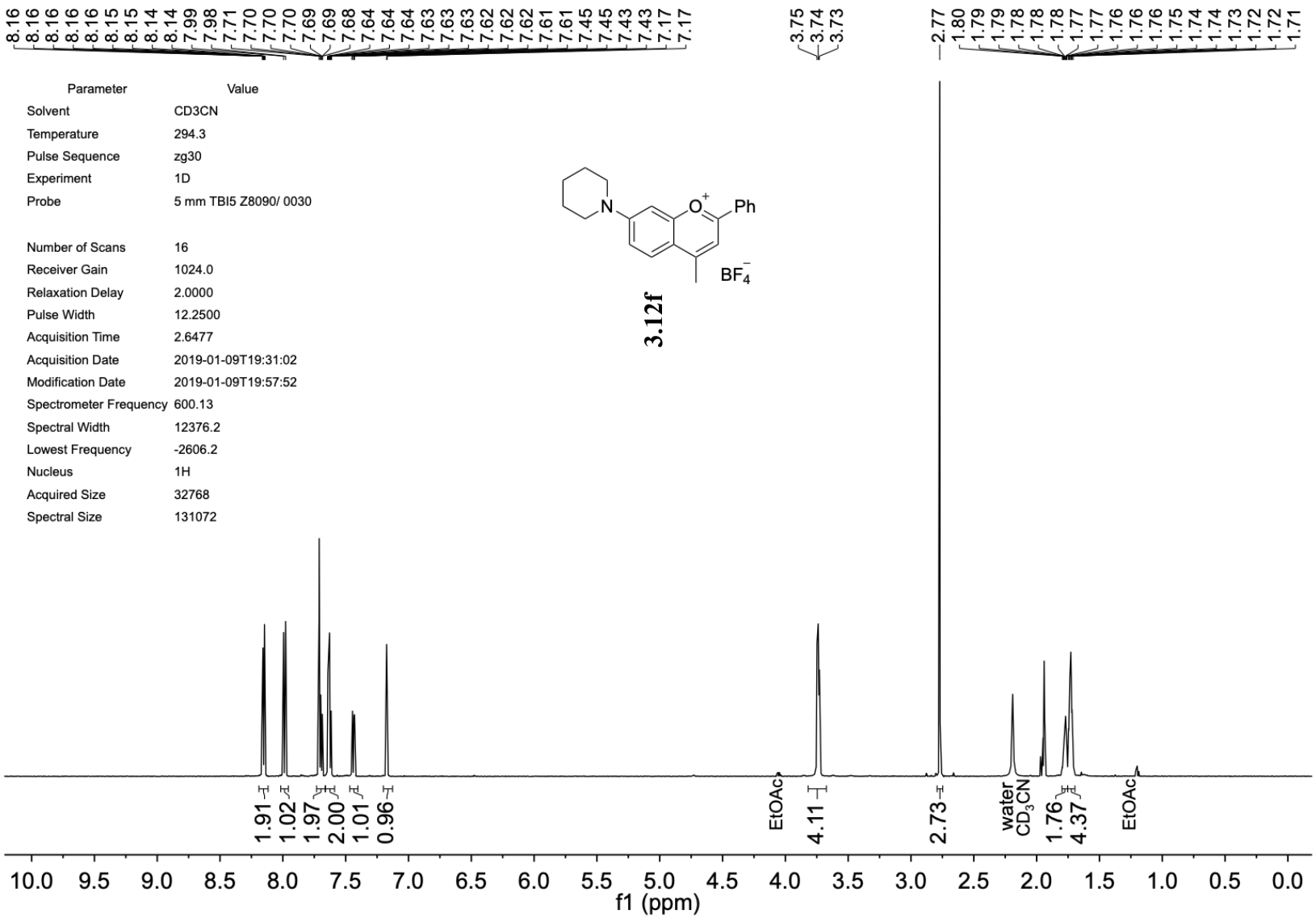
8.16 8.16 8.16 8.16 8.16 8.15 8.15 8.14 8.14 7.99 7.98 7.71 7.70 7.70 7.70 7.69 7.69 7.68 7.64 7.64 7.64 7.63 7.63 7.63 7.62 7.62 7.62 7.61 7.61 7.45 7.45 7.43 7.43 7.17 7.17
3.75 3.74 3.73
2.77 1.80 1.79 1.79 1.78 1.78 1.78 1.77 1.77 1.76 1.76 1.76 1.75 1.74 1.74 1.73 1.72 1.72 1.71
Parameter Value
Solvent CD3CN
Temperature 294.3
Pulse Sequence zg30
Experiment 1D
Probe 5 mm TBI5 Z8090/ 0030
Number of Scans 16
Receiver Gain 1024.0
Relaxation Delay 2.0000
Pulse Width 12.2500
Acquisition Time 2.6477
Acquisition Date 2019-01-09T19:31:02
Modification Date 2019-01-09T19:57:52
Spectrometer Frequency 600.13
Spectral Width 12376.2
Lowest Frequency -2606.2
Nucleus 1H
Acquired Size 32768
Spectral Size 131072
N
O+
Ph
BF4−
3.12f
1.91 1.02 1.97 2.00 1.01 0.96
EtOAc
4.11
2.73
water
CD3CN
1.76
4.37
EtOAc
10.0 9.5 9.0 8.5 8.0 7.5 7.0 6.5 6.0 5.5 5.0 4.5 4.0 3.5 3.0 2.5 2.0 1.5 1.0 0.5 0.0
f1 (ppm)

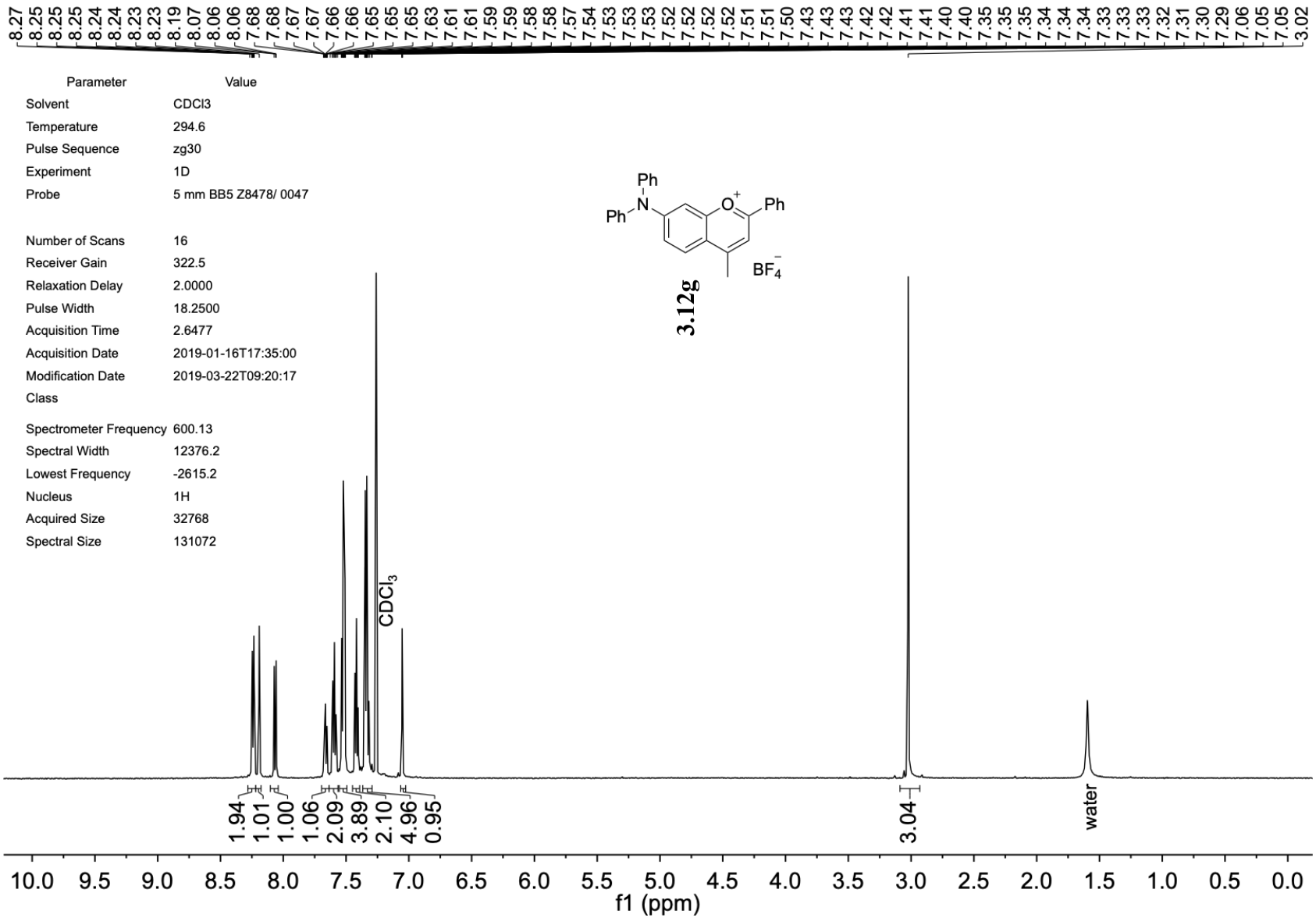
8.27 8.25 8.25 8.25 8.24 8.24 8.23 8.23 8.19 8.07 8.06 8.06 7.68 7.68 7.67 7.67 7.66 7.66 7.65 7.65 7.65 7.63 7.61 7.61 7.59 7.59 7.58 7.58 7.57 7.54 7.53 7.53 7.53 7.52 7.52 7.52 7.52 7.51 7.51 7.50 7.43 7.43 7.43 7.42 7.42 7.41 7.41 7.40 7.40 7.35 7.35 7.35 7.34 7.34 7.34 7.33 7.33 7.33 7.32 7.31 7.30 7.29 7.06 7.05 7.05 3.02
Parameter Value
Solvent CDCl3
Temperature 294.6
Pulse Sequence zg30
Experiment 1D
Probe 5 mm BB5 Z8478/ 0047
Number of Scans 16
Receiver Gain 322.5
Relaxation Delay 2.0000
Pulse Width 18.2500
Acquisition Time 2.6477
Acquisition Date 2019-01-16T17:35:00
Modification Date 2019-03-22T09:20:17
Class
Spectrometer Frequency 600.13
Spectral Width 12376.2
Lowest Frequency -2615.2
Nucleus 1H
Acquired Size 32768
Spectral Size 131072
Ph
N
Ph
O+
Ph
BF4−
3.12g
CDCl3
1.94 1.01 1.00 1.06 2.09 3.89 2.10 4.96 0.95
3.04
water
10.0 9.5 9.0 8.5 8.0 7.5 7.0 6.5 6.0 5.5 5.0 4.5 4.0 3.5 3.0 2.5 2.0 1.5 1.0 0.5 0.0
f1 (ppm)

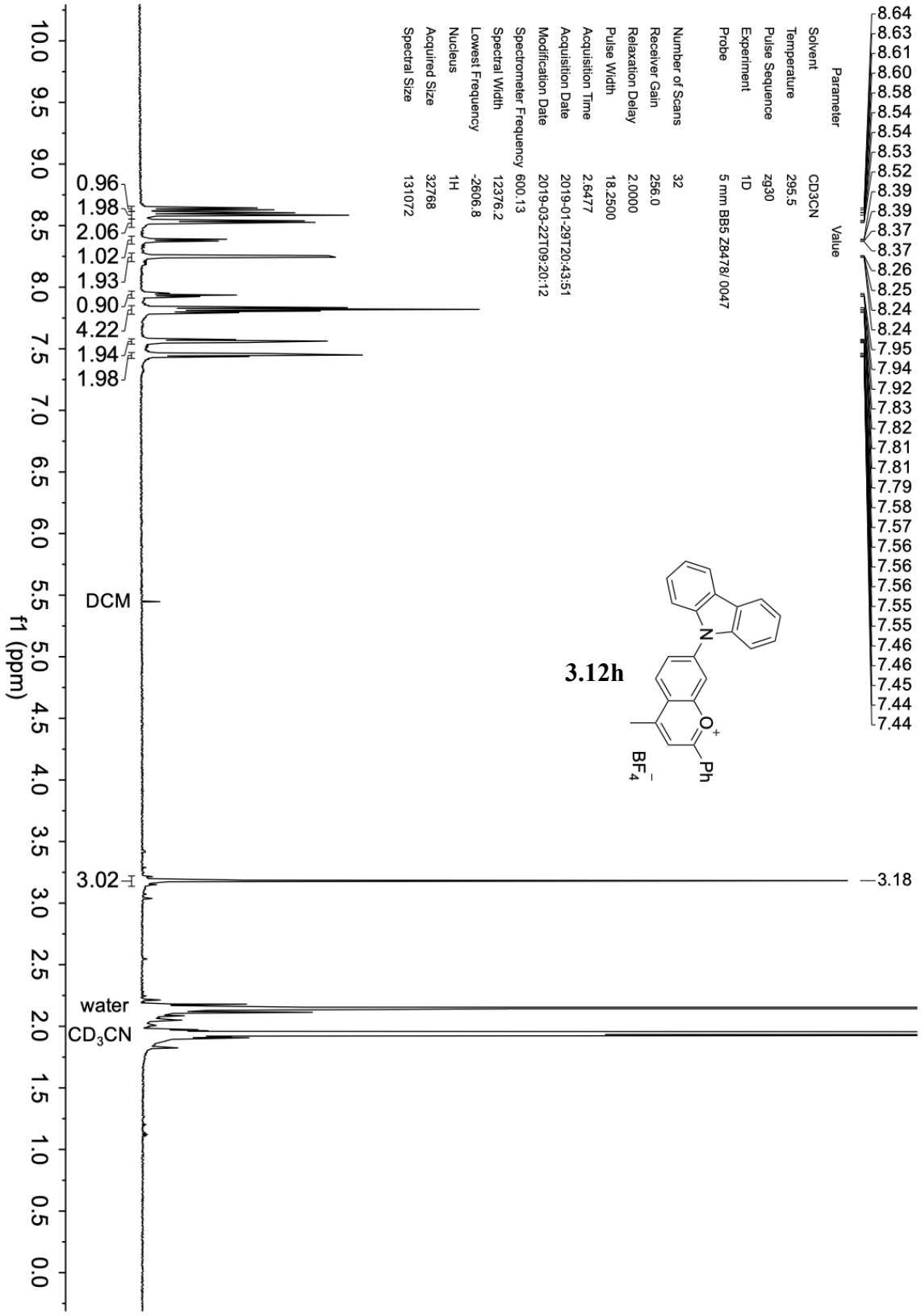
Parameter Value
Solvent CD3CN
Temperature 295.5
Pulse Sequence zg30
Experiment 1D
Probe 5 mm BB5 Z8478/ 0047
Number of Scans 32
Receiver Gain 256.0
Relaxation Delay 2.0000
Pulse Width 18.2500
Acquisition Time 2.6477
Acquisition Date 2019-01-29T20:43:51
Modification Date 2019-03-22T09:20:12
Spectrometer Frequency 600.13
Spectral Width 12376.2
Lowest Frequency -2606.8
Nucleus 1H
Acquired Size 32768
Spectral Size 131072
8.64 8.63 8.61 8.60 8.58 8.54 8.54 8.53 8.52 8.39 8.39 8.37 8.37 8.26 8.25 8.24 8.24 7.95 7.94 7.92 7.83 7.82 7.81 7.81 7.79 7.58 7.57 7.56 7.56 7.56 7.55 7.55 7.46 7.46 7.45 7.44 7.44
3.12h
0.96 1.98 2.06 1.02 1.93 0.90 4.22 1.94 1.98
DCM
3.02
3.18
water
CD3CN
f1 (ppm)

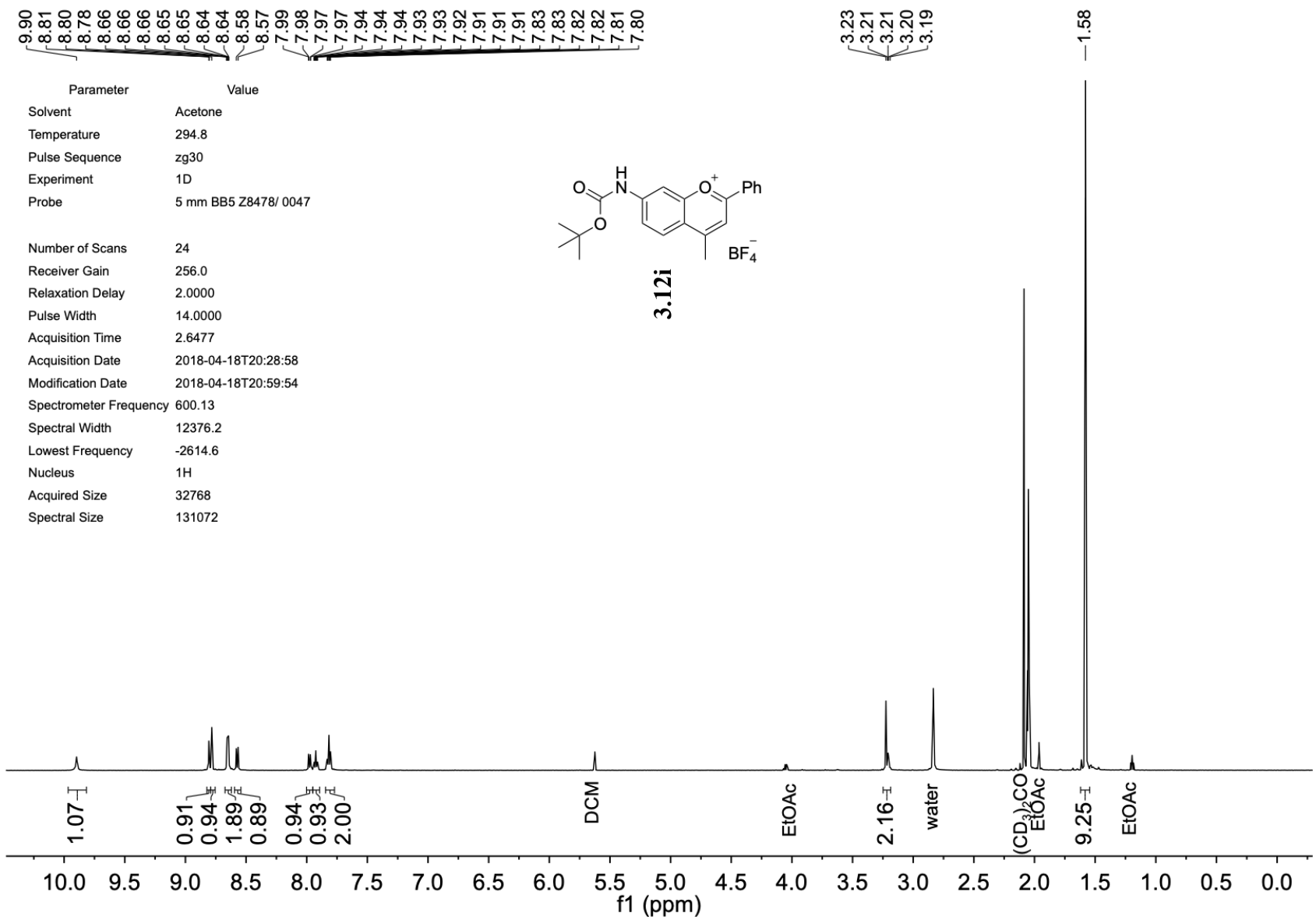
9.90 8.81 8.80 8.78 8.66 8.66 8.66 8.65 8.65 8.64 8.64 8.58 8.57
7.99 7.98 7.97 7.97 7.94 7.94 7.94 7.93 7.93 7.92 7.91 7.91 7.91 7.83 7.83 7.82 7.82 7.81 7.80
3.23 3.21 3.21 3.20 3.19
1.58
Parameter Value
Solvent Acetone
Temperature 294.8
Pulse Sequence zg30
Experiment 1D
Probe 5 mm BB5 Z8478/ 0047
Number of Scans 24
Receiver Gain 256.0
Relaxation Delay 2.0000
Pulse Width 14.0000
Acquisition Time 2.6477
Acquisition Date 2018-04-18T20:28:58
Modification Date 2018-04-18T20:59:54
Spectrometer Frequency 600.13
Spectral Width 12376.2
Lowest Frequency -2614.6
Nucleus 1H
Acquired Size 32768
Spectral Size 131072
Ph
BF4−
3.12i
1.07
0.91 0.94 1.89 0.89
0.94 0.93 2.00
DCM
EtOAc
2.16
water
(CD3)2CO
EtOAc
9.25
EtOAc
10.0 9.5 9.0 8.5 8.0 7.5 7.0 6.5 6.0 5.5 5.0 4.5 4.0 3.5 3.0 2.5 2.0 1.5 1.0 0.5 0.0
f1 (ppm)

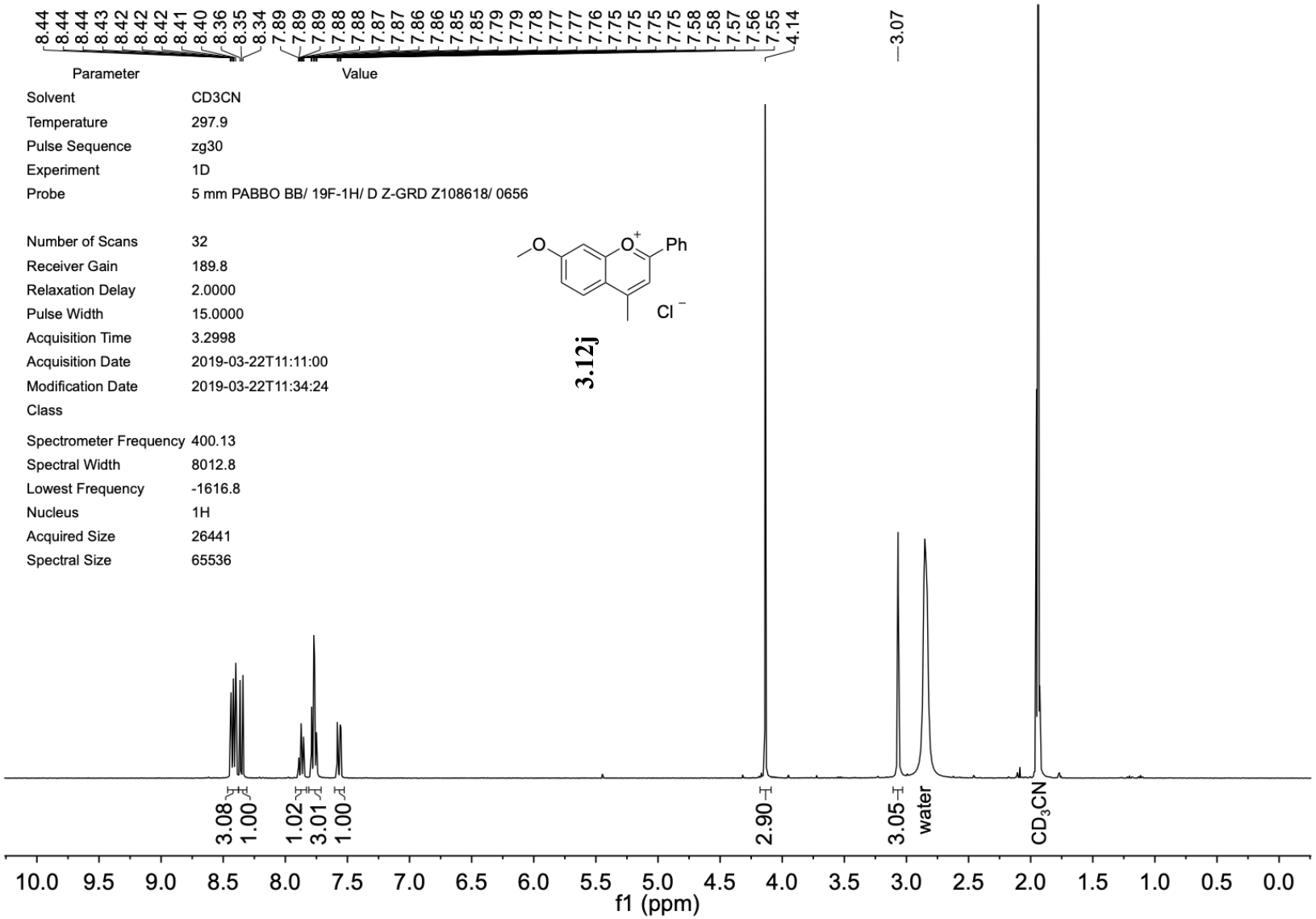
8.44 8.44 8.44 8.43 8.42 8.42 8.42 8.41 8.40 8.36 8.35 8.34 7.89 7.89 7.89 7.88 7.88 7.87 7.87 7.86 7.86 7.85 7.85 7.79 7.79 7.78 7.77 7.77 7.76 7.75 7.75 7.75 7.75 7.58 7.58 7.57 7.56 7.55 4.14
3.07
Parameter
Value
Solvent CD3CN
Temperature 297.9
Pulse Sequence zg30
Experiment 1D
Probe 5 mm PABBO BB/ 19F-1H/ D Z-GRD Z108618/ 0656
Number of Scans 32
Receiver Gain 189.8
Relaxation Delay 2.0000
Pulse Width 15.0000
Acquisition Time 3.2998
Acquisition Date 2019-03-22T11:11:00
Modification Date 2019-03-22T11:34:24
Class
Spectrometer Frequency 400.13
Spectral Width 8012.8
Lowest Frequency -1616.8
Nucleus 1H
Acquired Size 26441
Spectral Size 65536
O
O+
Ph
Cl −
3.12j
3.08
1.00
1.02
3.01
1.00
2.90
3.05
water
CD3CN
10.0 9.5 9.0 8.5 8.0 7.5 7.0 6.5 6.0 5.5 5.0 4.5 4.0 3.5 3.0 2.5 2.0 1.5 1.0 0.5 0.0
f1 (ppm)

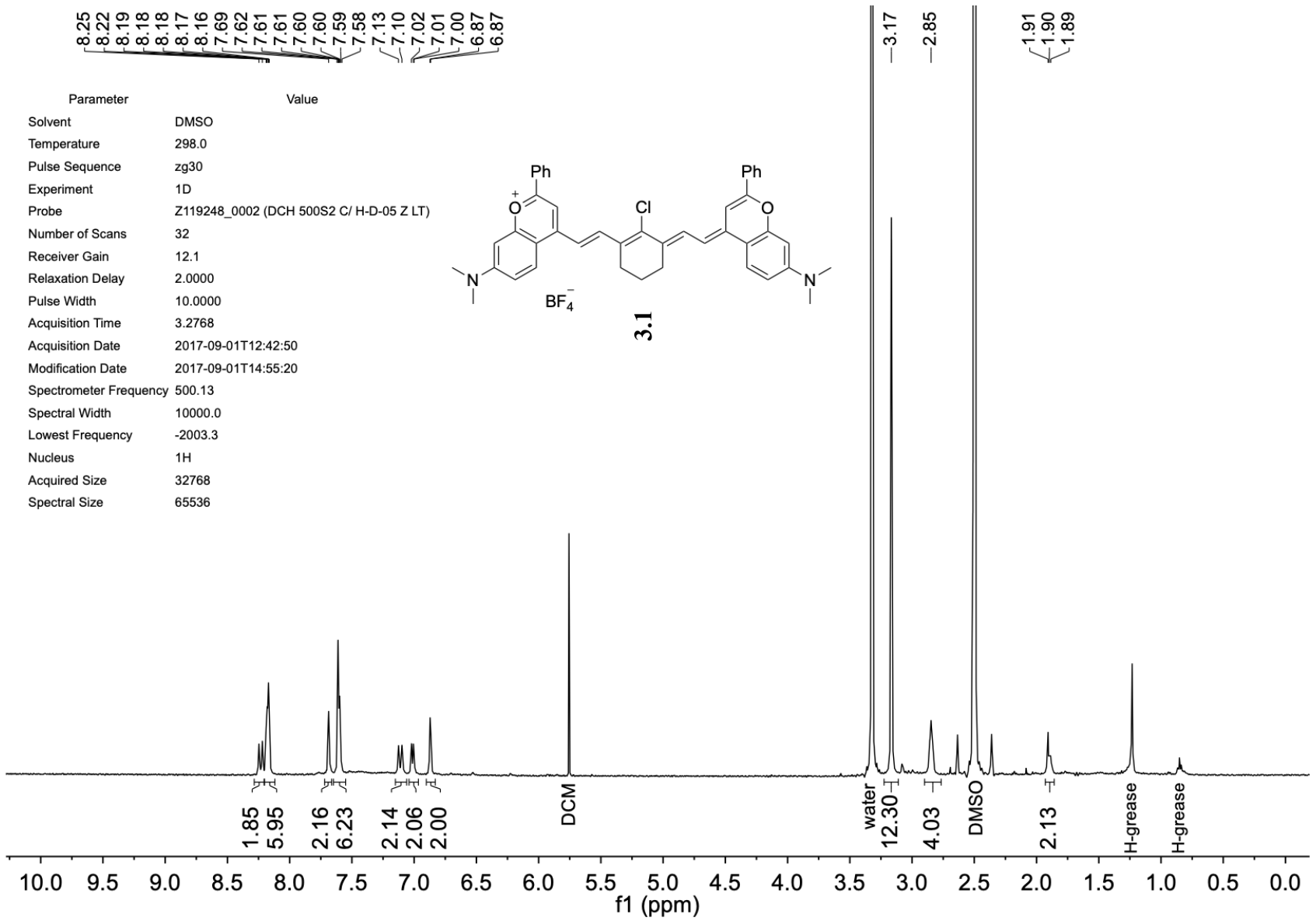
8.25
8.22
8.19
8.18
8.18
8.17
8.16
7.69
7.62
7.61
7.61
7.60
7.60
7.59
7.58
7.13
7.10
7.02
7.01
7.00
6.87
6.87
3.17
2.85
1.91
1.90
1.89
Parameter
Value
Solvent
DMSO
Temperature
298.0
Pulse Sequence
zg30
Experiment
1D
Probe
Z119248_0002 (DCH 500S2 C/ H-D-05 Z LT)
Number of Scans
32
Receiver Gain
12.1
Relaxation Delay
2.0000
Pulse Width
10.0000
Acquisition Time
3.2768
Acquisition Date
2017-09-01T12:42:50
Modification Date
2017-09-01T14:55:20
Spectrometer Frequency
500.13
Spectral Width
10000.0
Lowest Frequency
-2003.3
Nucleus
1H
Acquired Size
32768
Spectral Size
65536
Ph
Cl
Ph
N
N
BF4
3.1
1.85
5.95
2.16
6.23
2.14
2.06
2.00
DCM
water
12.30
4.03
DMSO
2.13
H-grease
H-grease
10.0
9.5
9.0
8.5
8.0
7.5
7.0
6.5
6.0
5.5
5.0
4.5
4.0
3.5
3.0
2.5
2.0
1.5
1.0
0.5
0.0
f1 (ppm)

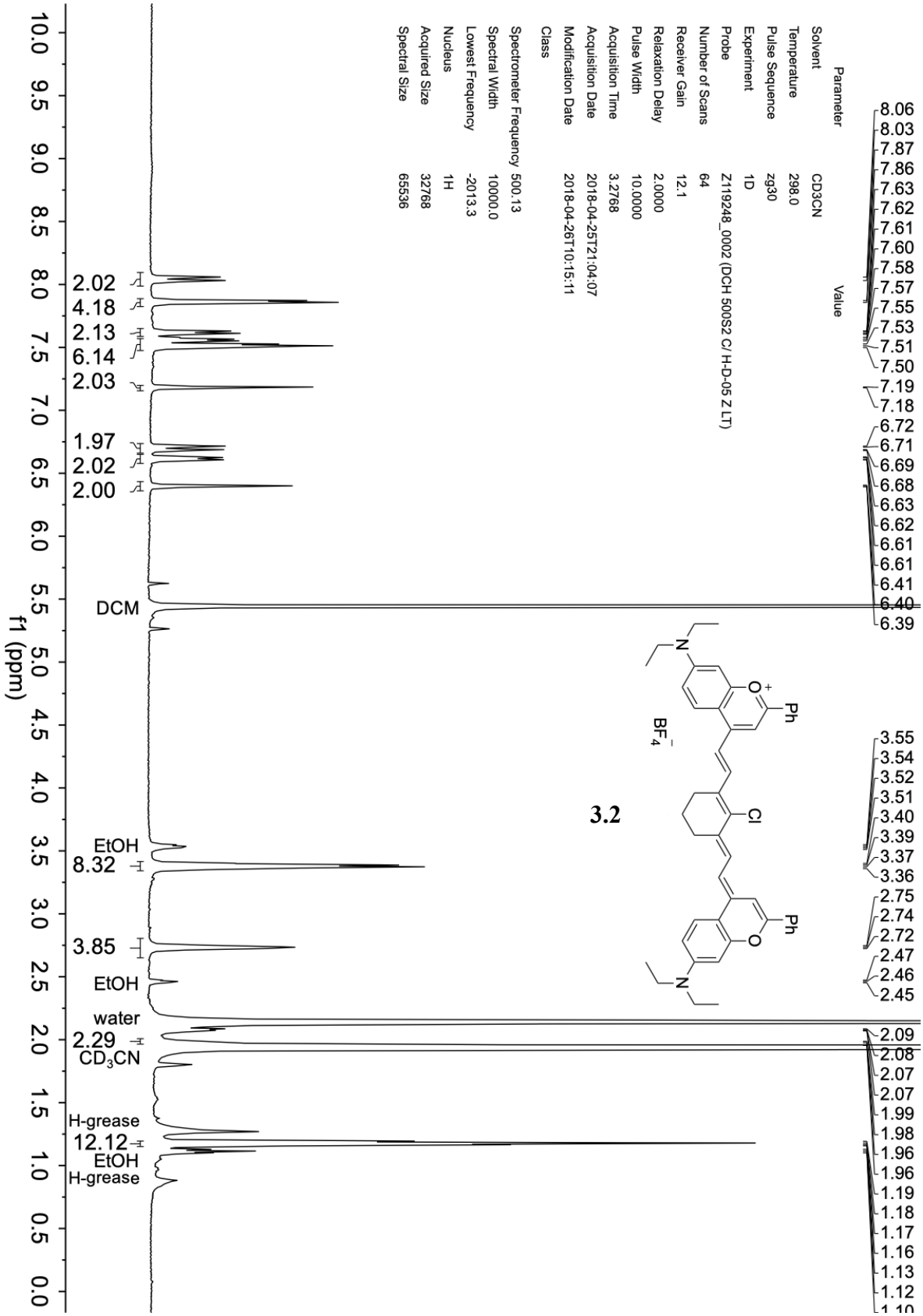
Parameter Value
Solvent CD3CN
Temperature 298.0
Pulse Sequence zg30
Experiment 1D
Probe Z119248_0002 (DCH 500S2 C/ H-D-05 Z LT)
Number of Scans 64
Receiver Gain 12.1
Relaxation Delay 2.0000
Pulse Width 10.0000
Acquisition Time 3.2768
Acquisition Date 2018-04-25T21:04:07
Modification Date 2018-04-26T10:15:11
Class
Spectrometer Frequency 500.13
Spectral Width 10000.0
Lowest Frequency -2013.3
Nucleus 1H
Acquired Size 32768
Spectral Size 65536
3.2
f1 (ppm)
DCM
EtOH
EtOH
water
CD3CN
H-grease
EtOH
H-grease

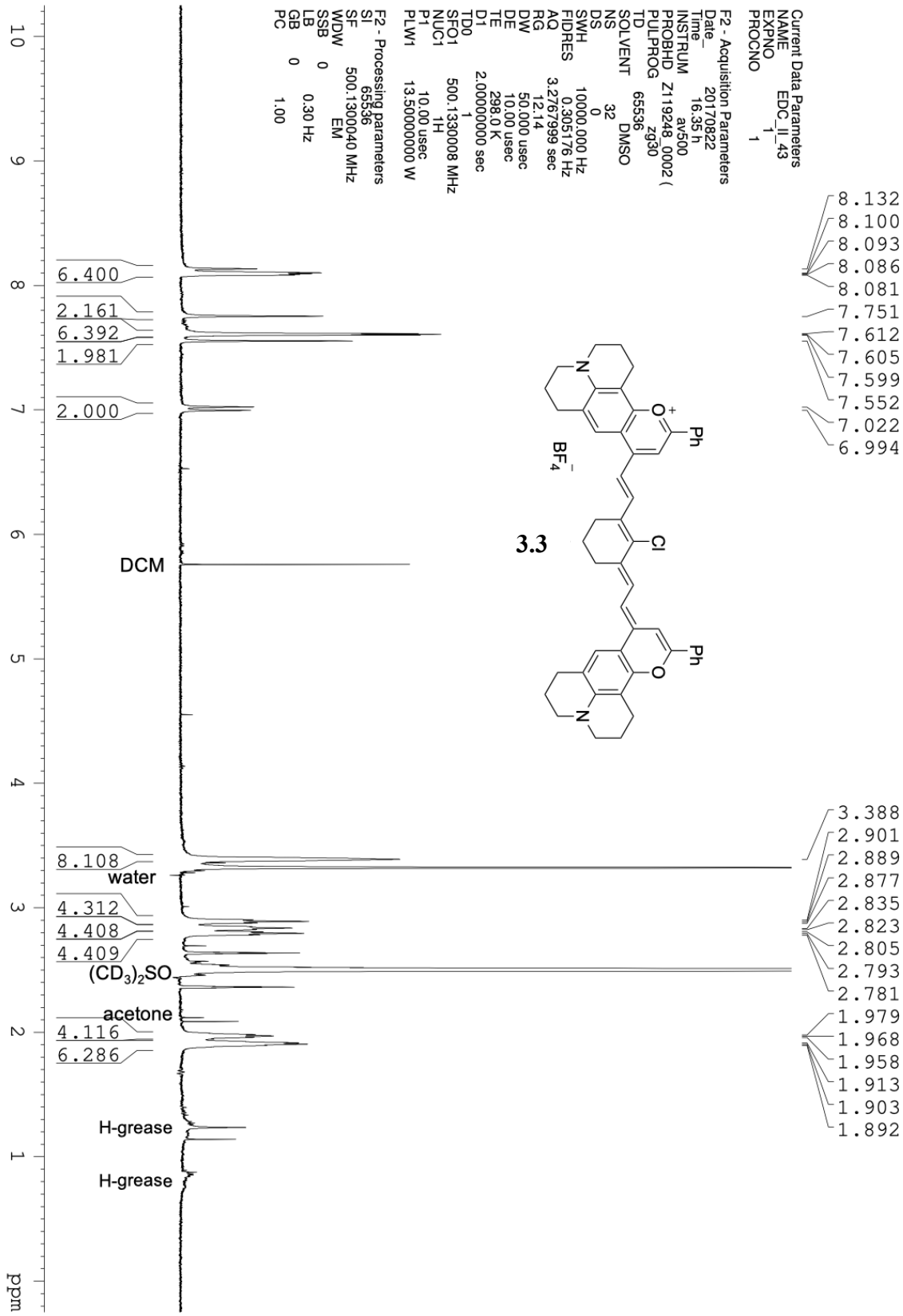
Current Data Parameters
NAME EDC_II_43
EXPNO 1
PROCNO 1
F2 - Acquisition Parameters
Date_ 20170822
Time 16.35 h
INSTRUM av500
PROBHD Z119248_0002 (
PULPROG zg30
TD 65536
SOLVENT DMSO
NS 32
DS 0
SWH 10000.000 Hz
FIDRES 0.305176 Hz
AQ 3.2767999 sec
RG 12.14
DW 50.000 usec
DE 10.00 usec
TE 298.0 K
D1 2.00000000 sec
TD0 1
SFO1 500.1330008 MHz
NUC1 1H
P1 10.00 usec
PLW1 13.50000000 W
F2 - Processing parameters
SI 65536
SF 500.1300040 MHz
WDW EM
SSB 0
LB 0.30 Hz
GB 0
PC 1.00
8.132
8.100
8.093
8.086
8.081
7.751
7.612
7.605
7.599
7.552
7.022
6.994
3.388
2.901
2.889
2.877
2.835
2.823
2.805
2.793
2.781
1.979
1.968
1.958
1.913
1.903
1.892
6.400
2.161
6.392
1.981
2.000
8.108
4.312
4.408
4.409
4.116
6.286
DCM
water
(CD3)2SO
acetone
H-grease
H-grease
3.3
Ph
Cl
Ph
BF4−
ppm

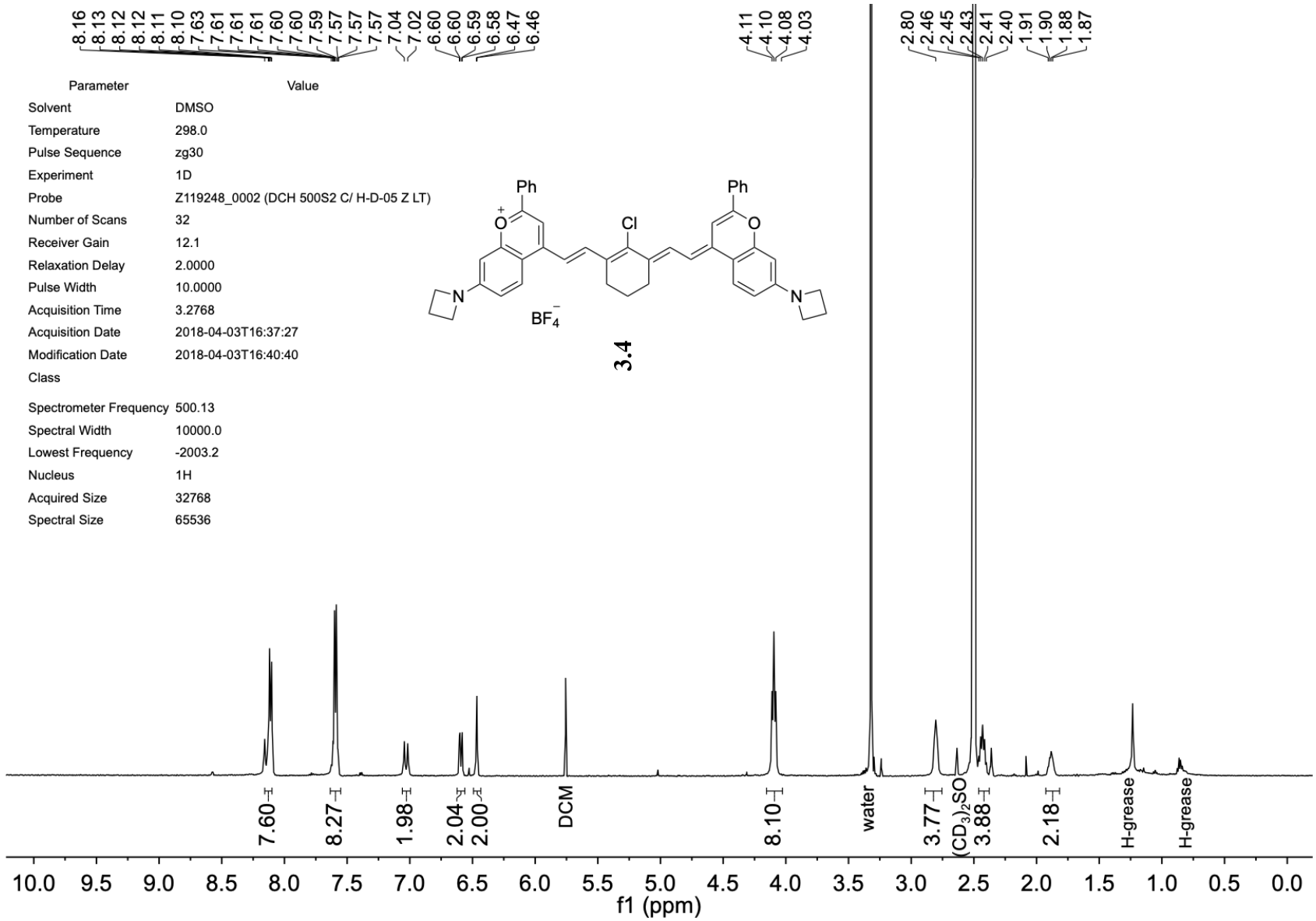
8.16 8.13 8.12 8.12 8.11 8.10 7.63 7.61 7.61 7.61 7.60 7.60 7.59 7.57 7.57 7.57 7.04 7.02 6.60 6.60 6.59 6.58 6.47 6.46
4.11 4.10 4.08 4.03
2.80 2.46 2.45 2.43 2.41 2.40 1.91 1.90 1.88 1.87
Parameter Value
Solvent DMSO
Temperature 298.0
Pulse Sequence zg30
Experiment 1D
Probe Z119248_0002 (DCH 500S2 C/ H-D-05 Z LT)
Number of Scans 32
Receiver Gain 12.1
Relaxation Delay 2.0000
Pulse Width 10.0000
Acquisition Time 3.2768
Acquisition Date 2018-04-03T16:37:27
Modification Date 2018-04-03T16:40:40
Class
Spectrometer Frequency 500.13
Spectral Width 10000.0
Lowest Frequency -2003.2
Nucleus 1H
Acquired Size 32768
Spectral Size 65536
Ph
Cl
Ph
N
N
BF_4^-
3.4
7.60
8.27
1.98
2.04
2.00
DCM
8.10
water
3.77
$(CD_3)_2SO$
3.88
2.18
H-grease
H-grease
10.0 9.5 9.0 8.5 8.0 7.5 7.0 6.5 6.0 5.5 5.0 4.5 4.0 3.5 3.0 2.5 2.0 1.5 1.0 0.5 0.0
f1 (ppm)

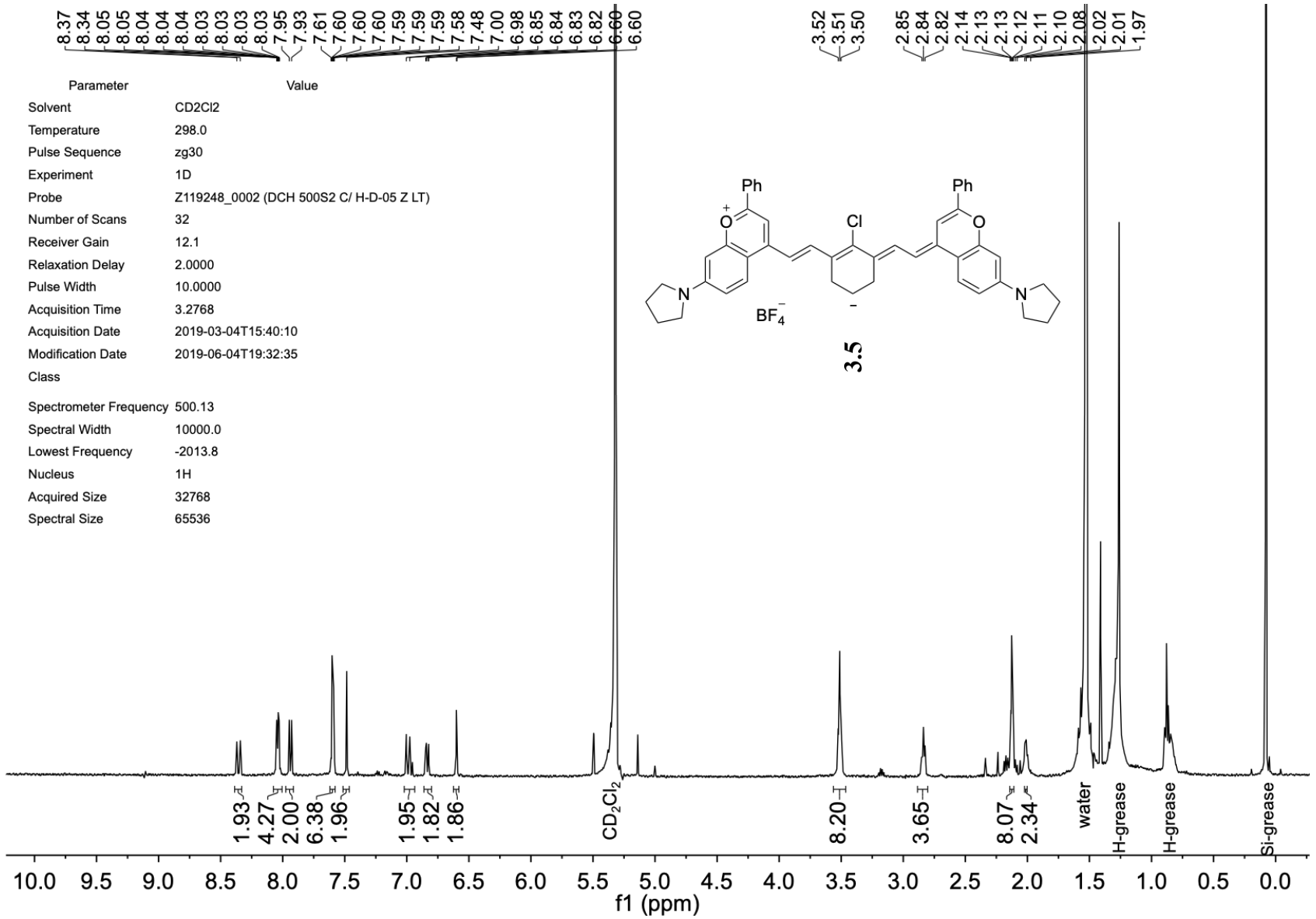
8.37 8.34 8.05 8.05 8.04 8.04 8.04 8.03 8.03 8.03 8.03 7.95 7.93 7.61 7.60 7.60 7.60 7.59 7.59 7.59 7.58 7.48 7.00 6.98 6.85 6.84 6.83 6.82 6.60 6.60
3.52 3.51 3.50 2.85 2.84 2.82 2.14 2.13 2.13 2.12 2.11 2.10 2.08 2.02 2.01 1.97
Parameter Value
Solvent CD2Cl2
Temperature 298.0
Pulse Sequence zg30
Experiment 1D
Probe Z119248_0002 (DCH 500S2 C/ H-D-05 Z LT)
Number of Scans 32
Receiver Gain 12.1
Relaxation Delay 2.0000
Pulse Width 10.0000
Acquisition Time 3.2768
Acquisition Date 2019-03-04T15:40:10
Modification Date 2019-06-04T19:32:35
Class
Spectrometer Frequency 500.13
Spectral Width 10000.0
Lowest Frequency -2013.8
Nucleus 1H
Acquired Size 32768
Spectral Size 65536
Ph
O
Cl
Ph
O
N
N
BF4
3.5
1.93 4.27 2.00 6.38 1.96 1.95 1.82 1.86
CD2Cl2
8.20 3.65 8.07 2.34
water
H-grease
H-grease
Si-grease
10.0 9.5 9.0 8.5 8.0 7.5 7.0 6.5 6.0 5.5 5.0 4.5 4.0 3.5 3.0 2.5 2.0 1.5 1.0 0.5 0.0
f1 (ppm)

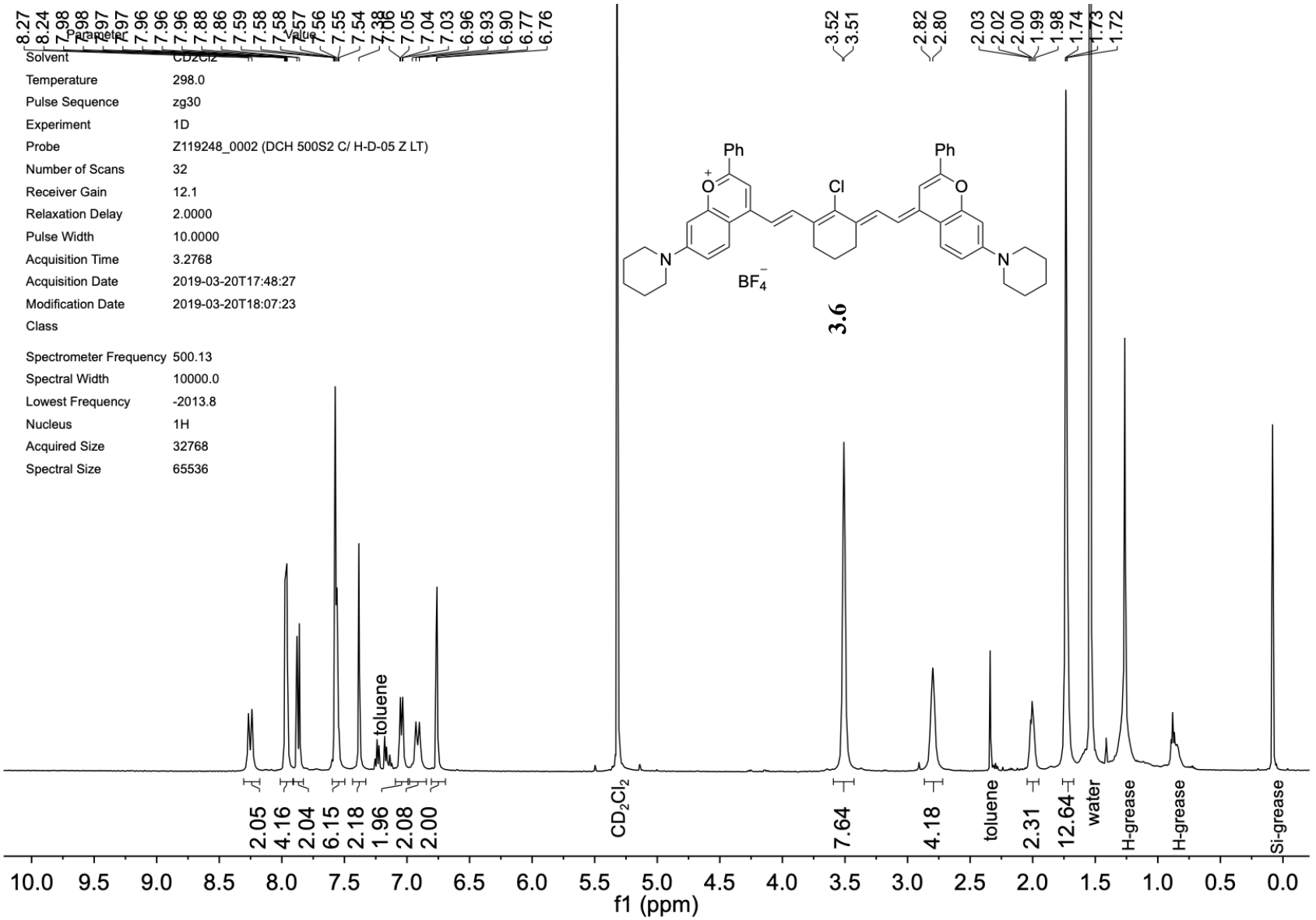
8.27 8.24 7.98 7.98 7.97 7.97 7.96 7.96 7.96 7.88 7.86 7.59 7.58 7.58 7.57 7.56 7.55 7.54 7.38 7.06 7.05 7.04 7.03 6.96 6.93 6.90 6.77 6.76
3.52 3.51 2.82 2.80 2.03 2.02 2.00 1.99 1.98 1.74 1.73 1.72
Parameter Value
Solvent CD2Cl2
Temperature 298.0
Pulse Sequence zg30
Experiment 1D
Probe Z119248_0002 (DCH 500S2 C/ H-D-05 Z LT)
Number of Scans 32
Receiver Gain 12.1
Relaxation Delay 2.0000
Pulse Width 10.0000
Acquisition Time 3.2768
Acquisition Date 2019-03-20T17:48:27
Modification Date 2019-03-20T18:07:23
Class
Spectrometer Frequency 500.13
Spectral Width 10000.0
Lowest Frequency -2013.8
Nucleus 1H
Acquired Size 32768
Spectral Size 65536
Ph
Ph
Cl
O
O
N
N
BF4−
3.6
toluene
2.05 4.16 2.04 6.15 2.18 1.96 2.08 2.00
CD2Cl2
7.64 4.18 toluene 2.31 12.64 water H-grease H-grease Si-grease
10.0 9.5 9.0 8.5 8.0 7.5 7.0 6.5 6.0 5.5 5.0 4.5 4.0 3.5 3.0 2.5 2.0 1.5 1.0 0.5 0.0
f1 (ppm)

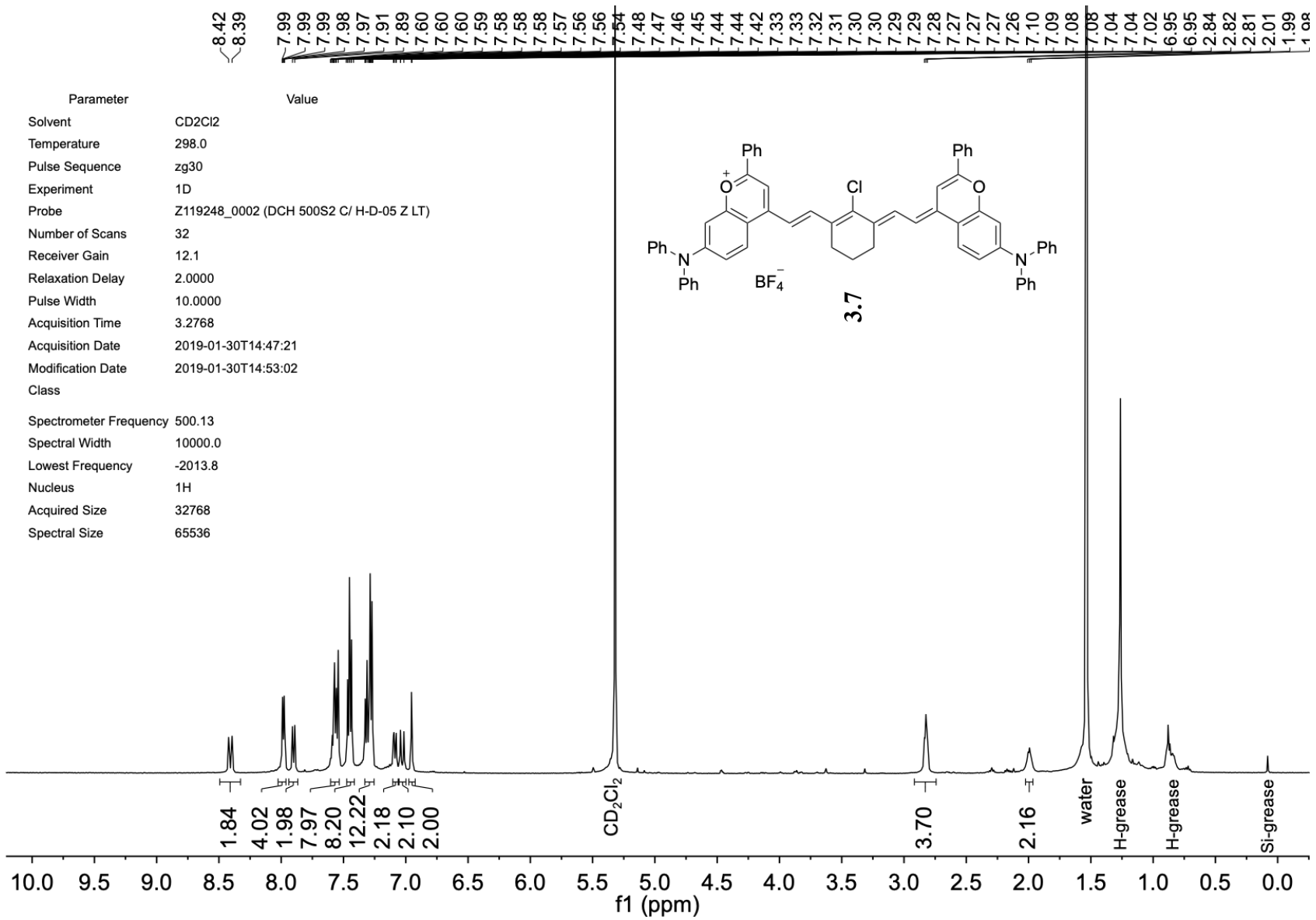
Parameter Value
Solvent CD2Cl2
Temperature 298.0
Pulse Sequence zg30
Experiment 1D
Probe Z119248_0002 (DCH 500S2 C/ H-D-05 Z LT)
Number of Scans 32
Receiver Gain 12.1
Relaxation Delay 2.0000
Pulse Width 10.0000
Acquisition Time 3.2768
Acquisition Date 2019-01-30T14:47:21
Modification Date 2019-01-30T14:53:02
Class
Spectrometer Frequency 500.13
Spectral Width 10000.0
Lowest Frequency -2013.8
Nucleus 1H
Acquired Size 32768
Spectral Size 65536
3.7
1.84
4.02
1.98
7.97
8.20
12.22
2.18
2.10
2.00
CD2Cl2
3.70
2.16
water
H-grease
H-grease
Si-grease
f1 (ppm)

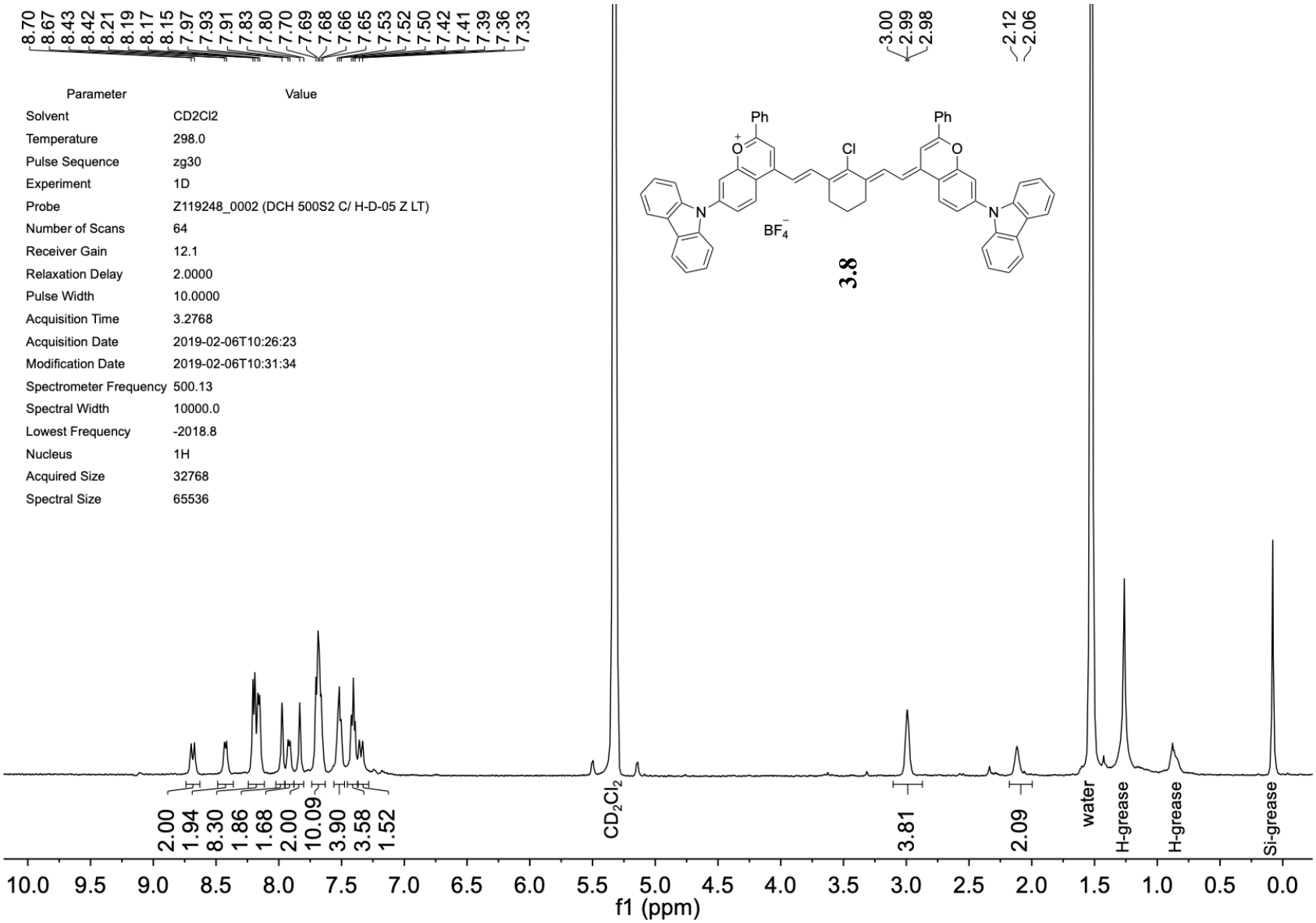
8.70
8.67
8.43
8.42
8.21
8.19
8.17
8.15
7.97
7.93
7.91
7.83
7.80
7.70
7.69
7.68
7.66
7.65
7.53
7.52
7.50
7.42
7.41
7.39
7.36
7.33
3.00
2.99
2.98
2.12
2.06
Parameter Value
Solvent CD2Cl2
Temperature 298.0
Pulse Sequence zg30
Experiment 1D
Probe Z119248_0002 (DCH 500S2 C/ H-D-05 Z LT)
Number of Scans 64
Receiver Gain 12.1
Relaxation Delay 2.0000
Pulse Width 10.0000
Acquisition Time 3.2768
Acquisition Date 2019-02-06T10:26:23
Modification Date 2019-02-06T10:31:34
Spectrometer Frequency 500.13
Spectral Width 10000.0
Lowest Frequency -2018.8
Nucleus 1H
Acquired Size 32768
Spectral Size 65536
Ph
Ph
Cl
O
O
N
N
BF4−
3.8
2.00
1.94
8.30
1.86
1.68
2.00
10.09
3.90
3.58
1.52
CD2Cl2
3.81
2.09
water
H-grease
H-grease
Si-grease
10.0 9.5 9.0 8.5 8.0 7.5 7.0 6.5 6.0 5.5 5.0 4.5 4.0 3.5 3.0 2.5 2.0 1.5 1.0 0.5 0.0
f1 (ppm)

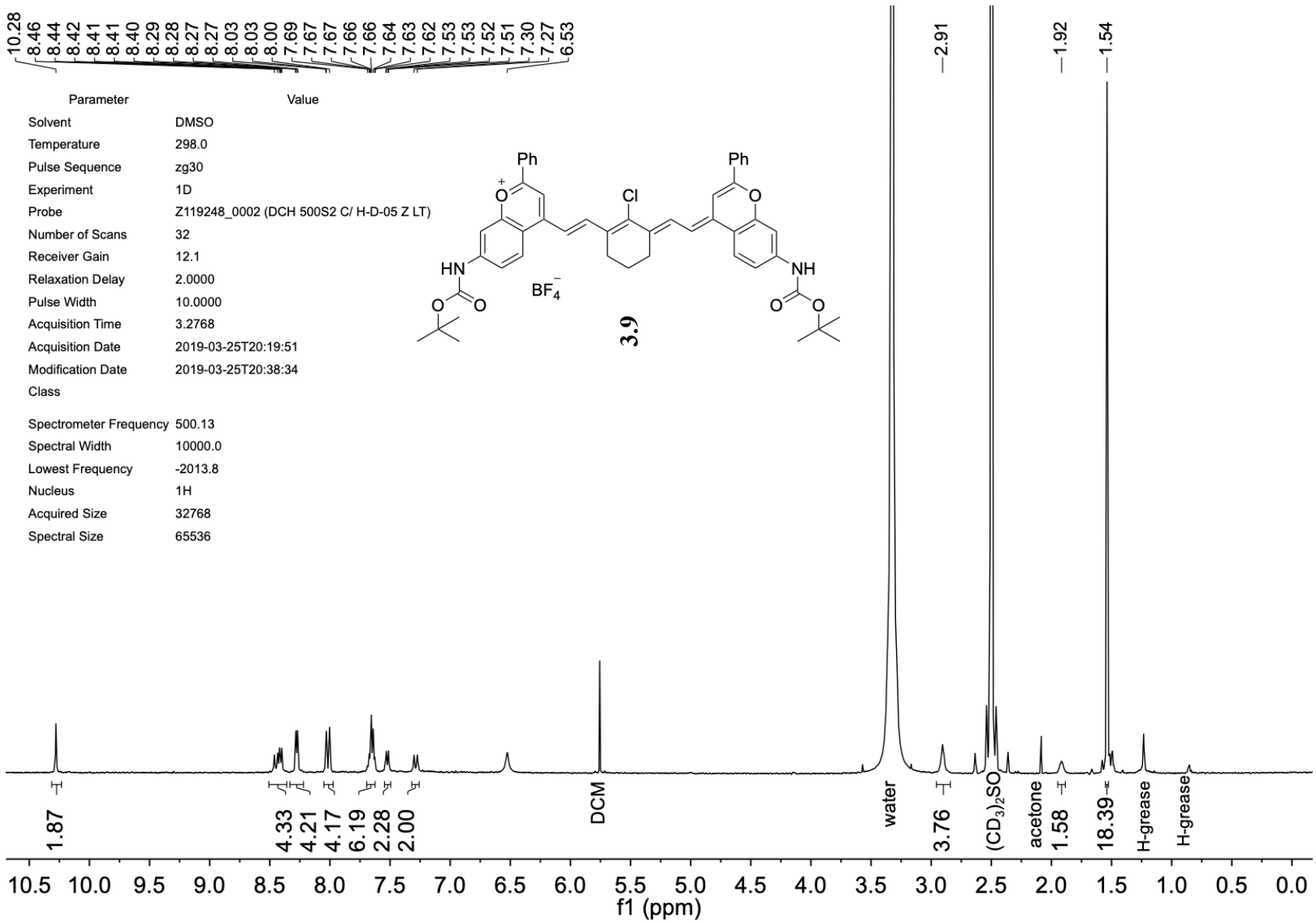
10.28
8.46
8.44
8.42
8.41
8.41
8.40
8.29
8.28
8.27
8.27
8.03
8.03
8.00
7.69
7.67
7.67
7.66
7.66
7.64
7.63
7.62
7.53
7.53
7.52
7.51
7.30
7.27
6.53
2.91
1.92
1.54
Parameter Value
Solvent DMSO
Temperature 298.0
Pulse Sequence zg30
Experiment 1D
Probe Z119248_0002 (DCH 500S2 C/ H-D-05 Z LT)
Number of Scans 32
Receiver Gain 12.1
Relaxation Delay 2.0000
Pulse Width 10.0000
Acquisition Time 3.2768
Acquisition Date 2019-03-25T20:19:51
Modification Date 2019-03-25T20:38:34
Class
Spectrometer Frequency 500.13
Spectral Width 10000.0
Lowest Frequency -2013.8
Nucleus 1H
Acquired Size 32768
Spectral Size 65536
Ph
Ph
Cl
HN
NH
BF4−
3.9
1.87
4.33
4.21
4.17
6.19
2.28
2.00
DCM
water
3.76
(CD3)2SO
acetone
1.58
18.39
H-grease
H-grease
10.5 10.0 9.5 9.0 8.5 8.0 7.5 7.0 6.5 6.0 5.5 5.0 4.5 4.0 3.5 3.0 2.5 2.0 1.5 1.0 0.5 0.0
f1 (ppm)

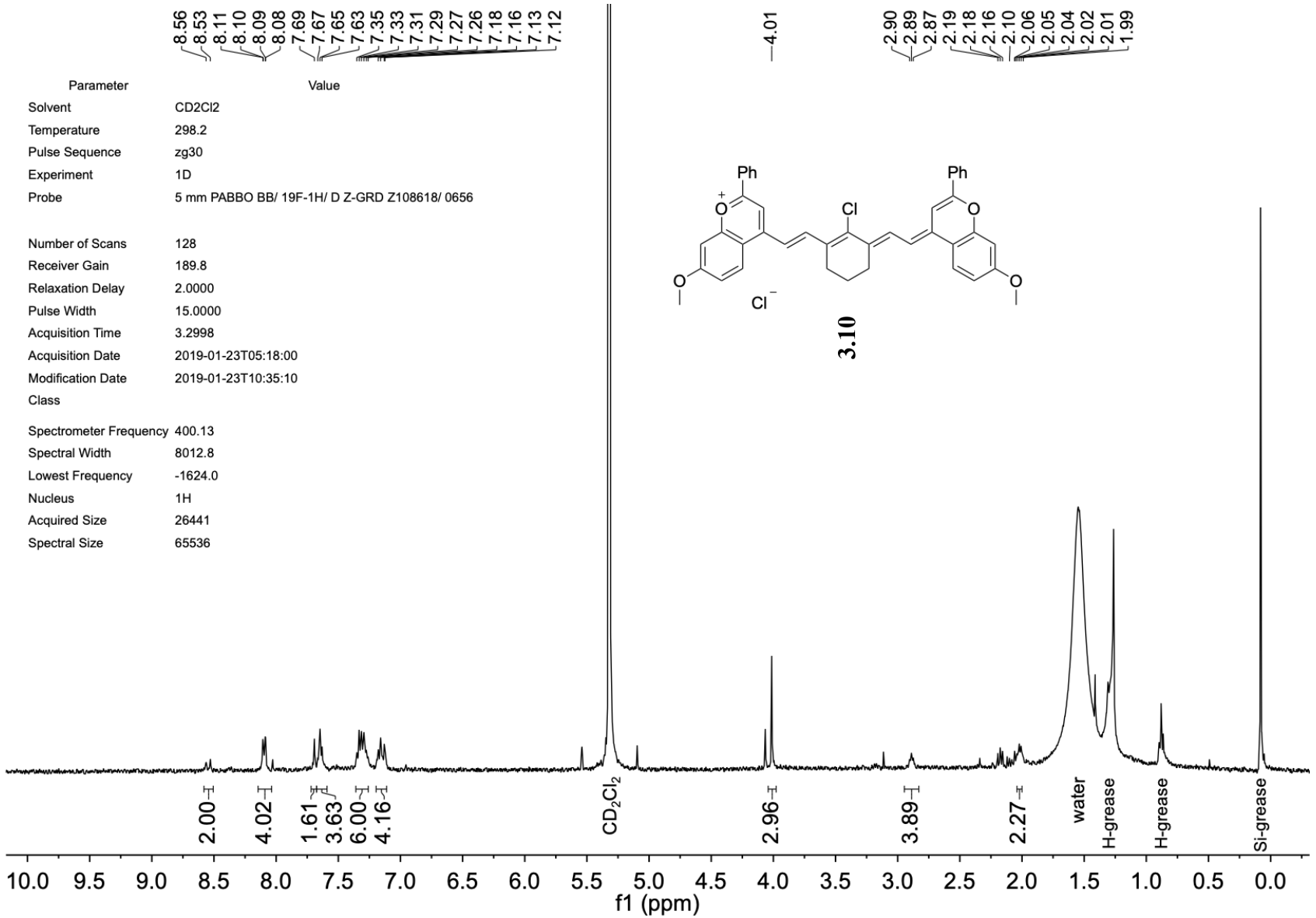
8.56
8.53
8.11
8.10
8.09
8.08
7.69
7.67
7.65
7.63
7.35
7.33
7.31
7.29
7.27
7.26
7.18
7.16
7.13
7.12
4.01
2.90
2.89
2.87
2.19
2.18
2.16
2.10
2.06
2.05
2.04
2.02
2.01
1.99
Parameter
Value
Solvent CD2Cl2
Temperature 298.2
Pulse Sequence zg30
Experiment 1D
Probe 5 mm PABBO BB/ 19F-1H/ D Z-GRD Z108618/ 0656
Number of Scans 128
Receiver Gain 189.8
Relaxation Delay 2.0000
Pulse Width 15.0000
Acquisition Time 3.2998
Acquisition Date 2019-01-23T05:18:00
Modification Date 2019-01-23T10:35:10
Class
Spectrometer Frequency 400.13
Spectral Width 8012.8
Lowest Frequency -1624.0
Nucleus 1H
Acquired Size 26441
Spectral Size 65536
Ph
Ph
Cl
O
O
O
O
Cl⁻
3.10
2.00
4.02
1.61
3.63
6.00
4.16
CD2Cl2
2.96
3.89
2.27
water
H-grease
H-grease
Si-grease
10.0 9.5 9.0 8.5 8.0 7.5 7.0 6.5 6.0 5.5 5.0 4.5 4.0 3.5 3.0 2.5 2.0 1.5 1.0 0.5 0.0
f1 (ppm)

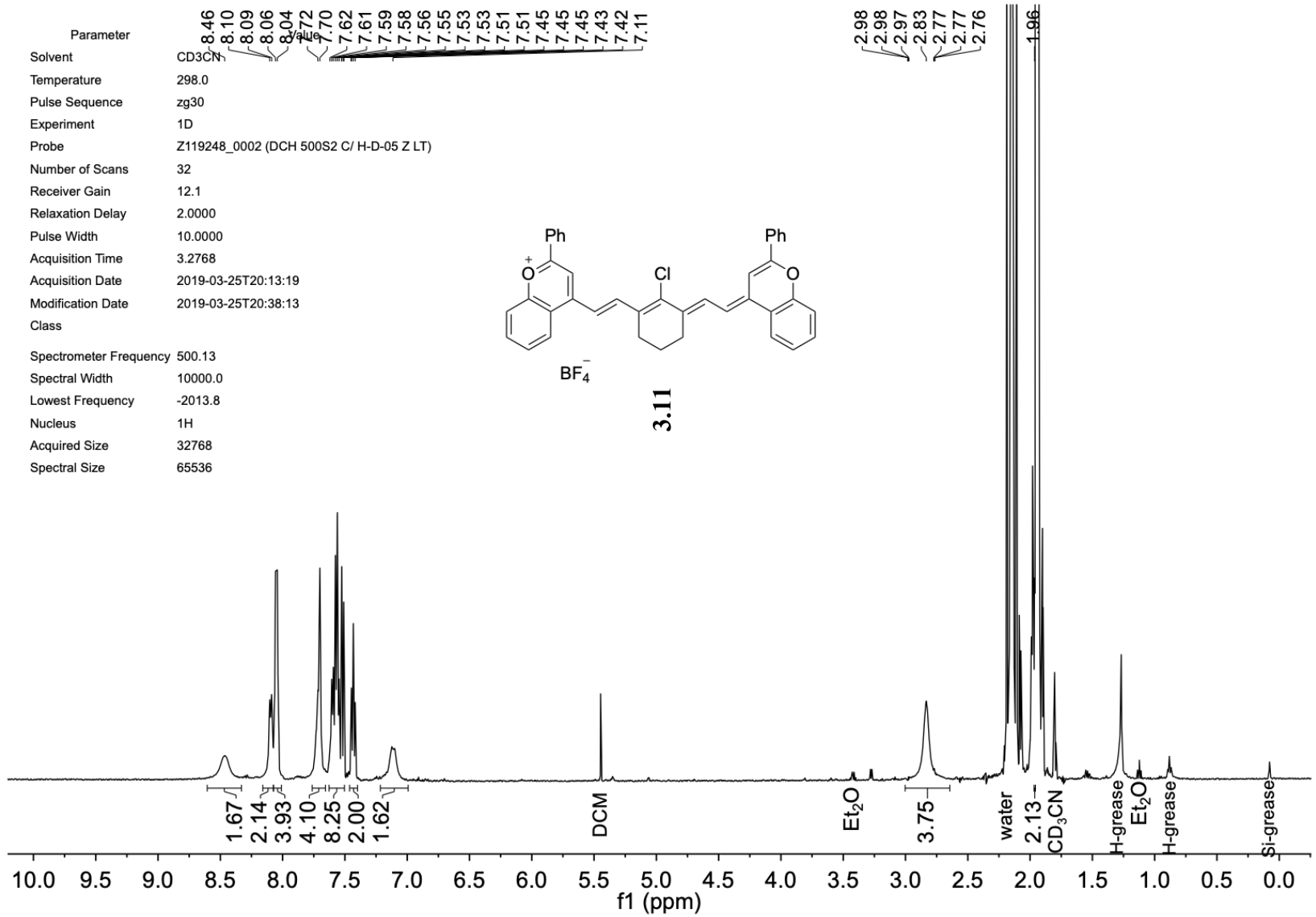
Parameter Value
Solvent CD3CN
Temperature 298.0
Pulse Sequence zg30
Experiment 1D
Probe Z119248_0002 (DCH 500S2 C/ H-D-05 Z LT)
Number of Scans 32
Receiver Gain 12.1
Relaxation Delay 2.0000
Pulse Width 10.0000
Acquisition Time 3.2768
Acquisition Date 2019-03-25T20:13:19
Modification Date 2019-03-25T20:38:13
Class
Spectrometer Frequency 500.13
Spectral Width 10000.0
Lowest Frequency -2013.8
Nucleus 1H
Acquired Size 32768
Spectral Size 65536
8.46 8.10 8.09 8.06 8.04 7.72 7.70 7.62 7.61 7.59 7.58 7.56 7.55 7.53 7.53 7.51 7.51 7.45 7.45 7.45 7.43 7.42 7.11
2.98 2.98 2.97 2.83 2.77 2.77 2.76 1.96
Ph
O
Cl
Ph
O
BF4−
3.11
1.67 2.14 3.93 4.10 8.25 2.00 1.62
DCM
Et2O
3.75
water
2.13
CD3CN
H-grease
Et2O
H-grease
Si-grease
10.0 9.5 9.0 8.5 8.0 7.5 7.0 6.5 6.0 5.5 5.0 4.5 4.0 3.5 3.0 2.5 2.0 1.5 1.0 0.5 0.0
f1 (ppm)

3.7.2 ^{13}C NMR Spectra

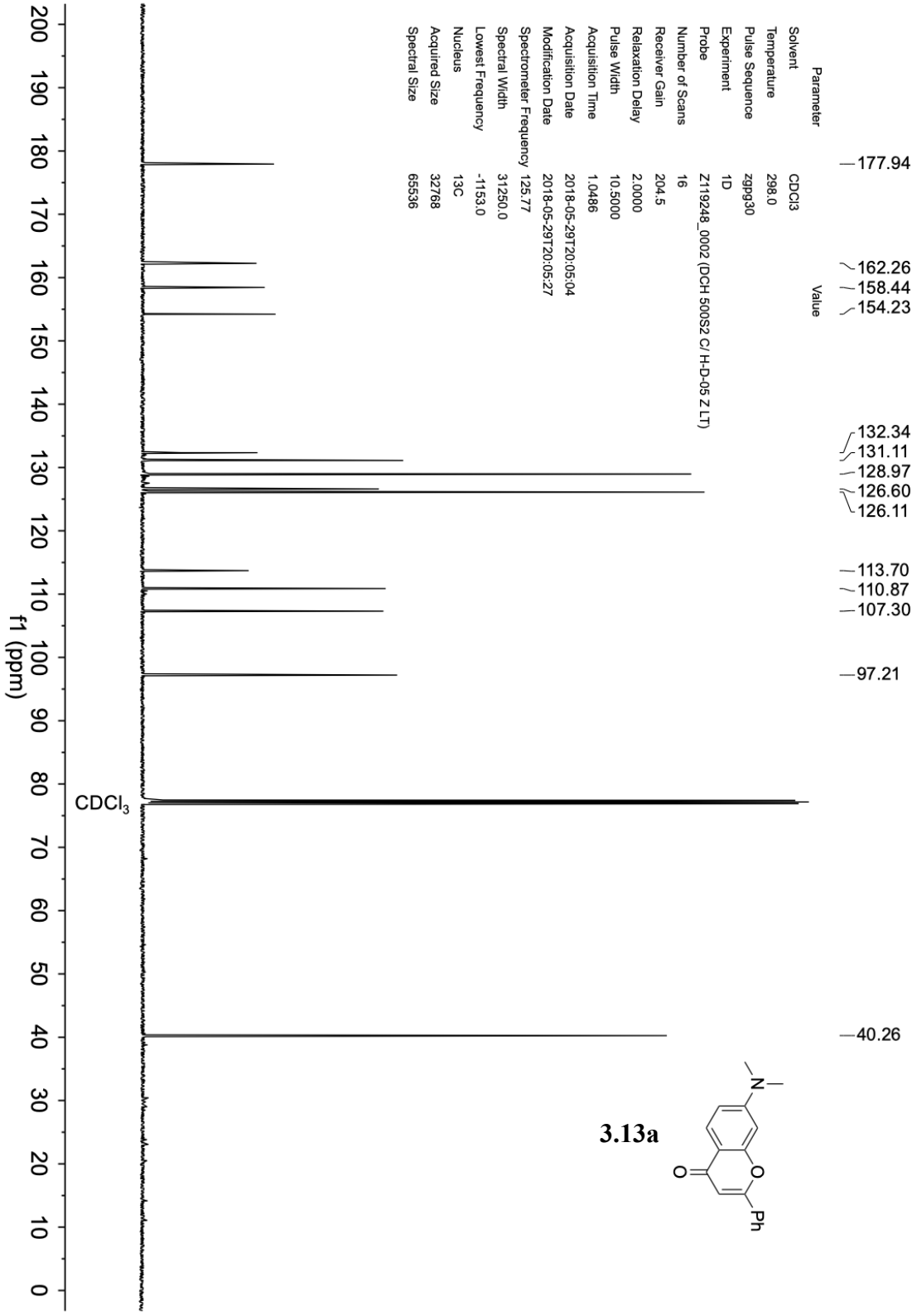

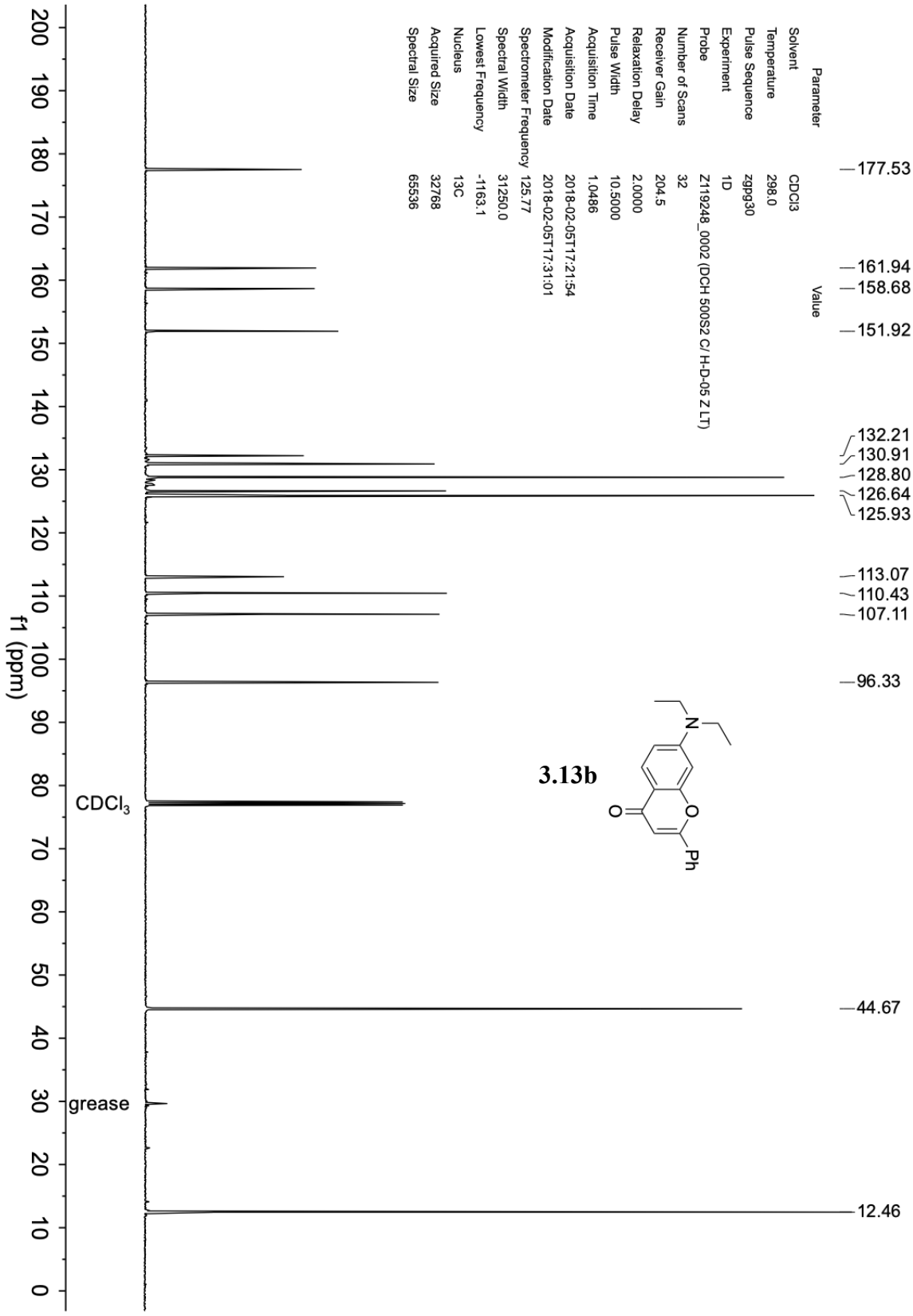
Parameter
Value
Solvent
CDCl3
Temperature
298.0
Pulse Sequence
zgpg30
Experiment
1D
Probe
Z119248_0002 (DCH 500S2 C/ H-D-05 Z LT)
Number of Scans
32
Receiver Gain
204.5
Relaxation Delay
2.0000
Pulse Width
10.5000
Acquisition Time
1.0486
Acquisition Date
2018-02-05T17:21:54
Modification Date
2018-02-05T17:31:01
Spectrometer Frequency
125.77
Spectral Width
31250.0
Lowest Frequency
-1163.1
Nucleus
13C
Acquired Size
32768
Spectral Size
65536
177.53
161.94
158.68
151.92
132.21
130.91
128.80
126.64
125.93
113.07
110.43
107.11
96.33
44.67
12.46
3.13b
N
O
O
Ph
CDCl3
grease
f1 (ppm)
200
190
180
170
160
150
140
130
120
110
100
90
80
70
60
50
40
30
20
10
0

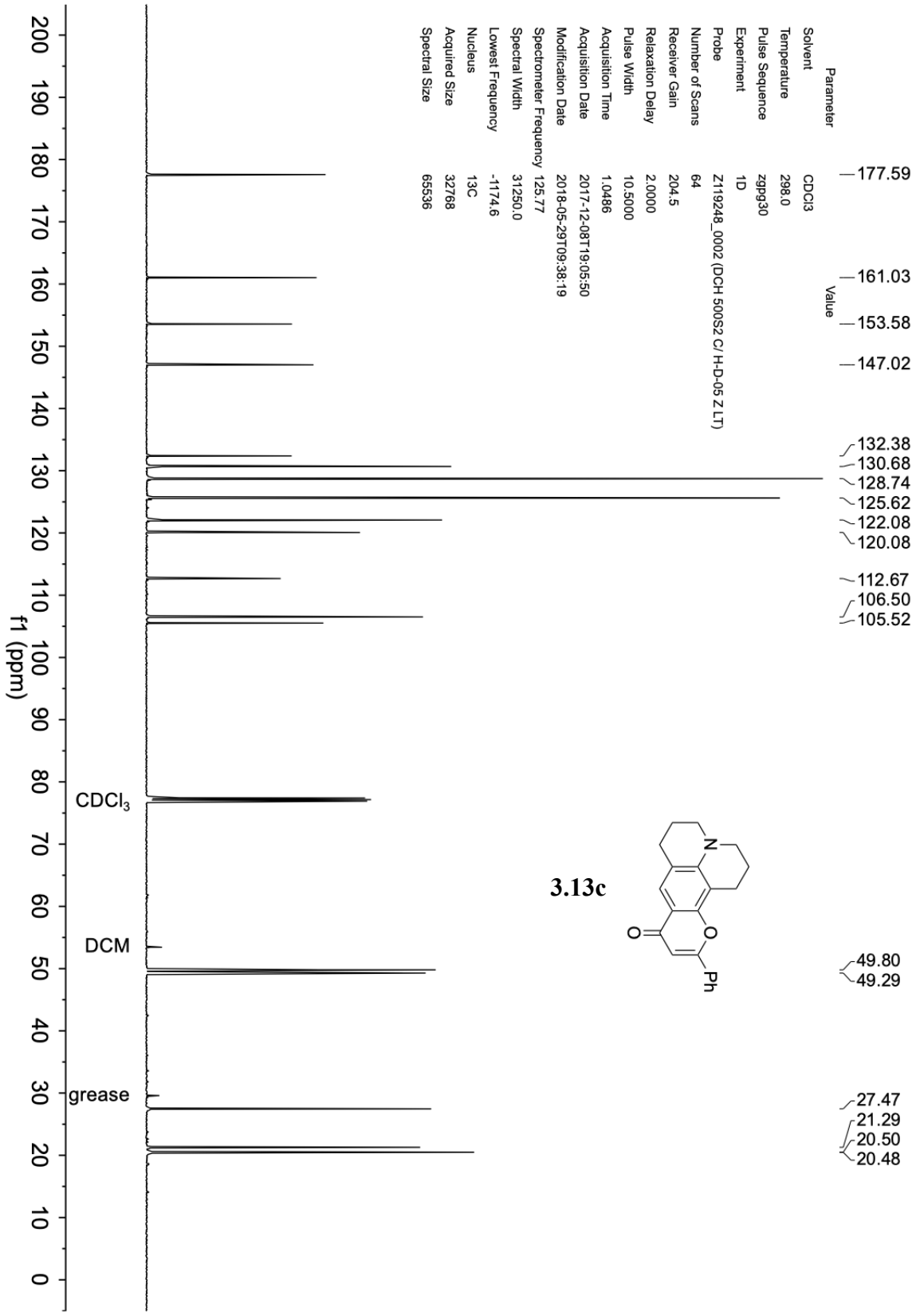
Parameter
Value
Solvent CDCl3
Temperature 298.0
Pulse Sequence zgpg30
Experiment 1D
Probe Z119248_0002 (DCH 500S2 C/ H-D-05 Z LT)
Number of Scans 64
Receiver Gain 204.5
Relaxation Delay 2.0000
Pulse Width 10.5000
Acquisition Time 1.0486
Acquisition Date 2017-12-08T19:05:50
Modification Date 2018-05-29T09:38:19
Spectrometer Frequency 125.77
Spectral Width 31250.0
Lowest Frequency -1174.6
Nucleus 13C
Acquired Size 32768
Spectral Size 65536
177.59
161.03
153.58
147.02
132.38
130.68
128.74
125.62
122.08
120.08
112.67
106.50
105.52
49.80
49.29
27.47
21.29
20.50
20.48
CDCl3
DCM
grease
f1 (ppm)
3.13c
N
O
O
Ph

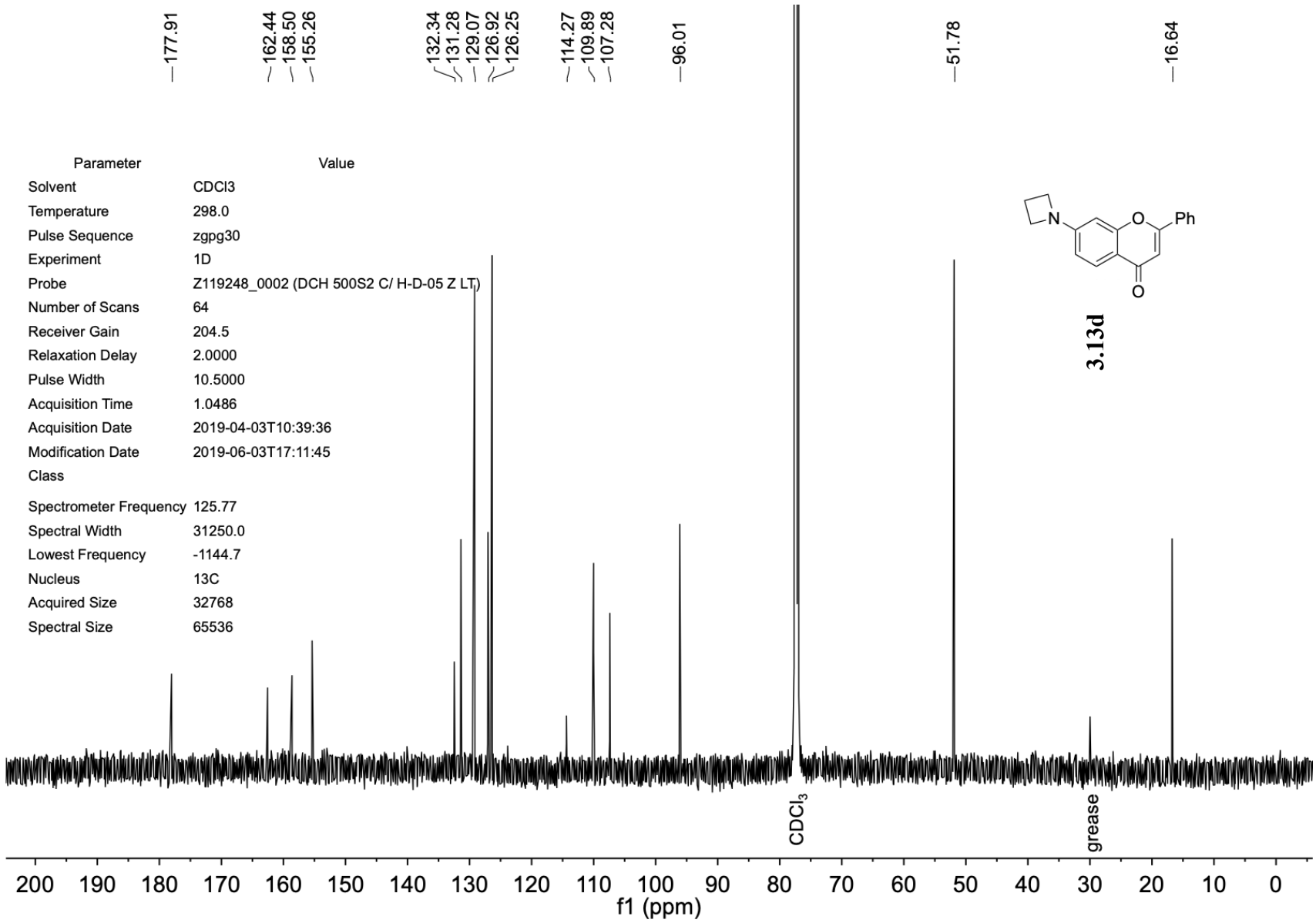
177.91
162.44
158.50
155.26
132.34
131.28
129.07
126.92
126.25
114.27
109.89
107.28
96.01
51.78
16.64
Parameter Value
Solvent CDCl3
Temperature 298.0
Pulse Sequence zgpg30
Experiment 1D
Probe Z119248_0002 (DCH 500S2 C/ H-D-05 Z LT)
Number of Scans 64
Receiver Gain 204.5
Relaxation Delay 2.0000
Pulse Width 10.5000
Acquisition Time 1.0486
Acquisition Date 2019-04-03T10:39:36
Modification Date 2019-06-03T17:11:45
Class
Spectrometer Frequency 125.77
Spectral Width 31250.0
Lowest Frequency -1144.7
Nucleus 13C
Acquired Size 32768
Spectral Size 65536
N
O
Ph
O
3.13d
CDCl3
grease
200 190 180 170 160 150 140 130 120 110 100 90 80 70 60 50 40 30 20 10 0
f1 (ppm)

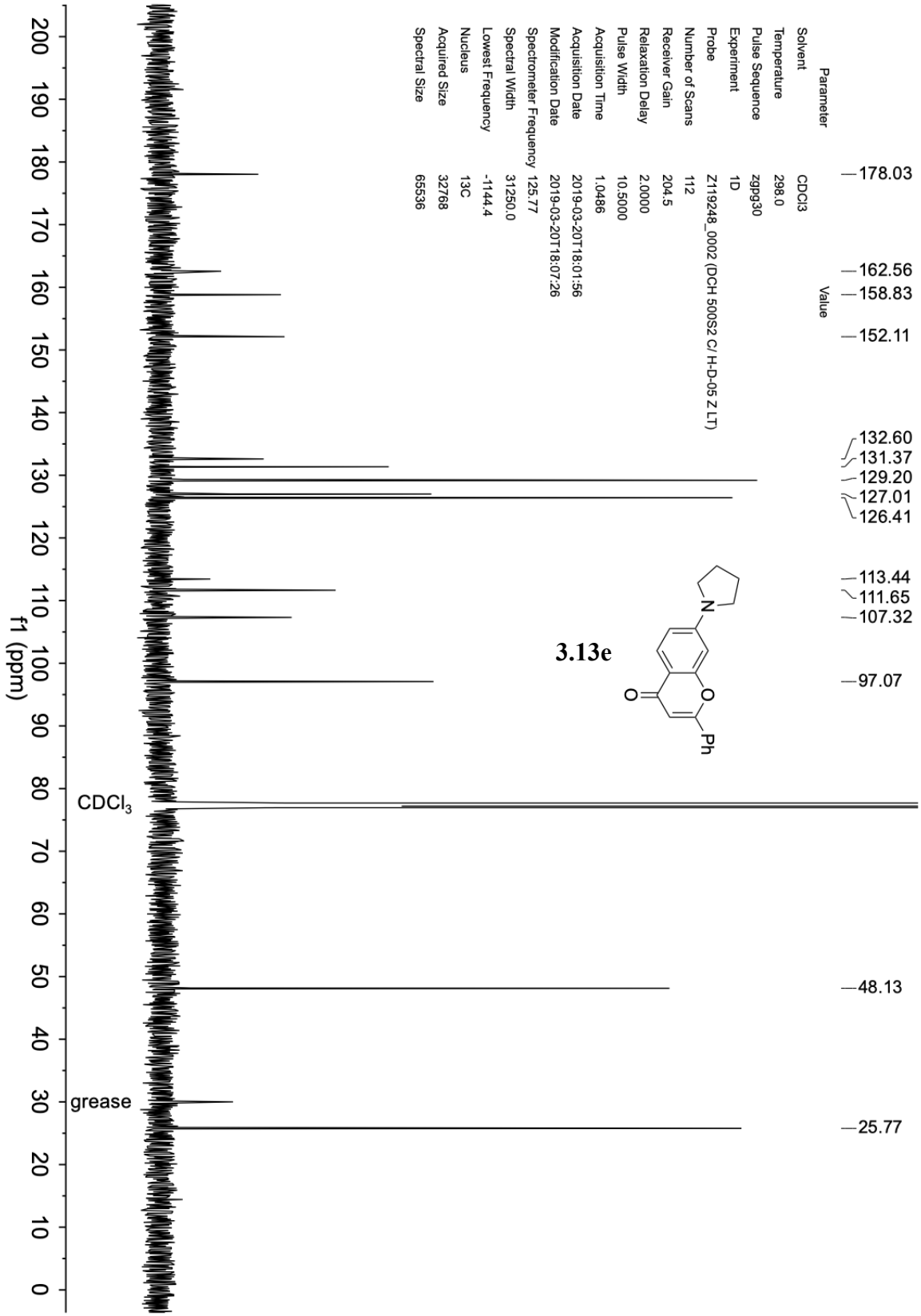
Parameter
Value
Solvent
CDCl3
Temperature
298.0
Pulse Sequence
zgpg30
Experiment
1D
Probe
Z119248_0002 (DCH 500S2 C/ H-D-05 Z LT)
Number of Scans
112
Receiver Gain
204.5
Relaxation Delay
2.0000
Pulse Width
10.5000
Acquisition Time
1.0486
Acquisition Date
2019-03-20T18:01:56
Modification Date
2019-03-20T18:07:26
Spectrometer Frequency
125.77
Spectral Width
31250.0
Lowest Frequency
-1144.4
Nucleus
13C
Acquired Size
32768
Spectral Size
65536
178.03
162.56
158.83
152.11
132.60
131.37
129.20
127.01
126.41
113.44
111.65
107.32
97.07
48.13
25.77
3.13e
N
O
O
Ph
CDCl3
grease
f1 (ppm)
200
190
180
170
160
150
140
130
120
110
100
90
80
70
60
50
40
30
20
10
0

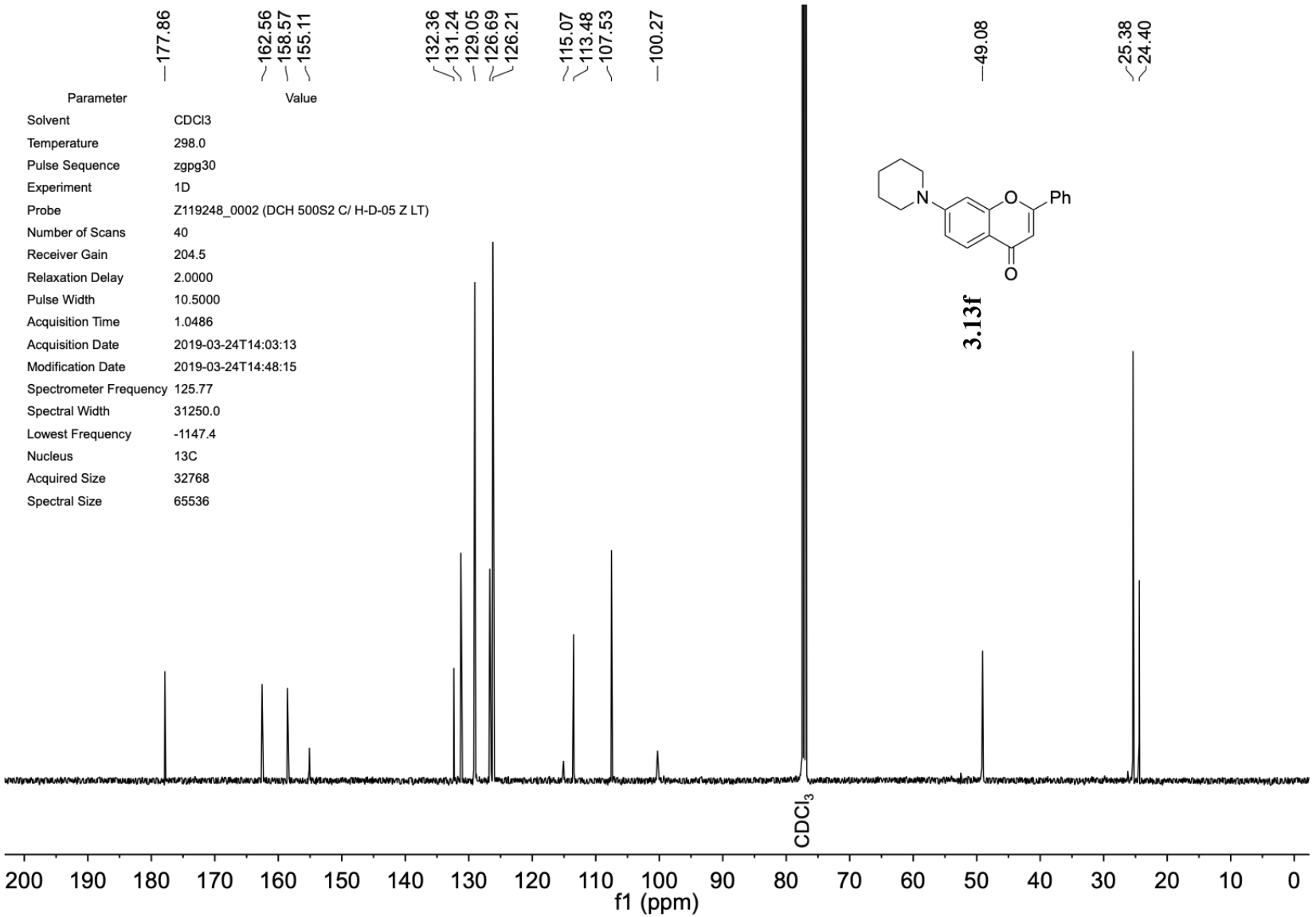
177.86
162.56
158.57
155.11
132.36
131.24
129.05
126.69
126.21
115.07
113.48
107.53
100.27
49.08
25.38
24.40
Parameter Value
Solvent CDCl3
Temperature 298.0
Pulse Sequence zgpg30
Experiment 1D
Probe Z119248_0002 (DCH 500S2 C/ H-D-05 Z LT)
Number of Scans 40
Receiver Gain 204.5
Relaxation Delay 2.0000
Pulse Width 10.5000
Acquisition Time 1.0486
Acquisition Date 2019-03-24T14:03:13
Modification Date 2019-03-24T14:48:15
Spectrometer Frequency 125.77
Spectral Width 31250.0
Lowest Frequency -1147.4
Nucleus 13C
Acquired Size 32768
Spectral Size 65536
N
O
Ph
O
3.13f
CDCl3
200 190 180 170 160 150 140 130 120 110 100 90 80 70 60 50 40 30 20 10 0
f1 (ppm)

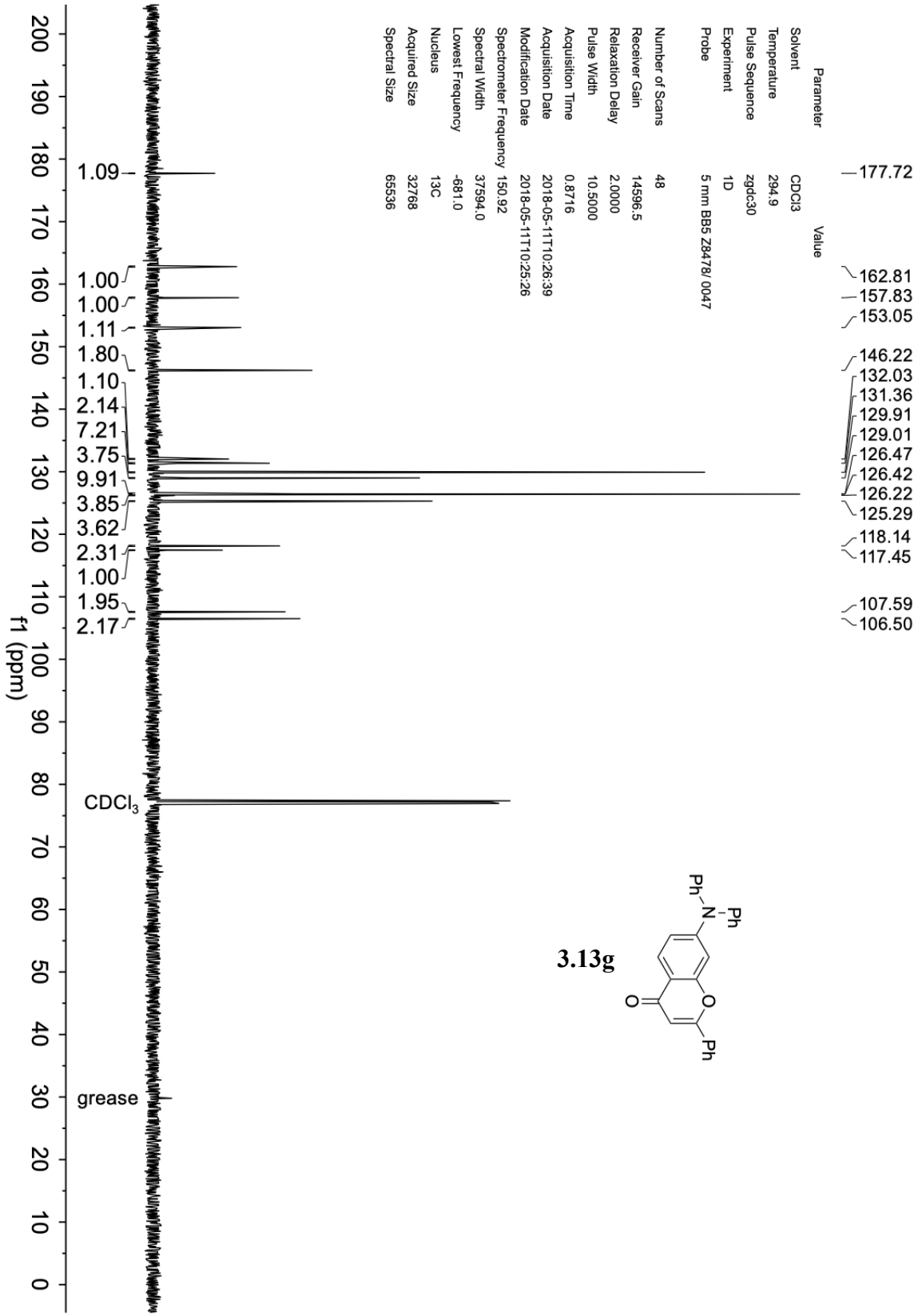
Parameter
Value
Solvent
CDCl3
Temperature
294.9
Pulse Sequence
zgdc30
Experiment
1D
Probe
5 mm BB5 Z84781 0047
Number of Scans
48
Receiver Gain
14596.5
Relaxation Delay
2.0000
Pulse Width
10.5000
Acquisition Time
0.8716
Acquisition Date
2018-05-11T10:26:39
Modification Date
2018-05-11T10:25:26
Spectrometer Frequency
150.92
Spectral Width
37594.0
Lowest Frequency
-681.0
Nucleus
13C
Acquired Size
32768
Spectral Size
65536
177.72
162.81
157.83
153.05
146.22
132.03
131.36
129.91
129.01
126.47
126.42
126.22
125.29
118.14
117.45
107.59
106.50
1.09
1.00
1.00
1.11
1.80
1.10
2.14
7.21
3.75
9.91
3.85
3.62
2.31
1.00
1.95
2.17
CDCl3
grease
f1 (ppm)
3.13g
Ph
N
Ph
O
O
Ph

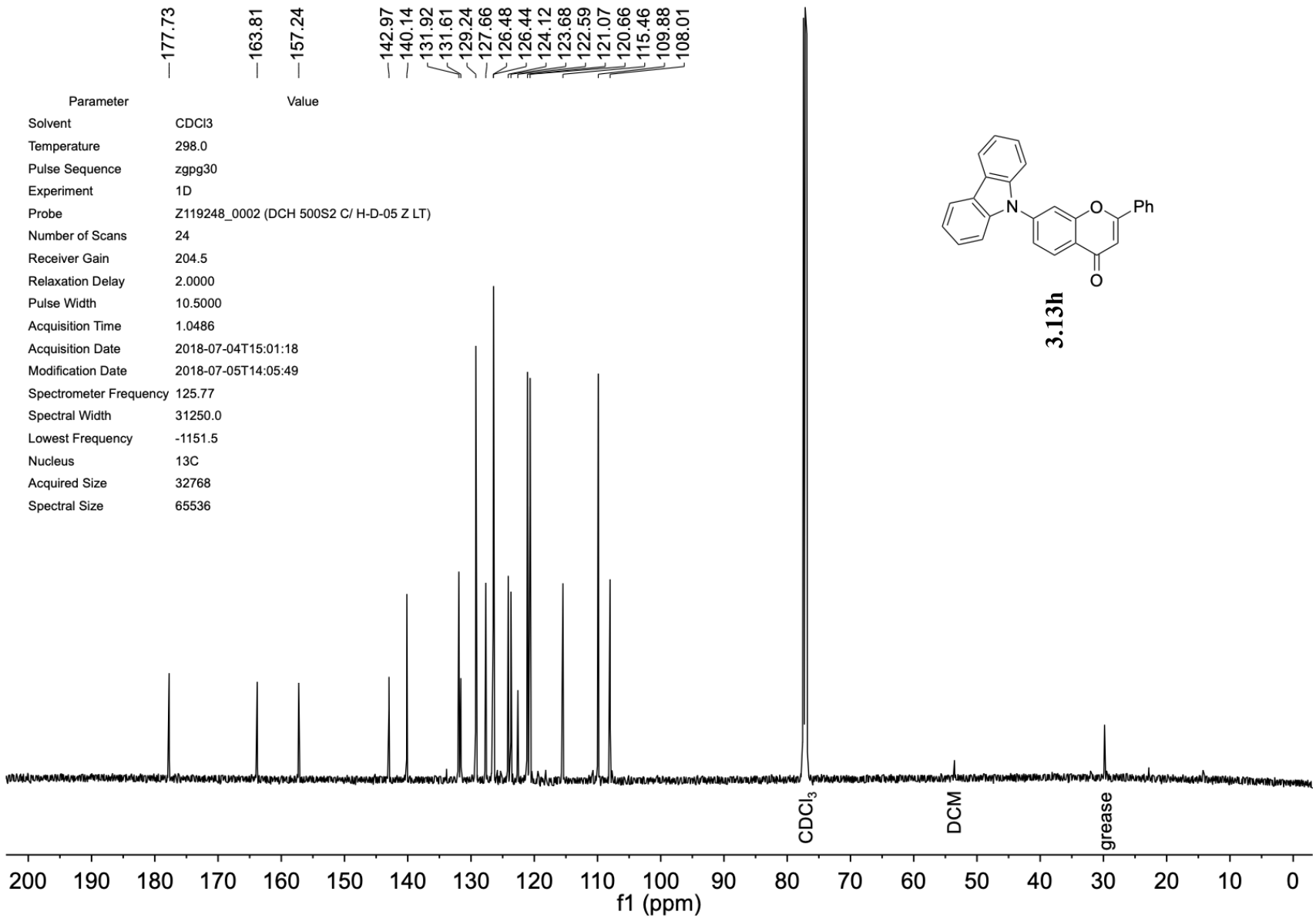
177.73
163.81
157.24
142.97
140.14
131.92
131.61
129.24
127.66
126.48
126.44
124.12
123.68
122.59
121.07
120.66
115.46
109.88
108.01
Parameter Value
Solvent CDCl3
Temperature 298.0
Pulse Sequence zgpg30
Experiment 1D
Probe Z119248_0002 (DCH 500S2 C/ H-D-05 Z LT)
Number of Scans 24
Receiver Gain 204.5
Relaxation Delay 2.0000
Pulse Width 10.5000
Acquisition Time 1.0486
Acquisition Date 2018-07-04T15:01:18
Modification Date 2018-07-05T14:05:49
Spectrometer Frequency 125.77
Spectral Width 31250.0
Lowest Frequency -1151.5
Nucleus 13C
Acquired Size 32768
Spectral Size 65536
N
O
Ph
O
3.13h
CDCl3
DCM
grease
200 190 180 170 160 150 140 130 120 110 100 90 80 70 60 50 40 30 20 10 0
f1 (ppm)

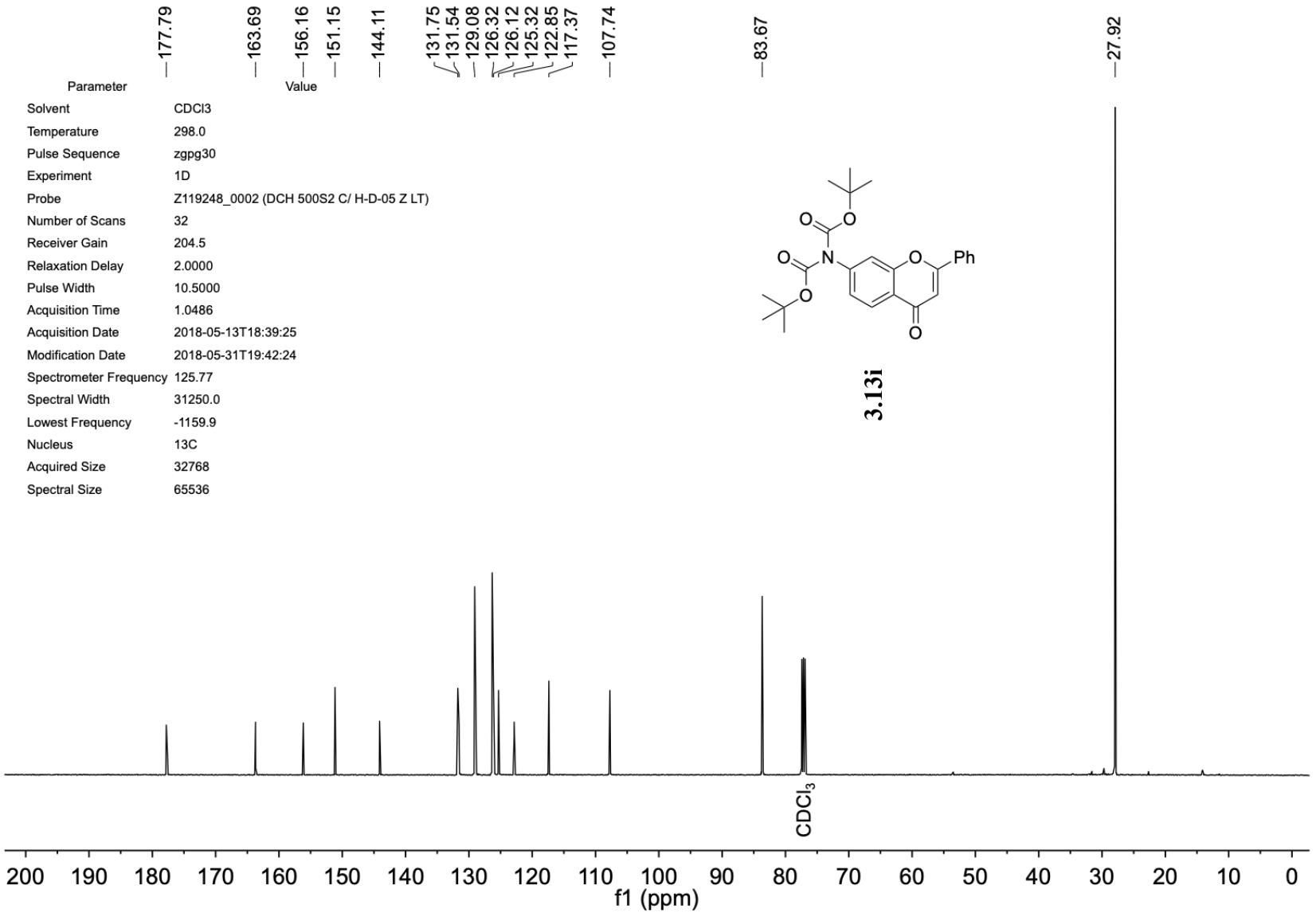
177.79
163.69
156.16
151.15
144.11
131.75
131.54
129.08
126.32
126.12
125.32
122.85
117.37
107.74
83.67
27.92
Parameter
Value
Solvent CDCl3
Temperature 298.0
Pulse Sequence zgpg30
Experiment 1D
Probe Z119248_0002 (DCH 500S2 C/ H-D-05 Z LT)
Number of Scans 32
Receiver Gain 204.5
Relaxation Delay 2.0000
Pulse Width 10.5000
Acquisition Time 1.0486
Acquisition Date 2018-05-13T18:39:25
Modification Date 2018-05-31T19:42:24
Spectrometer Frequency 125.77
Spectral Width 31250.0
Lowest Frequency -1159.9
Nucleus 13C
Acquired Size 32768
Spectral Size 65536
O
O
O
N
O
Ph
O
O
O
3.13i
CDCl3
200 190 180 170 160 150 140 130 120 110 100 90 80 70 60 50 40 30 20 10 0
f1 (ppm)

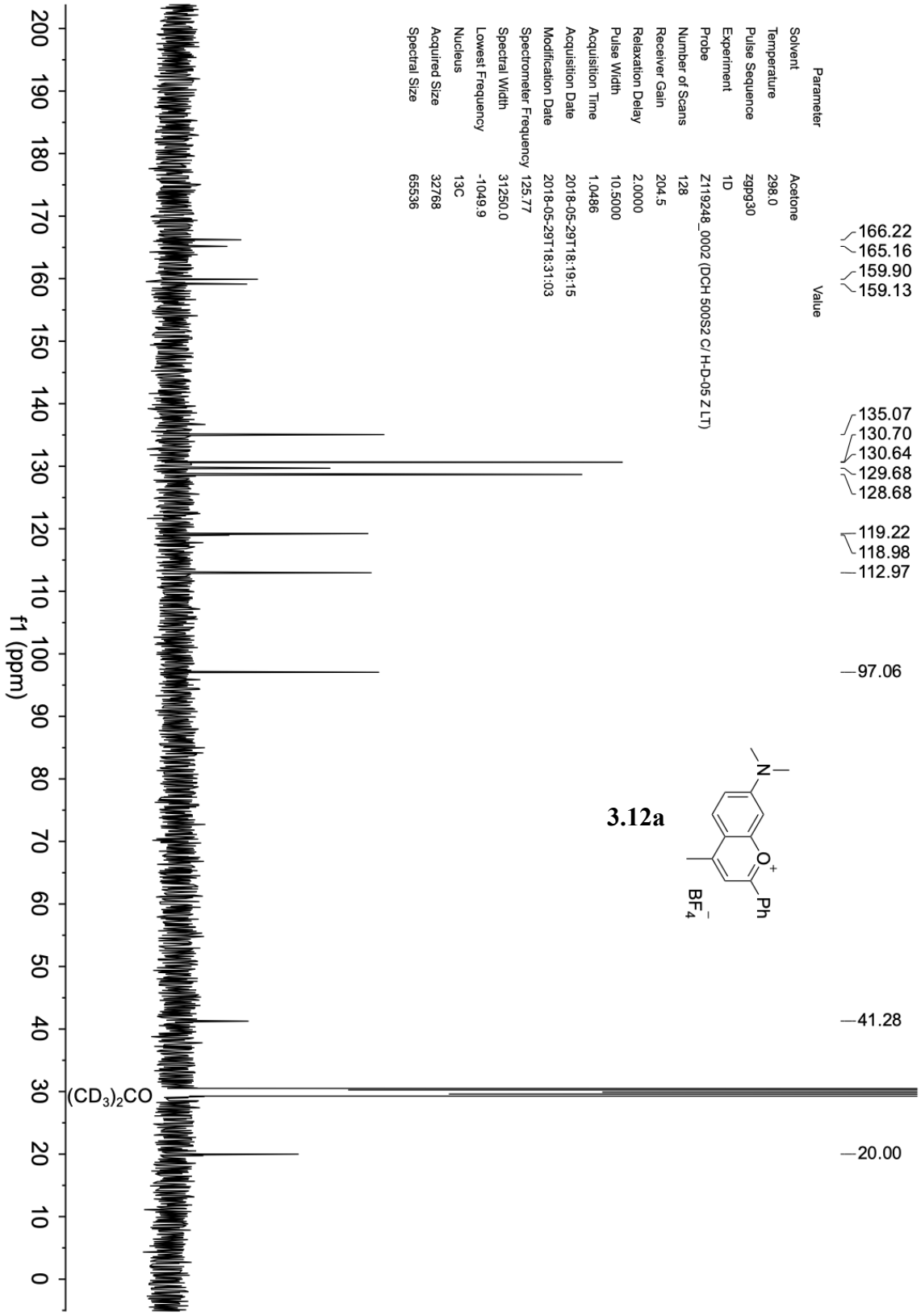
Parameter
Value
Solvent
Acetone
Temperature
298.0
Pulse Sequence
zgpg30
Experiment
1D
Probe
Z119248_0002 (DCH 500S2 C/ H-D-05 Z LT)
Number of Scans
128
Receiver Gain
204.5
Relaxation Delay
2.0000
Pulse Width
10.5000
Acquisition Time
1.0486
Acquisition Date
2018-05-29T18:19:15
Modification Date
2018-05-29T18:31:03
Spectrometer Frequency
125.77
Spectral Width
31250.0
Lowest Frequency
-1049.9
Nucleus
13C
Acquired Size
32768
Spectral Size
65536
166.22
165.16
159.90
159.13
135.07
130.70
130.64
129.68
128.68
119.22
118.98
112.97
97.06
41.28
20.00
(CD3)2CO
f1 (ppm)
3.12a
BF4−
Ph

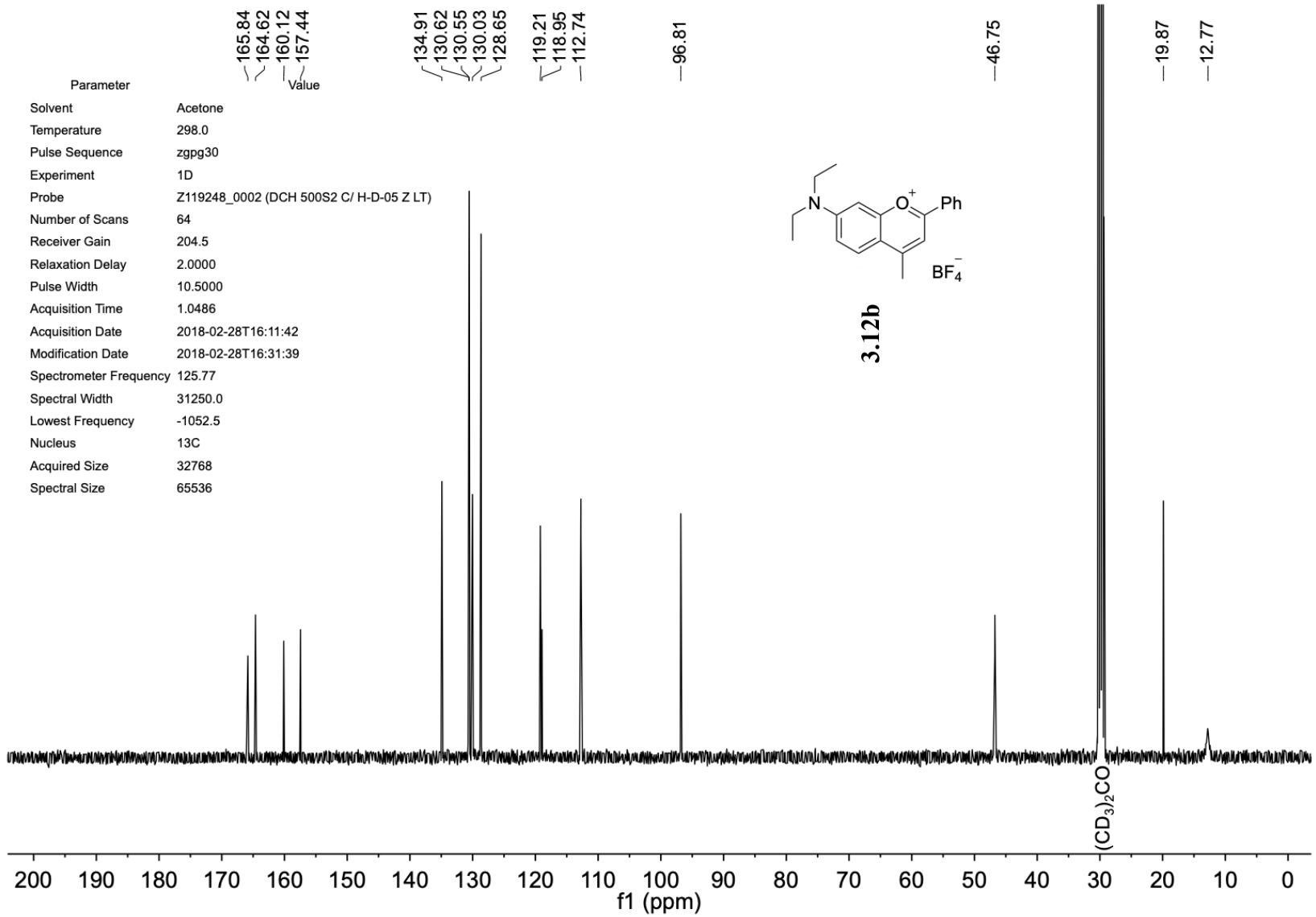
165.84
164.62
160.12
157.44
134.91
130.62
130.55
130.03
128.65
119.21
118.95
112.74
96.81
46.75
19.87
12.77
Parameter
Value
Solvent Acetone
Temperature 298.0
Pulse Sequence zgpg30
Experiment 1D
Probe Z119248_0002 (DCH 500S2 C/ H-D-05 Z LT)
Number of Scans 64
Receiver Gain 204.5
Relaxation Delay 2.0000
Pulse Width 10.5000
Acquisition Time 1.0486
Acquisition Date 2018-02-28T16:11:42
Modification Date 2018-02-28T16:31:39
Spectrometer Frequency 125.77
Spectral Width 31250.0
Lowest Frequency -1052.5
Nucleus 13C
Acquired Size 32768
Spectral Size 65536
N
O+
Ph
BF4−
3.12b
(CD3)2CO
200 190 180 170 160 150 140 130 120 110 100 90 80 70 60 50 40 30 20 10 0
f1 (ppm)

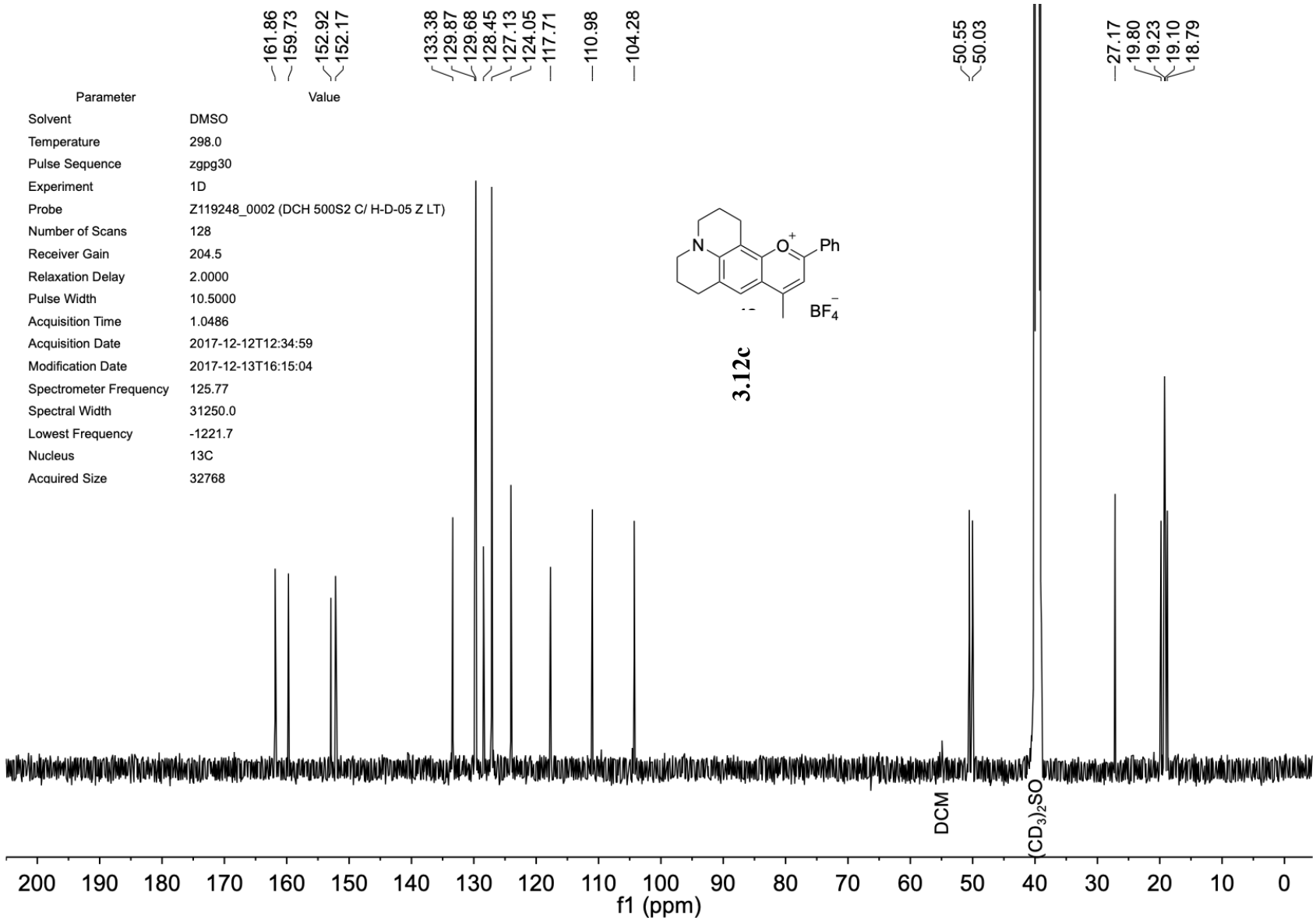
161.86
159.73
152.92
152.17
133.38
129.87
129.68
128.45
127.13
124.05
117.71
110.98
104.28
50.55
50.03
27.17
19.80
19.23
19.10
18.79
Parameter
Value
Solvent DMSO
Temperature 298.0
Pulse Sequence zgpg30
Experiment 1D
Probe Z119248_0002 (DCH 500S2 C/ H-D-05 Z LT)
Number of Scans 128
Receiver Gain 204.5
Relaxation Delay 2.0000
Pulse Width 10.5000
Acquisition Time 1.0486
Acquisition Date 2017-12-12T12:34:59
Modification Date 2017-12-13T16:15:04
Spectrometer Frequency 125.77
Spectral Width 31250.0
Lowest Frequency -1221.7
Nucleus 13C
Acquired Size 32768
N
O
Ph
BF4
3.12c
DCM
(CD3)2SO
200 190 180 170 160 150 140 130 120 110 100 90 80 70 60 50 40 30 20 10 0
f1 (ppm)

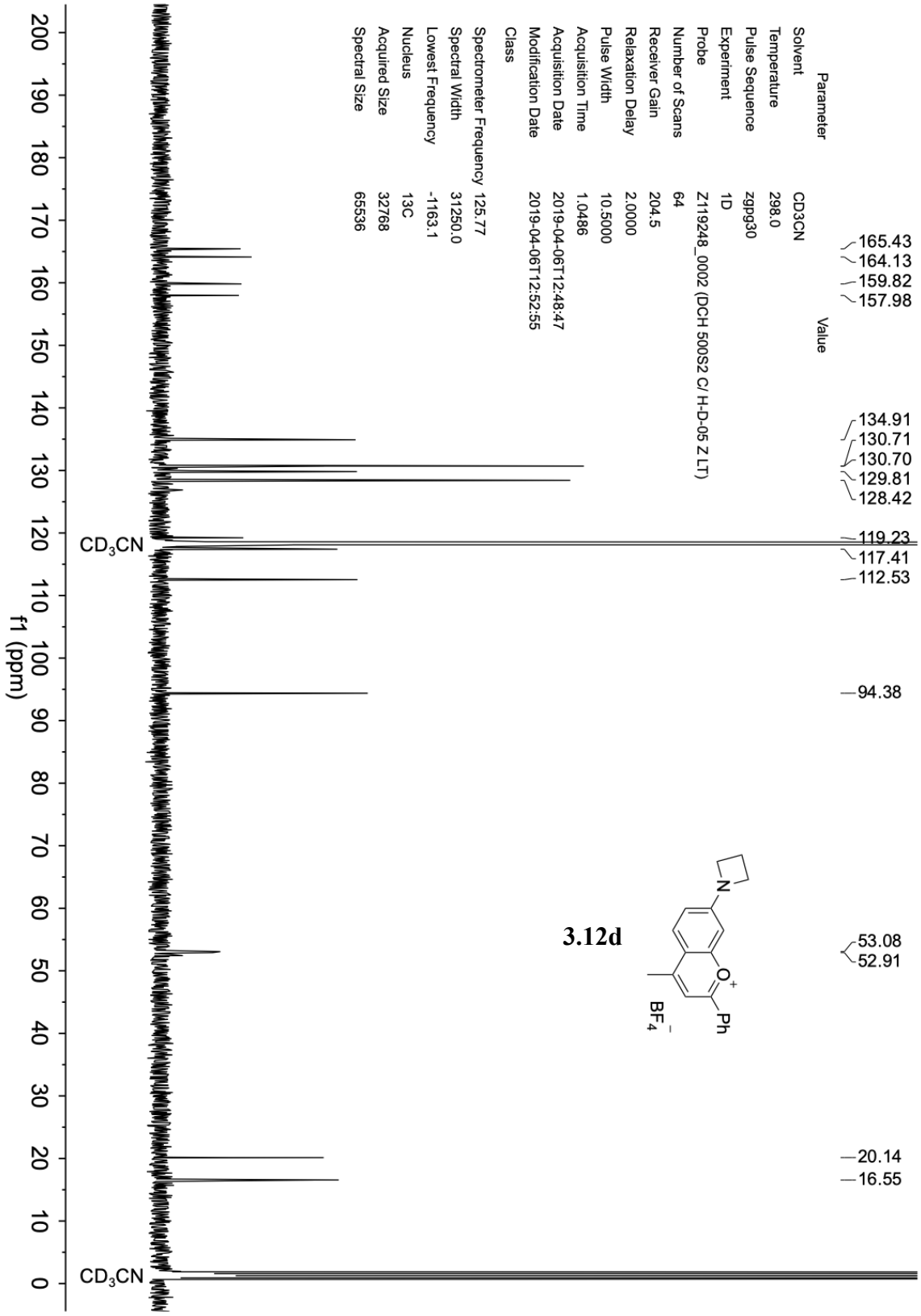
Parameter
Value
Solvent
CD3CN
Temperature
298.0
Pulse Sequence
zgpg30
Experiment
1D
Probe
Z119248_0002 (DCH 500S2 C/ H-D-05 Z LT)
Number of Scans
64
Receiver Gain
204.5
Relaxation Delay
2.0000
Pulse Width
10.5000
Acquisition Time
1.0486
Acquisition Date
2019-04-06T12:48:47
Modification Date
2019-04-06T12:52:55
Class
Spectrometer Frequency
125.77
Spectral Width
31250.0
Lowest Frequency
-1163.1
Nucleus
13C
Acquired Size
32768
Spectral Size
65536
165.43
164.13
159.82
157.98
134.91
130.71
130.70
129.81
128.42
119.23
117.41
112.53
94.38
53.08
52.91
20.14
16.55
CD3CN
CD3CN
3.12d
f1 (ppm)

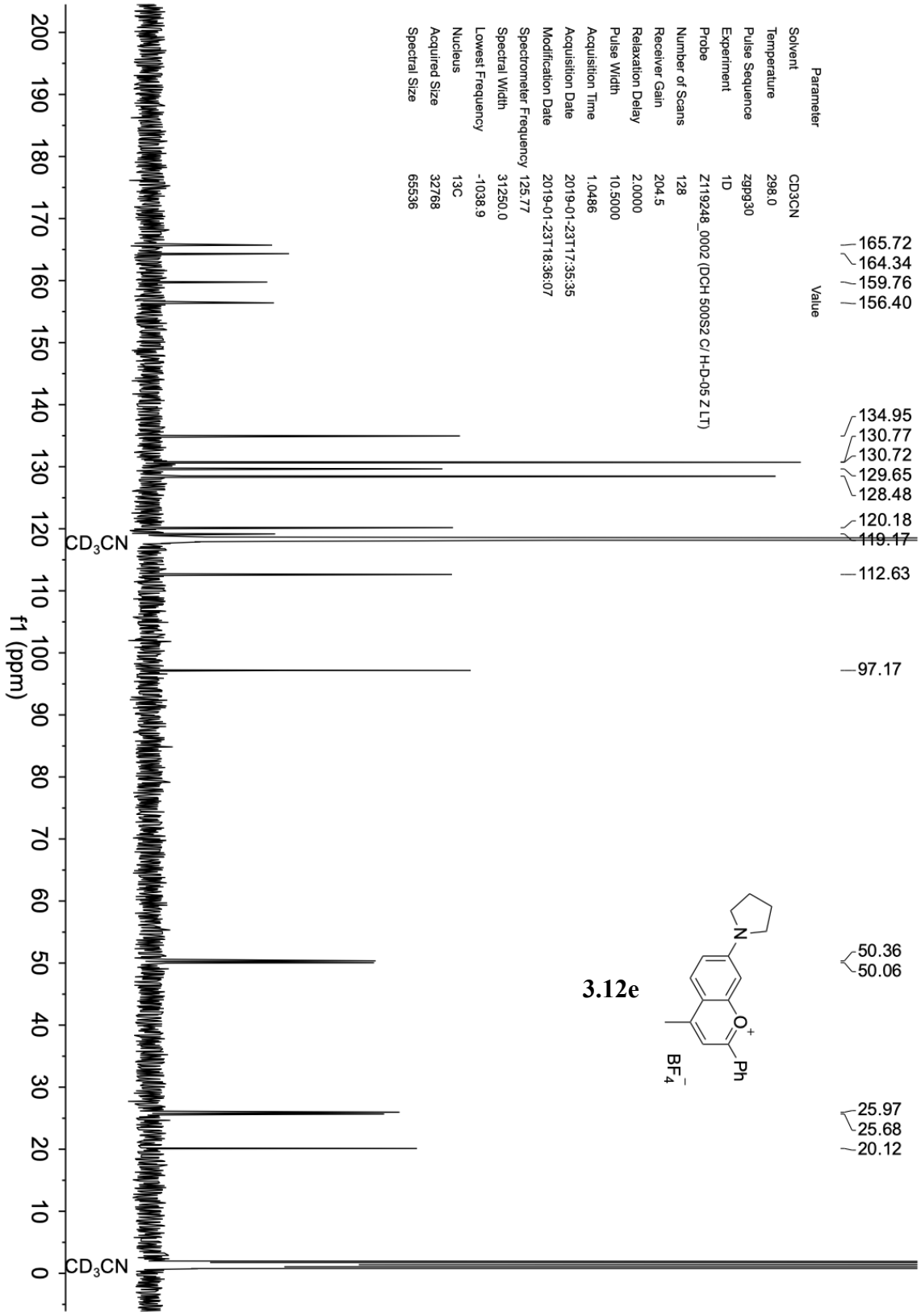
Parameter Value
Solvent CD3CN
Temperature 298.0
Pulse Sequence zgpg30
Experiment 1D
Probe Z119248_0002 (DCH 500S2 C/ H-D-05 Z LT)
Number of Scans 128
Receiver Gain 204.5
Relaxation Delay 2.0000
Pulse Width 10.5000
Acquisition Time 1.0486
Acquisition Date 2019-01-23T17:35:35
Modification Date 2019-01-23T18:36:07
Spectrometer Frequency 125.77
Spectral Width 31250.0
Lowest Frequency -1038.9
Nucleus 13C
Acquired Size 32768
Spectral Size 65536
165.72
164.34
159.76
156.40
134.95
130.77
130.72
129.65
128.48
120.18
119.17
112.63
97.17
50.36
50.06
25.97
25.68
20.12
CD3CN
CD3CN
f1 (ppm)
3.12e
N
O+
Ph
BF4−

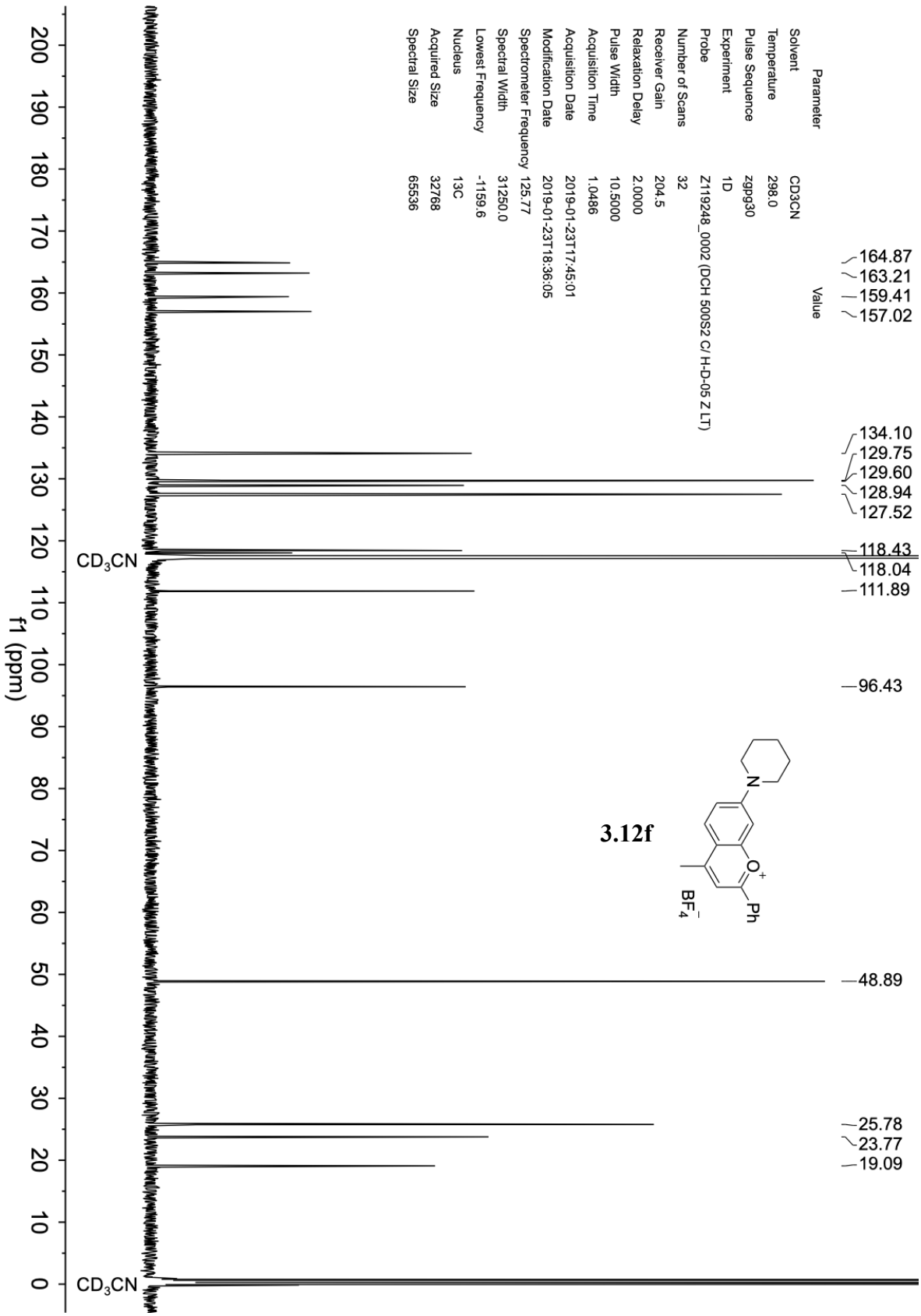
Parameter Value
Solvent CD3CN
Temperature 298.0
Pulse Sequence zgpg30
Experiment 1D
Probe Z119248_0002 (DCH 500S2 C/ H-D-05 Z LT)
Number of Scans 32
Receiver Gain 204.5
Relaxation Delay 2.0000
Pulse Width 10.5000
Acquisition Time 1.0486
Acquisition Date 2019-01-23T17:45:01
Modification Date 2019-01-23T18:36:05
Spectrometer Frequency 125.77
Spectral Width 31250.0
Lowest Frequency -1159.6
Nucleus 13C
Acquired Size 32768
Spectral Size 65536
164.87
163.21
159.41
157.02
134.10
129.75
129.60
128.94
127.52
118.43
118.04
111.89
96.43
48.89
25.78
23.77
19.09
CD3CN
CD3CN
f1 (ppm)
3.12f
N
O+
Ph
BF4−

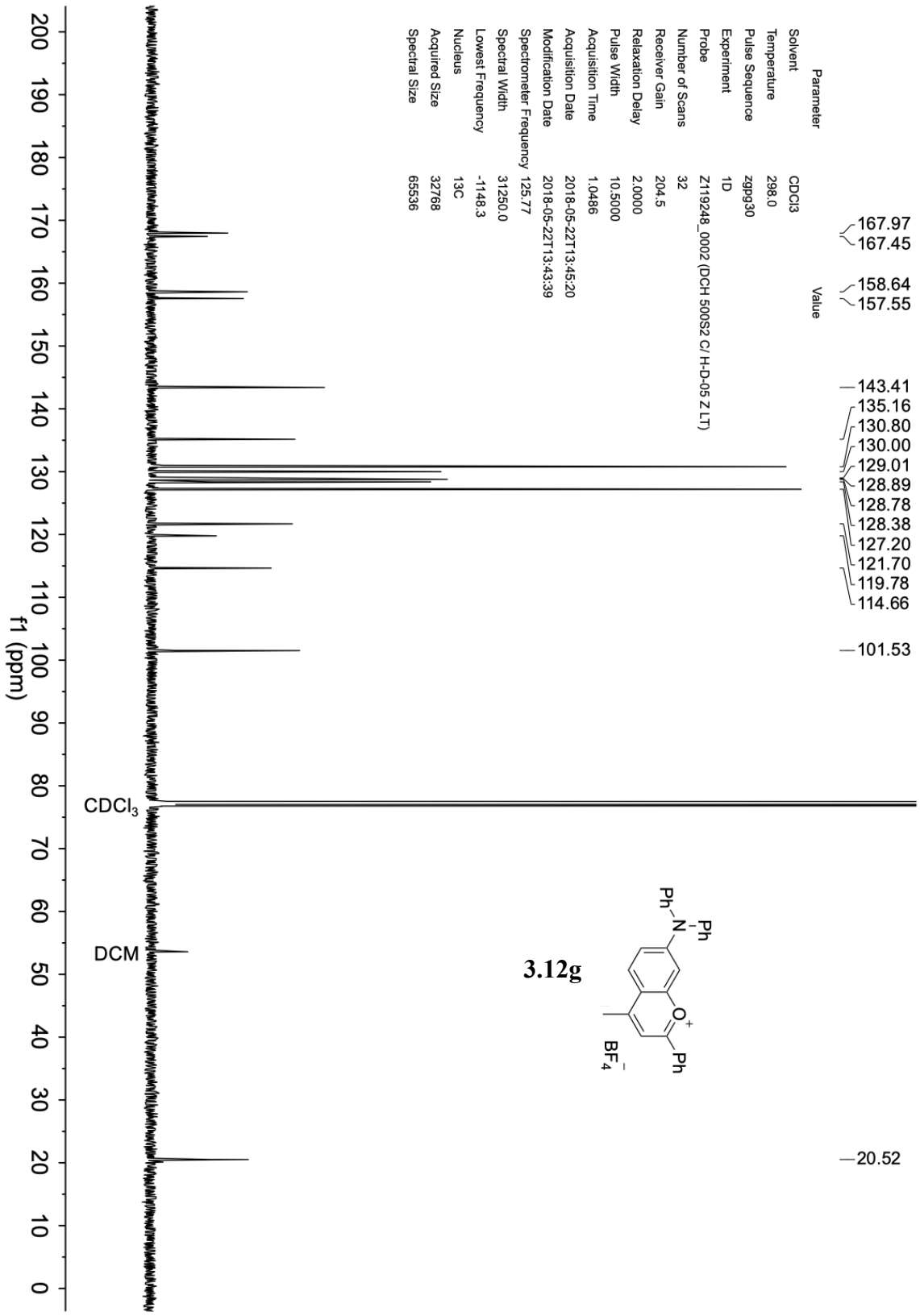
Parameter
Value
Solvent
CDCl3
Temperature
298.0
Pulse Sequence
zgpg30
Experiment
1D
Probe
Z119248_0002 (DCH 500S2 C/ H-D-05 Z LT)
Number of Scans
32
Receiver Gain
204.5
Relaxation Delay
2.0000
Pulse Width
10.5000
Acquisition Time
1.0486
Acquisition Date
2018-05-22T13:45:20
Modification Date
2018-05-22T13:43:39
Spectrometer Frequency
125.77
Spectral Width
31250.0
Lowest Frequency
-1148.3
Nucleus
13C
Acquired Size
32768
Spectral Size
65536
167.97
167.45
158.64
157.55
143.41
135.16
130.80
130.00
129.01
128.89
128.78
128.38
127.20
121.70
119.78
114.66
101.53
20.52
CDCl3
DCM
f1 (ppm)
3.12g

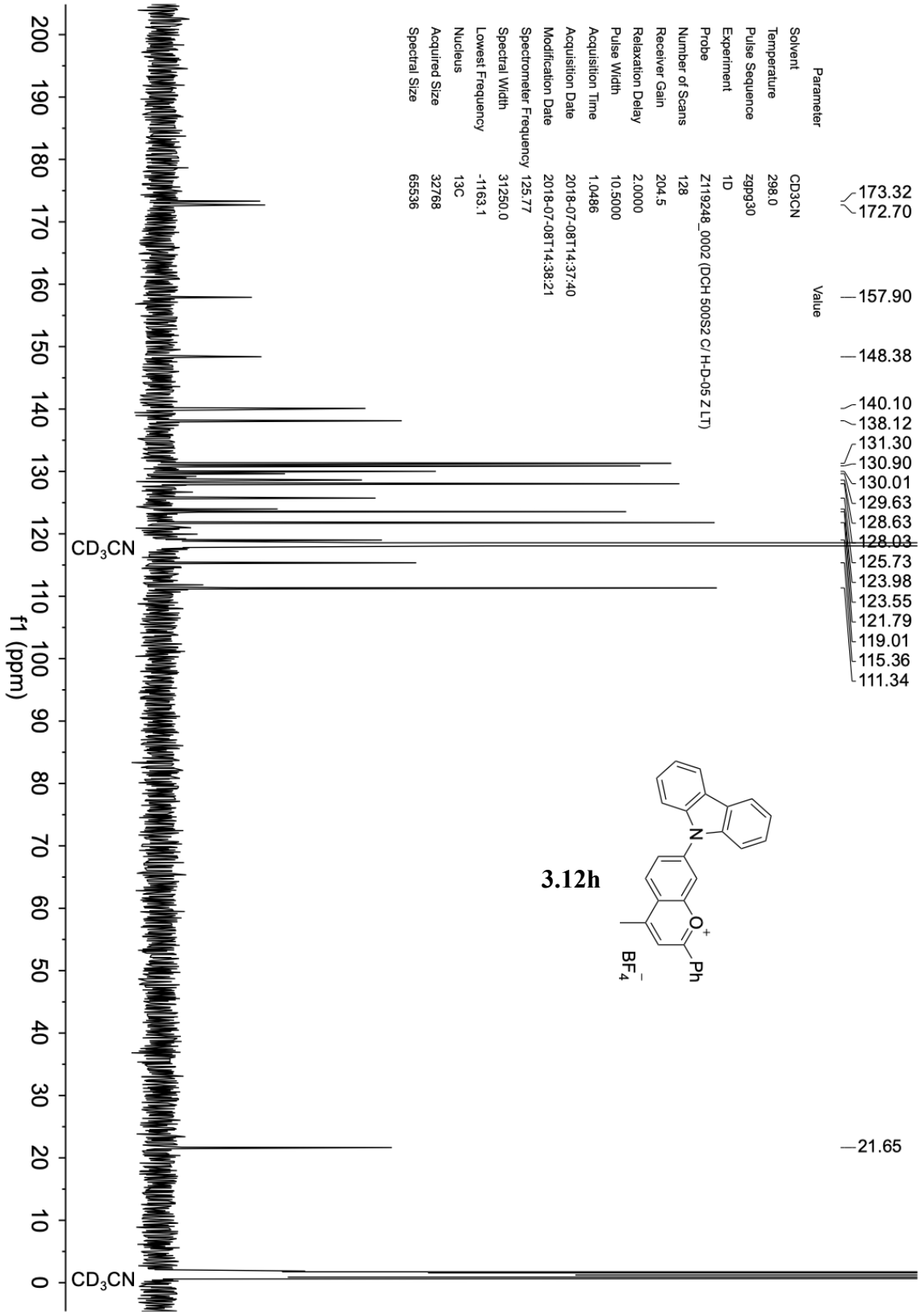
Parameter
Value
Solvent
CD3CN
Temperature
298.0
Pulse Sequence
zgpg30
Experiment
1D
Probe
Z119248_0002 (DCH 500S2 C/ H-D-05 Z LT)
Number of Scans
128
Receiver Gain
204.5
Relaxation Delay
2.0000
Pulse Width
10.5000
Acquisition Time
1.0486
Acquisition Date
2018-07-08T14:37:40
Modification Date
2018-07-08T14:38:21
Spectrometer Frequency
125.77
Spectral Width
31250.0
Lowest Frequency
-1163.1
Nucleus
13C
Acquired Size
32768
Spectral Size
65536
173.32
172.70
157.90
148.38
140.10
138.12
131.30
130.90
130.01
129.63
128.63
128.03
125.73
123.98
123.55
121.79
119.01
115.36
111.34
21.65
CD3CN
CD3CN
f1 (ppm)
3.12h
N
O+
Ph
BF4−

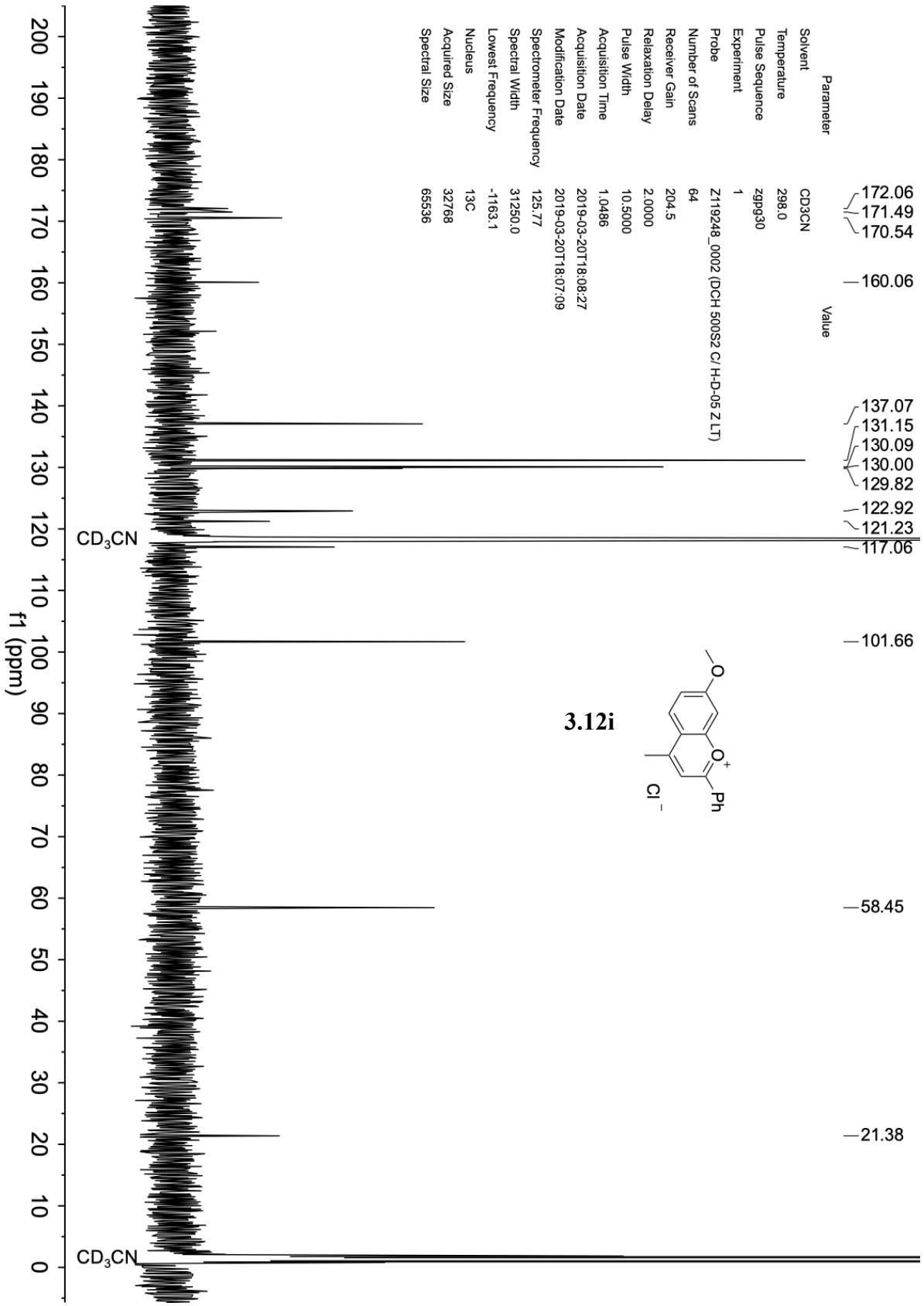
Parameter Value
Solvent CD3CN
Temperature 298.0
Pulse Sequence zgpg30
Experiment 1
Probe Z119248_0002 (DCH 500S2 C/ H-D-05 Z LT)
Number of Scans 64
Receiver Gain 204.5
Relaxation Delay 2.0000
Pulse Width 10.5000
Acquisition Time 1.0486
Acquisition Date 2019-03-20T18:08:27
Modification Date 2019-03-20T18:07:09
Spectrometer Frequency 125.77
Spectral Width 31250.0
Lowest Frequency -1163.1
Nucleus 13C
Acquired Size 32768
Spectral Size 65536
172.06
171.49
170.54
160.06
137.07
131.15
130.09
130.00
129.82
122.92
121.23
117.06
101.66
58.45
21.38
CD3CN
CD3CN
3.12i
Cl−
Ph
f1 (ppm)

3.7.3 ^{19}F NMR Spectra

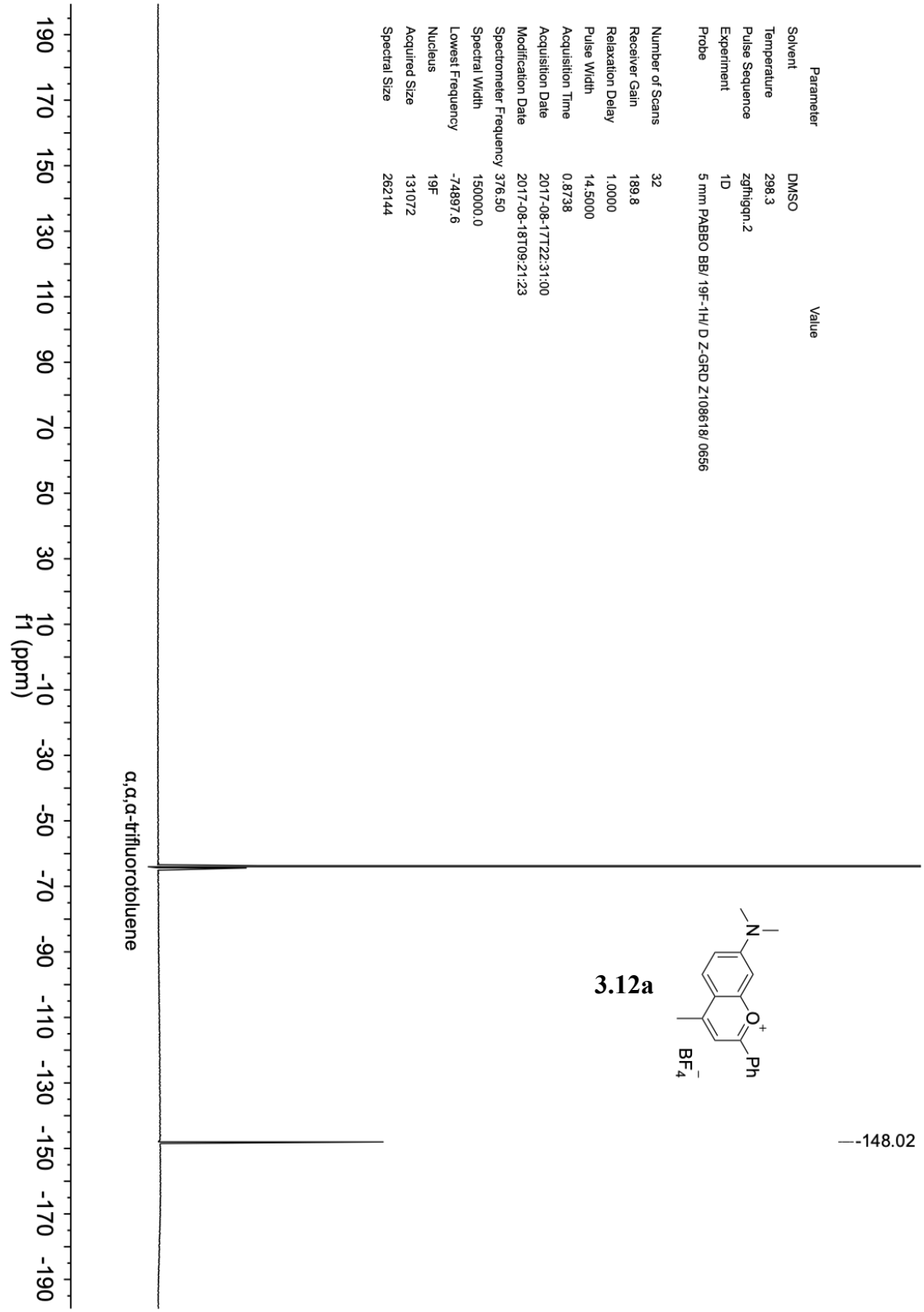

Parameter	Value
Solvent	DMSO
Temperature	298.2
Pulse Sequence	zgfhigqn.2
Experiment	1D
Probe	5 mm PABBO BB/ 19F-1H/ D Z-GRD Z108618/ 0656
Number of Scans	64
Receiver Gain	189.8
Relaxation Delay	1.0000
Pulse Width	14.5000
Acquisition Time	0.8738
Acquisition Date	2019-03-22T11:02:00
Modification Date	2019-03-22T11:34:22
Spectrometer Frequency	376.50
Spectral Width	150000.0
Lowest Frequency	-74888.2
Nucleus	19F
Acquired Size	131072
Spectral Size	262144

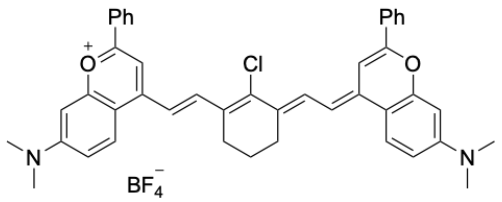

3.1

-148.00

α,α,α-trifluorotoluene

170 150 130 110 90 70 50 30 10 -10 -30 -50 -70 -90 -110 -130 -150 -170 -190

f1 (ppm)

3.7.4 Absorption and Emission Spectra

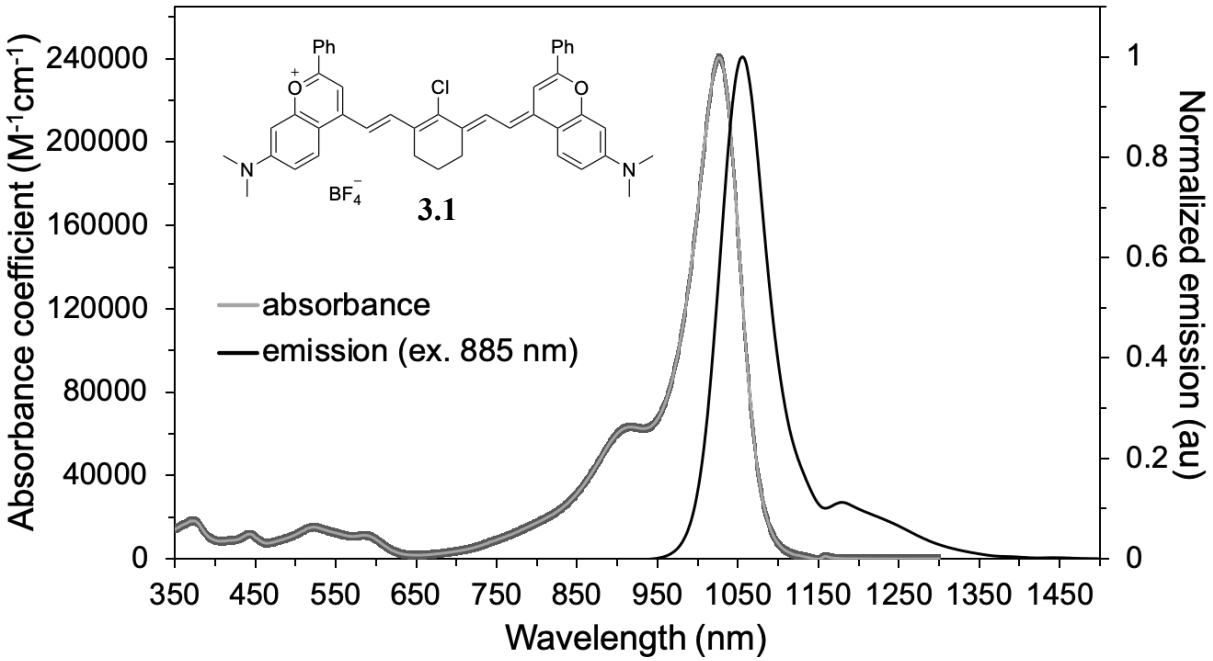

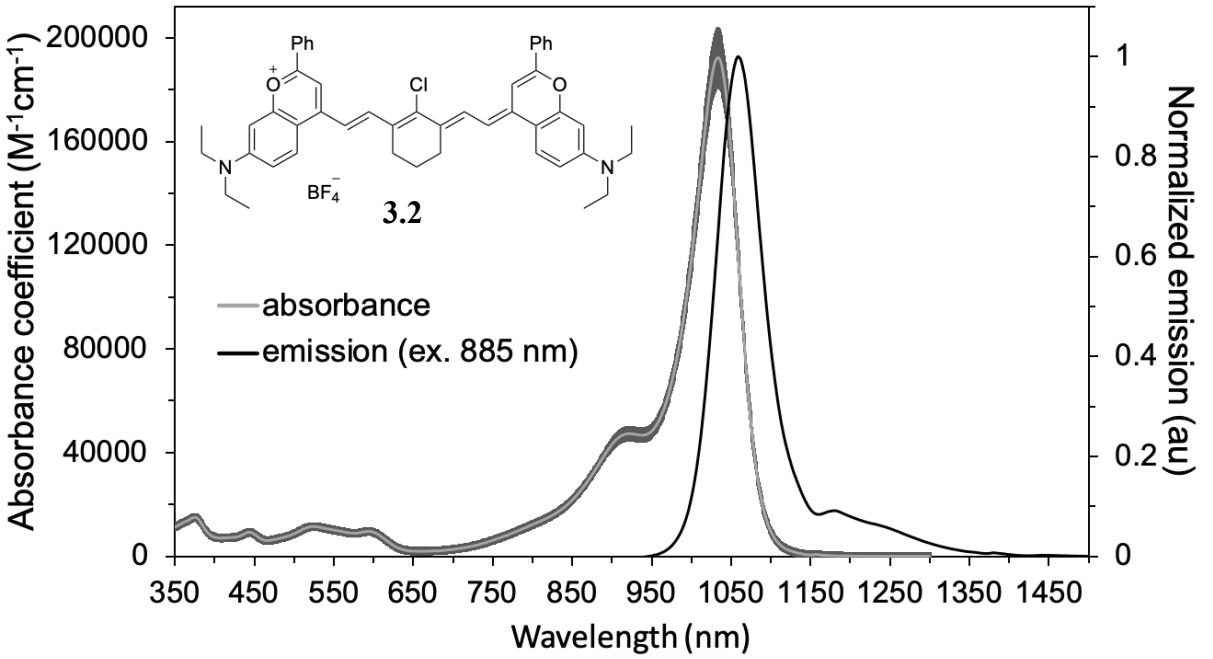

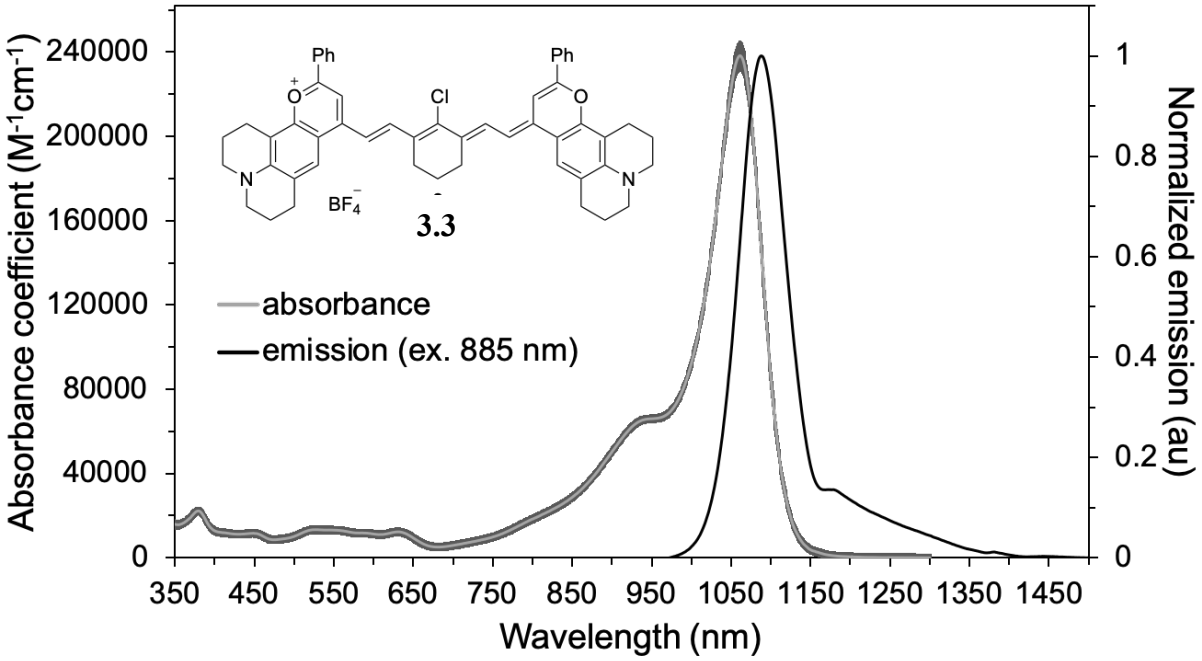
Absorbance coefficient (M-1cm-1)
Normalized emission (au)
Wavelength (nm)
absorbance
emission (ex. 885 nm)
Ph
Cl
Ph
BF4-
3.3

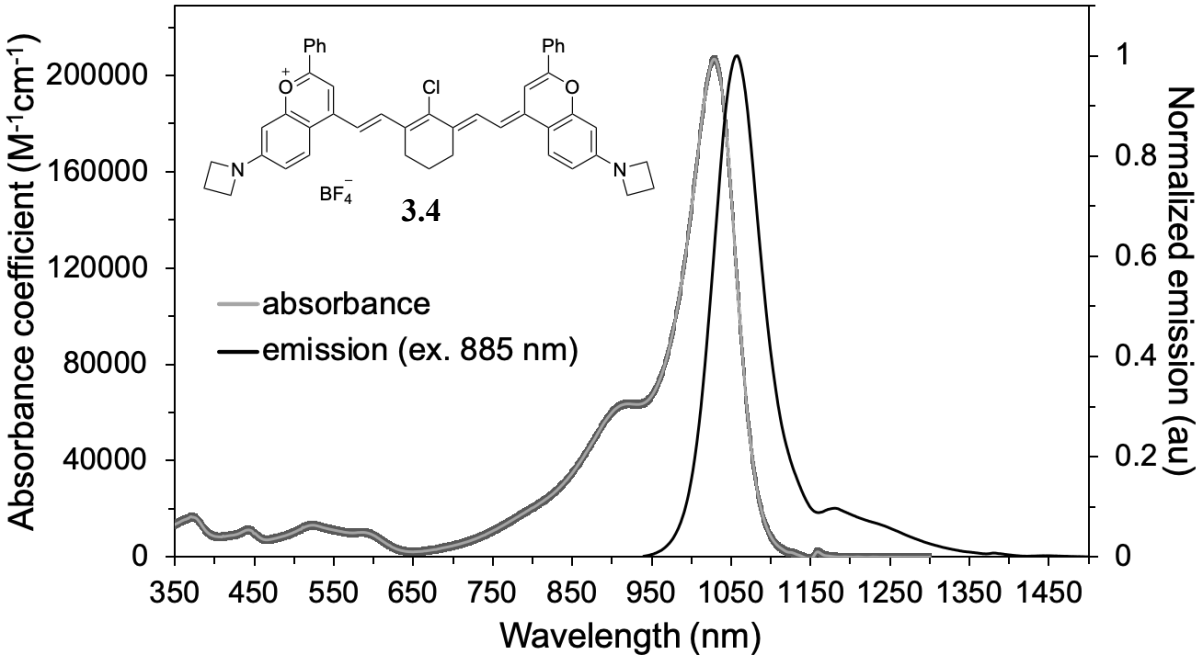
Absorbance coefficient (M-1cm-1)
Normalized emission (au)
Wavelength (nm)
absorbance
emission (ex. 885 nm)
Ph
Cl
Ph
BF4-
3.4

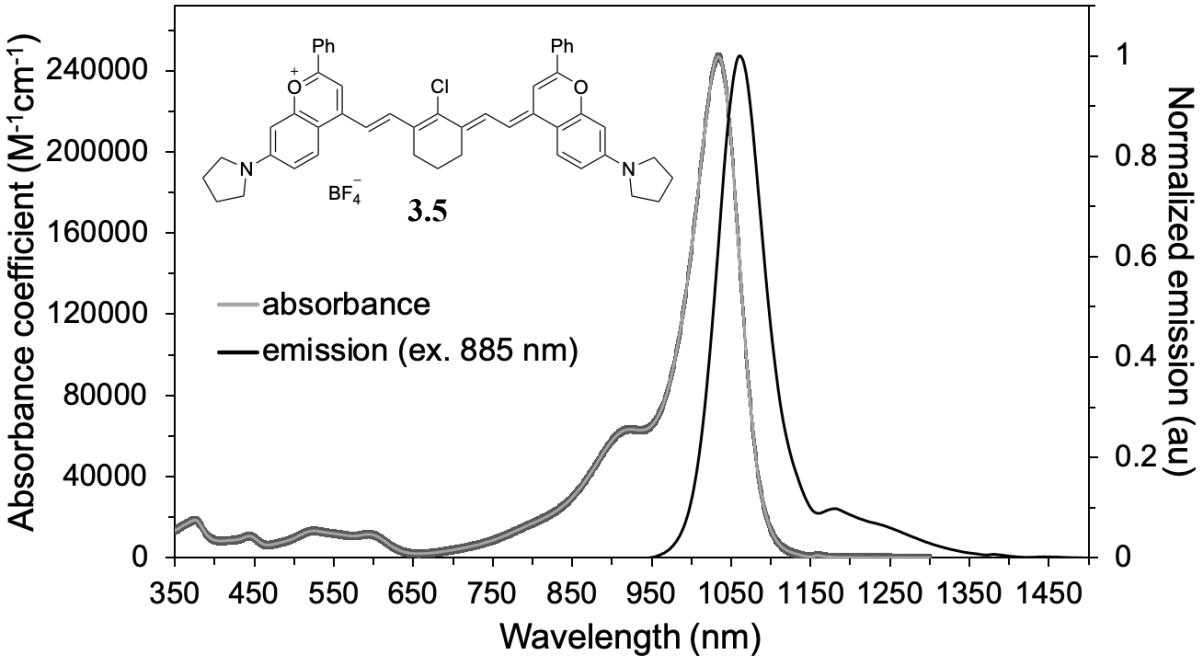
Absorbance coefficient (M-1cm-1)
Normalized emission (au)
Wavelength (nm)
absorbance
emission (ex. 885 nm)
Ph
Cl
BF4−
3.5

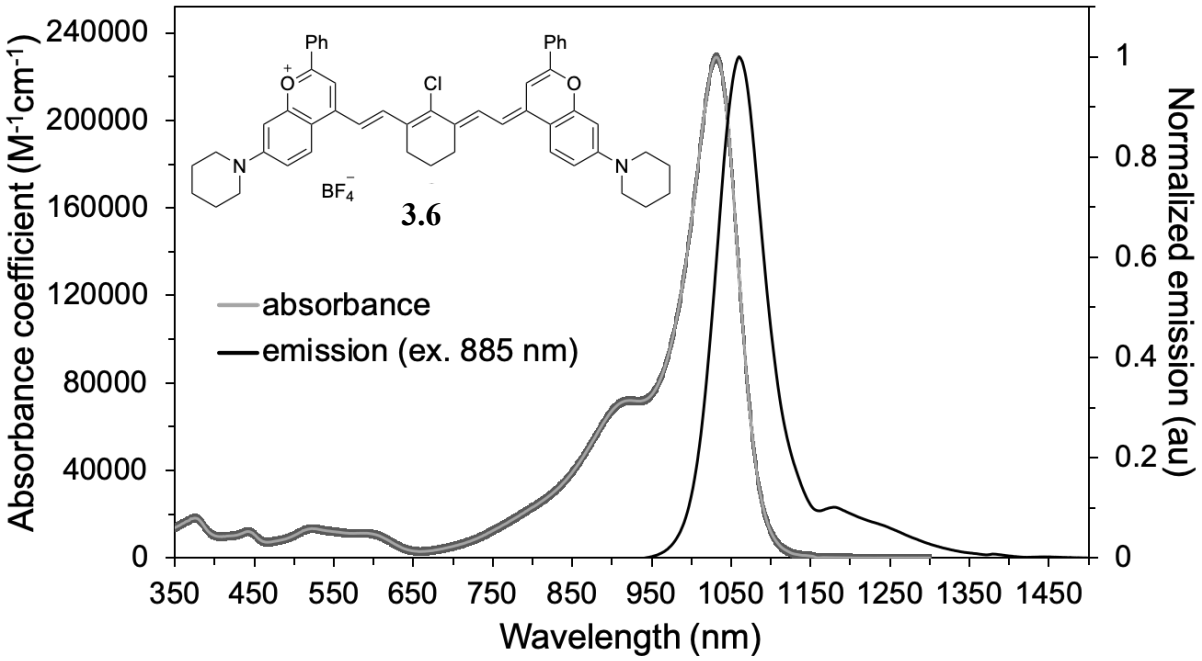
Absorbance coefficient (M-1cm-1)
Normalized emission (au)
Wavelength (nm)
absorbance
emission (ex. 885 nm)
Ph
Cl
BF4−
3.6

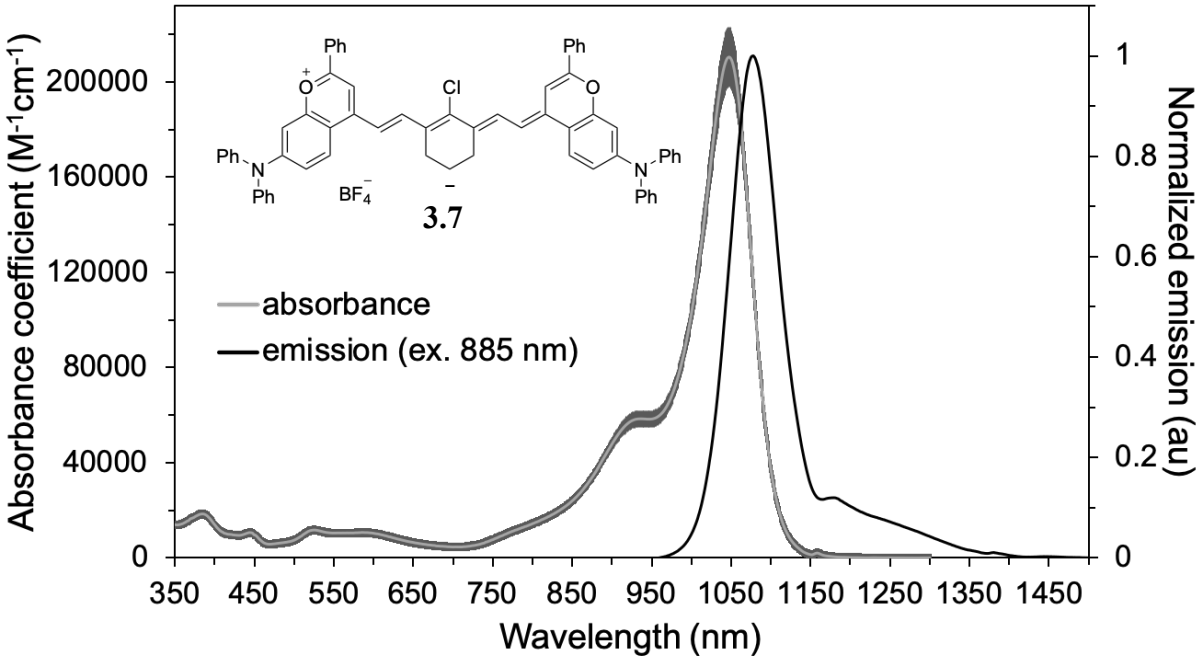
Absorbance coefficient (M-1cm-1)
Normalized emission (au)
Wavelength (nm)
absorbance
emission (ex. 885 nm)
3.7

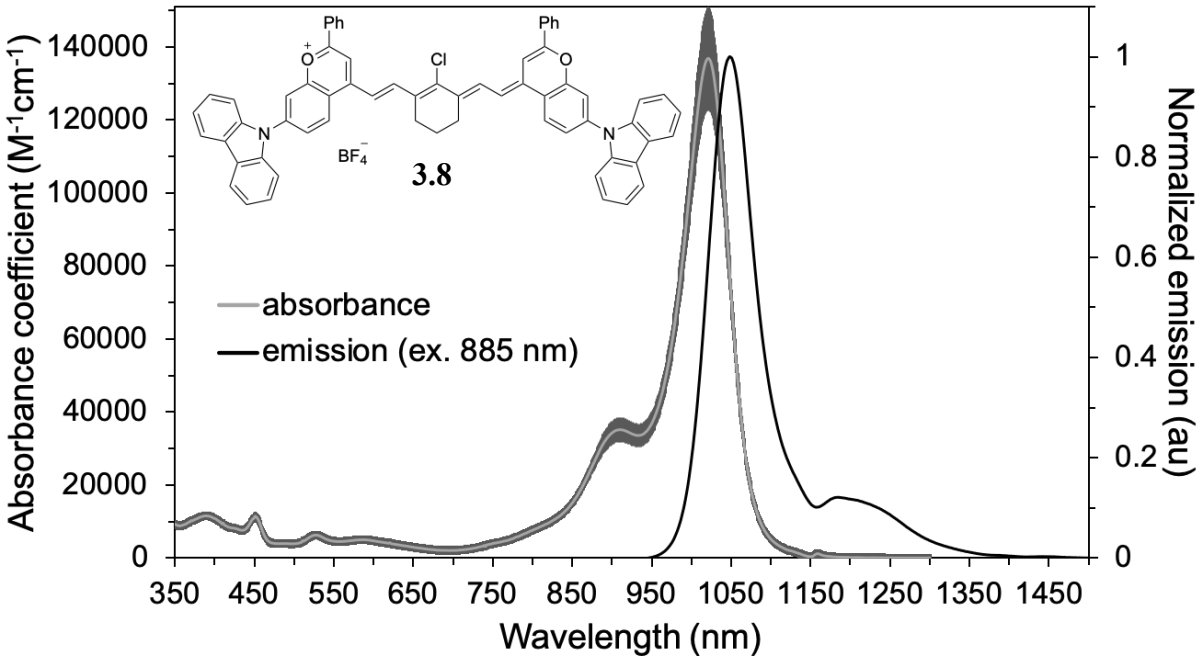
Absorbance coefficient (M-1cm-1)
Normalized emission (au)
Wavelength (nm)
absorbance
emission (ex. 885 nm)
3.8

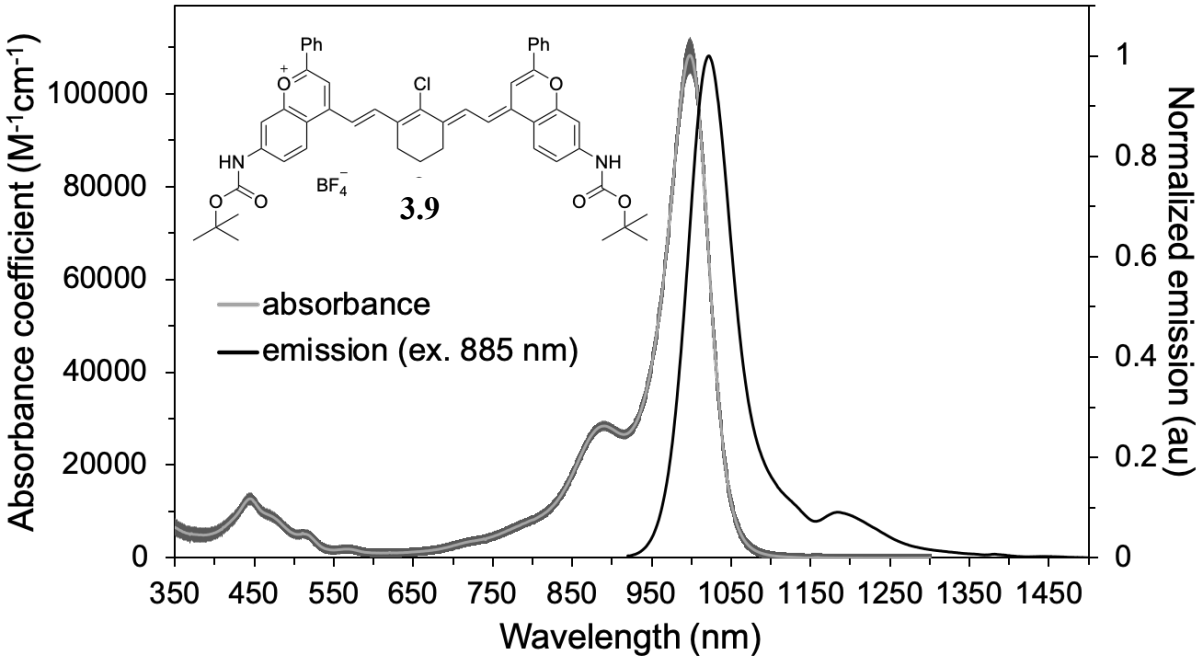
Absorbance coefficient (M-1cm-1)
Normalized emission (au)
Wavelength (nm)
absorbance
emission (ex. 885 nm)
3.9

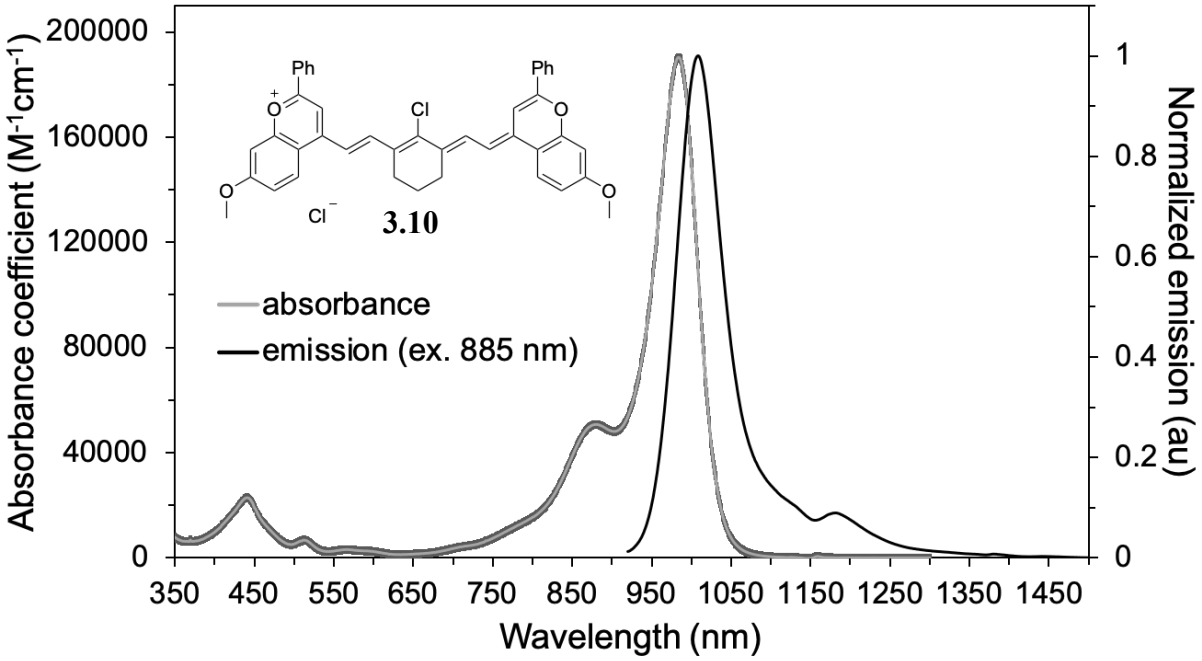
Absorbance coefficient (M-1cm-1)
Normalized emission (au)
Wavelength (nm)
absorbance
emission (ex. 885 nm)
3.10

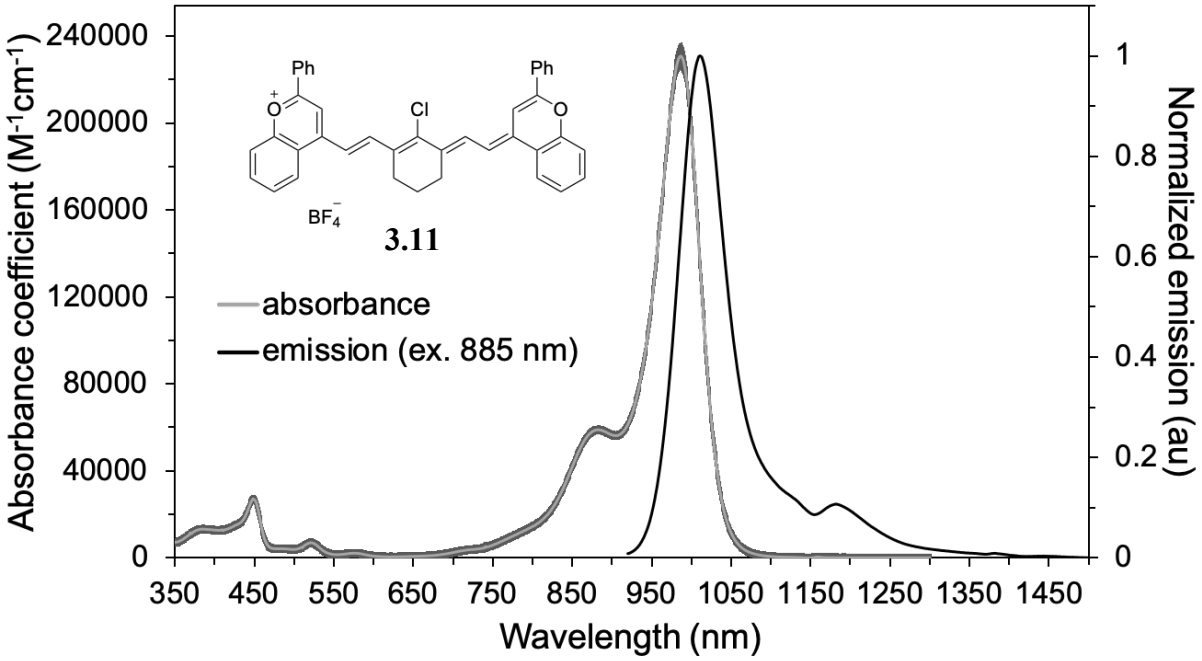

3.8 Data and Code Availability

Image datasets, including all raw and processed imaging data generated in this Chapter, are available at BioImage Archive (accession number: S-BIAD27). Custom computer programs used for the work are available at GitHub (https:// gitlab.com/brunslab/ccda).

3.9 List of Supplementary information relevant to Chapter Three

Supplementary Video 3.1 *Single-channel in vivo imaging with ex. 1,064 nm at 100 fps.* Image sequence was frame averaged by a factor of three to reduce file size and is displayed in real-time. Experimental details correspond to that of **Figure 3.13**.

Supplementary Video 3.2 *Video-rate multiplexed imaging in vivo – JuloFlav7 injection.* Image sequence was frame averaged by a factor of three to reduce file size and is displayed in 3x speed. *Experimental details correspond to that of **Figure 3.5G**.*

Supplementary Video 3.3 *Video-rate multiplexed imaging in vivo – ICG injection.* Image sequence was frame averaged by a factor of three to reduce file size and is displayed in 3x speed. Experimental details correspond to that of **Figure 3.5G**.

Supplementary Video 3.4 *Imaging of an awake mouse in three colors.* Image sequence was not frame averaged and is displayed in real-time. Experimental details correspond to that of **Figure 3.15A/Figure 3.5G.**

Supplementary Video 3.5 *Two-color demonstration of image guided necropsy.* Image sequence was frame averaged by a factor of eight to reduce file size and is displayed in 5x speed. Experimental details correspond to that of **Figure 3.15C**/**Figure 3.15E**.

Supplementary Video 3.6 *Orthogonal circulatory and lymphatic imaging.* Image sequence was frame averaged by a factor of two to reduce file size and is displayed in 3x speed. Experimental details correspond to that of **Figure 3.18B–C**.

3.10 References

[1] Dean, K. M.; Palmer, A. E. Advances in Fluorescence Labeling Strategies for Dynamic Cellular Imaging. *Nat. Chem. Biol.* **2014**, *10*, 512–523.

[2] Wei, L.; Chen, Z.; Shi, L.; Long, R.; Anzalone, A. V.; Zhang, L.; Hu, F.; Yuste, R.; Cornish, V. W.; Min, W. Super-Multiplex Vibrational Imaging. *Nature* **2017**, *544*, 465–470.

[3] Frangioni, J. V. In Vivo Near-Infrared Fluorescence Imaging. *Curr. Opin. Chem. Biol.* **2003**, *7*, 626–634.

[4] Kong, L.; Tang, J.; Little, J. P.; Yu, Y.; Lämmermann, T.; Lin, C. P.; Germain, R. N.; Cui, M. Continuous Volumetric Imaging via an Optical Phase-Locked Ultrasound Lens. *Nat. Methods* **2015**, *12*, 759–762.

[5] Grimm, J. B.; Muthusamy, A. K.; Liang, Y.; Brown, T. A.; Lemon, W. C.; Patel, R.; Lu, R.; Macklin, J. J.; Keller, P. J.; Ji, N.; et al. A General Method to Fine-Tune Fluorophores for Live-Cell and in Vivo Imaging. *Nat. Methods* **2017**, *14*, 987–994.

[6] Fenrich, K. K.; Weber, P.; Hocine, M.; Zalc, M.; Rougon, G.; Debarbieux, F. Long-Term in Vivo Imaging of Normal and Pathological Mouse Spinal Cord with Subcellular Resolution Using Implanted Glass Windows. *J. Physiol.* **2012**, *590*, 3665–3675.

[7] Rakhymzhan, A.; Leben, R.; Zimmermann, H.; Günther, R.; Mex, P.; Reismann, D.; Ulbricht, C.; Acs, A.; Brandt, A. U.; Lindquist, R. L.; et al. Synergistic Strategy for Multicolor Two-Photon Microscopy: Application to the Analysis of Germinal Center Reactions In Vivo. *Sci. Rep.* **2017**, *7*, 7101.

[8] Kim, P.; Puoris'haag, M.; Côté, D.; Lin, C. P.; Yun, S. H. In Vivo Confocal and Multiphoton Microendoscopy. *J. Biomed. Opt.* **2008**, *13*, 010501.

[9] Kosaka, N.; Ogawa, M.; Sato, N.; Choyke, P. L.; Kobayashi, H. In Vivo Real-Time, Multicolor, Quantum Dot Lymphatic Imaging. *J. Invest. Dermatol.* **2009**, *129*, 2818–2822.

[10] Erogbogbo, F.; Yong, K.-T.; Roy, I.; Hu, R.; Law, W.-C.; Zhao, W.; Ding, H.; Wu, F.; Kumar, R.; Swihart, M. T.; et al. In Vivo Targeted Cancer Imaging, Sentinel Lymph Node Mapping and Multi-Channel Imaging with Biocompatible Silicon Nanocrystals. *ACS Nano* **2011**, *5*, 413–423.

[11] Shcherbakova, D. M.; Verkhusha, V. V. Near-Infrared Fluorescent Proteins for Multicolor in Vivo Imaging. *Nat. Methods* **2013**, *10*, 751–754.

[12] Zavaleta, C. L.; Walton, I.; Gambhir, S. S.; Shojaei, B.; Doering, W.; Davis, G.; Natan, M. J.; Smith, B. R. Multiplexed Imaging of Surface Enhanced Raman Scattering Nanotags in Living Mice Using Noninvasive Raman Spectroscopy. *Proc. Natl. Acad. Sci.* **2009**, *106*, 13511–13516.

[13] Zhang, H.; Salo, D.; Kim, D. M.; Komarov, S.; Tai, Y.; Berezin, M. Y. Penetration Depth of Photons in Biological Tissues from Hyperspectral Imaging in Shortwave Infrared in Transmission and Reflection Geometries. *J. Biomed. Opt.* **2016**, *21*, 126006.

[14] Carr, J. A.; Aellen, M.; Franke, D.; So, P. T. C.; Bruns, O. T.; Bawendi, M. G. Absorption by Water Increases Fluorescence Image Contrast of Biological Tissue in the Shortwave Infrared. *Proc. Natl. Acad. Sci.* **2018**, *115*, 9080–9085.

[15] Naczynski, D. J.; Tan, M. C.; Zevon, M.; Wall, B.; Kohl, J.; Kulesa, A.; Chen, S.; Roth, C. M.; Riman, R. E.; Moghe, P. V. Rare-Earth-Doped Biological Composites as in Vivo Shortwave Infrared Reporters. *Nat. Commun.* **2013**, *4*, 2199.

[16] Welsher, K.; Liu, Z.; Sherlock, S. P.; Robinson, J. T.; Chen, Z.; Daranciang, D.; Dai, H. A Route to Brightly Fluorescent Carbon Nanotubes for Near-Infrared Imaging in Mice. *Nat. Nanotechnol.* **2009**, *4*, 773–780.

[17] Hong, G.; Robinson, J. T.; Zhang, Y.; Diao, S.; Antaris, A. L.; Wang, Q.; Dai, H. In Vivo Fluorescence Imaging with Ag2S Quantum Dots in the Second Near-Infrared Region. *Angew. Chemie Int. Ed.* **2012**, *51*, 9818–9821.

[18] Bruns, O. T.; Bischof, T. S.; Harris, D. K.; Franke, D.; Shi, Y.; Riedemann, L.; Bartelt, A.; Jaworski, F. B.; Carr, J. A.; Rowlands, C. J.; et al. Next-Generation in Vivo Optical Imaging with Short-Wave Infrared Quantum Dots. *Nat. Biomed. Eng.* **2017**, *1*, 0056.

[19] Tao, Z.; Hong, G.; Shinji, C.; Chen, C.; Diao, S.; Antaris, A. L.; Zhang, B.; Zou, Y.; Dai, H. Biological Imaging Using Nanoparticles of Small Organic Molecules with Fluorescence Emission at Wavelengths Longer than 1000 nm. *Angew. Chemie Int. Ed.* **2013**, *52*, 13002–13006.

[20] Yang, Q.; Ma, Z.; Wang, H.; Zhou, B.; Zhu, S.; Zhong, Y.; Wang, J.; Wan, H.; Antaris, A.; Ma, R.; et al. Rational Design of Molecular Fluorophores for Biological Imaging in the NIR-II Window. *Adv. Mater.* **2017**, *29*, 1605497.

[21] Zhu, S.; Herraiz, S.; Yue, J.; Zhang, M.; Wan, H.; Yang, Q.; Ma, Z.; Wang, Y.; He, J.; Antaris, A. L.; et al. 3D NIR-II Molecular Imaging Distinguishes Targeted Organs with High-Performance NIR-II Bioconjugates. *Adv. Mater.* **2018**, *30*, 1705799.

[22] Wan, H.; Yue, J.; Zhu, S.; Uno, T.; Zhang, X.; Yang, Q.; Yu, K.; Hong, G.; Wang, J.; Li, L.; et al. A Bright Organic NIR-II Nanofluorophore for Three-Dimensional Imaging into Biological Tissues. *Nat. Commun.* **2018**, *9*, 1171.

[23] Wang, F.; Wan, H.; Ma, Z.; Zhong, Y.; Sun, Q.; Tian, Y.; Qu, L.; Du, H.; Zhang, M.; Li, L.; et al. Light-Sheet Microscopy in the near-Infrared II Window. *Nat. Methods* **2019**, *16*, 545–552.

[24] Zhu, S.; Yang, Q.; Antaris, A. L.; Yue, J.; Ma, Z.; Wang, H.; Huang, W.; Wan, H.; Wang, J.; Diao, S.; et al. Molecular Imaging of Biological Systems with a Clickable Dye in the

Broad 800- to 1,700-nm Near-Infrared Window. *Proc. Natl. Acad. Sci.* **2017**, *114*, 962–967.

[25] Ma, B. L.; Zhai, X.; Du, G.; Zhou, J. Orthogonal Shortwave Infrared Emission Based on Rare Earth Nanoparticles for Interference-Free Logical Codes and Bio-Imaging. *Chem. Sci.* **2019**, *10*, 3281–3288.

[26] Hong, G.; Diao, S.; Chang, J.; Antaris, A. L.; Chen, C.; Zhang, B.; Zhao, S.; Atochin, D. N.; Huang, P. L.; Andreasson, K. I.; et al. Through-Skull Fluorescence Imaging of the Brain in a New Near-Infrared Window. *Nat. Photonics* **2014**, *8*, 723–730.

[27] Diao, S.; Blackburn, J. L.; Hong, G.; Antaris, A. L.; Chang, J.; Wu, J. Z.; Zhang, B.; Cheng, K.; Kuo, C. J.; Dai, H. Fluorescence Imaging In Vivo at Wavelengths beyond 1500 nm. *Angew. Chemie Int. Ed.* **2015**, *54*, 14758–14762.

[28] Kapanidis, A. N.; Laurence, T. A.; Nam, K. L.; Margeat, E.; Kong, X.; Weiss, S.; Lee, N. K.; Margeat, E.; Kong, X.; Weiss, S. Alternating-Laser Excitation of Single Molecules. *Acc. Chem. Res.* **2005**, *38*, 523–533.

[29] Müller, B. K.; Zaychikov, E.; Bräuchle, C.; Lamb, D. C.; Muller, B. K.; Zaychikov, E.; Brauchle, C.; Lamb, D. C. Pulsed Interleaved Excitation. *Biophys. J.* **2005**, *89*, 3508–3522.

[30] Lewis, E. K.; Haaland, W. C.; Nguyen, F.; Heller, D. A.; Allen, M. J.; MacGregor, R. R.; Berger, C. S.; Willingham, B.; Burns, L. A.; Scott, G. B. I.; et al. Color-Blind Fluorescence Detection for Four-Color DNA Sequencing. *Proc. Natl. Acad. Sci.* **2005**, *102*, 5346–5351.

[31] Garbacik, E. T.; Sanz-Paz, M.; Borgman, K. J. E.; Campelo, F.; Garcia-Parajo, M. F. Frequency-Encoded Multicolor Fluorescence Imaging with Single-Photon-Counting Color-Blind Detection. *Biophys. J.* **2018**, *115*, 725–736.

[32] Gómez-García, P. A.; Garbacik, E. T.; Otterstrom, J. J.; Garcia-Parajo, M. F.; Lakadamyali, M. Excitation-Multiplexed Multicolor Superresolution Imaging with Fm-STORM and Fm-DNA-PAINT. *Proc. Natl. Acad. Sci.* **2018**, *115*, 12991–12996.

[33] Thimsen, E.; Sadtler, B.; Berezin, M. Y. Shortwave-Infrared (SWIR) Emitters for Biological Imaging: A Review of Challenges and Opportunities. *Nanophotonics* **2017**, *6*, 1043–1054.

[34] Bricks, J. L.; Kachkovskii, A. D.; Slominskii, Y. L.; Gerasov, A. O.; Popov, S. V. Molecular Design of near Infrared Polymethine Dyes: A Review. *Dye. Pigment.* **2015**, *121*, 238–255.

[35] Marshall, M. V; Rasmussen, J. C.; Tan, I.; Aldrich, M. B.; Adams, K. E.; Wang, X.; Fife, C. E.; Maus, E. A.; Smith, L. A.; Sevick-Muraca, E. M. Near-Infrared Fluorescence Imaging in Humans with Indocyanine Green: A Review and Update. *Open Surg. Oncol. J.* **2010**, *2*, 12–25.

[36] Rurack, K.; Spieles, M. Fluorescence Quantum Yields of a Series of Red and Near-Infrared Dyes Emitting at 600−1000 Nm. *Anal. Chem.* **2011**, *83*, 1232–1242..

[37] Carr, J. A.; Franke, D.; Caram, J. R.; Perkinson, C. F.; Saif, M.; Askoxylakis, V.; Datta, M.; Fukumura, D.; Jain, R. K.; Bawendi, M. G.; et al. Shortwave Infrared Fluorescence Imaging with the Clinically Approved Near-Infrared Dye Indocyanine Green. *Proc. Natl. Acad. Sci.* **2018**, *115*, 4465–4470.

[38] Starosolski, Z.; Bhavane, R.; Ghaghada, K. B.; Vasudevan, S. A.; Kaay, A.; Annapragada, A. Indocyanine Green Fluorescence in Second Near-Infrared (NIR-II) Window. *PLoS One* **2017**, *12*, e0187563.

[39] Cosco, E. D.; Caram, J. R.; Bruns, O. T.; Franke, D.; Day, R. A.; Farr, E. P.; Bawendi, M. G.; Sletten, E. M. Flavylium Polymethine Fluorophores for Near- and Shortwave Infrared Imaging. *Angew. Chemie Int. Ed.* **2017**, *56*, 13126–13129.

[40] Henary, M.; Mojzych, M.; Say, M.; Strekowski, L. Functionalization of Benzo[c,d]Indole System for the Synthesis of Visible and Near-Infrared Dyes. *J. Heterocycl. Chem.* **2009**, *46*, 84–87.

[41] Li, B.; Lu, L.; Zhao, M.; Lei, Z.; Zhang, F. An Efficient 1064 nm NIR-II Excitation Fluorescent Molecular Dye for Deep-Tissue High-Resolution Dynamic Bioimaging. *Angew. Chemie Int. Ed.* **2018**, *57*, 7483–7487.

[42] Ding, B.; Xiao, Y.; Zhou, H.; Zhang, X.; Qu, C.; Xu, F.; Deng, Z.; Cheng, Z.; Hong, X. Polymethine Thiopyrylium Fluorophores with Absorption beyond 1000 nm for Biological Imaging in the Second Near-Infrared Subwindow. *J. Med. Chem.* **2019**, *62*, 2049–2059.

[43] Wang, S.; Fan, Y.; Li, D.; Sun, C.; Lei, Z.; Lu, L.; Wang, T.; Zhang, F. Anti-Quenching NIR-II Molecular Fluorophores for in Vivo High-Contrast Imaging and PH Sensing. *Nat. Commun.* **2019**, *10*, 1058.

[44] Lei, Z.; Sun, C.; Pei, P.; Wang, S.; Li, D.; Zhang, X.; Zhang, F. Stable, Wavelength-Tunable Fluorescent Dyes in the NIR-II Region for In Vivo High-Contrast Bioimaging and Multiplexed Biosensing. *Angew. Chemie Int. Ed.* **2019**, *58*, 8166–8171.

[45] Chen, J.-R.; Wong, J.-B.; Kuo, P.-Y.; Yang, D.-Y. Synthesis and Characterization of Coumarin-Based Spiropyran Photochromic Colorants. *Org. Lett.* **2008**, *10*, 4823–4826.

[46] Roehri-Stoeckel, C.; Gonzalez, E.; Fougerousse, A.; Brouillard, R. Synthetic Dyes: Simple and Original Ways to 4-Substituted Flavylium Salts and Their Corresponding Vitisin Derivatives. *Can. J. Chem.* **2001**, *79*, 1173–1178.

[47] Seijas, J. A.; Vázquez-Tato, M. P.; Carballido-Reboredo, R. Solvent-Free Synthesis of Functionalized Flavones under Microwave Irradiation. *J. Org. Chem.* **2005**, *70*, 2855–2858.

[48] Kónya, K.; Pajtás, D.; Kiss-Szikszai, A.; Patonay, T. Buchwald-Hartwig Reactions of Monohaloflavones. *European J. Org. Chem.* **2015**, *2015*, 828–839.

[49] Kopainsky, B.; Qiu, P.; Kaiser, W.; Sens, B.; Drexhage, K. H. Lifetime, Photostability, and Chemical Structure of IR Heptamethine Cyanine Dyes Absorbing beyond 1 μm. *Appl. Phys. B* **1982**, *29*, 15–18.

[50] Hansch, C.; Leo, A.; Taft, R. W. A Survey of Hammett Substituent Constants and Resonance and Field Parameters. *Chem. Rev.* **1991**, *91*, 165–195.

[51] Semonin, O. E.; Johnson, J. C.; Luther, J. M.; Midgett, A. G.; Nozik, A. J.; Beard, M. C. Absolute Photoluminescence Quantum Yields of IR-26 Dye, PbS, and PbSe Quantum Dots. *J. Phys. Chem. Lett.* **2010**, *1*, 2445–2450.

[52] Hatami, S.; Würth, C.; Kaiser, M.; Leubner, S.; Gabriel, S.; Bahrig, L.; Lesnyak, V.; Pauli, J.; Gaponik, N.; Eychmüller, A.; et al. Absolute Photoluminescence Quantum Yields of IR26 and IR-Emissive Cd1−xHgxTe and PbS Quantum Dots – Method- and Material-Inherent Challenges. *Nanoscale* **2015**, *7*, 133–143.

[53] Lukasik, V. M.; Gillies, R. J. Animal Anaesthesia for in Vivo Magnetic Resonance. *NMR Biomed.* **2003**, *16*, 459–467.

[54] Schwenke, D. O.; Pearson, J. T.; Mori, H.; Shirai, M. Long-Term Monitoring of Pulmonary Arterial Pressure in Conscious, Unrestrained Mice. *J. Pharmacol. Toxicol. Methods* **2006**, *53*, 277–283.

[55] Sato, M.; Matsumoto, N.; Noguchi, A.; Okonogi, T.; Sasaki, T.; Ikegaya, Y. Simultaneous Monitoring of Mouse Respiratory and Cardiac Rates through a Single Precordial Electrode. *J. Pharmacol. Sci.* **2018**, *137*, 177–186.

[56] Ceppi, L.; Bardhan, N. M.; Na, Y.; Siegel, A.; Rajan, N.; Fruscio, R.; Del Carmen, M. G.; Belcher, A. M.; Birrer, M. J. Real-Time Single-Walled Carbon Nanotube-Based Fluorescence Imaging Improves Survival after Debulking Surgery in an Ovarian Cancer Model. *ACS Nano* **2019**, *13*, 5356–5365.

[57] Zhu, S.; Tian, R.; Antaris, A. L.; Chen, X.; Dai, H. Near-Infrared-II Molecular Dyes for Cancer Imaging and Surgery. *Adv. Mater.* **2019**, *31*, 1900321.

[58] Cousins, A.; Thompson, S. K.; Wedding, A. B.; Thierry, B. Clinical Relevance of Novel Imaging Technologies for Sentinel Lymph Node Identification and Staging. *Biotechnol. Adv.* **2014**, *32*, 269–279.

[59] Rasmussen, J. C.; Fife, C. E.; Sevick-Muraca, E. M. Near-Infrared Fluorescence Lymphatic Imaging in Lymphangiomatosis. *Lymphat. Res. Biol.* **2015**, *13*, 195–201.

[60] Tozzi, M.; Boni, L.; Soldini, G.; Franchin, M.; Piffaretti, G. Vascular Fluorescence Imaging Control for Complex Renal Artery Aneurysm Repair Using Laparoscopic Nephrectomy and Autotransplantation. *Case Rep. Transplant.* **2014**, *2014*, 563408.

[61] Bexrud, J. A.; Eisenberger, P.; Leitch, D. C.; Payne, P. R.; Schafer, L. L. Selective C-H Activation α to Primary Amines. Bridging Metallaaziridines for Catalytic, Intramolecular α-Alkylation. *J. Am. Chem. Soc.* **2009**, *131*, 2116–2118.

[62] Kövér, J.; Antus, S. Facile Deoxygenation of Hydroxylated Flavonoids by Palladium-Catalysed Reduction of Its Triflate Derivatives. *Z. Naturforsch.* **2005**, *60b*, 792–796.

[63] Schindelin, J.; Arganda-Carreras, I.; Frise, E.; Kaynig, V.; Longair, M.; Pietzsch, T.; Preibisch, S.; Rueden, C.; Saalfeld, S.; Schmid, B.; et al. Fiji: An Open-Source Platform for Biological-Image Analysis. *Nat. Methods* **2012**, *9*, 676–682.

[64] Rueden, C. T.; Schindelin, J.; Hiner, M. C.; DeZonia, B. E.; Walter, A. E.; Arena, E. T.; Eliceiri, K. W. ImageJ2: ImageJ for the next Generation of Scientific Image Data. *BMC Bioinformatics* **2017**, *18*, 529.

[65] Garcia, P. P.; Lee, J. W.; Marshall, J. L.; McGowan, D. A.; Puttick, A. J.; Spencer, T. K.; Stroud, S. G.; Telfer, S. J.; Zuraw, M. J. Squarylium Compounds, and Processes and Intermediats for the Synthesis of These Compunds. U.S. Patent 5,919,950, **1999**.

CHAPTER FOUR

Bright Chromenylium Polymethine Dyes Enable Fast, Four-Color in vivo Imaging with Shortwave Infrared Detection

Work in this chapter is incorporated into a submitted manuscript with authors Emily D. Cosco, Bernardo A. Arús, Anthony L. Spearman, Timothy L. Atallah, Olivia S. Leland, Justin R. Caram, Thomas S. Bischof, Oliver T. Bruns*, and Ellen M. Sletten*

4.1 Abstract

Optical imaging within the shortwave infrared (SWIR, 1,000–2,000 nm) region of the electromagnetic spectrum has enabled high-resolution and high-contrast imaging in mice, non-invasively. Polymethine dyes, with narrow absorption spectra and high absorption coefficients, are optimal probes for fast and multiplexed SWIR imaging. Here, we expand upon the multiplexing capabilities in SWIR imaging by obtaining brighter polymethine dyes with varied excitation wavelengths spaced throughout the near infrared (NIR, 700–1,000 nm) region. Building on the flavylium polymethine dye scaffold, we explored derivatives with functional group substitution at the 2-position, deemed chromenylium polymethine dyes. The reported dyes have reduced non-radiative rates and enhanced emissive properties, enabling non-invasive imaging in mice in a single color at 300 fps and in three colors at 100 fps. Combined with polymethine dyes containing a red-shifted julolidine flavylium heterocycle (JuloFlav7), and indocyanine green (ICG), distinct channels with well-separated excitation wavelengths provide non-invasive video-rate in vivo imaging in four colors.

4.2 Introduction

Optical detection in the shortwave infrared (SWIR, 1,000–2,000 nm) region of the electromagnetic spectrum furnishes high sensitivity and high-resolution imaging in small animals. The enhanced performance arises from lower scattering coefficients, reduced tissue autofluorescence, and water absorption improving the contrast in the SWIR compared to the near-infrared (NIR, 700–1,000 nm) and visible (VIS, 350–700 nm) regions.[1–4] Since the initial report of SWIR detection for deep-tissue optical imaging in 2009,[5] diverse emitters for this region, including carbon nanotubes[6] quantum dots[7–8] rare-earth containing nanoparticles[9–10] and small molecules[11–12] have been optimized. These efforts have enabled improvements in imaging speed, up to ~100 fps[10,13] and the translation of advanced imaging techniques, such as multicolor imaging[13–15] confocal microscopy[16–17] and light-sheet microscopy[18], to this long wavelength region.

Recent efforts in multiplexing *in vivo* using non-invasive modalities such as bioluminescence,[19] magnetic resonance,[20] and photoacoustic[21] imaging have paved the way to study multiple biological parameters simultaneously. We recently reported a strategy for multiplexed non-invasive optical imaging in mice, namely, excitation-multiplexing with single-channel SWIR detection.[13] This approach hinges on SWIR-emissive fluorescent probes with well-spaced absorption spectra that can be preferentially excited with orthogonal wavelengths of light (Figure 4.1A) and detected in the SWIR (Figure 4.1B) in tandem on the millisecond time scale. An additional benefit of the excitation multiplexing approach is that similar contrast and resolution in all channels is achieved by maintaining the same SWIR detection window. In the initial report, non-invasive, real-time, multi-channel imaging in living mice in video rate (27 frames per second, fps) was demonstrated. However, it was limited to three colors and produced

some challenges in motion artifacts due to the ~10 ms separation between channels. Faster acquisition speeds would allow for enhanced temporal resolution in three-color imaging, and/or increased number of orthogonal excitation channels (and thus biological parameters) that can be acquired while maintaining video-rate acquisition.

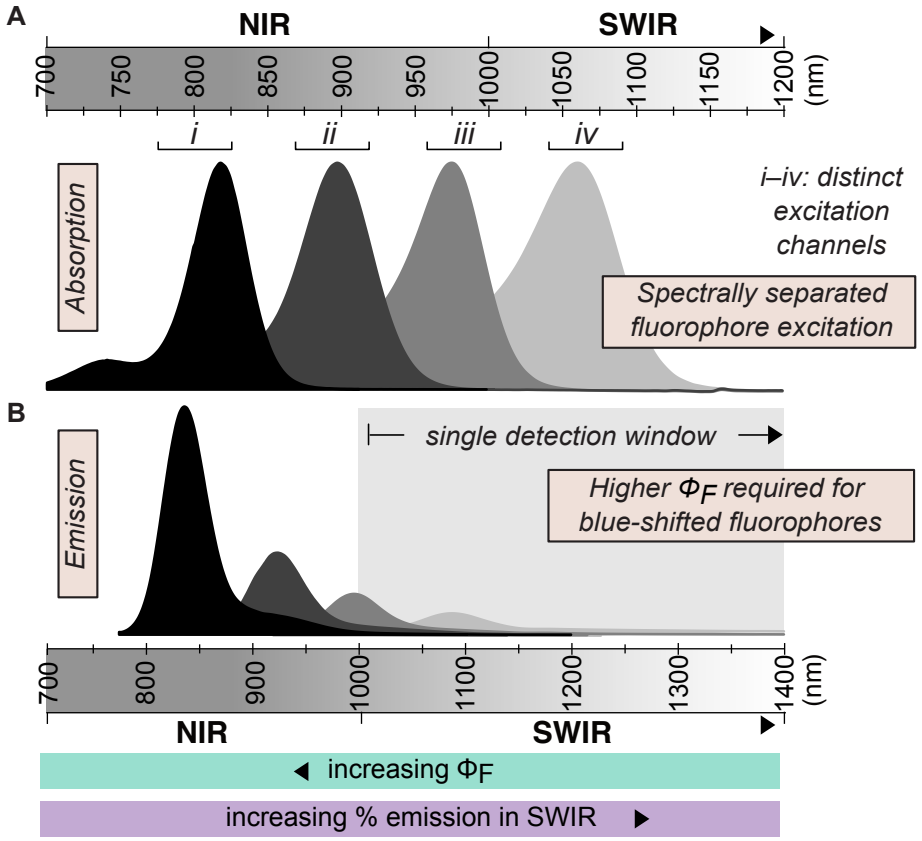

Figure 4.1 Excitation multiplexing concepts. A) Absorption properties of select fluorophores aligned with distinct excitation channels across the NIR and SWIR. B) Emission properties of select fluorophores across the NIR and SWIR overlaid with a SWIR detection window, defined here as 1,000–1,700 nm. Intensities are schematized to represent the key imaging concepts defined below.

To produce orthogonal signals from differing, well-separated (~75-100 nm) excitation wavelengths across the NIR and SWIR, two classifications of emitters are necessary: 1) fluorophores with SWIR absorption and emission, and 2) NIR-absorbing dyes which exhibit long wavelength emission tails extending into the SWIR region (Figure 4.1). Imaging NIR dyes in the SWIR requires a higher brightness to compensate for the small fraction of the emission signal that

is collected (Figure 4.1B). Fortuitously, this concept aligns well with the energy gap laws[22], allowing drastically higher fluorescence quantum yields (Φ_F) to be obtained with more blue-shifted dyes. However, apart from the FDA-approved indocyanine green[22–23], (ICG), and analogues[25–28] (Figure 4.2A, *i*) which are commonly excited between 785–808 nm, currently, there are few bright probes with NIR absorption greater than 800 nm (Figure 4.2A, *ii–iii*, Chart 4.1).[12–13, 29–33] To improve both the speed and degree of multiplexing for non-invasive imaging in small animals, brighter dyes with narrow excitation spectra at wavelengths between 800–1,000 nm are necessary.

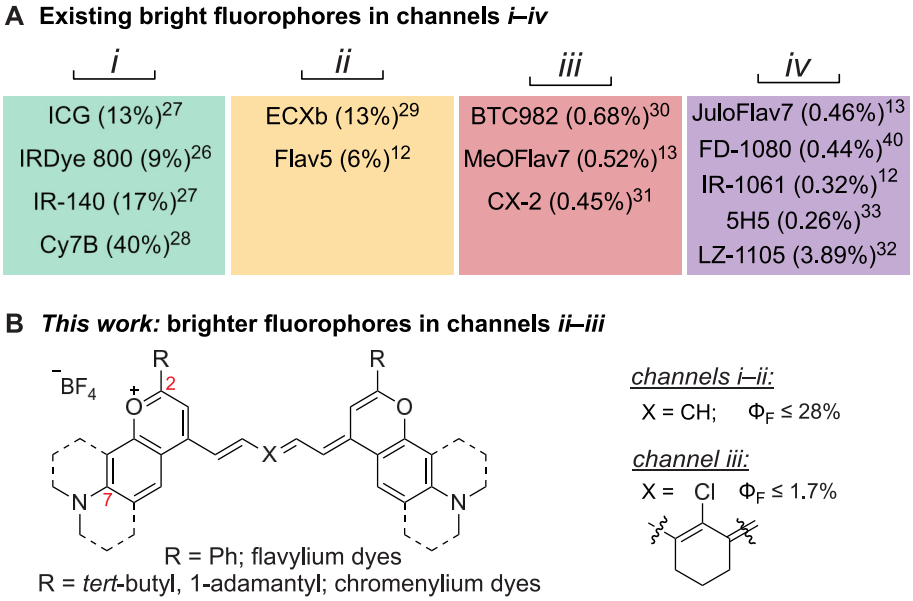

Figure 4.2 Fluorophores in the context of excitation multiplexed SWIR imaging. C) Existing fluorophores with high Φ_F (Φ_F in parenthesis) values for their respective absorption wavelength aligned with the excitation channels defined in (A). B) Pentamethine and heptamethine fluorophores reported in this manuscript. Positions 2- and 7- on the flavylium and chromenylium heterocycles are indicated in red.

Chart 4.1 Structures of dyes listed in Figure 4.2A.

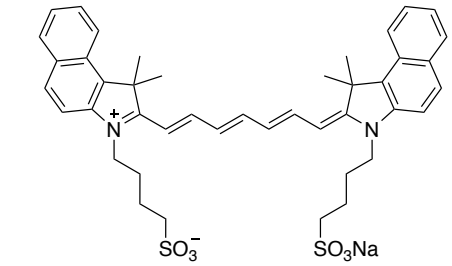

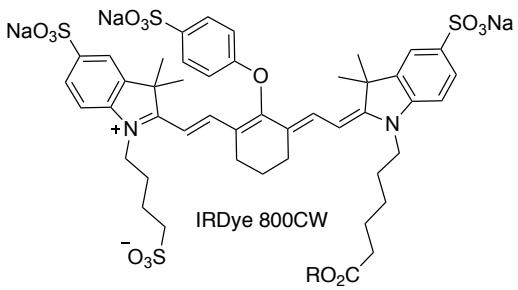

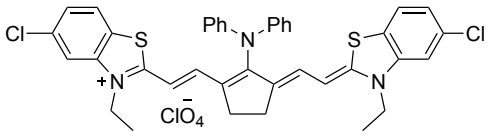

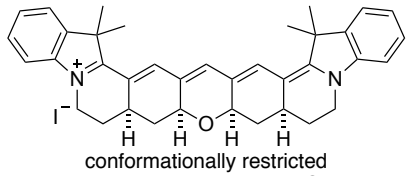

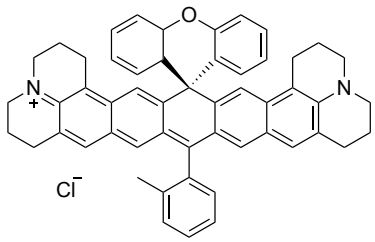

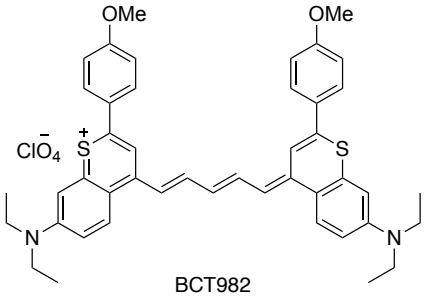

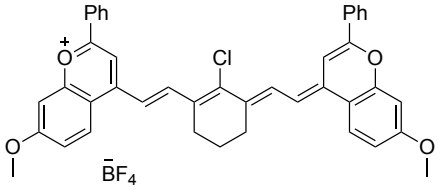

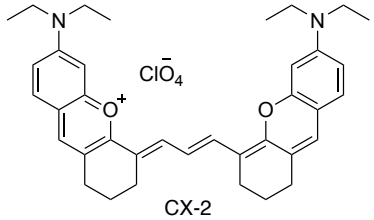

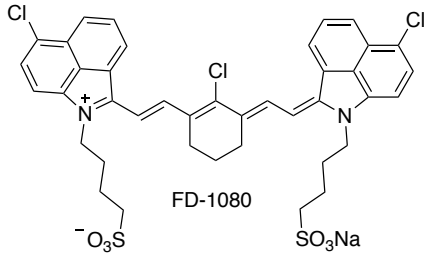

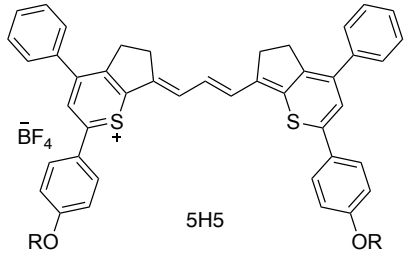

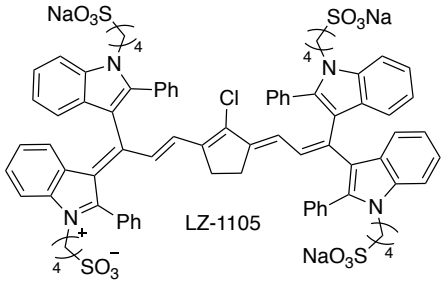

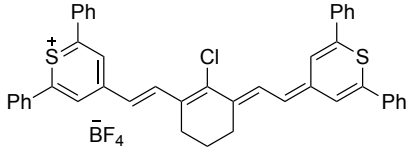

Small molecules are desirable contrast agents due to their small size, biocompatibility, and simple bioconjugation approaches.[34] Polymethine dyes, fluorophores composed of two heterocyclic terminal groups connected by a vinylene chain[35–36], are ideal candidates for excitation multiplexing, due to high absorption coefficients (ε), often above ~10^5 $M^{-1}cm^{-1}$, and narrow absorption profiles which can be fine-tuned to match excitation channels.[13,37] While red-shifted polymethine dyes often retain favorable absorptive properties, Φ_F values drop drastically in the NIR to SWIR regions. As brightness is reliant on both absorptive and emissive properties (brightness = $\varepsilon_{max} \times \Phi_F$; ε_{max} = absorbance coefficient at $\lambda_{max,abs}$), an ideal fluorophore will undergo both excitation and emission efficiently. Efforts to increase the quantum yield of polymethine dyes have included reducing non-radiative processes by interactions with biomolecules[25, 39–40], introducing conformational restraint on the polymethine chain[41–42], or by decreasing intersystem crossing by replacing heavy atoms[12, 43]. Further efforts to increase brightness in polymethine dyes include reducing aggregation effects to increase the amount of actively absorbing and emitting species that can be detected.[26, 30, 44]

As a starting point to obtain NIR polymethine dyes with absorption maxima >800 nm and high brightness, we looked to the oxygen-containing flavylium dyes, which have previously furnished bright NIR and SWIR-light absorbing molecules. Fluorophores constructed from a 4-methyl-7-dimethylamino flavylium heterocycle include heptamethine dye **4.1** (Flav7, $\lambda_{max,abs}$ = 1,027 nm, Φ_F ~0.6%) and pentamethine dye **4.2** (Flav5, $\lambda_{max,abs}$ = 862 nm, Φ_F ~5%),[12] (Figure 4.2A) which are ~10-fold more emissive than the thiaflavylium counterparts[30, 45], likely due to reduction in intersystem crossing (in addition to the effects of energy gap laws). Investigation of structure-property relationships by systematic substitution of the flavylium heterocycle produced trends which could reliably red- or blue-shift excitation wavelengths but did not produce

significant enhancements in the emissive properties, offering little insight into further increasing the brightness of the scaffold.[13, 46] Here, we explore structural features on the heterocycle that increase the emissive behavior in long wavelength polymethine dyes. The resulting dyes are applied to fast and multiplexed SWIR imaging in mice.

4.3 Results and Discussion

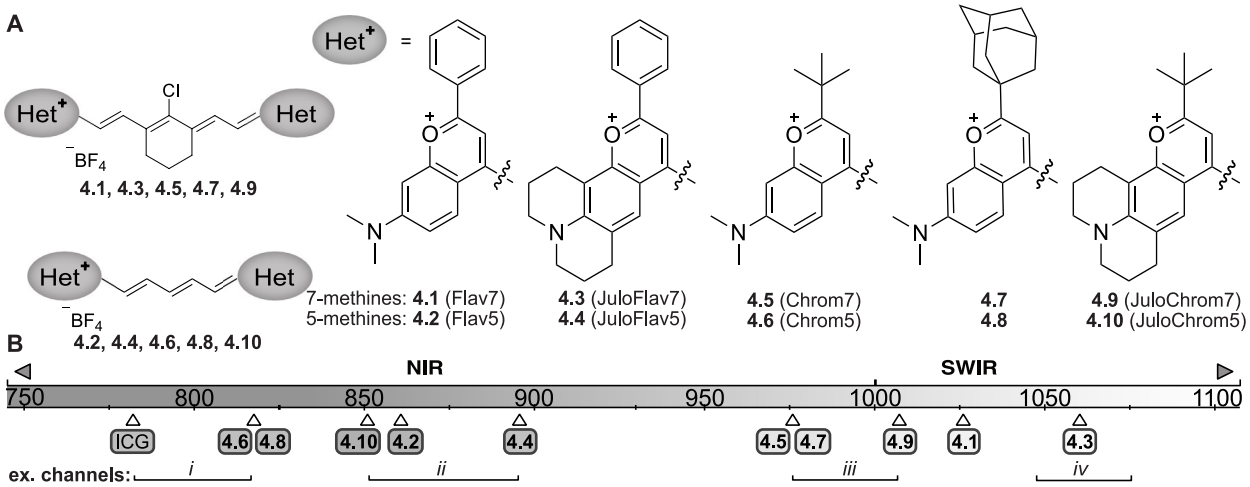

Figure 4.3 Structures absorption wavelengths of heptamethine and pentamethine dyes. A) Chemical structures of heptamethine and pentamethine dyes explored in this study (see Chart 4.1 for full structures). B) Absorption maxima of ICG and dyes **4.1**–**4.10** displayed graphically on the electromagnetic spectrum and aligned with the distinct excitation channels used for excitation-multiplexed, single-channel SWIR imaging.

4.3.1 Design, Synthesis, and Photophysical Characterization of SWIR-Emitting Polymethine Dyes

We hypothesized that rotational and vibrational modes within the phenyl group at the 2-position on flavylium (Figure 4.2B) could be contributing to internal conversion in the resulting polymethine dyes. To investigate this question, we targeted 4-methyl chromenylium heterocycles containing either a tert-butyl or a 1-adamanyl group at their 2-positions and applied them to synthesize pentamethine and heptamethine dyes with absorption between 800–1000 nm (Figure 4.3). We found that the chromenylium heterocycles could be synthesized by an analogous route to

the prior flavylium variants[13] (Scheme 4.1A). From these heterocycles, we synthesized the hepta- and pentamethine chromenylium dyes **4.5**–**4.8** (Scheme 4.1B–C, Chart 4.1) through the polymethine condensation reaction with the corresponding conjugated bis(phenylimine) (**4.13** and **4.14**, respectively).

Scheme 4.1 Synthesis of chromenylium heterocycles (A), heptamethine dyes (B) and pentamethine dyes (C).

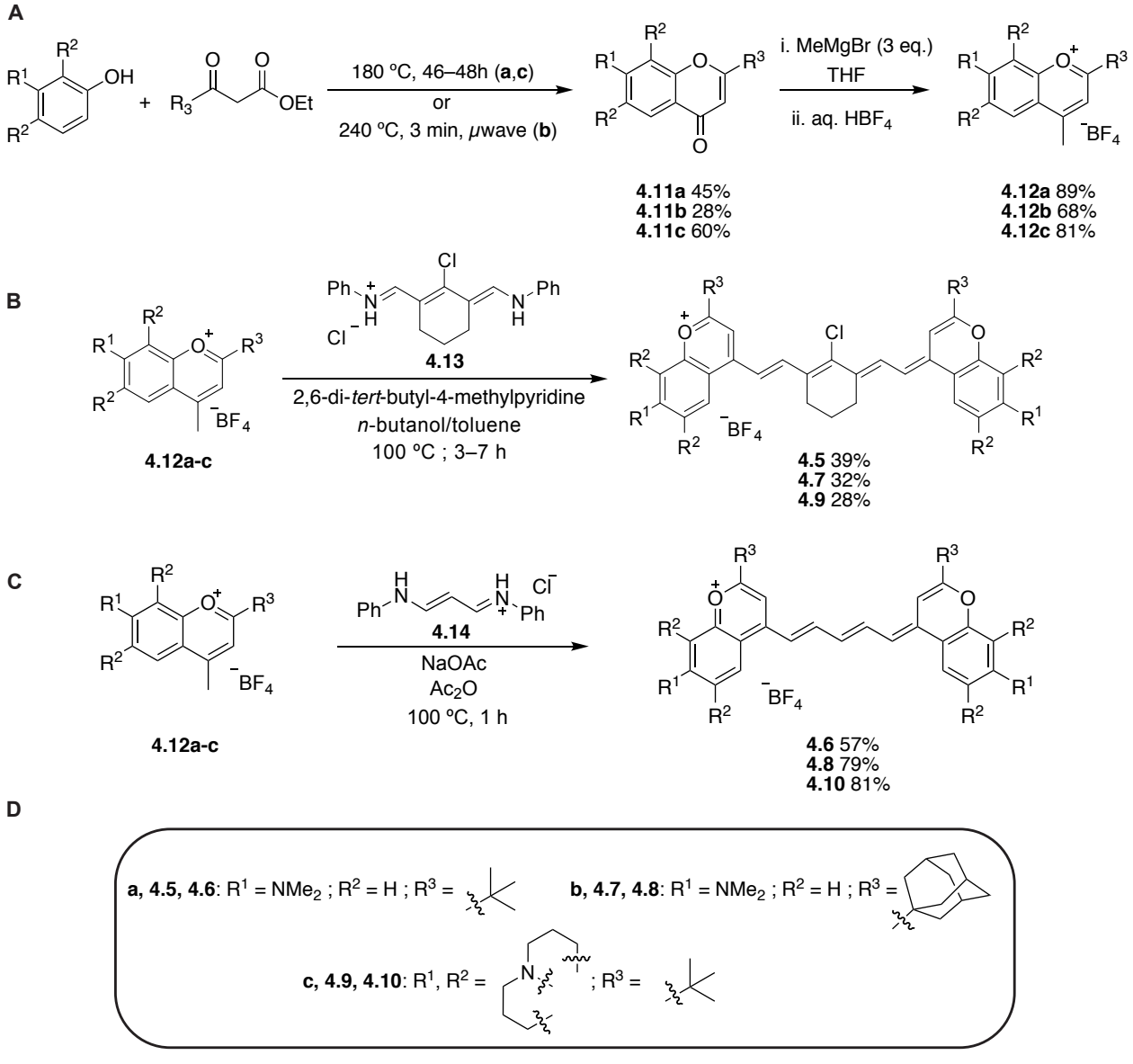

Chart 4.2 Full Structures of dyes **4.1**–**4.10**.

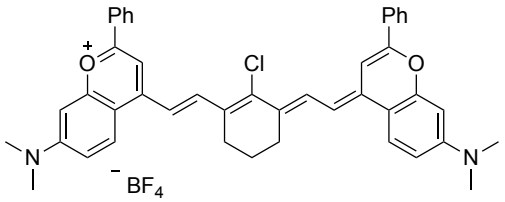

4.1 (Flav7)

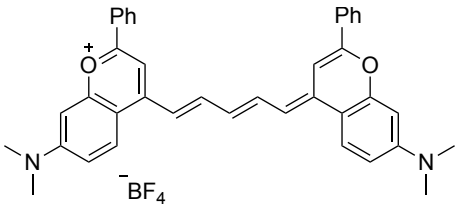

4.2 (Flav5)

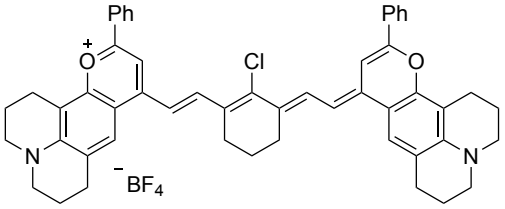

4.3 (JuloFlav7)

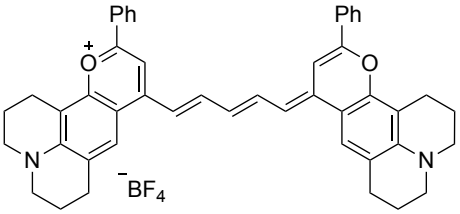

4.4 (JuloFlav5)

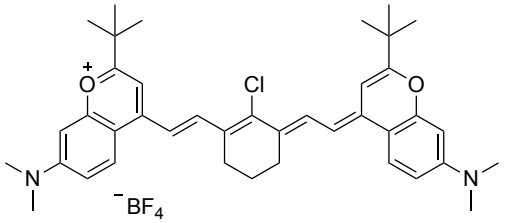

4.5 (Chrom7)

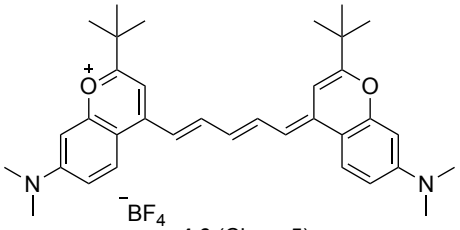

4.6 (Chrom5)

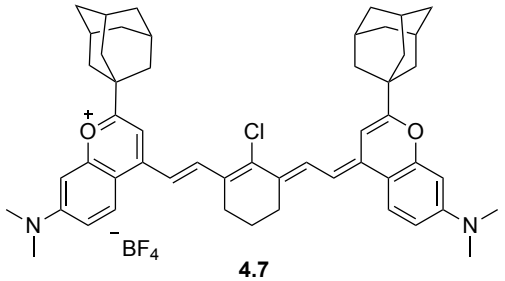

4.7

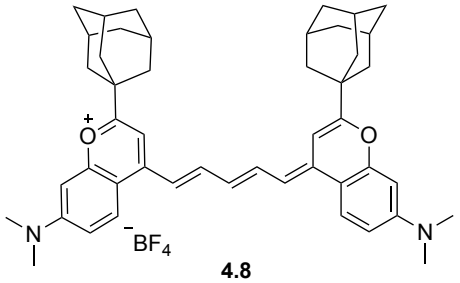

4.8

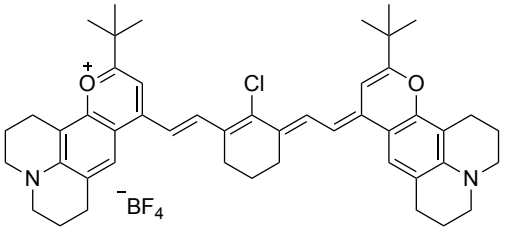

4.9 (JuloChrom7)

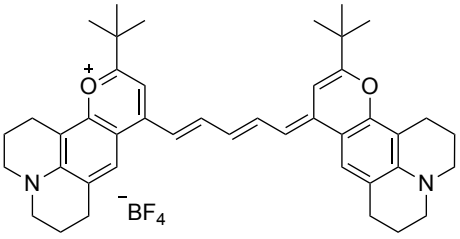

4.10 (JuloChrom5)

In previous work, we found that the introduction of a julolidine-containing flavylium heterocycle provided advantageous red-shifts (**4.3,** JuloFlav7, $\lambda_{max,abs}$ = 1,061 nm, Φ_F ~0.46%) compared to Flav7 (**4.1**)[13]. Consequently, we were also interested in investigating the pentamethine flavylium dye that would result from this same julolidine-containing heterocycle, (**4.4**), and the chromenylium pentamethine and heptamethine fluorophores containing the julolidine functionality (**4.9**, **4.10**, respectively, Figure 4.3A, Chart 4.2).

Scheme 4.2 Synthesis of flavylium pentamethine dyes.

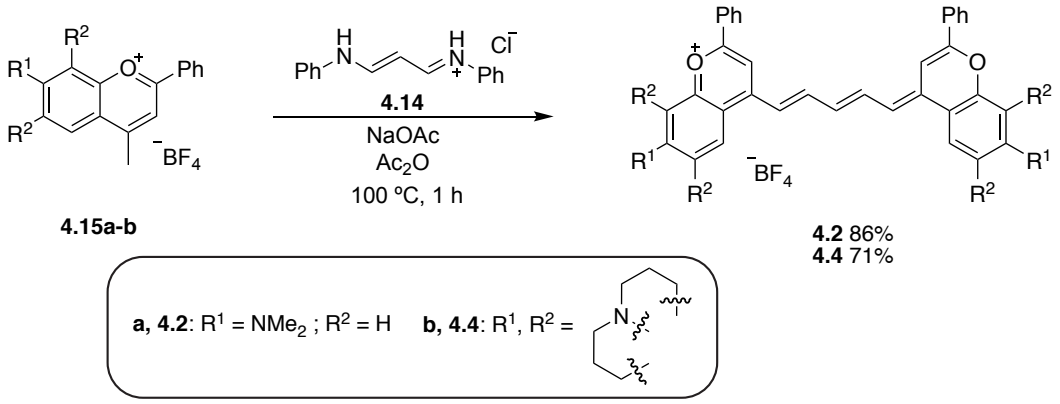

After preparation of the chromenylium dyes **4.5**–**4.10** as well as the previously reported flavylium dyes **4.1**–**4.3** and the new flavylium dye **4.4** (Scheme 4.2, select dyes are named after the heterocycle and the number of methine units in the polymethine chain), we performed a comparative investigation of their photophysical properties. The photophysical properties in dichloromethane reveal that the absorption and emission of the chromenylium heptamethine derivatives are blue shifted by λ ~52 nm (ν ~500 cm^{-1}), and the chromenylium pentamethine dyes by λ ~44 nm (ν ~600 cm^{-1}), from their flavylium counterparts (Figure 4.4A, Table 4.1). The absorption coefficients remain characteristically high, with the pentamethines having, on average, higher values than the heptamethines, at ~360,000 $M^{-1}cm^{-1}$ and ~250,000 $M^{-1}cm^{-1}$, respectively (Table 4.1). Remarkably, the emissive properties increased substantially, with heptamethine chromenylium dyes Φ_F = 1.6–1.7% (relative measurements to IR-26 = 0.05%)[45] and

pentamethine chromenylium dyes Φ_F = 18–28% (absolute quantum yield measurements) (Figure 4.4 C–D, Section 4.6.1). Combining the absorptive and emissive properties, **4.5** and **4.7** have the highest brightness of the heptamethines at 4,300 $M^{-1}cm^{-1}$, while **4.6** is the brightest pentamethine (106,000 $M^{-1}cm^{-1}$).

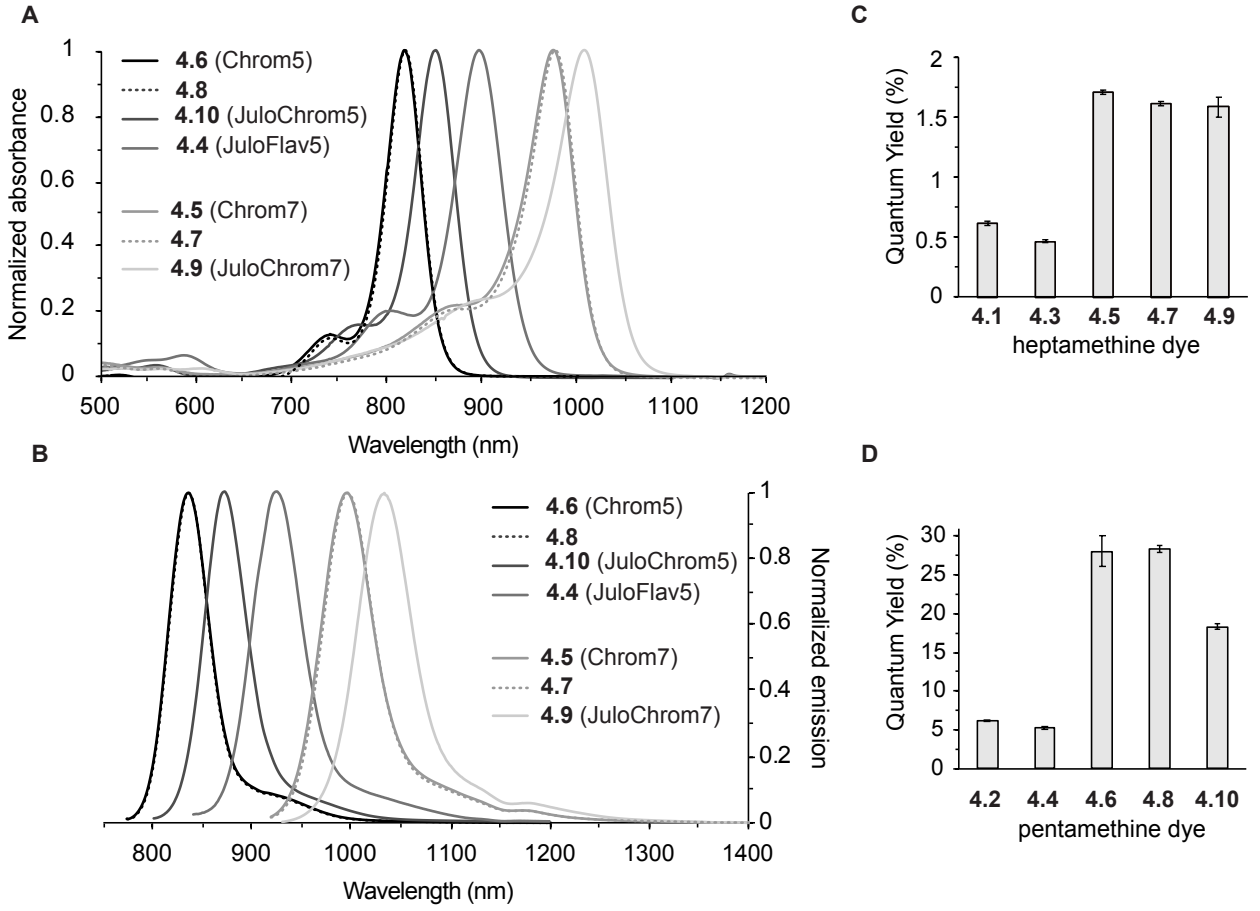

Figure 4.4 Photophysics of penta- and heptamethine dyes. A) Absorbance spectra of newly reported dyes. B) Emission spectra of newly reported dyes, ex. = 755 nm for pentamethine dyes; ex. = 885 nm for heptamethine dyes. C–D) Quantum yields of heptamethine dyes (C) and pentamethine dyes (D) displayed graphically; error bars represent standard deviation, n = 3 measurements.

Table 4.1 Photophysics of penta- and heptamethine dyes in DCM.

	dye	$\lambda_{max,abs}$ (nm)	ε_{max} ($M^{-1}cm^{-1}$)	$\lambda_{max,em}$ (nm)	Φ_F (%)	brightness(ε_{max}) ($M^{-1}cm^{-1}$)[c]	SWIR brightness ($M^{-1}cm^{-1}$)[d]
heptamethine	**4.1** (Flav7)[a]	1027	241,000 ± 1,000	1053	0.61 ± 0.02	1,470 ± 50	1,430 ± 50
	4.3 (JuloFlav7)[a]	1061	238,000 ± 7,000	1088	0.46 ± 0.01	1,090 ± 50	1,090 ± 40
	4.5 (Chrom7)	975	252,000 ± 5,000	996	1.70 ± 0.02	4,300 ± 100	2,420 ± 60
	4.7	977	267,000 ± 8,000	997	1.61 ± 0.02	4,300 ± 100	2,480 ± 80
	4.9 (JuloChrom7)	1008	228,000 ± 6,000	1033	1.58 ± 0.08	3,600 ± 200	3,300 ± 200
pentamethine	**4.2** (Flav5)[b]	862	327,000 ± 7,000	883	6.1 ± 0.1	19,900 ± 500	910 ± 20
	4.4 (JuloFlav5)	897	254,000 ± 5,000	925	5.3 ± 0.2	13,500 ± 600	1,200 ± 50
	4.6 (Chrom5)	819	380,000 ± 10,000	836	28 ± 2	106,000 ± 8000	1,140 ± 90
	4.8	818	320,000 ± 10,000	837	28.3 ± 0.5	91,000 ± 3000	940 ± 30
	4.10 (JuloChrom5)	852	389,000 ± 3,000	872	18.3 ± 0.4	71,000 ± 2000	1,240 ± 30

[a]previously reported measurements, ref. 13
[b]previously reported as the perchlorate salt, ref. 12
[c]brightness = $\varepsilon_{max} \cdot \Phi_F$
[d]SWIR brightness = brightness · α; α = emission ≥1000 nm / total emission

When compared to current state of the art organic fluorophores with similar absorption wavelengths in each excitation channel (dyes outlined in Figure 4.2 C, Table 4.2), the chromenylium dyes fare quite well. For example, in region (*i*), dye **4.6** is brighter than ICG[27], IRDye-800[26], and IR-140[27] and displays similar brightness to the conformationally restricted heptamethine indocyanine[28] (notated here as Cy7B). Dye **4.10** (in region *ii*) is ~3.5-fold and ~4 fold brighter than Flav5 (**4.2**) [12] and ECXb[29], respectively, while dye **4.5** (in region *iii*) is between ~2.5–5-fold brighter than current standards BCT982[30], MeOFlav7 (**3.10**)[13], and CX-2[31]. Thus, the series of chromenylium dyes provide bright organic chromophores with NIR-absorption.

Table 4.2 Photophysics of existing bright NIR dyes.

Relevant spectral region	dye	Solvent	$\lambda_{max,abs}$ (nm)	ε_{max} ($M^{-1}cm^{-1}$)	Φ_F (%)	brightness ($M^{-1}cm^{-1}$)	citation
i	ICG	EtOH	787	194,000	13.2	25,600	27
i	IRDye 800CW	PBS	775	240,000	8.7	23,490	26
i	IR-140	EtOH	804	174,000	16.7	29,000	27
i	Cy7B	DCM	775	303,000	40	121,200	28
ii	ECXb	DCM	879	132,000	13.3	17,500	29
iii	BTC892	DCM	944	260,000	0.68	1,800	30
iii	MeOFlav7	DCM	984	190,000	0.52	990	13
iii	CX-2	chloroform	981	191,000	0.45	860	31

While overall brightness is an important comparative metric, the more relevant brightness metric for excitation-multiplexed imaging with single channel SWIR detection is the percent of emission that is within the SWIR region. We accounted for this parameter by defining SWIR brightness = $\varepsilon_{max} \times \Phi_F \times \alpha$, where α = emission ≥1000 nm/total emission, calculated from the emission spectra. All of the chromenylium heptamethine dyes have higher SWIR brightness than the flavylium heptamethine dyes, despite their more blue-shifted photophysics (Table. 4.1). For the pentamethines, flavylium dye **4.4** and chromenylium dyes **4.6** and **4.10** are the brightest SWIR emitters of the series.

4.3.2 Investigation of Enhanced Φ_F of Chromenylium Dyes

The chromenylium dyes display significant improvements in their Φ_F compared to their flavylium analogues. To investigate this enhancement, we measured the fluorescence lifetimes (τ) of dyes **4.1**–**4.10** by time-correlated single-photon counting (TCSPC) (see Section 4.6.2). We found that in all cases, τ increased considerably for the chromenylium dyes compared to the flavylium dyes, corresponding to the increase in Φ_F (Table 4.3). A ~2.5-fold increase in τ to ~140

ps for the heptamethines (**4.5**, **4.7**, **4.9**) and a ~3.1-fold enhancement to τ ~1 ns for the pentamethines **4.6** and **4.8** (Table 4.3, Figure 4.5A–B) is observed. A slightly shorter τ (~750 ps), and corresponding lower Φ_F is determined for the more red-shifted pentamethine **4.10**. By calculating the radiative (k_r) and non-radiative (k_{nr}) rates from these data, we discovered that while modest increases in k_r are observed for the brighter dyes, the k_{nr} are more drastically affected. There is an average of 2.3-fold decrease in k_{nr} for the heptamethines and a 3.8-fold decrease in k_{nr} for the pentamethines when comparing chromenylium to flavylium dyes (Table 4.3).

Table 4.3 Table of photoluminescence lifetimes and rates in DCM.

	dye	Φ_F (%)	τ (ps)	k_r (ns^{-1})	k_{nr} (ns^{-1})
heptamethine	**4.1** (Flav7)	0.61 ± 0.02	68 ± 1	0.090 ± 0.003	14.6 ± 0.5
	4.3 (JuloFlav7)	0.46 ± 0.01	56 ± 1	0.083 ± 0.003	17.9 ± 0.7
	4.5 (Chrom7)	1.70 ± 0.04	148 ± 1	0.117 ± 0.003	6.7 ± 0.09
	4.7	1.61 ± 0.04	151 ± 1	0.106 ± 0.003	6.5 ± 0.2
	4.9 (JuloChrom7)	1.58 ± 0.08	118 ± 1	0.134 ± 0.007	8.3 ± 0.4
pentamethine	**4.2** (Flav5)	6.1 ± 0.1	311 ± 1	0.197 ± 0.003	3.02 ± 0.05
	4.4 (JuloFlav5)	5.3 ± 0.2	296 ± 1	0.180 ± 0.008	3.2 ± 0.1
	4.6 (Chrom5)	28 ± 2	1022 ± 1	0.27 ± 0.02	0.70 ± 0.04
	4.8	28.3 ± 0.5	1054 ± 1	0.268 ± 0.004	0.68 ± 0.01
	4.10 (JuloChrom5)	18.3 ± 0.4	753 ± 1	0.243 ± 0.005	1.09 ± 0.02

This effect can be visualized by comparing analogous chromenylium and flavylium structures (Figure 4.5C) and observing the relative contribution of changes in k_r or k_{nr} to $\Delta\Phi_F$ between the two scaffolds (Figure 4.5D, Section 4.6.3). The finding that the decreased k_{nr} is the dominant contributor to the increased Φ_F in the chromenylium dyes lead us to hypothesize that the bulky alkyl groups at the 2-poistion provide fewer vibrational modes that enable relaxation by internal conversion as compared to a phenyl group. We are unable to decouple the vibrational

mode effects from those imparted by the energy gap laws: blue-shifted dyes will have both increased k_r, and decreased k_{nr} compared to "vibrational mode equivalent" molecules with smaller HOMO-LUMO gaps. Nonetheless, the significantly increased Φ_F seen here that is absent in other polymethine dyes with a similar wavelength of absorption, supports that reducing vibrational modes is playing an important role in the increase in emissive behavior.

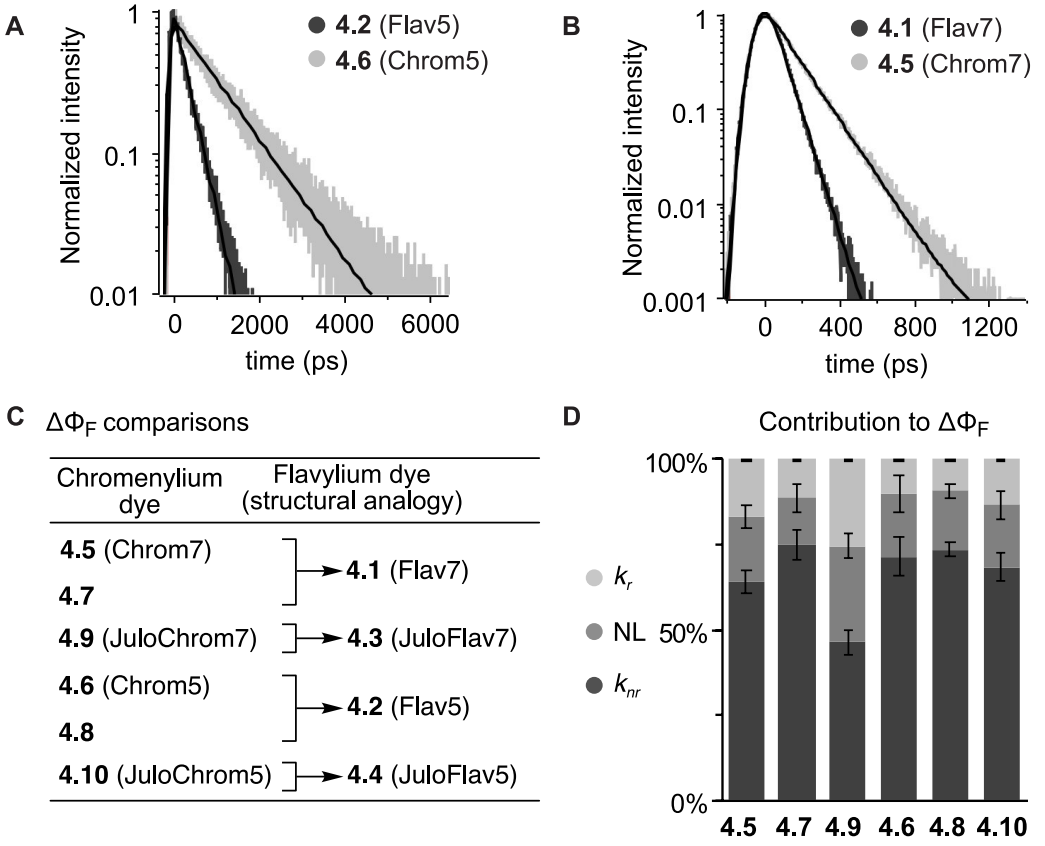

Figure 4.5 Analysis of heptamethine and pentamethine dye emissive properties. A–B) Time-correlated emission of selected dyes **4.2** and **4.6** (A) or **4.1** and **4.5** (B) and fitting curves. C) Chart outlining comparisons made between chromenylium and flavylium dyes for $\Delta\Phi_F$ analysis in (D). D) Relative contribution of non-radiative rate (k_{nr}), radiative rate (k_r), or a non-linear contribution (NL) composed of a combination of both k_{nr} and k_r to $\Delta\Phi_F$ between chromenylium and flavylium dyes (Section 4.6.3).

To further understand the differences between the two dye types, we obtained the X-ray crystal structures of dyes **4.4** and **4.5** as exemplars of the flavylium and chromenylium scaffolds,

respectively (Figure 4.6). Focusing on the 2-position of the heterocycle, the phenyl group on the flavylium dye **4.4** lies ~10–20˚ out of plane of the polymethine chain and the C1–C2 and C3–C4 bonds have an average bond length of 1.47 Å, indicating single bond C(sp^2)–C(sp^2) character. These metrics suggest that free rotation of the phenyl groups occur in solution. Chromenylium dye **4.5** displays the expected C2–C1 and C4–C3 bond lengths of 1.51 Å for a C(sp^2)–C(sp^3) bond. Taken together, the crystal structure and fluorescence lifetime analyses suggest that the added degrees of freedom in the chromophore associated with the 2-phenyl substituent contributes to the increased k_{nr} in the flavylium dyes.

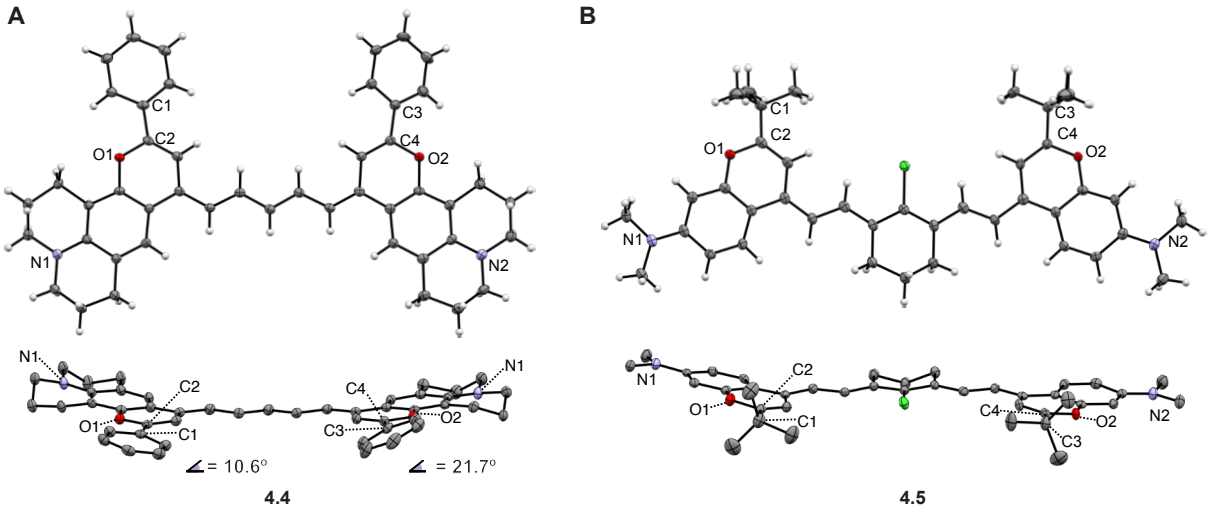

Figure 4.6 Thermal Ellipsoid Plots (ORTEP) for compound **4.4** (A) and **4.5** (B), arbitrary numbering, shown at two viewpoints. Counterions and solvent molecules are omitted for clarity. Lower structures omit all H atoms for clarity. Atomic displacement parameters are drawn at the 50% probability level.

4.3.3 In vitro Comparative Brightness Experiments[1]

While photophysical characterization is essential for understanding chromophore properties, there are many additional parameters that contribute to a dye's *in vivo* performance,

[1] Imaging experiments in this chapter with Bernardo Arús

including: delivery strategy, interaction with biological tissues, and the excitation and detection parameters of the imaging configuration. To begin to understand the translation to *in vivo* experiments, we used an excitation-multiplexed SWIR imaging configuration to compare emission of the fluorophores in different biologically-relevant media when excited at different wavelengths. The imaging set-up includes excitation lasers that correspond to each channel (*i–iv*, Figure 4.1A) (785, 892, and 968, 1,065 nm), which are diffused and delivered uniformly to the biological sample. Excitation irradiation is scaled to the approved values, as outlined by the International Commission on Non-Ionizing Radiation Protection (ICNIRP) guidelines. The guidelines indicate that within the spectral region of interest (~785–1,065 nm), higher photon doses are tolerated as the wavelength is increased. This results in a factor of 3.4-fold higher irradiation power allowed at 1,000 nm compared to 785 nm.[50] Importantly, the excitation-multiplexed imaging configuration provides fast switching of the excitation lasers (on the μs time scale), allowing for real-time multicolor imaging. Collection is achieved through a single-channel ("color-blind") SWIR detector that records individual frames for each excitation channel in tandem. Multiplexed frames are obtained by merging the adjacent frames from each excitation channel. As multiplexed frame rates are related to the exposure time multiplied by the number of channels used in the experiment, to obtain video-rate speeds, bright probes and short exposure times are necessary.

To compare brightness of the chromenylium dyes *in vitro*, we first dissolved dyes **4.5**, **4.6**, **4.9** and **4.10**, in organic solvent (DCM) at 0.25 μM, and measured the emission with 1,000 nm longpass (LP) filtering on an InGaAs camera upon sequential excitation with 785, 892, and 968 nm lasers. ICG (in EtOH), **4.4**, and MeOFlav7 (**3.10**) were used as benchmarks for excitation channels, *i–iii*, respectively (Figure 4.7). When the raw count data are normalized to the exposure time used in image collection, it is clear that **4.5**, in channel *iii*, produces the brightest SWIR

emission in organic solvent with excitation with the 968 nm laser, providing a ~3-fold advantage in brightness over MeOFlav7 (**3.10**), previously employed for 3-color imaging.[12] The other two channels offered lower signal overall, but the best performers in channels *i* and *ii* were ICG and **4.4**, respectively.

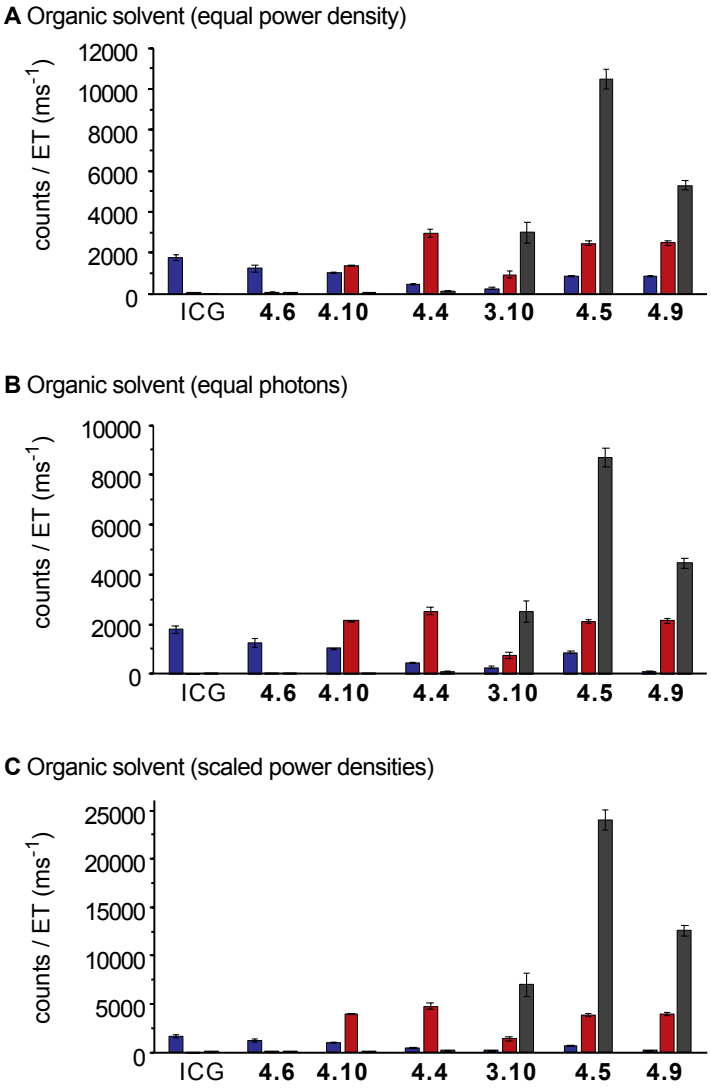

Figure 4.7 Brightness comparisons in organic solvent obtained in a SWIR imaging setup with different excitation and collection 1,100–1,700 nm. Quantification of mean intensity over ROI/exposure time (ms) from SWIR images of Eppendorf tubes containing 0.25 μM of each dye in organic solvent (flavylium and chromenylium dyes in DCM; ICG in EtOH) after excitation with 785 nm, 892 nm, or 968 nm lasers of equal power densities (A; 785 nm = 100 $mWcm^{-2}$, 892 nm = 101 $mWcm^{-2}$, 968 nm = 100 $mWcm^{-2}$), equal photon number (B; 785 nm = 100 $mWcm^{-2}$, 892 = 88 $mWcm^{-2}$, 968 nm = 81 $mWcm^{-2}$), or power densities scaled to INCIRP guidelines (C; 785 nm = 100 $mWcm^{-2}$, 892 nm = 163 $mWcm^{-2}$; 968 nm = 232 $mWcm^{-2}$) and LP1000 nm detection

(variable exposure time (ET) and frame rate). Error represents variation in concentration assessed by UV-VIS spectrometry measurements.

Next, to more closely approximate *in vivo* performance, we formulated each chromenylium or flavylium dye into water-soluble poly(ethylene) glycol-phospholipid micelles, a biocompatible nanomaterial for delivery (Scheme 4.3, Figures 4.8–4.9).

Scheme 4.3 Assembly of PEG-phospholipid micelles of chromenylium and flavylium polymethine dyes **4.3** (JuloFlav7), **4.4** (JuloFlav5), **4.5** (Chrom7), **4.6** (Chrom5), **4.9** (JuloChrom7), and **4.10** (JuloChrom5).

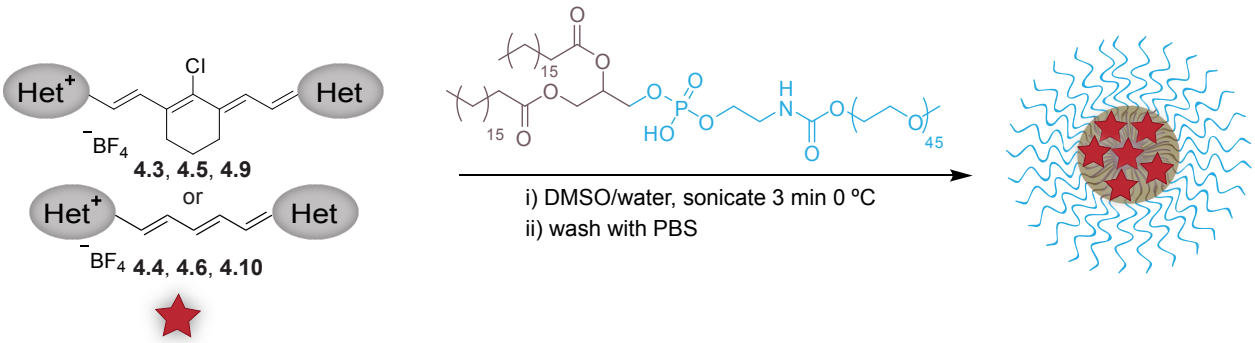

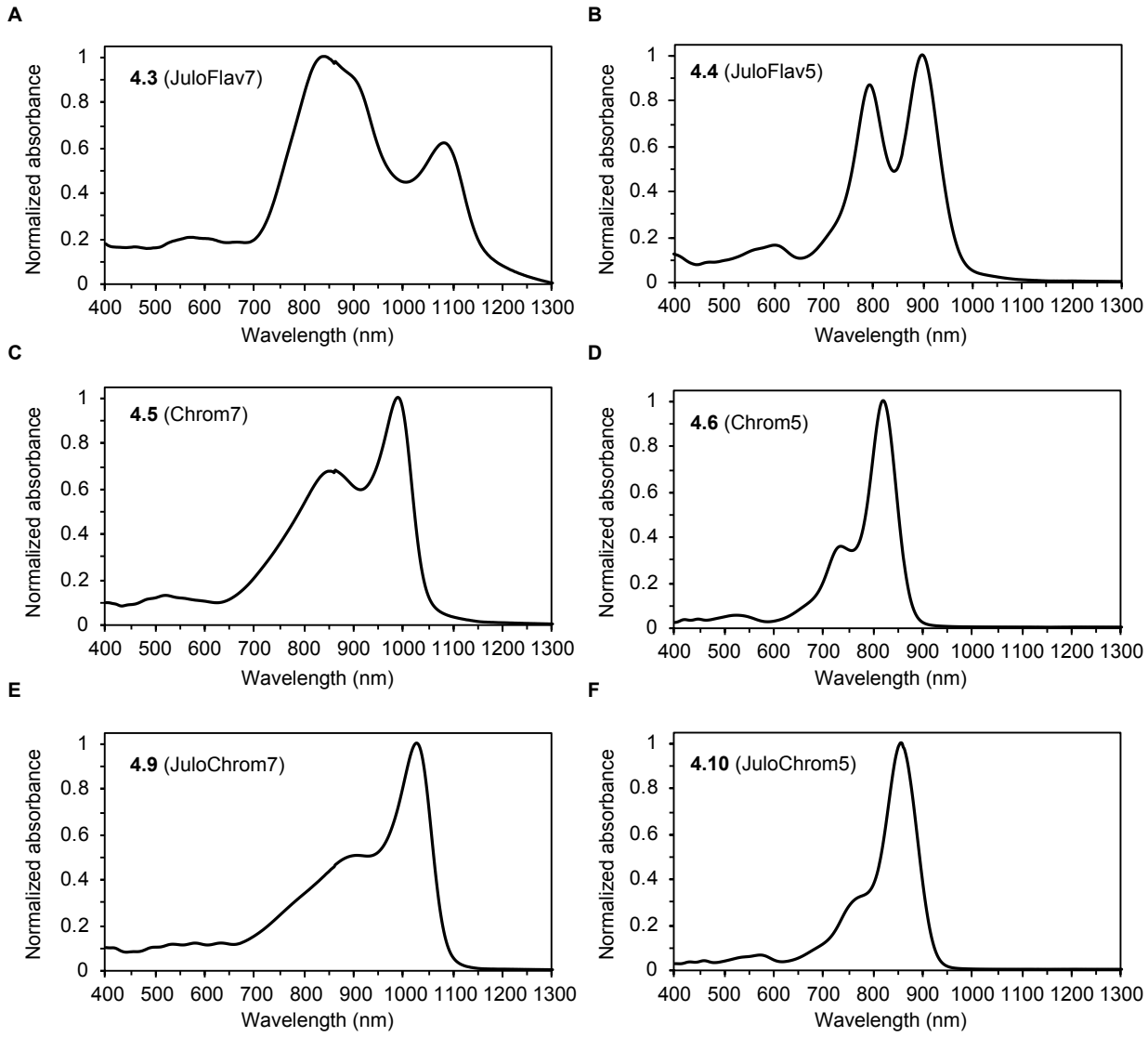

Figure 4.8 Normalized absorbance traces of PEG-phospholipid micelles of chromenylium and flavylium polymethine dyes in PBS buffer at 3–5 μM (path length = 2.0 mm).

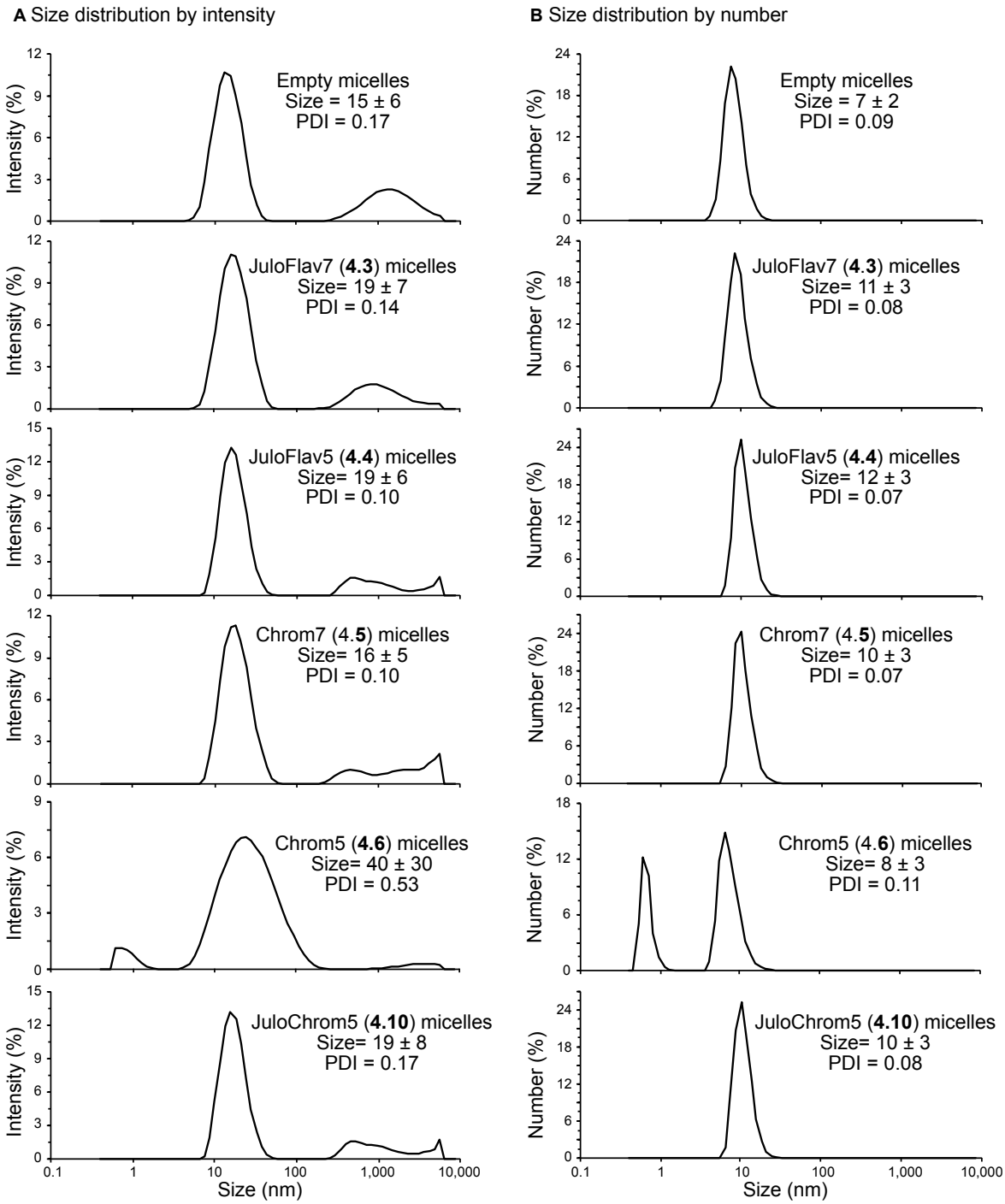

Figure 4.9 Dynamic light scattering (DLS) characterization of PEG-phospholipid micelles composed of 18:0 PEG2000 lipids containing either no dye, or one of dyes used for imaging: **4.3**–**4.6**, **4.10**. Data are the average of three replicate measurements. A) Size distribution by intensity. B) Size distribution by number. Size values and PDI values are taken and calculated from the majority peak. Note: minor micelle aggregation is occurring between 0.5–10,000 μm. As intensity is proportional to diameter to the sixth power, aggregate species is a small amount of the total sample and cannot be observed in the size distribution by number graphs in (B).

Solutions with equal dye concentration (flavylium and chromenylium dyes in micelles; ICG, free; see Section 4.6.4) were dispersed in water (Figure 4.10A–4.11A), fetal bovine serum (FBS) (Figure 4.10B–4.11B), and sheep blood (Figure 4.10C–4.11C) and loaded into capillary tubes (Figure 4.12). As many polymethine dyes, most notably ICG,[51] are known to increase in brightness in serum and blood, it is essential to perform benchmarking experiments in these biologically-relevant media. Evaluating brightness in these media changed the results drastically compared to those in the organic solvent experiment, likely due to variable amounts of aggregation or interactions within the micelles and/or biological media. Notably, in all media, two dyes stand out with significantly high SWIR brightness, **4.10**, when excited with the 892 nm laser, and **4.5**, when excited with the 968 nm laser. While ICG is the brightest SWIR emitter upon 785 nm laser excitation in both FBS and blood, both chromenylium dyes produce greater signal in their respective channels (*ii* and *iii*) compared to that of ICG (in channel *i*). In blood, the most representative media, this quantitates to a ~2.8-fold and ~1.7-fold improvement in signal over ICG for **4.10** and **4.5**, respectively. Additionally, comparing the performance of the chromenylium dyes between media, it is clear that, similar to ICG, an increase in brightness is occurring in FBS and blood compared to water. Interestingly, the opposite effect is observed for MeOFlav7, likely due to instability in more complex environments. Similar experiments using either equal laser power, or equal photon number at all excitation wavelengths have an expected reduced performance at the longer excitation wavelengths compared to those using ICNIRP-suggested powers, but still predict a ~2-fold brightness advantage of **4.10** over ICG (Figure 4.10D–I). As **4.5** and **4.10** will be further applied in multiplexed SWIR imaging in the *in vivo* experiments we will refer to them as Chrom7 (**4.5**) and JuloChrom5 (**4.10**), respectively.

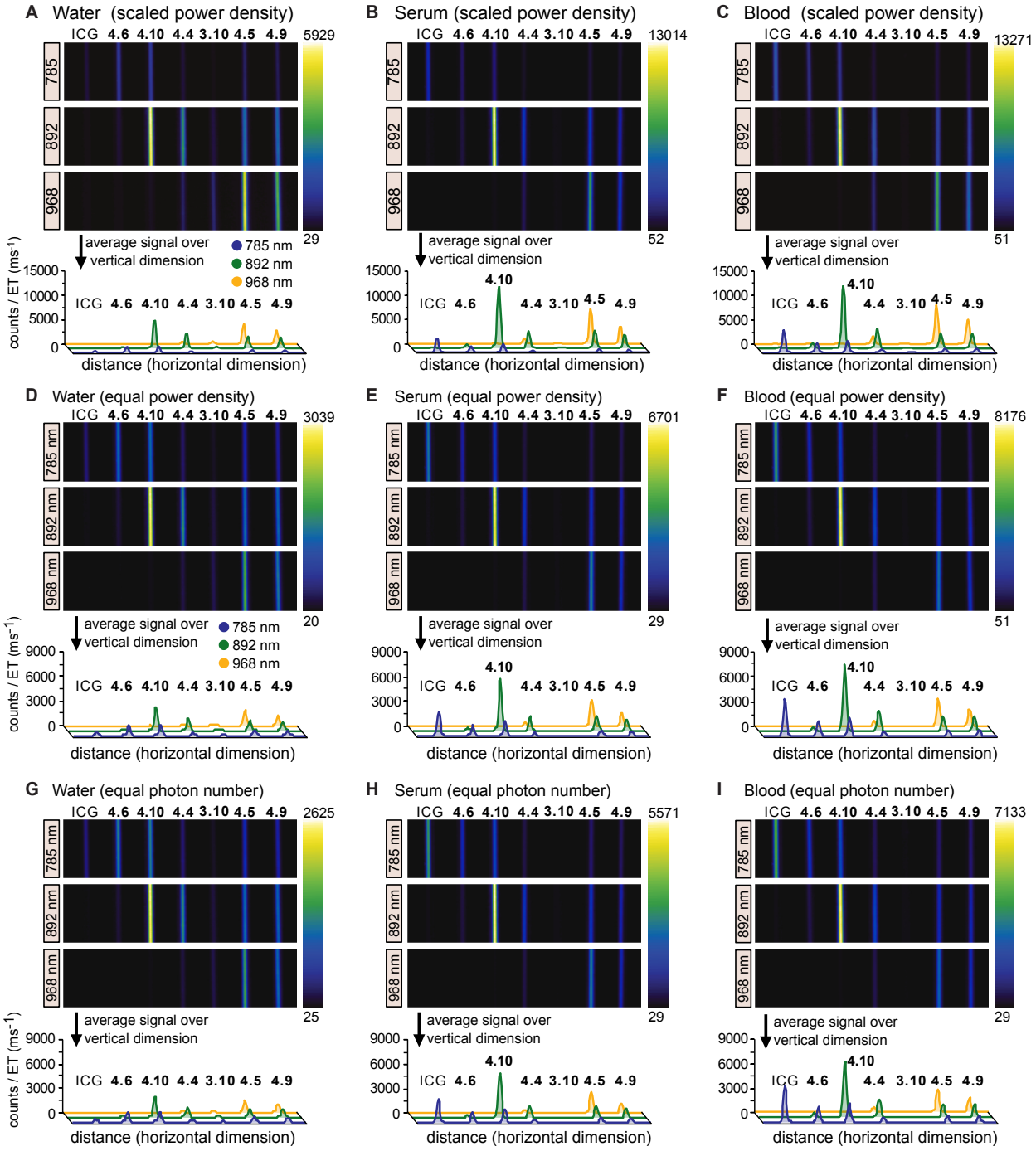

Figure 4.10 Brightness comparisons in imaging configuration using scaled power densities (A–C), equal power densities (D–F), and equal photon numbers (G–I) across laser wavelengths. Images upon 785 (A–I = 33 mW cm^{-2}), 892 (A–C = 54; D–F = 33; G–I = 29 mW cm^{-2}), and 968 (A–C = 77; D–F = 33; G–I = 27 mW cm^{-2}) nm ex. and LP1000 nm detection (variable exposure time (ET) and frame rate) of capillaries containing equal moles of dyes **4.4**–**4.6**, **4.9**, **4.10** (lipid formulations) and benchmark dyes ICG (free) and MeOFlav7 (**3.10**) (lipid formulation) when

dissolved in water (A, D, G), fetal bovine serum (FBS) (B, E, H), or sheep blood (C, F, I). Displayed images were averaged over 200 frames and normalized to the ET used in each image. The intensities are averaged over the vertical dimension and are plotted over distance in the horizontal dimension below each image.

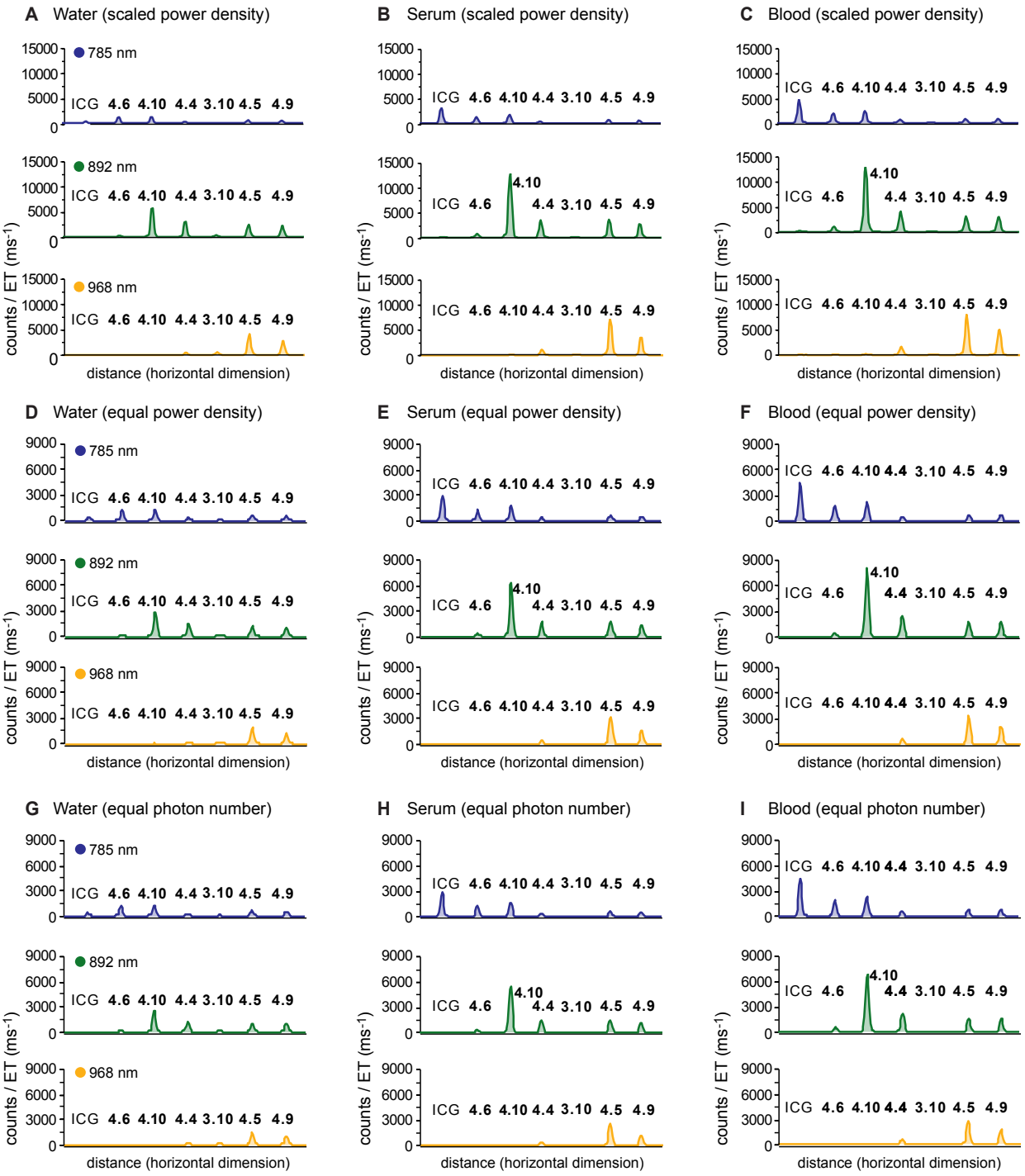

Figure 4.11 Graphs from brightness comparison in Figure 4.10 displayed individually for visual clarity. A–C) Scaled power densities. D–F) Equal power densities. G–I) Equal photon numbers.

Power densities: 785 (A–I = 33 mWcm^{-2}), 892 (A–C = 54; D–F = 33; G–I = 29 mWcm^{-2}), 968 (A–C = 77; D–F = 33; G–I = 27 mWcm^{-2}). LP1000 nm detection (variable ET and frame rate). Capillaries contain equal moles of dyes **4.4**–**4.6**, **4.9**, and **4.10** (lipid formulations) and benchmark dyes ICG (free) and MeOFlav7 (**3.10**) (lipid formulation) when dissolved in water (A, D, G), fetal bovine serum (FBS) (B, E, H), or sheep blood (C, F, I). Graphs represent the intensity of each image averaged over the vertical dimension, and plotted over the horizontal dimension.

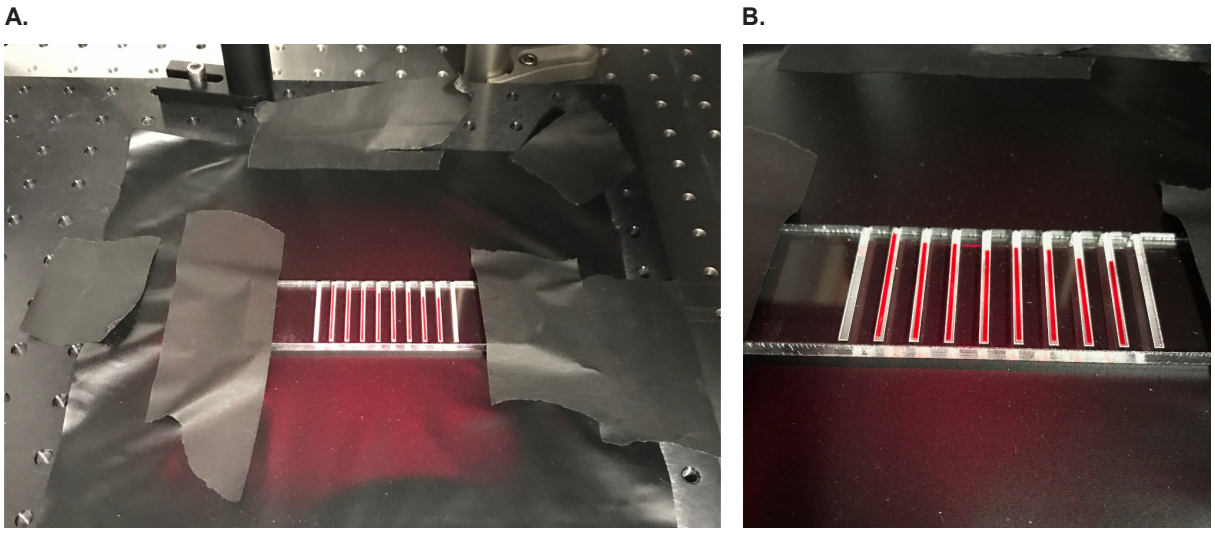

Figure 4.12 Visible light photographs of the capillary imaging configuration. A) Image of dye-filled capillaries in a transparent plastic holder placed in the imaging configuration. Lasers and camera are situated directly above the field of view. B) Close-up of the capillary holder and dye-filled capillaries. The red color is due to reflections from a 650 nm pilot light on the lasers.

4.3.4 Comparative in vivo Imaging Experiment

To most closely assess the brightness performance for SWIR imaging, we designed an *in vivo* comparative experiment between the highest performing chromenylium dye, JuloChrom5 (**4.10**) and ICG. To note, while many SWIR imaging agents have been compared to the benchmark dye, ICG, these comparisons are often difficult due to the diverse photophysical and biological properties of different emitters. In our case, the *in vivo* comparison is complicated by differing biodistribution properties of the two dyes. While this difference cannot be entirely decoupled from the conclusions, we aimed to reduce uncertainty in other aspects of the experiment and the analysis. We capitalized on the multiplexing capabilities of the two dyes to perform a comparative

experiment of both agents in a single mouse, thus reducing biological sample variance. As signal from ICG upon 892 nm laser irradiation is negligible with these acquisition settings (Figure 4.15), we performed temporally-separated tail-vein injections of equal moles of ICG, followed by JuloChrom5 (**4.10**) into mice and imaged each injection in two channels, with 785 nm and 892 nm lasers and collection with 1,000 nm LP filtering (Figures 4.13–4.14). Normalizing each acquisition to the injection start time, we quantified the signal over time over the whole mouse (yellow), a section of the vasculature (red), and the liver (black). Looking at the whole mouse region of interest (ROI) (Figure 4.13E), signal from JuloChrom5 (**4.10**) is significantly higher than signal from ICG. However, the ratio of counts between **4.10** and ICG (Figure 4.13E) increases when looking only at the vasculature. Conversely, the ratio (**4.10** to ICG) decreases when observing the liver, due to the faster hepatic clearance time of ICG compared to the PEG-coated micelles containing **4.10**. Despite this difference, **4.10** still demonstrates slightly higher signal than ICG in the liver over the observed time frame. While differential biodistribution could result in variable probe depths and differing amounts of attenuation, the higher signal among several regions of interest *in vivo*, combined with the more controlled in vitro quantification leads us to conclude that JuloChrom5 (**4.10**) displays an overall higher signal in the SWIR compared to ICG. Importantly, the advantageous brightness of **4.10** enables imaging with high signal-to-noise ratios (SNR) at low exposure times (1.6–2.0 ms). Accordingly, we can now image a whole mouse in a single color at frame rates up to 300 fps, limited by the collection rate of the current detector. Notably, the more red-shifted dye, Chrom7 (**4.5**), in channel *iii*, can also be employed to image in a single color at 300 fps, with good SNR and similar acquisition parameters (Figure 4.16, Supplementary Video 4.1), enabling rapid, multiplexed SWIR imaging.

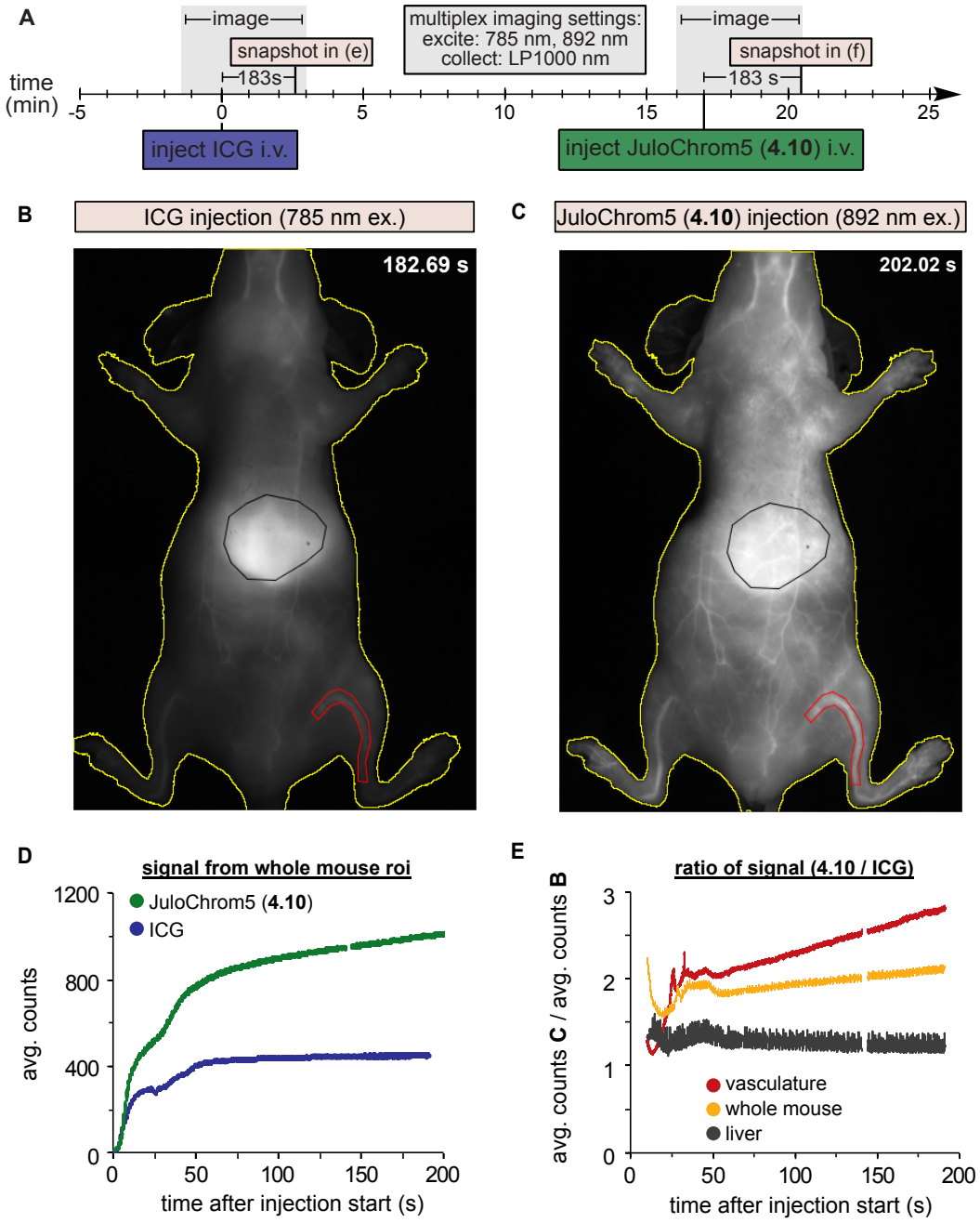

Figure 4.13 *In vivo* comparative imaging experiment. A) Experimental timeline for the imaging experiment in B–C. B–C) Images after injection of ICG (50 nmol) upon 785 nm (64 mWcm^{-2}) ex. (B) and after injection of JuloChrom5 (**4.10**) (50 nmol) upon 892 nm (104 mWcm^{-2}) ex. (C). Collect: LP1000 nm, 2.0 ms ET, 150 fps (for 2-channel collection, see Figure 4.15 for cross-talk evaluation). Single frames at the time point which displayed the highest intensity over the whole mouse ROI obtained during acquisition are displayed. D) Intensity quantification from images in B–C, taken by averaging intensity over the whole mouse at each frame after i.v. injection, where t = 0 is the initial frame in which signal is visualized. E) Ratio of intensities (JuloChrom5 (**4.10**)/ICG) from ROIs quantified in B–C.

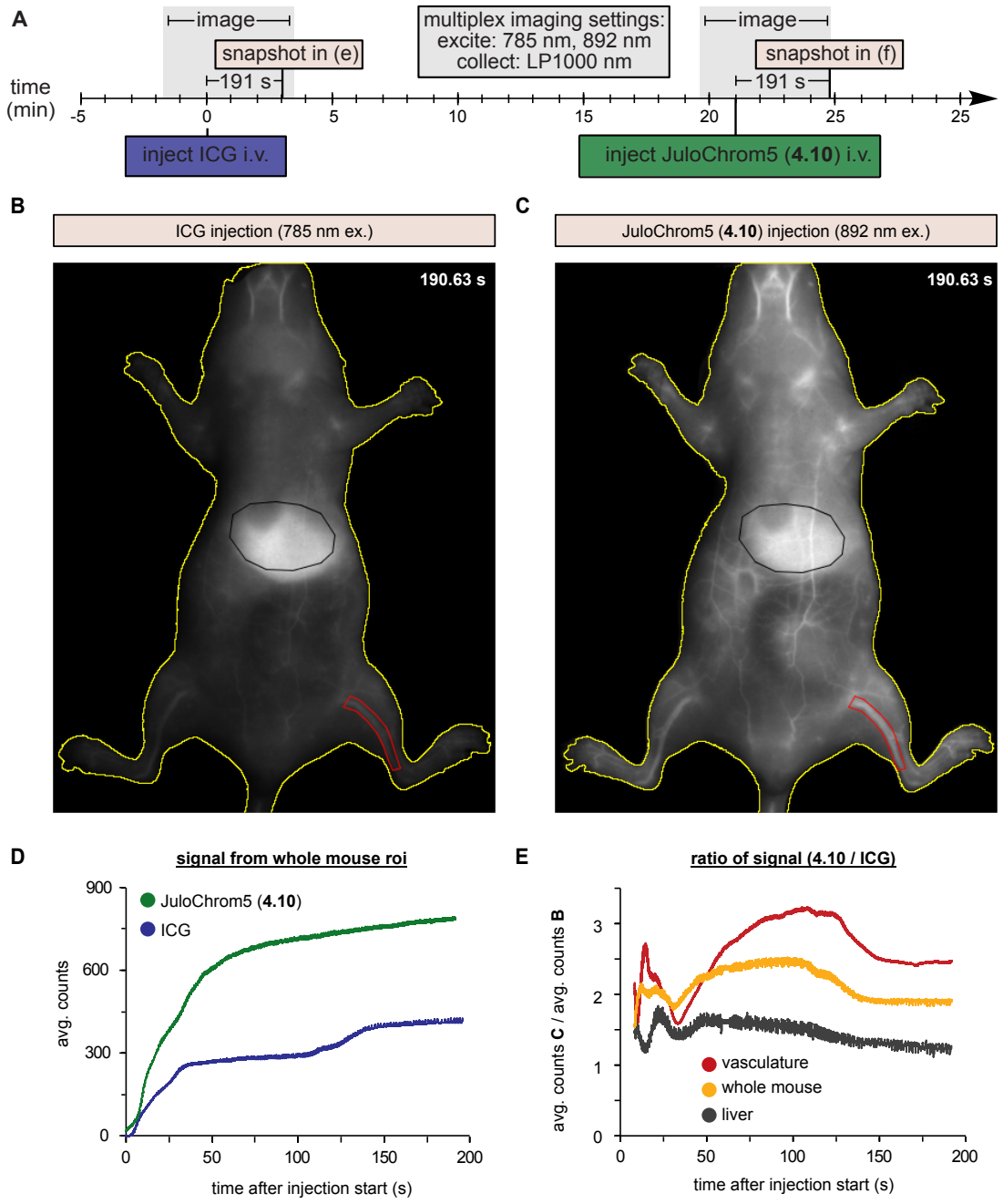

Figure 4.14 *In vivo* comparative imaging experiment, replicate. A) Experimental timeline for the imaging experiment in B–C. B–C) Images after injection of ICG (50 nmol) upon 785 nm (64 $mWcm^{-2}$) ex. (B) and after injection of JuloChrom5 (**4.10**) (50 nmol) upon 892 nm (104 $mWcm^{-2}$) ex. (C). Collect: LP1000 nm, 2.0 ms ET, 150 fps (for 2-channel collection, see Figure 4.15 for cross-talk evaluation). Single frames at the time point which displayed the highest intensity over the whole mouse ROI obtained during acquisition are displayed. D) Intensity quantification from images in B–C, taken by averaging intensity over the whole mouse at each frame after i.v. injection, where t = 0 is the initial frame in which signal is visualized. E) Ratio of intensities (JuloChrom5 (**4.10**)/ICG) from ROIs quantified in B–C.

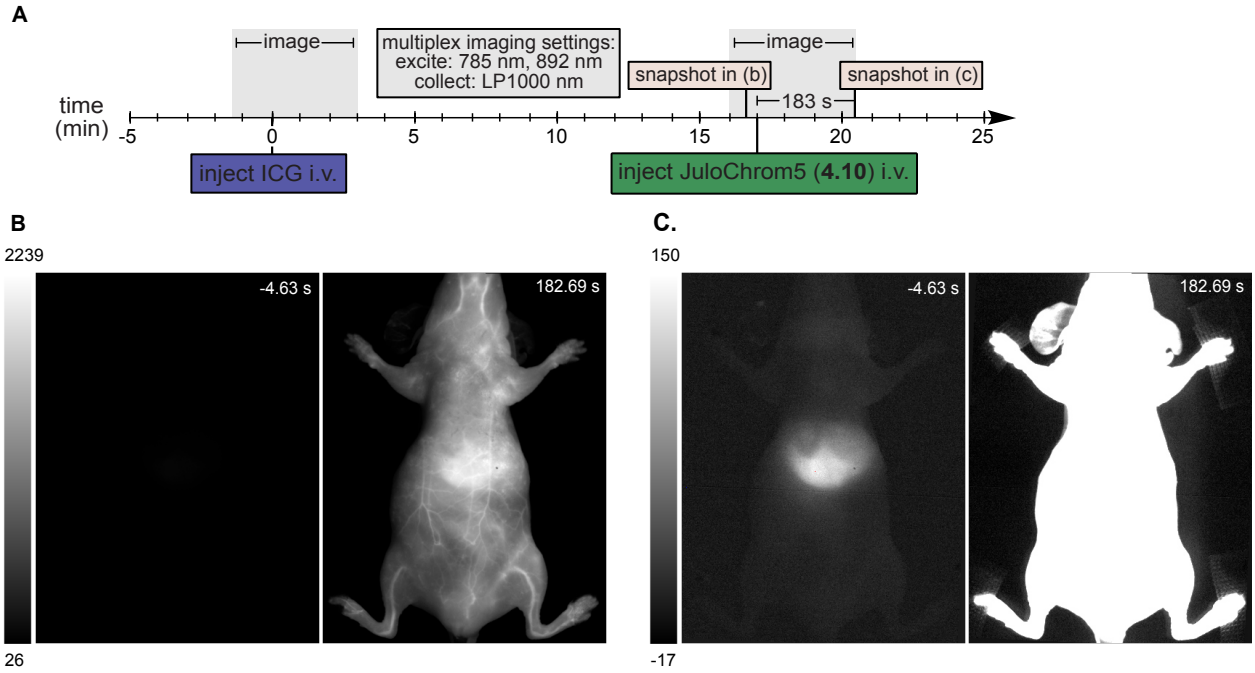

Figure 4.15 Images from comparative brightness experiment (Figure 4.13) taken after ICG injection and before injection (left) and after injection (right) of JuloChrom5 (**4.10**), showing residual signal from ICG in the 892 nm channel. A) Experimental timeline for the imaging experiment in B–C. B) Normal contrast images. C) Contrast-enhanced images. Ex. 892 nm (104 $mWcm^{-2}$); collect: LP1000 nm, 2.0 ms ET, 150 fps. Single frames are displayed.

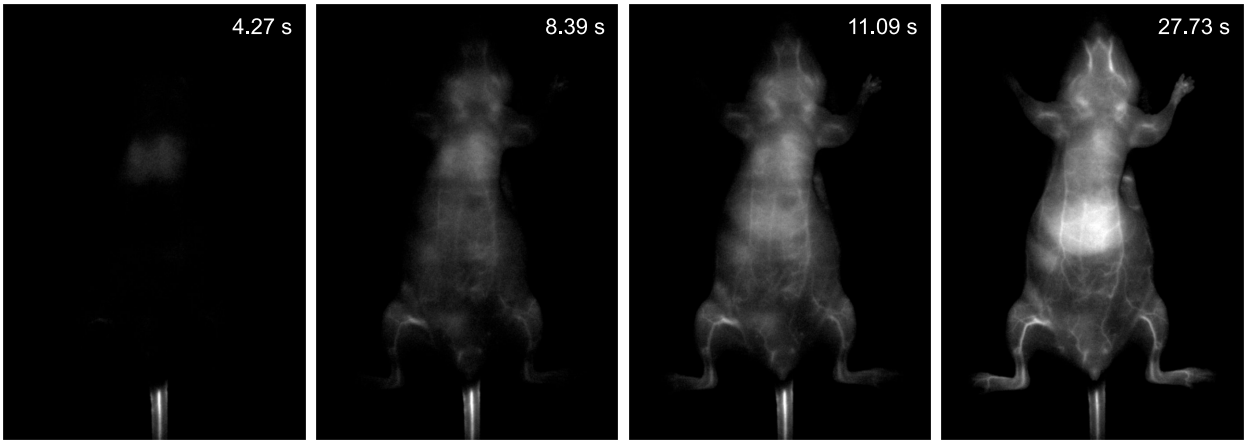

Figure 4.16 Single color imaging at 300 fps. Images after injection of Chrom7 (**4.5**) (141 nmol) upon 968 nm (100 $mWcm^{-2}$) laser ex. Collect: LP1500 nm, 3 ms ET, 300 fps. Single frames are displayed. Images are representative of two replicate experiments.

4.3.5 Fast, Multiplexed in vivo SWIR Imaging

We next moved to examine how the brighter dyes can be used to improve excitation-multiplexed, single-channel detection, SWIR imaging. Previously, we demonstrated 3-color imaging in real time (up to 27 fps)[13]. Here, we aimed to improve the temporal resolution of the method as well as increase the number of channels at which orthogonal signals can be detected. The high brightness of the chromenylium dyes and the flavylium pentamethines, coupled with the varied absorption profiles across the far-NIR provides several candidate dyes for multiplexed imaging using channels *i–iii*. First, we used **4.6** (referred to here as Chrom5), **4.4** (referred to here as JuloFlav5), and Chrom7 (**4.5**) together, preferentially excited by 785, 892, and 968 nm lasers, respectively, with collection using 1,000 nm LP filtering. The three dyes were injected at differing times or routes to ensure varied biodistribution of the different channels during imaging. The injection amounts of each dye were optimized to provide similar brightness using the ICNIRP-scaled power densities. Images with excellent signal to noise ratio (Figure 4.17, Supplementary Video 4.2) were collected with 3.3 ms exposure time (ET), and 100 fps multiplexed frame rate (multiplexed frame rate = 1/(n x ET), where n = number of channels), which is over 3x the speed obtained previously.[13] Multiplexing at these high frame rates ensures that macroscopic biological motion is negligible within the collection time for each frame that contributes to the composite image and will offer increased benefits in applications such as image-guided surgery or imaging animals in the absence of anesthesia.

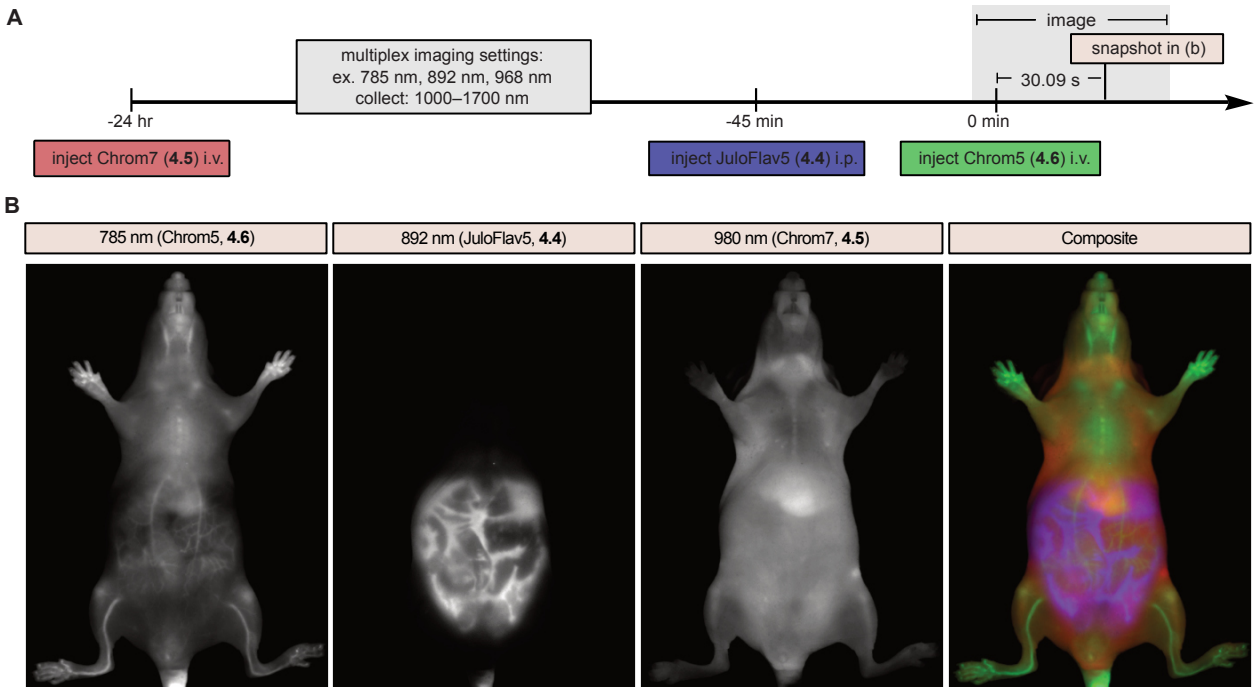

Figure 4.17 High-speed three-color imaging. A) Experimental timeline for experiment in B. (not to scale). B) Single channel and composite images from three-color excitation multiplexed SWIR imaging at 100 fps. Injection amounts are as follows: Chrom5 (**4.6**) = 130 nmol; JuloFlav5 (**4.4**) = 80 nmol; Chrom7 (**4.5**) = 110 nmol. Ex. 785 nm (80 $mWcm^{-2}$). 892 nm (87 $mWcm^{-2}$), 968 nm (94 $mWcm^{-2}$), collect LP1000 nm, 3.3 ms, 100 fps, single frames are displayed.

Finally, the new NIR fluorophores allowed the addition of a fourth channel such that 4-color SWIR imaging could be performed for the first time. We chose ICG, JuloChrom5 (**4.10**), Chrom7 (**4.5**), and JuloFlav7 (**4.3**) as spectrally distinct fluorophores with preferential excitation at 785, 892, 968, and 1,065 nm, respectively, and collection with 1,100 nm LP filtering (Figure 4.18–4.19, Supplementary Video 4.3). Again, we optimized injection routes, times, and amounts to ensure different biodistribution of probes would be present with similar brightness at the time of imaging. First, JuloChrom5 (**4.10**) was injected i.v. 27 hours prior to serve as a structural reference. Next, ICG was injected i.v., and allowed to clear for 5 hours through the liver into the intestine. JuloFlav7 (**4.3**) was then administered into the i.p. space 7 min before imaging, and finally, Chrom7 (**4.5**) was injected i.v. to obtain the time-course images of the injection displayed

in Figure 4.18B–C. For multiplexed experiments employing 1,065 nm laser excitation, longer exposure times were needed due to the smaller, more red-shifted collection window decreasing the percentage of emissive-tails of the dyes collected. Regardless, signal in each channel was sufficient for collection at 30 fps, with a 7.8 ms ET for each channel. The 4 color experiment was able to be performed at similar speeds to previously reported 3-color experiments which used 1,064 nm laser excitation, providing video-rate temporal resolution of biological function, visualized in the heart and breathing rates (Figure 4.20).[13] The lower exposure times used herein (7.8 ms vs. 10 ms) were possible due to the improved brightness of the chromenylium dyes and the scaled power densities of the excitation wavelengths.[13] Notably, we have also improved the linear unmixing procedure compared to the initial report, to accommodate 4-color data (see Section 4.6.5).

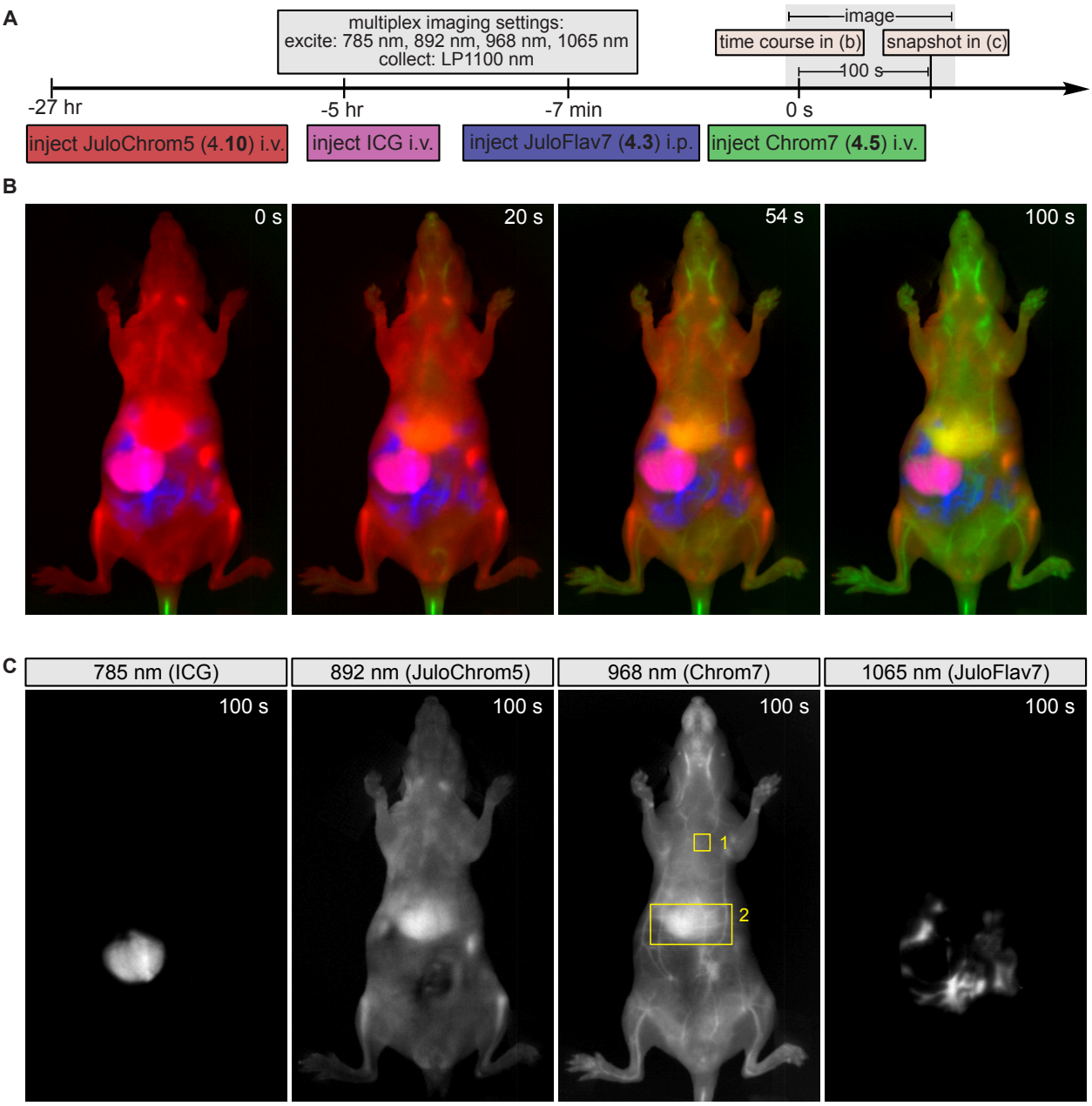

Figure 4.18 Video-rate four-color imaging. A) Experimental timeline for experiment in (B-C) (not to scale). B-C) Composite images (B) and single frames (C) from four-color excitation multiplexed SWIR imaging at 30 fps. Injection amounts are as follows: ICG = 200 nmol; JuloChrom5 (**4.10**) = 50 nmol; Chrom7 (**4.5**) = 45 nmol; JuloFlav7 (**4.3**) = 45 nmol. Ex. 785 nm (45 mWcm-2), 892 nm (75 mWcm-2), 968 nm (103 mWcm-2), 1065 nm (156 mWcm-2); collect LP1100 nm, 7.8 ms, 30 fps, single frames are displayed.

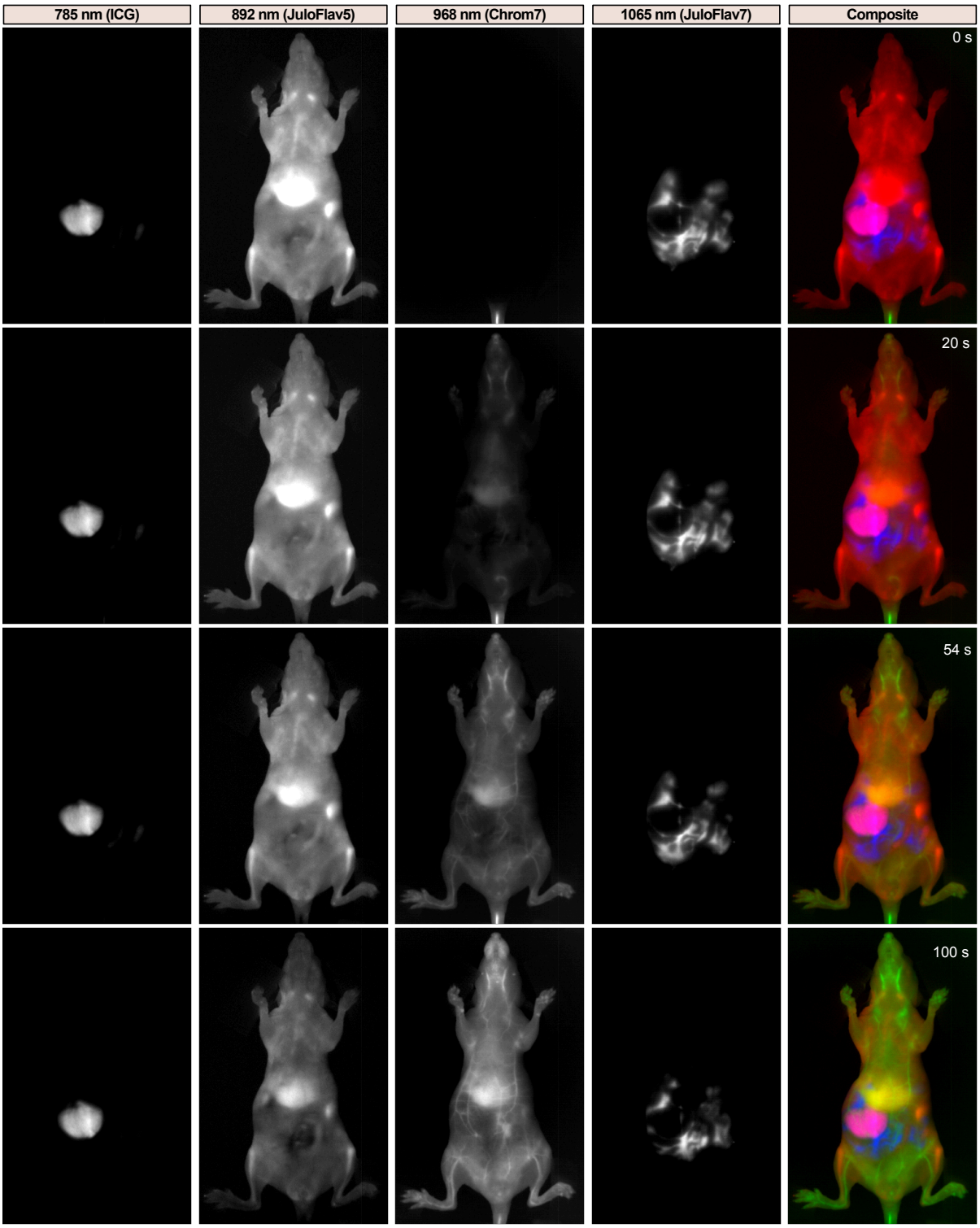

Figure 4.19 Video-rate 4-color imaging, with individual channels displayed at all time points. Injection amounts are: ICG = 200 nmol; JuloChrom5 (**4.10**) = 50 nmol; Chrom7 (**4.5**) = 45 nmol; JuloFlav7 (**4.3**) = 45 nmol. Ex. 785 nm (45 $mWcm^{-2}$). 892 nm (75 $mWcm^{-2}$), 968 nm (103 $mWcm^{-2}$), 1065 nm (156 $mWcm^{-2}$); collect LP1100 nm, 7.8 ms, 30 fps, single frames are displayed.

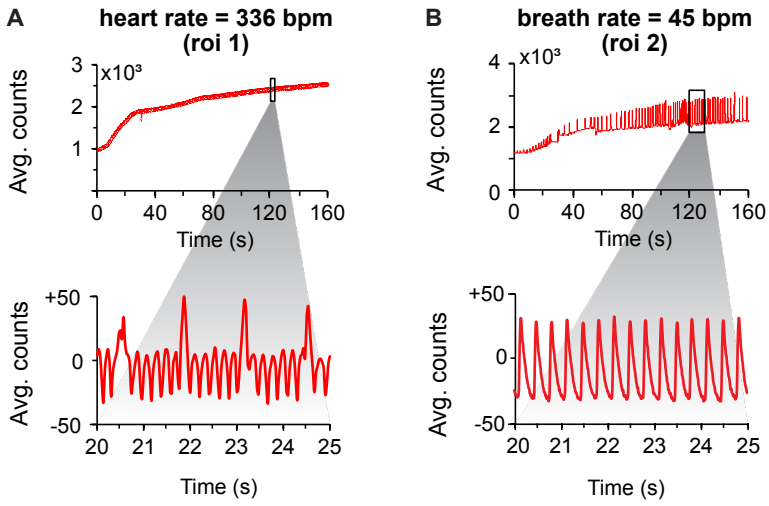

Figure 4.20 Heart rate (D) and Breath rate (E) calculated from ROIs specified in 4.18C.

4.4 Conclusions

The ability to non-invasively and longitudinally track multiple probes within living animals will be key to studying causes and interventions of human disease. Fluorescence is an optimal tool for high resolution and high sensitivity detection, but non-invasive experiments are limited by light scattering in tissue. Longer wavelength detection benefits from increased penetration depth and contrast, but lacks bright enough probes that can be concurrently detected orthogonally. Here, we designed and synthesized seven new polymethine dyes with flavylium or chromenylium heterocycles, which are brighter than their predecessors. The pentamethine and heptamethine chromenylium dyes benefit from significantly higher quantum yields due to decreased non-radiative rates compared to the flavylium dyes. We capitalize on the excitation-multiplexed strategy to compare performance and biodistribution of two probes in the same mouse. In this experiment, we found that JuloChrom5 (**4.10**), excitable when excited at 892 nm, is brighter than ICG for *in vivo* experiments. The panel of bright dyes enables single-channel imaging at up to 300 fps, while dyes excitable at orthogonal excitation wavelengths can be used together providing

three-channel imaging at up to 100 fps. These experiments represent the fastest single and multi-channel SWIR imaging to date. Combining these dyes with ICG and JuloFlav7 (**4.3**), video-rate (30 fps) imaging in mice in 4-colors is demonstrated for the first time. The contribution puts forth a greater understanding of how to increase the performance and utility of long wavelength probes to visualize complex organisms. Specifically, by improving the brightness of dyes in key wavelength regions and integrating their use into excitation-multiplexed SWIR imaging, we open up opportunities for non-invasive and high-resolution imaging of multiple biological parameters *in vivo*.

4.5 Experimental procedures

4.5.1 General experimental procedures

Instrumentation Thin layer chromatography was performed using Silica Gel 60 F_{254} (EMD Millipore) plates. Flash chromatography was executed with technical grade silica gel with 60 Å pores and 40–63 μm mesh particle size (Sorbtech Technologies). Solvent was removed under reduced pressure with a Büchi Rotavapor with a Welch self-cleaning dry vacuum pump and further dried with a Welch DuoSeal pump. Aqueous solvent was removed by lyophilization with a LABCONCO FreeZone Benchtop Freeze Dryer. Bath sonication was performed using a Branson 3800 ultrasonic cleaner or an Elma S15Elmasonic. Nuclear magnetic resonance (^{1}H NMR, ^{13}C NMR) spectra were taken on Bruker Avance 300, AV-500 or AV-600 instruments and processed with MestReNova software. All ^{1}H NMR and ^{13}C NMR peaks are reported in ppm in reference to their respective solvent signals. High resolution mass spectra (electrospray ionization (ESI)) were obtained on a Thermo Scientific Q Exactive™ Plus Hybrid Quadrupole-Orbitrap™ M with Dionex UltiMate 3000 RSLCnano System. IR spectra were obtained on a Perkin-Elmer UATR Two FT-

IR spectrometer and are reported in terms of frequency of absorption (cm^{-1}). Nanomaterial size was analyzed with a Malvern Zetaziser Nano dynamic light scattering in plastic 1 cm cuvettes. Absorbance spectra were collected on a JASCO V-770 UV-Visible/NIR spectrophotometer with a 2000 nm/min scan rate after blanking with the appropriate solvent or on a PerkinElmer LAMBDA 1050+ UV/VIS/NIR Spectrophotometer with a reference sample. Photoluminescence spectra were obtained on a Horiba Instruments PTI QuantaMaster Series fluorometer with InGaAs detector Horiba Edison DSS IGA 020L. Absolute quantum yields were taken in a Horiba KSPHERE-Petite. Quartz cuvettes (1 cm) were used for absorbance and photoluminescence measurements. Absorption coefficients in DCM were calculated with serial dilutions with Hamilton syringes in volumetric glassware. Error was taken as the standard deviation of the triplicate experiments. Relative quantum yields were determined in DCM relative to IR-26 in DCM (see Note S1 for details on photoluminescence quantum yield measurements).

Abbreviations DCM = dichloromethane; DMSO = dimethylsulfoxide; ET = exposure time; EtOH = ethanol; EtOAc = ethyl acetate; fps = frames per second; i.v. = intravenous; i.p. intraperitoneal; LP = longpass; NIR = near-infrared; NMR = nuclear magnetic resonance; PBS = phosphate buffered saline; PEG = polyethylene glycol; ROI = region of interest; SP = shortpass; SWIR = shortwave infrared; THF = tetrahydrofuran; VIS = visible.

General synthetic procedures Chemical reagents were purchased from Accela, Acros Organics, Alfa Aesar, Carl Roth, Fisher Scientific, Sigma-Aldrich, or TCI and used without purification unless noted otherwise. Anhydrous and deoxygenated solvents (toluene, THF) were dispensed from a Grubb's-type Phoenix Solvent Drying System constructed by JC Meyer. Anhydrous solvent (*n*-butanol) was prepared by drying over 4 Å molecular sieves for at least 3 days. Oxygen was removed by three consecutive freeze–pump–thaw cycles in air-free glassware directly before use.

Animal procedures Animal experiments were conducted in conformity with the institutional guidelines. Non-invasive whole mouse imaging was performed on athymic nude female mice (6-15 weeks old, weight between 20-25 g), purchased from Envigo or Charles River Laboratories. Mice were anesthetized with inhaled isoflurane/oxygen. Tail vein injections were performed with a catheter assembled from a 30-gauge needle connected through plastic tubing to a syringe prefilled with isotonic saline solution. The bevel of the needle was then inserted into the tail vein and secured using tissue adhesive. The plastic tubing was then connected to a syringe (30-gauge needle) prefilled with the probe of interest. All probes were filtered through a 0.22 μm syringe filter prior to i.v. injection.

SWIR imaging apparatus For whole mouse imaging, a custom-built setup was used. Lumics laser units: LU1064DLD350-S70AN03 (35 W) “1065 nm”; LU0980D350-D30AN (35W) “968 nm”, and LU0890D400-U10AF (40W) “892 nm”, LU0785DLU250-S70AN03 (25 W) "785 nm” were used for excitation. Laser modules are specced to ± 10 nm. Laser outputs were coupled in a 4x1 fan-out fiber-optic bundle (Thorlabs BF46LS01) of 600 μm core diameter for each optical path. The output from the fiber was fixed in an excitation cube (Thorlabs KCB1EC/M), reflected off of a mirror (Thorlabs BBE1-E03), and passed through a positive achromat (Thorlabs AC254-050-B), SP filter (specified for each experiment) and an engineered diffuser (Thorlabs ED1-S20-MD or ED1-S50-MD) to provide uniform illumination over the working area. In a typical experiment, the excitation flux at the object was adjusted to be close to 100 $mWcm^{-2}$ (power density used is defined separately in each experiment, with an error of ± 3%). The working area was covered by a heating mat coated with blackout fabric (Thorlabs BK5). Emitted light was directed onto an Allied Vision Goldeye G-032 Cool TEC2 camera with a sensor temperature set point of -30 °C or a Goldeye G-033 TECless camera. Emitted light was directed through a custom

filter set (defined for each experiment) and a C-mount camera lens (Navitar, SWIR-35). The assembly was partially enclosed to avoid excess light while enabling manipulation of the field of view during operation. Camera and lasers were externally controlled and synchronized by delivering trigger pulses of 5V TTL (5V Transistor-Transistor Logic) to the laser drivers and camera using a programmable trigger controller with pulses generated with an Atmel Atmega328 micro-controller unit and programmed using Arduino Nano Rev 3 MCU (A000005) in the Arduino integrated development environment (IDE). Acquired imaging data is then transferred to the PC via either a Gigabit Ethernet (GigE), or CameraLink (CL) interface. For image acquisition with the G-032 camera, the toolbox of MATLAB programming environment was used in combination with a MATLAB script (github) to preview and collect the required image data in 14-bit depth. For image acquisition with the G-033 camera, FireBird Camera Link Frame Grabber (1xCLD-2PE8 or 1xCLD-2PE4, Active Silicon) along with ActiveCapture (Active Silicon) was used to collect image data in 8-bit or 12-bit depth.

Image processing procedures Images were processed using the Fiji distribution[52] of ImageJ[53] and Python3. All images were background corrected to correct for non-linearities in the detector and/or excitation. Raw images underwent no further processing. Multiplexed images that underwent unmixing were subjected to either manual or an automated linear unmixing method (see Note S5), specified in the experimental procedures for each figure. All still images are displayed as single frames and converted to 8-bit PNG files for display, unless stated otherwise. Videos were frame averaged to reduce file size, if necessary, before compression with FFmpeg to a .mov file.

4.5.2 Experimental procedures[2]

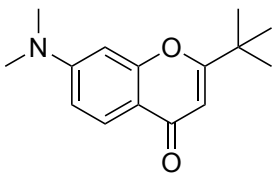

2-(*tert*-butyl)-7-(dimethylamino)-4*H*-chromen-4-one (**4.11a**): 3-(dimethylamino)phenol (299 mg, 2.18 mmol, 1.00 equiv.) and ethyl pivaloylacetate (700 μL, 3.93 mmol, 1.00 equiv.) were combined in an oven-dried 1 dram vial and heated at 180 ºC for 40 h. The solution was cooled to room temperature, evaporated onto silica, and purified via column chromatography with a 10:1 to 4:1 hexanes/EtOAc gradient. The procedure gave a light pink solid (238 mg, 0.970 mmol, 45%). R_f = 0.4 in 1:2 hexanes/EtOAc. ^{1}H NMR (300 MHz, Chloroform-*d*) δ 7.96 (d, *J* = 9.0 Hz, 1H), 6.70 (dd, *J* = 9.0, 2.4 Hz, 1H), 6.45 (d, *J* = 2.4 Hz, 1H), 6.10 (s, 1H), 3.05 (s, 6H), 1.30 (s, 9H). ^{13}C NMR (126 MHz, Chloroform-*d*) δ 178.4, 174.7, 158.6, 154.1, 126.4, 113.1, 110.5, 106.1, 97.0, 40.2, 36.3, 28.0. HRMS (ESI$^+$) calcd for $C_{15}H_{20}NO_2^+$ $[M+H]^+$: 246.1489; found: 246.1482. Absorbance (CH_2Cl_2): 264, 296, 337 nm.

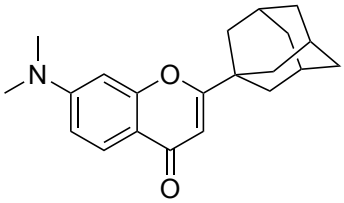

2-((3*r*,5*r*,7*r*)-adamantan-1-yl)-7-(dimethylamino)-4*H*-chromen-4-one (**4.11b**): 3-(dimethylamino)phenol (150 mg, 1.09 mmol, 1.00 equiv.) and ethyl 3-(1-adamantyl)-3-oxopropionate (316 μL, 1.31 mmol, 1.20 equiv.) were added to a glass 10 mL microwave vial and heated to 240 ºC for 3 min. The crude product was cooled and evaporated onto silica for purification via column chromatography with a 10:1 to 3:1 hexanes/EtOAc gradient. Impure fractions were further purified with a 250:1 to 14:1 toluene/acetone gradient to obtain a grey solid (99.6 mg, 0.308 mmol, 28%). R_f = 0.4 in 1:2 hexanes/EtOAc. ^{1}H NMR (500 MHz, Chloroform-*d*) δ 7.96 (d, *J* = 9.0 Hz, 1H),

[2] Anthony Spearman contributed to work in this section

6.71 (dd, J = 9.1, 2.5 Hz, 1H), 6.46 (d, J = 2.4 Hz, 1H), 6.03 (s, 1H), 3.06 (s, 6H), 2.17 – 2.03 (m, 3H), 1.93 (d, J = 3.0 Hz, 6H), 1.84 – 1.65 (m, 6H). ^{13}C NMR (126 MHz, Chloroform-*d*) δ 178.6, 174.6, 158.7, 154.1, 126.5, 113.4, 110.5, 106.0, 97.1, 40.3, 39.6, 38.0, 36.6, 28.1. HRMS (ESI^+) calcd for $C_{21}H_{26}NO_2^+$ $[M+H]^+$: 324.1958; found: 324.1949. Absorbance (CH_2Cl_2): 264, 297, 339 nm.

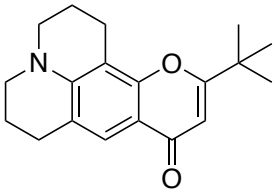

11-(*tert*-butyl)-2,3,6,7-tetrahydro-1*H*,5*H*,9*H*-pyrano[2,3-*f*]pyrido[3,2,1-*ij*]quinolin-9-one (**4.11c**): 8- hydroxyjulolidine (315 mg, 1.66 mmol, 1.00 equiv) and ethyl pivaloylacetate (500 μL, 2.81 mmol, 1.69 equiv.) were added to a 20 mL vial, and heated at 180 ºC for 48 h. The solution was cooled to room temperature, evaporated onto silica, and purified via column chromatography with an 8:1 to 3:1 hexanes/EtOAc gradient to yield an off-white solid (295 mg, 0.992 mmol, 60%). R_f = 0.4 in 1:2 hexanes/EtOAc. ^{1}H NMR (600 MHz, Chloroform-*d*) δ 7.53 (s, 1H), 6.05 (s, 1H), 5.25 (s, 1H), 3.27 – 3.15 (m, 4H), 2.83 (t, J = 6.5 Hz, 2H), 2.74 (t, J = 6.2 Hz, 2H), 1.96 (p, J = 6.3 Hz, 2H), 1.90 (p, J = 6.2 Hz, 2H), 1.27 (s, 9H). ^{13}C NMR (126 MHz, Chloroform-*d*) δ 178.4, 173.9, 153.9, 146.9, 122.1, 119.9, 112.2, 105.58, 105.55, 49.9, 49.4, 36.4, 28.1, 27.6, 21.5, 20.7, 20.5. HRMS (ESI^+) calcd for $C_{19}H_{24}NO_2^+$ $[M+H]^+$: 298.1802; found: 298.1793. Absorbance (CH_2Cl_2): 272, 300, 355 nm.

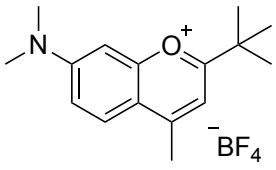

2-(*tert*-butyl)-7-(dimethylamino)-4-methylchromenylium tetrafluoroborate (**4.12a**): Chromone **4.11a** (500 mg, 2.04 mmol, 1.00 equiv.) was dissolved in THF (20 mL) in a flame-dried 100 mL 3-neck flask in an N_2 atmosphere. The solution was cooled to 0 ºC, and methylmagnesium bromide (1.0

M in THF, 5.1 mL, 2.5 equiv.) was added dropwise. The reaction mixture was warmed to room temperature and stirred for 21 h. The reaction was quenched with fluoroboric acid (50% aqueous, 300 μL), and with the addition of 5% fluoroboric acid, extracted into DCM. The extract was dried with Na_2SO_4, filtered, and evaporated. The crude product was purified by precipitation upon addition of EtOAc, filtration, and rinsing with additional EtOAc to yield a bright orange solid (604 mg, 1.82 mmol, 89%). ^{1}H NMR (500 MHz, Acetone-d_6) δ 8.27 (d, J = 9.6 Hz, 1H), 7.59 (dd, J = 9.6, 2.5 Hz, 1H), 7.50 (s, 1H), 7.25 (d, J = 2.6 Hz, 1H), 3.45 (s, 6H), 2.93 (s, 3H), 1.52 (s, 9H). ^{13}C NMR (126 MHz, Acetone-d_6) δ 181.0, 166.1, 160.5, 159.1, 129.7, 119.2, 118.3, 112.5, 96.7, 41.2, 38.7, 28.3, 20.0. HRMS (ESI$^+$) calcd for $C_{16}H_{22}NO^+$ [M]$^+$: 244.1696; found: 244.1693. Absorbance (CH_2Cl_2): 285, 331, 468 nm. Emission (CH_2Cl_2, ex. 450 nm): 534 nm.

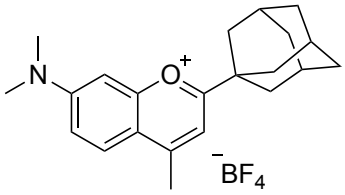

2-((3*r*,5*r*,7*r*)-adamantan-1-yl)-7-(dimethylamino)-4-methylchromenylium tetrafluoroborate (**4.12b**): Chromone **4.11b** (79 mg, 0.24 mmol, 1.0 equiv.) was added to a flame dried 25 mL 2-neck flask in a N_2 atmosphere and dissolved in THF (3.2 mL). The solution was cooled to 0 ºC and methylmagnesium bromide (1.0 M in THF, 0.75 mL, 3.1 equiv.) was added dropwise. The reaction was warmed to room temperature and stirred for 14 h before quenching with fluoroboric acid (50%, aqueous, 150 μL). After further addition of 5% fluoroboric acid, the product was extracted into DCM, dried with Na_2SO_4, filtered, and evaporated. The crude product was purified by precipitation upon addition of toluene, collected by vacuum filtration, and rinsed briefly with cold EtOAc to yield a bright orange solid (68 mg, 0.17 mmol, 68%). ^{1}H NMR (500 MHz, Acetone-d_6) δ 8.26 (d, J = 9.7 Hz, 1H), 7.58 (dd, J = 9.6, 2.5 Hz, 1H), 7.42 (s, 1H), 7.25 (d, J = 2.6 Hz, 1H), 3.45 (s, 6H), 2.94 (s, 3H), 2.17 (d, J = 1.4 Hz, 9H), 1.95 – 1.79 (m, 6H). ^{13}C NMR (126 MHz,

Acetone-d_6) δ 180.5, 166.1, 160.5, 159.0, 129.6, 119.1, 118.3, 112.5, 96.7, 41.2, 40.6, 40.3, 36.7, 28.8, 20.0. HRMS (ESI^+) calcd for $C_{22}H_{28}NO^+$ $[M]^+$: 322.2165; found: 322.2164. Absorbance (CH_2Cl_2): 286, 331, 469 nm. Emission (CH_2Cl_2, ex. 450 nm): 534 nm.

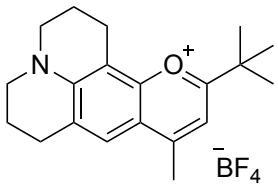

11-(*tert*-butyl)-9-methyl-2,3,6,7-tetrahydro-1*H*,5*H*-pyrano[2,3-*f*]pyrido[3,2,1-*ij*]quinolin-12-ium tetrafluoroborate (**4.12c**): Chromone **4.11c** (256 mg, 0.861 mmol, 1.00 equiv.) was added to a flame dried 50 mL 2-neck flask in a N_2 atmosphere and dissolved in THF (8.8 mL). Methylmagnesium bromide (1.0 M in THF, 2.6 mL, 3.0 equiv.) was added dropwise and the solution was stirred at room temperature for 12 h. The reaction was quenched with fluoroboric acid (50% aqueous, 200 µL). The product was extracted into DCM with the addition of 5% fluoroboric acid, dried with Na_2SO_4, filtered, and evaporated. The product was purified by precipitation upon addition of cold EtOAc, filtration and rinsing with cold EtOAc to obtain a magenta solid (268 mg, 0.669 mmol, 81%). ^{1}H NMR (500 MHz, Acetonitrile-d_3) δ 7.65 (s, 1H), 7.02 (s, 1H), 3.53 (q, J = 5.4 Hz, 4H), 2.95 (t, J = 6.4 Hz, 2H), 2.93 – 2.87 (m, 2H), 2.67 (s, 3H), 2.05 – 1.96 (m, 4H), 1.44 (s, 9H). ^{13}C NMR (126 MHz, Acetonitrile-d_3) δ 178.3, 161.6, 155.2, 153.7, 129.7, 124.7, {peak at 118.6–118.1 beneath CD_3CN solvent peak}, 111.1, 105.6, 51.8, 51.3, 38.5, 28.4, 28.4, 21.0, 20.2, 19.9, 19.7. HRMS (ESI^+) calcd for $C_{20}H_{26}NO^+$ $[M]^+$: 296.2009; found: 296.2002. Absorbance (CH_2Cl_2): 300, 351, 488 nm. Emission (CH_2Cl_2, ex. 450 nm): 557 nm.

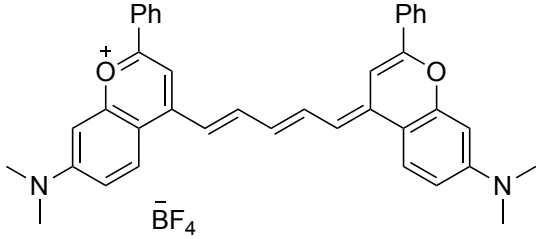

7-(dimethylamino)-4-((1*E*,3*E*)-5-((*E*)-7-(dimethylamino)-2-phenyl-4*H*-chromen-4-ylidene)penta-1,3-dien-1-yl)-2-

phenylchromenylium tetrafluoroborate (**4.2, Flav5)**: Flavylium **4.15a** (see [13] for synthesis) (164 mg, 0.467 mmol, 1.00 equiv.), malonaldehyde bis(phenylimine) monohydrochloride (59.0 mg, 0.228 mmol, 0.490 equiv.) and sodium acetate (128 mg, 1.25 mmol, 2.68 equiv.) were added to a 25 mL Schlenk tube under a N_2 atmosphere. Acetic anhydride (4.0 mL) was added and the solution was freeze-pump-thawed x3 before heating to 100 ºC for 65 min. The reaction was cooled, ~16 mL of toluene was added, and the product was collected by vacuum filtration. The product was rinsed with toluene and water before drying *in vacuo*. A bronze solid resulted (127 mg, 0.194 mmol, 86%). ^{1}H NMR (500 MHz, DMSO-d_6) δ 8.20 (t, J = 12.9 Hz, 2H), 8.13 – 8.03 (m, 4H), 7.99 (d, J = 9.4 Hz, 2H), 7.66 (s, 2H), 7.62 – 7.53 (m, 6H), 7.08 (d, J = 13.3 Hz, 2H), 6.91 (dd, J = 9.3, 2.6 Hz, 2H), 6.83 (t, J = 12.4 Hz, 1H), 6.77 (d, J = 2.6 Hz, 2H), 3.13 (s, 12H). ^{13}C NMR (126 MHz, DMSO-d_6) δ 156.1, 155.3, 154.1, 148.9, 145.5, 131.5, 131.1, 129.1, 126.0, 125.8, 115.3, 113.1, 110.8, 101.5, 97.3 {peak at 38.9–40.1 beneath DMSO- d_6 solvent peak.}. HRMS (ESI$^+$) calcd for $C_{39}H_{35}N_2O_2^+$ [M]$^+$: 563.2693; found: 563.2675. IR (film): 2926, 2867, 1629, 1456, 1052, 995, 902, 883 cm^{-1}. Absorbance (CH_2Cl_2): 548, 778, 862 nm. Emission (CH_2Cl_2, ex. 755 nm): 883 nm.

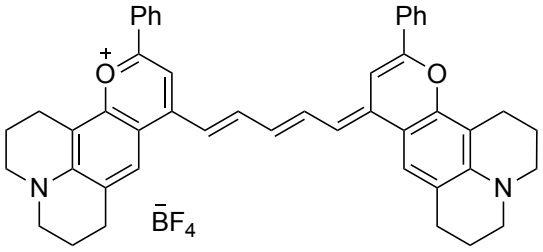

11-phenyl-9-((1*E*,3*E*,5*E*)-5-(11-phenyl-2,3,6,7-tetrahydro-1*H*,5*H*,9*H*-pyrano[2,3-*f*]pyrido[3,2,1-*ij*]quinolin-9-ylidene)penta-1,3-dien-1-yl)-2,3,6,7-tetrahydro-1*H*,5*H*-pyrano[2,3-*f*]pyrido[3,2,1-*ij*]quinolin-12-ium tetrafluoroborate (**4.4**, JuloFlav5): Flavylium **4.15b** (see [13] for synthesis) (150 mg, 0.372 mmol, 1.00 equiv.), malonaldehyde bis(phenylimine) monohydrochloride (47.2 mg, 0.182 mmol, 0.490 equiv.) and sodium acetate (92.6 mg, 1.13 mmol, 3.03 equiv.) were added

to a 25 mL Schlenk tube under a N_2 atmosphere. Acetic anhydride (4.0 mL) was added and the solution was freeze-pump-thawed x3 before heating to 100 ºC for 60 min. The reaction was cooled, ~10 mL of toluene was added, and the product was collected by vacuum filtration. The product was rinsed with toluene until filtrate runs clear, followed by a water rinse. The product was further purified by column chromatography, after dry-loading onto silica, in a three-way gradient of 1:1 toluene/DCM plus 1% EtOH to 0:1 toluene/DCM plus 20% EtOH. An iridescent red solid resulted (97.9 mg, 0.130 mmol, 71%). ^{1}H NMR (500 MHz, DMSO-d_6) δ 8.15 (t, J = 13.0 Hz, 2H), 8.13 – 8.08 (m, 4H), 7.70 – 7.58 (m, 10H), 7.05 (d, J = 13.4 Hz, 2H), 6.79 (t, J = 12.4 Hz, 1H), 3.41 – 3.38 (m, 8H), 2.92 (t, J = 6.5 Hz, 4H), 2.78 (t, J = 6.5 Hz, 4H), 1.98 (p, J = 5.7 Hz, 4H), 1.91 (p, J = 5.8 Hz, 4H). ^{13}C NMR (126 MHz, DMSO-d_6) δ 154.9, 150.4, 147.6, 144.2, 131.5, 131.2, 129.1, 125.6, 122.6, 121.6, 114.5, 110.4, 105.5, 100.9, 49.6, 49.0, 27.1, 20.5, 19.8, 19.6. HRMS (ESI$^+$) calcd for $C_{47}H_{43}N_2O_2^+$ [M]$^+$: 667.3319; found: 667.3296. IR (film): 2928, 2849, 1631, 1431, 1091, 1038, 916 cm^{-1}. Absorbance (CH_2Cl_2): 588, 805, 897 nm. Emission (CH_2Cl_2, ex. 755 nm): 925 nm.

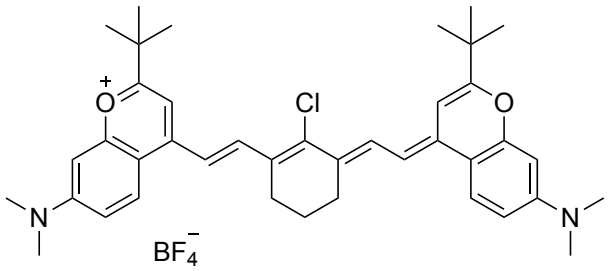

2-(*tert*-butyl)-4-((*E*)-2-((*E*)-3-(2-((*E*)-2-(*tert*-butyl)-7-(dimethylamino)-4*H*-chromen-4-ylidene)ethylidene)-2-chlorocyclohex-1-en-1-yl)vinyl)-7-(dimethylamino)chromenylium tetrafluoroborate (**4.5**, Chrom7): Chromenylium **4.12a** (300 mg, 0.900 mmol, 1.00 equiv.), *N*-[(3-(anilinomethylene)-2-chloro-1-cyclohexen-1-yl)methylene]aniline hydrochloride (153 mg, 0.426 mmol, 0.47 equiv.) and 2,6-di-*tert*-butyl-4-methyl pyridine (555 mg, 2.70 mmol, 2.98 equiv.) were added to a flame-dried 50 mL Schlenk tube under a N_2 atmosphere. Toluene (2.1 mL) and *n*-butanol (4.8 mL) were added and the solution was freeze-pump-thawed x3 before heating

to 100 ºC for 3 h. The reaction was cooled and evaporated. The product was precipitated in toluene and collected by vacuum filtration, washing with ~200 mL toluene, ~50 mL trifluorotoluene, ~50 mL cold THF. The product was further purified by column chromatography after dry-loading onto silica in DCM plus a gradient of 0.5–5% EtOH. After a second column in a three-way gradient of 3:7 toluene/DCM plus 0.5 % EtOH to 0:1 toluene/DCM plus 5% EtOH, the procedure resulted in a red iridescent product (108 mg, 0.152 mmol, 36%). ^{1}H NMR (500 MHz, Acetonitrile-d_3) δ 8.00 (d, J = 13.8 Hz, 2H), 7.82 (d, J = 9.3 Hz, 2H), 6.86 (dd, J = 9.4, 2.6 Hz, 2H), 6.79 (s, 2H), 6.73 (d, J = 13.8 Hz, 2H), 6.50 (d, J = 2.5 Hz, 2H), 3.04 (s, 12H), 2.71 (t, J = 6.3 Hz, 4H), 1.89 (p, J = 6.2 Hz, 2H), 1.42 (s, 18H). ^{13}C NMR (126 MHz, Acetonitrile-d_3) δ 170.8, 157.2, 155.3, 146.8, 146.1, 139.1, 130.5, 126.3, 113.9, 112.9, 112.3, 100.4, 98.0, 40.5, 37.4, 28.2, 27.6, 21.8. HRMS (ESI$^+$) calcd for $C_{40}H_{48}ClN_2O_2^+$ [M]$^+$: 623.3399; found: 623.3383. IR (film): 2964, 2927, 2872, 2811, 1627, 1377, 1227, 1155, 982, 934, 884 cm^{-1}. Absorbance (CH_2Cl_2): 499, 562, 975 nm. Emission (CH_2Cl_2, ex. 885 nm): 996 nm.

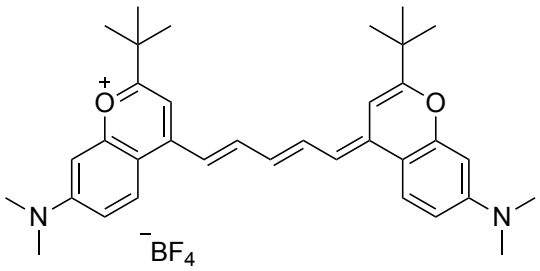

2-(*tert*-butyl)-4-((1*E*,3*E*)-5-((*E*)-2-(*tert*-butyl)-7-(dimethylamino)-4*H*-chromen-4-ylidene)penta-1,3-dien-1-yl)-7-(dimethylamino)chromenylium tetrafluoroborate (**4.6**, Chrom5): Chromenylium **4.12a** (150 mg, 0.45 mmol, 1.0 equiv.), malonaldehyde bis(phenylimine) monohydrochloride (57.3 mg, 0.221 mmol, 0.490 equiv.), and sodium acetate (117 mg, 1.43 mmol, 3.16 equiv.) were added to a 25 mL Schlenk tube under a N_2 atmosphere. Acetic anhydride (3.5 mL) was added and the solution was freeze-pump-thawed x3 before heating to 120 ºC for 60 min. The reaction was cooled, ~14 mL of toluene was added, and the product was collected by vacuum filtration. The

product was rinsed with toluene until filtrate runs clear, followed by a water rinse. The product was further purified by column chromatography, after dry-loading onto silica, in a three-way gradient of 1:1 toluene/DCM plus 1% EtOH to 0:1 toluene/DCM plus 12% EtOH. An iridescent dark purple solid resulted (76.6 mg, 0.125 mmol, 57%). ^{1}H NMR (500 MHz, Acetonitrile-d_3) δ 7.93 (t, J = 13.0 Hz, 2H), 7.87 (d, J = 9.4 Hz, 2H), 6.91 (dd, J = 9.3, 2.6 Hz, 2H), 6.86 (s, 2H), 6.83 (d, J = 13.5 Hz, 2H), 6.68 (t, J = 12.5 Hz, 1H), 6.61 (d, J = 2.6 Hz, 2H), 3.10 (s, 12H), 1.40 (s, 18H). ^{13}C NMR (126 MHz, Acetonitrile-d_3) δ 171.3, 157.5, 155.6, 150.1, 148.2, 128.3, 126.5, 114.5, 114.0, 112.0, 100.3, 98.1, 40.6, 37.5, 28.2. HRMS (ESI$^+$) calcd for $C_{35}H_{43}N_2O_2^+$ [M]$^+$: 523.3319; found: 523.3312. IR (film): 2961, 2923, 2870, 1631, 1457, 124, 977, 929, 882 cm^{-1}. Absorbance (CH_2Cl_2): 521, 741, 819 nm. Emission (CH_2Cl_2, ex. 755 nm): 836 nm.

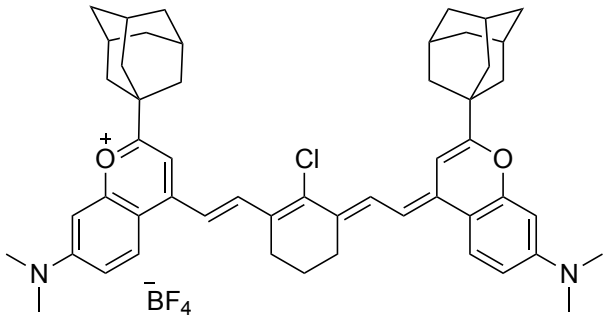

2-((3*r*,5*r*,7*r*)-adamantan-1-yl)-4-((*E*)-2-((*E*)-3-(2-((*E*)-2-((3*r*,5*r*,7*r*)-adamantan-1-yl)-7-(dimethylamino)-4*H*-chromen-4-ylidene)ethylidene)-2-chlorocyclohex-1-en-1-yl)vinyl)-7-(dimethylamino)chromenylium tetrafluoroborate (**4.7**): Chromenylium **4.12b** (30.5 mg, 0.0745 mmol, 1.00 equiv.), *N*-[(3-(anilinomethylene)- 2-chloro-1-cyclohexen-1-yl)methylene]aniline hydrochloride (11.9 mg, 0.0331 mmol, 0.440 equiv.) and 2,6-di-*tert*-butyl-4-methyl pyridine (46.1 mg, 0.225 mmol, 3.01 equiv.) were added to a flame-dried 25 mL Schlenk tube under a N_2 atmosphere. Toluene (0.20 mL) and *n*-butanol (0.50 mL) were added and the solution was freeze-pump-thawed x3 before heating to 100 ºC for 6.5 h. The reaction was cooled and evaporated. The crude product was purified by column chromatography after dry-loading onto silica in DCM plus a gradient of 0.5–

4% EtOH. After a second column in a three-way gradient of 3:7 toluene/DCM plus 0.4% EtOH to 0:1 toluene/DCM plus 7% EtOH, the procedure resulted in a dark blue product (9.2 mg, 0.011 mmol, 32%). ^{1}H NMR (500 MHz, DMSO-d_6) δ 8.15 (d, J = 9.6 Hz, 2H), 7.93 (d, J = 13.6 Hz, 2H), 7.14 – 6.90 (m, 4H), 6.71 (s, 2H), 6.68 (d, J = 2.5 Hz, 2H), 3.07 (s, 12H), 2.76 (m, 4H), 2.13 – 2.11 (m, 6H), 2.03 – 2.02 (m, J = 12H), 1.86 – 1.76 (m, 14H). ^{13}C NMR (126 MHz, DMSO-d_6) δ 169.0, 155.8, 154.2, 145.0, 144.4, 137.7, 129.4, 126.2, 113.3, 111.84, 111.81, 99.2, 97.0, {two peaks at 40.4–38.8, beneath DMSO-d_6 solvent peak} 37.9, 35.9, 27.6, 26.5, 20.8. HRMS (ESI$^+$) calcd for $C_{52}H_{60}ClN_2O_2^+$ [M]$^+$: 779.4338; found: 779.4307. IR (film): 2902, 2850, 1634, 1363, 1230, 1143, 987, 932, 885 cm^{-1}. Absorbance (CH_2Cl_2): 500, 562, 876, 977 nm. Emission (CH_2Cl_2, ex. 885 nm): 997 nm.

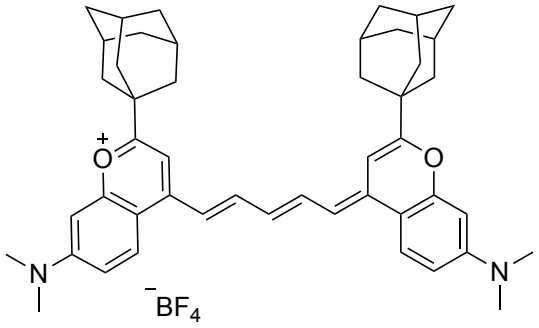

2-((3*r*,5*r*,7*r*)-adamantan-1-yl)-4-((1*E*,3*E*)-5-((*E*)-2-((3*r*,5*r*,7*r*)-adamantan-1-yl)-7-(dimethylamino)-4*H*-chromen-4-ylidene)penta-1,3-dien-1-yl)-7-(dimethylamino)chromenylium tetrafluoroborate (**4.8**). Chromenylium **4.12b** (15.1 mg, 0.0369 mmol, 1.00 equiv.), malonaldehyde bis(phenylimine) monohydrochloride (4.5 mg, 0.020 mmol, 0.47 equiv.), and sodium acetate (10.2 mg, 0.124 mmol, 3.37 equiv.) were added to a 25 mL Schlenk tube under a N_2 atmosphere. Acetic anhydride (0.41 mL) was added and the solution was freeze-pump-thawed x3 before heating to 100 ºC for 70 min. The reaction was cooled, ~5 mL of toluene was added, and the product was collected by vacuum filtration. An iridescent dark purple solid resulted (10.5 mg, 0.0137 mmol, 79%). ^{1}H NMR (500 MHz, Methylene Chloride-d_2) δ 7.87 (d, J = 9.4 Hz, 2H), 7.80 (t, J = 12.9 Hz, 2H), 6.91 (dd, J = 9.3, 2.6 Hz, 2H), 6.82 (d, J = 13.4 Hz, 2H),

6.76-6.71 (m, 3H), 6.57 (d, *J* = 2.6 Hz, 2H), 3.16 (s, 12H), 2.16 (t, *J* = 3.1 Hz, 6H), 2.05 (d, *J* = 2.8 Hz, 12H), 1.89 – 1.75 (m, 12H). ^{13}C NMR (126 MHz, Methylene Chloride-d_2) δ 170.9, 157.1, 154.8, 148.9, 147.9, 127.3, 125.8, 113.5, 113.3, 111.7, 99.9, 97.6, 40.6, 40.2, 39.0, 36.8, 28.6. HRMS (ESI$^+$) calcd for $C_{47}H_{55}N_2O_2^+$ [M]$^+$: 679.4258; found: 679.4240. IR (film): 2905, 2851, 1631, 1463, 1122, 984, 929, 884. Absorbance (CH_2Cl_2): 521, 742, 818 nm. Emission (CH_2Cl_2, ex. 755 nm): 837 nm.

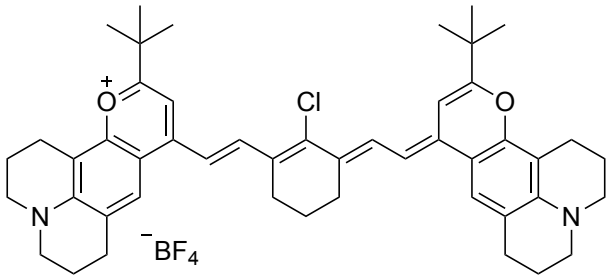

11-(Tert-butyl)-9-((E)-2-((E)-3-((E)-2-(11-(tert-butyl)-2,3,6,7-tetrahydro-1H,5H,9H-pyrano[2,3-f]pyrido[3,2,1-ij]quinolin-9-ylidene)ethylidene)-2-chlorocyclohex-1-en-1-yl)vinyl)-2,3,6,7-tetrahydro-1H,5H-pyrano[2,3-f]pyrido[3,2,1-ij]quinolin-12-ium tetrafluoroborate (4.9, JuloChrom7). Chromenylium **4.12c** (52 mg, 0.13 mmol, 1.0 equiv.), *N*-[(3-(anilinomethylene)- 2-chloro-1-cyclohexen-1-yl)methylene]aniline hydrochloride (22 mg, 0.062 mmol, 0.48 equiv.), and 2,6-di-*tert*-butyl-4-methyl pyridine (80 mg, 0.4 mmol, 3 equiv.) were dissolved in a mixture of *n*-butanol (820 µL) and toluene (350 µL) in a 25 mL Schlenk flask and heated to 105 °C for 7 hours. The solution was cooled to rt and evaporated onto silica gel. The crude product was purified via silica gel chromatography, eluting with a DCM/toluene/EtOH solvent gradient of 7:3 + 0.2% EtOH, increasing up to 10% EtOH gradually, followed by a trituration with ice cold THF. The procedure gave a dark purple solid (30. mg, 0.036 mmol, 28 %). ^{1}H NMR (500 MHz, Methylene Chloride-d_2) δ 8.15 (d, J = 13.8 Hz, 2H), 7.48 (s, 2H), 6.79 (s, 4H), 3.39 (s, 8H), 2.89 (s, 8H), 2.77 (s, 4H), 2.02 (d, J = 7.2 Hz, 8H), 1.41 (s, 18H), 0.08 (s, 2H). HRMS (ESI$^+$) calcd for $C_{48}H_{56}ClN_2O_2+^+$ [M]$^+$: 727.4025; found: 727.4003. IR (film): 2925, 2854,

1628, 1234, 1144, 1048, 960, 929, 895 cm^{-1}. Absorbance (CH_2Cl_2): 524, 563, 608, 1008 nm. Emission (CH_2Cl_2): 1033 nm..

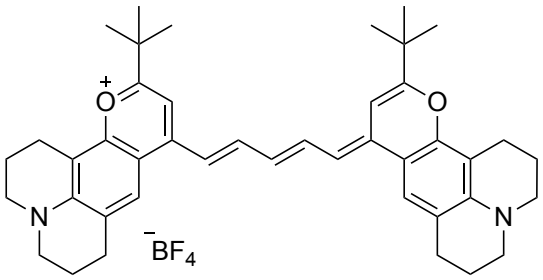

11-(*tert*-butyl)-9-((1*E*,3*E*,5*E*)-5-(11-(*tert*-butyl)-2,3,6,7-tetrahydro-1*H*,5*H*,9*H*-pyrano[2,3-*f*]pyrido[3,2,1-*ij*]quinolin-9-ylidene)penta-1,3-dien-1-yl)-2,3,6,7-tetrahydro-1*H*,5*H*-pyrano[2,3-*f*]pyrido[3,2,1-*ij*]quinolin-12-ium tetrafluoroborate (**4.10,** JuloChrom5). Chromenylium **4.12c** (150 mg, 0.39 mmol, 1.0 equiv.), malonaldehyde bis(phenylimine) monohydrochloride (49.7 mg, 0.192 mmol, 0.490 equiv.), and sodium acetate (99.1 mg, 1.21 mmol, 3.09 equiv.) were added to a 25 mL Schlenk tube under a N_2 atmosphere. Acetic anhydride (3.5 mL) was added and the solution was freeze-pump-thawed x3 before heating to 100 ºC for 60 min. The reaction was cooled, ~10 mL of toluene was added, and the product was collected by vacuum filtration. A bronze solid resulted (111 mg, 0.155 mmol, 81%). ^{1}H NMR (500 MHz, Acetonitrile-d_3) δ 7.85 (t, J = 13.0 Hz, 2H), 7.51 (s, 2H), 6.81 (s, 2H), 6.78 (d, J = 13.6 Hz, 2H), 6.61 (t, J = 12.5 Hz, 1H), 3.36 (q, J = 6.5 Hz, 8H), 2.85 (t, J = 6.4 Hz, 4H), 2.81 (t, J = 6.1 Hz, 4H), 1.99 – 1.96 (m, 8H), 1.39 (s, 18H). ^{13}C NMR (126 MHz, Acetonitrile-d_3) δ 170.0, 152.6, 149.1, 148.4, 146.9, 127.3, 124.1, 122.3, 113.7, 111.6, 107.0, 99.7, 50.9, 50.4, 37.6, 28.5, 28.4, 21.8, 20.91, 20.87. HRMS (ESI^+) calcd for $C_{43}H_{51}N_2O_2^+$ $[M]^+$: 627.3945; found: 627.3927. IR (film): 2955, 2847, 1633, 1439, 1091, 951, 925, 886 cm^{-1}. Absorbance (CH_2Cl_2): 560, 771, 852 nm. Emission (CH_2Cl_2, ex. 755 nm): 872 nm.

4.5.3 Figure experimental procedures

Figure 4.4A–B Absorption spectra were obtained of dilute dye solutions in DCM (approx. OD = 1) in a 10 mm cuvette. Spectra were baseline corrected to the signal at 1,300 nm for the heptamethine dyes and to 1,000 nm for **4.6** and **4.8**, 1,100 nm for **4.10**, and 1,200 nm for **4.4**. Spectra for **4.6** and **4.8**were corrected for non-linearity between gratings. Displayed spectra are normalized to 1.0. Emission spectra were obtained in dilute solutions of dyes in DCM (OD < 0.1) in a 10 mm cuvette, with excitation at 885 nm for the heptamethine dyes and at 755 nm for the pentamethine dyes.

Figure 4.4C–D Quantum yields were acquired as described in Seciton 4.6.1. Photophysics were acquired as described in the general experimental procedures. Brightness and "SWIR brightness" were calculated from the listed equations.

Figure 4.5A–B Excited state lifetimes were acquired and calculated as described in Section 4.6.2.

Figure 4.5C–D The contribution of change in k_r and k_{nr} to the $\Delta\Phi_F$ for chromenylium vs. flavylium dyes was obtained as described in Section 4.6.3

Figure 4.6 Single crystals of dye **4.4** were obtained by slow evaporation from DMSO. Single crystals of dye **4.5** were obtained by layered diffusion of DCM with *n*-hexane. Crystallization parameters are provided in Section 4.7.

Figure 4.7. Solutions in DCM of each flavylium/chromenylium dye and in EtOH of ICG at 0.25 μM were prepared and transferred to 1.5 mL Eppendorf tubes. Imaging was performed with Goldeye G-032 in an upright configuration with Navitar (SWIR-35) SWIR C-mount lens and LP filters (1x FELH1000 (Thorlabs), 3x LP1000 (#84-766 Edmund Optics). Camera settings were as follows: gain = 1, temperature = -30 ºC, ET = 0.3–2.5 ms. The excitation used 785 nm, 892 nm, and 968 nm lasers in an excitation unit with SP filters 2x FESH1000 (Thorlabs) and engineered

diffuser ED1-S50 (Thorlabs). Power densities for each irradiation wavelength were as follows: equal power densities (A): 785 nm = 100 $mWcm^{-2}$, 892 nm = 101 $mWcm^{-2}$, 968 nm = 100 $mWcm^{-2}$; equal photon number (B): 785 nm = 100 $mWcm^{-2}$, 892 = 88 $mWcm^{-2}$, 968 nm = 81 $mWcm^{-2}$; power densities scaled to INCIRP guidelines (C) 785 nm = 100 $mWcm^{-2}$, 892 nm = 163 $mWcm^{-2}$; 968 nm = 232 $mWcm^{-2}$. Images were averaged over 200 frames before analysis. Rectangular ROIs were drawn over the Eppendorf locations and used to obtain intensity values for each sample. Intensities were divided by the exposure time used for each acquisition to obtain counts/ms.

Figure 4.8 Micelles were fabricated according to the following procedure: 0.4 mg of each dye (dyes **4.3**, **4.4**, **4.5**, **4.6**, **4.8**, **4.10**) was dissolved in 4 mL DMSO and added to 2 mL of a 6 mg/mL solution of 18:0 PEG2000 PE (1,2-distearoyl-*sn*-glycero-3-phosphoethanolamine-*N*-[methoxy(polyethylene glycol)-2000] ammonium salt (Avanti Polar Lipids) in a 50 mL falcon tube. The solution was sonicated in a probe sonicator for 3 min on ice. The solution was then transferred to a 10 kDa MW cutoff filter (Amicon Ultra-15) and centrifuged at 4000 rpm. Sequential washes with 1x PBS were performed, until the remaining DMSO consisted of <1%. The micelles were then concentrated by centrifugation (4000 rpm) to ~12.5 mL. Concentrations were calculated according to Section 4.6.4. Absorbance traces were obtained without dilution in a 2 mm cuvette. Spectra were baseline corrected to the signal at 1,300 nm. Displayed spectra are normalized to 1.0.

Figure 4.9 Size data by DLS were acquired after a 1:100 (20 μL to 2 mL, 14 μM with respect to the lipid) dilution in MilliQ water, after filtering through a 0.22 μm cellulose acetate syringe filter. SOP parameters were as follows: sample refractive index 1.4, 3 measurements, no delay between measurements, 25 °C with 120 second equilibration time.

Figure 4.10–4.12 Micelles were prepared as described in experimental procedures for Figure 4.8. MeOFlav7 (**3.10**) micelles were prepared following literature procedure.[13] ICG was prepared in water. 2 μM solutions were prepared using dilutions from water into water, FBS, and sheep blood. Solutions were transferred to capillary tubes (Perschman DEM18 Mini Caps ISO7000), and placed in a transparent plastic holder for imaging. Imaging was performed with Goldeye G-032 in an upright configuration with Navitar (SWIR-35) SWIR C-mount lens and LP filters (1x FELH1000 (Thorlabs), 3x LP1000 (#84-766 Edmund Optics). Camera settings were as follows: gain = 1, temperature = -30 ºC, ET = 35 ms. The excitation used 785 nm, 892 nm, and 968 nm lasers in an excitation unit with SP filters 2x FESH1000 (Thorlabs) and engineered diffuser ED1-S50 (Thorlabs). Power densities for each irradiation wavelength and image are listed in the figure legend. Excitation was modulated using external triggering, with variable "on" time to modulate effective exposure time while keeping camera exposure time at 35 ms. Images were divided by the laser "on" time used in acquisition to normalize signal across all images. A rectangular ROI was drawn over the relevant area and used to crop images to the displayed size. The intensity over this ROI (averaged in the Y dimension) is plotted below each figure. LUT table CET-L16[54] was applied to all images for manuscript display in 8-bit format.

Figure 4.13–4.15 Imaging was performed with Goldeye G-033 in an upright configuration with Navitar (SWIR-35) SWIR C-mount lens and LP filters 1x FELH1000 (Thorlabs), 3x LP1000 (#84-766 Edmund Optics). Camera settings were as follows: gain = 1, ET = 2 ms, frame rate = 300 fps. The Arduino-programmed laser/camera "on" time = 2000 microseconds; "off" time = 1300 microseconds. The excitation used 785 nm and 892 nm lasers in an excitation unit with SP filters 2x FESH1000 (Thorlabs) and engineered diffuser ED1-S50 (Thorlabs). Power densities for each irradiation wavelength were as follows: 785 nm = 64 $mWcm^{-2}$; 892 nm =104 $mWcm^{-2}$. The mouse

was dosed with 50 nmol of each dye, delivered i.v. at the timepoints listed in the timelines. Micelles of **4.10** were prepared as described in experimental procedures for Figure 4.8. Images were analyzed by taking the intensities over the ROIs and graphing signal over the injection time (D) and relative signal of **4.10**/ICG (E).

Figure 4.16 Imaging was performed with Goledye G-033 in an upright configuration with Navitar (SWIR-35) SWIR C-mount lens and LP filters 1x FELH1150 (Thorlabs), and 1x LP1100 (#84-768 Edmund Optics). Camera settings were as follows: gain = 1, ET = 3 ms, frame rate = 300 fps. The excitation used 968 nm laser in an excitation unit with SP filter 1x SP1100 (#64-339 Edmund Optics) and engineered diffuser ED1-S50 (Thorlabs). Power density of irradiation was 100 $mWcm^{-2}$. The mouse was dosed with 141 nmol Chrom7 (**4.5**) i.v.

Figure 4.17 Imaging was performed with Goldeye G-033 in an upright configuration with Navitar (SWIR-35) SWIR C-mount lens and LP filters 1x FELH1000 (Thorlabs), 2x LP1000 (#84-768 Edmund Optics). Camera settings were as follows: gain = 1, ET = 3.3 ms, frame rate = 300 fps. The Arduino-programmed laser/camera "on" time = 2800 microseconds; "off" time = 500 microseconds. The excitation used 785 nm, 892 nm, 968 nm lasers in an excitation unit with SP filters 2x FESH1000 (Thorlabs) and engineered diffuser ED1-S50 (Thorlabs). Power densities for each irradiation wavelength were as follows: 785 nm = 80 $mWcm^{-2}$; 892 nm =87 $mWcm^{-2}$; 968 nm = 94 $mWcm^{-2}$. The mouse was dosed with: Chrom5 (**4.6**) = 130 nmol; JuloFlav5 (**4.4**) = 80 nmol; Chrom7 (**4.5**) = 110 nmol with delivery i.v. (Chrom5 (**4.6**), Chrom7 (**4.5**)) or i.p. (JuloFlav5 (**4.4**)) at the timepoints indicated in the timeline in (A). Micelles of **4.6, 4.5**, and **4.4** were prepared as described in experimental procedures for Figure 4.8. The mouse was imaged at the time points after injection listed in the timeline in (A). Images were manually unmixed using the following equations:

$$980_f = 980_r - (0.28 * 892_r) \quad \text{Eq. 4.1}$$

$$892_f = 892_r - (0.4 * 785_r - (0.6 * 968_f)) \quad \text{Eq. 4.2}$$

$$785_f = 785_r - (0.2 * 980_r - (0.11 * 785_r)) \quad \text{Eq. 4.3}$$

Where the subscripts (f) and (r) represent "final" and "raw" images, respectively.

Figure 4.18–4.20 Imaging was performed with Goldeye G-033 in an upright configuration with Navitar (SWIR-35) SWIR C-mount lens and LP filters 1x FELH1100 (Thorlabs), 2x LP1100 (#84-768 Edmund Optics). Camera settings were as follows: gain = 1, ET = 7.8 ms, frame rate = 120 fps. The Arduino-programmed laser/camera "on" time = 7800 microseconds; "off" time = 500 microseconds. The excitation used 785 nm, 892 nm, 968 nm, and 1065 nm lasers in an excitation unit with SP filters 2x SP1100 (#64-339 Edmund Optics) and engineered diffuser ED1-S50 (Thorlabs). Power densities for each irradiation wavelength were as follows: 785 nm = 45 $mWcm^{-2}$; 892 nm =75 $mWcm^{-2}$; 968 nm = 103 $mWcm^{-2}$; 1065 nm = 156 $mWcm^{-2}$. The mouse was dosed with: ICG = 200 nmol; JuloChrom5 (**4.10**) = 50 nmol; Chrom7 (**4.5**) = 45 nmol; JuloFlav7 (**4.3**) = 45 nmol with delivery i.v. (JuloChrom5 (**4.10**), ICG, Chrom7 (**4.5**)) or i.p. (JuloFlav7 (**4.3**)) at the time points listed in the timeline in (a). Micelles of **4.10**, **4.5**, and **4.3** were prepared as described in experimental procedures for Figure 4.8. The mouse was imaged at the time points after injection listed in the timeline in (a). Heart rate and breathing rate traces were obtained from plotting the intensity over time from the ROIs in (4.18c). Images were linearly unmixed using an automated unmixing method described in Section 4.6.5. Data are representative of two biological replicates.

4.6 Notes related to Chapter Four

4.6.1 Photoluminescence Quantum Yield Measurements

The photoluminescence quantum yield (Φ_F) of a molecule or material is defined as follows,

$$\Phi_F = \frac{P_E}{P_A} \qquad \text{(Eq. 4.4)}$$

where P_E and P_A are the number of photons absorbed and emitted, respectively. To determine the quantum yield, we either use a relative method with a known standard in the same region of the electromagnetic spectrum, or an absolute method, in which the number of photons absorbed and emitted are measured independently. Here, we used (1) a relative method with IR-26 as the known standard for all new heptamethine derivatives (**4.5**, **4.7**, **4.9**) and (2) an absolute method for all pentamethine derivatives (**4.2**, **4.4**, **4.6**, **4.8**, **4.10**). Quantum yields for dyes **4.1** and **4.3** were taken from measurements acquired previously.[13]

(1) For the relative method, to compare an unknown to a reference with a known quantum yield, the following relationship was used:

$$\Phi_{F,x} = \Phi_{F,r}(m_x/m_f)(\eta_x{}^2/\eta_r{}^2) \qquad \text{(Eq. 4.5)}$$

where m represents the slope of the line (y = mx + b) obtained from graphing integrated fluorescence intensity versus optical density across a series of samples, η is the refractive index of the solvent, and the subscripts x and r represent values of the unknown and reference, respectively. The ($\Phi_{F,r}$) of IR-26 was taken to be a constant, 0.05%, as we have previously measured,[12] and which agrees with several recent measurements.[45, 55]

Here, we measured relative fluorescence quantum yields of each dye in DCM. To obtain a plot of integrated fluorescence intensity versus absorbance for the reference and unknown, five solutions and a solvent blank were prepared and their absorbance and emission spectra (with an

excitation wavelength of 885 nm) were acquired. IR-26 and the unknown dyes were diluted in DCM to concentrations with optical densities less than 0.1 to minimize effects of reabsorption. The baseline corrected (to 1,500 nm) fluorescence traces were integrated, and the raw integrals were corrected by subtracting the integral over an identical range from fluorescence traces of the blank solvent. The integrated fluorescence intensities were then plotted against the baseline corrected absorbance values at the relevant wavelength (885 nm), and the slope and error in slope were obtained ($R^2 > 0.99$ for all traces) (Figure 4.21).

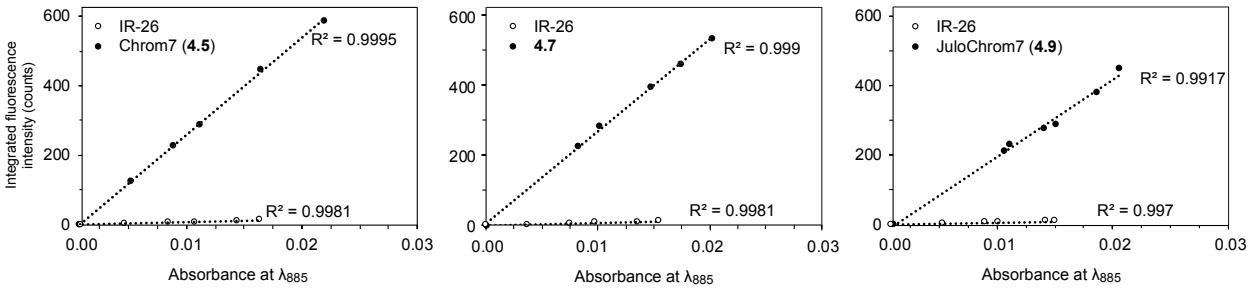

Figure 4.21 Integrated fluorescence intensity vs. absorbance at 885 nm plots for IR-26 vs. each unknown dye sample in DCM.

The refractive indices were omitted from the calculation as all samples were measured in the same solvent (DCM). The fluorescence quantum yields were then calculated using Eq. 4.5 and are reported in Table 4.1. Error measurements were propagated from the error in slope of the reference and the unknown.

The methods employed here were validated with comparison of IR-26 to IR-1061, giving a Φ_F value of 0.32 ± 0.01 %, which agrees with our prior absolute quantum yield measurement.[12] Acquisition settings for relative fluorescence quantum yield measurements: For quantum yield measurements, fluorescence traces were acquired with ex. 885 nm with a 900 nm SP filter (Thorlabs FES 900) and collection from 920– or 930–1,500 nm. The slits were 5.76 mm (15 nm) for excitation and 11.52 mm (30 nm) for emission. The step size used was 1.0 nm, integration time

0.1 s, and traces were acquired after an automatic detector background subtraction, and with the default excitation correction. Absorbances traces were acquired with a 2,000 nm/min acquisition speed, and a 1 nm step size, after blanking with dichloromethane. All samples were observed an OD of ≤0.1 to minimize sample reabsorption effects.

(2) For absolute quantum yield measurements, an integrating sphere was used (Horiba KSPHERE-Petite). Detector-corrected emission traces (collecting over the spectral region containing emission of the sample, λ_{em}) and "excitation traces" (emission spectra collecting over the spectral region containing the excitation wavelength, λ_{ex}) of the sample dissolved in DCM (sample, x) and DCM in the absence of sample (solvent, r) were collected. From these traces, absolute quantum yields were calculated from the following equation:

$$\Phi_F = \frac{P_E}{P_A} = \frac{\int_{\lambda_{em}} \left(I_x(\lambda_{em}) - I_r(\lambda_{em})\right) d\lambda_{em}}{\int_{\lambda_{ex}} \left(I_r(\lambda_{ex}) - I_x(\lambda_{ex})\right) d\lambda_{ex}} \qquad \text{(Eq. 4.6)}$$

Where, I = intensity. All reported quantum yields are the average of three independent measurements and the error is taken as the standard deviation.

Acquisition settings for absolute fluorescence quantum yield measurements: Samples in a 10 mm x 10 mm quartz cuvette were illuminated with the excitation lamp on the fluorometer and detected at 90º. Direct scatter into the detector is obfuscated by a Teflon baffle. Step sizes of 1 nm, and integration times of 0.1 s were used. A correction file was used to account for the non-linearity of the detector. All samples were observed an OD of ≤0.1 to minimize sample reabsorption effects. Parameters which were variable for each sample are outlined in Table 4.4**.**

Table 4.4 Acquisition settings for fluorescence quantum yield measurements.

Dye	**Excitation λ (nm)**	λ_{ex}**(nm)**	λ_{em} **(nm)**	**Ex. slits (nm)**	**Em. slits (nm)**
4.2 (Flav5)	808	778–830	850–1300	14	21
4.4 (JuloFlav5)	770	740–800	810–1230	11.5	11.5
4.6 (Chrom5)	750	720–780	780–1200	12	12
4.8	750	720–780	780–1200	12	12
4.10 (JuloChrom5)	770	740–800	800–1220	12	12

Photoluminescence quantum yields are displayed in Table 4.1.

4.6.2 Time Resolved Photoluminescence (TRPL) Measurements[3]

We recorded PL lifetimes using a home-built, all-reflective epifluorescence setup. Dye sample solutions (OD ~1.0) were excited at the front of a 1 cm cuvette using the pulsed laser output from an optical parametric amplifier [Spirit-OPA, MKS-Spectra Physics] pumped by ytterbium-fiber amplified pulsed laser (1040 nm, 29μJ, ~300 fs, at 10 kHz with pulse-picker) [Spirit HE 30, MKS-Spectra Physics]:

For the heptamethine dyes, the OPA excitation was tuned to 970 nm (70 μJcm^{-2}, ~200 fs) and the emission was then collected and filtered with a 90:10 beamsplitter [BSX10R, Thorlabs], two 1,000 nm longpass filters [10CGA-1000, Newport], one 1050 nm longpass filter [FELH1050, Thorlabs], and a hot mirror [10HMR-0, Newport] and finally reflectively coupled into a single-mode fiber [F-SMF-28-C-10FC, Newport] and detected using a superconducting nanowire single photon detector (SNSPD, IRF = 47 ± 1 ps) [Quantum Opus One].

[3] With Timothy Atallah

For the pentamethine dyes, the OPA excitation was tuned to 780 nm (900-100 μJcm^{-2}, ~200 fs) and the emission was then collected and filtered with the 90:10 beamsplitter, one 800 nm longpass filters [10CGA-800, Newport], two 830 nm longpass filter [10CGA-800, Newport], and the hot mirror and finally reflectively coupled into the single-mode fiber and detected using a superconducting nanowire single photon detector (SNSPD) (IRF = 59 ± 1 ps) [Quantum Opus One].

Time correlated single photon counting (TCSPC) traces were histogrammed using a HydraHarp 400 and corresponding software [Picoquant]. All measurements were carried out at room temperature. Curve fitting was performed with Igor Pro.

The instrument response function (IRF) was determined from the weighted average of two gaussian curves (Figure 4.22).

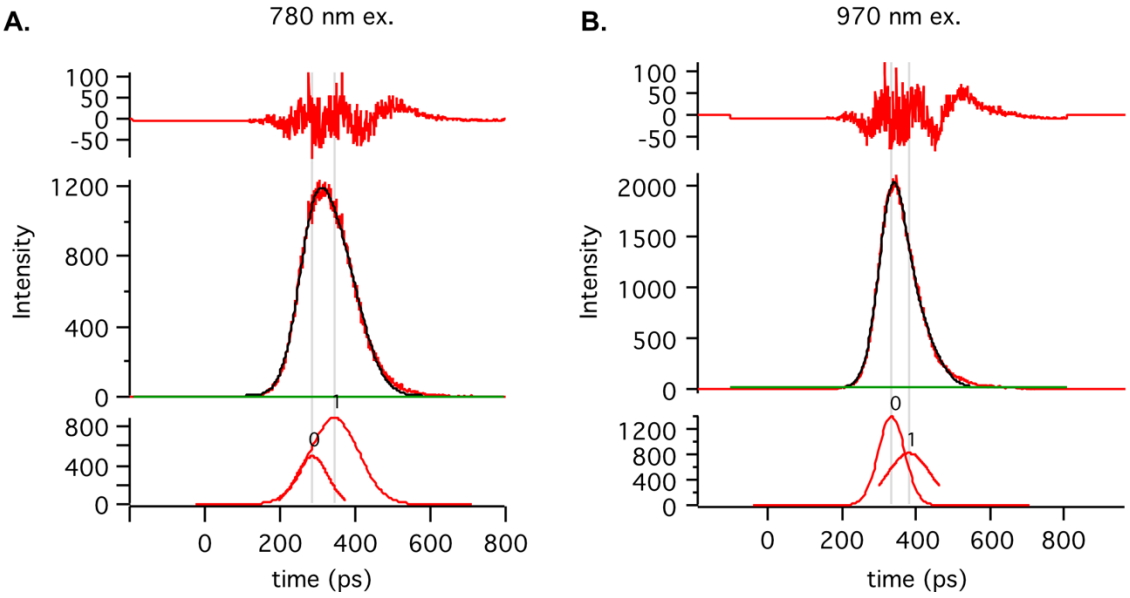

Figure 4.22 Integrated fluorescence intensity vs. absorbance at 885 nm plots for IR-26 vs. each unknown dye sample in DCM.

TRPL decay curves were fit to a single exponential using the convolution integral of the IRF and the impulse response function (Figure 4.23):

$$I(t) = \left(\frac{a}{2}\right)\left(e^{-k\left((t-t_o)-\frac{\sigma^2 k}{2}\right)}\right)\left(1+\operatorname{erf}\left[\frac{(t-t_o)-\sigma^2 k}{\sqrt{2}\sigma}\right]\right)+c \qquad \text{(Eq. 4. 7)}$$

where I = intensity, a = amplitude, k = total excited state decay rate, t = time, t_o = initial time, σ = IRF width, and c = constant.

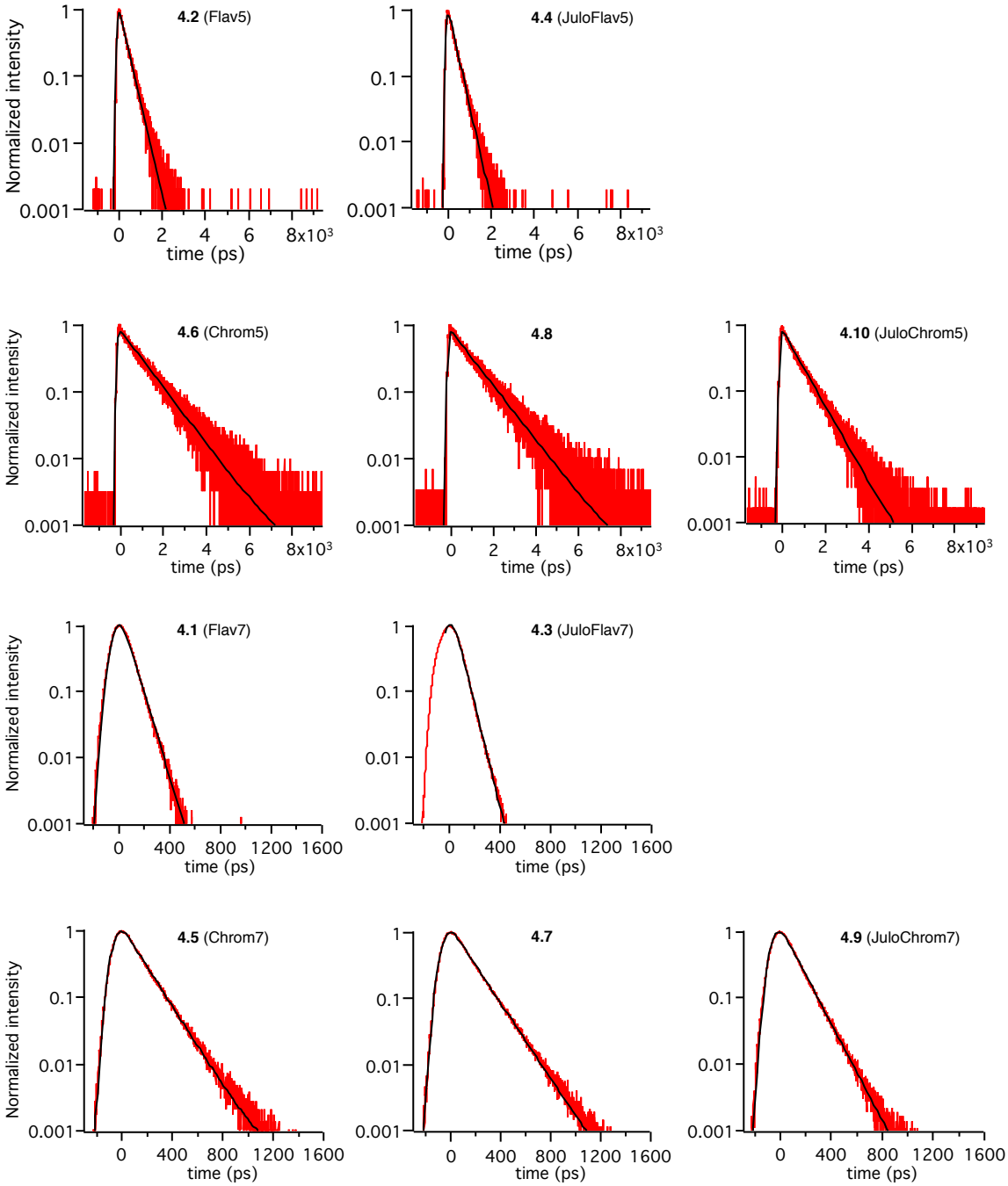

Figure 4.23 Decay curves (red) and single exponential fits (black).

The excited state lifetime is defined as the inverse of total excited state decay rate:

$$\tau = \frac{1}{k} \quad \text{(Eq. 4.8)}$$

Errors in τ were taken as ± 1 ps, the value of the detector resolution. Errors in fitting parameters were sufficiently small such that they are negligible when considering the detector resolution.

The radiative (k_r) and non-radiative (k_{nr}) rates were calculated according to the following equations:

$$k_r = \frac{\Phi_F}{\tau} \quad \text{(Eq. 4.9)}$$

$$k_{nr} = \frac{1-\Phi_F}{\tau} \quad \text{(Eq. 4.10)}$$

Errors in k_r and k_{nr} were taken as the propagated error from the errors in τ and Φ_F.

Lifetimes and radiative and non-radiative rates, are displayed in Table 4.

4.6.3 Contribution of Change in k_r and k_{nr} to the $\Delta\Phi_F$ for Chromenylium vs. Flavylium Dyes[4]

The relative contribution of k_r and k_{nr} to the $\Delta\Phi_F$ between the chromenylium and flavylium dye structures was determined according to the following analysis.

From the definition of Φ_F in terms of k_r and k_{nr}:

$$\Phi_F(k_r, k_{nr}) = \frac{k_r}{k_r + k_{nr}} \quad \text{(Eq. 4.11)}$$

The change in fluorescence quantum yield, $\Delta\Phi_F$, can be determined by:

$$\Delta\Phi_F(k_r, k_{nr}, \Delta k_r, \Delta k_{nr}) = \Phi_F(k_r + \Delta k_r, k_{nr} + \Delta k_{nr}) - \Phi_F(k_r, k_{nr}) \quad \text{(Eq. 4.12)}$$

[4] Analysis by Timothy Atallah

Where each rate constant (k_r, k_{nr}) represents that of the flavylium dye and each change in rate constant, ($\Delta k_r, \Delta k_{nr}$) represents the difference in rate constant between the chromenylium and flavylium dyes (chromenylium – flavylium). Eq. 4.12 can be divided into components:

$$\Delta\Phi_F(k_r, k_{nr}, \Delta k_r, \Delta k_{nr}) =$$

$$\Delta\Phi_F(k_r, k_{nr}, \Delta k_r, 0) + \Delta\Phi_F(k_r, k_{nr}, 0, \Delta k_{nr}) + \mathcal{O}_{\Delta k_r \Delta k_{nr}} \qquad \text{(Eq. 4.13)}$$

Since the mixed partial derivatives of $\Phi_F(k_r, k_{nr})$ with respect to k_r and k_{nr} are non-zero, i.e. $\frac{\partial}{\partial k_r}\frac{\partial}{\partial k_{nr}}\Phi_F(k_r, k_{nr}) \neq 0$, then $\mathcal{O}_{\Delta k_r \Delta k_{nr}} \neq 0$. Simultaneous changes in k_r and k_{nr} result in a component that can change $\Phi_F(k_r, k_{nr})$ depending on both k_r and k_{nr} together. Hence accounting for the total change in $\Phi_F(k_r, k_{nr})$ in terms of the separate changes of k_r and k_{nr} is not possible. Therefore, we determine the remaining term requiring the non-linear mixing of changes in both k_r and k_{nr} together, $\mathcal{O}_{\Delta k_r \Delta k_{nr}}$, from the unaccounted fraction in the change. The relative contribution from each component in the equation to the overall $\Delta\Phi_F$ can be calculated as a ratio of $\Delta\Phi_F$ attributed to each component over the total $\Delta\Phi_F$ resulting from all components:

$$R_{\Delta k_r} = \frac{\Delta\Phi_F(k_r, k_{nr}, \Delta k_r, 0)}{\Delta\Phi_F(k_r, k_{nr}, \Delta k_r, \Delta k_{nr})} \qquad \text{(Eq. 4.14)}$$

Eq. 4.14 gives the ratio component of the $\Delta\Phi_F$ attributed solely to the change in k_r.

$$R_{\Delta k_{nr}} = \frac{\Delta\Phi_F(k_r, k_{nr}, 0, \Delta k_{nr})}{\Delta\Phi_F(k_r, k_{nr}, \Delta k_r, \Delta k_{nr})} \qquad \text{(Eq. 4.15)}$$

Eq. 4.15 gives the ratio component of the $\Delta\Phi_F$ attributed solely to the change in k_{nr}.

$$R_{\mathcal{O}_{\Delta k_r \Delta k_{nr}}} = 1 - \left(R_{\Delta k_r} + R_{\Delta k_{nr}}\right) = \frac{\mathcal{O}_{\Delta k_r \Delta k_{nr}}}{\Delta\Phi_F(k_r, k_{nr}, \Delta k_r, \Delta k_{nr})} \qquad \text{(Eq. 4.16)}$$

Eq. 4.16 gives the ratio component of the $\Delta\Phi_F$ due to both the non-radiative and radiative component simultaneously changed leading to even further non-linear change of the quantum yield as the non-radiative and radiative rates act together.

The values of $R_{\Delta k_r}$, $R_{\Delta k_{nr}}$, and $R_{\mathcal{O}_{\Delta k_r \Delta k_{nr}}}$ were determined for each chromenylium dye compared to the closest structurally analogous flavylium dye, to best represent the impact of structural changes at the C2 position of the heterocycle. These pairs are outlined in the Figure 3d. The resulting contributions to overall $\Delta\Phi_F$ are plotted in Figure 3e.

The analysis used here to compare of k_r and k_{nr} contributions to $\Delta\Phi_F$ is limited to cases where a change in Φ_F is observed between chromophores, and to cases where the non-linear component is non-negative and is not the dominating contributor to change in Φ_F.

4.6.4 Determination of Dye Concentration within Micelles

As micelle fabrication includes several washing and transfer steps, and various amounts of dye could be lost from the nanomaterial during these steps, we applied a method to allow accurate quantification of the amount of dye in a micelle solution.

After micelle fabrication (see experimental procedures for Figure 4.5), an aliquot was removed from the micelle stock and lyophilized overnight. The resulting dry powder was dissolved in DCM for analysis by UV-VIS spectroscopy. The concentration of the dye in organic solvent was determined using Beer's law, $c = \frac{\varepsilon \times l}{A}$ and correlated to the appropriate volume of the original aliquot to determine dye concentration in the aqueous micellular solution.

4.6.5 Method Description – Linear Unmixing[5]

The excitation spectra of the dyes used in these experiments have some overlap between imaging channels. We use a linear unmixing method to generate images representing the quantity of each

[5] Analysis by Thomas Bischof and Bernardo Arús

dye present in an image, enhancing contrast and simplifying interpretation. We assume that each dye has a consistent excitation spectrum, which is linear with concentration. We also assume that the signals are additive, such that the signal measured at each pixel for a given laser can be expressed as:

$$I(\lambda_1) = \eta(\lambda_1) + c_{dye1}A_{dye1}(\lambda_1) + c_{dye2}A_{dye2}(\lambda_1)\ldots \quad \text{(Eq. 4.17)}$$

where η is the background signal (camera noise, stray light, etc), c is the concentration of the dye, and A is the signal generated by that dye. Overall this leads to a system of equations:

$$\underline{I} = \underline{\underline{A}}\underline{c} + \underline{\eta} \quad \text{(Eq. 4.18)}$$

where the number of underlines represents the number of dimensions for the quantity (vector vs. matrix). Thus, our task is to determine A and η, such that we can convert from a signal measured in intensity space to a signal in concentration space.

We measure noise by obtaining images of a blank field of view, which are then subtracted from subsequent measurements. To calibrate the relative amount of signal emitted by each dye in each imaging channel, we begin by placing vials containing solutions of each dye in the field of view and acquire images, using the same conditions as in the *in vivo* experiments. We select regions of interest (ROI) representing each vial, and determine the mean signal generated by each dye, in each imaging channel. Inversion of Eq. 4.15 yields a value for A, which is then used to generate unmixed images representing the contribution of each dye to the overall signal.

4.7 Crystallographic Information Relevant to Chapter Four

Table 4.5 Crystal data and structure refinement for **4.4** (JuloFlav5).

Empirical formula	C53 H61 B F4 N2 O5 S3	
Formula weight	989.02	
Temperature	100(2) K	
Wavelength	1.54178 Å	
Crystal system	Triclinic	
Space group	P -1	
Unit cell dimensions	a = 12.9984(5) Å	a= 101.472(2)°.
	b = 13.0604(5) Å	b= 90.570(2)°.
	c = 15.5647(6) Å	g = 111.570(2)°.
Volume	2398.17(16) Å3	
Z	2	
Density (calculated)	1.370 Mg/m3	
Absorption coefficient	1.969 mm-1	
F(000)	1044	
Crystal size	.2 x .2 x .18 mm3	
Theta range for data collection	2.909 to 69.453°.	
Index ranges	-15<=h<=15, -15<=k<=15, -18<=l<=18	
Reflections collected	45262	
Independent reflections	8621 [R(int) = 0.0437]	
Completeness to theta = 67.679°	96.6 %	
Absorption correction	Semi-empirical from equivalents	
Max. and min. transmission	0.75 and 0.67	
Refinement method	Full-matrix least-squares on F2	
Data / restraints / parameters	8621 / 0 / 619	
Goodness-of-fit on F2	1.066	
Final R indices [I>2sigma(I)]	R1 = 0.0453, wR2 = 0.1234	
R indices (all data)	R1 = 0.0522, wR2 = 0.1287	
Extinction coefficient	n/a	
Largest diff. peak and hole	0.643 and -0.600 e.Å-3	

Table 4.6 Crystal data and structure refinement for **4.5** (Chrom7).

Empirical formula	C43 H54 B Cl7 F4 N2 O2	
Formula weight	965.84	
Temperature	100(2) K	
Wavelength	1.54178 Å	
Crystal system	Triclinic	
Space group	P-1	
Unit cell dimensions	a = 14.0234(3) Å	a= 88.1450(10)°.
	b = 18.9593(5) Å	b= 79.6560(10)°.
	c = 19.1502(4) Å	g = 70.0770(10)°.
Volume	4706.73(19) Å3	
Z	4	
Density (calculated)	1.363 Mg/m3	
Absorption coefficient	4.298 mm-1	
F(000)	2008	
Crystal size	0.200 x 0.200 x 0.100 mm3	
Theta range for data collection	2.346 to 69.503°.	
Index ranges -	16<=h<=17, -21<=k<=22, -22<=l<=23	
Reflections collected	96540	
Independent reflections	16916 [R(int) = 0.0414]	
Completeness to theta = 67.679°	96.5 %	
Absorption correction	Semi-empirical from equivalents	
Max. and min. transmission	0.75 and 0.58	
Refinement method	Full-matrix least-squares on F2	
Data / restraints / parameters	16916 / 0 / 1101	
Goodness-of-fit on F2	1.038	
Final R indices [I>2sigma(I)]	R1 = 0.0486, wR2 = 0.1211	
R indices (all data)	R1 = 0.0585, wR2 = 0.1269	
Extinction coefficient	n/a	
Largest diff. peak and hole	0.826 and -0.894 e.Å-3	

4.8 Spectra Relevant to Chapter Four

4.8.1 ^{1}H NMR Spectra

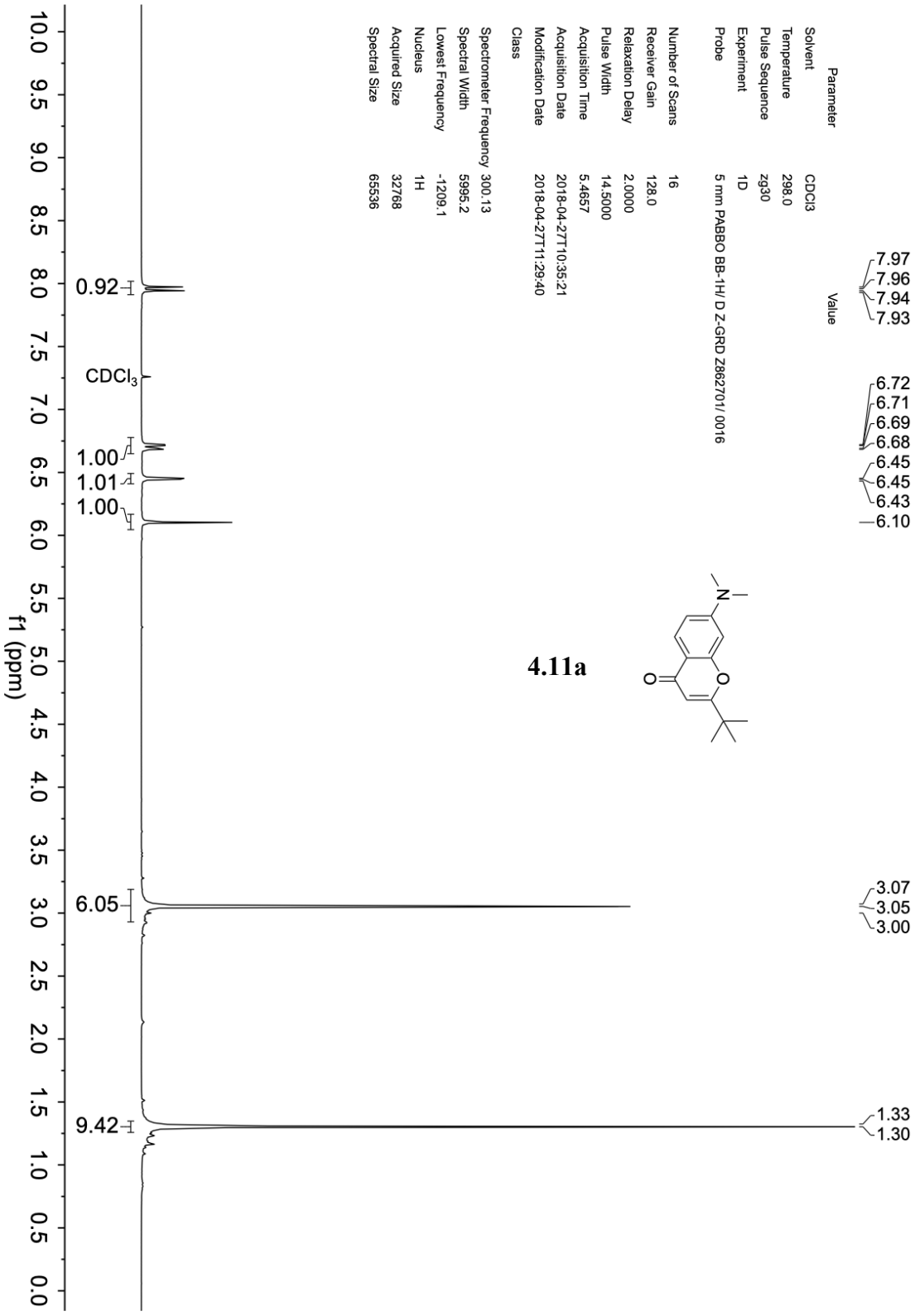

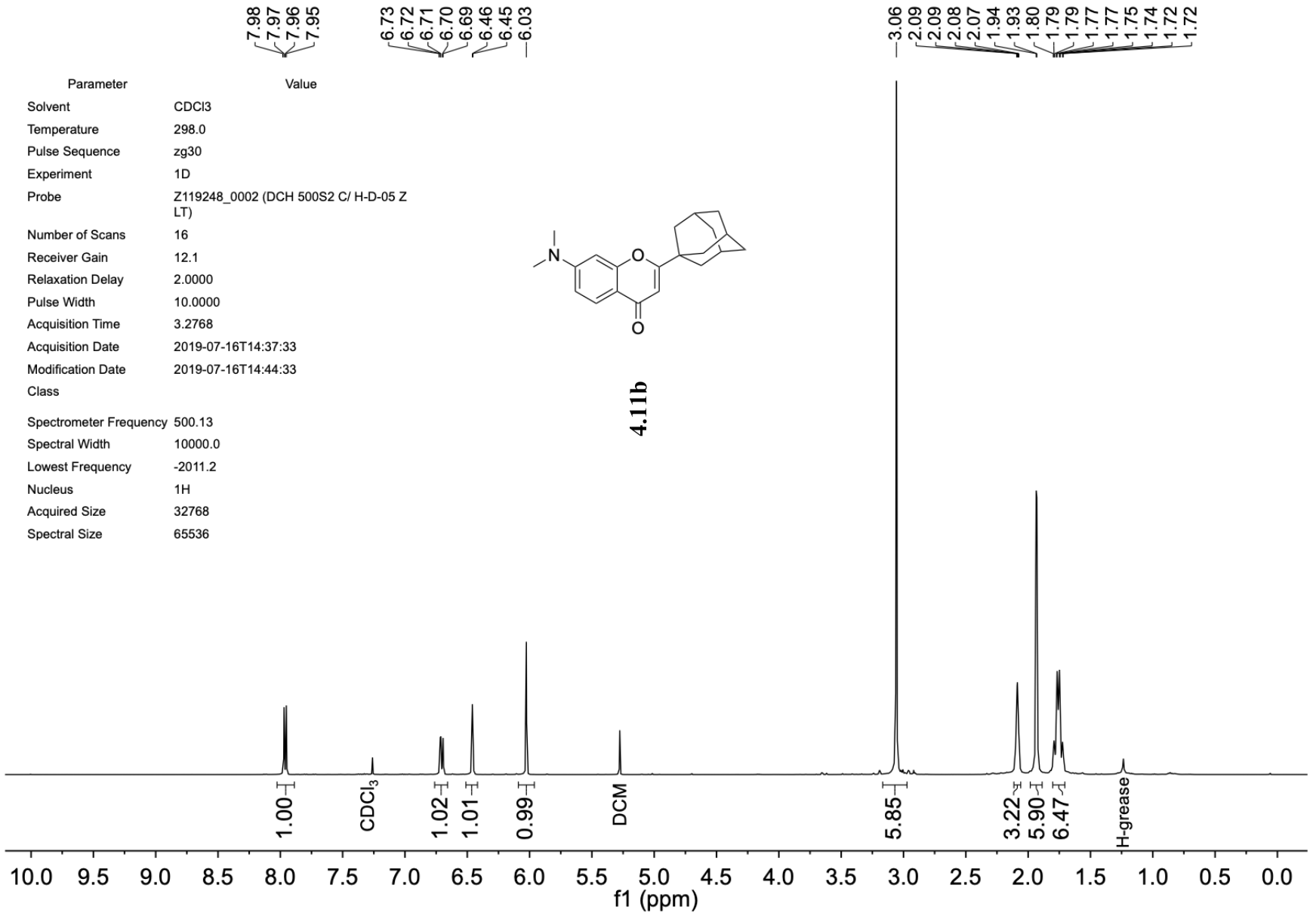
7.98
7.97
7.96
7.95
6.73
6.72
6.71
6.70
6.69
6.46
6.45
6.03
3.06
2.09
2.09
2.08
2.07
1.94
1.93
1.80
1.79
1.79
1.77
1.77
1.75
1.74
1.72
1.72
Parameter Value
Solvent CDCl3
Temperature 298.0
Pulse Sequence zg30
Experiment 1D
Probe Z119248_0002 (DCH 500S2 C/ H-D-05 Z LT)
Number of Scans 16
Receiver Gain 12.1
Relaxation Delay 2.0000
Pulse Width 10.0000
Acquisition Time 3.2768
Acquisition Date 2019-07-16T14:37:33
Modification Date 2019-07-16T14:44:33
Class
Spectrometer Frequency 500.13
Spectral Width 10000.0
Lowest Frequency -2011.2
Nucleus 1H
Acquired Size 32768
Spectral Size 65536
N
O
O
4.11b
1.00
CDCl3
1.02
1.01
0.99
DCM
5.85
3.22
5.90
6.47
H-grease
10.0 9.5 9.0 8.5 8.0 7.5 7.0 6.5 6.0 5.5 5.0 4.5 4.0 3.5 3.0 2.5 2.0 1.5 1.0 0.5 0.0
f1 (ppm)

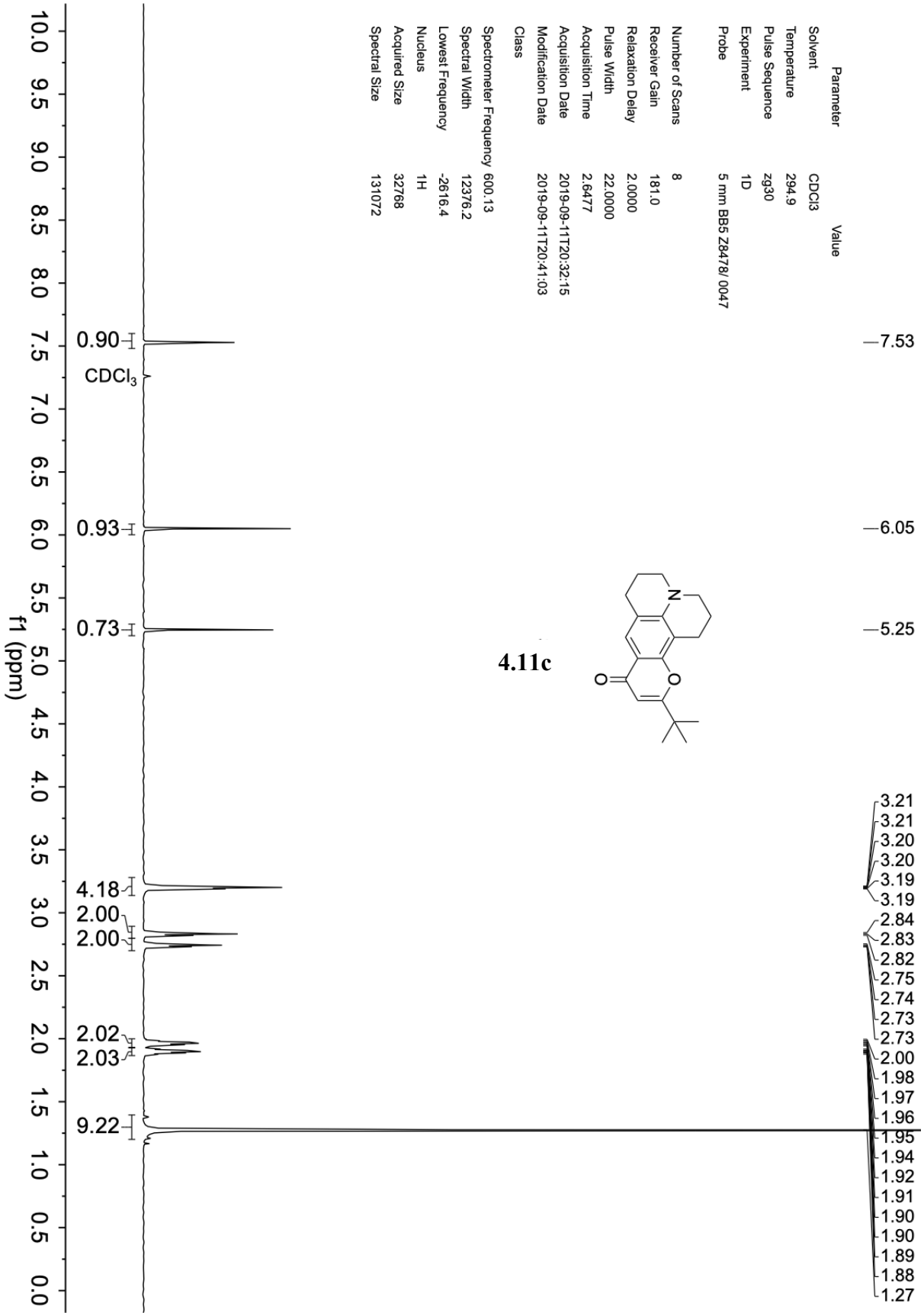
Parameter Value
Solvent CDCl3
Temperature 294.9
Pulse Sequence zg30
Experiment 1D
Probe 5 mm BB5 Z8478/ 0047
Number of Scans 8
Receiver Gain 181.0
Relaxation Delay 2.0000
Pulse Width 22.0000
Acquisition Time 2.6477
Acquisition Date 2019-09-11T20:32:15
Modification Date 2019-09-11T20:41:03
Class
Spectrometer Frequency 600.13
Spectral Width 12376.2
Lowest Frequency -2616.4
Nucleus 1H
Acquired Size 32768
Spectral Size 131072
4.11c
7.53
6.05
5.25
3.21
3.21
3.20
3.20
3.19
3.19
2.84
2.83
2.82
2.75
2.74
2.73
2.73
2.00
1.98
1.97
1.96
1.95
1.94
1.92
1.91
1.90
1.90
1.89
1.88
1.27
0.90
CDCl3
0.93
0.73
4.18
2.00
2.00
2.02
2.03
9.22
f1 (ppm)

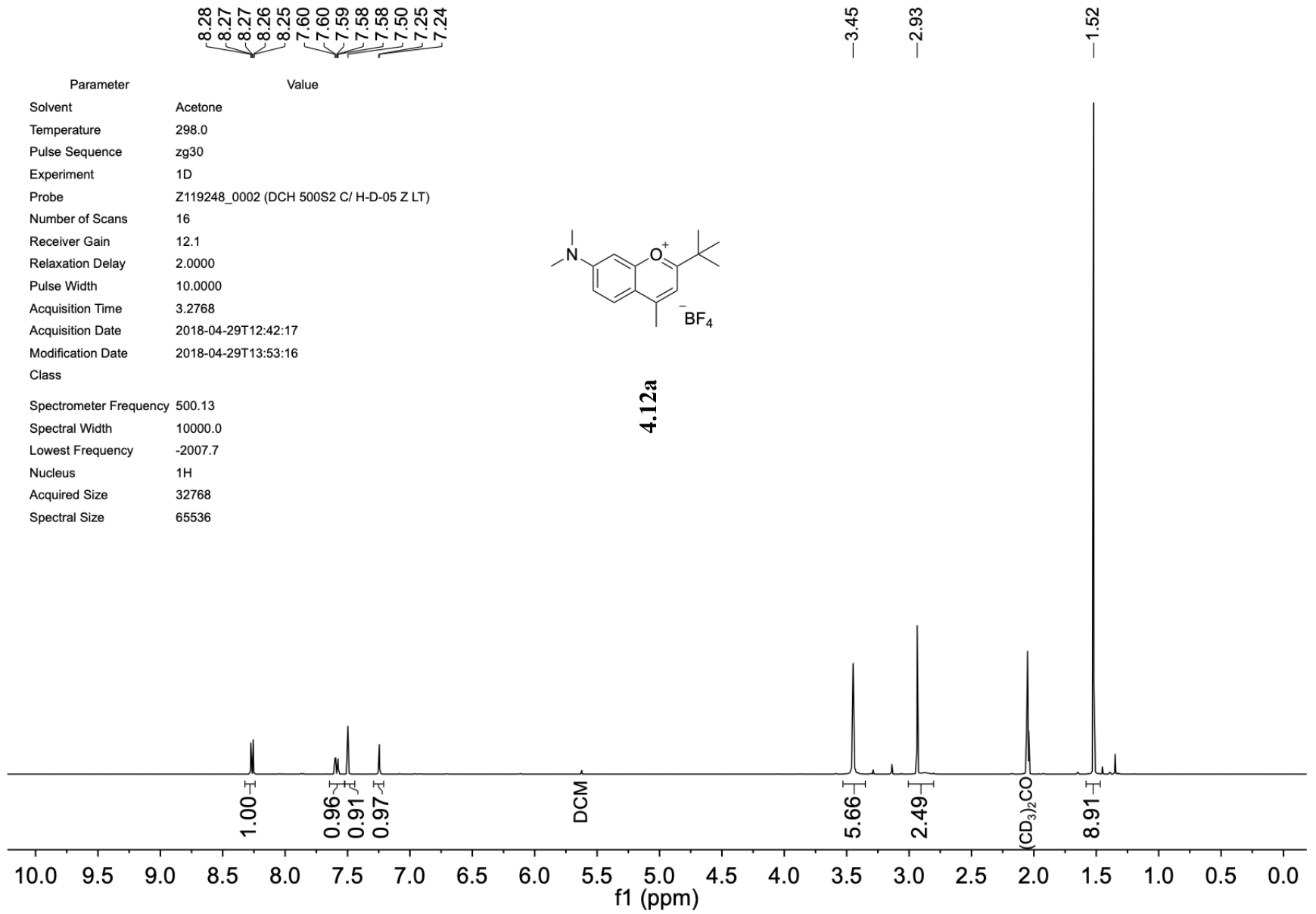
8.28
8.27
8.27
8.26
8.25
7.60
7.60
7.59
7.58
7.58
7.50
7.25
7.24
3.45
2.93
1.52
Parameter Value
Solvent Acetone
Temperature 298.0
Pulse Sequence zg30
Experiment 1D
Probe Z119248_0002 (DCH 500S2 C/ H-D-05 Z LT)
Number of Scans 16
Receiver Gain 12.1
Relaxation Delay 2.0000
Pulse Width 10.0000
Acquisition Time 3.2768
Acquisition Date 2018-04-29T12:42:17
Modification Date 2018-04-29T13:53:16
Class
Spectrometer Frequency 500.13
Spectral Width 10000.0
Lowest Frequency -2007.7
Nucleus 1H
Acquired Size 32768
Spectral Size 65536
N
O+
BF4
4.12a
1.00
0.96
0.91
0.97
DCM
5.66
2.49
(CD3)2CO
8.91
10.0 9.5 9.0 8.5 8.0 7.5 7.0 6.5 6.0 5.5 5.0 4.5 4.0 3.5 3.0 2.5 2.0 1.5 1.0 0.5 0.0
f1 (ppm)

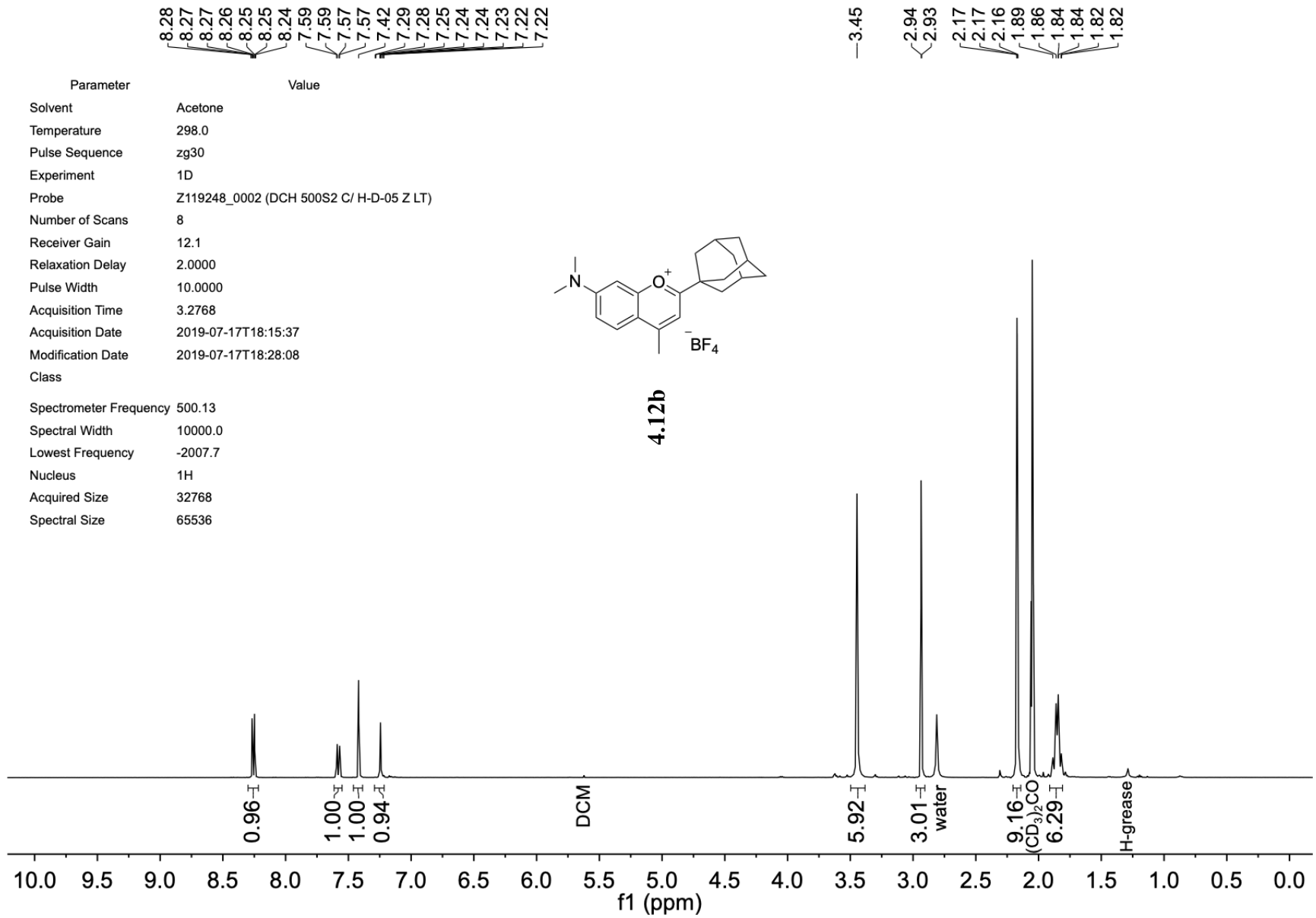
8.28
8.27
8.27
8.26
8.25
8.25
8.24
7.59
7.59
7.57
7.57
7.42
7.29
7.28
7.25
7.24
7.24
7.23
7.22
7.22
3.45
2.94
2.93
2.17
2.17
2.16
1.89
1.86
1.84
1.84
1.82
1.82
Parameter Value
Solvent Acetone
Temperature 298.0
Pulse Sequence zg30
Experiment 1D
Probe Z119248_0002 (DCH 500S2 C/ H-D-05 Z LT)
Number of Scans 8
Receiver Gain 12.1
Relaxation Delay 2.0000
Pulse Width 10.0000
Acquisition Time 3.2768
Acquisition Date 2019-07-17T18:15:37
Modification Date 2019-07-17T18:28:08
Class
Spectrometer Frequency 500.13
Spectral Width 10000.0
Lowest Frequency -2007.7
Nucleus 1H
Acquired Size 32768
Spectral Size 65536
N
O+
BF4
4.12b
0.96
1.00
1.00
0.94
DCM
5.92
3.01
water
9.16
(CD3)2CO
6.29
H-grease
10.0 9.5 9.0 8.5 8.0 7.5 7.0 6.5 6.0 5.5 5.0 4.5 4.0 3.5 3.0 2.5 2.0 1.5 1.0 0.5 0.0
f1 (ppm)

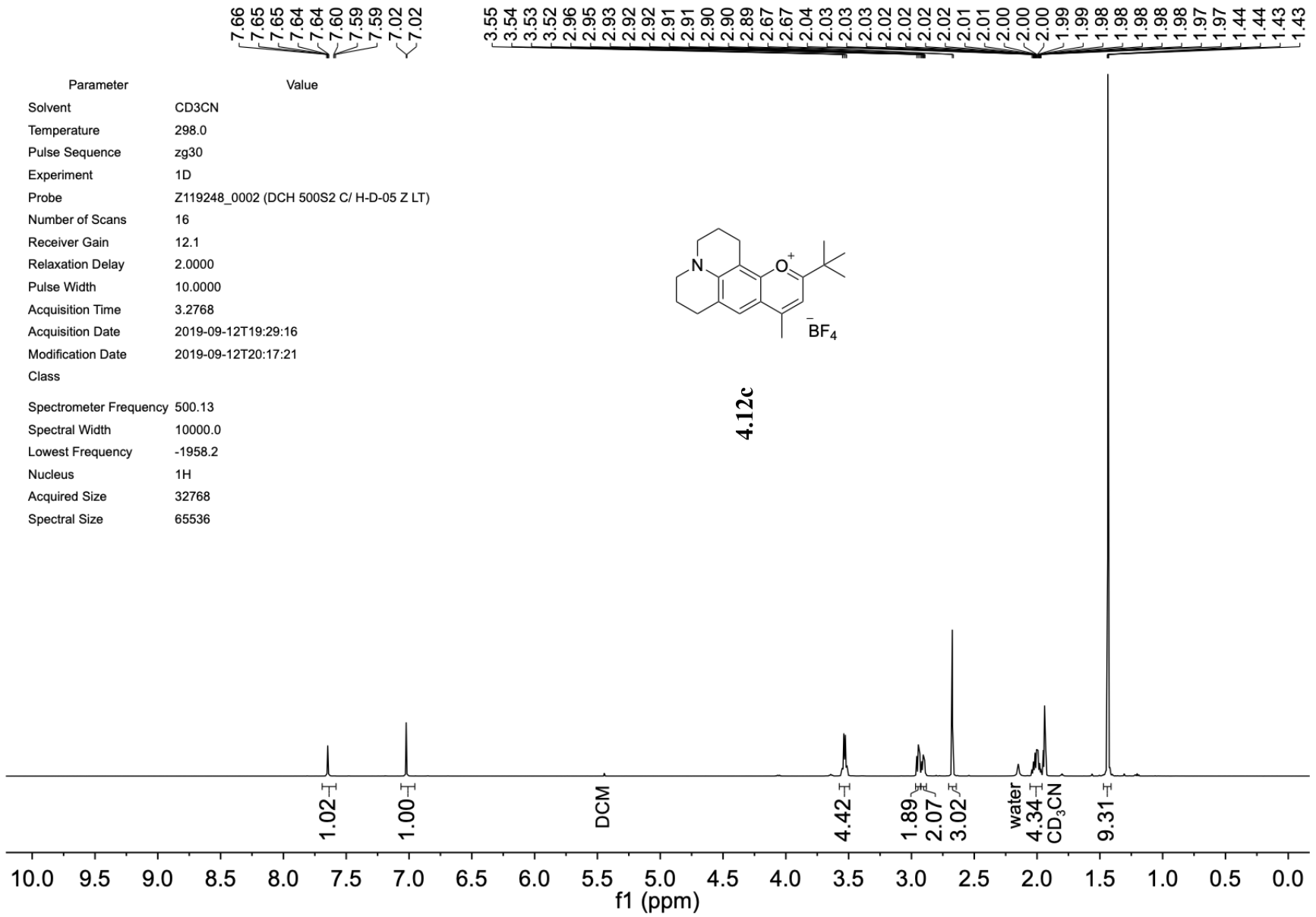
7.66 7.65 7.65 7.64 7.64 7.60 7.59 7.59 7.02 7.02
3.55 3.54 3.53 3.52 2.96 2.95 2.93 2.92 2.92 2.91 2.91 2.90 2.90 2.89 2.67 2.67 2.04 2.03 2.03 2.03 2.02 2.02 2.02 2.01 2.01 2.00 2.00 2.00 1.99 1.99 1.98 1.98 1.98 1.98 1.97 1.97 1.44 1.44 1.43 1.43
Parameter Value
Solvent CD3CN
Temperature 298.0
Pulse Sequence zg30
Experiment 1D
Probe Z119248_0002 (DCH 500S2 C/ H-D-05 Z LT)
Number of Scans 16
Receiver Gain 12.1
Relaxation Delay 2.0000
Pulse Width 10.0000
Acquisition Time 3.2768
Acquisition Date 2019-09-12T19:29:16
Modification Date 2019-09-12T20:17:21
Class
Spectrometer Frequency 500.13
Spectral Width 10000.0
Lowest Frequency -1958.2
Nucleus 1H
Acquired Size 32768
Spectral Size 65536
N
O+
BF4
4.12c
1.02
1.00
DCM
4.42
1.89
2.07
3.02
water
4.34
CD3CN
9.31
10.0 9.5 9.0 8.5 8.0 7.5 7.0 6.5 6.0 5.5 5.0 4.5 4.0 3.5 3.0 2.5 2.0 1.5 1.0 0.5 0.0
f1 (ppm)

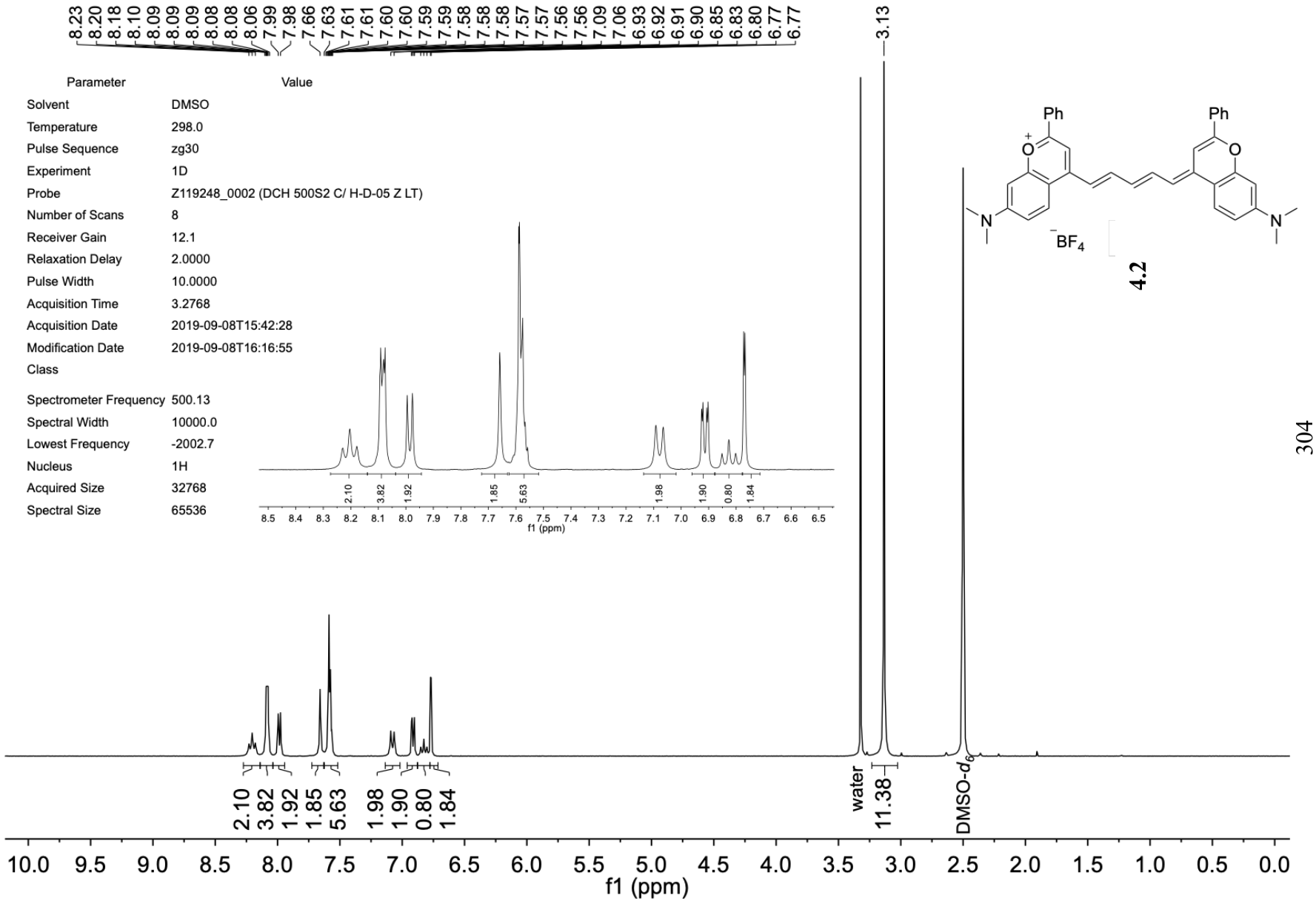
8.23 8.20 8.18 8.10 8.09 8.09 8.09 8.08 8.08 8.06 7.99 7.98 7.66 7.63 7.61 7.61 7.60 7.60 7.59 7.59 7.58 7.58 7.58 7.57 7.57 7.56 7.56 7.09 7.06 6.93 6.92 6.91 6.90 6.85 6.83 6.80 6.77 6.77
3.13
Parameter Value
Solvent DMSO
Temperature 298.0
Pulse Sequence zg30
Experiment 1D
Probe Z119248_0002 (DCH 500S2 C/ H-D-05 Z LT)
Number of Scans 8
Receiver Gain 12.1
Relaxation Delay 2.0000
Pulse Width 10.0000
Acquisition Time 3.2768
Acquisition Date 2019-09-08T15:42:28
Modification Date 2019-09-08T16:16:55
Class
Spectrometer Frequency 500.13
Spectral Width 10000.0
Lowest Frequency -2002.7
Nucleus 1H
Acquired Size 32768
Spectral Size 65536
2.10 3.82 1.92 1.85 5.63 1.98 1.90 0.80 1.84
f1 (ppm)
Ph
Ph
O
O
N
N
BF4
4.2
2.10 3.82 1.92 1.85 5.63 1.98 1.90 0.80 1.84
water 11.38
DMSO-d6
10.0 9.5 9.0 8.5 8.0 7.5 7.0 6.5 6.0 5.5 5.0 4.5 4.0 3.5 3.0 2.5 2.0 1.5 1.0 0.5 0.0
f1 (ppm)

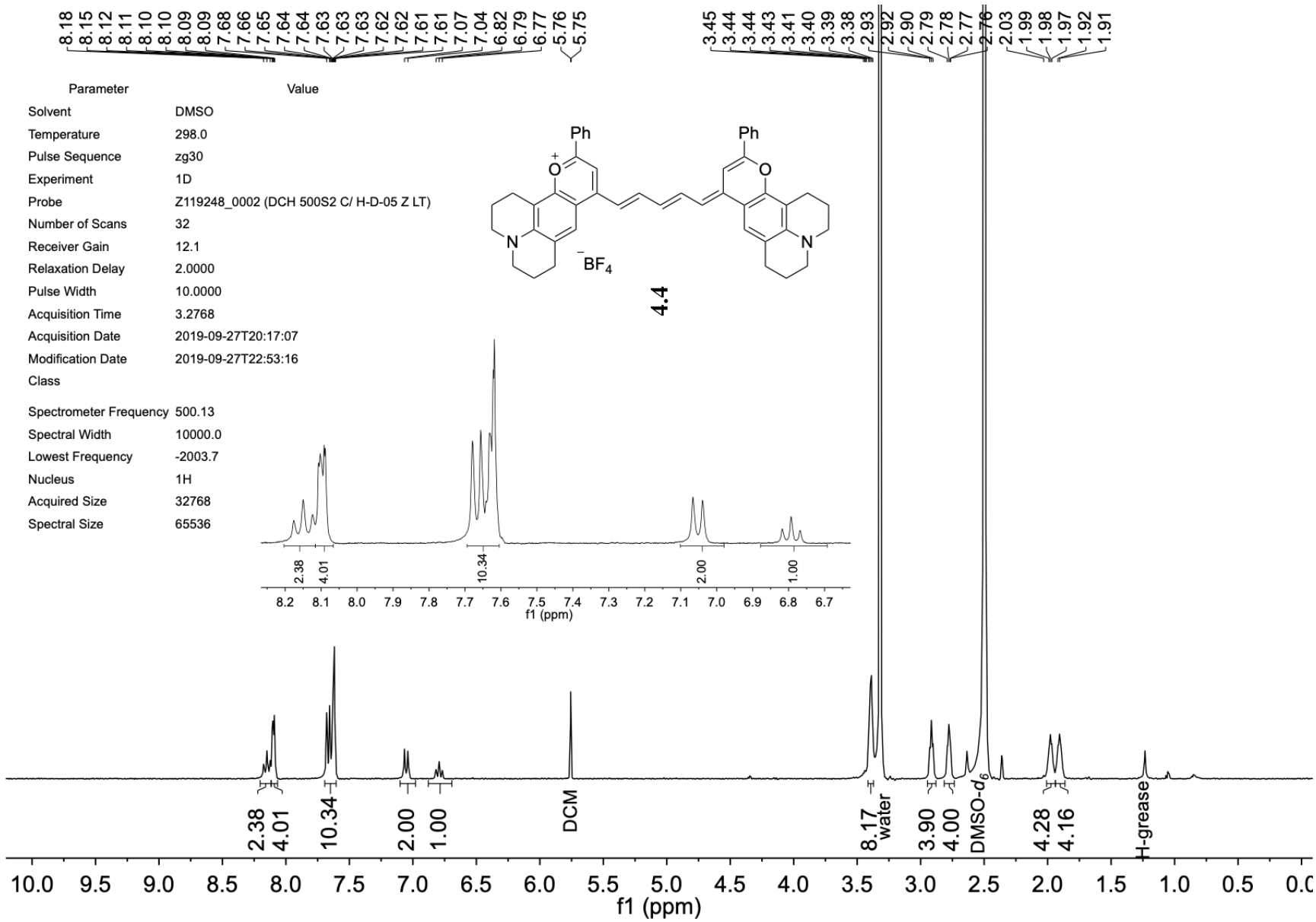
8.18 8.15 8.12 8.11 8.10 8.10 8.09 8.09 7.68 7.66 7.65 7.64 7.64 7.63 7.63 7.63 7.62 7.62 7.61 7.61 7.07 7.04 6.82 6.79 6.77 5.76 5.75
3.45 3.44 3.44 3.43 3.41 3.40 3.39 3.38 2.93 2.92 2.90 2.79 2.78 2.77 2.76 2.03 1.99 1.98 1.97 1.92 1.91
Parameter Value
Solvent DMSO
Temperature 298.0
Pulse Sequence zg30
Experiment 1D
Probe Z119248_0002 (DCH 500S2 C/ H-D-05 Z LT)
Number of Scans 32
Receiver Gain 12.1
Relaxation Delay 2.0000
Pulse Width 10.0000
Acquisition Time 3.2768
Acquisition Date 2019-09-27T20:17:07
Modification Date 2019-09-27T22:53:16
Class
Spectrometer Frequency 500.13
Spectral Width 10000.0
Lowest Frequency -2003.7
Nucleus 1H
Acquired Size 32768
Spectral Size 65536
Ph
Ph
O
N
N
BF4
4.4
2.38 4.01 10.34 2.00 1.00
8.2 8.1 8.0 7.9 7.8 7.7 7.6 7.5 7.4 7.3 7.2 7.1 7.0 6.9 6.8 6.7
f1 (ppm)
2.38 4.01 10.34 2.00 1.00 DCM 8.17 water 3.90 4.00 DMSO-d6 4.28 4.16 H-grease
10.0 9.5 9.0 8.5 8.0 7.5 7.0 6.5 6.0 5.5 5.0 4.5 4.0 3.5 3.0 2.5 2.0 1.5 1.0 0.5 0.0
f1 (ppm)

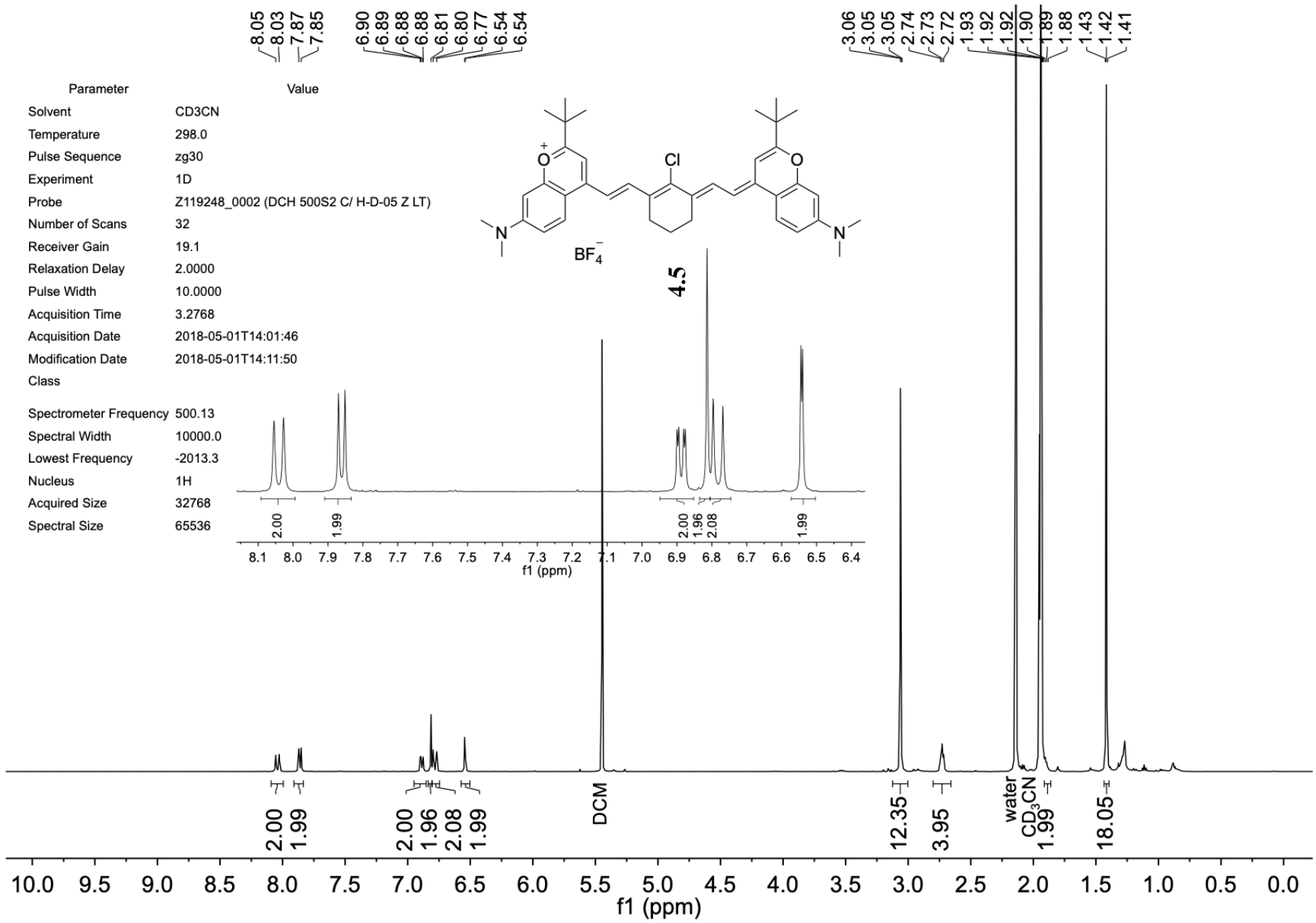
8.05
8.03
7.87
7.85
6.90
6.89
6.88
6.88
6.81
6.80
6.77
6.54
6.54
3.06
3.05
3.05
2.74
2.73
2.72
1.93
1.92
1.92
1.90
1.89
1.88
1.43
1.42
1.41
Parameter Value
Solvent CD3CN
Temperature 298.0
Pulse Sequence zg30
Experiment 1D
Probe Z119248_0002 (DCH 500S2 C/ H-D-05 Z LT)
Number of Scans 32
Receiver Gain 19.1
Relaxation Delay 2.0000
Pulse Width 10.0000
Acquisition Time 3.2768
Acquisition Date 2018-05-01T14:01:46
Modification Date 2018-05-01T14:11:50
Class
Spectrometer Frequency 500.13
Spectral Width 10000.0
Lowest Frequency -2013.3
Nucleus 1H
Acquired Size 32768
Spectral Size 65536
Cl
O
O
N
N
BF4−
4.5
2.00
1.99
2.00
1.96
2.08
1.99
f1 (ppm)
2.00
1.99
2.00
1.96
2.08
1.99
DCM
12.35
3.95
water
CD3CN
1.99
18.05
f1 (ppm)

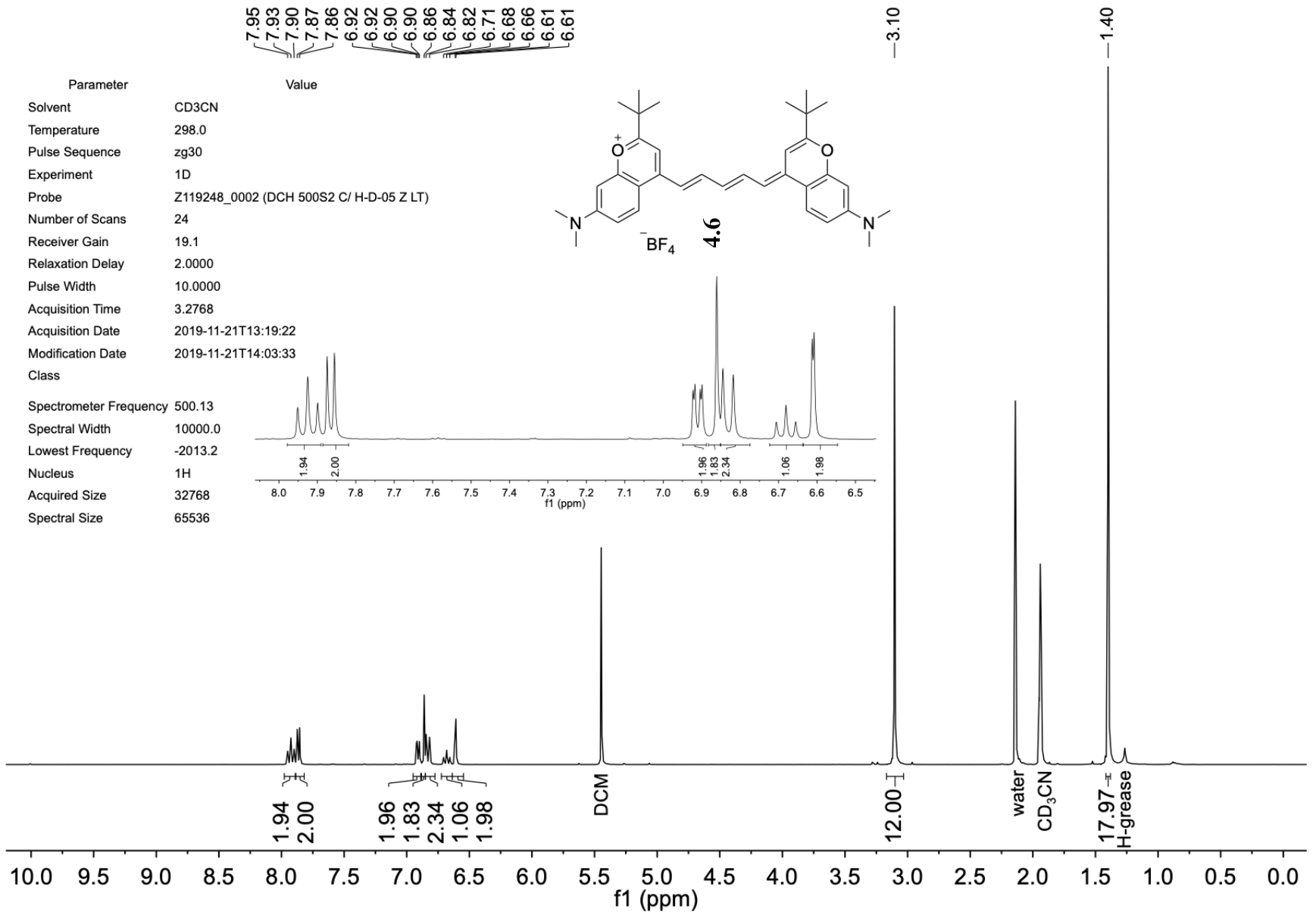
7.95
7.93
7.90
7.87
7.86
6.92
6.92
6.90
6.90
6.86
6.84
6.82
6.71
6.68
6.66
6.61
6.61
3.10
1.40
Parameter
Value
Solvent CD3CN
Temperature 298.0
Pulse Sequence zg30
Experiment 1D
Probe Z119248_0002 (DCH 500S2 C/ H-D-05 Z LT)
Number of Scans 24
Receiver Gain 19.1
Relaxation Delay 2.0000
Pulse Width 10.0000
Acquisition Time 3.2768
Acquisition Date 2019-11-21T13:19:22
Modification Date 2019-11-21T14:03:33
Class
Spectrometer Frequency 500.13
Spectral Width 10000.0
Lowest Frequency -2013.2
Nucleus 1H
Acquired Size 32768
Spectral Size 65536
BF_4^-
4.6
1.94
2.00
1.96
1.83
2.34
1.06
1.98
DCM
12.00
water
CD_3CN
17.97
H-grease
f1 (ppm)

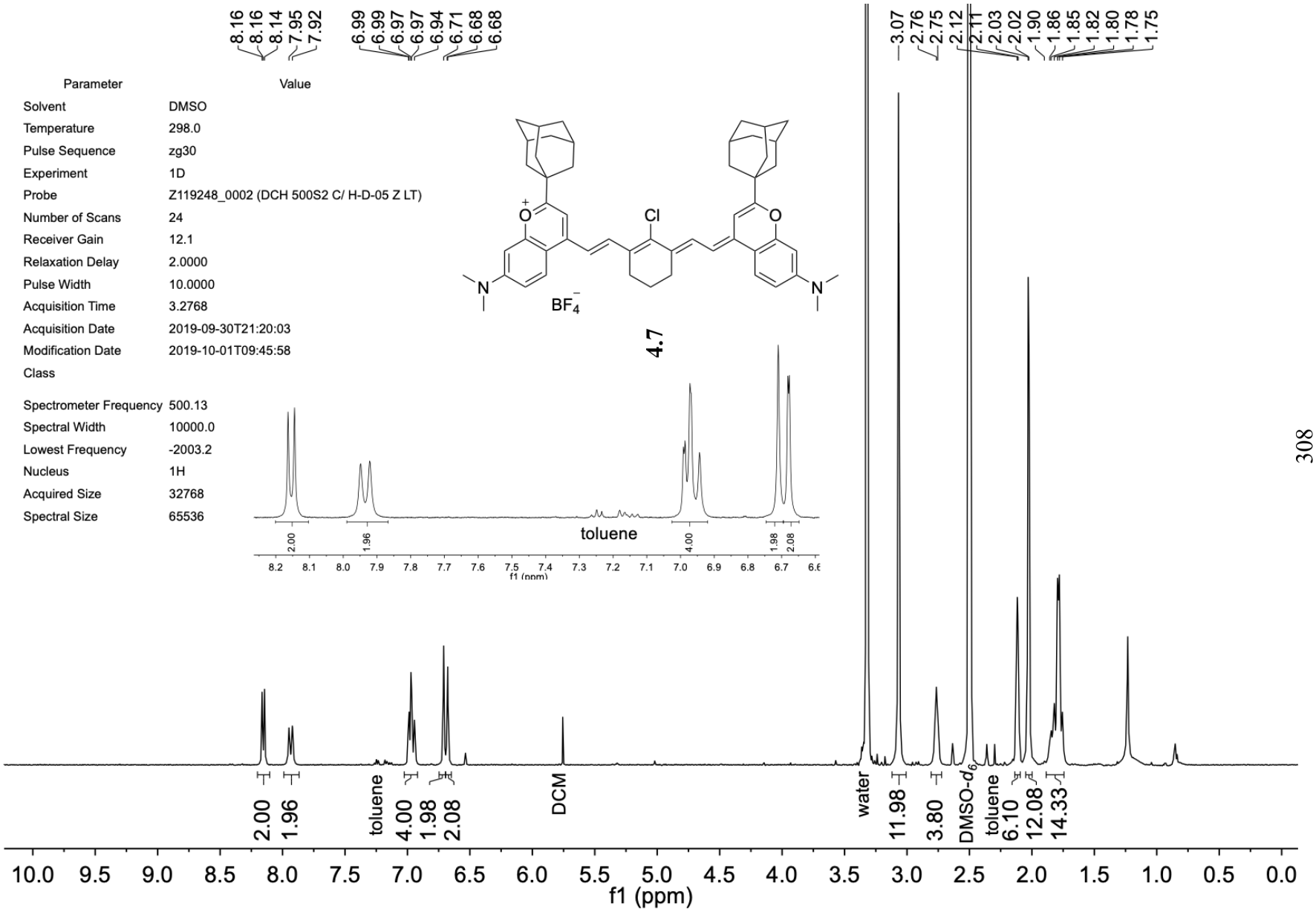
8.16
8.16
8.14
7.95
7.92
6.99
6.99
6.97
6.97
6.94
6.71
6.68
6.68
3.07
2.76
2.75
2.12
2.11
2.03
2.02
1.90
1.86
1.85
1.82
1.80
1.78
1.75
Parameter
Value
Solvent DMSO
Temperature 298.0
Pulse Sequence zg30
Experiment 1D
Probe Z119248_0002 (DCH 500S2 C/ H-D-05 Z LT)
Number of Scans 24
Receiver Gain 12.1
Relaxation Delay 2.0000
Pulse Width 10.0000
Acquisition Time 3.2768
Acquisition Date 2019-09-30T21:20:03
Modification Date 2019-10-01T09:45:58
Class
Spectrometer Frequency 500.13
Spectral Width 10000.0
Lowest Frequency -2003.2
Nucleus 1H
Acquired Size 32768
Spectral Size 65536
Cl
O
N
BF4
4.7
toluene
2.00
1.96
4.00
1.98
2.08
DCM
water
11.98
3.80
DMSO-d6
toluene
6.10
12.08
14.33
f1 (ppm)

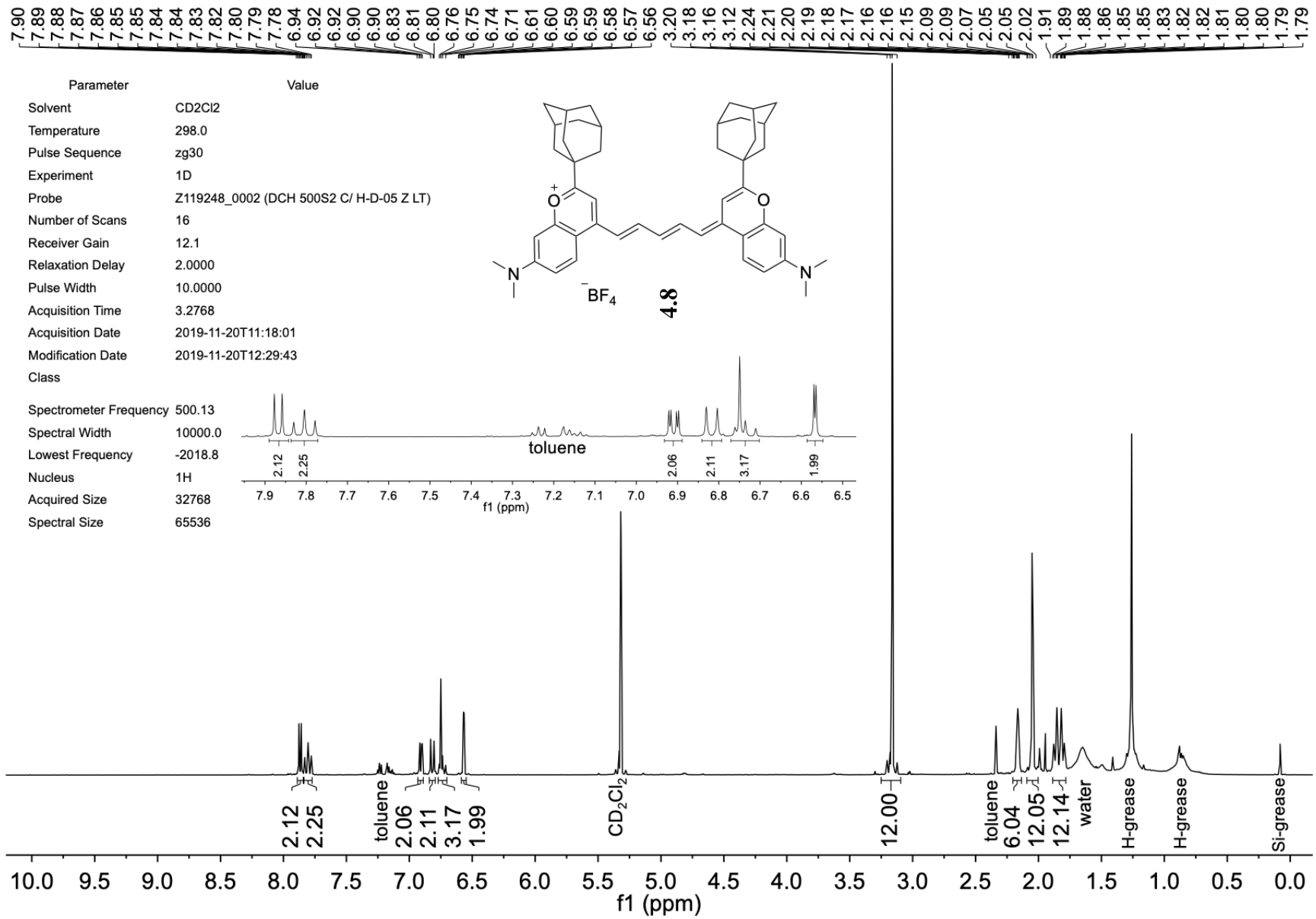
Parameter Value
Solvent CD2Cl2
Temperature 298.0
Pulse Sequence zg30
Experiment 1D
Probe Z119248_0002 (DCH 500S2 C/ H-D-05 Z LT)
Number of Scans 16
Receiver Gain 12.1
Relaxation Delay 2.0000
Pulse Width 10.0000
Acquisition Time 3.2768
Acquisition Date 2019-11-20T11:18:01
Modification Date 2019-11-20T12:29:43
Class
Spectrometer Frequency 500.13
Spectral Width 10000.0
Lowest Frequency -2018.8
Nucleus 1H
Acquired Size 32768
Spectral Size 65536
BF4
4.8
toluene
f1 (ppm)
CD2Cl2
water
H-grease
Si-grease

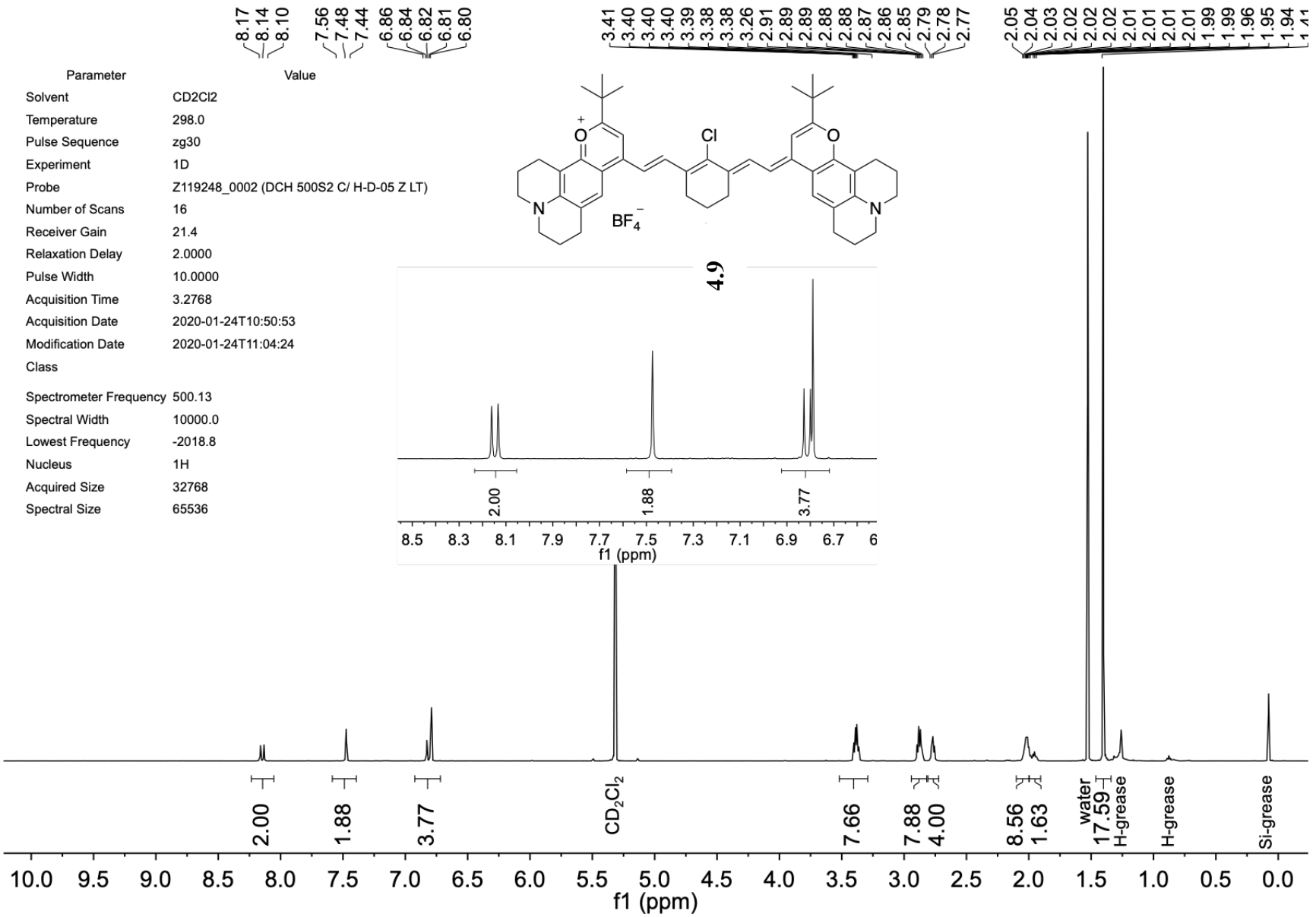
8.17
8.14
8.10
7.56
7.48
7.44
6.86
6.84
6.82
6.81
6.80
3.41
3.40
3.40
3.39
3.38
3.38
3.26
2.91
2.89
2.89
2.88
2.88
2.87
2.86
2.85
2.79
2.78
2.77
2.05
2.04
2.03
2.02
2.02
2.02
2.01
2.01
2.01
2.01
1.99
1.99
1.96
1.95
1.94
Parameter Value
Solvent CD2Cl2
Temperature 298.0
Pulse Sequence zg30
Experiment 1D
Probe Z119248_0002 (DCH 500S2 C/ H-D-05 Z LT)
Number of Scans 16
Receiver Gain 21.4
Relaxation Delay 2.0000
Pulse Width 10.0000
Acquisition Time 3.2768
Acquisition Date 2020-01-24T10:50:53
Modification Date 2020-01-24T11:04:24
Class
Spectrometer Frequency 500.13
Spectral Width 10000.0
Lowest Frequency -2018.8
Nucleus 1H
Acquired Size 32768
Spectral Size 65536
O
Cl
O
N
N
BF4−
4.9
2.00
1.88
3.77
8.5 8.3 8.1 7.9 7.7 7.5 7.3 7.1 6.9 6.7
f1 (ppm)
2.00
1.88
3.77
CD2Cl2
7.66
7.88
4.00
8.56
1.63
water
17.59
H-grease
H-grease
Si-grease
10.0 9.5 9.0 8.5 8.0 7.5 7.0 6.5 6.0 5.5 5.0 4.5 4.0 3.5 3.0 2.5 2.0 1.5 1.0 0.5 0.0
f1 (ppm)

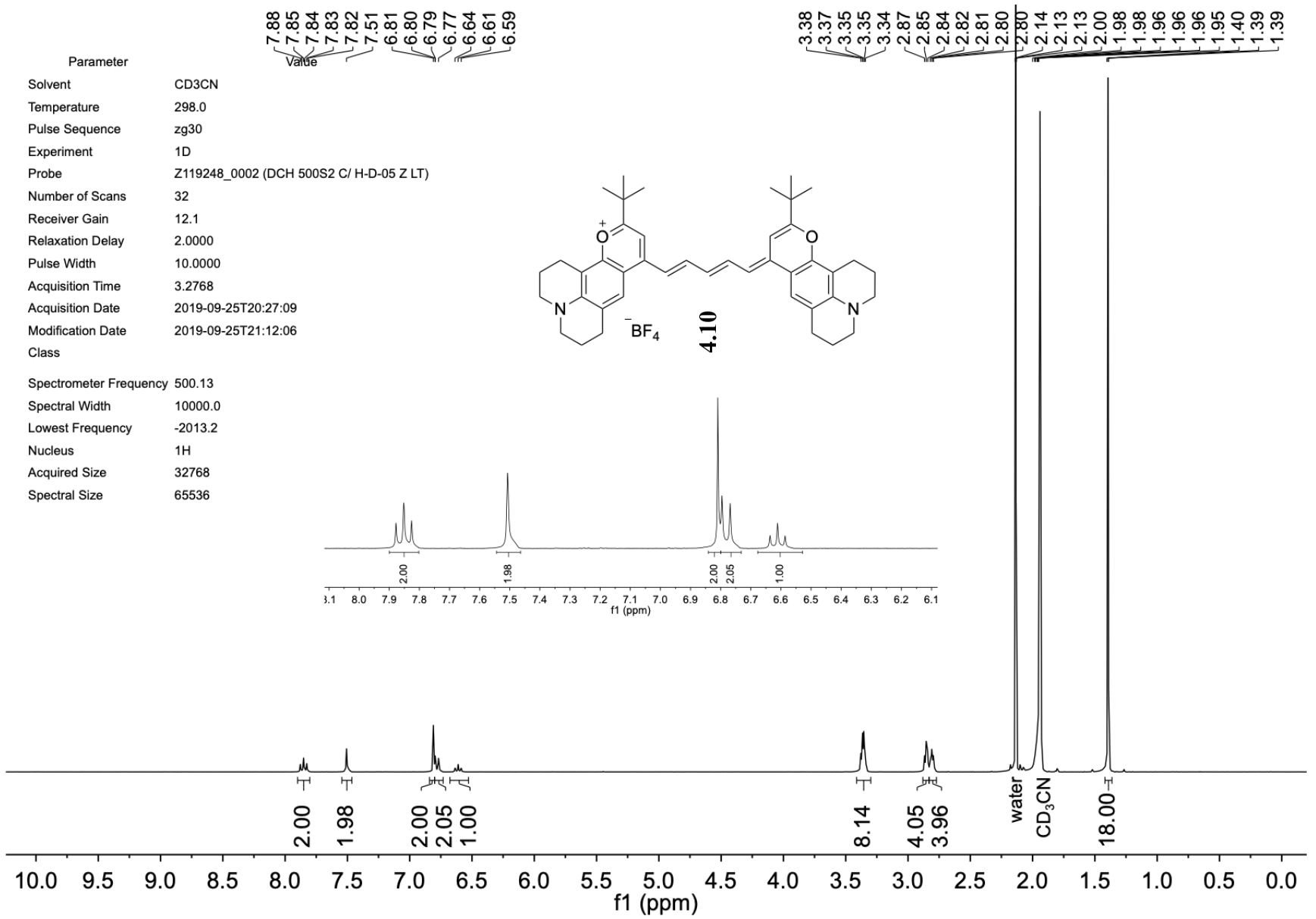
7.88 7.85 7.84 7.83 7.82 7.51 6.81 6.80 6.79 6.77 6.64 6.61 6.59
3.38 3.37 3.35 3.35 3.34 2.87 2.85 2.84 2.82 2.81 2.80 2.80 2.14 2.13 2.13 2.00 1.98 1.98 1.96 1.96 1.96 1.95 1.40 1.39 1.39
Parameter Value
Solvent CD3CN
Temperature 298.0
Pulse Sequence zg30
Experiment 1D
Probe Z119248_0002 (DCH 500S2 C/ H-D-05 Z LT)
Number of Scans 32
Receiver Gain 12.1
Relaxation Delay 2.0000
Pulse Width 10.0000
Acquisition Time 3.2768
Acquisition Date 2019-09-25T20:27:09
Modification Date 2019-09-25T21:12:06
Class
Spectrometer Frequency 500.13
Spectral Width 10000.0
Lowest Frequency -2013.2
Nucleus 1H
Acquired Size 32768
Spectral Size 65536
O
N
N
BF4
4.10
2.00 1.98 2.00 2.05 1.00
f1 (ppm)
2.00 1.98 2.00 2.05 1.00 8.14 4.05 3.96 water CD3CN 18.00
10.0 9.5 9.0 8.5 8.0 7.5 7.0 6.5 6.0 5.5 5.0 4.5 4.0 3.5 3.0 2.5 2.0 1.5 1.0 0.5 0.0
f1 (ppm)

4.8.2 ^{13}C NMR Spectra

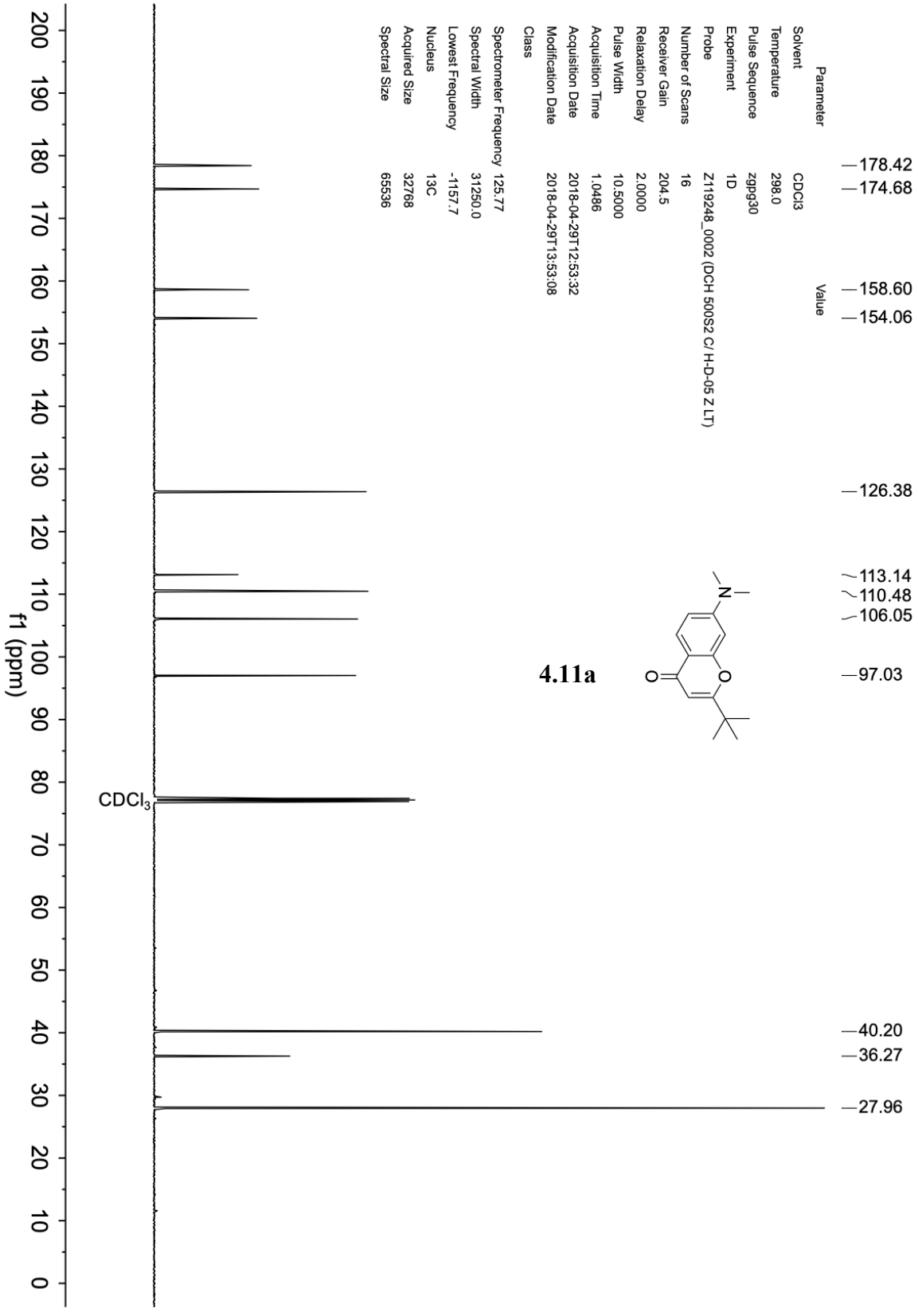

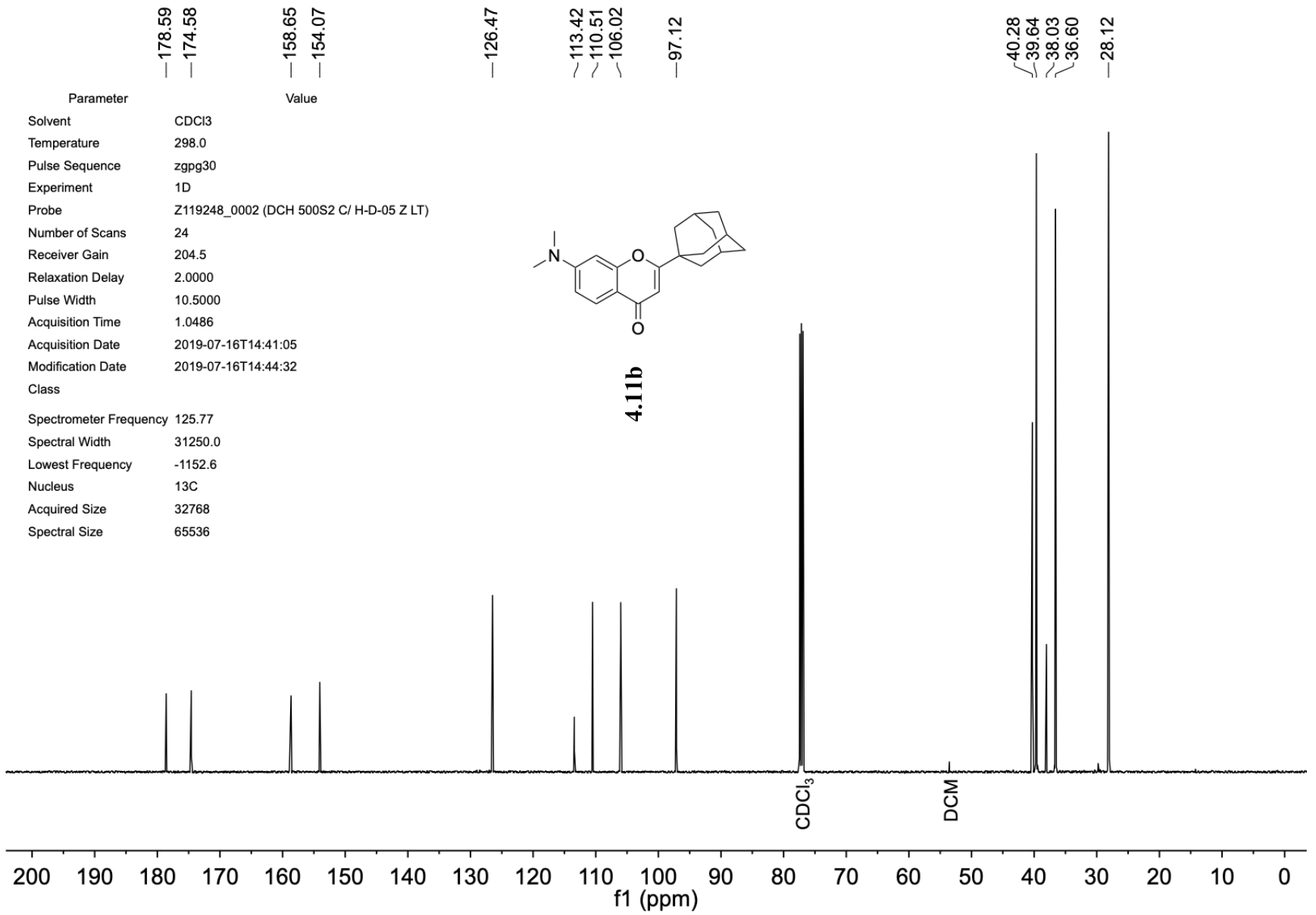
178.59
174.58
158.65
154.07
126.47
113.42
110.51
106.02
97.12
40.28
39.64
38.03
36.60
28.12
Parameter
Value
Solvent CDCl3
Temperature 298.0
Pulse Sequence zgpg30
Experiment 1D
Probe Z119248_0002 (DCH 500S2 C/ H-D-05 Z LT)
Number of Scans 24
Receiver Gain 204.5
Relaxation Delay 2.0000
Pulse Width 10.5000
Acquisition Time 1.0486
Acquisition Date 2019-07-16T14:41:05
Modification Date 2019-07-16T14:44:32
Class
Spectrometer Frequency 125.77
Spectral Width 31250.0
Lowest Frequency -1152.6
Nucleus 13C
Acquired Size 32768
Spectral Size 65536
N
O
O
4.11b
CDCl3
DCM
200 190 180 170 160 150 140 130 120 110 100 90 80 70 60 50 40 30 20 10 0
f1 (ppm)

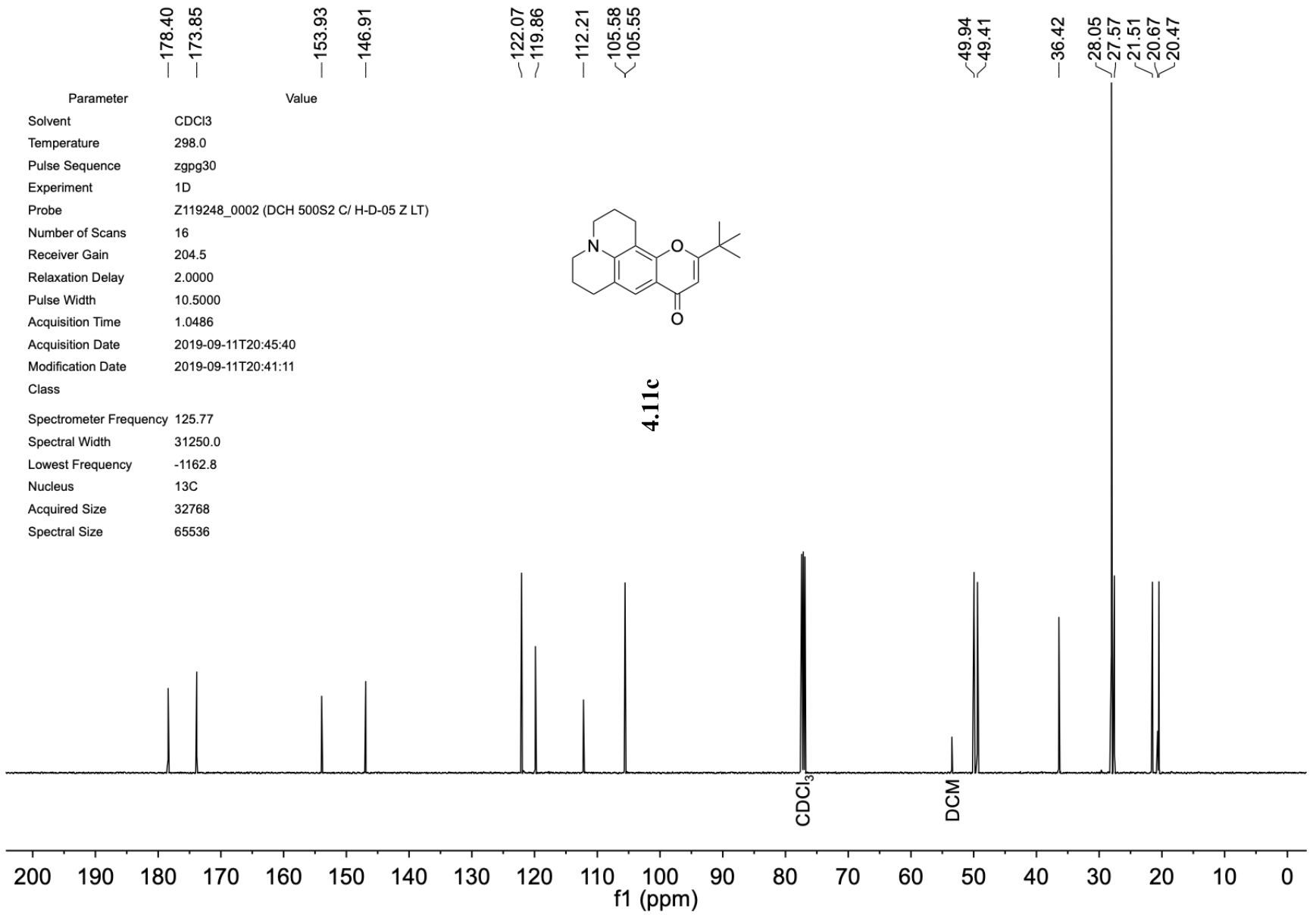
178.40
173.85
153.93
146.91
122.07
119.86
112.21
105.58
105.55
49.94
49.41
36.42
28.05
27.57
21.51
20.67
20.47
Parameter Value
Solvent CDCl3
Temperature 298.0
Pulse Sequence zgpg30
Experiment 1D
Probe Z119248_0002 (DCH 500S2 C/ H-D-05 Z LT)
Number of Scans 16
Receiver Gain 204.5
Relaxation Delay 2.0000
Pulse Width 10.5000
Acquisition Time 1.0486
Acquisition Date 2019-09-11T20:45:40
Modification Date 2019-09-11T20:41:11
Class
Spectrometer Frequency 125.77
Spectral Width 31250.0
Lowest Frequency -1162.8
Nucleus 13C
Acquired Size 32768
Spectral Size 65536
N
O
O
4.11c
CDCl3
DCM
200 190 180 170 160 150 140 130 120 110 100 90 80 70 60 50 40 30 20 10 0
f1 (ppm)

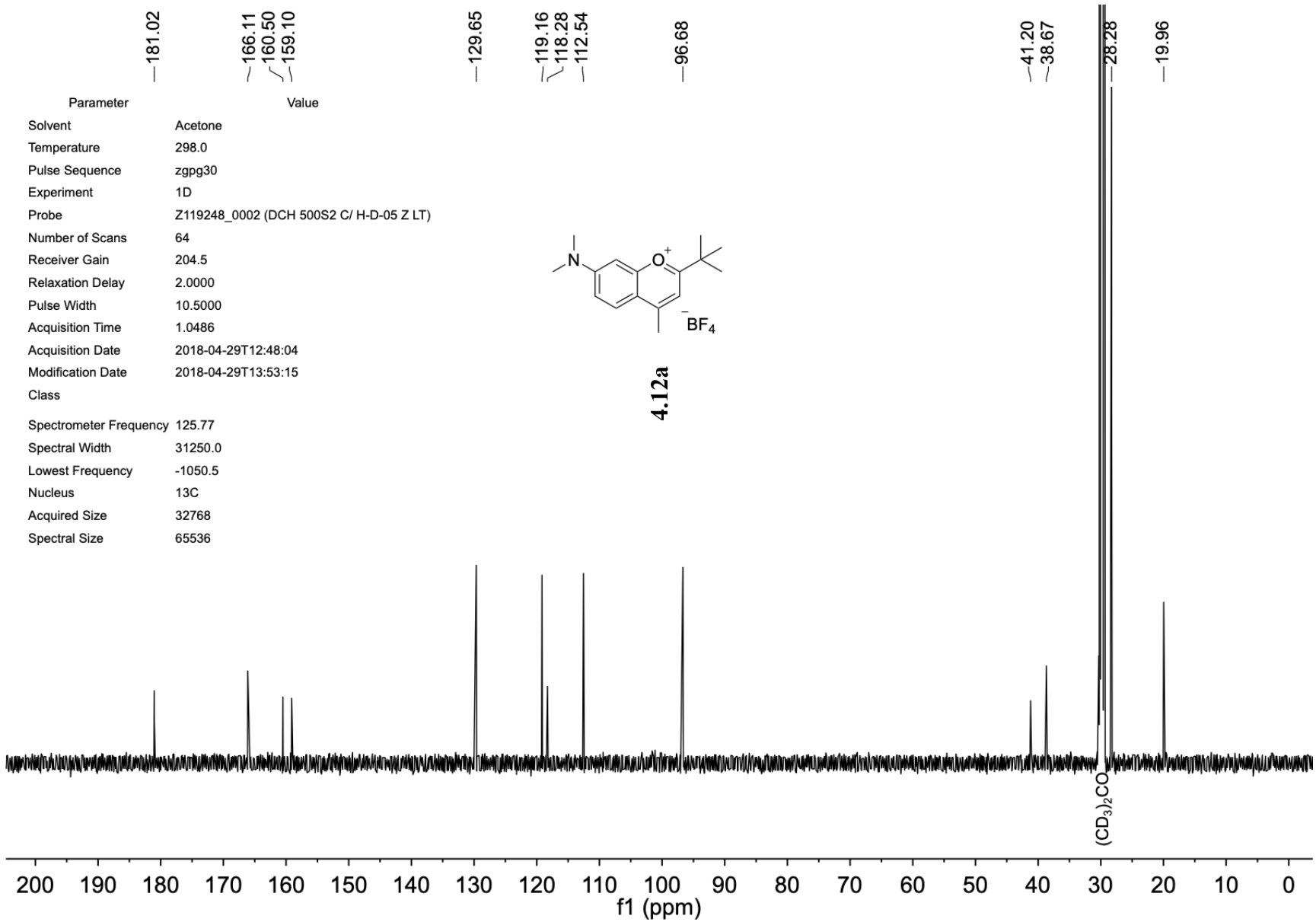
181.02
166.11
160.50
159.10
129.65
119.16
118.28
112.54
96.68
41.20
38.67
28.28
19.96
Parameter Value
Solvent Acetone
Temperature 298.0
Pulse Sequence zgpg30
Experiment 1D
Probe Z119248_0002 (DCH 500S2 C/ H-D-05 Z LT)
Number of Scans 64
Receiver Gain 204.5
Relaxation Delay 2.0000
Pulse Width 10.5000
Acquisition Time 1.0486
Acquisition Date 2018-04-29T12:48:04
Modification Date 2018-04-29T13:53:15
Class
Spectrometer Frequency 125.77
Spectral Width 31250.0
Lowest Frequency -1050.5
Nucleus 13C
Acquired Size 32768
Spectral Size 65536
N
O+
BF4
4.12a
(CD3)2CO
200 190 180 170 160 150 140 130 120 110 100 90 80 70 60 50 40 30 20 10 0
f1 (ppm)

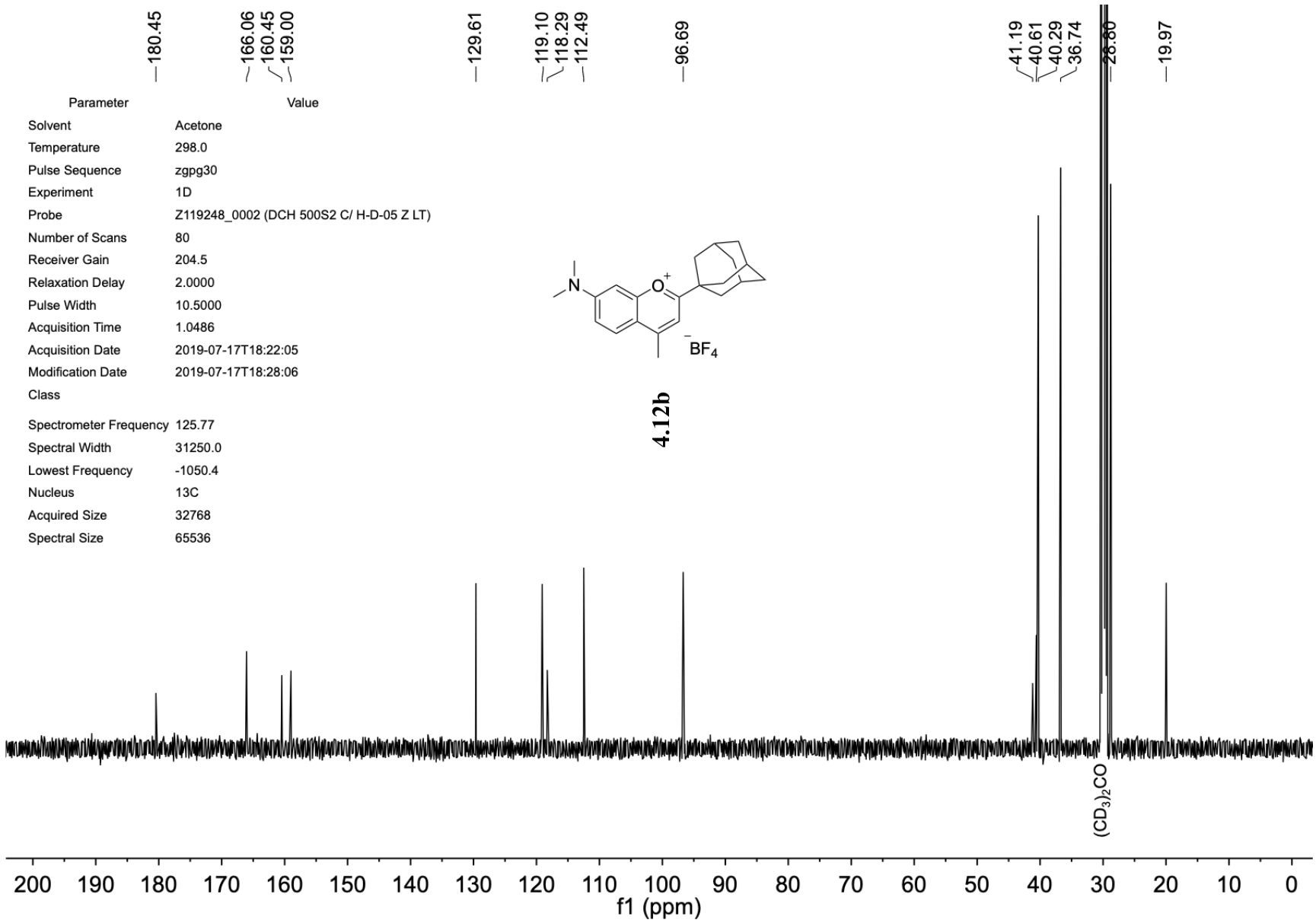
180.45
166.06
160.45
159.00
129.61
119.10
118.29
112.49
96.69
41.19
40.61
40.29
36.74
28.80
19.97
Parameter Value
Solvent Acetone
Temperature 298.0
Pulse Sequence zgpg30
Experiment 1D
Probe Z119248_0002 (DCH 500S2 C/ H-D-05 Z LT)
Number of Scans 80
Receiver Gain 204.5
Relaxation Delay 2.0000
Pulse Width 10.5000
Acquisition Time 1.0486
Acquisition Date 2019-07-17T18:22:05
Modification Date 2019-07-17T18:28:06
Class
Spectrometer Frequency 125.77
Spectral Width 31250.0
Lowest Frequency -1050.4
Nucleus 13C
Acquired Size 32768
Spectral Size 65536
N
O+
BF4
4.12b
(CD3)2CO
200 190 180 170 160 150 140 130 120 110 100 90 80 70 60 50 40 30 20 10 0
f1 (ppm)

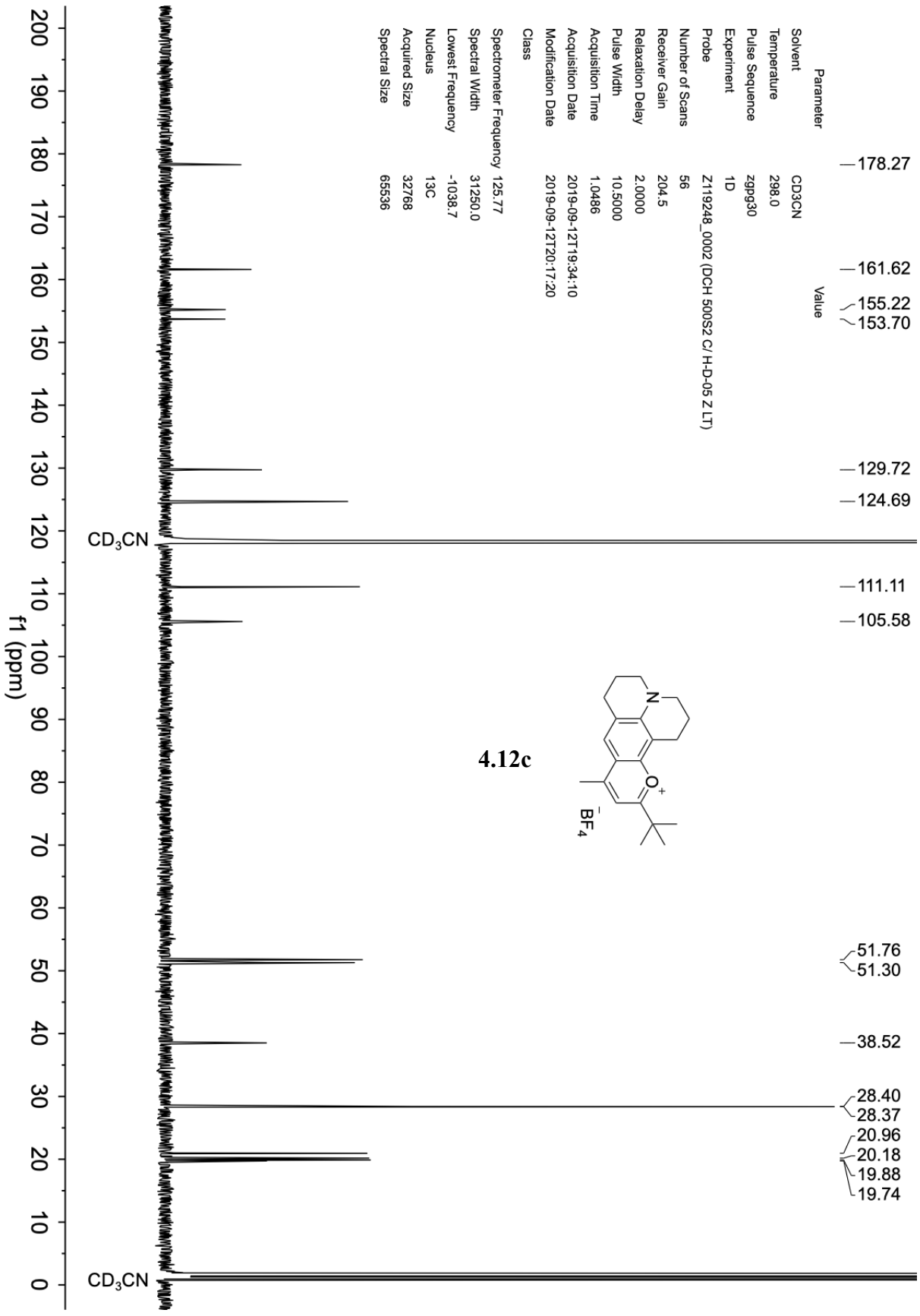
Parameter
Value
Solvent
CD3CN
Temperature
298.0
Pulse Sequence
zgpg30
Experiment
1D
Probe
Z119248_0002 (DCH 500S2 C/ H-D-05 Z LT)
Number of Scans
56
Receiver Gain
204.5
Relaxation Delay
2.0000
Pulse Width
10.5000
Acquisition Time
1.0486
Acquisition Date
2019-09-12T19:34:10
Modification Date
2019-09-12T20:17:20
Class
Spectrometer Frequency
125.77
Spectral Width
31250.0
Lowest Frequency
-1038.7
Nucleus
13C
Acquired Size
32768
Spectral Size
65536
178.27
161.62
155.22
153.70
129.72
124.69
111.11
105.58
51.76
51.30
38.52
28.40
28.37
20.96
20.18
19.88
19.74
CD3CN
CD3CN
4.12c
f1 (ppm)

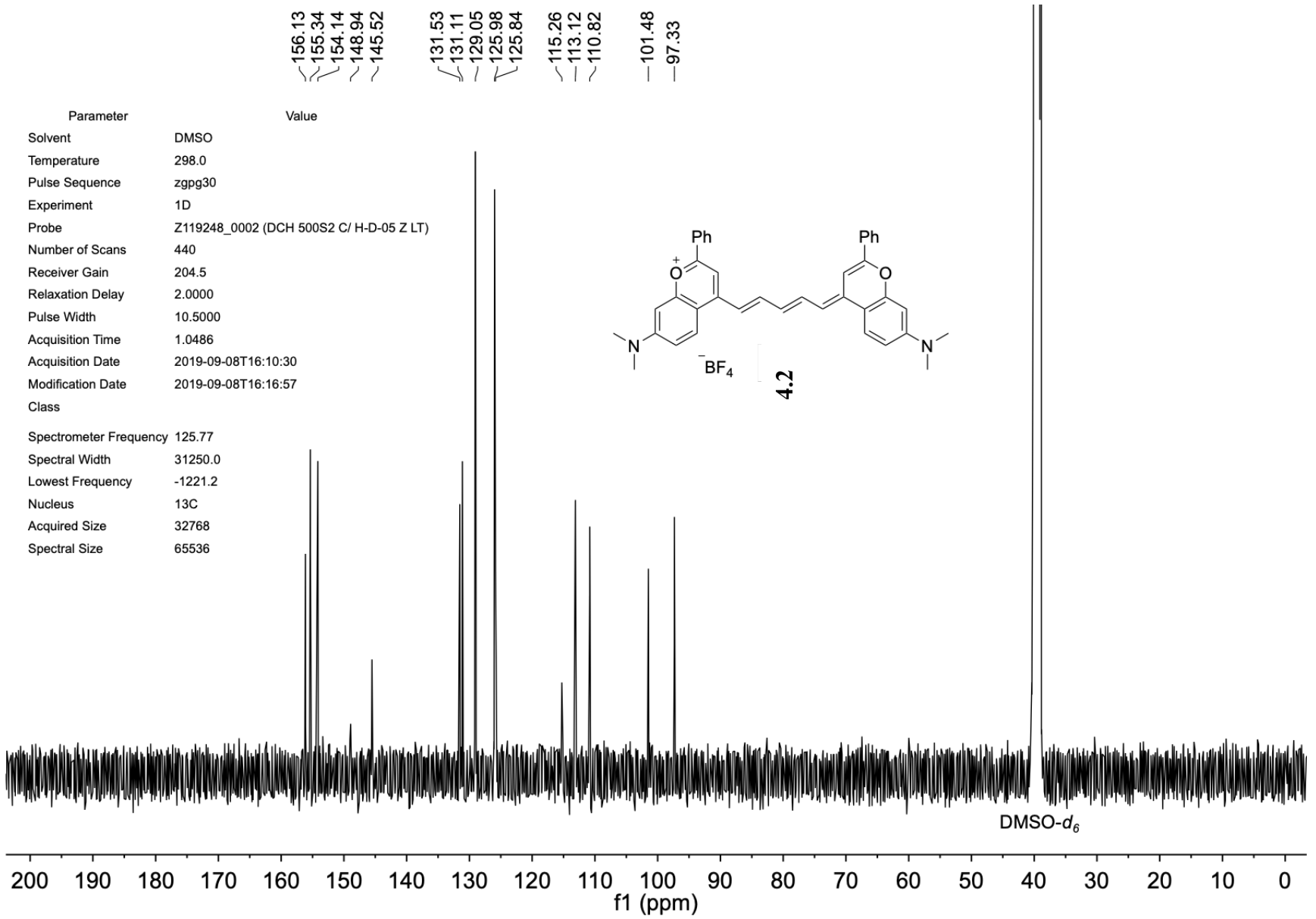
156.13
155.34
154.14
148.94
145.52
131.53
131.11
129.05
125.98
125.84
115.26
113.12
110.82
101.48
97.33
Parameter Value
Solvent DMSO
Temperature 298.0
Pulse Sequence zgpg30
Experiment 1D
Probe Z119248_0002 (DCH 500S2 C/ H-D-05 Z LT)
Number of Scans 440
Receiver Gain 204.5
Relaxation Delay 2.0000
Pulse Width 10.5000
Acquisition Time 1.0486
Acquisition Date 2019-09-08T16:10:30
Modification Date 2019-09-08T16:16:57
Class
Spectrometer Frequency 125.77
Spectral Width 31250.0
Lowest Frequency -1221.2
Nucleus 13C
Acquired Size 32768
Spectral Size 65536
Ph
Ph
O
O
N
N
BF4
4.2
DMSO-d6
200 190 180 170 160 150 140 130 120 110 100 90 80 70 60 50 40 30 20 10 0
f1 (ppm)

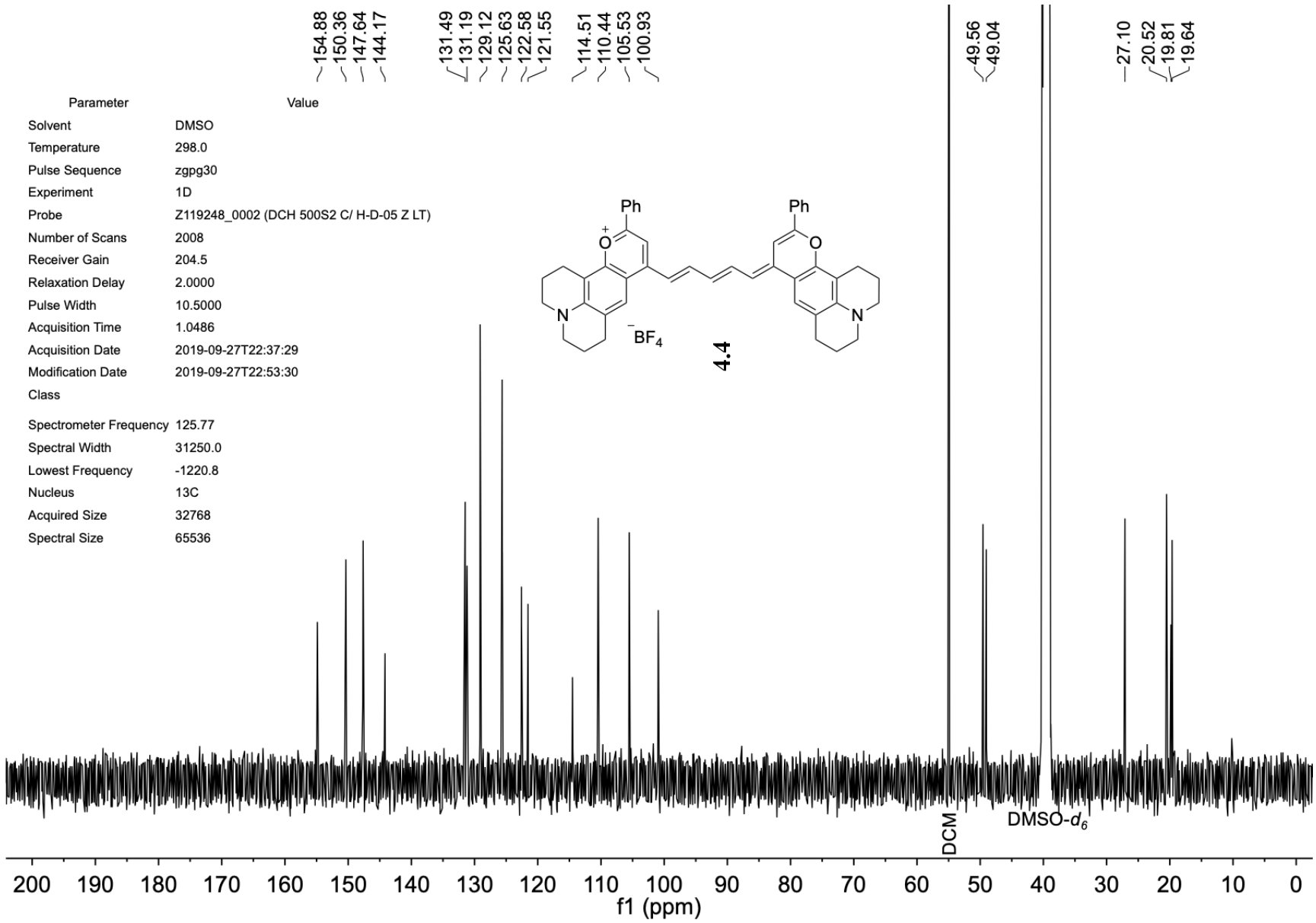
154.88
150.36
147.64
144.17
131.49
131.19
129.12
125.63
122.58
121.55
114.51
110.44
105.53
100.93
49.56
49.04
27.10
20.52
19.81
19.64
Parameter Value
Solvent DMSO
Temperature 298.0
Pulse Sequence zgpg30
Experiment 1D
Probe Z119248_0002 (DCH 500S2 C/ H-D-05 Z LT)
Number of Scans 2008
Receiver Gain 204.5
Relaxation Delay 2.0000
Pulse Width 10.5000
Acquisition Time 1.0486
Acquisition Date 2019-09-27T22:37:29
Modification Date 2019-09-27T22:53:30
Class
Spectrometer Frequency 125.77
Spectral Width 31250.0
Lowest Frequency -1220.8
Nucleus 13C
Acquired Size 32768
Spectral Size 65536
Ph
Ph
O
O
N
N
BF4
4.4
DCM
DMSO-d6
200 190 180 170 160 150 140 130 120 110 100 90 80 70 60 50 40 30 20 10 0
f1 (ppm)

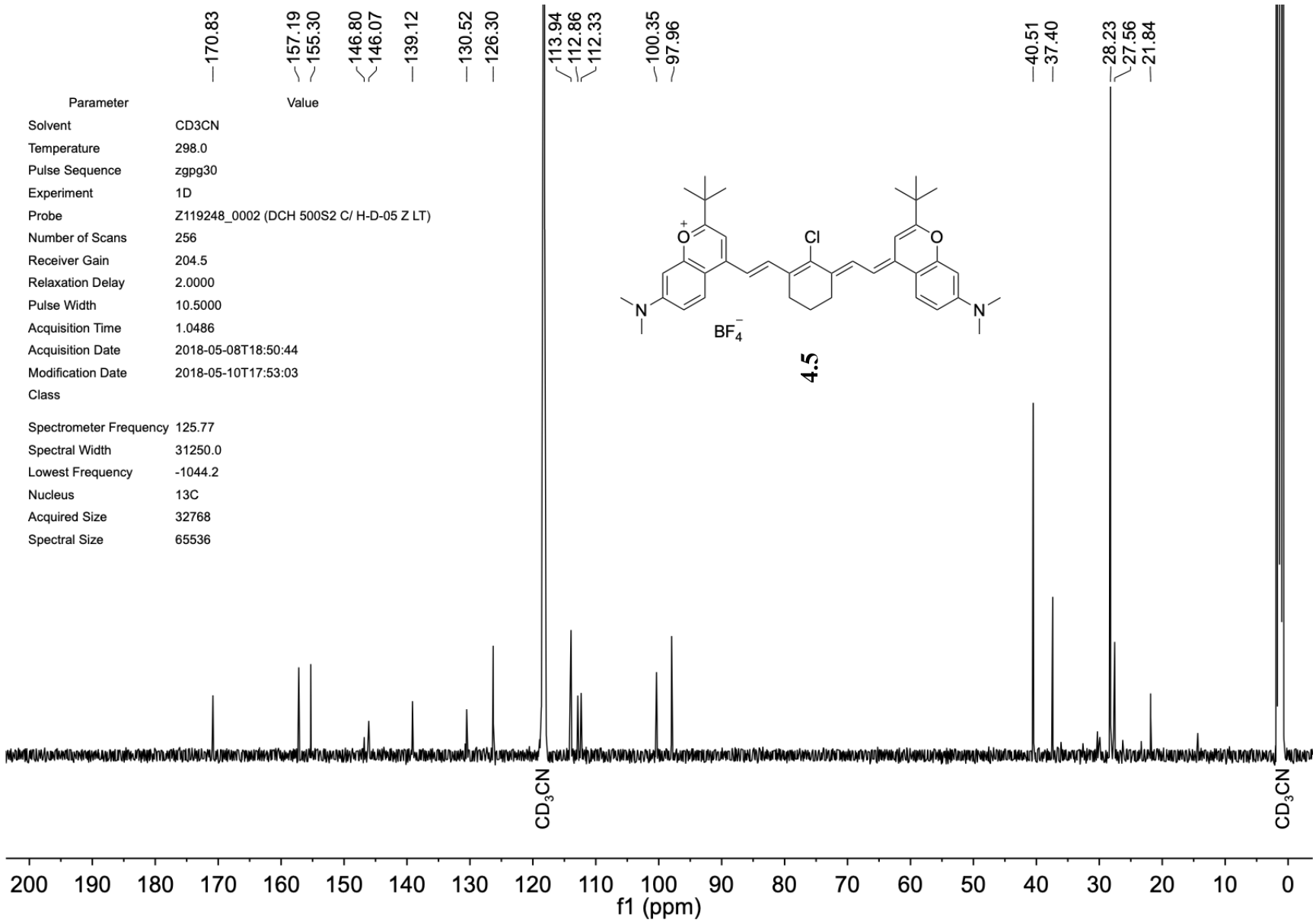
170.83
157.19
155.30
146.80
146.07
139.12
130.52
126.30
113.94
112.86
112.33
100.35
97.96
40.51
37.40
28.23
27.56
21.84
Parameter Value
Solvent CD3CN
Temperature 298.0
Pulse Sequence zgpg30
Experiment 1D
Probe Z119248_0002 (DCH 500S2 C/ H-D-05 Z LT)
Number of Scans 256
Receiver Gain 204.5
Relaxation Delay 2.0000
Pulse Width 10.5000
Acquisition Time 1.0486
Acquisition Date 2018-05-08T18:50:44
Modification Date 2018-05-10T17:53:03
Class
Spectrometer Frequency 125.77
Spectral Width 31250.0
Lowest Frequency -1044.2
Nucleus 13C
Acquired Size 32768
Spectral Size 65536
Cl
BF4−
4.5
CD3CN
CD3CN
200 190 180 170 160 150 140 130 120 110 100 90 80 70 60 50 40 30 20 10 0
f1 (ppm)

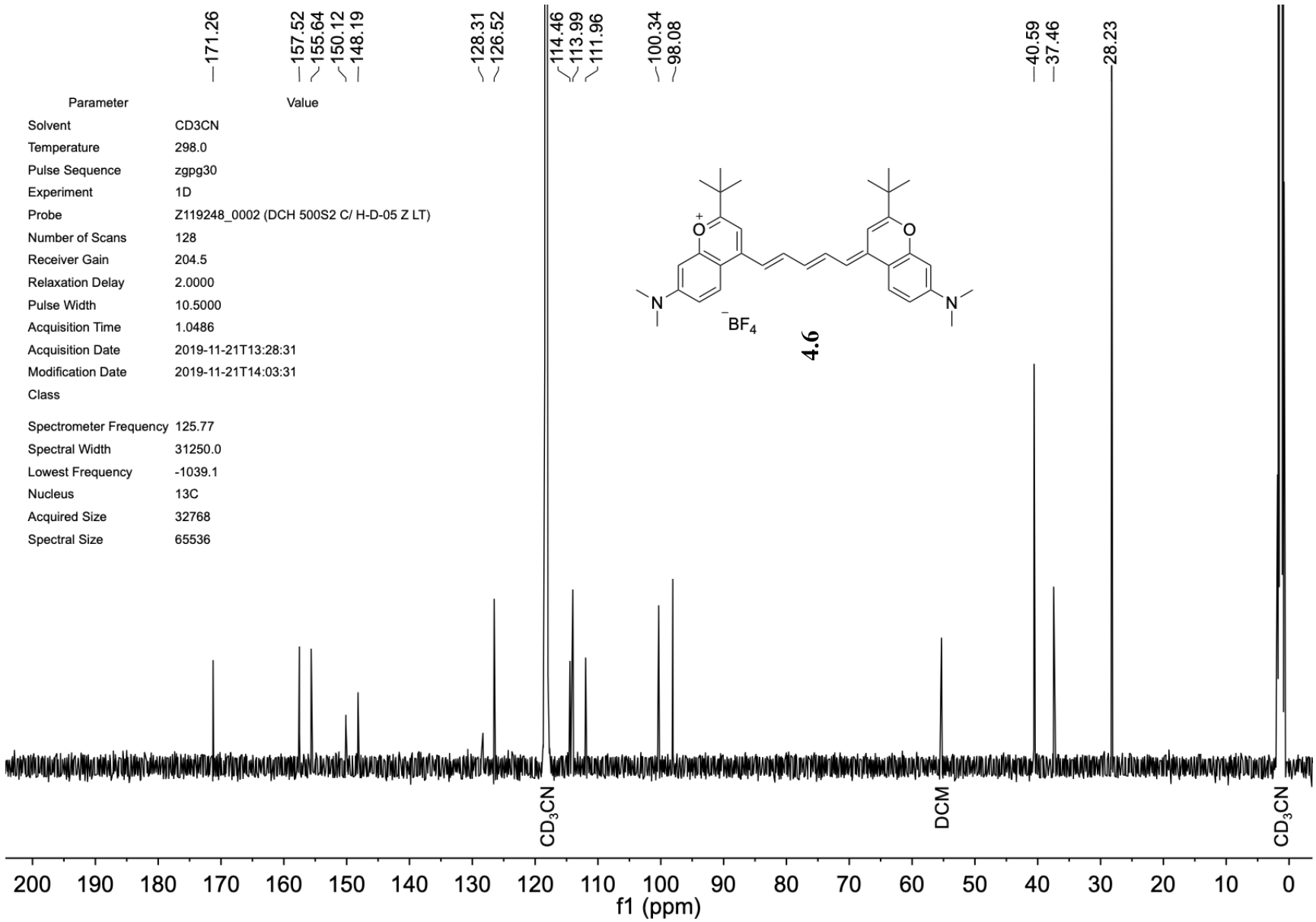
171.26
157.52
155.64
150.12
148.19
128.31
126.52
114.46
113.99
111.96
100.34
98.08
40.59
37.46
28.23
Parameter Value
Solvent CD3CN
Temperature 298.0
Pulse Sequence zgpg30
Experiment 1D
Probe Z119248_0002 (DCH 500S2 C/ H-D-05 Z LT)
Number of Scans 128
Receiver Gain 204.5
Relaxation Delay 2.0000
Pulse Width 10.5000
Acquisition Time 1.0486
Acquisition Date 2019-11-21T13:28:31
Modification Date 2019-11-21T14:03:31
Class
Spectrometer Frequency 125.77
Spectral Width 31250.0
Lowest Frequency -1039.1
Nucleus 13C
Acquired Size 32768
Spectral Size 65536
$^-BF_4$
4.6
CD_3CN
DCM
CD_3CN
200 190 180 170 160 150 140 130 120 110 100 90 80 70 60 50 40 30 20 10 0
f1 (ppm)

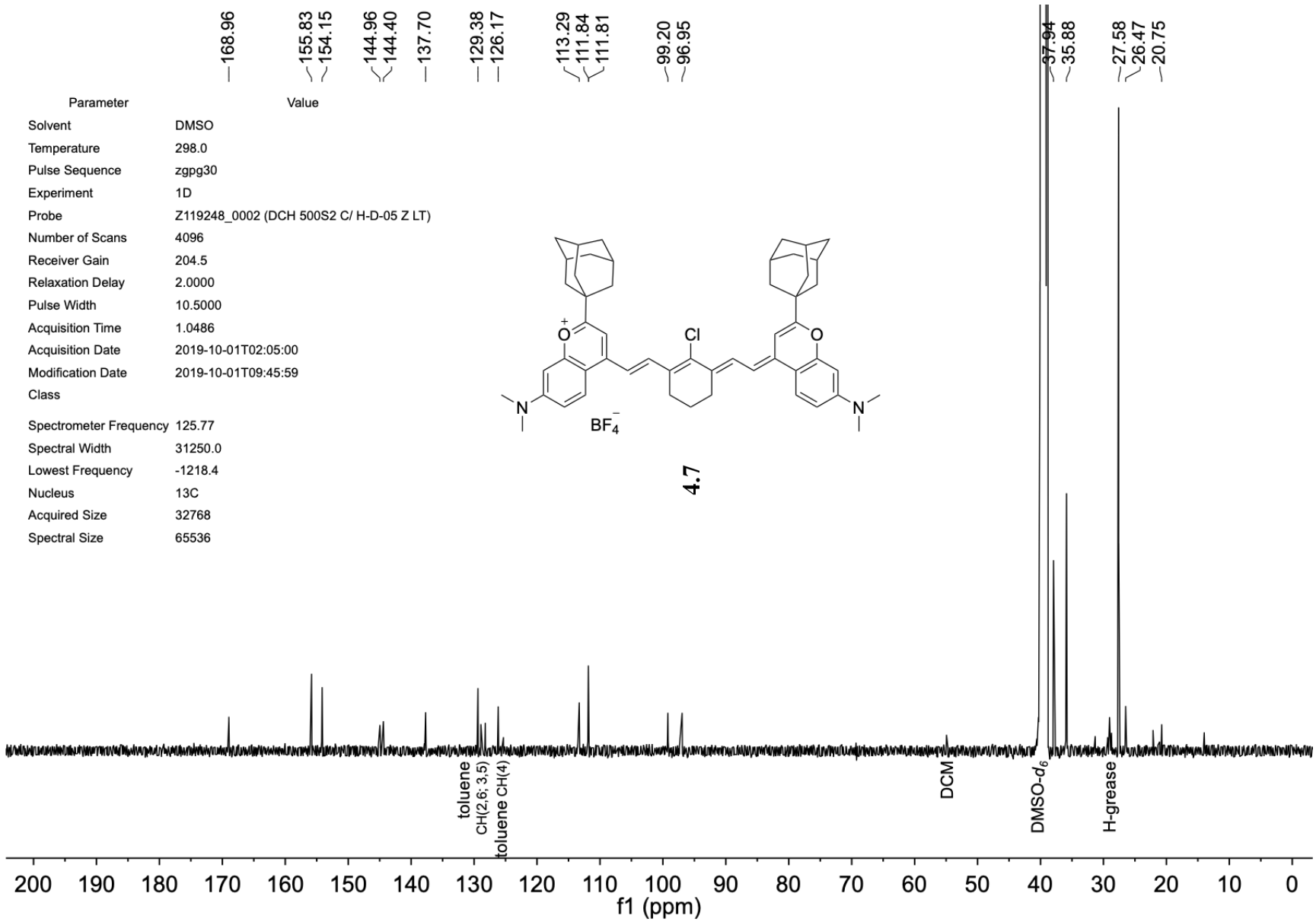
168.96
155.83
154.15
144.96
144.40
137.70
129.38
126.17
113.29
111.84
111.81
99.20
96.95
37.94
35.88
27.58
26.47
20.75
Parameter Value
Solvent DMSO
Temperature 298.0
Pulse Sequence zgpg30
Experiment 1D
Probe Z119248_0002 (DCH 500S2 C/ H-D-05 Z LT)
Number of Scans 4096
Receiver Gain 204.5
Relaxation Delay 2.0000
Pulse Width 10.5000
Acquisition Time 1.0486
Acquisition Date 2019-10-01T02:05:00
Modification Date 2019-10-01T09:45:59
Class
Spectrometer Frequency 125.77
Spectral Width 31250.0
Lowest Frequency -1218.4
Nucleus 13C
Acquired Size 32768
Spectral Size 65536
Cl
O
N
BF4
4.7
toluene
CH(2,6; 3,5)
toluene CH(4)
DCM
DMSO-d6
H-grease
200 190 180 170 160 150 140 130 120 110 100 90 80 70 60 50 40 30 20 10 0
f1 (ppm)

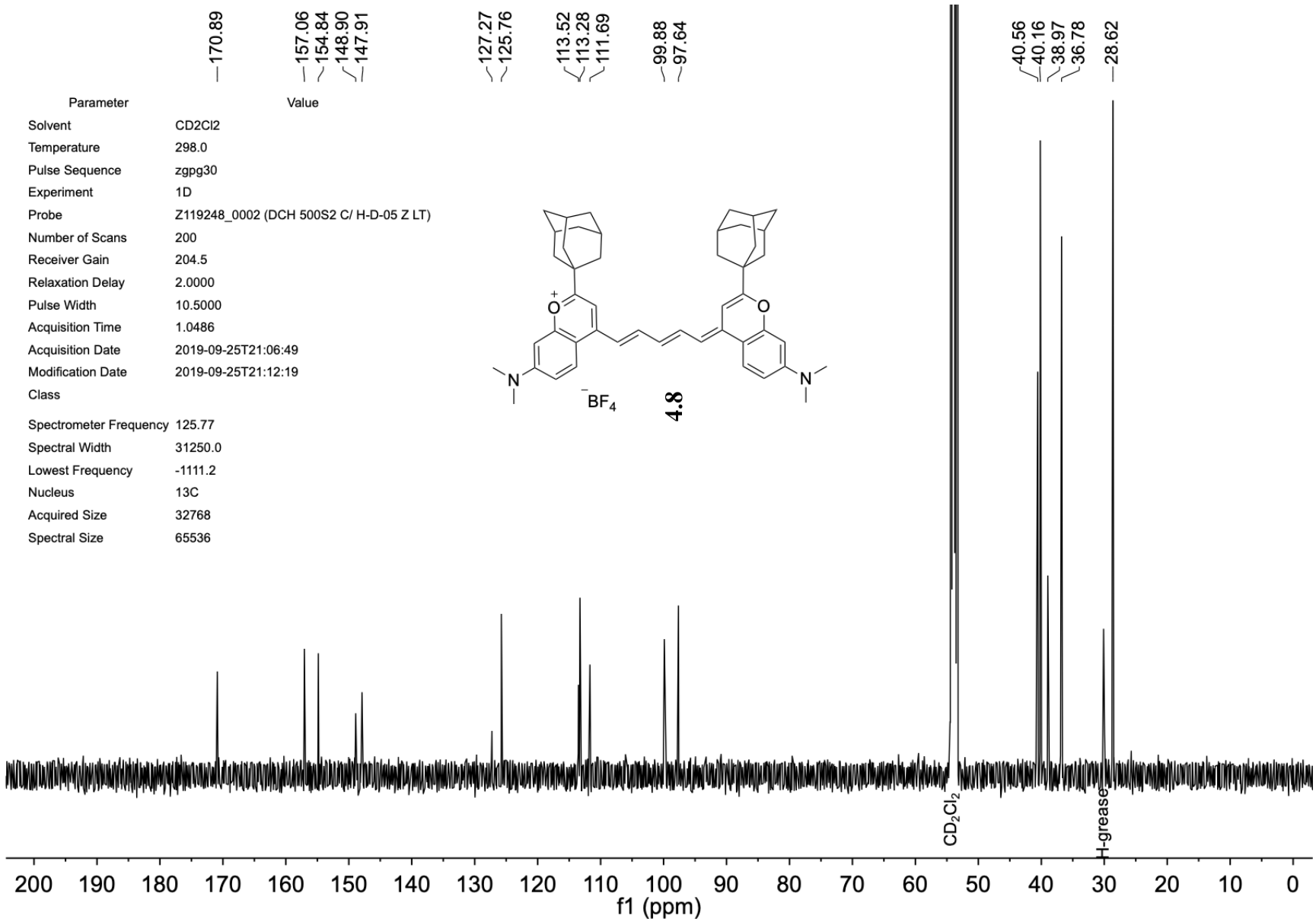
170.89
157.06
154.84
148.90
147.91
127.27
125.76
113.52
113.28
111.69
99.88
97.64
40.56
40.16
38.97
36.78
28.62
Parameter Value
Solvent CD2Cl2
Temperature 298.0
Pulse Sequence zgpg30
Experiment 1D
Probe Z119248_0002 (DCH 500S2 C/ H-D-05 Z LT)
Number of Scans 200
Receiver Gain 204.5
Relaxation Delay 2.0000
Pulse Width 10.5000
Acquisition Time 1.0486
Acquisition Date 2019-09-25T21:06:49
Modification Date 2019-09-25T21:12:19
Class
Spectrometer Frequency 125.77
Spectral Width 31250.0
Lowest Frequency -1111.2
Nucleus 13C
Acquired Size 32768
Spectral Size 65536
$^{-}BF_4$
4.8
CD_2Cl_2
H-grease
200 190 180 170 160 150 140 130 120 110 100 90 80 70 60 50 40 30 20 10 0
f1 (ppm)

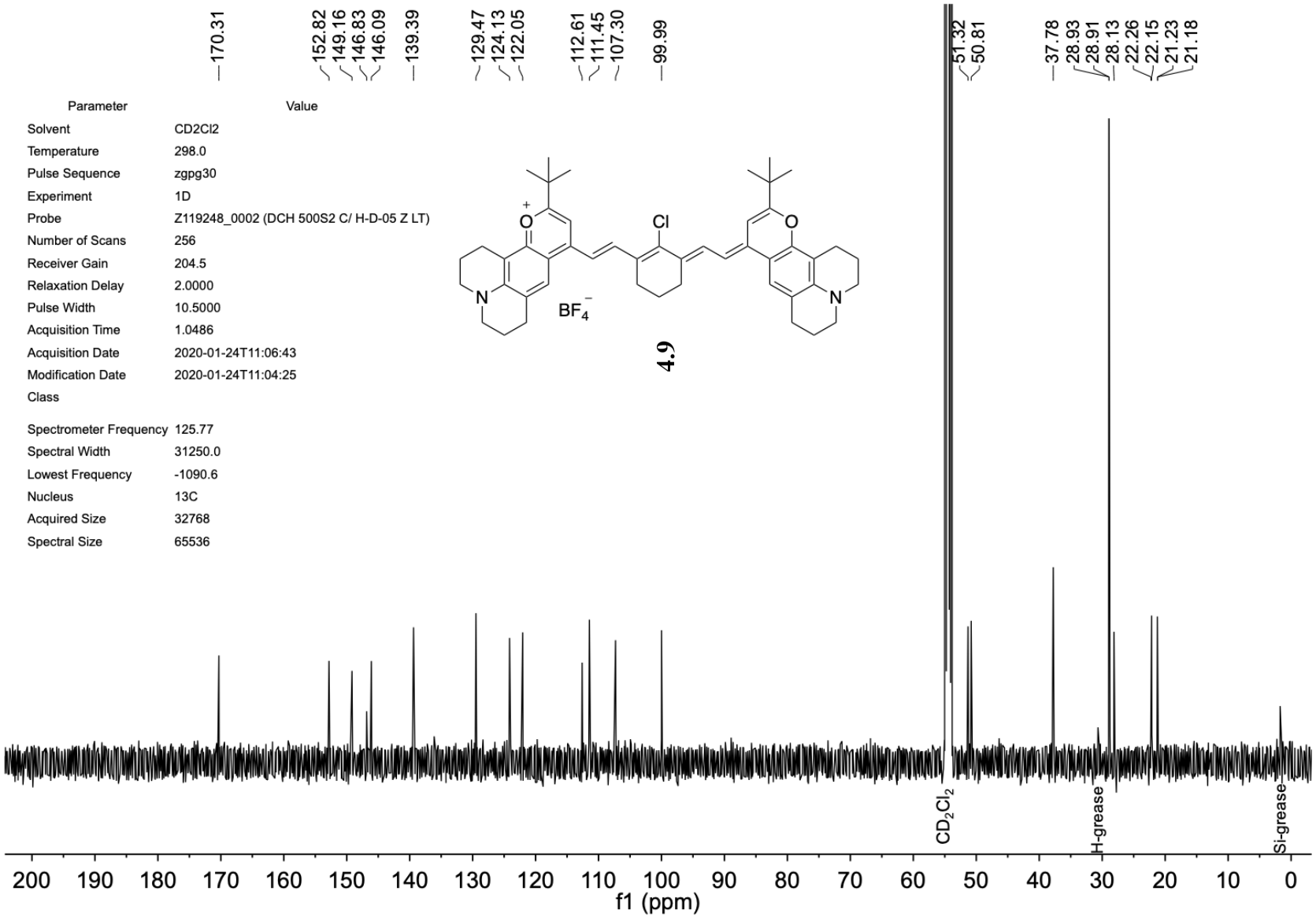
170.31
152.82
149.16
146.83
146.09
139.39
129.47
124.13
122.05
112.61
111.45
107.30
99.99
51.32
50.81
37.78
28.93
28.91
28.13
22.26
22.15
21.23
21.18
Parameter
Value
Solvent CD2Cl2
Temperature 298.0
Pulse Sequence zgpg30
Experiment 1D
Probe Z119248_0002 (DCH 500S2 C/ H-D-05 Z LT)
Number of Scans 256
Receiver Gain 204.5
Relaxation Delay 2.0000
Pulse Width 10.5000
Acquisition Time 1.0486
Acquisition Date 2020-01-24T11:06:43
Modification Date 2020-01-24T11:04:25
Class
Spectrometer Frequency 125.77
Spectral Width 31250.0
Lowest Frequency -1090.6
Nucleus 13C
Acquired Size 32768
Spectral Size 65536
Cl
O
N
BF4−
4.9
CD2Cl2
H-grease
Si-grease
200 190 180 170 160 150 140 130 120 110 100 90 80 70 60 50 40 30 20 10 0
f1 (ppm)

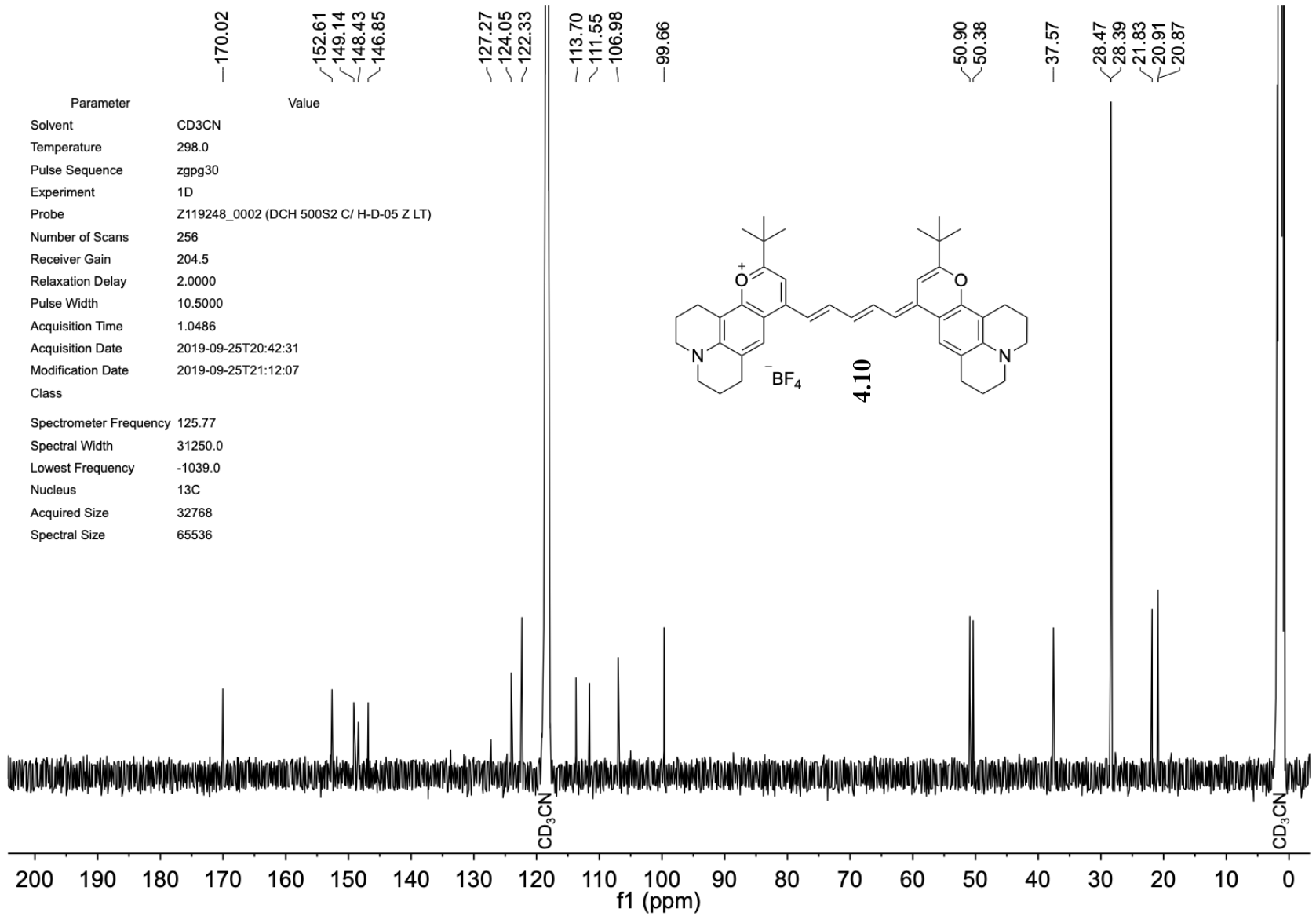
170.02
152.61
149.14
148.43
146.85
127.27
124.05
122.33
113.70
111.55
106.98
99.66
50.90
50.38
37.57
28.47
28.39
21.83
20.91
20.87
Parameter Value
Solvent CD3CN
Temperature 298.0
Pulse Sequence zgpg30
Experiment 1D
Probe Z119248_0002 (DCH 500S2 C/ H-D-05 Z LT)
Number of Scans 256
Receiver Gain 204.5
Relaxation Delay 2.0000
Pulse Width 10.5000
Acquisition Time 1.0486
Acquisition Date 2019-09-25T20:42:31
Modification Date 2019-09-25T21:12:07
Class
Spectrometer Frequency 125.77
Spectral Width 31250.0
Lowest Frequency -1039.0
Nucleus 13C
Acquired Size 32768
Spectral Size 65536
BF4
4.10
CD3CN
CD3CN
200 190 180 170 160 150 140 130 120 110 100 90 80 70 60 50 40 30 20 10 0
f1 (ppm)

4.8.3 FT-IR Spectra

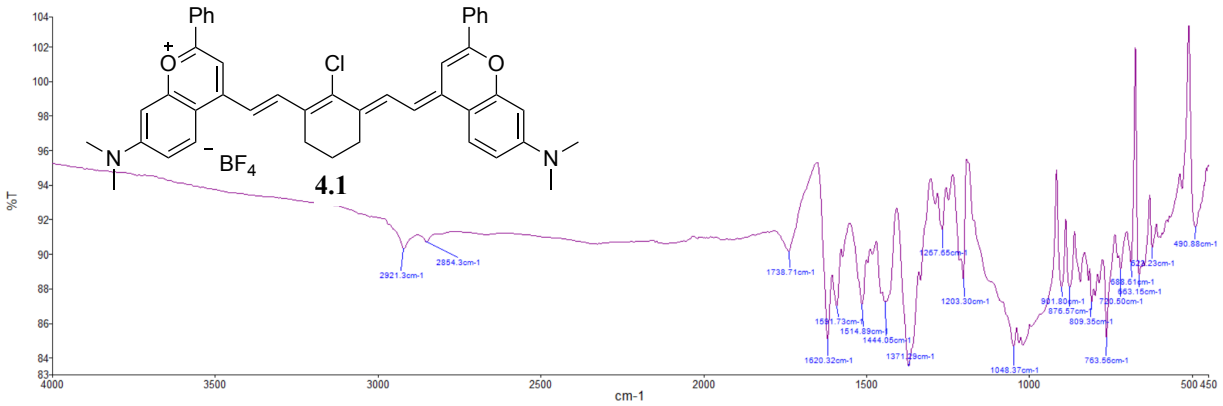

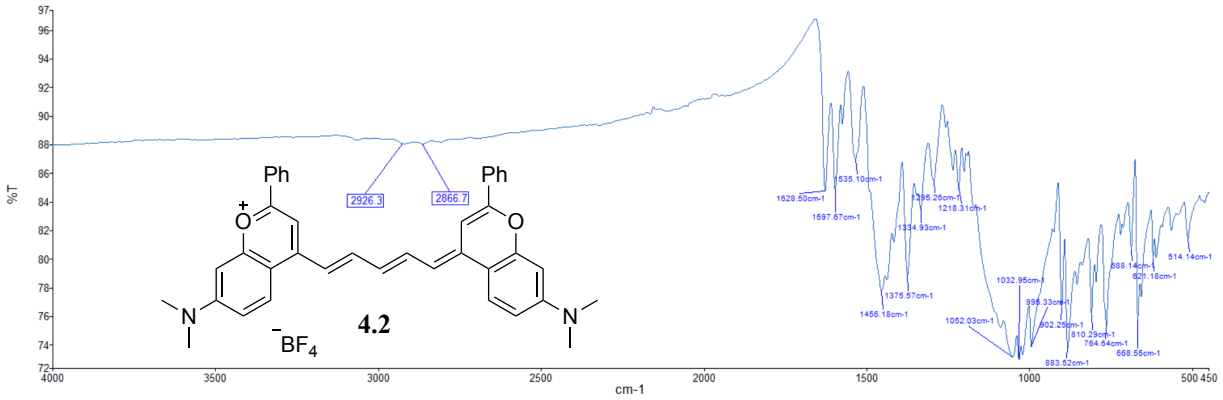

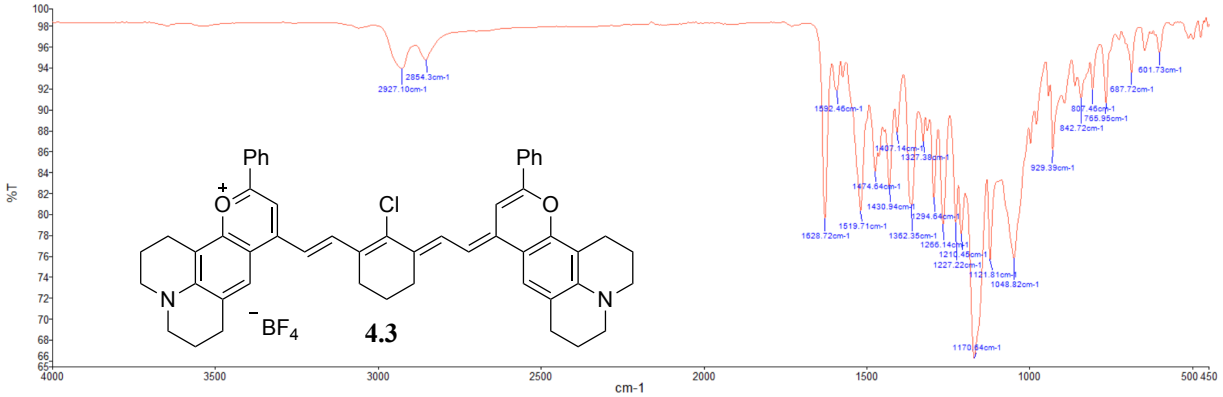

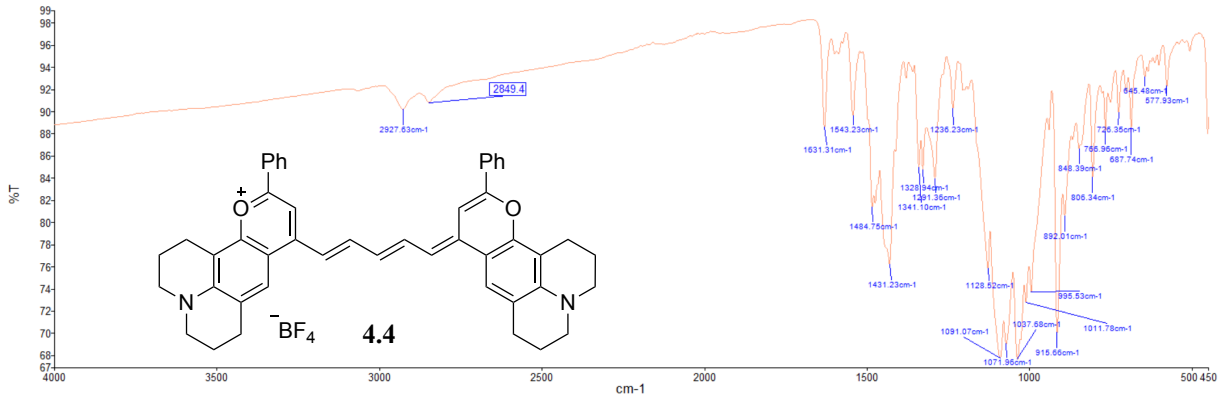
%T
cm-1
Ph
Ph
O
O
N
N
BF4
4.4
2927.63cm-1
2849.4
1631.31cm-1
1543.23cm-1
1484.75cm-1
1431.23cm-1
1328.94cm-1
1391.36cm-1
1341.10cm-1
1236.23cm-1
1128.52cm-1
1091.07cm-1
1071.96cm-1
1037.68cm-1
995.53cm-1
915.66cm-1
892.01cm-1
1011.78cm-1
848.39cm-1
806.34cm-1
766.96cm-1
726.35cm-1
687.74cm-1
645.48cm-1
577.93cm-1

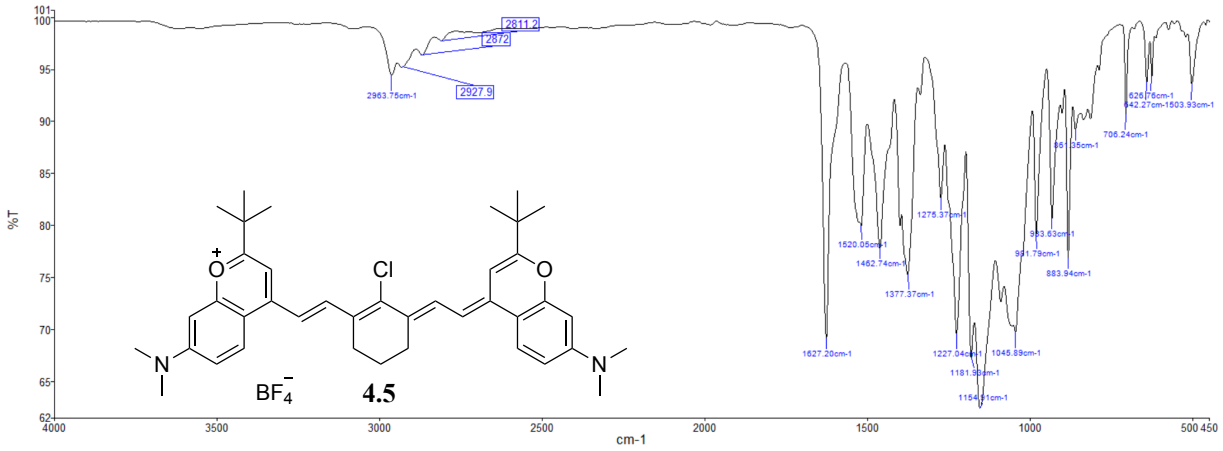
%T
cm-1
Cl
O
O
N
N
BF4
4.5
2963.75cm-1
2927.9
2872
2811.2
1627.20cm-1
1520.05cm-1
1462.74cm-1
1377.37cm-1
1275.37cm-1
1227.04cm-1
1181.38cm-1
1154.91cm-1
1045.89cm-1
963.63cm-1
921.79cm-1
883.94cm-1
706.24cm-1
661.35cm-1
642.27cm-1
626.76cm-1
503.93cm-1

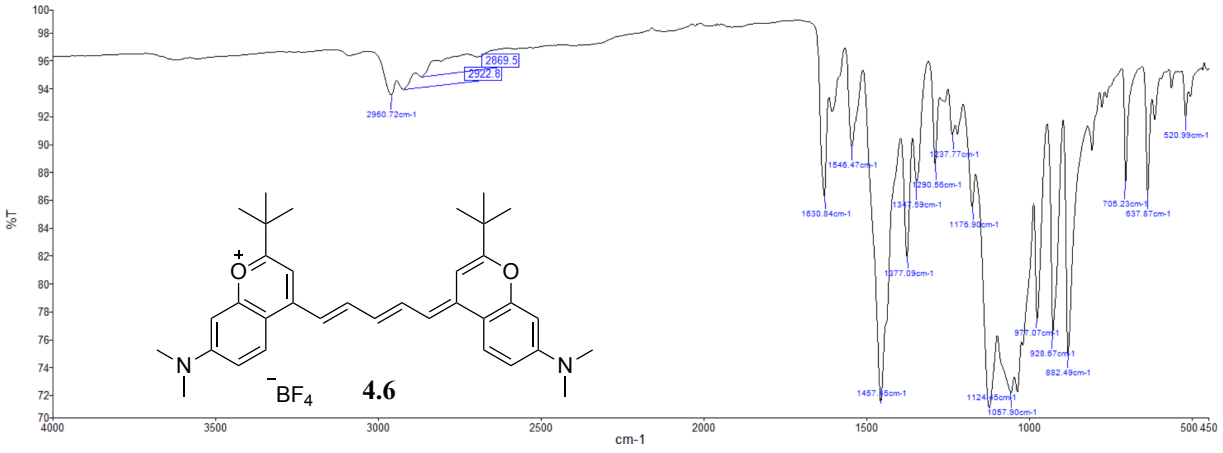
%T
cm-1
O
O
N
N
BF4
4.6
2960.72cm-1
2922.8
2869.5
1630.84cm-1
1546.47cm-1
1457.18cm-1
1377.09cm-1
1347.59cm-1
1290.56cm-1
1237.77cm-1
1176.96cm-1
1124.45cm-1
1057.90cm-1
977.07cm-1
928.67cm-1
882.49cm-1
705.23cm-1
637.87cm-1
520.99cm-1

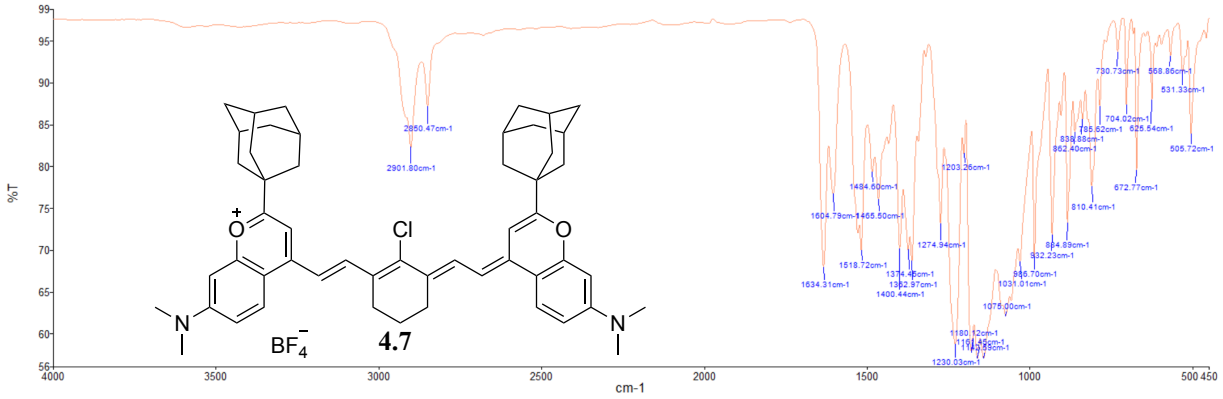
%T
cm-1
2850.47cm-1
2901.80cm-1
1634.31cm-1
1604.79cm-1
1518.72cm-1
1484.60cm-1
1465.50cm-1
1400.44cm-1
1374.45cm-1
1352.97cm-1
1274.94cm-1
1203.26cm-1
1180.12cm-1
1161.46cm-1
1143.89cm-1
1230.03cm-1
1075.00cm-1
1031.01cm-1
966.70cm-1
932.23cm-1
884.89cm-1
862.40cm-1
838.86cm-1
810.41cm-1
785.62cm-1
730.73cm-1
704.02cm-1
672.77cm-1
625.54cm-1
568.85cm-1
531.33cm-1
505.72cm-1
Cl
O
N
BF4
4.7

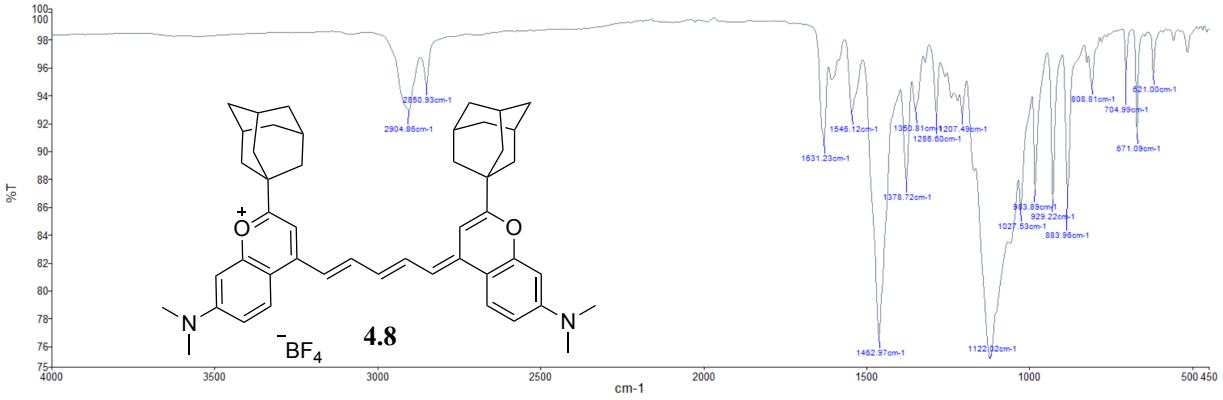
%T
cm-1
2850.93cm-1
2904.86cm-1
1631.23cm-1
1546.12cm-1
1462.97cm-1
1378.72cm-1
1350.81cm-1
1286.60cm-1
1207.49cm-1
1122.02cm-1
1027.53cm-1
983.89cm-1
929.22cm-1
883.96cm-1
808.81cm-1
704.99cm-1
671.09cm-1
621.00cm-1
O
N
BF4
4.8

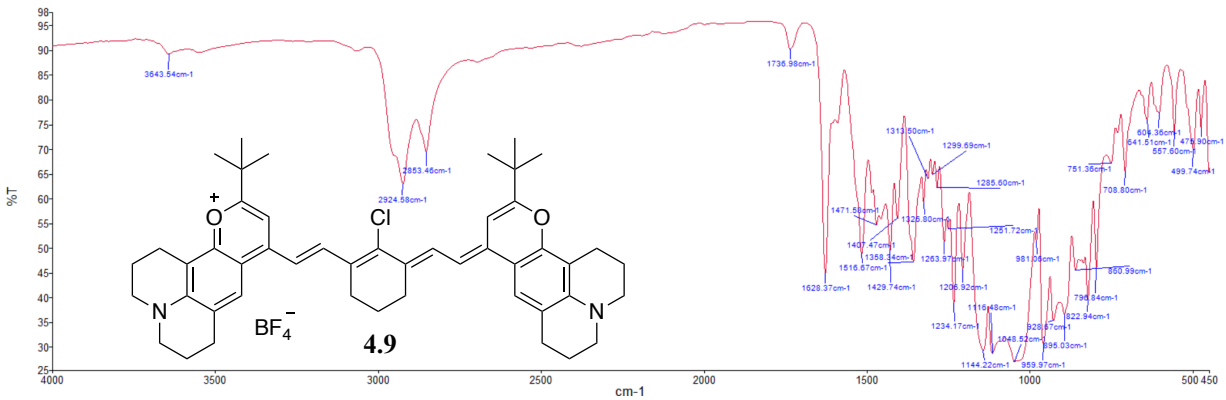
%T
cm-1
3643.54cm-1
2853.46cm-1
2924.58cm-1
1736.98cm-1
1628.37cm-1
1516.67cm-1
1471.58cm-1
1429.74cm-1
1407.47cm-1
1358.34cm-1
1328.80cm-1
1313.50cm-1
1299.69cm-1
1285.60cm-1
1263.97cm-1
1251.72cm-1
1206.92cm-1
1144.22cm-1
1116.48cm-1
1048.52cm-1
981.09cm-1
959.97cm-1
926.67cm-1
895.03cm-1
860.99cm-1
822.94cm-1
796.84cm-1
751.36cm-1
708.80cm-1
609.36cm-1
557.60cm-1
499.74cm-1
Cl
O
N
BF4
4.9

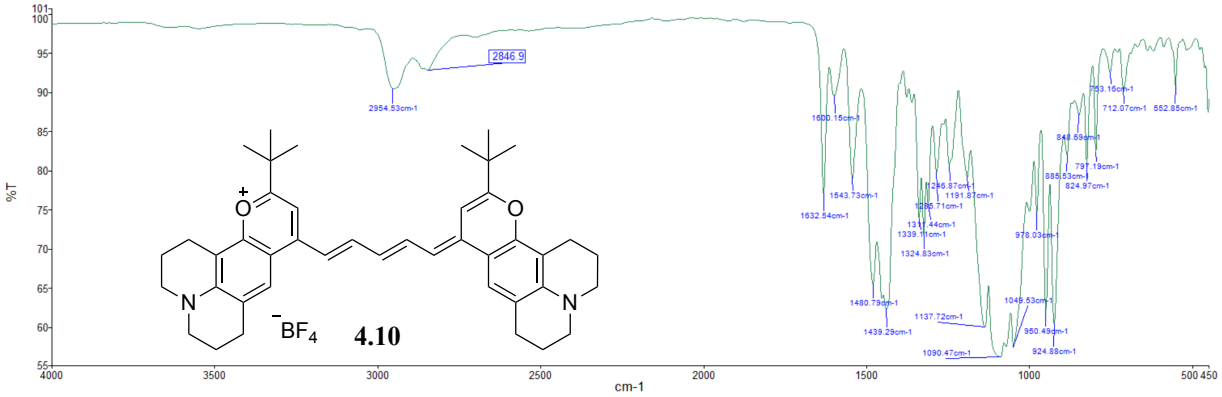
%T
cm-1
2954.53cm-1
2846.9
1600.15cm-1
1632.54cm-1
1543.73cm-1
1480.79cm-1
1439.29cm-1
1324.83cm-1
1339.11cm-1
1311.44cm-1
1295.71cm-1
1246.87cm-1
1191.87cm-1
1137.72cm-1
1090.47cm-1
1049.53cm-1
978.03cm-1
950.49cm-1
924.88cm-1
885.53cm-1
846.69cm-1
824.97cm-1
797.19cm-1
753.15cm-1
712.07cm-1
552.85cm-1
BF4
4.10

4.8.4 Absorption and Emission Spectra

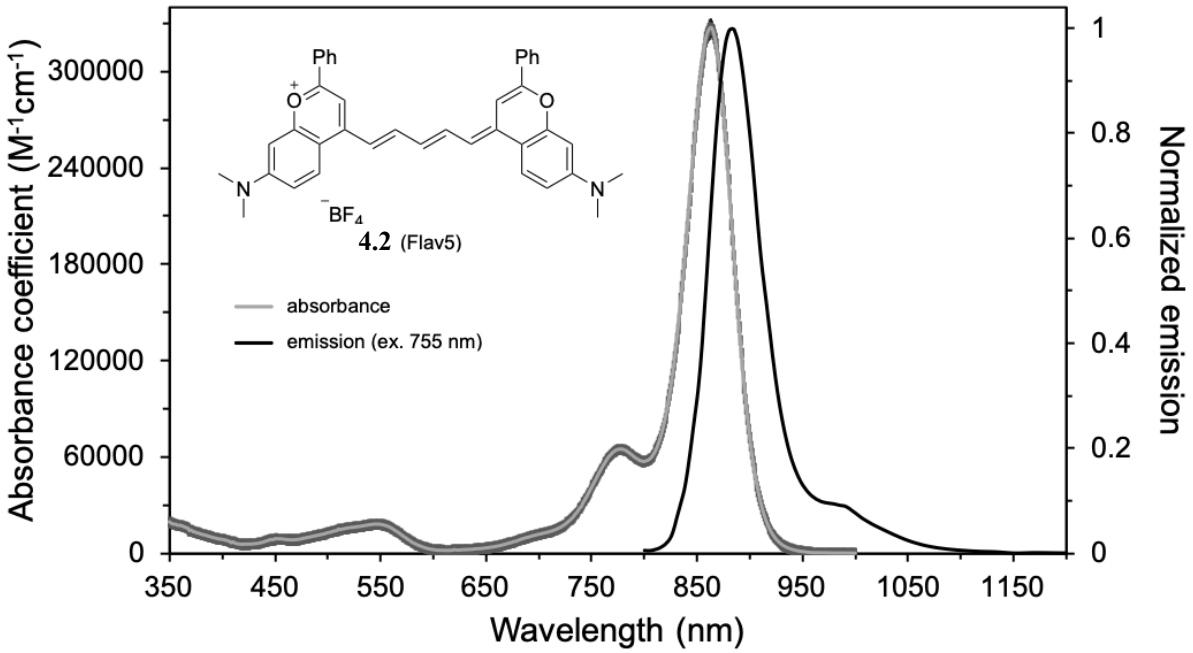

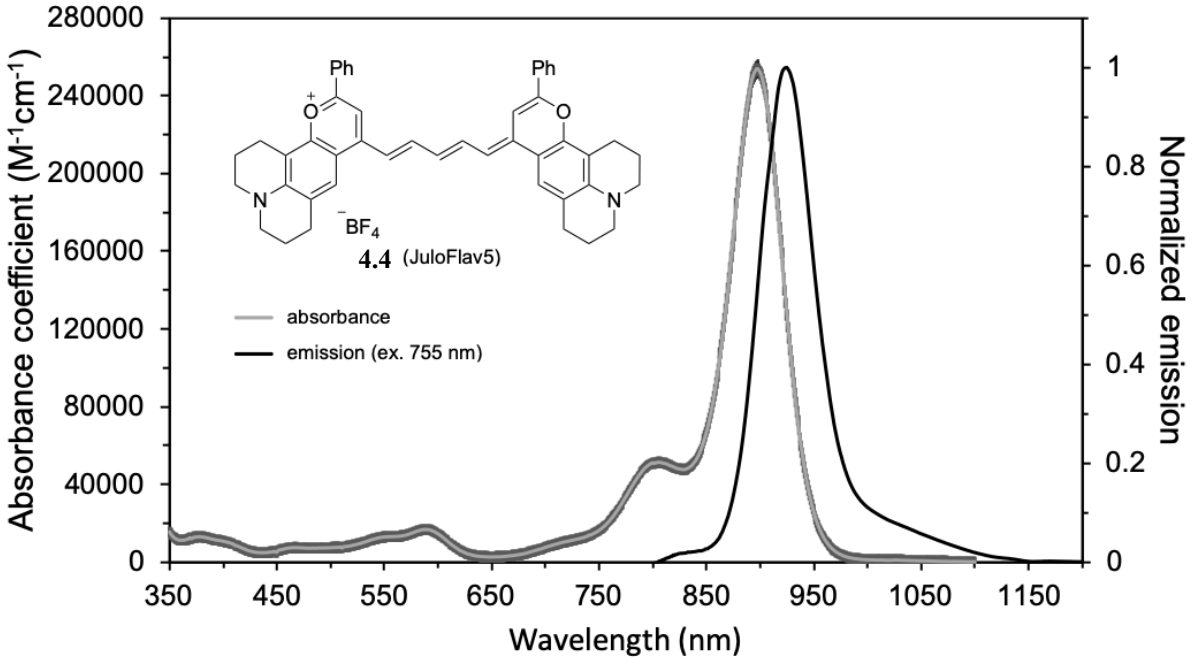

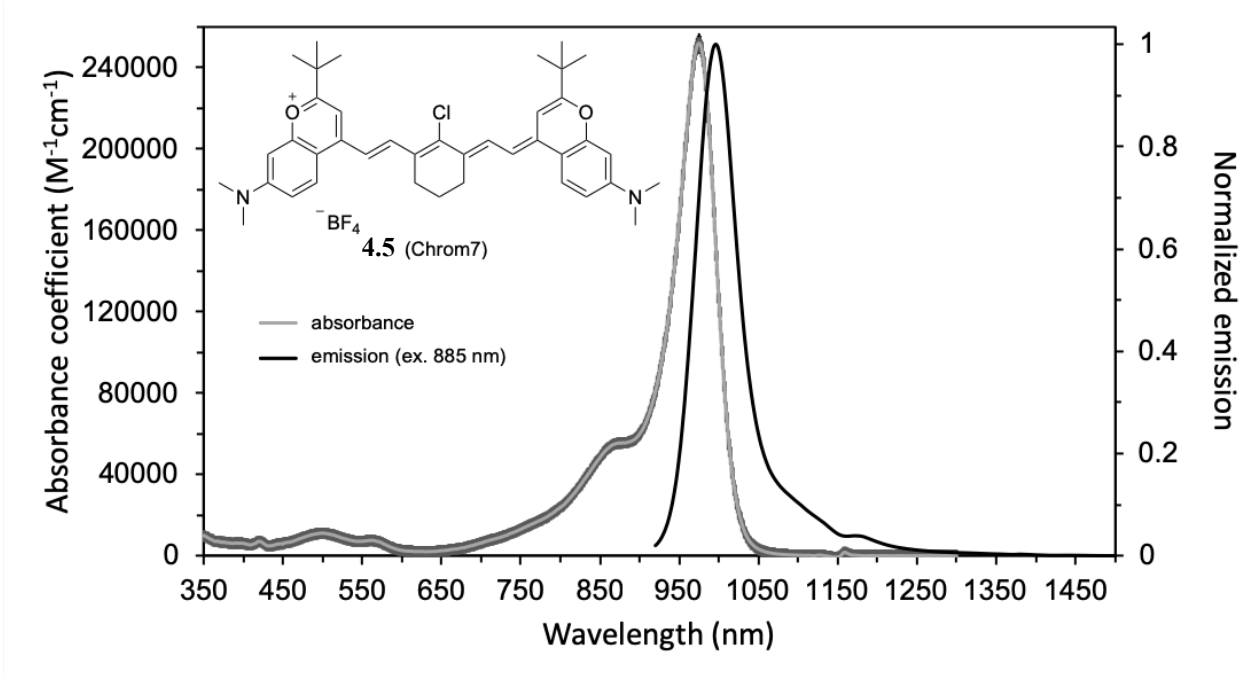

4.5 (Chrom7)

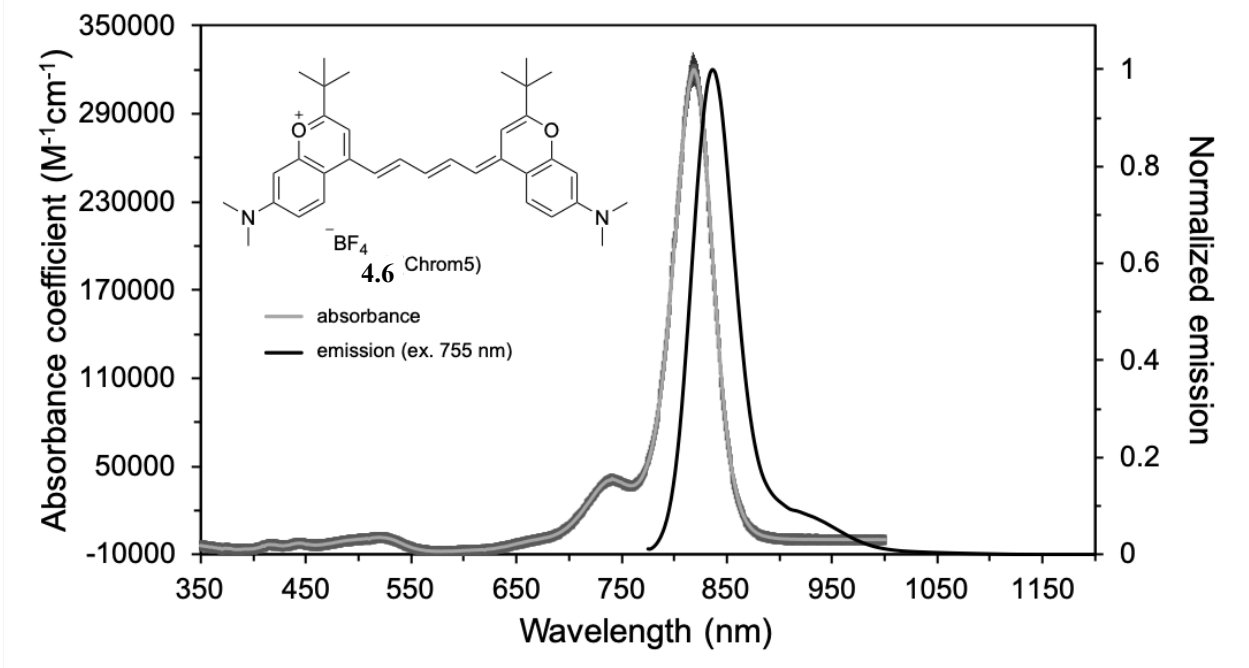

4.6 Chrom5)

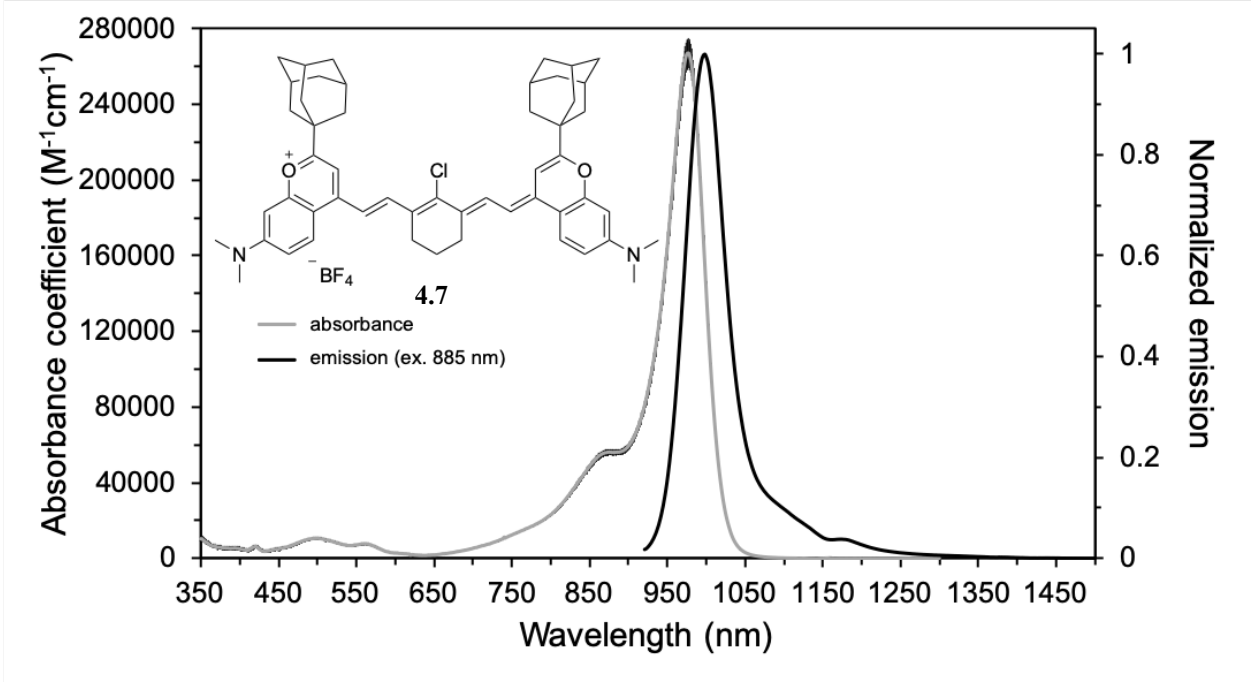
Absorbance coefficient (M-1cm-1)
Normalized emission
Wavelength (nm)
absorbance
emission (ex. 885 nm)
4.7

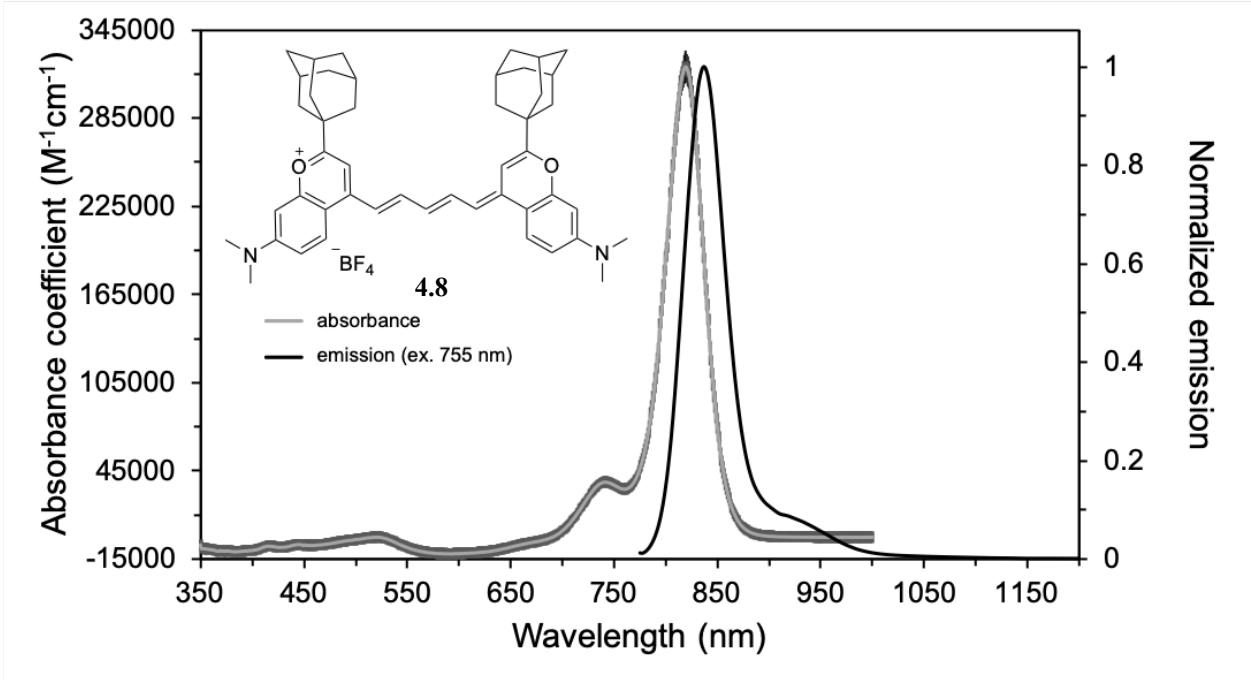
Absorbance coefficient (M-1cm-1)
Normalized emission
Wavelength (nm)
absorbance
emission (ex. 755 nm)
4.8

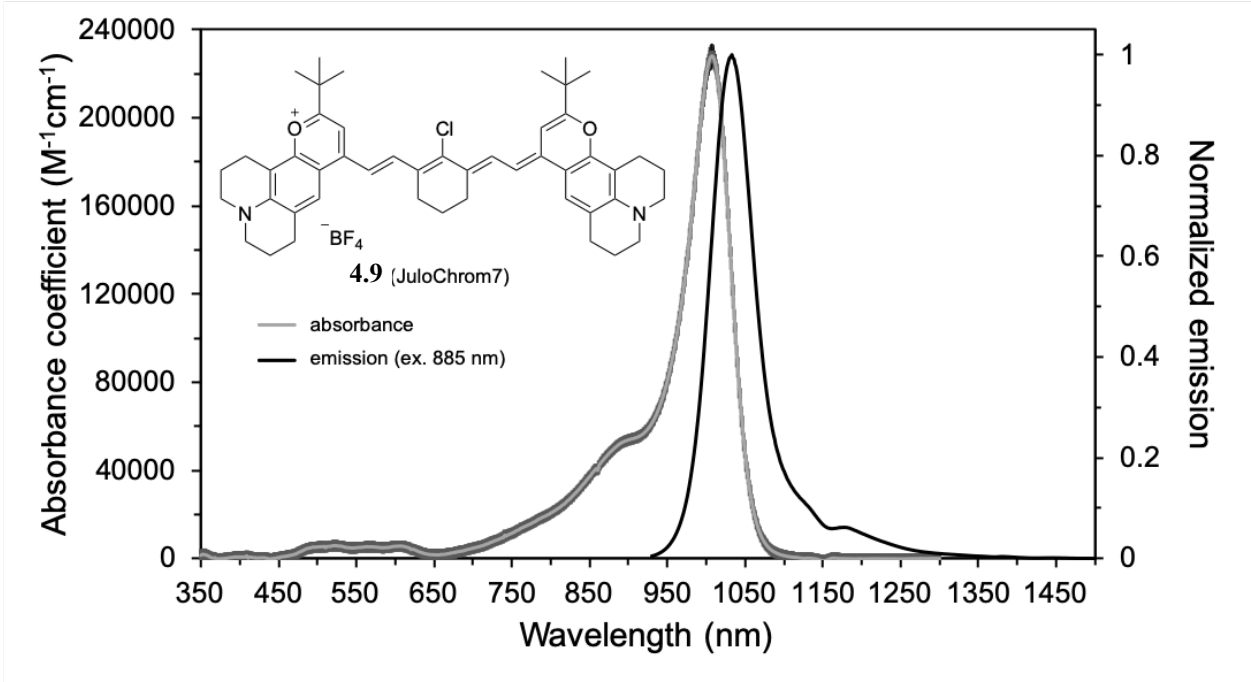

4.9 (JuloChrom7)

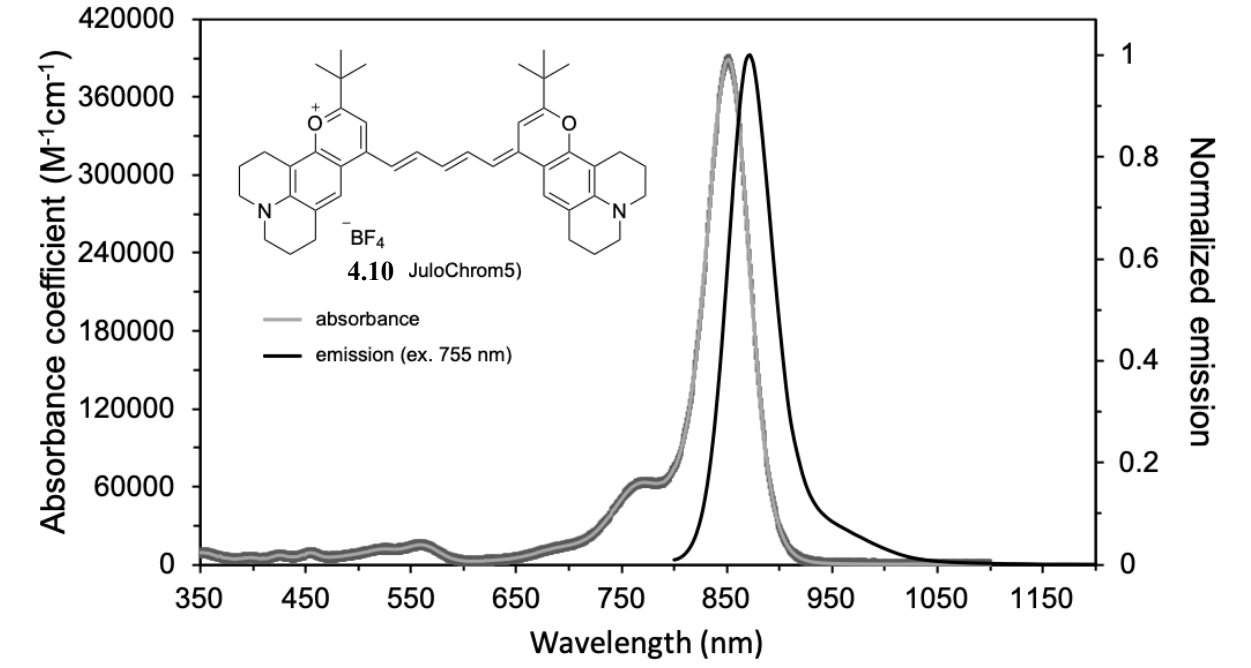

4.10 JuloChrom5)

4.9 Data and Code Availability

Crystal structures are available at the Cambridge Crystallographic Data Centre. Custom computer programs used for the work are available at GitHub (https:// gitlab.com/brunslab/ccda).

4.10 List of Supplementary Information Relevant to Chapter Four

Supplementary Video 4.1 *Single color imaging at 300 fps*

One per every 4 frames was kept in an image sequence. Image sequence was reduced in file size by constant rate factor of 12, using ffmpeg (vcodec h264) and is displayed in 3-fold slow motion. Experimental details correspond to that of **Figure 4.16**.

Supplementary Video 4.2 *High speed 3-color imaging*

One per every 4 frames was kept in an image sequence. Image sequence was reduced in file size by constant rate factor of 5, using ffmpeg (vcodec h264) and is displayed in real-time.

Experimental details correspond to that of **Figure 4.17**

Supplementary Video 4.3 *Video rate 4-color imaging*

No frames were omitted. Image sequence was reduced in file size by constant rate factor of 14. using ffmpeg (vcodec h264) and is displayed in real-time.

Experimental details correspond to that of **Figure 4.18.**

4.11 References and Notes

[1] Bashkatov, A. N.; Genina, E. A.; Kochubey, V. I.; Tuchin, V. V. Optical properties of human skin, subcutaneous and mucous tissues in the wavelength range from 400 to 2000 nm. *J. Phys. D. Appl. Phys.* **2005**, *38*, 2543–2555.

[2] Zhang, H.; Salo, D.; Kim, D. M.; Komarov, S.; Tai, Y.; Berezin, M. Y. Penetration depth of photons in biological tissues from hyperspectral imaging in shortwave infrared in transmission and reflection geometries. *J. Biomed. Opt.* **2016**, *21*, 126006.

[3] Lim, Y. T.; Kim, S.; Nakayama, A.; Stott, N. E.; Bawendi, M. G.; Frangioni, J. V. Selection of quantum dot wavelengths for biomedical assays and imaging. *Mol. Imaging* **2003**, *2*, 50–64.

[4] Carr, J. A.; Aellen, M.; Franke, D.; So, P. T. C.; Bruns, O. T.; Bawendi, M. G. Absorption by Water Increases Fluorescence Image Contrast of Biological Tissue in the Shortwave Infrared. *Proc. Natl. Acad. Sci.* **2018**, *115*, 9080–9085.

[5] Welsher, K.; Liu, Z.; Sherlock, S. P.; Robinson, J. T.; Chen, Z.; Daranciang, D.; Dai, H. A route to brightly fluorescent carbon nanotubes for near-infrared imaging in mice. *Nat. Nanotechnol.* **2009**, *4*, 773–780.

[6] Ceppi, L.; Bardhan, N. M.; Na, Y.; Siegel, A.; Rajan, N.; Fruscio, R.; Del Carmen, M. G.; Belcher, A. M.; Birrer, M. J. Real-time single-walled carbon nanotube-based fluorescence imaging improves survival after debulking surgery in an ovarian cancer model. *ACS Nano* **2019**, *13*, 5356–5365.

[7] Hong, G.; Robinson, J. T.; Zhang, Y.; Diao, S.; Antaris, A. L.; Wang, Q.; Dai, H. In vivo fluorescence imaging with Ag2S quantum dots in the second near-infrared region. Angew. Chem. Int. Ed. 2012, 51, 9818–9821.

[8] Bruns, O. T.; Bischof, T. S.; Harris, D. K.; Franke, D.; Shi, Y.; Riedemann, L.; Bartelt, A.; Jaworski, F. B.; Carr, J. A.; Rowlands, C. J.; et al. Next-generation in vivo optical imaging with short-wave infrared quantum dots. *Nat. Biomed. Eng.* **2017**, *1*, 0056.

[9] Naczynski, D. J.; Tan, M. C.; Zevon, M.; Wall, B.; Kohl, J.; Kulesa, A.; Chen, S.; Roth, C. M.; Riman, R. E.; Moghe, P. V. Rare-earth-doped biological composites as in vivo shortwave infrared reporters. *Nat. Commun.* **2013**, *4*, 2199.

[10] Zhong, Y.; Ma, Z.; Wang, F.; Wang, X.; Yang, Y.; Liu, Y.; Zhao, X.; Li, J.; Du, H.; Zhang, M.; et al. In vivo molecular imaging for immunotherapy using ultra-bright near-infrared-IIb rare-earth nanoparticles. *Nat. Biotechnol.* **2019**, 37, 1322–1331.

[11] Yang, Q.; Ma, Z.; Wang, H.; Zhou, B.; Zhu, S.; Zhong, Y.; Wang, J.; Wan, H.; Antaris, A.; Ma, R.; et al. Rational Design of Molecular Fluorophores for Biological Imaging in the NIR-II Window. *Adv. Mater.* **2017**, *29*, 1605497.

[12] Cosco, E. D.; Caram, J. R.; Bruns, O. T.; Franke, D.; Day, R. A.; Farr, E. P.; Bawendi, M. G.; Sletten, E. M. Flavylium Polymethine fluorophores for near- and shortwave infrared imaging. *Angew. Chem. Int. Ed.* **2017**, *56*, 13126–13129.

[13] Cosco, E. D.; Spearman, A. L.; Ramakrishnan, S.; Lingg, J. G. P.; Saccomano, M.; Pengshung, M.; Arús, B. A.; Wong, K. C. Y.; Glasl, S.; Ntziachristos, V.; et al. Shortwave Infrared Polymethine Fluorophores Matched to Excitation Lasers Enable Non-Invasive, Multicolour in Vivo Imaging in Real Time. *Nat. Chem.* **2020**, *12*, 1123–1130.

[14] Zhu, S.; Herraiz, S.; Yue, J.; Zhang, M.; Wan, H.; Yang, Q.; Ma, Z.; Wang, Y.; He, J.; Antaris, A. L.; et al. 3D NIR-II molecular imaging distinguishes targeted organs with high-performance NIR-II bioconjugates. *Adv. Mater.* **2018**, *30*, 1705799.

[15] Wan, H.; Yue, J.; Zhu, S.; Uno, T.; Zhang, X.; Yang, Q.; Yu, K.; Hong, G.; Wang, J.; Li, L.; et al. A bright organic NIR-II manofluorophore for three-dimensional imaging into biological tissues. *Nat. Commun.* **2018**, *9*, 1171.

[16] Zhu, S.; Yang, Q.; Antaris, A. L.; Yue, J.; Ma, Z.; Wang, H.; Huang, W.; Wan, H.; Wang, J.; Diao, S.; et al. Molecular imaging of biological systems with a clickable dye in the broad 800- to 1,700-nm near-infrared window. *Proc. Natl. Acad. Sci.* **2017**, *114*, 962–967.

[17] Zubkovs, V.; Antonucci, A.; Schuergers, N.; Lambert, B.; Latini, A.; Ceccarelli, R.; Santinelli, A.; Rogov, A.; Ciepielewski, D.; Boghossian, A. A. Spinning-disc confocal microscopy in the second near-infrared window (NIR-II). *Sci. Rep.* **2018**, *8*, 13770.

[18] Wang, F.; Wan, H.; Ma, Z.; Zhong, Y.; Sun, Q.; Tian, Y.; Qu, L.; Du, H.; Zhang, M.; Li, L.; et al. Light-sheet microscopy in the near-infrared II window. *Nat. Methods* **2019**, *16*, 545–552.

[19] Williams, S. J.; Prescher, J. A. Building Biological Flashlights: Orthogonal Luciferases and Luciferins for in Vivo Imaging. *Acc. Chem. Res.* **2019**, *52*, 3039–3050.

[20] Lu, G. J.; Farhadi, A.; Szablowski, J. O.; Lee-Gosselin, A.; Barnes, S. R.; Lakshmanan, A.; Bourdeau, R. W.; Shapiro, M. G. Acoustically Modulated Magnetic Resonance Imaging of Gas-Filled Protein Nanostructures. *Nat. Mater.* **2018**, 17, 456–463.

[21] Chen, M.; Knox, H. J.; Tang, Y.; Liu, W.; Nie, L.; Chan, J.; Yao, J. Simultaneous Photoacoustic Imaging of Intravascular and Tissue Oxygenation. *Opt. Lett.* **2019**, *44*, 3773.

[22] Thimsen, E.; Sadtler, B.; Berezin, M. Y. Shortwave-infrared (SWIR) emitters for biological imaging: a review of challenges and opportunities. *Nanophotonics.* **2017**, *6*, 1043–1054.

[23] Carr, J. A.; Franke, D.; Caram, J. R.; Perkinson, C. F.; Saif, M.; Askoxylakis, V.; Datta, M.; Fukumura, D.; Jain, R. K.; Bawendi, M. G.; et al. Shortwave infrared fluorescence

imaging with the clinically approved near-infrared dye indocyanine green. *Proc. Natl. Acad. Sci.* **2018**, *115*, 4465–4470.

[24] Starosolski, Z.; Bhavane, R.; Ghaghada, K. B.; Vasudevan, S. A.; Kaay, A.; Annapragada, A. Indocyanine green fluorescence in second near-infrared (NIR-II) window. *PLoS One* **2017**, *12*, e0187563.

[25] Zhu, S.; Hu, Z.; Tian, R.; Yung, B. C.; Yang, Q.; Zhao, S.; Kiesewetter, D. O.; Niu, G.; Sun, H.; Antaris, A. L.; et al. Repurposing cyanine NIR-I dyes accelerates clinical translation of near-infrared-II (NIR-II) bioimaging. *Adv. Mater.* **2018**, *30*, 1802546.

[26] Luciano, M. P.; Crooke, S. N.; Nourian, S.; Dingle, I.; Nani, R. R.; Kline, G.; Patel, N. L.; Robinson, C. M.; Difilippantonio, S.; Kalen, J. D.; et al. A nonaggregating heptamethine cyanine for building brighter labeled biomolecules. *ACS Chem. Biol.* **2019**, *14*, 934–940.

[27] Rurack, K.; Spieles, M. Fluorescence quantum yields of a series of red and near-infrared dyes emitting at 600−1000 nm. *Anal. Chem.* **2011**, *83*, 1232–1242.

[28] Matikonda, S. S.; Hammersley, G.; Kumari, N.; Grabenhorst, L.; Glembockyte, V.; Tinnefeld, P.; Ivanic, J.; Levitus, M.; Schnermann, M. J. Impact of cyanine conformational restraint in the near-infrared range. *J. Org. Chem.* **2020**, *85*, 5907–5915.

[29] Lei, Z.; Li, X.; Luo, X.; He, H.; Zheng, J.; Qian, X.; Yang, Y. Bright, stable, and biocompatible organic fluorophores absorbing/emitting in the deep near-infrared spectral region. *Angew. Chem. Int. Ed.* **2017**, *56*, 2979–2983.

[30] Wang, S.; Fan, Y.; Li, D.; Sun, C.; Lei, Z.; Lu, L.; Wang, T.; Zhang, F. Anti-quenching NIR-II molecular fluorophores for in vivo high-contrast imaging and pH sensing. *Nat. Commun.* **2019**, *10*, 1058.

[31] Lei, Z.; Sun, C.; Pei, P.; Wang, S.; Li, D.; Zhang, X.; Zhang, F. Stable, Wavelength-tunable fluorescent dyes in the NIR-II region for in vivo high-contrast bioimaging and multiplexed biosensing. *Angew. Chem. Int. Ed.* **2019**, *58*, 8166–8171.

[32] Li, B.; Zhao, M.; Feng, L.; Dou, C.; Ding, S.; Zhou, G.; Lu, L.; Zhang, H.; Chen, F.; Li, X.; et al. Organic NIR-II molecule with long blood half-life for in vivo dynamic vascular imaging. *Nat. Commun.* **2020**, *11*, 3102.

[33] Ding, B.; Xiao, Y.; Zhou, H.; Zhang, X.; Qu, C.; Xu, F.; Deng, Z.; Cheng, Z.; Hong, X. Polymethine thiopyrylium fluorophores with absorption beyond 1000 nm for biological imaging in the second near-infrared subwindow. *J. Med. Chem.* **2019**, *62*, 2049–2059.

[34] Lavis, L. D. Chemistry is dead. Long live chemistry! *Biochemistry* **2017**, *56*, 5165–5170.

[35] Bricks, J. L.; Kachkovskii, A. D.; Slominskii, Y. L.; Gerasov, A. O.; Popov, S. V. Molecular Design of near infrared polymethine dyes: a review. *Dye. Pigment.* **2015**, *121*, 238–255.

[36] Strekowski, L. *Heterocyclic Polymethine Dyes*; Strekowski, L., Ed.; Topics in Heterocyclic Chemistry; Springer Berlin Heidelberg: Berlin, Heidelberg, 2008; Vol. 14.

[37] Štacková, L.; Muchová, E.; Russo, M.; Slavíček, P.; Štacko, P.; Klán, P. Deciphering the Structure–Property Relations in Substituted Heptamethine Cyanines. *J. Org. Chem*. **2020**, *85*, 9776–9790.

[38] Ishchenko, A. A. The length of the polymethine chain and the spectral-luminescent properties of symmetrical cyanine dyes. *Russ. Chem. Bull.* **1994**, *43*, 1161–1174.

[39] Tatikolov, A. S.; Costa, S. M. B. Complexation of polymethine dyes with human serum albumin: a spectroscopic study. *Biophys. Chem.* **2004**, *107*, 33–49.

[40] Li, B., Lu, L., Zhao, M., Lei, Z. & Zhang, F. An efficient 1064 nm NIR-II excitation fluorescent molecular dye for deep-tissue high-resolution dynamic bioimaging. *Angew. Chem. Int. Ed.* **2018**, *57*, 7483–7487.

[41] Waggoner, A. S.; Mujumdar, R. B. Rigidized trimethine cyanine dyes. U.S. Patent 6133445A, Oct. 17, 2000.

[42] Michie, M. S.; Götz, R.; Franke, C.; Bowler, M.; Kumari, N.; Magidson, V.; Levitus, M.; Loncarek, J.; Sauer, M.; Schnermann, M. J. Cyanine conformational restraint in the far-red range. *J. Am. Chem. Soc.* **2017**, *139*, 12406–12409.

[43] Ohulchanskyy, T. Y.; Donnelly, D. J.; Detty, M. R.; Prasad, P. N. Heteroatom substitution induced changes in excited-state photophysics and singlet oxygen generation in chalcogenoxanthylium dyes: effect of sulfur and selenium substitutions. *J. Phys. Chem. B* **2004**, *108*, 8668–8672.

[44] Choi, H. S.; Nasr, K.; Alyabyev, S.; Feith, D.; Lee, J. H.; Kim, S. H.; Ashitate, Y.; Hyun, H.; Patonay, G.; Strekowski, L.; et al. Synthesis and in vivo fate of zwitterionic near-infrared fluorophores. *Angew. Chem. Int. Ed.* **2011**, *50*, 6258–6263.

[45] Semonin, O. E.; Johnson, J. C.; Luther, J. M.; Midgett, A. G.; Nozik, A. J.; Beard, M. C. Absolute photoluminescence quantum yields of IR-26 dye, PbS, and PbSe quantum dots. *J. Phys. Chem. Lett.* **2010**, *1*, 2445–2450.

[46] Pengshung, M.; Li, J.; Mukadum, F.; Lopez, S. A.; Sletten, E. M. Photophysical Tuning of Shortwave Infrared Flavylium Heptamethine Dyes via Substituent Placement. *Org. Lett.* **2020**, *22*, 6150–6154.

[47] While many SWIR-emissive donor-acceptor donor (DAD) dyes have been developed (Ref. 11, 14–16), broad absorption spectra and low absorption coefficients limit applications within excitation-multiplexed SWIR imaging.

[48] Englman, R.; Jortner, J. The energy gap law for radiationless transitions in large molecules. *Mol. Phys.* **1970**, *18*, 145–164.

[49] Allen, F. H.; Kennard, O.; Watson, D. G.; Brammer, L.; Orpen, A. G.; Taylor, R. Tables of bond lengths determined by X-Ray and neutron diffraction. Part 1. Bond lengths in organic compounds. *J. Chem. Soc. Perkin Trans. II* **1987**, *12*, S1–S19.

[50] International Commission on Non-Ionizing Radiation Protection. ICNIRP guidelines on limits of exposure to laser radiation of wavelengths between 180 nm and 1,000 μm. *Health Phys.* **2013**, *105*, 271–295.

[51] Philip, R.; Penzkofer, A.; Baumler, W.; Szeimies, R. M.; Abels, C. absorption and fluorescence spectroscopic investigation of indocyanine green. *J. Photochem. Photobiol., A* **1996**, *96*, 137–148.

[52] Schindelin, J.; Arganda-Carreras, I.; Frise, E.; Kaynig, V.; Longair, M.; Pietzsch, T.; Preibisch, S.; Rueden, C.; Saalfeld, S.; Schmid, B.; et al. Fiji: An Open-Source Platform for Biological-Image Analysis. *Nat. Methods* **2012**, *9*, 676–682.

[53] Rueden, C. T.; Schindelin, J.; Hiner, M. C.; DeZonia, B. E.; Walter, A. E.; Arena, E. T.; Eliceiri, K. W. ImageJ2: ImageJ for the next Generation of Scientific Image Data. *BMC Bioinformatics* **2017**, *18*, 529.

[54] Kovesi, P. Good Colour Maps: How to Design Them. 2005, arXiv:1509.03700 [cs.GR].

[55] Hatami, S.; Würth, C.; Kaiser, M.; Leubner, S.; Gabriel, S.; Bahrig, L.; Lesnyak, V.; Pauli, J.; Gaponik, N.; Eychmüller, A.; et al. Absolute Photoluminescence Quantum Yields of IR26 and IR-Emissive Cd1−xHgxTe and PbS Quantum Dots – Method- and Material-Inherent Challenges. *Nanoscale* **2015**, *7*, 133–143.

CHAPTER FIVE

Investigating Solubility Changes and Nanomaterial Encapsulation of Polymethine dyes for Shortwave Infrared in vivo Imaging

5.1 Abstract

A major aspect imaging probe development is efficient delivery of the imaging probe into biological environments. The hydrophobicity of the flavylium and chromenylium polymethine dyes reported in Chapters 2–4 renders aqueous solubility or dispersion a major challenge for their widespread use in biological experiments. Here, we explore diverse strategies towards enabling delivery of these chromophores by encapsulation in nanomaterials composed of poly(lactic-*co*-glycolic acid) or poly(ethylene glycol)-phospholipid amphiphiles, exploring weakly coordinating anions as counterions, and by appending diverse solubilizing groups onto the chromophore. Polymethine dyes with fluorophobic, lipophilic, and hydrophilic tags are synthesized and the solubility properties are investigated towards their use as shortwave infrared contrast agents.

5.2 Nanomaterial Encapsulation of Flavylium and Chromenylium Polymethine Dyes[1]

5.2.1 Background

Delivery in nanomaterials is advantageous for facilitating solubility of organic molecules as well as for increasing avidity for targeting to cell-type specific surface receptors, particularly to solid tumors. Efficient nanomaterial encapsulation is a challenge for many organic dyes, and often results in formation of a blue-shifted, non-emissive, H-aggregate species in addition to a

[1] Olivia Leland and Zhumin Zhang contributed to work in this section

monomeric species. In the studies described in Chapters 2–4, the flavylium and chromenylium dyes used are hydrophobic and thus required delivery within nanoparticles. We used poly(ethylene glycol)-phospholipid amphiphiles to solubilize the dyes inside micelles which are dispersed in water or phosphate buffered saline (PBS) and deliver them to living species. Upon loading in phospholipid micelles composed of 18:0 PEG2000 PE (1,2-distearoyl-sn-glycero-3-phosphoethanolamine-N-[methoxy(polyethylene glycol)-2000] ammonium salt) or 18:0 PEG5000 PE (1,2-distearoyl-sn-glycero-3-phosphoethanolamine-N-[methoxy(polyethylene glycol)-5000] ammonium salt), Flav7 indeed has a large H-aggregate peak observable by absorption spectroscopy (see Ch. 2) that is present alongside the monomer. Optimizing the dye loading within nanoparticles to reduce H-aggregation would increase the amount of dye that is in an active species, increase the overall brightness of the material, and enable a reduction in the amount of dye delivered. Thus far, we have taken several diverse approaches to pursue improved nanomaterial encapsulation.

Initial work focused on screening micelle formation conditions, buffers, and additives (organic host molecules and charged polymers) with Flav7 and IR-1061 dyes in the PEG5000 PE amphiphile-based micelles. These experiments, with additives including poly(acrylic acid) (average MW ~1,800), poly(sodium 4-styrenesulfonate) (average MW ~70,000), β-cyclodextrin, β-cyclodextrin polymer, γ-cyclodextrin, and curcurbit[7]uril (CB[7]), and buffers such as 4-(2-hydroxyethyl)-1-piperazineethanesulfonic acid (HEPES), (3-(N-morpholino)propanesulfonic acid) (MOPS), piperazine-N,N′-bis(2-ethanesulfonic acid) (PIPES), and tris(hydroxymethyl)aminomethane (TRIS), were largely unsuccessful; the conditions screened did not improve the ratio of monomer to H-aggregated species compared to formation with no additive in PBS buffer at physiological pH.

5.2.2 Loading Polymethine Dyes in PLGA Nanoparticles

We also explored other polymer amphiphiles for dye encapsulation, specifically poly(lactic-*co*-glycolic acid) (PLGA) using JuloFlav7 (**4.3**) as a model dye. The fabrication procedure[1] involved dissolving dye and PLGA into a co-solvent mixture composed of organic solvents, adding this solution dropwise to an aqueous solution of poly(vinyl alcohol) (PVA) and sonicating the immiscible phases together using a probe sonicator. Organic solvent was removed by evaporation under stirring, and finally, the particles were spun down by centrifugation and washed with phosphate buffered saline (PBS) (Figure 5.1A). Within this procedure, aggregation would occur during the organic solvent evaporation step (step 5), naturally once the dye no longer can benefit from organic solvent solubilization. Modifications to this procedure included optimizing the dye loading concentration and testing two PLGA polymers containing different lactide to glycolide (hydrophobic to hydrophilic) ratios (50:50 and 75:25 lactide:glycolide) (Figure 5.1B). A range of co-solvents in which to initially dissolve the dye and polymer were screened (Figure 5.1C). Finally, PVA concentrations, from 0.1–2.0% were also investigated (5.1D). Regardless of the parameters tested, these experiments resulted in nanoparticles with a diameter of 130–190 nm (Figure 5.1 E–F), but with minimal monomer behavior of JuloFlav7.

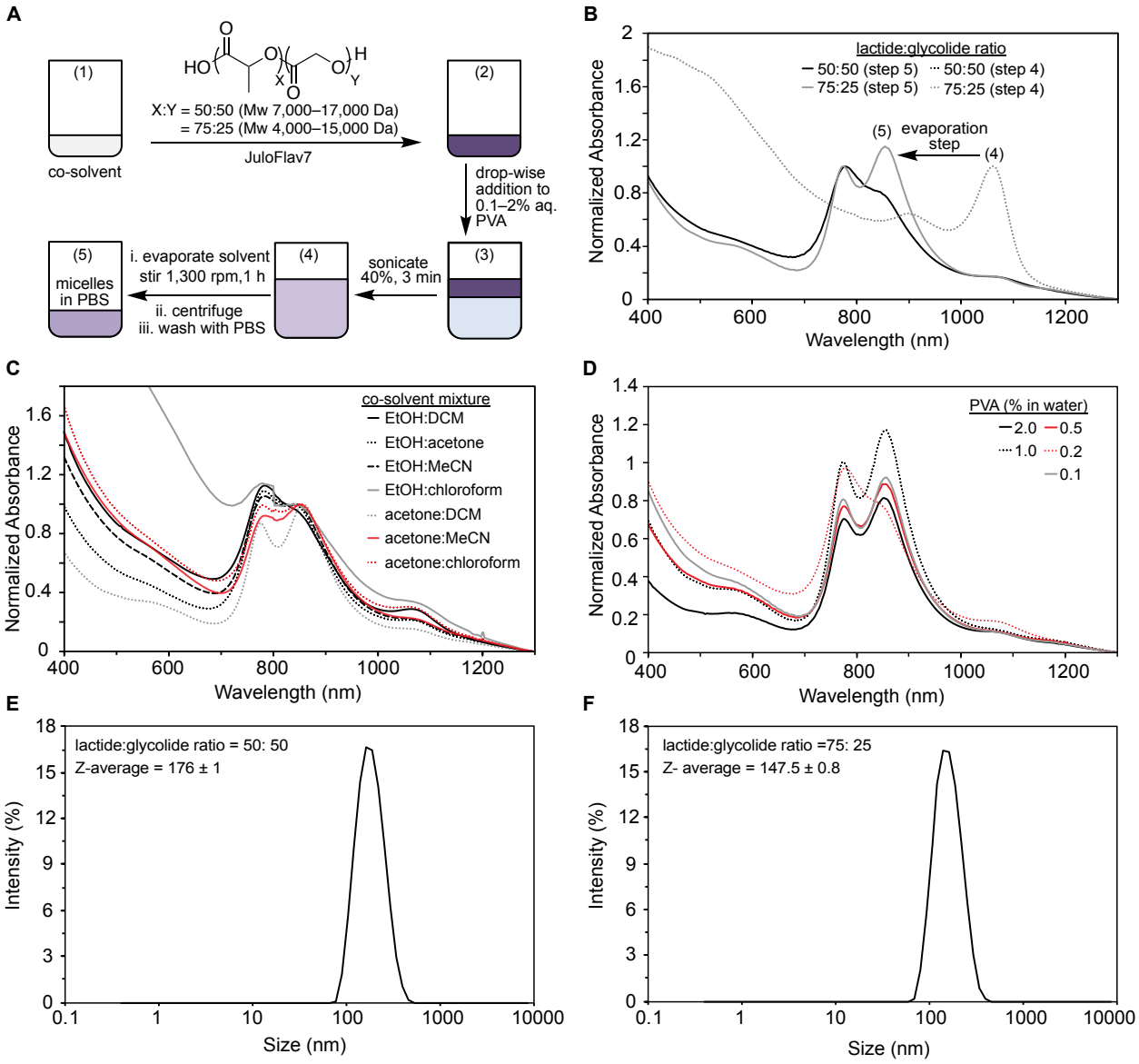

Figure 5.1 Fabrication and absorption characterization on JuloFlav7 encapsulated in PLGA nanoparticles. A) Fabrication scheme. B) Absorption of JuloFlav7 in PLGA using amphiphiles with 50:50 (black) and 75:25 (grey) lactide:glycolide ratios before solvent evaporation (step 4, dotted) and after solvent evaporation and washing (step 5, solid). C) Absorption of JuloFlav7 in the 50:50 PLGA nanoparticles, fabricated using a variety of different co-solvent mixtures (step 1). D) Absorption of JuloFlav7 in 50:50 PLGA nanoparticles, fabricated by dropwise addition of 0.1–2% PVA in water solutions. E–F) DLS data on PLGA nanoparticles fabricated with polymers with a 50:50 lactide:glycolide (E) and a 75:25 lactide:glycolide ratio (F). Data is displayed as the average of three measurements, error represents the standard deviation.

To contextualize the behavior of JuloFlav7 in PLGA micelles, loading of several other dyes was also explored. In contrast, ICG did not display any H-aggregation upon encapsulation in

PLGA nanoparticles, however, upon washing and dilution, (after steps 4.ii–4.iii, Figure 5.1), a significant amount of J-aggregation was observed (Figure 5.2A). This result was unexpected but not unsurprising, as ICG has been shown to have concentration and time-dependent J-aggregation in micellar and protein environments.[2–3] Finally, the indolenine heptamethine dye, HITCI (,1′,3,3,3′,3′-hexamethylindotricarbocyanine iodide) showed successful encapsulation without signs of either H- or J-aggregation (Figure 5.2B). Further, the absorption of monomeric HITCI in the particles was stable for at least 2 days when stored at 4 ºC.

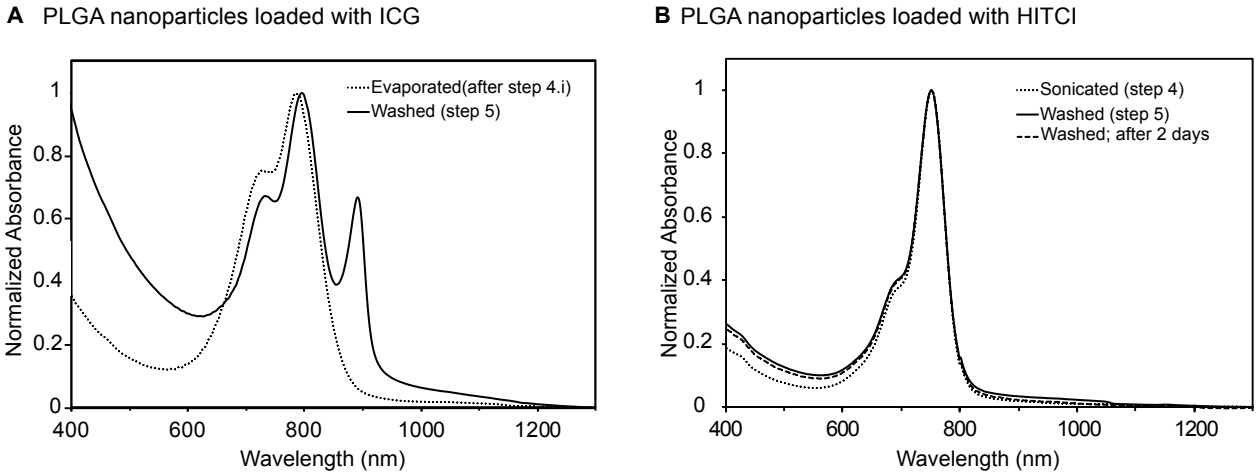

Figure 5.2 Absorption characterization on ICG (A) and HITCI (B) encapsulated in PLGA (50:50 lactide:glycolide ratio) nanoparticles at several steps in the fabrication process.

5.2.3 Loading Flavylium and Chromenylium Polymethine Dyes in Phospholipid Micelles

Next, (as described in Ch. 4) we introduced bulky substituents at the 2-position of the dye heterocycles, such as *tert*-butyl and 1-adamantyl, hypothesizing that these groups could disfavor face-to-face stacking of the molecules. Addition of bulky substituents onto polymethine dyes has been studied by Marder and coworkers, in which they demonstrate decreased aggregation of polymethine dyes in thin films,[4–5] an environment with close dye packing, similar to the inside of a nanomaterial. Using the Charton steric parameters (ν) to estimate the relative steric bulk of the functional groups tested, Ph is the smallest (ν = 0.57), *tert*-butyl is substantially larger (ν =

1.24), and 1-adamantyl is the largest, although by a smaller margin (ν = 1.33))[6]. In our system, for the heptamethine dyes, the hypothesis that increased steric bulk could decrease H-aggregation held for the comparison of 2-phenyl (flavylium) dyes to 2-*tert*-butyl (chromenylium) dyes. The increase in steric bulk of the 2-*tert*-butyl group correlated with a higher percentage of monomer vs H-aggregate present upon micellular encapsulation (Figure 5.3B). However, the trend did not extend to the 2-adamantyl heptamethine dye **4.7** despite a further increase in steric bulk. Upon encapsulation, dye **4.7** displayed a substantially smaller monomer/aggregate ratio than the *tert*-butyl containing dyes (Figure 5.3B), with similar behavior to the flavylium dye JuloFlav7 (**4.3**). Additionally, changes to the micelle fabrication method, including using a thin-film method from chloroform or dichloromethane did not improve the amount of monomer present (Figure 5.3C–D). This result implies that more subtle packing behaviors are at play in addition to simply the substituent size. Further investigation into structure-property relationships with groups of varying steric parameters is needed to understand this behavior.

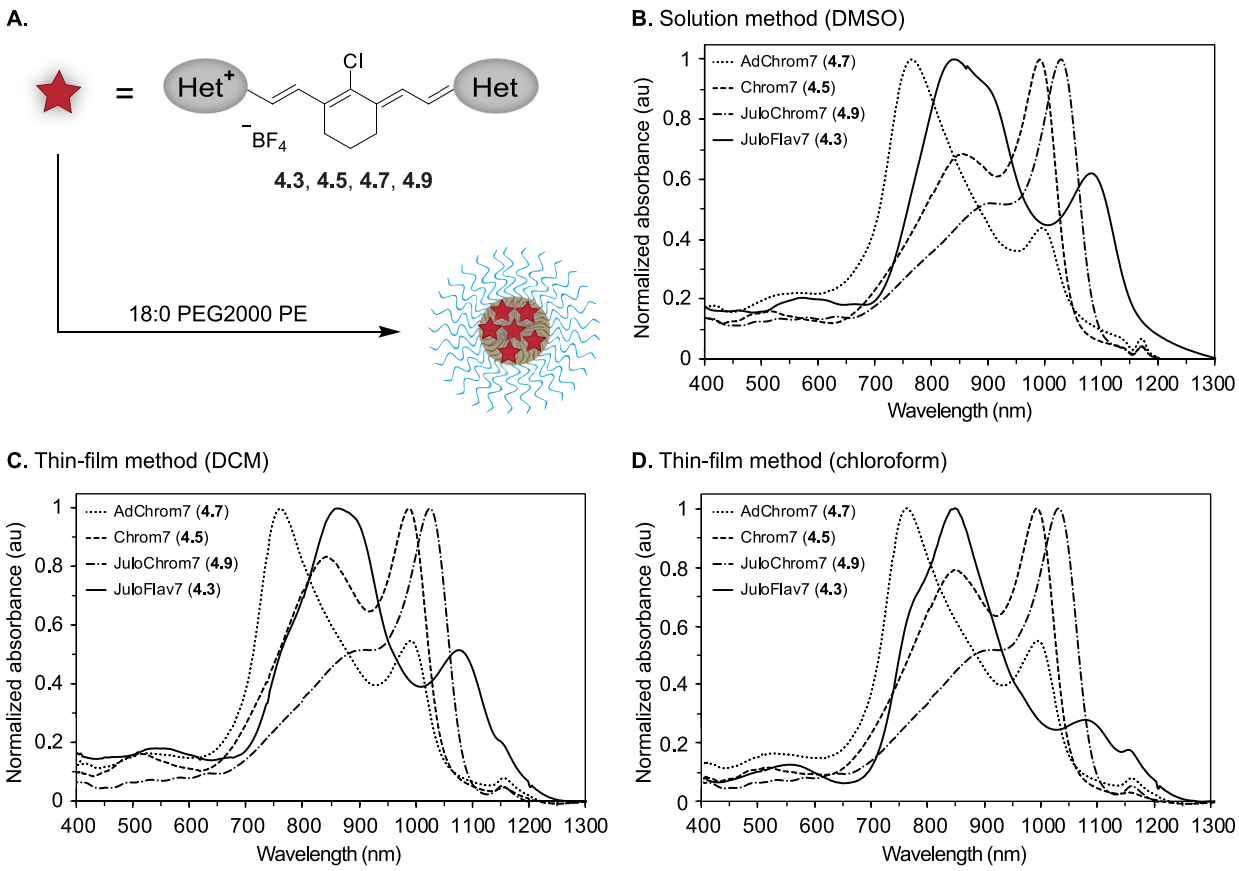

Figure 5.3 Normalized absorbance traces of PEG-phospholipid micelles composed of 18:0 PEG2000 lipids containing heptamethine flavylium or chromenylium dyes.

For the pentamethine dyes, overall less aggregate formation is observed upon micelle encapsulation compared to the heptamethine dyes, yet in this case both *t*-Bu and 1-Ad groups at the 2-position on the heterocycle improved the amount of monomer present compared to the flavylium dyes with a 2-position phenyl group (Figure 5.4). Note that although these data cannot be directly compared to the heptamethine micelle data in Figure 5.4, as amphiphiles with different length PEG chains were used, similar results are obtained by loading heptamethine dyes in both PEG2000 and PEG5000 containing lipids.

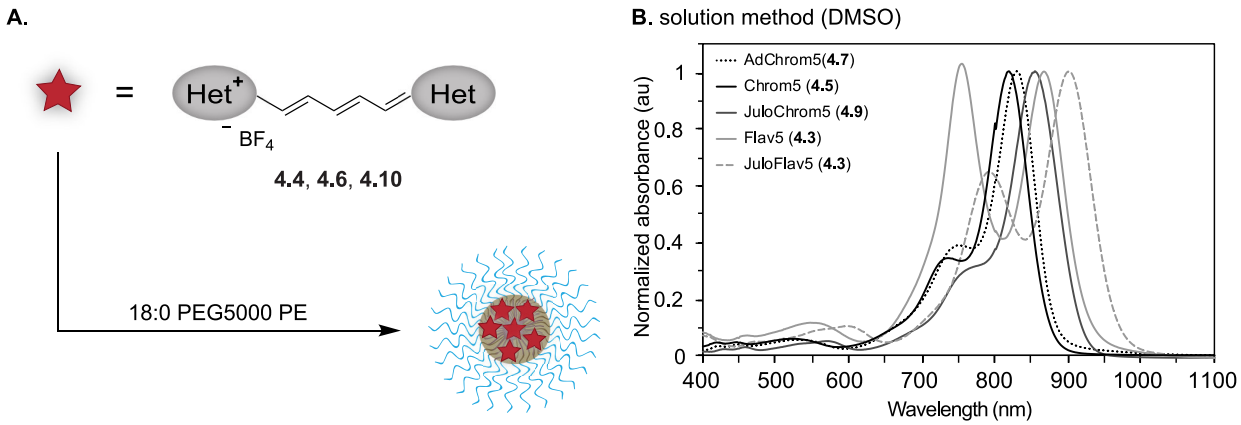

Figure 5.4 Normalized absorbance traces of PEG-phospholipid micelles composed of 18:0 PEG2000 lipids containing pentamethine flavylium or chromenylium dyes.

5.2.4 Exploring Weakly Coordinating Anions as Counterions for Flav7

As an alternate route to reduce aggregation upon nanoparticle encapsulation by increasing steric bulk, we also explored the use of large and weakly-coordinating counterions. Weakly coordinating anions and their effects on dye aggregation within nanoparticles has been studied extensively by Klymchenko and coworkers in rhodamine dyes[7–10] and cyanine dyes.[11–13] Further, alongside increasing molecular steric bulk, large anions have shown improvement for cyanine dye aggregation in thin films.[2,14] Additionally, anion exchange in polymethine dyes can produce diverse changes in molecular photophysical properties, such as absorption coefficient, quantum yield, and stokes shift.[12]

Three counterions of increasing size were chosen to exchange with the original tetrafluoroborate: tetraphenyl borate (TPB), tetrakis[3,5-bis(trifluoromethyl)phenyl]borate (F_{24}TPB) and tetrakis[3,5-bis(1,1,1,3,3,3-hexafluoro-2-methoxy-2-propyl)phenyl]borate (F_{48}TBP).[15] The three counterions have a molecular diameter of ~10.8 Å, for TPB, ~12.4 Å for F_{24}TPB, and ~16.0 Å for F_{48}TPB.[9] Counterion exchanges were performed by treating the tetrafluoroborate salt of Flav7 (Flav7·BF_4) with sodium salts of each counterion (Scheme 5.1).

Flav7·BF_4 was dissolved in DCM, and the counterion was either co-dissolved in DCM or dissolved in water and combined together with the DCM layer in a biphasic solution. The solution was then sonicated in a bath sonicator for 5 min to induce thorough mixing, washed with water, and purified via column chromatography. The resulting Flav salts, Flav7·TPB (**5.1**), Flav7·F_{24}TPB (**5.2**), and Flav7·F_{48}TPB (**5.3**) were characterized by ^{1}H NMR, ^{19}F NMR (compounds **5.2** and **5.3**) and ^{11}B NMR (compound **5.2**). Characterizing the photophysics of the salts, the $\lambda_{max,abs}$ in DCM was unchanged at 1027 nm for all variants. However, the absorption coefficients of the series in DCM varied between 180,000–283,000 $M^{-1}cm^{-1}$, with the lowest number corresponding to Flav7·TPB (**5.1**) and the highest to Flav7·F_{24}TPB (**5.2**) (Figure 5.5A-B).

Scheme 5.1 Counterion-exchange on Flav7.

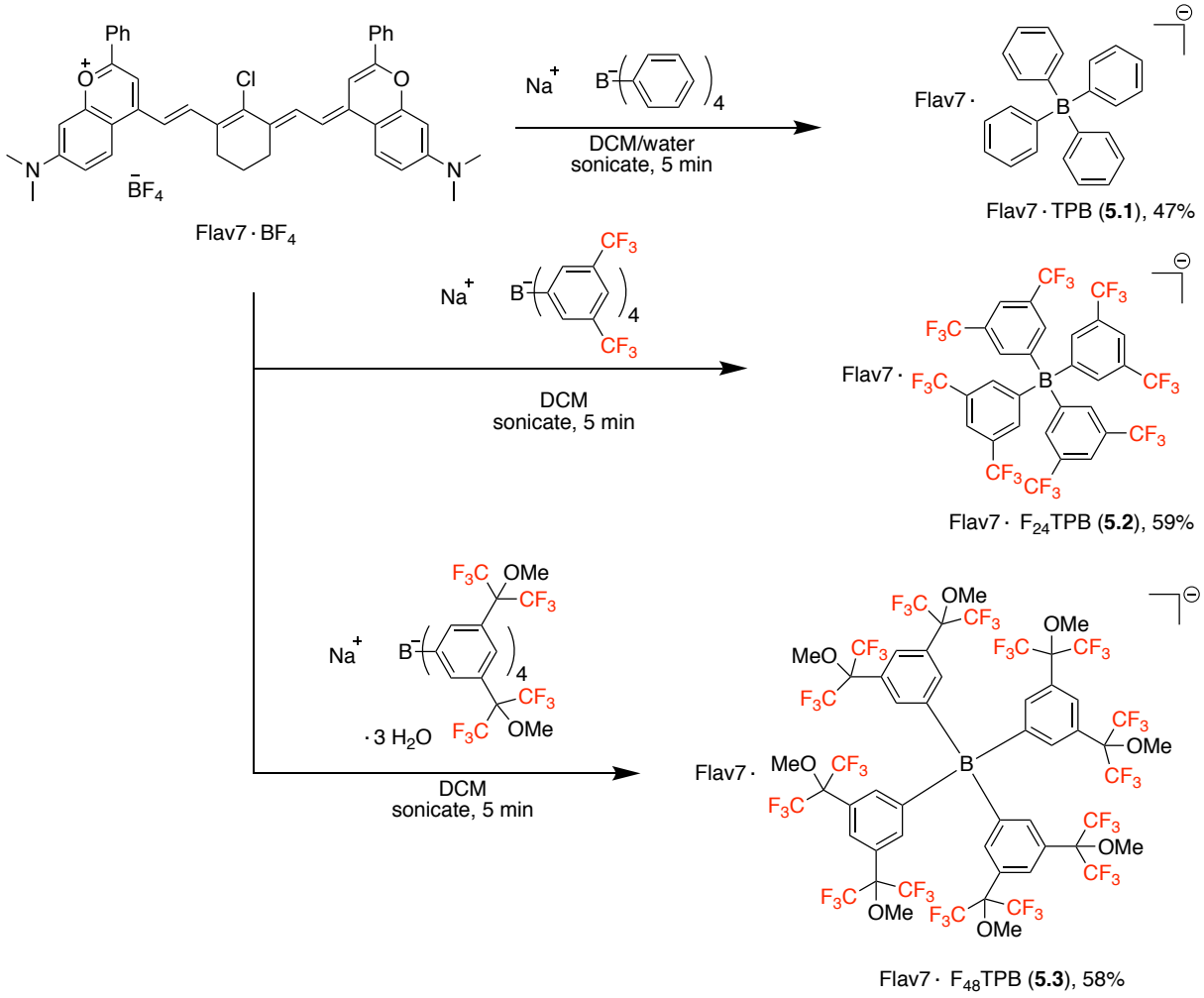

Upon micellar encapsulation with PEG2000 PE amphiphiles, the increasing counterion size trended to increase H-aggregation of Flav7, contrary to our initial hypothesis (Figure 5.5C–D). It is possible that the environment within relatively small micelles is limiting in volume, and the addition of large counterions further restricts the free volume available to dye species, further decreasing the amount of monomeric species present. With a clear trend related to counterion size, moving to smaller counterions, such as Cl^- and NO_3^- may have the opposite effect, but substantial improvement is not likely as BF_4^- is already quite small with a diameter of ~3.3 Å.[8] Sequestration in thin films, polymer matrices, or within larger nanoparticles such as PLGA nanoparticles[7,10], oil based emulsions, or in ion-associated nanoparticles[8] could allow for more volume for dyes and counterions to pack without aggregation, compared to the PEG-phospholipid micelles. Additionally, indication that weakly coordinating anions can decrease the ion pairing effect to favor the cyanine over a dipolar electronic structure in non-polar environments[16–17] prompts more solvent dependent studies on these dye–weakly coordinating anion pairs. With the limited solubility of Flav7 in nonpolar solvents, decoupling the effects of aggregation from electronic structure changes could be challenging. Its possible that to fully elucidate these effect, Flav7 derivatives with higher solubility in nonpolar solvents would be required. These studies, as well as investigation into the emissive behavior of the Flav7 counterion salt species are needed to fully understand the effects of large weakly-coordinating anions on the Flav7 scaffold.

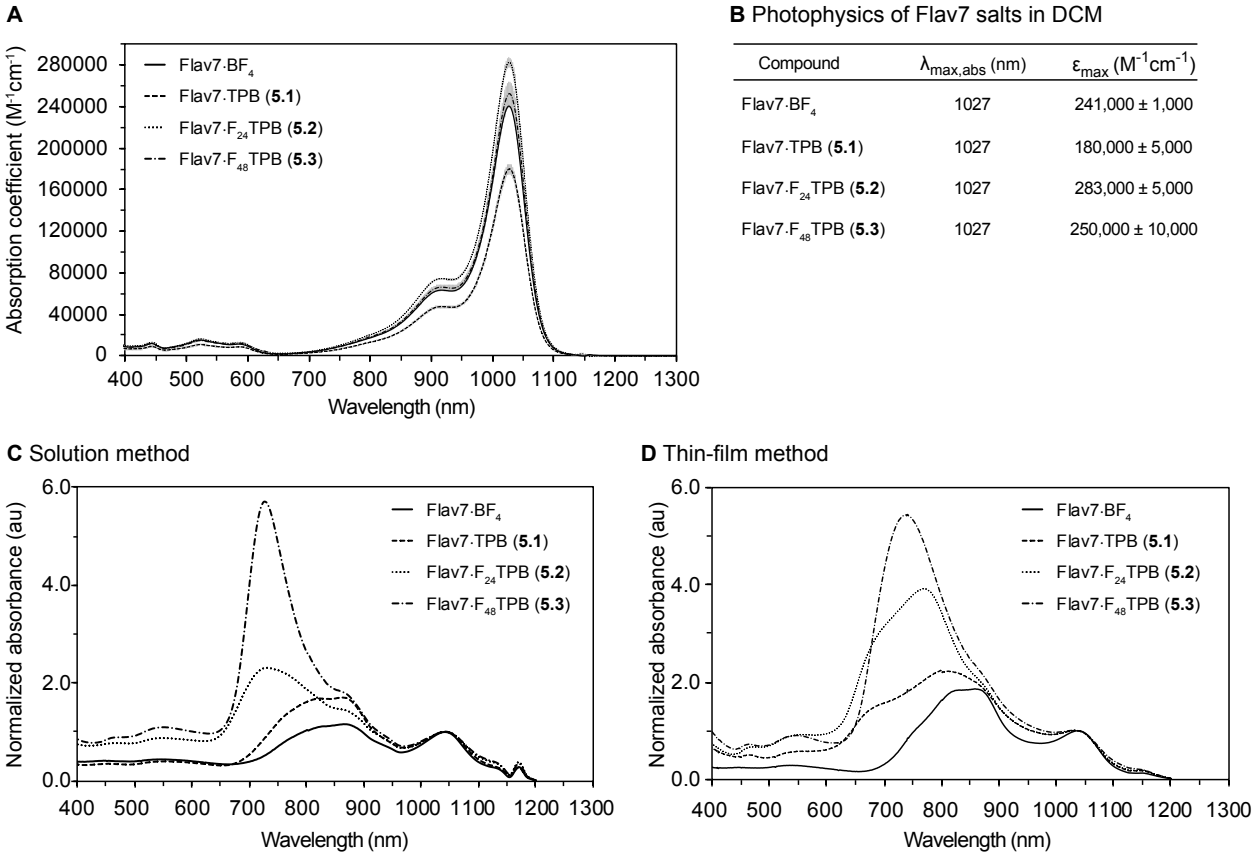

Figure 5.5 Photophysics of Flav7 salts with weakly coordinating anions. A) Absorption coefficient spectra in DCM. B) Table of photophysical values C) Normalized absorption spectra of PEG2000 PE micelles containing Flav7 salts, fabricated by a solution method. D) Normalized absorption spectra of PEG2000 PE micelles containing Flav7 salts, fabricated by a thin-film evaporation method.

With minimal success in all of the attempts to better solubilize the dyes within nanoparticles, we realized that covalent modifications to alter the solubility behavior of the flavylium and chromenylium dyes could be a more promising approach to improve the efficiency of biological delivery. The remainder of this chapter is devoted to covalent dye modifications intended to alter the dye solubility and offer possibilities of diverse strategies for delivery into biological environments.

5.3. SWIR Imaging with a Fluorous Soluble Dye in Perfluorocarbon Nanoemulsions

5.3.1 Background

Biological delivery using nanoparticles with a hydrophobic or aqueous core, including micelles, liposomes, and oil-based emulsions aids in solubilization of organic cargo, and offers opportunities for targeting to a site of interest with increased avidity compared to a single molecule. Importantly, the nanoparticle gives the cargo increased protection from reactive biological species until it reaches the target location. However, nanomaterials with an aqueous or organic core can readily interact with biological species in either aqueous (extracellular space, cytosol) or organic (lipid membranes) environments, which can limit the stability and selectivity of the cargo delivery. In contrast, perfluorocarbon nanoemulsions, droplets of perfluorocarbon-in-water stabilized by surfactant, offer a delivery strategy with a vehicle that is orthogonal to the molecules and liquid phases found in biology. Perfluorocarbons (PFCs), molecules containing sp^3 C–F bonds instead of the sp^3 C–H bonds found in organic molecules, will separate entirely from aqueous and organic phases, forming a separate fluorous phase. This behavior is primarily due to the large size and high electronegativity of fluorine atoms and the resulting low polarizability of perfluorocarbons.[18] The clinical applicability of PFC nanoemulsions is reinforced by Fluosol-DA, a previously FDA-approved PFC nanoemulsion formulation for oxygen delivery.[19] PFC nanoemulsions have been widely employed as imaging agents in mammalian model organisms, specifically in ^{19}F-MRI[20–22] and ultrasound experiments.[23–25] In contrast, the application of PFC nanoemulsions to *in vivo* optical imaging is minimally explored, and is often performed in combination with ^{19}F-MRI.[26–30] This lack of optical imaging experiments in animals is likely due to the challenges associated with encapsulating fluorophores within the fluorous phase. Prior and concurrent work in the Sletten group has focused on developing fluorous-soluble optical tools including

photosensitizers[31–32] and dyes within the visible[33–34] and NIR[35] regions which can be successfully encapsulated and delivered within PFC nanoemulsions. Imaging and phototherapy experiments with the fluorous-soluble tools have been performed in mammalian cells[26–27,36–37] and in zebrafish.[30] Fluorous optical tools which absorb and emit longer wavelengths of light could successfully extend these experiments to applications in mice. Here, we pursue this challenge by targeting a fluorous-soluble flavylium heptamethine dye with shortwave infrared (SWIR) absorption and emission. We hypothesized that, in addition to enabling optical detection of perfluorocarbons in mammalian model organisms, the rigidity of perfluorocarbons, as well as isolation from C-H bonds, which are a large source of vibrational quenching for molecules in the SWIR,[38] could generate SWIR contrast agents with superior brightness.

5.3.2 Design and Synthesis of a Fluorous Flavylium Heptamethine Dye

Fluorous solubility is often imparted by molecules that have a high wt-% fluorine (>60%).[39] In addition, increased solubility is observed for branched fluorous groups, as well as molecules which have fluoroalkyl chains appended to several different locations.[40] With these parameters in mind and knowledge of existing perfluoroalkylated starting materials, we chose compound **5.4** as a synthetic target. We envisioned that **5.4**, a flavylium heptamethine dye with fluoroalkyl chains appended to the 7-amino group, could be synthesized by an analogous route to that used in Chapter 3 (Scheme 5.2). Initially, following route 1, alkylation of 3-aminophenol was achieved in good agreement with the literature.[33] The Mentzer-pyrone reaction between aminophenol **5.4** and ethyl benzoyl acetate proceeded in moderate yield, but difficulties in separating product **5.5** from reaction by-products with similar retention times on silica gel chromatography prompted direct alkylation of 7-aminoflavone in a second route. In route 2,

alkylation could be obtained in moderate yields using excess sodium hydride and heat, and allowed for more facile purification. A Grignard reaction on the flavone efficiently produced the flavylium **5.6** in 83% yield. Finally, the fluoroalkylated heptamethine dye **5.8** (named F_{68}Flav7, for the number of fluorine atoms contained in the molecule) was obtained in good yield by reacting flavylium **5.6** with the relevant pentamethine imine-enamine linker **5.7** using 2,6-di-*tert*-butyl-4-methylpyridine in DMF. To note, due to the low solubility of flavylium **5.6** in many organic solvents, including those typically used for polymethine dye formation, such as *n*-butanol and toluene, and instability in heated, basic acetic anhydride, DMF was necessary to solubilize **5.6** and produce significant and selective conversion to the heptamethine dye.

Scheme 5.2 Synthesis of a fluoroalkylated 7-amino flavylium heptamethine dye **5.8**.

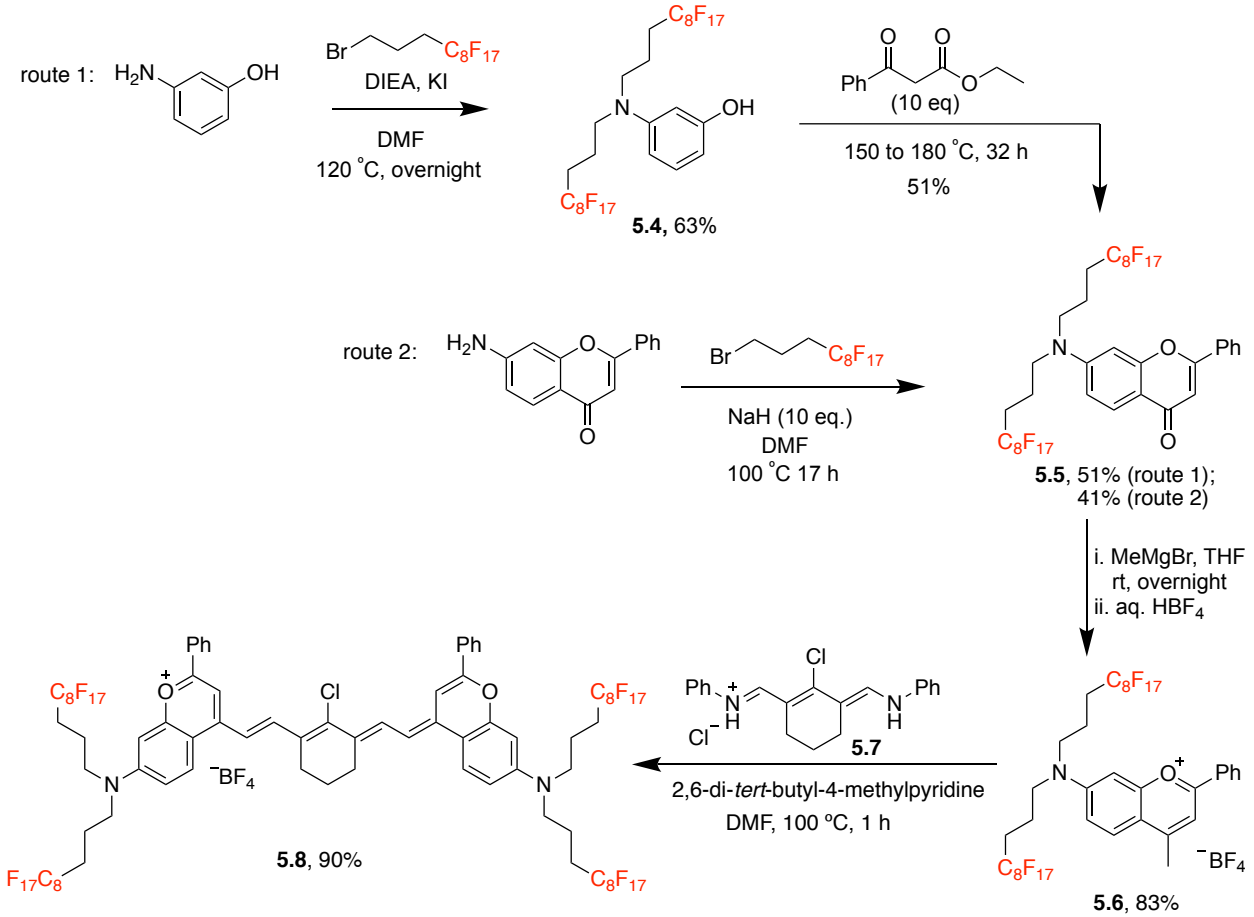

5.3.3 Photophysical Characterization and Perfluorocarbon Solubility

Upon characterizing the photophysics of the heptamethine dye **5.8** in DCM, we found that the behavior was similar, yet slightly blue shifted (~5 nm) from the original, non-fluorinated dye, Flav7, with $\lambda_{max,abs}$ = 1022 nm, $\lambda_{max,em}$ = 1044 nm and Φ_F = 0.73% (Figure 5.6A–B). Moving to characterize the photophysics of **5.8** in other organic, fluorinated or fluorous solvents, we encountered challenges in solubilizing the dye. We observed low and no solubility in the organic solvents acetone and DMSO, respectively, and very minimal and no solubility in the fluorous, polar solvents perfluorooctyl bromide (PFOB) and perfluorotripropylamine (PFTPA), respectively (Figure 5.6C). The dye was unstable in the more polar hexafluroisopropanol (HFIPA), but we were able to observe some solubility in the partially fluorinated solvent, nonafluorobutyl methyl ether (HFE-7100). In HFE-7100, significant H-aggregation occurred in the absorption spectrum, with a $\lambda_{max,abs}$ = 727 nm, but some monomer could be observed as a long wavelength shoulder. Excitation at the shoulder (900 nm) resulted in emission at $\lambda_{max,em}$ = 1011 nm, which is ~30 nm blue shifted from the absorption maximum of **5.8** in DCM.

A Absorption and emission traces of F_{68}Flav7·BF_4 (**5.8**)

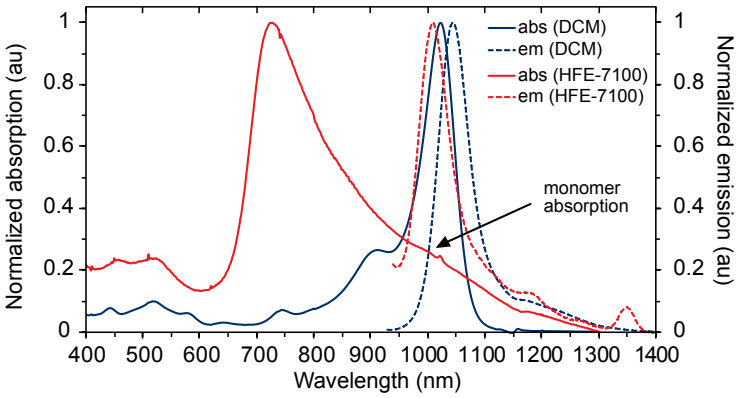

B Photophysics of F_{68}Flav7·BF_4 (**5.8**)

Solvent	$\lambda_{max,abs}$ (nm)	$\lambda_{max,em}$ (nm)	Φ_F (%)
DCM	1022	1044 (ex. 890 nm)	0.73 ± 0.04
HFE-7100	727	1011 (ex. 900 nm)	–

C Solubility of F_{68}Flav7·BF_4 (**5.8**)

Solvent	Solubility	Solvent	Solubility
DCM	high	HFE-7100	low
acetone	low	HFIPA	unstable
DMSO	none	PFOB	none
		PFTPA	none

Figure 5.6 Photophysical properties of heptamethine dye F_{68}Flav7 (**5.8**). A) Absorption and emission spectra of **5.8**. Excitation = 890 nm (DCM); excitation = 900 nm (HFE-7100). B–C) Photophysical properties (B) and solubility observations (C) of **5.8** in various organic and fluorinated solvents.

To enable solubility in perfluorocarbons, we hypothesized that exchanging the $^{-}BF_4$ counterion for one with higher fluorous content could help increase the amount of fluorous character of the resulting salt. We screened a variety of counterions containing CF_3 and fluoroalkyl groups. The counterions tested (Scheme 5.3) include trifluoroacetate (TFA), perfluorooctanoic acetate (PFOA acetate), two of the TPB counterions used in Section 5.1, F_{24}TPB and F_{48}TPB, as well as the more highly fluorinated TPB derivative **5.13**,[41] which we will refer to here as F_{104}TPB. The Gladysz group (Texas A&M) previously optimized the synthesis of this compound[42], and kindly provided it to us for testing. The counterion exchanges were performed by mixing or sonicating an aqueous solution of counterion with a solution of F_{68}Flav7·BF_4 (**5.8**) in DCM (**5.9**, **5.10**, **5.11**) or by co-dissolving dye and counterion salts in DCM (**5.12**) or HFE-7100 (**5.14**) and washing with water.

Scheme 5.3 Counterion exchange on F_{68}Flav7 (**5.8**).

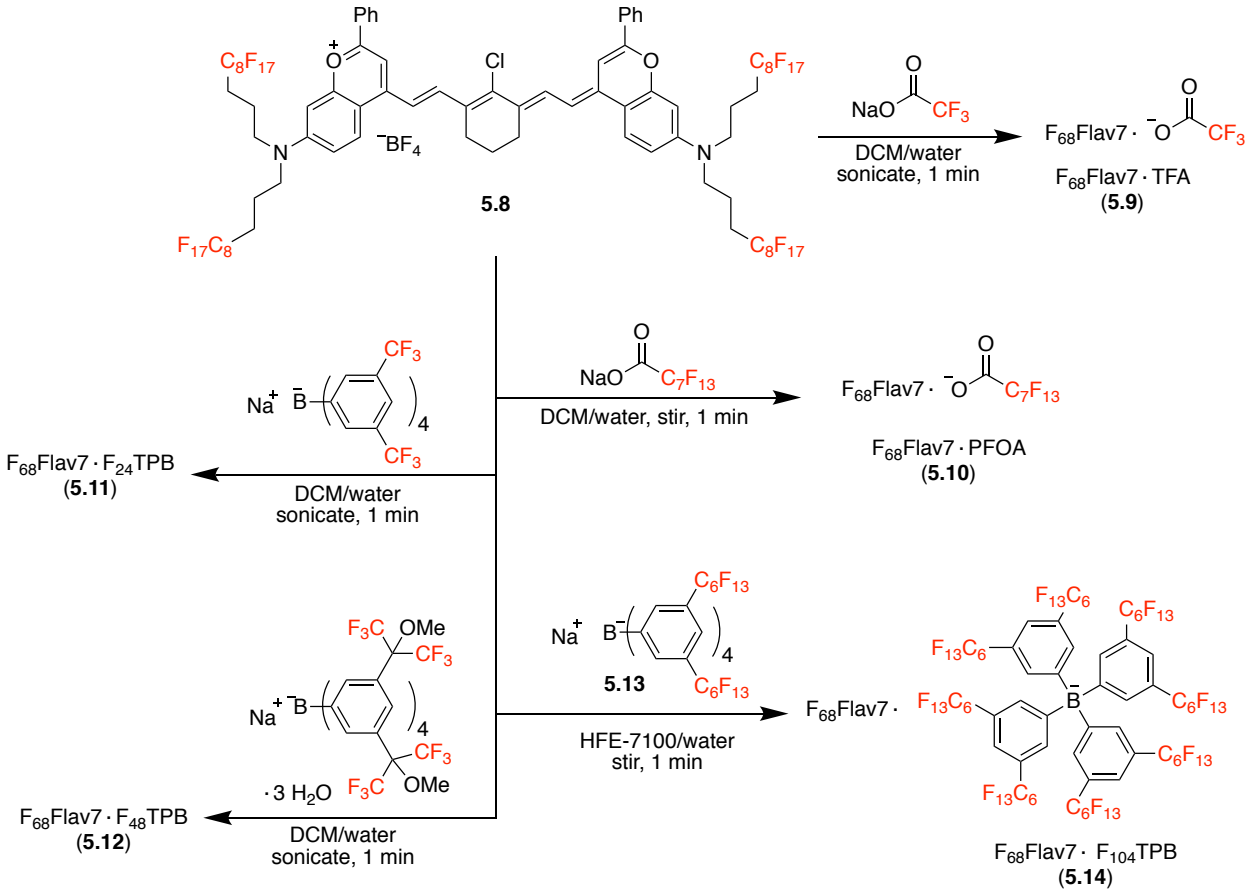

In a photophysics screen, we observed absorption and emission of the F_{68}Flav7 fluorinated salts **5.9**, **5.10**, and **5.11** in HFE-7100 (Figure 5.7A–B). The TFA counterion in F_{68}Flav7·TFA (**5.9**) worsened the H-aggregation and solubility in HFE-7100 compared to **5.8**, with a more blue-shifted H-aggregate peak now visible at 649 nm and displays only minimal emission. The PFOA counterion produced a dye, F_{68}Flav7·PFOA (**5.10**), which displayed similar H-aggregation in HFE-7100 to **5.8**, but for which a monomer absorption peak could be visualized at 992 nm in addition to the H-aggregate peak at 726 nm. In contrast, good solubility in HFE-7100 is obtained with F_{68}Flav7·F_{24}TPB (**5.11**), with the $\lambda_{max,abs}$ = 994 nm and $\lambda_{max,em}$ = 1014 nm (Figure 5.7D). Despite solubility in the partially fluorinated solvent HFE-7100, stable PFC nanoemulsions could not be obtained with this solvent due to its low boiling point (60 ºC). Thus, fluorous solubility needed to

be increased further to enable the use of higher boiling perfluorocarbon, such as PFOB. The absorption and emission spectra in PFOB were observed for the dye salts with more highly fluorinated counterions, **5.12** and **5.14** (Figure 5.7C). While dye **5.12** displays monomer absorption in addition to a large H-aggregate peak, dye **5.14** displays solely monomer behavior in PFOB.[43] From these spectral data of the counterion salts of F_{68}Flav7, we learned that while some improvement in solubility was observed for the salts with an increasing number of CF_3 groups, namely **5.11** and **5.12**, the counterions that did not substantially increase the wt% fluorine were insufficient. It was not until we moved to the F_{104}TPB counterion which increased the wt% fluorine to 66% that we were able to obtain solubility in an entirely fluorous solvent.

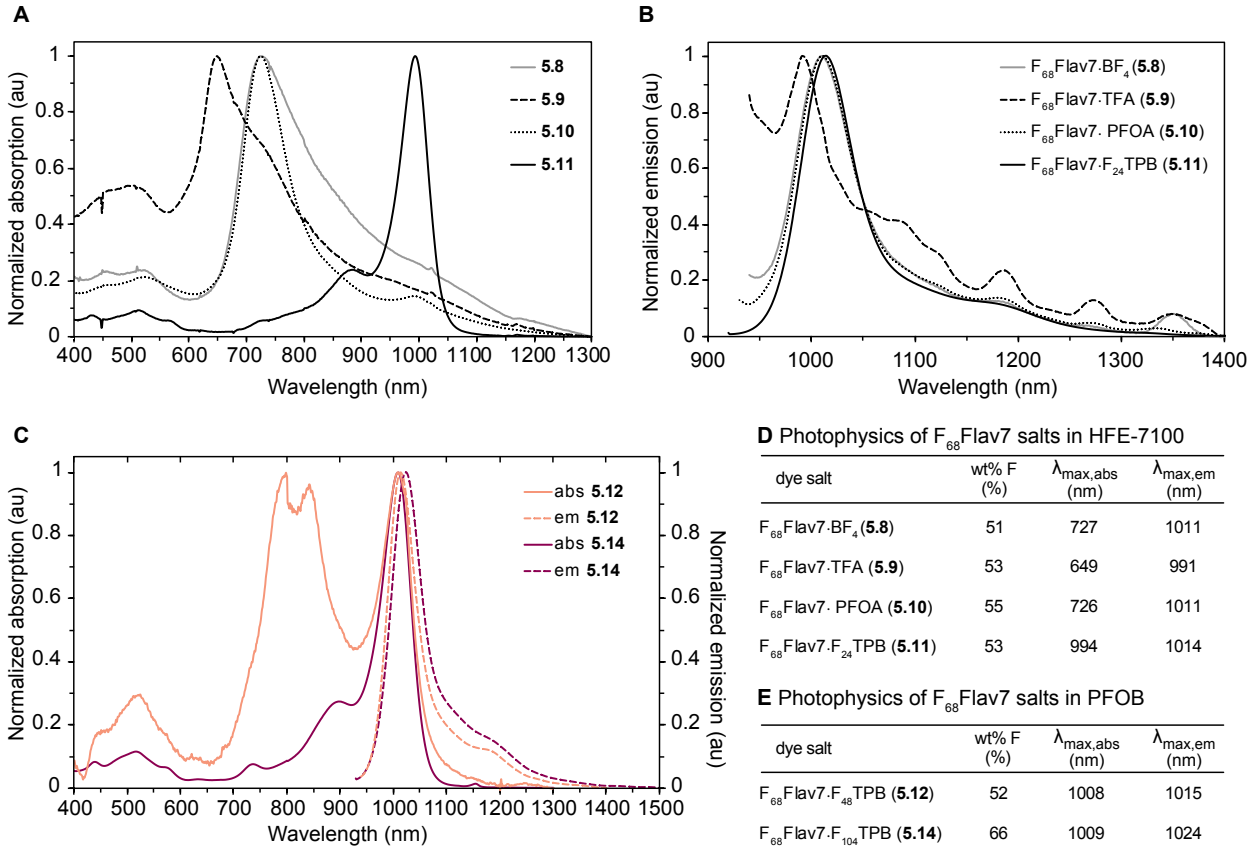

D Photophysics of F_{68}Flav7 salts in HFE-7100

dye salt	wt% F (%)	$\lambda_{max,abs}$ (nm)	$\lambda_{max,em}$ (nm)
F_{68}Flav7·BF_4 (**5.8**)	51	727	1011
F_{68}Flav7·TFA (**5.9**)	53	649	991
F_{68}Flav7· PFOA (**5.10**)	55	726	1011
F_{68}Flav7·F_{24}TPB (**5.11**)	53	994	1014

E Photophysics of F_{68}Flav7 salts in PFOB

dye salt	wt% F (%)	$\lambda_{max,abs}$ (nm)	$\lambda_{max,em}$ (nm)
F_{68}Flav7·F_{48}TPB (**5.12**)	52	1008	1015
F_{68}Flav7·F_{104}TPB (**5.14**)	66	1009	1024

Figure 5.7 Photophysics of F_{68}Flav7 salts. A–B) Absorption (A) and emission (B) traces of F_{68}Flav7 salts in HFE-7100. C) Absorption and emission traces of F_{68}Flav7 salts in PFOB. D–E) Table of photophysical measurements for F_{68}Flav7 salts in HFE-7100 (D) and in PFOB (D).

5.3.4 SWIR Imaging with Perfluorocarbon Nanoemulsions

With solubility obtained in PFOB with **5.14**, PFC emulsions were fabricated with **5.14** using Pluronic F-68 or poly(2-oxazoline) (POx) amphiphiles (Figure 5.8A–B). The alkyne-containing POx amphiphile **5.15** developed by Estabrook *et al*.[31] offers a functionalizable handle on the surface of the emulsions for modification with vitamins, peptides, or small-molecule targeting agents to control biodistribution. Initial experiments screening dye loading in PFC emulsions with Pluronic F-68 revealed that although **5.14** appears to be soluble in PFOB at spectroscopy-relevant concentrations (μM range), significant aggregation occurs upon encapsulation in the emulsions, in which dye is solubilized in perfluorocarbon at the mM concentration range (Figure 5.8C). In the absorption traces for at all concentrations tested, between 0.77–3.1 mM, a large H-aggregation peak is visible at ~804 nm.[44] Other parameters which remain to be explored beyond concentration could also be playing roles here, such as the amphiphilic nature of the fluorous ions or interactions with the surfactant.

Despite the aggregation observed, we moved forward to test the performance of the SWIR PFC nanoemulsions *in vivo*, using dye **5.14** inside emulsions stabilized with POx **5.15**. Emulsions with dye at 1.6 mM enabled a total of 34 nmol of **5.14** to be contained within a 190 μL volume for delivery. The SWIR-fluorescent emulsions were injected into the tail vein, and subsequently, the head (Figure 5.8D) and the hindlimb (Figure 5.8E) of the mouse and were immediately imaged using 968 nm excitation and collecting with 1100 nm longpass filtering. While high-resolution images were obtained upon injection, exposure times were limited to 60–120 ms, and imaging speeds to 8–16 fps. The moderate brightness is likely due to the aggregation within the PCF nanoemulsions. For targeted experiments, it will be necessary to image at later time points, to allow for accumulation at a site(s) of interest and clearance from the non-targeted areas. Thus, high

brightness is an essential characteristics of a targeted imaging agent. While these studies produced a promising initial result, the difficulties in formulating and delivering the F_{68}Flav7 dye in PFC nanoemulsions prompted us pause imaging experiments at this point, and re-evaluate the dye structure before pursuing targeted imaging experiments.

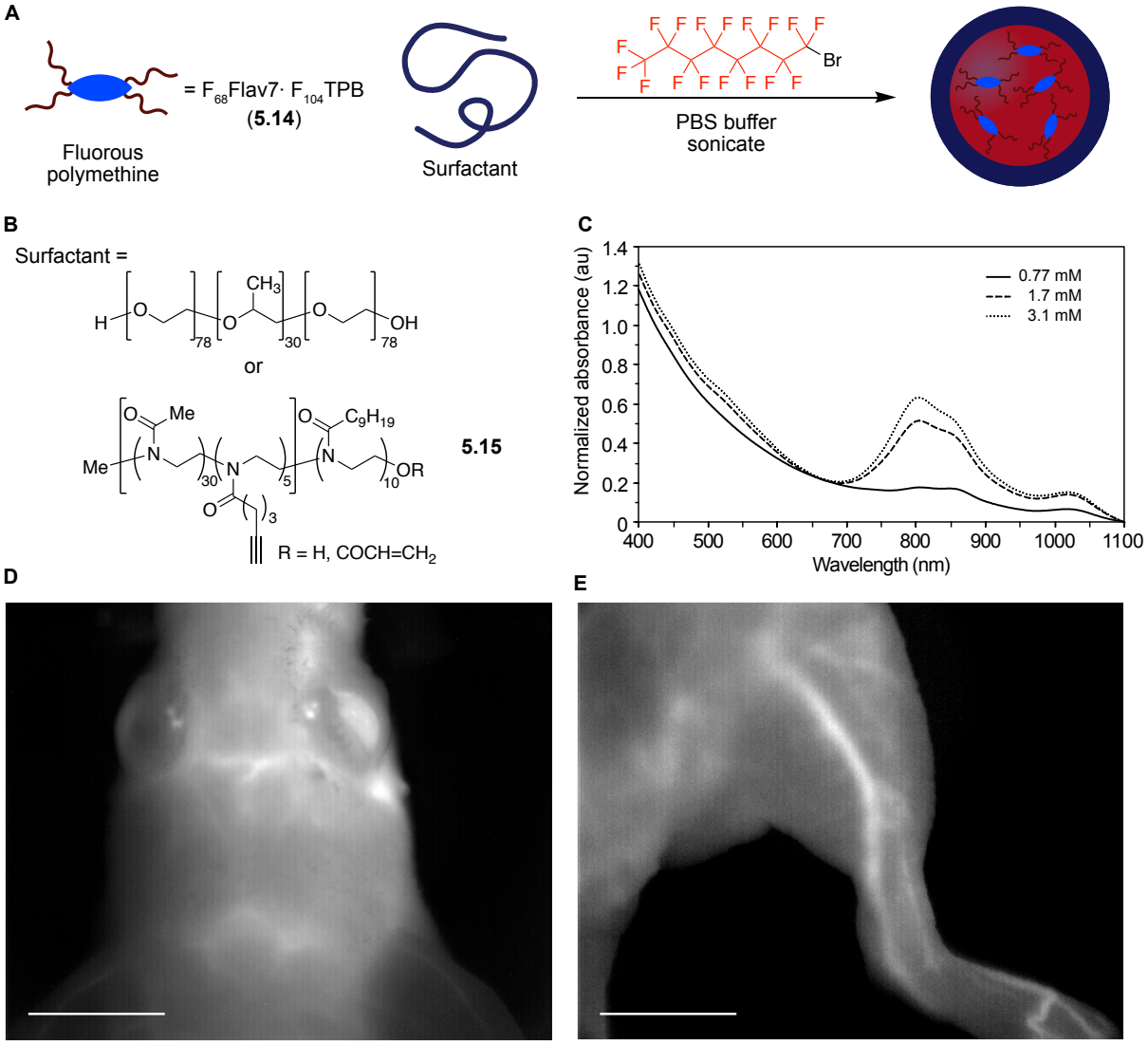

Figure 5.8 PFC nanoemulsion formation and in vivo imaging with F_{68}Flav7·F_{104}TPB (**5.14**). A) PFC nanoemulsion fabrication scheme. B) Structures of the surfactants used to stabilize the PFC nanoemulsions. C) Absorption spectra of Pluronic F-68-stabilized PFC nanoemulsions containing **5.14**. D–E) *In vivo* imaging of the mouse head (D) and hindlimb (E) with PFC emulsions containing emulsions of **5.14** (34 nmol of dye) immediately after tail vein injection. Acquisition

settings: excitation wavelength: 968 nm (100 $mWcm^{-2}$), collection with 1100 nm longpass, exposure time = 60 ms, 16.6 fps (D); exposure time = 120 ms, 8.3 fps (E). Scale bar = 1 cm.

5.3.5 Outlook for Fluorous Soluble Flavylium or Chromenylium Dyes

Ultimately, we concluded that the F_{68}Flav7 dye is not soluble enough in fluorous solvent to render it a useful dye for studying perfluorocarbons *in vivo*, particularly for targeted imaging experiments. Strategies towards other derivatives are now en route by others in the lab. Specifically, chromenylium derivatives, which are both brighter than the flavylium counterparts, and include derivatives which have shown decreased aggregation in nanomaterials with a hydrophobic core, could be a more promising scaffold from which to build a fluorous dye. Additionally, it could be advantageous to have additional fluorination locations on the dye scaffold, such as at the C2 or C4' locations on the dye. Lim *et al.* have demonstrated increased fluorous solubility of indolenine cyanine dyes with the presence of three fluoroalkyl chains on each heterocycle.[35] Concurrent studies on fluoroalkylated cyanine dyes which aims to decipher structure-property relationships between the location and amount of fluoroalkyl chains on fluorous solubility should be highly useful for providing similar insights into the behavior of the flavylium scaffold. Nevertheless, as we were able to show here, counterion exchange with fluorine-containing counterions, particularly with the F_{104}TPB (**5.13**) is a promising route to significantly increase fluorous solubility of the dye. I began early work to pursue these aims by targeting a chromenylium dye with a 2-trifluoromethyl substituent. The initial target molecule, **5.16** (Scheme 5.4), focused on installing the 2-CF_3 modification, and excluded the fluoroalkyl chain modifications at the 7-amino position that we envisioned would be employed for a fluorous soluble dye. The proposed synthesis began with a Kostanecki-Robinson reaction of 2',4'-dihydroxyacetophenone and trifluoroacetic anhydride to obtain the 2-trifluoromethyl substituted

7-hydroxyflavone **5.16**.[45] The hydroxyl group in **5.16** was converted to the triflate **5.17** by treatment with trifluoromethanesulfonic anhydride in pyridine. Initial attempts at Buchwald-Hartwig coupling reactions with dimethyl amine were unsuccessful, however a more recent methodology study of coupling reactions on molecule **5.17** offers a more promising starting point.[46]

Scheme 5.4 Progress towards 2-CF_3 chromenylium dyes.

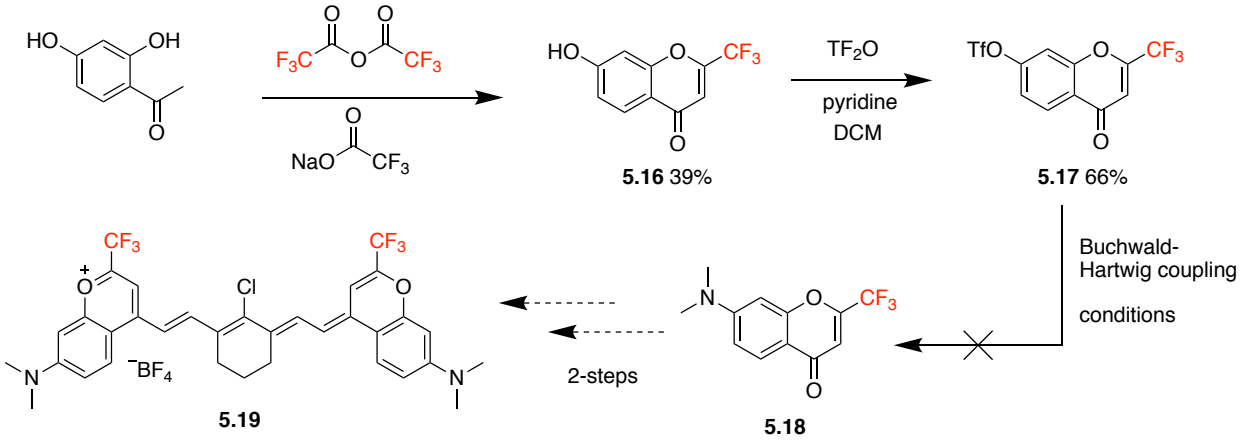

An alternate attempt to arrive at flavone **5.18**, using the analogous "Mentzer-pyrone" conditions did not produce the desired product but instead selectively furnished the coumarin isomer **5.20** in high yield (Scheme 5.5). This transformation was previously observed using a $ZnCl_2$ catalyst,[47] but has not been reported neat and without the use of catalyst.

Scheme 5.5 Synthesis of a CF_3-substituted coumarin.

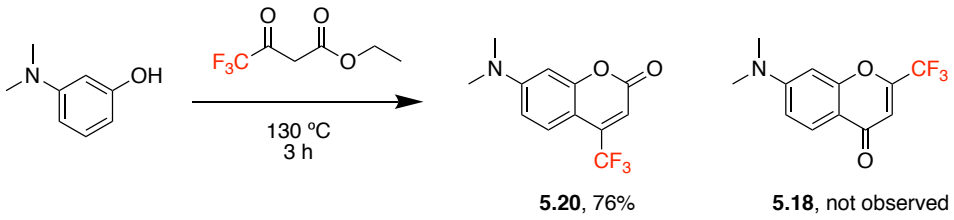

Overall, upon further optimization of the flavylium or chromenylium dye structure to increase solubility in perfluorocarbons, reduce H-aggregation, and increase dye loading within PFC emulsions, the material should offer a bright and orthogonal system for *in vivo* experiments.

This optimization should include targeting molecules with shorter fluoroalkyl chain (C_6F_{13}) or smaller, to reduce bioaccumulation. Alongside current complementary work in the Sletten lab to optimize the stabilization, surface functionalization, delivery, and disassembly of PFC emulsions, the ability to efficiently label the perfluorocarbons with SWIR-emitting fluorophores will enable diverse imaging, phototherapy, and theranostic applications of this bioorthogonal delivery vessel in mammalian model organisms.

5.4 Synthesis of Lipophilic Chromenylium Polymethine Dyes

Lipophilic chromophores are a staple in optical microscopy and spectroscopy experiments to study biological membrane structure and composition,[48] diffusion dynamics,[49–51] tension,[52–53] polarization,[54] as well as for tracking lipid droplets,[55] and lipoproteins.[56] A wide variety of chromophore structures have been utilized for these experiments, and with a key focus on environmentally sensitive structures.[57] However, commonly employed dyes for these experiments absorb and emit VIS and NIR light while longer wavelength lipophilic chromophores optimized for SWIR absorption and emission have yet to be reported. We envisioned that lipophilic chromenylium polymethine dyes could have applications in labelling lipoproteins, lipids, and membranes *in vivo*, as well as offer improved loading in lipophilic nanomaterial environments. As an initial structure to test and explore its properties in lipophilic environments, we targeted a 7-amino chromenylium heterocycle **5.23**, with two C-12 alkyl chains appended to the amine, and envisioned that the penta- and heptamethine dyes synthesized from this heterocycle could be used in SWIR imaging experiments at 785 nm and 980 nm excitation, respectively. The synthesis of the polymethine dyes followed a similar route as the perfluoroalkyl dyes in section 5.2, beginning with alkylation of 3-aminophenol to yield aminophenol **5.21** (Scheme 5.6).[Error! Bookmark not defined.] The

chromone **5.22** was obtained in moderate yield through a Mentzer pyrone reaction of **5.21** with ethyl pivaloylacetate. Addition of a methyl nucleophile and dehydration transformed chromone **5.22** to chromenylium **5.23** quantitatively. The lipophilic pentamethine dye **5.25** (named lipo-Chrom5) was produced in good yield through reaction of **5.23** with the relevant polymethine chains **5.24** with sodium acetate in acetic anhydride. Finally, the heptamethine dye **5.26** (named lipo-Chrom7) was accessed from chromenylium **5.23** and the polymethine chain **5.7** by reaction using the sterically hindered base, 2,6-di-*tert*-butyl-4-methylpyridine in *n*-butanol and toluene. It is possible that further optimization of this reaction solvent could improve the efficiency of the transformation to **5.26**.

Scheme 5.6. Synthesis of lipophilic chromenylium penta- and heptamethine derivatives.

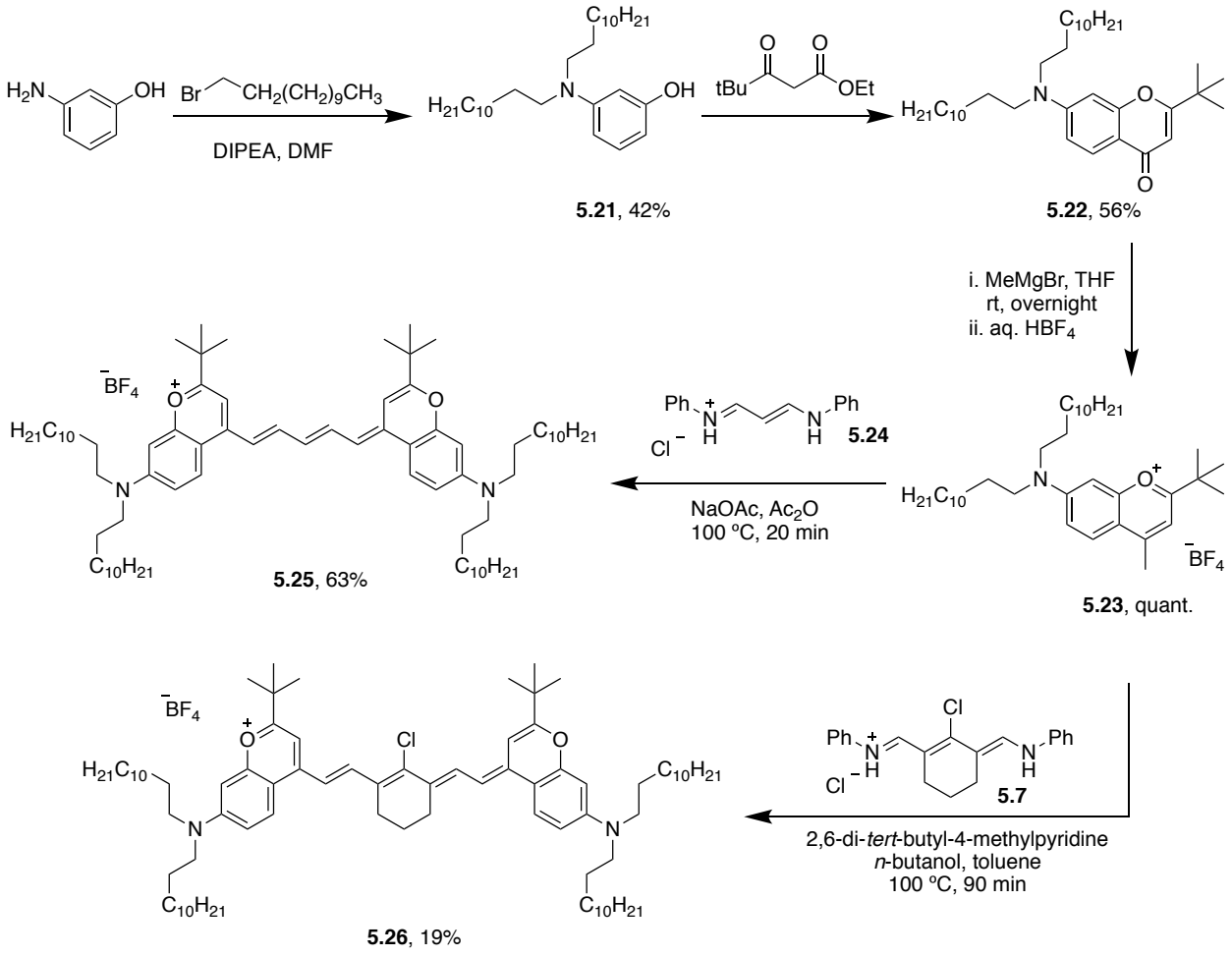

We oberserved absorption and emission properties of lipo-Chrom5 (**5.25**) and lipo-Chrom7 (**5.26**) in DCM and 1-octanol, a solvent commonly used to mimic the environment of lipid membranes (Figure 5.9A–B). Lipo-Chrom5 (**5.25**) has a $\lambda_{max,abs}$ = 830 nm $\lambda_{max,em}$ = 849 nm in DCM, while in 1-octanol, these values are blue-shifted by ~4 nm. Lipo-Chrom7 (**5.26**) has a $\lambda_{max,abs}$ = 988 nm $\lambda_{max,em}$ = 1003 nm in DCM, but instead displays slightly red-shifted values in 1-octanol (Figure 5.9C). Additionally, we examined the solvatochromic behavior of the absorbance spectra of lipo-Chrom5 (**5.25**) at 5 μM in a variety of solvents with different dielectric constants (Figure 5.9D–F). In the most non-polar solvents, hexanes and cyclohexane, lowered absorption intensity is observed. The highest absorption intensities are observed for the moderately non-polar solvents tolene and diethyl ether, indicating that these solvent environements are most favorable for **5.25**. In more polar solvents, intensities decreased again, with moderate intensities for all of the long chain alcohols and lowered intensity for the most polar solvents tested, MeCN and DMSO. Additionally, **5.25** generally displayed positive solvatochromism in the more non-polar solvents, (hexanes to chloroform), while negative solvatochromism was observed in the more polar solvents (DCM to MeCN). These experiments give some initial insight into the solvent behavior of the lipophilic chromenylium dyes. Further work is needed to understand the solubility of **5.25** and **5.26** in natural and unnatural lipid environments, including the labelling of lipophilic biological structures such as membranes and lipoporoteins.

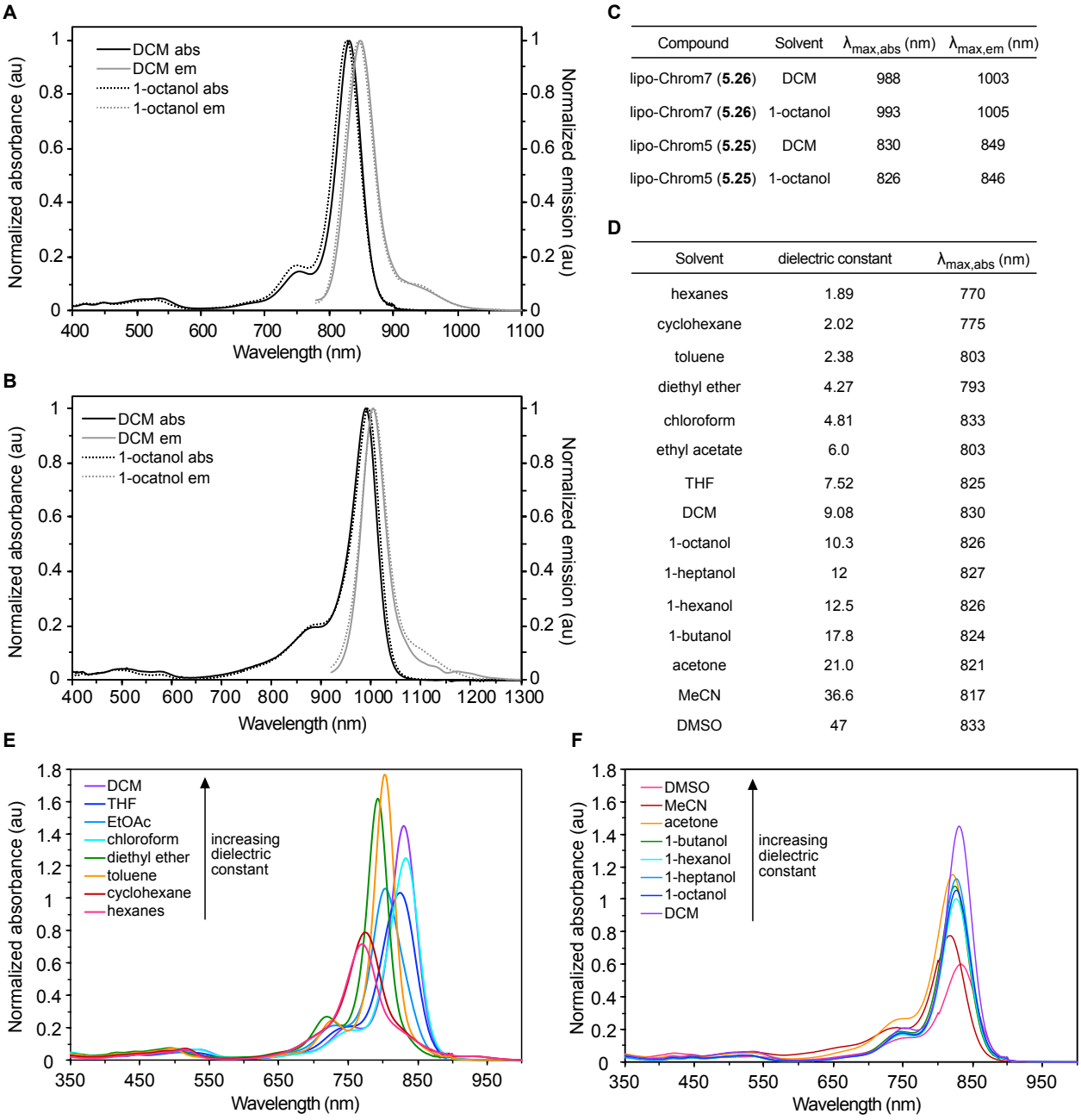

C

Compound	Solvent	$\lambda_{max,abs}$ (nm)	$\lambda_{max,em}$ (nm)
lipo-Chrom7 (**5.26**)	DCM	988	1003
lipo-Chrom7 (**5.26**)	1-octanol	993	1005
lipo-Chrom5 (**5.25**)	DCM	830	849
lipo-Chrom5 (**5.25**)	1-octanol	826	846

D

Solvent	dielectric constant	$\lambda_{max,abs}$ (nm)
hexanes	1.89	770
cyclohexane	2.02	775
toluene	2.38	803
diethyl ether	4.27	793
chloroform	4.81	833
ethyl acetate	6.0	803
THF	7.52	825
DCM	9.08	830
1-octanol	10.3	826
1-heptanol	12	827
1-hexanol	12.5	826
1-butanol	17.8	824
acetone	21.0	821
MeCN	36.6	817
DMSO	47	833

Figure 5.9 Photophysical properties of lipophilic polymethine dyes in different solvents. A–B) Absorbance (black) and emission (grey) traces of **5.25** (A) and **5.26** (B) in DCM (solid) and 1-octanol (dotted). Excitation wavelengths were 755 nm for (A) and 885 nm for (B). C) Table of absorption and emission wavelengths observed in (A–B). D) Table of absorption wavelengths for **5.25** in solvents with a range of dielectric constants. E–F) Absorbance of **5.25** at 5 μM in solvents of different dielectric constants. The more non-polar solvents are displayed in (E) and the more polar solvents are displayed in (F).

5.5 Progress towards Sulfonated Flavylium Heptamethine Dyes

Regardless of the success of nanomaterials for delivery of SWIR fluorophores, ultimately, acquisition of water-soluble derivatives will open a new realm of applications and experiments which can be performed in animals. These include understanding the *in vivo* biodistribution of the aqueous-soluble small molecules by delivering free untargeted derivatives, as well as in combination with conjugation methods, efficient labelling of peptides, proteins, antibodies, or other targeting agents to alter biodistribution and preferentially target healthy or diseased tissues. Additionally, water-compatible dyes will facilitate the development of responsive probes which require attachment to peptides or proteins, or can directly react with biological molecules. Imparting water solubility to the flavylium polymethine dye scaffold is not nominal, as these aromatic compounds are quite large and hydrophobic. We began work towards this goal with several strategies that were ultimately unsuccessful up to this point, but did offer insight into directions which were not promising, and inform strategies that might offer more potential. Currently, others in the Sletten Group are now pursing these more recent aims towards water soluble derivatives of Flav7 and other flavylium and chromenylium dyes.

We focused here on the installation of sulfonate groups on Flav7, as sulfonates have shown success in imparting water solubility in cyanine scaffolds including ICG, without substantially increasing the size of the molecule. Concurrently, we were also pursuing functional group modifications at the 7-position on flavylium (see Ch. 3), and found that we could leverage this position to predictably red- or blue-shift absorption and emission wavelengths. Thus, we aimed for an orthogonal modification which we hoped would only minimally impart photophysical changes, and leave the 7-position open for tuning the wavelength of absorption and emission. This left the phenyl group on flavylium as an ideal open site for sulfonate modification. The first target

dye, **5.27** (Scheme 5.7), contained two meta-sulfonates on each flavylium phenyl group. Upon attempting the synthesis of this molecule, we quickly realized that the installation of sulfonate groups early in the synthesis was problematic due to minimal solubility of the sulfonate containing molecules in organic solvents and the necessity of organic solvents for the subsequent transformations. Beginning from 3,5-disulfobenzoic acid, which we prepared using literature procedure,[58] we attempted reactions which would install a leaving group on the acid which could facilitate a Claisen condensation to produce ethyl benzoyl acetate **5.26**. Reaction of 3,5-disulfobenzoic acid with carbonyl diimidazole in DMF or pentafluorophenyl trifluoroacetate with *N*,*N*-diisopropylethylamine (DIEA) in DMF or DMSO proved unsuccessful. Some success was seen in transesterification reactions performed in concentrated HCl (12 M) with methanol or ethanol, however these compounds were not entirely purified and could not be dissolved in organic solvents, prompting us to reconsider the molecular design and synthetic route.

Scheme 5.7. Proposed route to a flavylium heptamethine dye with directly sulfonated phenyl groups.

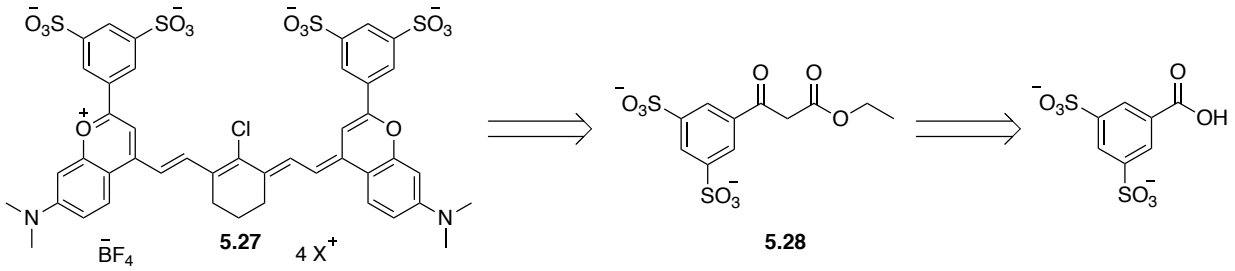

Inspired by synthetic work by Jasti and coworkers,[59] we anticipated that we could enable late-stage installation of sulfonate groups on the dye by leveraging protected phenols which could be carried through the synthesis before deprotection and reaction with a cyclic sulfonate ester, such as 1,3-propane sultone (Scheme 5.8). Beginning with the methyl methoxy methyl (MOM) protected acetophenone **5.29**, which we synthesized according to literature procedures,[60] we performed a Claisen condensation with diethyl carbonate, using sodium hydride in toluene to yield

the β-keto ester **5.30** in moderate yield. Previous attempts to obtain an ethyl benzoylacetate compound with protected phenols, but with *tert*-butyldimethylsilyl ether (TBDMS) as a protecting group, was unsuccessful due to considerable hydrolysis of the protecting groups in hot, basic conditions required for the Claisen condensation. The ethyl benzoylacetate **5.30** was then subjected to a Mentzer pyrone reaction with 3-dimethylamino phenol to obtain the flavone **5.31** in low yield. This transformation proved to be lower yielding than most of the previous Mentzer pyrone reactions, likely due to heat instability of the ethyl benzoylacetate **5.30**, which at temperatures as low as 130 ºC, would revert back to the corresponding acetophenone **5.29**. This proved difficult, as typically 180 ºC is required for conversion in Mentzer pyrone reactions we had performed previously. Indeed, attempting typical Mentzer pyrone conditions (neat, 180 ºC) produced acetophenone **5.29** as the major product. Attempting the reaction at lower temperatures, such as 130 ºC, or in DMF solvent, instead of the neat reaction was significantly worse for product conversion. Some improvement in the conversion could be obtained by ramping the temperature slowly over time, beginning at 100 ºC for the first ~24 h and then raising it to 140 ºC by 3 days. While this helped somewhat with conversion, the purification of product **5.31** was also challenging, particularly as it was not present in a high percentage in the crude reaction mixture and badly streaks on silica gel columns. Thus, it was only isolated up to ~80% purity. Despite difficulties in purity, attempts at performing a Grignard reaction on **5.31** were pursued, hoping that purification would be more facile at the flavylium stage. Unfortunately, all attempts at methyl nucleophile addition with MeMgBr were unsuccessful.

Scheme 5.8 Attempted route towards a heptamethine dye with protected phenols.

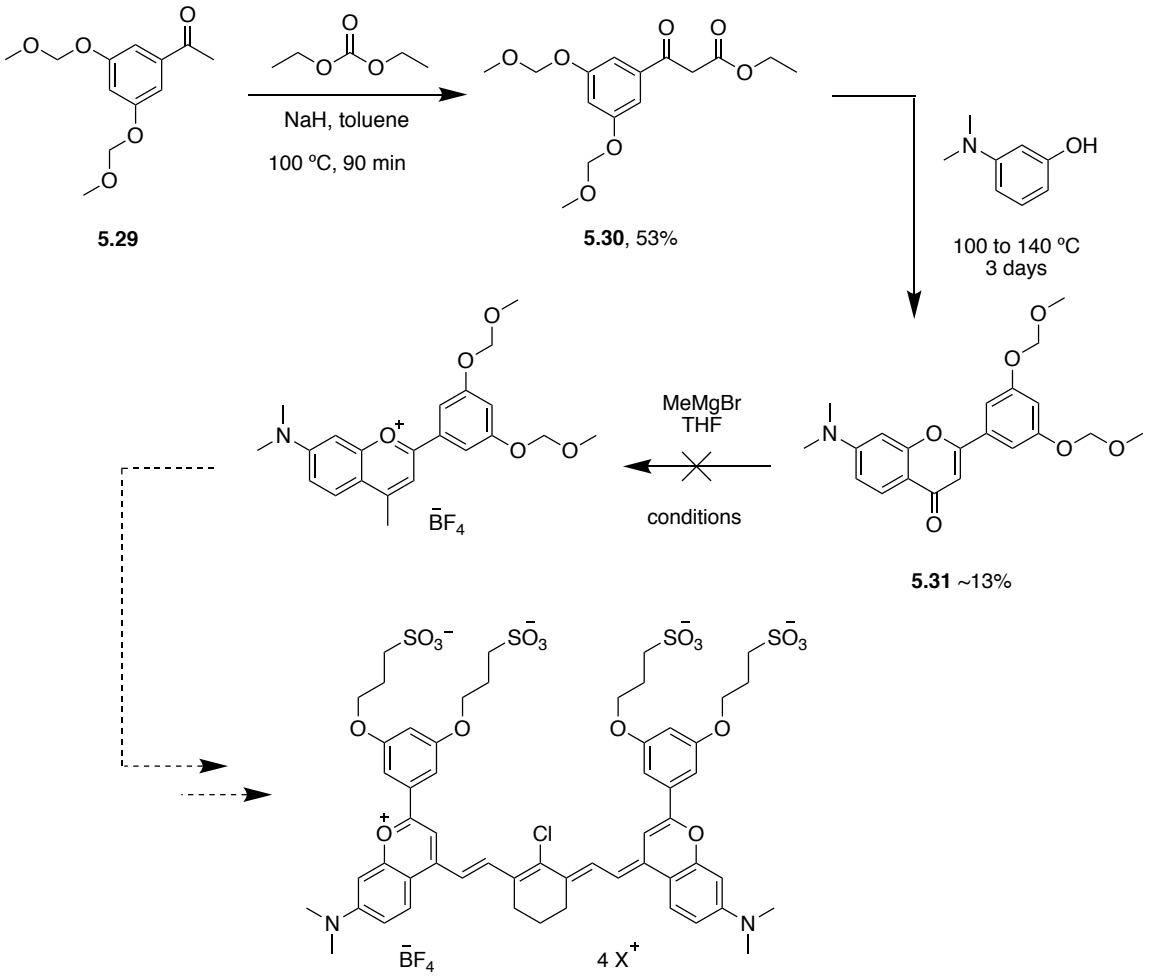

In light of these challenges, but still optimistic about a route in which the polar sulfonate groups could be installed in the final step, we attempted a synthesis of an alternate target sulfonated dye **5.32**, using a different deprotection strategy (Scheme 5.8, route 1). Using the 7-BOC derivative we reported in Ch. 3 (**3.9**), we envisioned that upon BOC deprotection, alkylation of the amino flavylium could be possible with 1,3-propane sultone. On attempting the BOC deprotection on **3.9**, we found that treatment with trifluoroacetic acid (TFA) in DCM or TFA in neat propane sultone resulted in complete loss of the chromophore, as observed by absorption spectroscopy.

Scheme 5.9. Attempted routes towards a 7-aminoalkyl sulfonated flavylium heptamethine dye.

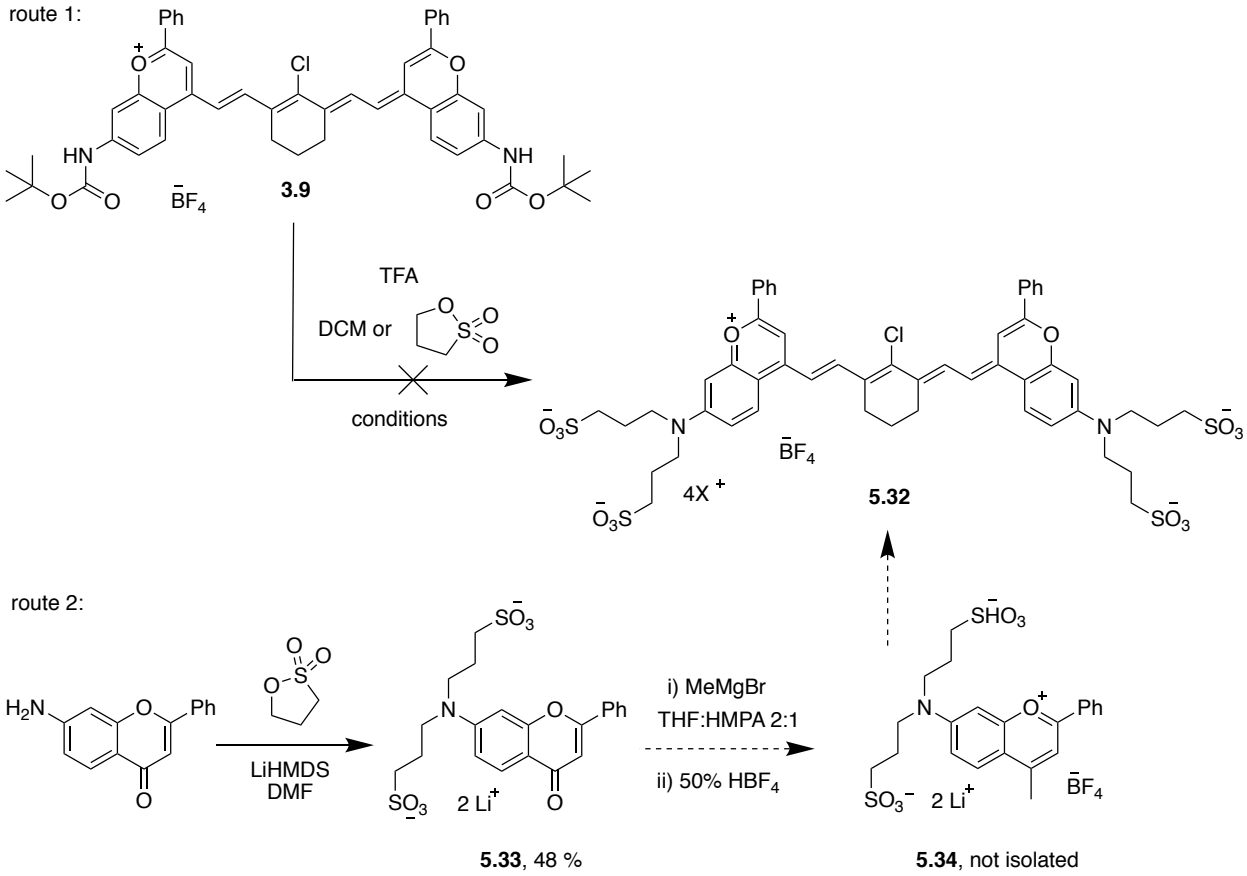

Alternately, we targeted the same sulfonated dye without a deprotection strategy. In this approach (Scheme 5.8, route 2), we were able to install two alkyl sulfonates on the amine of 7-aminoflavone to yield the sulfonated flavone **5.33**. After screening several bases (DIEA, 1,8-Diazabicyclo[5.4.0]undec-7-ene, (DBU), Potassium carbonate), reasonable conversion to the di-alkylated product was obtained with Lithium bis(trimethylsilyl)amide (LiHMDS) in excess, which after purification obtained 48% yield on small scale. The purification of this reaction upon scale up became particularly problematic by column chromatography, and appropriate recrystallization conditions were not arrived at. The Grignard reaction on flavone **5.33** was challenging due to the insolubility of **5.33** in most commonly employed solvents for Grignard reactions, including THF, dioxane, dimethoxyethane (DME), and diglyme. When using a 2:1 mixture of THF and HMPA

we were able to increase the solubility of the starting material and obtain some indication of conversion to the desired product flavylium **5.34**. Observing the absorption spectrum after reacting overnight, but before quenching the reaction, minimal absorption could be seen at ~500 nm. However, upon addition of 50% aq. HBF_4, the reaction solution turned dark red to the eye, and a clear increase in absorbance could be visualized at $\lambda_{max,abs}$ = 500 nm (Figure 5.10). However, this reaction was done on a small scale and the collected dark red crystals were not further characterized. With further optimization of the purification conditions of compound **5.33** such that better scale up conditions can be obtained, the Grignard reaction could be appropriately scaled and compound **5.34** fully characterized. Given that this route shows indication that the flavylium derivative is stable and isolable, I still believe it to be a viable option for obtaining a sulfonated flavylium dye. In light of the difficulties in obtaining fully water soluble flavylium heptamethine dye with other water solubilizing groups, such as oligo ethylene glycol units, this could be a route to revisit for the installation of sulfonates.

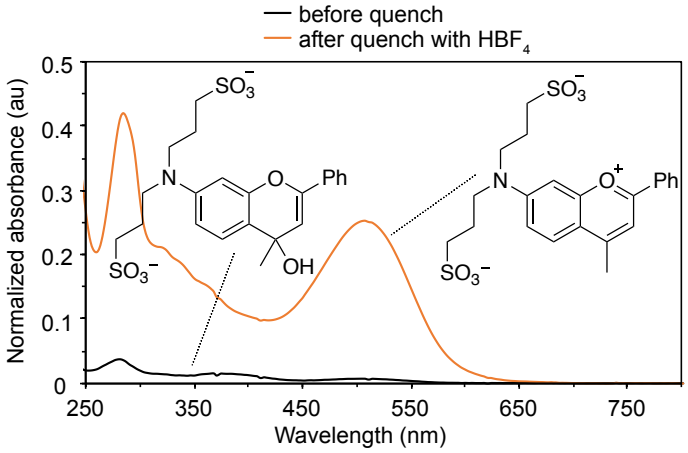

Figure 5.10 Absorption traces and hypothesized chromophore species taken on the Grignard reaction of **5.33**, after reacting overnight but before quenching (black) and after quenching with 50% aq. fluoroboric acid (orange).

5.6 Experimental Procedures

5.6.1 General Experimental Procedures

Materials and instrumentation Acid-terminated poly(lactic-co-glycolic acid) (PLGA) with lactide:glycoside ratios of 50:50 and 75:25 and polyvinyl alcohol (PVA) (Mw=31,000) were purchased from Sigma-Aldrich. Lipids (18:0 PEG2000 PE and 18:0PEG5000 PE) were purchased from Avanti Polar Lipids. Dichloromethane (DCM), hexanes, cyclohexane, toluene, diethyl ether, THF, 1-octanol, 1-heptanol, 1-hexanol, DMSO, ethanol, acetone, acetonitrile, and chloroform were purchased from Fischer Scientific. All materials were used as received. Thin layer chromatography was performed using Silica Gel 60 F_{254} (EMD Millipore) plates. Flash chromatography was executed with technical grade silica gel with 60 Å pores and 40–63 μm mesh particle size (Sorbtech Technologies). Solvent was removed under reduced pressure with a Büchi Rotavapor with a Welch self-cleaning dry vacuum pump and further dried with a Welch DuoSeal pump. Bath sonication was performed using a Branson 3800 ultrasonic cleaner or an Elma S15Elmasonic. Probe sonication was performed on a QSonica (Q125) sonicator. Nuclear magnetic resonance (^{1}H NMR, ^{11}B NMR,^{13}C NMR, ^{19}F NMR) spectra were taken on Bruker Avance 300, AV-500 or AV-600 instruments and processed with MestReNova software. All ^{1}H NMR and ^{13}C NMR peaks are reported in ppm in reference to their respective solvent signals. The calibrated ^{19}F NMRs were calibrated to α,α,α-trifluorotoluene at -63.90 ppm as an internal standard.[61] ^{11}B NMRs were calibrated to BF_3 at 0.0 ppm as an external standard. High resolution mass spectra (electrospray ionization (ESI)) were obtained on a Thermo Scientific Q Exactive™ Plus Hybrid Quadrupole-Orbitrap™ M with Dionex UltiMate 3000 RSLCnano System. Matrix assisted laser desorption ionization (MALDI) time of flight (TOF) analysis was performd on a Bruker Ultraflex

MALDI TOF-TOF. Masses for analytical measurements were taken on a Sartorius MSE6.6S-000-DM Cubis Micro Balance.

Photophysical measurements Absorbance data were collected using a Jasco V-770 UV-Visible/NIR Spectrophotometer after blanking with the appropriate solvent with a 2,000 nm/min scan rate. The spectrophotometer used a D2/WI light source and a 1.0 nm grating for UV-visible measurements and 8.0 nm grating for NIR measurements. All spectra were corrected to 0 at 1,300 nm. Photoluminescence spectra were obtained on a Horiba Instruments PTI QuantaMaster Series fluorometer with InGaAs detector Horiba Edison DSS IGA 020L. Absolute quantum yields were taken in a Horiba KSPHERE-Petite. Quartz cuvettes (1 cm) were used for absorbance and photoluminescence measurements. Absorption coefficients in DCM were calculated with serial dilutions with Hamilton syringes in volumetric glassware. Error was taken as the standard deviation of the triplicate experiments.

Dynamic light scattering (DLS) characterization Nanomaterial size was analyzed with a Malvern Zetaziser Nano dynamic light scattering in plastic 1 cm cuvettes. Size data by DLS were acquired after a 1:100 dilution in MilliQ water, after filtering through a 0.22 μm syringe filter. SOP parameters were as follows: sample refractive index 1.4, 3 measurements, no delay between measurements, 25 °C with 120 second equilibration time.

5.6.2 Experimental procedures [2]

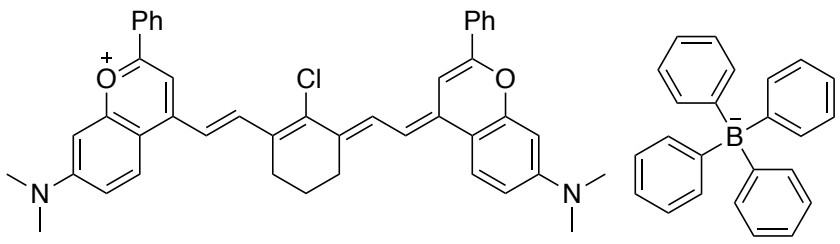

Flav7·TPB 5.1: 7-Dimethylamino flavylium heptamethine dye

[2] Counterion exchange on Flav7 by Zhumin Zhang

tetrafluoroborate (Flav7·BF_4) (15 mg, 0.020 mmol, 1.0 equiv.) was dissolved in DCM (15 mL) and combined with an aqueous solution (15 mL deionized water) of sodium tetraphenylborate (TPB) (10 mg, 0.030 mmol, 1.5 equiv.). The biphasic mixture was sonicated at rt for 5 minutes and then washed with water x3. The organic layer was extracted, dried with sodium sulfate and evaporated onto silica gel. The dye was purified via column chromatography, eluting with a toluene:EtOH solvent ratio of 10:1 followed by a DCM/Toluene/EtOH solvent gradient of 50:50:1, 70:30:1, 80:20:1. This procedure gave pure **5.1** (9.6 mg, 0.0094 mmol, 47%). R_f = 0.3 in 100:1 DCM:EtOH. ^{1}H NMR (500 MHz, DMSO-d_6) δ 8.22 (d, J = 13.5 Hz, 2H), 8.19 – 8.12 (m, 6H), 7.66 (s, 2H), 7.64 – 7.55 (m, 6H), 7.17 (t, J = 6.3, 8H), 7.09 (d, J = 14.0 Hz, 2H), 7.00 (dd, J = 10.2, 2.3 Hz, 2H), 6.92 (t, J = 7.3 Hz, 8H), 6.84 (d, J = 1.6 Hz, 2H), 6.78 (t, J = 7.1 Hz, 2H), 3.16 (s, 12H), 2.84 (p, J = 6.0, 4H), 1.94 – 1.85 (p, J = 5.2, 1H). Absorbance (CH_2Cl_2) = 1027 nm.

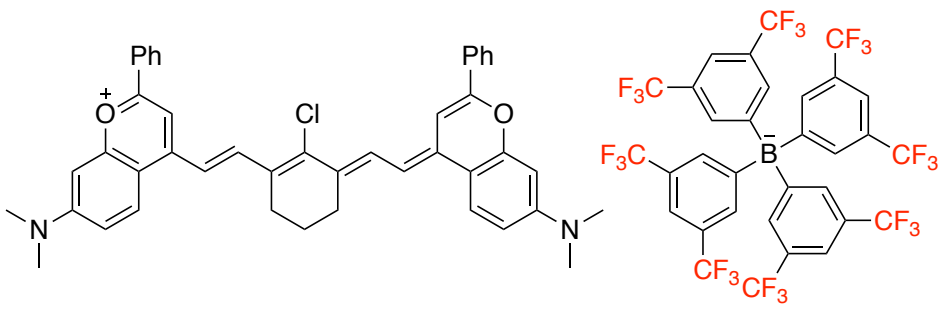

Flav7·F_{24}TPB 5.2: 7-Dimethylamino flavylium heptamethine dye tetrafluoroborate (Flav7·BF_4) (50.1 mg, 0.0667 mmol, 1.00 equiv.) and sodium tetrakis[3,5-bis(trifluoromethyl)phenyl]borate (88.5 mg, 0.0999 mmol, 1.50 equiv.) were dissolved in DCM (50 mL) at rt. The mixture was sonicated for 5 minutes and then washed with water x3. The organic layer was extracted, dried with sodium sulfate, and evaporated onto silica gel. The dye was purified via column chromatography, eluting with a toluene:EtOH solvent ratio of 20:1 followed by a DCM:toluene:EtOH solvent ratio of 50:50:1. This procedure gave pure **5.2** (61.7 mg, 0.0393 mmol, 59%). R_f = 0.6 in 90:10:0.1 DCM:toluene:EtOH. ^{1}H NMR (500 MHz, Acetone-d_6) δ 8.18

(d, J = 13.8 Hz, 2H), 7.92 (dd, J = 7.3, 1.8 Hz, 4H), 7.88 (d, J = 9.3 Hz, 2H), 7.81 – 7.77 (m, 8H), 7.67 (bs, 4H), 7.62 – 7.54 (m, 2H), 7.54 – 7.49 (m, 4H), 7.39 (s, 2H), 6.90 (d, J = 13.9 Hz, 2H), 6.81 (dd, J = 9.2, 2.6 Hz, 2H), 6.60 (d, J = 2.6 Hz, 2H), 3.12 (s, 12 H), 2.81 (p, 4H) {partially obscured under H_2O and HDO peaks}, 2.03 – 1.96 (p, J = 6.0 Hz, 2H) {partially obscured under $(CD_3)_2CO$ peak}. ^{11}B NMR (161 MHz, Acetone-d_6) δ -5.84. ^{19}F NMR (376 MHz, Acetone-d_6) δ -62.55. Absorbance (CH_2Cl_2) = 1027 nm.

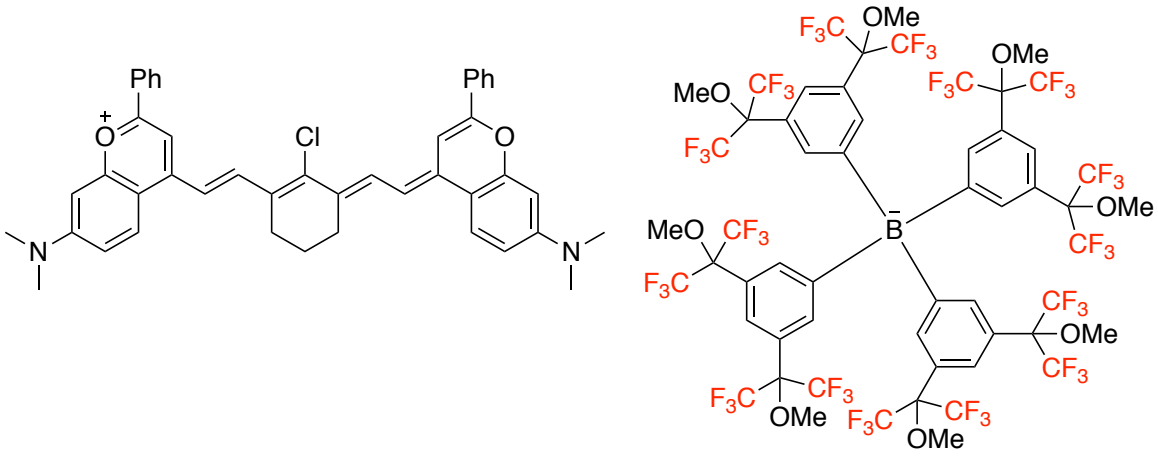

Flav7·F_{48}TPB 5.3: 7-Dimethylamino flavylium heptamethine dye tetrafluoroborate (Flav7·BF_4) (12.3 mg, 0.0164 mmol, 1.0 equiv.) and sodium tetrakis[3,5-bis(1,1,1,3,3,3-hexafluoro-2-methoxy-2-propyl)phenyl]borate trihydrate (27 mg, 0.015 mmol, 0.90 equiv.) were dissolved in DCM (13 mL) at rt. The mixture was sonicated for 5 minutes and then washed with water x3. The organic layer was extracted, dried with sodium sulfate and evaporated onto silica gel. The dye was purified via column chromatography, eluting with a toluene:EtOH solvent ratio of 20:1 followed by a DCM:toluene:EtOH solvent ratio of 50:50:1. This procedure gave pure **5.3** (20.7 mg, 0.00854 mmol, 58%). R_f = 0.2 in 10:1 toluene:EtOH. ^1H NMR (500 MHz, Acetone-d_6) δ 8.07 (d, J = 13.5 Hz, 2H), 7.82 (d, J = 7.1 Hz, 4H), 7.75 (d, J = 9.2 Hz, 2H), 7.64 – 7.57 (m, 8H), 7.56 (t, J = 7.4 Hz, 2H), 7.48 (t, J = 7.5 Hz, 4H), 7.44 – 7.41 (m, 4H), 7.23 (s, 2H), 6.76 (d, J = 13.9 Hz, 2H), 6.70 (dd, J = 9.2, 2.6 Hz, 2H), 6.46 (d, J = 2.5 Hz, 2H), 3.30 (s, 24H), 3.05 (s, 12H), 2.73 (p, J = 6.0

Hz, 4H), 1.99 (p, J = 6.2 Hz, 2H). ^{19}F NMR (376 MHz, Acetone-d_6) δ -71.01. Absorbance (CH_2Cl_2) = 1027 nm.

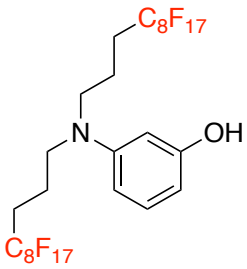

Aminophenol 5.4: The preparation was adapted with modifications from Sletten *et al.*[Error! Bookmark not defined.] 3-Aminophenol (129 mg, 1.19 mmol, 1.00 equiv.), 3-(perfluorooctyl)propyl iodide (1.36 g, 2.51 mmol, 2.13 equiv.), *N*,*N*-diisopropylethylamine (0.415 mL, 2.38 mmol, 2.02 equiv.), and potassium iodide (206 mg, 1.24 mmol, 1.05 equiv.), were dissolved in DMF (2.5 mL) in a 20 mL oven-dried vial. The solution was heated to 120 ºC overnight, then cooled to rt. The crude product was purified via column chromatography, by loading the mixture in DMF directly on to a silica gel column and eluting with 25:1 to 16:1 hexanes:ethyl acetate. This procedure yielded pure **5.4** as a peach colored solid (765 mg, 0.743 mmol, 63%).^{1}H NMR (400 MHz, Acetone-d_6) δ 7.97 (s, 1H), 6.99 (t, J = 8.0 Hz, 1H), 6.39 – 6.26 (m, 2H), 6.19 (dd, J = 8.0, 2.1 Hz, 1H), 3.50 (t, J = 7.5 Hz, 4H), 2.35 (tt, J = 18.9, 7.7 Hz, 4H), 1.94 (p, J = 7.8, 7.2 Hz, 4H). {The ^{1}H NMR spectrum agrees with the literature.}

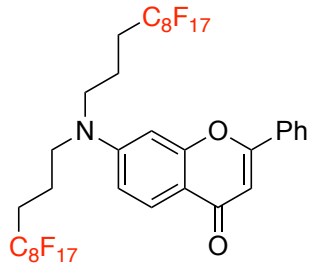

Flavone 5.5: The compound was accessed by two routes. **Route 1**: Fluoroalkyl aminophenol **5.4** (206 mg, 0.200 mmol, 1.00 equiv) was combined neat with ethyl benzoylacetate (0.346 mL, 2.00 mmol, 9.98 equiv.) in a one-dram vial and heated to 150 ºC. After 10 h, the heat was increased to 180 ºC and heated for an additional 22 h. The crude product was purified via column chromatography by dry loading onto silica gel and eluting with 9:1 to 5:1 hexanes:ethyl acetate. This procedure yielded pure **5.5** (118 mg, 0.102 mmol, 51% yield). **Route 2**: 7-

Aminoflavone (99.8 mg, 0.420 mmol, 1.00 equiv.), 3-(perfluorooctyl)propyl iodide (545 mg, 1.01 mmol, 2.4 equiv.) and sodium hydride (60% wt percent in mineral oil, 168 mg, 4.2 mmol, 9.99 equiv.) were added to a flame-dried 25 mL flask. The flask was flushed with N_2 before adding DMF (2.0 mL). The solution was heated to 100 ºC for 17 h and let cool to rt. The crude mixture was dissolved in trifluorotoluene to facilitate dry loading onto silica gel. The crude product was purified by column chromatography, eluted with 8:1 to 4:1 hexanes:ethyl acetate. This procedure yielded pure **5.4** (199 mg, 0.172 mmol, 41%). ^{1}H NMR (400 MHz, Acetone-d_6) δ 8.08 – 7.99 (m, 2H), 7.94 (d, J = 9.0 Hz, 1H), 7.65 – 7.55 (m, 3H), 7.06 (dd, J = 9.1, 2.5 Hz, 1H), 7.02 (d, J = 2.4 Hz, 1H), 6.70 (s, 1H), 3.86 – 3.75 (m, 4H), 2.47 (tt, J = 19.5, 8.2 Hz,4H), 2.17 – 2.07 (m, 4H, partially underneath Acetone-d_6 peak). ^{13}C NMR (126 MHz, Acetone-d_6) δ 176.9, 162.7, 159.5, 153.1, 133.2, 132.0, 130.0 – 106.3 (m, CF_n peaks), 129.8, 127.3, 126.9, 114.8, 111.8, 1078, 98.5, 50.3, 28.6 (t, J = 22 Hz), 19.0. ^{19}F NMR (376 MHz, Acetone-d_6) δ -81.7 (t, J = 10 Hz, 6F), -114.3 (p, J = 16 Hz 4F), -121.5 – -122.7 (m, 12F), -123.3 (bs, 4F), -123.9 (bs, 4F), -126.5 – -126.8 (m, 4F).

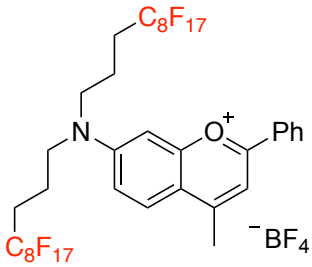

Flavylium 5.6: Fluoroalkyl flavone **5.5** (183 mg, 0.158 mmol, 1.00 equiv.) was added to a flame-dried 25 mL Schlenk flask and dissolved in THF (1.5 mL). The solution was submerged in liquid N_2 and MeMgBr (1.0 M in THF, 0.27 mL, 1.7 equiv.) was added. After freeze-pump-thawing x3, the solution was let warm to rt and stirred overnight. The reaction was quenched with 5 drops of 50% aq. fluoroboric acid. The product was extracted into trifluorotoluene and washed x3 with ~50 mL 5% aq. fluoroboric acid, dried with sodium sulfate, filtered (sodium sulfate was rinsed with acetone to remove all product) and evaporated. The crude product was then precipitated from cold ethyl acetate, filtered, and rinsed with cold ether. This procedure yielded

pure **5.6** (164 mg, 0.132 mmol, 83%). ^{1}H NMR (500 MHz, Acetone-d_6) δ 8.36 (t, J = 9.0 Hz, 3H), 8.24 (s, 1H), 7.83 – 7.76 (m,2H), 7.73 (t, J = 7.7 Hz, 2H), 7.66 (d, J = 2.5 Hz, 1H), 4.08 (t, J = 7.5 Hz 2H), 3.03 (s, 1H), 2.52 (tt, J = 19.0, 8.1 Hz, 4H), 2.20 (p, J = 15.8, 9.4 Hz, 4H). ^{13}C NMR (126 MHz, Acetone-d_6) δ 165.9, 165.1, 159.3, 157.1, 134.3, 129.73, 129.69, 129.3, 128.0, 125.0 – 105.0 (m, CF_n peaks), 118.4, 1183, 112.5, 96.7, 50.2, 27.5 (t, J = 22 Hz), 19.2. ^{19}F NMR (376 MHz, Acetone-d_6) δ -81.7 (t, J = 10 Hz, 6F), -114.3 (p, J = 16 Hz, 4F), -121.9 – -122.7 (m, 12F), -123.3 (bs, 4F), -123.9 (bs, 4F), -126.7 (m, 4F), -152.2 (s, 4F). HRMS (ESI): calcd for $C_{38}H_{24}F_{34}NO^{+}$ $[M]^{+}$: 1156.13095; found: 1156.13281. Absorbance (acetone): 505 nm.

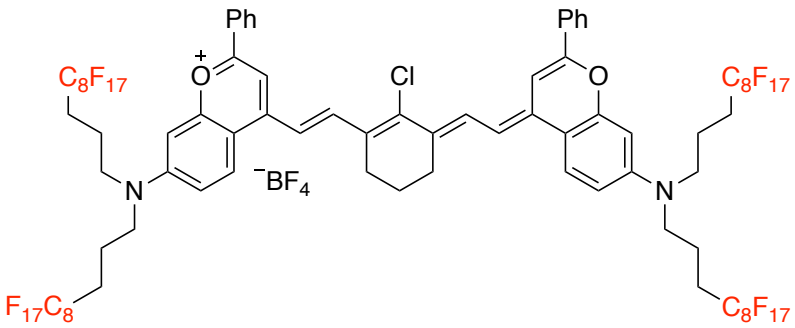

Heptamethine dye 5.8: Fluoroalkyl flavylium **5.6** (50 mg, 0.040 mmol, 1.0 equiv.), *N*-[(3-(anilinomethylene)-2-chloro-1-cyclohexen-1-yl)methylene]aniline hydrochloride (**5.7**) (6.8 mg, 0.019 mmol, 0.47 equiv.), and 2,6-di-*tert*-butyl-4-methylpyridine (26 mg, 0.13 mmol, 3.2 equiv.) were added to a flame-dried 25 mL Schlenk tube. The starting materials were dissolved in DMF (2.0 mL), freeze-pump-thawed x3, and heated to 100 ºC for 1 h. The crude product was evaporated onto silica gel and purified by column chromatography, eluted with 0.25% to 5% acetone in DCM. This procedure yielded **5.7** (92 mg, .036 mmol, 90%). MS (MALDI): calcd for $C_{84}H_{52}ClF_{68}N_2O_2^{+}$ $[M]^{+}$: 2447.26; found: 2447.38. Absorbance (CH_2Cl_2) = 1022 nm.

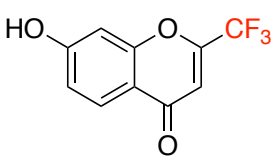

7-hydroxy-2-(trifluoromethyl)-flavone 5.16: The preparation was adapted from Bolós *et al.*[Error! Bookmark not defined.] 2',4'-dihydroxyacetophenone (151 mg, 0.992 mmol, 1.00 equiv.) and sodium trifluoroacetate (266 mg, 1.96 mmol, 1.97 equiv.) were added to a flame-dried 1-dram vial. Trifluoroacetic anhydride (554 µL, 5.85 mmol, 5.90 equiv.) was added dropwise and stirred at 100 ºC. After 1h, the heat was increased to 125 ºC and run overnight. The reaction was cooled to rt, HCl (2 M) was added, the mixture was filtered, and the precipitate was collected. The precipitate was heated at 45 ºC in water, and NaOH (0.2 M) was dripped in until the precipitate dissolved. This solution was filtered, and the filtrate was collected, washed with water and dried. To the filtrate, 0.2 M HCl was dripped in until a light pink precipitate formed which was collected. This procedure yielded pure **6.16** as a light pink solid (88.8 mg, 39 %). ^{1}H NMR (400 MHz, Acetone-d_6) δ 9.93 (bs, 1H), 7.99 (d, J = 8.7 Hz, 1H), 7.07 (dd, J = 8.8, 2.2 Hz, 1H), 7.00 (d, J = 2.3 Hz, 1H), 6.71 (s, 1H). {The ^{1}H NMR spectrum agrees with the literature, but with a different ppm shift for the OH.}

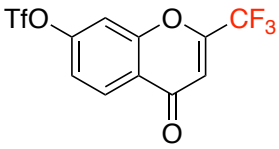

4-oxo-2-(trifluoromethyl)-4*H*-chromen-7-yl trifluoromethanesulfonate 5.17: 7-hydroxy-2-(trifluoromethyl)-flavone (**5.16**) (77.6 mg, 0.337 mmol, 1.00 equiv.) was added to a 15 mL flame-dried 2-neck flask. DCM (1.5 mL) and dry pyridine (150 µL, 1.86 mmol, 5.52 equiv.) were added. Trifluoromethanesulfonic anhydride (146 µL, 0.867 mmol, 2.57 equiv.) was dripped in over ice and the reaction was stirred at 0 ºC for 45 min. The reaction was quenched with aqueous sodium bicarbonate, and the crude product was extracted in DCM, dried with sodium sulfate, and evaporated. The crude product was purified by column chromatography in hexanes:ether 50:1 to 25:1 to yield pure **5.17** (80.5 mg,

0.222 mmol, 66%). ^{1}H NMR (400 MHz, Chloroform-d) δ 8.31 (d, *J* = 8.9 Hz, 1H), 7.54 (d, *J* = 2.4 Hz, 1H), 7.40 (dd, *J* = 8.8, 2.3 Hz, 1H), 6.77 (s, 1H). ^{19}F NMR (376 MHz, Chloroform-*d*) δ -71.71, -72.58.

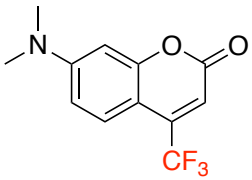

7-(dimethylamino)-4-(trifluoromethyl)-coumarin 5.20: 3-dimethylaminophenol (100 mg, 0.729 mmol, 1.00 equiv.) and ethyl 4,4,4-trifluoroacetate (210 µL, 1.43 mmol, 1.96 equiv.) were added to an oven dried 1-dram vial and flushed with N_2. The reaction was stirred at 130 ºC for 3 hours before cooling to room temperature. The crude product was purified by column chromatography with a 50:1 to 20:1 hexanes:ethyl acetate solvent gradient to yield pure **5.20** as a yellow solid (143 mg, 0.554 mmol, 76%). ^{1}H NMR (600 MHz, Chloroform-*d*) δ 7.46 (dd, *J* = 9.1, 2.0 Hz, 1H), 6.61 (dd, *J* = 9.1, 2.6 Hz, 1H), 6.48 (d, *J* = 2.6 Hz, 1H), 6.35 (s, 1H), 3.06 (s, 7H). ^{13}C NMR (151 MHz, Chloroform-*d*) δ 160.47, 156.75, 153.28, 141.80 (q, *J* = 32.2 Hz), 125.96, 121.99 (q, *J* = 275.6 Hz), 109.61, 108.30, 102.93, 98.26, 40.09. ^{19}F NMR (376 MHz, Acetone-d_6) δ -72.39.

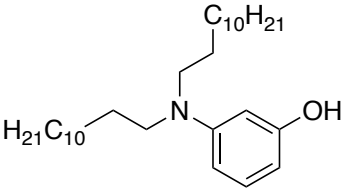

Aminophenol 5.21: The preparation was adapted from Sletten *et al.*[Error! Bookmark not defined.] 3-Aminophenol (1.00 g, 9.16 mmol, *N*,*N*-diisopropylethylamine1.05 equiv.), 1-bromododecane (4.18 mL, 17.4 mol, 2.00 equiv.), and *N*,*N*-diisopropylethylamine (1.92 mL, 11.0 mmol, 1.27 equiv.) were added to an 100 mL flame-dried round bottom flask and dissolved in DMF (18 mL). The solution was heated to 120 ºC for 20 h. After cooling to rt, the DMF was evaporated and the crude product was evaporated onto silica gel. The product was purified via column chromatography, using two columns, each with an 100:1 to 25:1 hexanes:ethyl acetate eluent gradient. This procedure yielded

pure **5.21** (1.62 g, 3.64 mmol, 42%). ^{1}H NMR (500 MHz, Chloroform-*d*) δ 7.05 (t, *J* = 8.1 Hz, 1H), 6.25 (dd, *J* = 8.4, 2.3 Hz, 1H), 6.16 (bs, 1H), 6.12 (d, *J* = 7.9 Hz, 1H), 4.97 (bs, 1H), 3.23 (t, *J* = 7.7 Hz, 4H), 1.58 (p, *J* = 7.4 Hz, 4H), 1.35 – 1.25 (m, 36H), 0.92 (t, *J* = 6.8 Hz, 6H). ^{1}H NMR matches the literature.

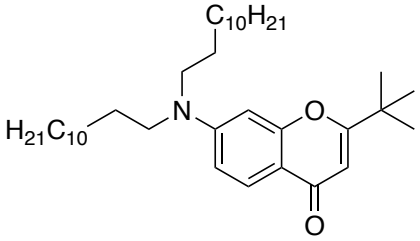

Chromone 5.22: Aminophenol **5.21** (1.53g, 3.42 mmol, 1.00 equiv.) and ethyl pivaloylacetate (1.22 mL, 6.85 mmol, 2.00 equiv.) were each divided into 4 aliquots and combined into 4 1-dram vials. The neat solutions were heated at 80 ºC for 72 h. The crude products were combined for purification by column chromatography with a 25:1 to 12.5:1 hexanes:ethyl acetate eluent system. Pure fractions were collected, and impure fractions were run on a second column under the same eluent. This procedure yielded pure **5.22** (1.10 g, 1.92 mmol, 58%). ^{1}H NMR (500 MHz, Chloroform-*d*) δ 7.94 (d, *J* = 9.1 Hz, 1H), 6.65 (dd, *J* = 9.1, 2.4 Hz, 1H), 6.38 (d, *J* = 2.4 Hz, 1H), 6.10 (s, 1H), 3.43 – 3.24 (m, 4H), 1.61 (p, *J* = 8.6, 7.9, 7.6 Hz, 4H), 1.44 – 1.23 (m, 45H), 0.87 (t, *J* = 6.9 Hz, 6H). ^{13}C NMR (126 MHz, Chloroform-*d*) δ 178.2, 174.4, 158.9, 152.2, 126.5, 112.6, 110.3, 106.0, 96.3, 51.1, 36.2, 31.9, 29.7, 29.64, 29.62, 29.61, 29.5, 29.4, 28.0, 27.13, 27.05, 22.7, 14.1.

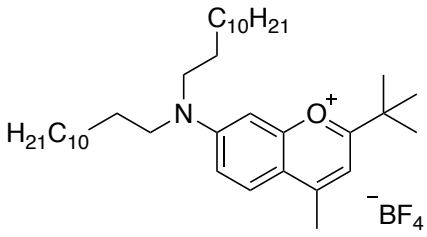

Chromenylium 5.23: Chromone **5.22** (500 mg, 0.90 mmol, 1.0 equiv.) was added to a flame-dried 50 mL 2-neck flask and dissolved in THF (5.5 mL). The solution was cooled to 0 ºC and MeMgBr (1.4 M in THF, 1.2 mL, 1.9 equiv.) was added dropwise. The solution was let warm to rt and stirred for 25 hours. The reaction was quenched

with 200 μL of 50% aqueous fluoroboric acid followed by an extraction with DCM and 5% fluoroboric acid. The organic layer was dried with sodium sulfate, filtered, and evaporated to yield pure **5.23** (579 mg, 0.91 mmol, 100%) as an orange solid. ^{1}H NMR (400 MHz, Chloroform-*d*) δ 8.14 (d, *J* = 9.7 Hz, 1H), 7.33 (dd, *J* = 9.7, 2.5 Hz, 1H), 7.15 (s, 1H), 6.73 (d, *J* = 1.8 Hz, 1H), 3.55 (bs, 4H), 2.87 (s, 3H), 1.70 (p, *J* = 9.1, 7.0 Hz, 4H), 1.49 (s, 9H), 1.44 – 1.21 (m, 36H), 0.90 – 0.85 (m, 6H). ^{13}C NMR (126 MHz, Chloroform-*d*) δ 178.0, 164.7, 159.7, 156.7, 129.4, 118.5, 117.6, 111.6, 95.4, 52.2, 38.0, 31.9, 29.7, 29.64, 29.59, 29.5, 29.37, 29.35, 28.2, 26.8, 22.7, 20.0, 14.2. HRMS (ESI): calcd for $C_{38}H_{66}NO^{+}$ $[M]^{+}$: 552.51389; found: 552.51440.

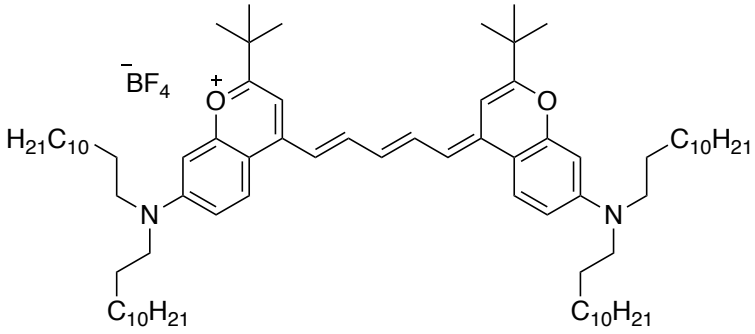

Lipo-Chrom5 5.25: Chromenylium **5.23** (203 mg, 0.317 μmol, 1.00 equiv.), malonaldehyde bis(phenylimine) (40.0 mg, 0.155 μmol, 0.490 equiv.) and sodium acetate (82.1 mg, 1.00 mmol, 3.15 equiv.) were added to a flame-dried 25 mL Schlenk flask. Acetic anhydride (3.6 mL) was added and the solution was freeze-pump-thawed x3 before heating to 100 ºC for 20 min. The cooled solution was evaporated directly onto silica gel and purified via column chromatography with 2 columns run with a DCM:toluene:EtOH solvent gradient of 50:50:0.1 to 50:50:10, followed by a column with a hexanes:ethyl acetate solvent gradient of 20:1 to 4:1. This procedure yielded pure **5.25** (120 mg, 0.98 μmol, 63%) as a maroon solid. ^{1}H NMR (500 MHz, Chloroform-*d*) δ 8.01 (t, *J* = 12.9 Hz, 2H), 7.84 (d, *J* = 9.6 Hz, 2H), 6.94 (s, 2H), 6.83 – 6.71 (m, 5H), 6.37 (d, *J* = 2.5 Hz, 2H), 3.37 (t, *J* = 7.8 Hz, 8H), 1.63 (p, *J* = 7.1 Hz, 8H), 1.40 (s, 18H), 1.37 – 1.21 (m, 72H), 0.87 (t, *J* = 6.9 Hz, 12H). ^{13}C NMR (126 MHz, Chloroform-*d*) δ 170.1, 156.8,

152.6, 150.0, 147.1, 128.5, 126.0, 114.0, 112.8, 111.3, 100.1, 96.8, 51.4, 36.9, 32.0, 29.8, 29.74, 29.71, 29.54, 29.45, 28.3, 27.4, 27.1, 22.8, 14.2. HRMS (ESI): calcd for $C_{79}H_{131}N_2O_2^+$ $[M]^+$: 1140.02051; found: 1140.02234. Absorbance (CH_2Cl_2): 830 nm.

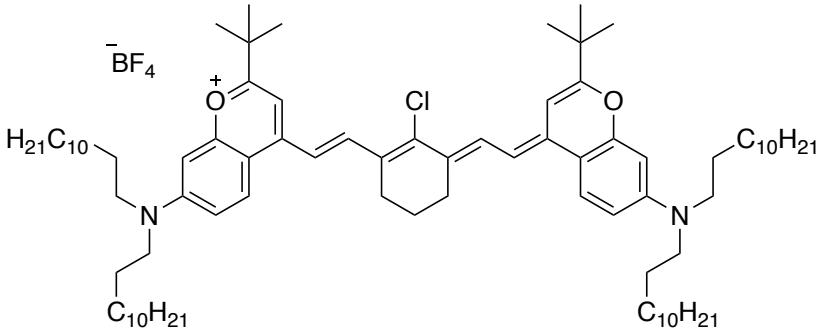

Lipo-Chrom7 5.26: Chromenylium **5.23** (148 mg, 0.239 mmol, 1.00 equiv.), *N*-[(3-(anilinomethylene)-2-chloro-1-cyclohexen-1-yl)methylene]aniline hydrochloride (40.2 mg, 0.112 mmol, 0.490 equiv.), and 2,6-di-*tert*-butyl-4-methyl pyridine (143 mg, 0.696 mmol, 3.00 equiv.) were dissolved in *n*-butanol (0.90 mL) and toluene (2.1 mL) in a flame-dried 25 mL Schlenk tube. The mixture was freeze-pump-thawed x3 before heating to 100 ºC for 1.5 h. The crude product was purified by column chromatography with a 20:1 to 1:1 hexane:ethyl acetate solvent gradient followed by a second column with a 10:1 to 1:1 hexanes:ethyl acetate solvent gradient. This procedure yielded pure **5.26** as a purple solid (28.7 mg, 0.0210 mmol, 19%. ^{1}H NMR (500 MHz, Chloroform-*d*) δ 8.13 (d, *J* = 13.2 Hz, 2H), 7.97 (d, *J* = 9.3 Hz, 2H), 6.92 (d, *J* = 10.2 Hz, 4H), 6.77 (s, 2H), 6.43 (d, *J* = 2.3 Hz, 2H), 3.42 (t, *J* = 7.7 Hz, 8H), 2.79 (s, 4H), 1.97 (d, *J* = 6.5 Hz, 2H), 1.69 – 1.56 (m, 8H), 1.40 (s, 18H), 1.38 – 1.16 (m, 72H), 0.88 (t, *J* = 6.8 Hz, 12H). ^{13}C NMR (126 MHz, Chloroform-*d*) δ 169.9, 157.0, 153.0, 146.9, 145.6, 139.3, 130.2, 126.3, 113.6, 112.2, 111.6, 99.6, 97.0, 51.6, 36.8, 32.1, 29.79, 29.77, 29.74, 29.73, 29.6, 29.5, 28.2, 27.5, 27.3, 27.1, 22.8, 21.3, 14.3. HRMS (ESI): calcd for $C_{79}H_{131}N_2O_2^+$ $[M]^+$: 1240.02979; found: 1240.02234. Absorbance (CH_2Cl_2): 988 nm.

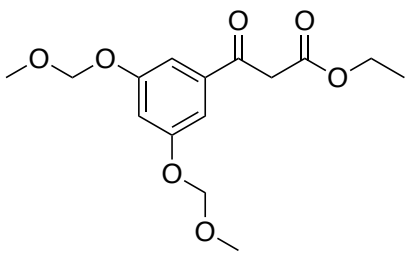

ethyl 3-(3,5-bis(methoxymethoxy)phenyl)-3-oxopropanoate 5.30: Sodium hydride (350 mg, 60% in mineral oil, 8.8 mmol, 1.9 equiv.) was added to a flame-dried 50 mL round bottom flask, and dissolved in toluene (5 mL). Diethyl carbonate (1.2 mL, 9.9 mmol, 2.1 equiv.) was added dropwise. Finally, **5.29** (1.13 g, 4.69 mmol, 1.0 equiv.) in toluene (2.5 mL) was added to the solution before heating to 100 ºC for 1.5 h. After cooling, acetic acid (1.5 mL) was added, followed by water, and the crude product was extracted with ethyl acetate, washed with brine, dried with sodium sulfate, filtered, and evaporated. The crude product was purified by column chromatography with a solvent gradient of 30:1 to 16:1 hexanes:ethyl acetate to yield pure **5.30** (771 mg, 2.47 mmol, 53%). ^{1}H NMR (300 MHz, Chloroform-*d*) δ 12.52 (s, 0.3H), 7.25 (m, 2H), 7.11 (d, *J* = 2.2 Hz, 0.6H), 6.96 (t, *J* = 2.2 Hz, 1H), 6.83 (t, *J* = 2.2 Hz, 0.3H), 5.62 (s, 0.3H), 5.19 (s, 4H), 5.18 (s, 1.2H), 4.24 (dq, *J* = 14.2, 7.1 Hz, 2.6H), 3.94 (s, 2H), 3.48 (s, 7.8H), 1.33 (t, *J* = 7.1 Hz, 0.9H), 1.26 (t, *J* = 7.1 Hz, 3H). ^{13}C NMR (126 MHz, Chloroform-*d*) δ 192.0, 173.2, 171.0, 167.5, 158.6, 158.6, 158.5, 138.1, 135.7, 110.3, 109.8, 107.9, 107.6, 94.7, 88.0, 61.6, 60.5, 56.4, 56.3, 46.3, 14.4, 14.2.

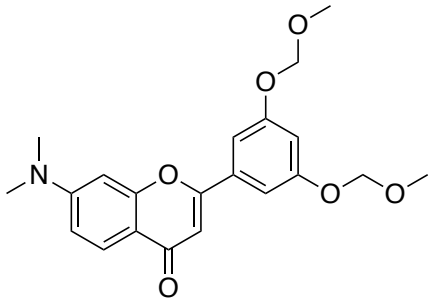

2-(3,5-bis(methoxymethoxy)phenyl)-7-(dimethylamino)-4*H*-chromen-4-one 5.31: Compound **5.30** (114 mg, 0.366 mmol, 2.00 equiv.) and 3-dimethylaminophenol (25.1 mg, 0.183 mmol, 1.00 equiv.) were added to a flame dried vial under N_2 atmosphere. The mixture was heated to 100 ºC and stirred for 23 hours. The heat was then increased to 130 ºC and the reaction was stirred for another 25 hours, before increasing the heat to 140 ºC for a final 24 hours. The reaction was cooled, and

the crude product was purified via column chromatography using a hexanes:ethyl acetate solvent gradient of 12:1 to 4:1. This procedure yielded **5.31** (16.5 mg, ~60% purity, 0.026 mmol, 14%). ^{1}H NMR (400 MHz, Chloroform-*d*) δ 7.35 (dd, *J* = 8.5, 0.7 Hz, 1H), 6.85 (t, *J* = 2.3 Hz, 1H), 6.77 (d, *J* = 2.2 Hz, 2H), 6.62 – 6.49 (m, 2H), 6.07 (s, 1H), 5.19 (s, 4H), 3.50 (s, 6H), 3.06 (s, 6H).

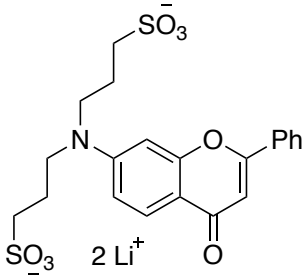

Flavone 5.33: 7-aminoflavone (20.3 mg, .0856 mmol, 1.0 equiv.) and propane sultone (61.5 mg, 0.504 mmol, 5.89 equiv.) were added to an oven-dried 1-dram vial and dissolved in DMF (650 μL). LiHMDS (1 M in THF, 197 μL, 2.30 equiv.) was added and the solution was stirred to 6 hours at rt, before heating to 100 ºC for 14 hours. The crude mixture was purified via column chromatography with a 100:3:1 EtOAc:MeOH:H_2O+ 1% AcOH solvent system to 10:3:1 +1% AcOH. This procedure yielded pure **5.33** (91.6 mg, 0.0397 mmol, 46%). ^{1}H NMR (500 MHz, Deuterium Oxide) δ 7.60 (d, *J* = 7.3 Hz, 2H), 7.47 (t, *J* = 7.2 Hz, 1H), 7.40 (t, *J* = 7.5 Hz, 2H), 7.32 (d, *J* = 9.1 Hz, 1H), 6.43 (dd, *J* = 9.0, 2.3 Hz, 1H), 6.19 (s, 1H), 3.15 (t, *J* = 7.8 Hz, 4H), 2.90 (t, *J* = 7.6 Hz, 4H), 1.92 (p, *J* = 8.4, 7.4, Hz, 4H).

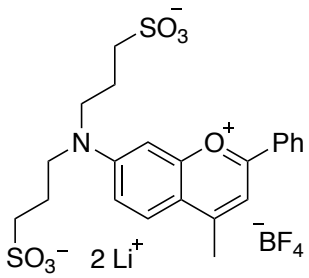

Flavylium 5.34: Flavone **5.33** (10 mg, 0.02 mmol, 1 equiv.) was dissolved in THF (400 μL) and HMPA (100 μL) and cooled to 0 ºC. MeMgBr (1 M in THF, 85 μL, .085 mmol, 4.2 equiv.) was added dropwise and the reaction was let warm and stirred at rt. After 24 hours, additional HMPA (100 μL) and MeMgBr (1 M in THF, 100 μL, .10 mmol, 4.9 equiv.) were added, and the reaction was stirred for an additional 12 hours. The reaction was quenched with 50% aq. HBF_4 (6 μL). Ether was added to the reaction mixture and all solvent was evaporated to dryness.

MeCN was added and resulting the sticky red precipitate was filtered. MeOH was added and the resulting principate was filtered to yield a red powder product, as a trace amount adhered to the filter paper, which is putatively assigned to be flavylium **5.34**. Absorbance (water): 506 nm.

5.6.3 PLGA nanoparticle fabrication methods[3]

JuloFlav7 PLGA nanoparticle preparation The fabrication of the nanoemulsions was adapted from the modified spontaneous emulsion method as described by Lee and Lai.[1] The general procedure consisted of preparing PLGA (50:50) (30 mg/mL) and JuloFlav7 (**4.3**) (0.55 mg/mL) in an EtOH:DCM solution (v/v 3:7). A 0.2% PVA solution was made, sonicated in a bath sonicator for thirty minutes, and filtered through a 0.22μm PFTE syringe filter. The JuloFlav7-PLGA solution (100 μL) was added dropwise to 1.5mL 0.2% PVA solution over ice. The mixture was sonicated at 40% intensity for three minutes in a probe sonicator. The sonicated solution was then stirred at 1,300 rpm for 1 hour while open to air. The evaporated solution was centrifuged in a 10 kDa MW cutoff filter (Amicon Ultra-15) and centrifuged at 5,000 rpm for 15 min, washed with an equal volume of PBS, and finally, resuspended and stored in 0.5 mL PBS. Variations in this procedure included using PGLA with 75:25 lactide:glycolide ratio, adjusting the % PVA in water between 0.1–2%, and changing the cosolvent ratio, all kept at a 3:7 v/v ratio.

ICG PLGA nanoparticle preparation ICG (1 mg/mL) and PLGA (50:50 lactide:glycolide ratio) (30 mg/mL) were dissolved in a 3:7 (v/v) solution of ethanol/DCM. A separate solution of 0.2% PVA in water was bath sonicated until complete dissolution, before filtering through a 0.22μm PFTE syringe filter. The dye solution (100 μL) was added dropwise into the PVA solution (1.5 mL) over ice. This mixture was sonicated in a probe sonicator (40%) for 3 min at 0 ºC. The sonicated solution was then stirred at 1,300 rpm for 1 hour while open to air. The evaporated

[3] PLGA loading and characterization by Olivia Leland

solution was centrifuged at 18,000 x *g* for 20 min, washed twice with an equal volume of PBS, and finally the centrifuged pellet was resuspended and stored in 0.5 mL PBS.

HITCI PLGA nanoparticle preparation HITCI (0.35 mg/mL) and PLGA (50:50 lactide:glycolide ratio) (30 mg/mL) were dissolved in a 3:7 (v/v) solution of ethanol/DCM. A separate solution of 0.2% PVA in water was bath sonicated until complete dissolution, before filtering through a 0.22μm PFTE syringe filter. The dye- PLGA solution (100 μL) was added dropwise into the PVA solution (1.5 mL) over ice. This mixture was sonicated in a probe sonicator (40%) for 3 min at 0 ºC. The sonicated solution was then stirred at 1,300 rpm for 1 hour while open to air to evaporate organic solvent. The evaporated solution was centrifuged at 18,000 x *g* for 20 min, washed twice with an equal volume of PBS, and the centrifuged pellet was resuspended and stored in 0.5 mL PBS.

3.6.4 Micelle fabrication methods

Micelles with heptamethine dyes (DMSO method) 0.4 mg of each heptamethine dye was dissolved in 4 mL DMSO and added to 2 mL of a 6 mg/mL solution of 18:0 PEG2000 PE (1,2-distearoyl-*sn*-glycero-3-phosphoethanolamine-*N*-[methoxy(polyethylene glycol)-2000] ammonium salt (Avanti Polar Lipids) in a 50 mL falcon tube. The solution was sonicated in a probe sonicator for 3 min on ice. The solution was then transferred to a 10 kDa MW cutoff filter (Amicon Ultra-15) and centrifuged at 4,000 rpm. Sequential washes with 1x PBS were performed, until the remaining DMSO consisted of <1%. The micelles were then concentrated by centrifugation (4,000 rpm) to ~12.5 mL.

Micelles with heptamethine dyes (Thin film method) The thin film method was adapted from Lei *et al*.[62] Each heptamethine dye (0.1 mg) and 18:0 PEG2000 PE (11 mg) were combined in

either chloroform or DCM (~600 uL) in a vial, mixed until dissolution, and evaporated in on a rotary evaporator. To this thin film, DI water (10 mL) at 80 ºC was added, and the mixture was sonicated in a bath sonicator for 1 min.

Micelles with pentamethine dyes (DMSO method) Each pentamethine dye (0.233 μmol) was dissolved in 4 mL DMSO and added to 2 mL of a 10 mg/mL solution of 18:0 PEG5000 PE (1,2-distearoyl-sn-glycero-3-phosphoethanolamine-N-[methoxy(polyethylene glycol)-5000] ammonium salt) (Avanti Polar Lipids) in a 50 mL falcon tube. The solution was sonicated in a probe sonicator for 3 min on ice. The solution was then transferred to a 10 kDa MW cutoff filter (Amicon Ultra-15) and centrifuged at 4,000 rpm. Sequential washes with 1x PBS were performed, until the remaining DMSO consisted of <1%. The micelles were then concentrated by centrifugation (4,000 rpm) to ~3 mL.

3.6.5 Counterion exchanges on F_{68}Flav7

Small scale counterion exchanges from F_{68}Flav7·BF_4 (**5.8**) were performed to screen solubility and photophysical properties in fluorous solvents of the dye salts. These compounds were not explicitly purified or characterized beyond what was necessary for photophysical measurements.

F_{68}Flav7·TFA (5.9) A small amount of F_{68}Flav7·BF_4 (**5.8**) was dissolved in DCM and added to an aqueous solution of sodium trifluoroacetate. The biphasic solution was sonicated in a bath sonicator for ~1 min, in which a color change to a lighter shade of pink is observed. The DCM layer was extracted, dried with sodium sulfate, filtered, and evaporated to yield 0.9 mg of **5.9** as a pink solid.

F_{68}Flav7·PFOA (5.10) Perfluorooctanoic acid (15.5 μL) was dissolved in 0.1 M NaOH (~500 μL) and the pH was adjusted with the addition of NaOH until the solution pH = 7. F_{68}Flav7·BF_4 (**5.8**)

was dissolved in DCM and added to the aqueous solution. The biphasic mixture was mixed for ~1 min until a color change occurred, to a lighter pink color. The organic phase was then extracted, dried with sodium sulfate, filtered, and evaporated to obtain **5.10** as a pink solid.

F_{68}Flav7·F_{24}TPB (5.11) A small amount of F_{68}Flav7·BF_4 (**5.8**) was dissolved in DCM (~1 mL) and added to an aqueous solution (~1 mL) of sodium tetrakis[3,5-bis(trifluoromethyl)phenyl] borate (2.4 mg). The biphasic solution was sonicated for ~1 min, until the aqueous layer turns from clear and colorless to opaque. The organic layer was extracted, dried with sodium sulfate, and evaporated to yield 2.7 mg of **5.11.**

F_{68}Flav7·F_{48}TPB (5.12) Sodium tetrakis[3,5-bis(1,1,1,3,3,3-hexafluoro-2-methoxy-2-propyl) phenyl]borate trihydrate (0.875 mg, 0.476 μmol, 1.00 equiv.) and F_{68}Flav7·BF_4 (**5.8**) (1.10 mg, 0.434 μmol, 0.911 equiv.) were dissolved in DCM (1 mL). The DCM solution was added to water and the biphasic solution was sonicated in a bath sonicator for ~ 1 min. The organic layer was extracted, dried with sodium sulfate, and evaporated to yield **5.12** (2.0 mg, 0.47 μmol, quant.).

F_{68}Flav7·F_{104}TPB (5.14) Sodium tetrakis[3,5-bis(perfluorohexyl)phenyl]borate (**5.13**) (1.71 mg, 0.592 μmol, 1.47 equiv.) and F_{68}Flav7·BF_4 (**5.8**) (1.02 mg, 0.402 μmol, 1.00 equiv.) were dissolved in HFE-7100 (~2 mL), and washed with water for ~1 min. The fluorous layer was extracted, dried with sodium sulfate, filtered, and evaporated to yield **5.14** (~2.5 mg, 0.50 μmol, 85%).

5.6.6 Perfluorocarbon nanoemulsion formation

Nanoemulsion formation used in dye loading optimization F_{68}Flav7·F_{104}TPB (**5.14**), was dissolved in PFOB at either 0.77 mM, 1.6 mM, or 3.1 mM. Of these solutions, 40 μL was transferred to an Eppendorf tube and Pluronic F-68 in PBS (400 μL, 28 mg/mL solution) was added. The biphasic mixture was sonicated with a probe sonicator (35%, 3 min) at 0 ºC.

Nanoemulsion formation used for imaging F_{68}Flav7·F_{104}TPB (**5.14**) (0.662 mg) with a 2:1 ratio of F_{104}TPB counterion to F_{68}Flav7 dye, was dissolved in PFOB (50 μL). Polymer **5.15** (1.2 mg) was added to an Eppendorf tube and dissolved in DMF (20 μL). The dye solution and PBS (400 μL) were added to the Eppendorf tube and sonicated with a probe sonicator (35%, 3 min) at 0 ºC.

5.6.7 In vivo SWIR imaging with F_{68}Flav7·F_{104}TPB (5.14)

SWIR imaging apparatus For whole mouse imaging, a custom-built set-up was used. A Lumics laser unit LU0980D350-D30AN (35 W) was used for excitation. Laser modules are specced to ±10 nm. Laser output were coupled in a 4 × 1 fan-out fibre-optic bundle (Thorlabs BF46LS01) of 600 μm core diameter for each optical path. The output from the fibre was fixed in an excitation cube (Thorlabs KCB1EC/M), reflected off of a mirror (Thorlabs BBE1-E03) and passed through a positive achromat (Thorlabs AC254-050-B), SP filter (Thorlabs FESH1000) and an engineered diffuser (Thorlabs ED1-S20-MD) to provide uniform illumination over the working area. The excitation flux at the object was adjusted to be 100 mW cm^{-2} with an error of ± 3%. The working area was covered by a heating mat coated with blackout fabric (Thorlabs BK5). Emitted light was directed onto an Allied Vision Goldeye G-032 Cool TEC2 camera with a sensor temperature set point of −20 °C. The custom lens system consists of a 4f configuration with three lenses with focal length (f) = 500.0 mm (Thorlabs LB1909-C) and two f = 200.0 mm lenses (Thorlabs LB1199-C) with a custom filter set (Thorlabs FELH1100 x2). For ergonomic reasons, a 2-inch protected silver-coated elliptical mirror (PFE20-P01) mounted to a kinematic mount (Thorlabs KCB2EC/M) was used. The assembly was partially enclosed to avoid excess light while enabling manipulation of the field of view during operation. The image acquisition toolbox of the MATLAB programming

environment was used in combination with a custom MATLAB script to preview and collect the required image data in 8-bit format.

Animal procedures Animal experiments were conducted in conformity with the institutional guidelines. Non-invasive whole mouse imaging was performed on athymic nude female mice (6–16 weeks old, weight between 20–25 g), purchased from Envigo. Mice were anaesthetized with an i.p. injection of a ketamine/xylazine mixture. Tail vein injections were performed with a catheter assembled from a 30-gauge needle connected through plastic tubing to a syringe prefilled with isotonic saline solution. The bevel of the needle was then inserted into the tail vein and secured using tissue adhesive. The plastic tubing was then connected to a syringe (30-gauge needle) prefilled with the probe of interest. All probes were filtered through a 0.22 μm syringe filter prior to i.v. injection.

Imaging procedures PFC nanoemulsions, fabricated with polymer **5.15** in PBS (190 μL) containing 34 nmol of **5.14,** were injected via tail vein into an anesthetized mouse and immediately imaged on the SWIR imaging apparatus using an exposure time = 60 ms, 16.6 fps for the head (in Figure 5.8D); exposure time = 120 ms, 8.3 fps for the hindlimb (in Figure 5.8E).

Image processing procedures Images were processed using the Fiji distribution[63] of ImageJ[64]. All images were background corrected with a ten-frame averaged background file to correct for non-linearities in the detector and/or excitation. Displayed images were averaged over 200 frames and outliers were removed (2.0 pixels, threshold = 20).

5.7 Spectra related to Chapter Five

5.7.1 ^{1}H NMR spectra

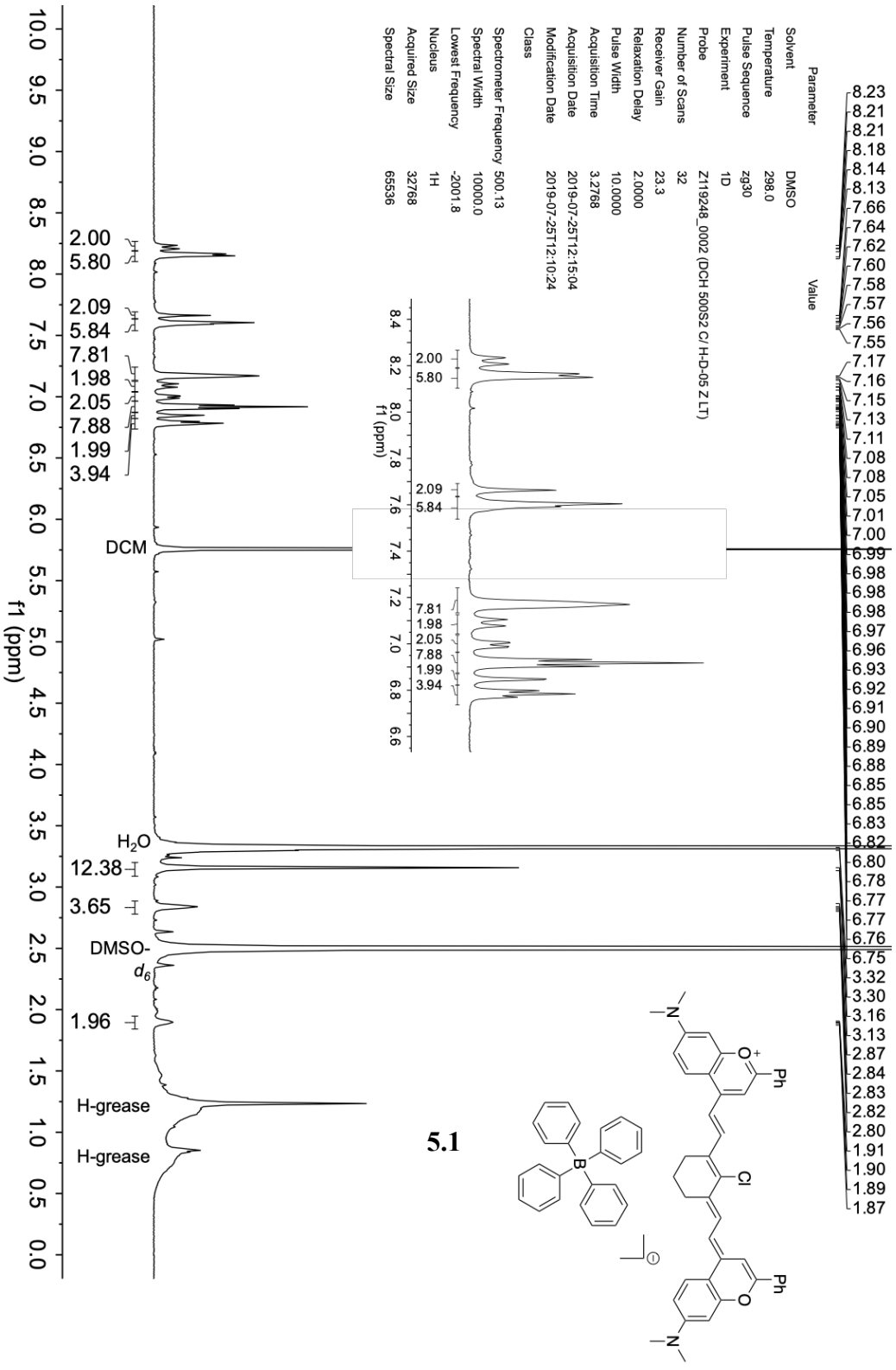

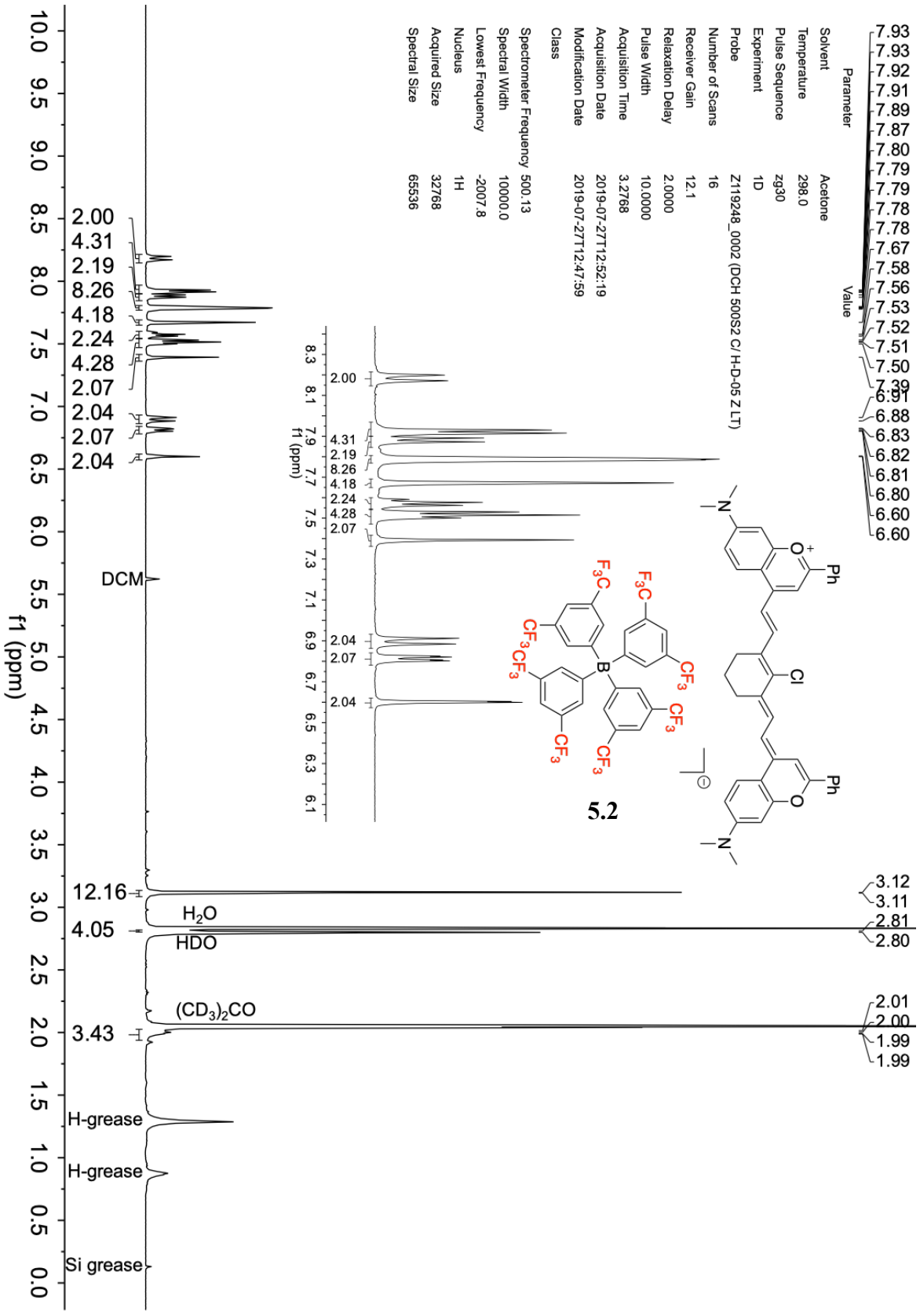
Parameter Value
Solvent Acetone
Temperature 298.0
Pulse Sequence zg30
Experiment 1D
Probe Z119248_0002 (DCH 500S2 C/H-D-05 Z LT)
Number of Scans 16
Receiver Gain 12.1
Relaxation Delay 2.0000
Pulse Width 10.0000
Acquisition Time 3.2768
Acquisition Date 2019-07-27T12:52:19
Modification Date 2019-07-27T12:47:59
Class
Spectrometer Frequency 500.13
Spectral Width 10000.0
Lowest Frequency -2007.8
Nucleus 1H
Acquired Size 32768
Spectral Size 65536
7.93 7.93 7.92 7.91 7.89 7.87 7.80 7.79 7.79 7.78 7.78 7.67 7.58 7.56 7.53 7.52 7.51 7.50 7.39 6.91 6.88 6.83 6.82 6.81 6.80 6.60 6.60
2.00 4.31 2.19 8.26 4.18 2.24 4.28 2.07 2.04 2.07 2.04
DCM
12.16 4.05 3.43
H2O
HDO
(CD3)2CO
H-grease
H-grease
Si grease
3.12 3.11 2.81 2.80 2.01 2.00 1.99 1.99
f1 (ppm)
5.2

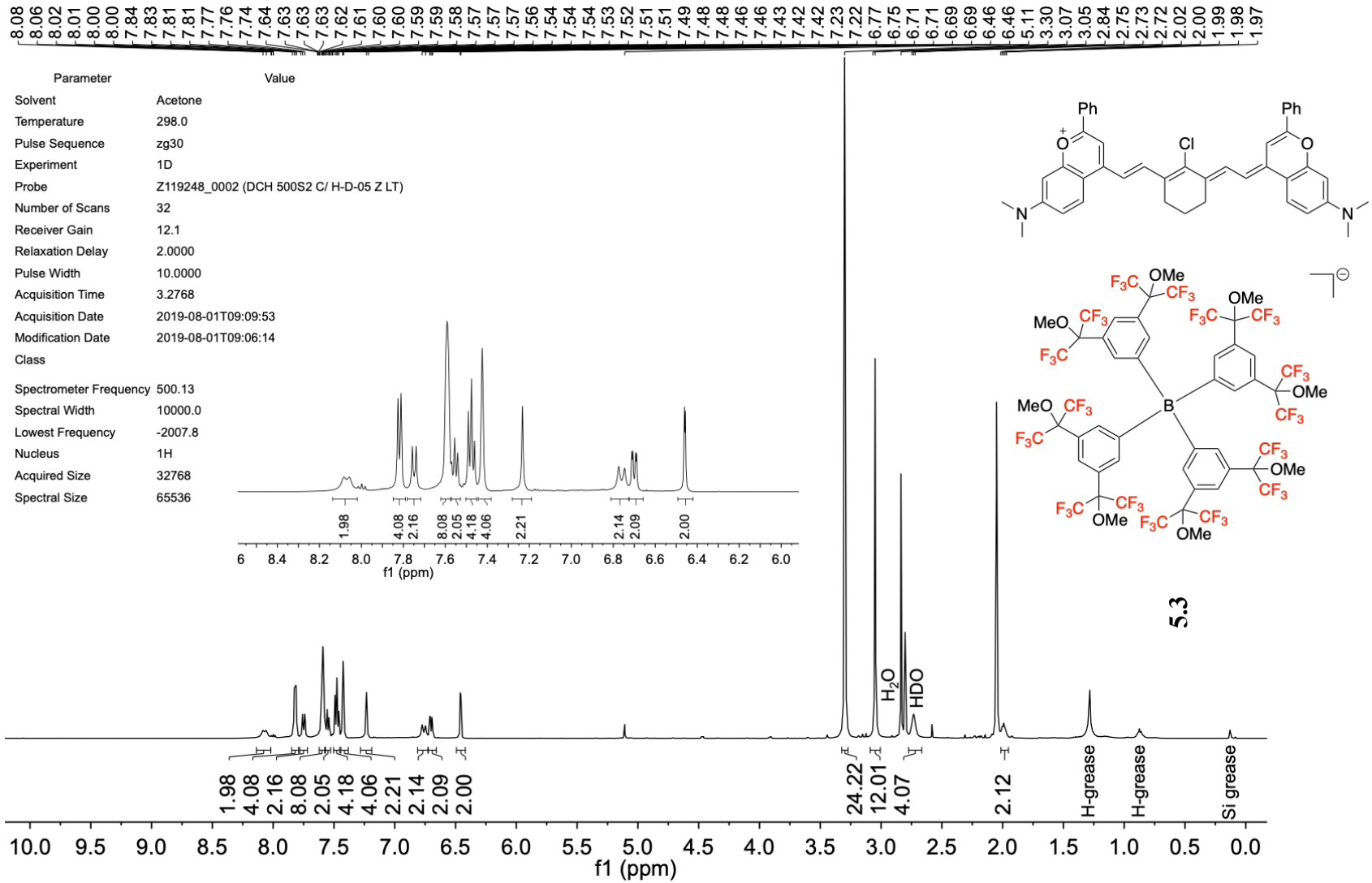
Parameter Value
Solvent Acetone
Temperature 298.0
Pulse Sequence zg30
Experiment 1D
Probe Z119248_0002 (DCH 500S2 C/ H-D-05 Z LT)
Number of Scans 32
Receiver Gain 12.1
Relaxation Delay 2.0000
Pulse Width 10.0000
Acquisition Time 3.2768
Acquisition Date 2019-08-01T09:09:53
Modification Date 2019-08-01T09:06:14
Class
Spectrometer Frequency 500.13
Spectral Width 10000.0
Lowest Frequency -2007.8
Nucleus 1H
Acquired Size 32768
Spectral Size 65536
f1 (ppm)
H2O
HDO
H-grease
H-grease
Si grease
5.3

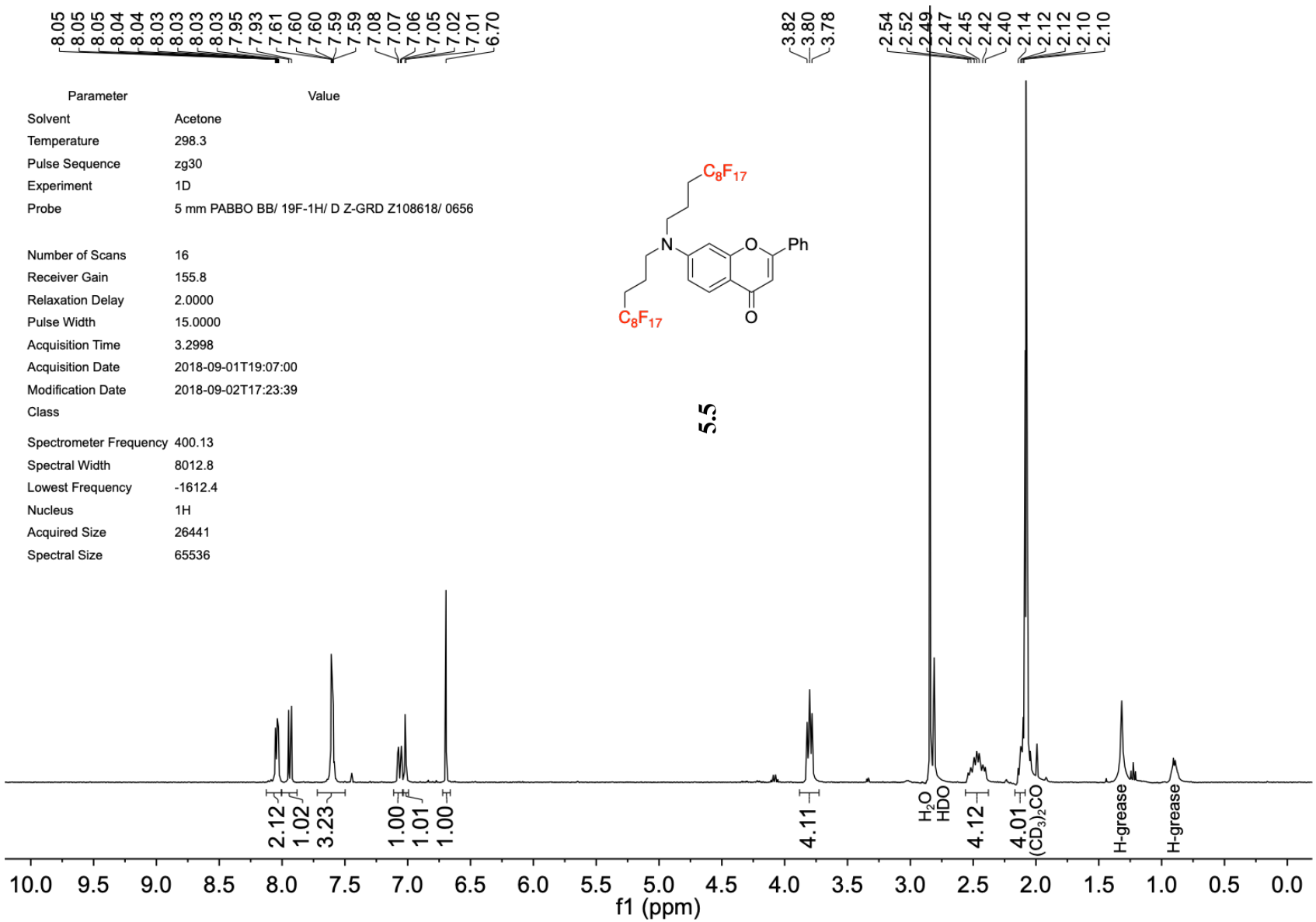
8.05 8.05 8.05 8.04 8.04 8.03 8.03 8.03 8.03 7.95 7.93 7.61 7.60 7.60 7.59 7.59 7.08 7.07 7.06 7.05 7.02 7.01 6.70
3.82 3.80 3.78
2.54 2.52 2.49 2.47 2.45 2.42 2.40 2.14 2.12 2.12 2.10 2.10
Parameter Value
Solvent Acetone
Temperature 298.3
Pulse Sequence zg30
Experiment 1D
Probe 5 mm PABBO BB/ 19F-1H/ D Z-GRD Z108618/ 0656
Number of Scans 16
Receiver Gain 155.8
Relaxation Delay 2.0000
Pulse Width 15.0000
Acquisition Time 3.2998
Acquisition Date 2018-09-01T19:07:00
Modification Date 2018-09-02T17:23:39
Class
Spectrometer Frequency 400.13
Spectral Width 8012.8
Lowest Frequency -1612.4
Nucleus 1H
Acquired Size 26441
Spectral Size 65536
C8F17
N
O
Ph
O
C8F17
5.5
2.12 1.02 3.23 1.00 1.01 1.00 4.11 H2O HDO 4.12 4.01 (CD3)2CO H-grease H-grease
10.0 9.5 9.0 8.5 8.0 7.5 7.0 6.5 6.0 5.5 5.0 4.5 4.0 3.5 3.0 2.5 2.0 1.5 1.0 0.5 0.0
f1 (ppm)

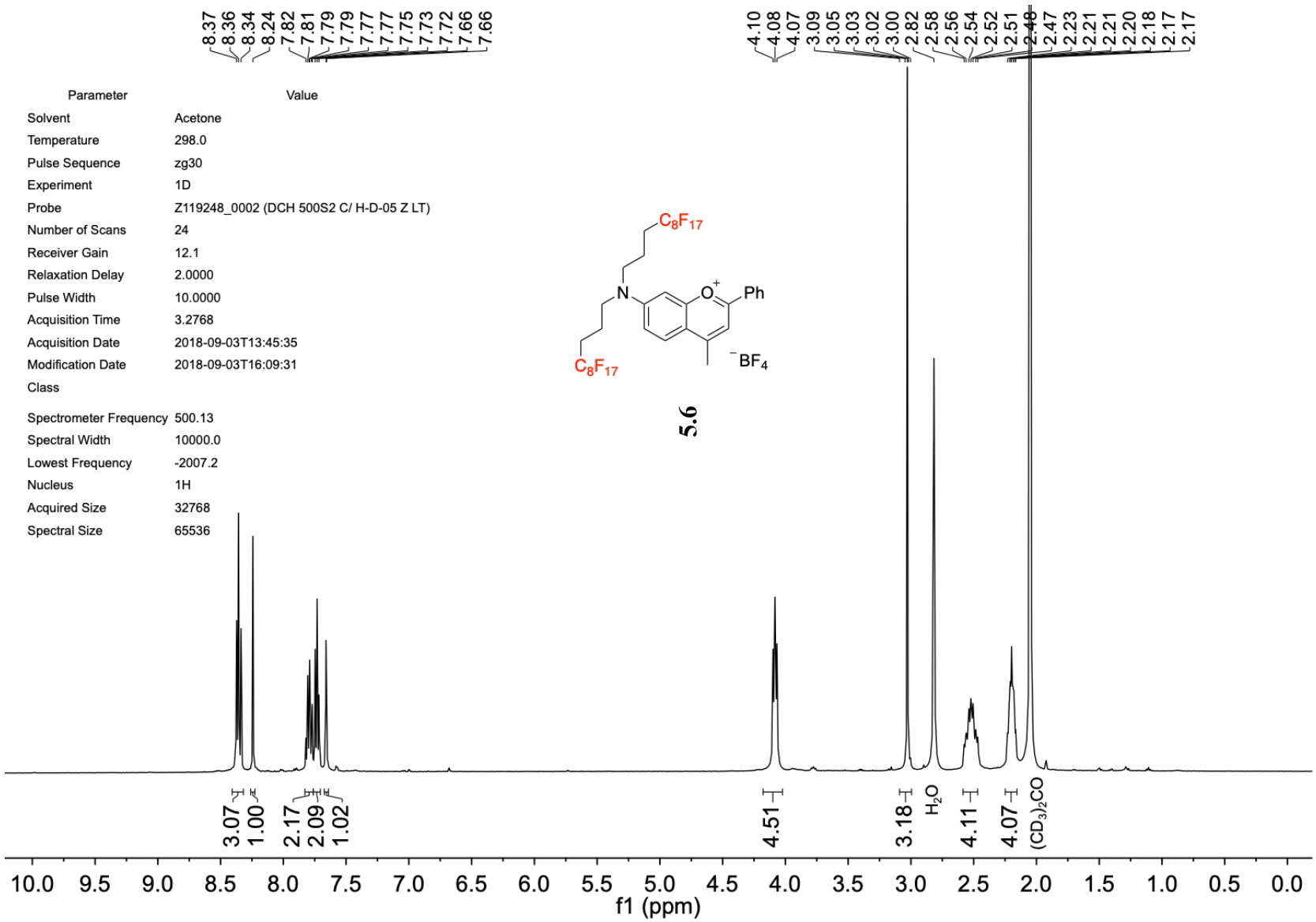
8.37
8.36
8.34
8.24
7.82
7.81
7.79
7.79
7.77
7.77
7.75
7.73
7.72
7.66
7.66
4.10
4.08
4.07
3.09
3.05
3.03
3.02
3.00
2.82
2.58
2.56
2.54
2.52
2.51
2.48
2.47
2.23
2.21
2.21
2.20
2.18
2.17
2.17
Parameter Value
Solvent Acetone
Temperature 298.0
Pulse Sequence zg30
Experiment 1D
Probe Z119248_0002 (DCH 500S2 C/ H-D-05 Z LT)
Number of Scans 24
Receiver Gain 12.1
Relaxation Delay 2.0000
Pulse Width 10.0000
Acquisition Time 3.2768
Acquisition Date 2018-09-03T13:45:35
Modification Date 2018-09-03T16:09:31
Class
Spectrometer Frequency 500.13
Spectral Width 10000.0
Lowest Frequency -2007.2
Nucleus 1H
Acquired Size 32768
Spectral Size 65536
C8F17
N
O+
Ph
C8F17
−BF4
5.6
3.07
1.00
2.17
2.09
1.02
4.51
3.18
H2O
4.11
4.07
(CD3)2CO
10.0 9.5 9.0 8.5 8.0 7.5 7.0 6.5 6.0 5.5 5.0 4.5 4.0 3.5 3.0 2.5 2.0 1.5 1.0 0.5 0.0
f1 (ppm)

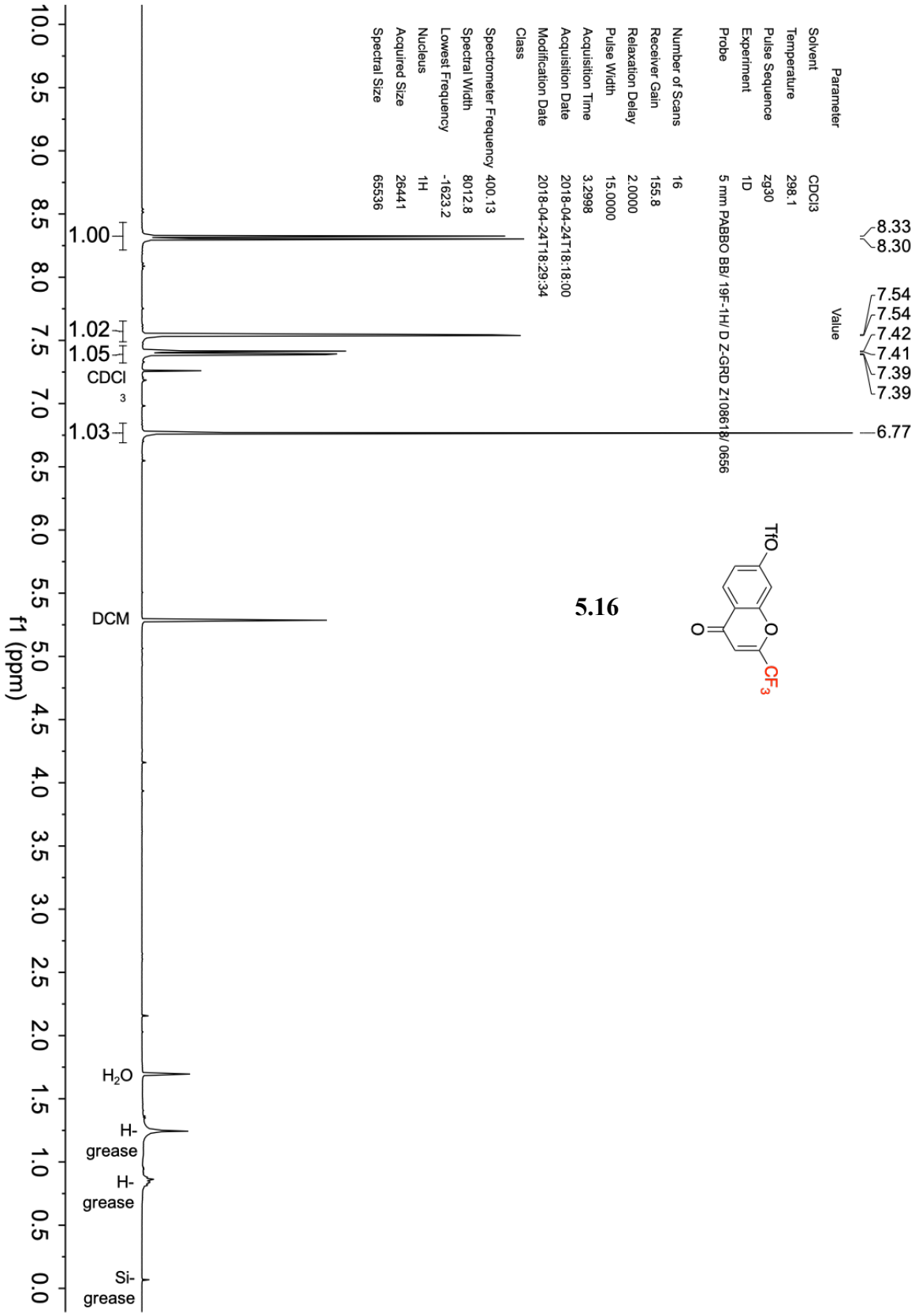
Parameter
Value
Solvent
CDCl3
Temperature
298.1
Pulse Sequence
zg30
Experiment
1D
Probe
5 mm PABBO BB/ 19F-1H/ D Z-GRD Z108618/ 0656
Number of Scans
16
Receiver Gain
155.8
Relaxation Delay
2.0000
Pulse Width
15.0000
Acquisition Time
3.2998
Acquisition Date
2018-04-24T18:18:00
Modification Date
2018-04-24T18:29:34
Class
Spectrometer Frequency
400.13
Spectral Width
8012.8
Lowest Frequency
-1623.2
Nucleus
1H
Acquired Size
26441
Spectral Size
65536
8.33
8.30
7.54
7.54
7.42
7.41
7.39
7.39
6.77
TfO
O
O
CF3
5.16
1.00
1.02
1.05
CDCl3
1.03
DCM
H2O
H-grease
H-grease
Si-grease
f1 (ppm)

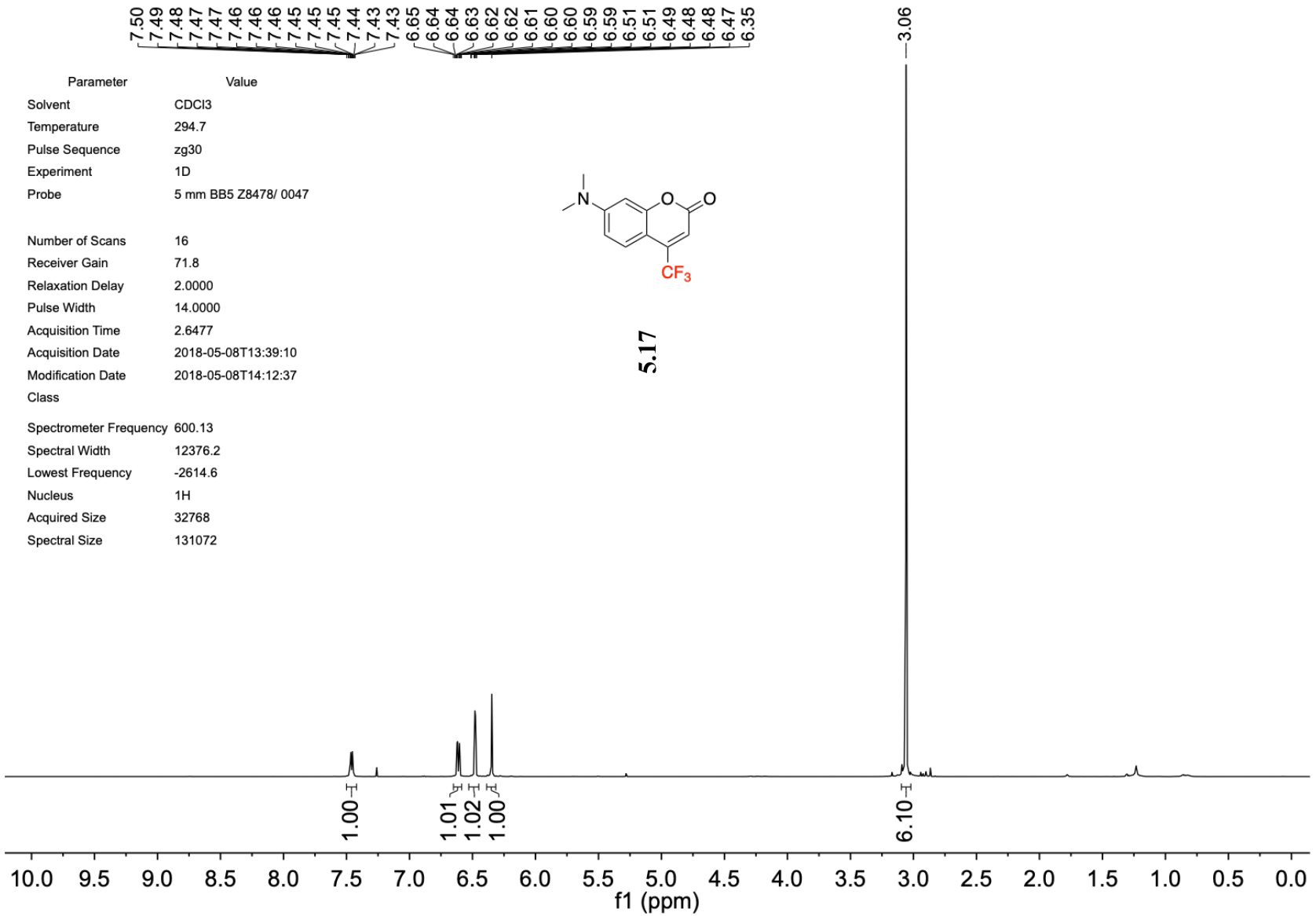
7.50 7.49 7.48 7.47 7.47 7.46 7.46 7.46 7.45 7.45 7.45 7.44 7.43 7.43
6.65 6.64 6.64 6.63 6.62 6.62 6.61 6.60 6.60 6.59 6.59 6.51 6.51 6.49 6.48 6.48 6.47 6.35
3.06
Parameter Value
Solvent CDCl3
Temperature 294.7
Pulse Sequence zg30
Experiment 1D
Probe 5 mm BB5 Z8478/ 0047
Number of Scans 16
Receiver Gain 71.8
Relaxation Delay 2.0000
Pulse Width 14.0000
Acquisition Time 2.6477
Acquisition Date 2018-05-08T13:39:10
Modification Date 2018-05-08T14:12:37
Class
Spectrometer Frequency 600.13
Spectral Width 12376.2
Lowest Frequency -2614.6
Nucleus 1H
Acquired Size 32768
Spectral Size 131072
N
O
O
CF3
5.17
1.00
1.01
1.02
1.00
6.10
10.0 9.5 9.0 8.5 8.0 7.5 7.0 6.5 6.0 5.5 5.0 4.5 4.0 3.5 3.0 2.5 2.0 1.5 1.0 0.5 0.0
f1 (ppm)

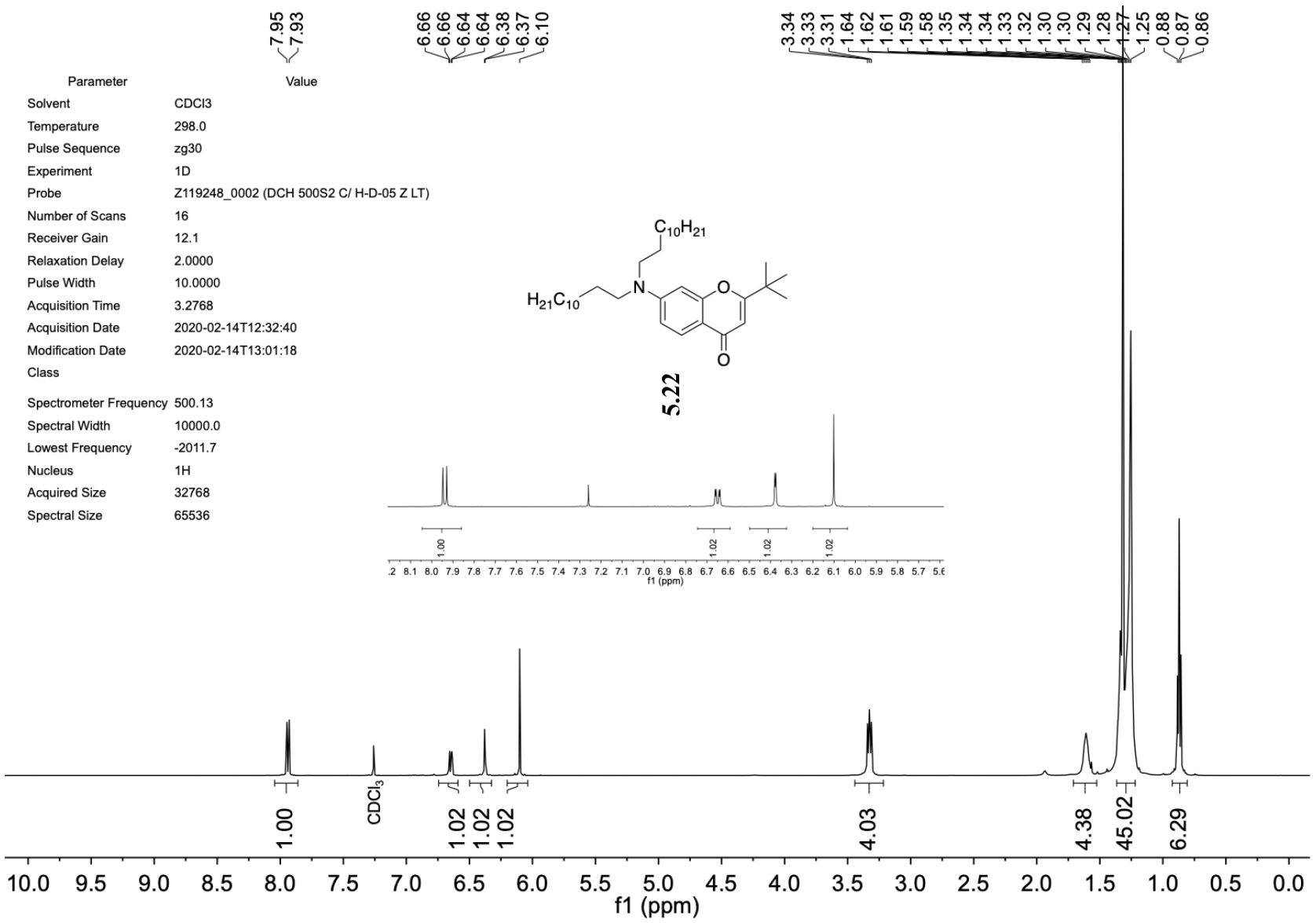
7.95
7.93
6.66
6.66
6.64
6.64
6.38
6.37
6.10
3.34
3.33
3.31
1.64
1.62
1.61
1.59
1.58
1.35
1.34
1.34
1.33
1.32
1.30
1.30
1.29
1.28
1.27
1.25
0.88
0.87
0.86
Parameter Value
Solvent CDCl3
Temperature 298.0
Pulse Sequence zg30
Experiment 1D
Probe Z119248_0002 (DCH 500S2 C/ H-D-05 Z LT)
Number of Scans 16
Receiver Gain 12.1
Relaxation Delay 2.0000
Pulse Width 10.0000
Acquisition Time 3.2768
Acquisition Date 2020-02-14T12:32:40
Modification Date 2020-02-14T13:01:18
Class
Spectrometer Frequency 500.13
Spectral Width 10000.0
Lowest Frequency -2011.7
Nucleus 1H
Acquired Size 32768
Spectral Size 65536
C10H21
H21C10
N
O
O
5.22
1.00
1.02
1.02
1.02
f1 (ppm)
CDCl3
1.00
1.02
1.02
1.02
4.03
4.38
45.02
6.29
10.0 9.5 9.0 8.5 8.0 7.5 7.0 6.5 6.0 5.5 5.0 4.5 4.0 3.5 3.0 2.5 2.0 1.5 1.0 0.5 0.0
f1 (ppm)

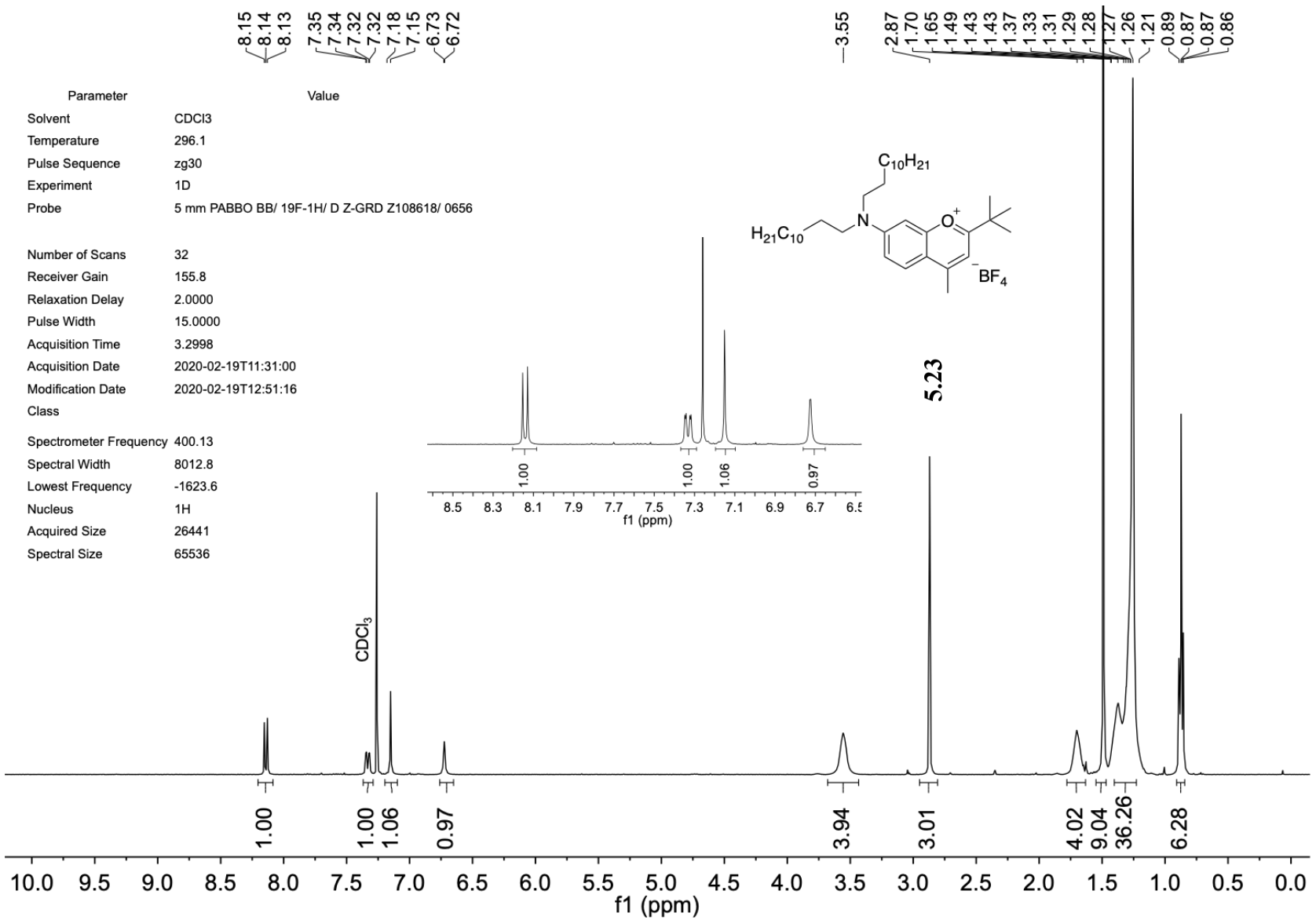
8.15
8.14
8.13
7.35
7.34
7.32
7.32
7.18
7.15
6.73
6.72
3.55
2.87
1.70
1.65
1.49
1.43
1.43
1.37
1.33
1.31
1.29
1.28
1.27
1.26
1.21
0.89
0.87
0.87
0.86
Parameter Value
Solvent CDCl3
Temperature 296.1
Pulse Sequence zg30
Experiment 1D
Probe 5 mm PABBO BB/ 19F-1H/ D Z-GRD Z108618/ 0656
Number of Scans 32
Receiver Gain 155.8
Relaxation Delay 2.0000
Pulse Width 15.0000
Acquisition Time 3.2998
Acquisition Date 2020-02-19T11:31:00
Modification Date 2020-02-19T12:51:16
Class
Spectrometer Frequency 400.13
Spectral Width 8012.8
Lowest Frequency -1623.6
Nucleus 1H
Acquired Size 26441
Spectral Size 65536
$C_{10}H_{21}$
$H_{21}C_{10}$
N
O+
BF_4^-
5.23
$CDCl_3$
1.00
1.00
1.06
0.97
3.94
3.01
4.02
9.04
36.26
6.28
f1 (ppm)

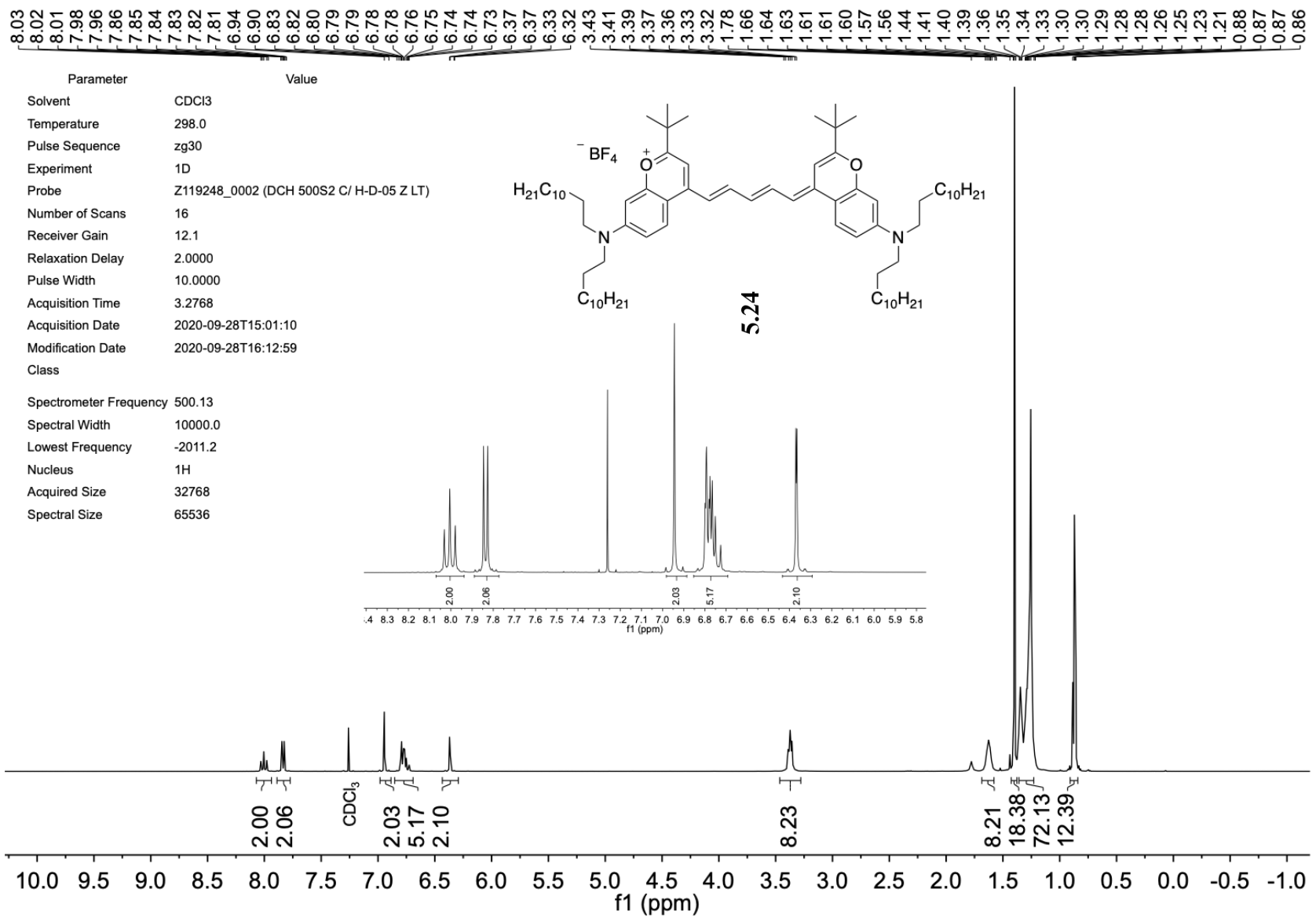
8.03 8.02 8.01 7.98 7.96 7.86 7.85 7.84 7.83 7.82 7.81 6.94 6.90 6.83 6.82 6.80 6.79 6.79 6.78 6.78 6.76 6.75 6.74 6.74 6.73 6.37 6.37 6.33 6.32 3.43 3.41 3.39 3.37 3.36 3.33 3.32 1.78 1.66 1.64 1.63 1.61 1.61 1.60 1.57 1.56 1.44 1.41 1.40 1.39 1.36 1.35 1.34 1.33 1.30 1.30 1.29 1.28 1.28 1.26 1.25 1.23 1.21 0.88 0.87 0.87 0.86
Parameter Value
Solvent CDCl3
Temperature 298.0
Pulse Sequence zg30
Experiment 1D
Probe Z119248_0002 (DCH 500S2 C/ H-D-05 Z LT)
Number of Scans 16
Receiver Gain 12.1
Relaxation Delay 2.0000
Pulse Width 10.0000
Acquisition Time 3.2768
Acquisition Date 2020-09-28T15:01:10
Modification Date 2020-09-28T16:12:59
Class
Spectrometer Frequency 500.13
Spectral Width 10000.0
Lowest Frequency -2011.2
Nucleus 1H
Acquired Size 32768
Spectral Size 65536
BF4
H21C10
C10H21
N
O
5.24
2.00 2.06 2.03 5.17 2.10
f1 (ppm)
CDCl3
2.00 2.06 2.03 5.17 2.10 8.23 8.21 18.38 72.13 12.39
10.0 9.5 9.0 8.5 8.0 7.5 7.0 6.5 6.0 5.5 5.0 4.5 4.0 3.5 3.0 2.5 2.0 1.5 1.0 0.5 0.0 -0.5 -1.0
f1 (ppm)

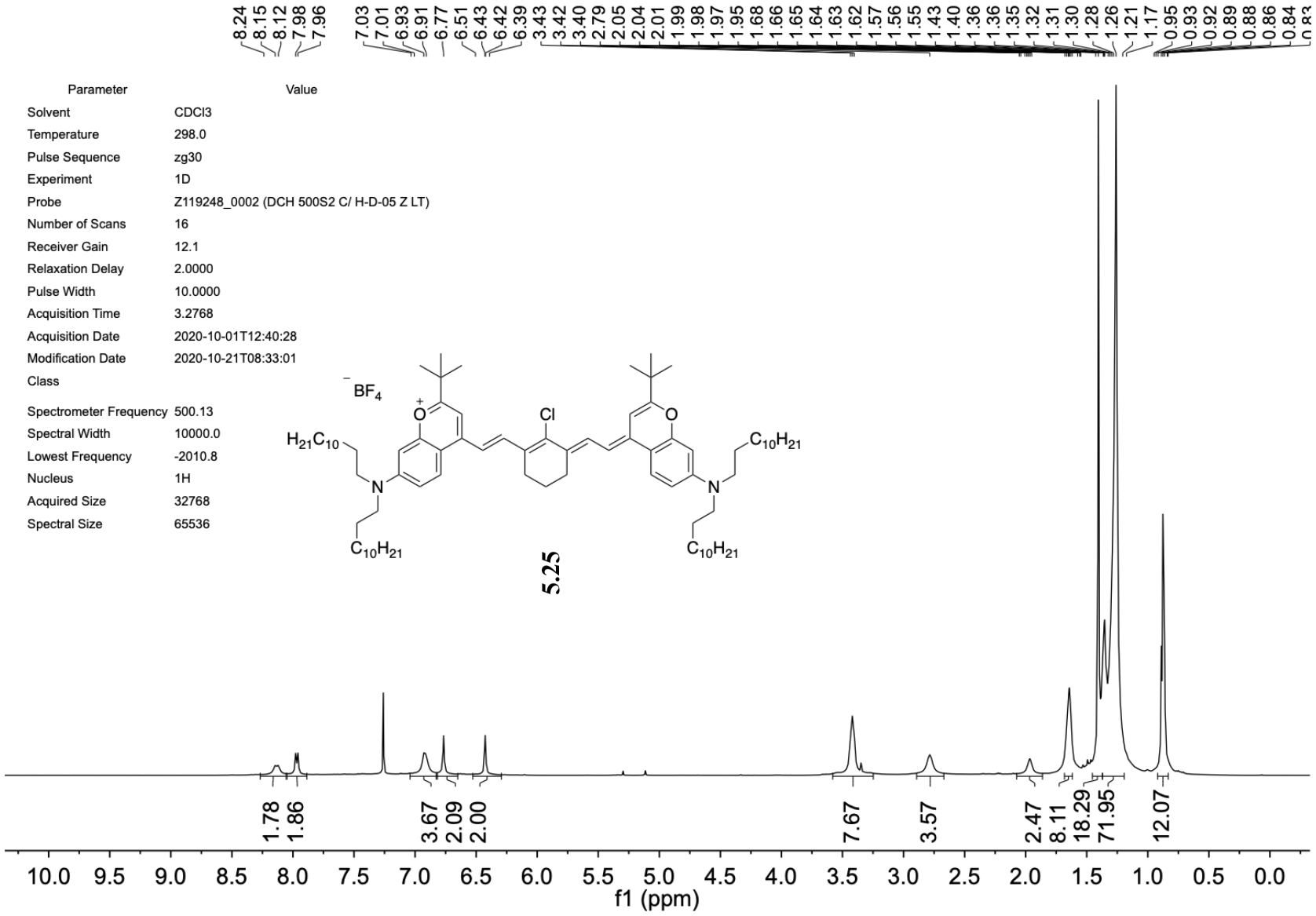
8.24 8.15 8.12 7.98 7.96 7.03 7.01 6.93 6.91 6.77 6.51 6.43 6.42 6.39 3.43 3.42 3.40 2.79 2.05 2.04 2.01 1.99 1.98 1.97 1.95 1.68 1.66 1.65 1.64 1.63 1.62 1.57 1.56 1.55 1.43 1.40 1.36 1.36 1.35 1.32 1.31 1.30 1.28 1.26 1.21 1.17 0.95 0.93 0.92 0.89 0.88 0.86 0.84
Parameter Value
Solvent CDCl3
Temperature 298.0
Pulse Sequence zg30
Experiment 1D
Probe Z119248_0002 (DCH 500S2 C/ H-D-05 Z LT)
Number of Scans 16
Receiver Gain 12.1
Relaxation Delay 2.0000
Pulse Width 10.0000
Acquisition Time 3.2768
Acquisition Date 2020-10-01T12:40:28
Modification Date 2020-10-21T08:33:01
Class
Spectrometer Frequency 500.13
Spectral Width 10000.0
Lowest Frequency -2010.8
Nucleus 1H
Acquired Size 32768
Spectral Size 65536
BF4
Cl
H21C10
C10H21
5.25
1.78 1.86 3.67 2.09 2.00 7.67 3.57 2.47 8.11 18.29 71.95 12.07
10.0 9.5 9.0 8.5 8.0 7.5 7.0 6.5 6.0 5.5 5.0 4.5 4.0 3.5 3.0 2.5 2.0 1.5 1.0 0.5 0.0
f1 (ppm)

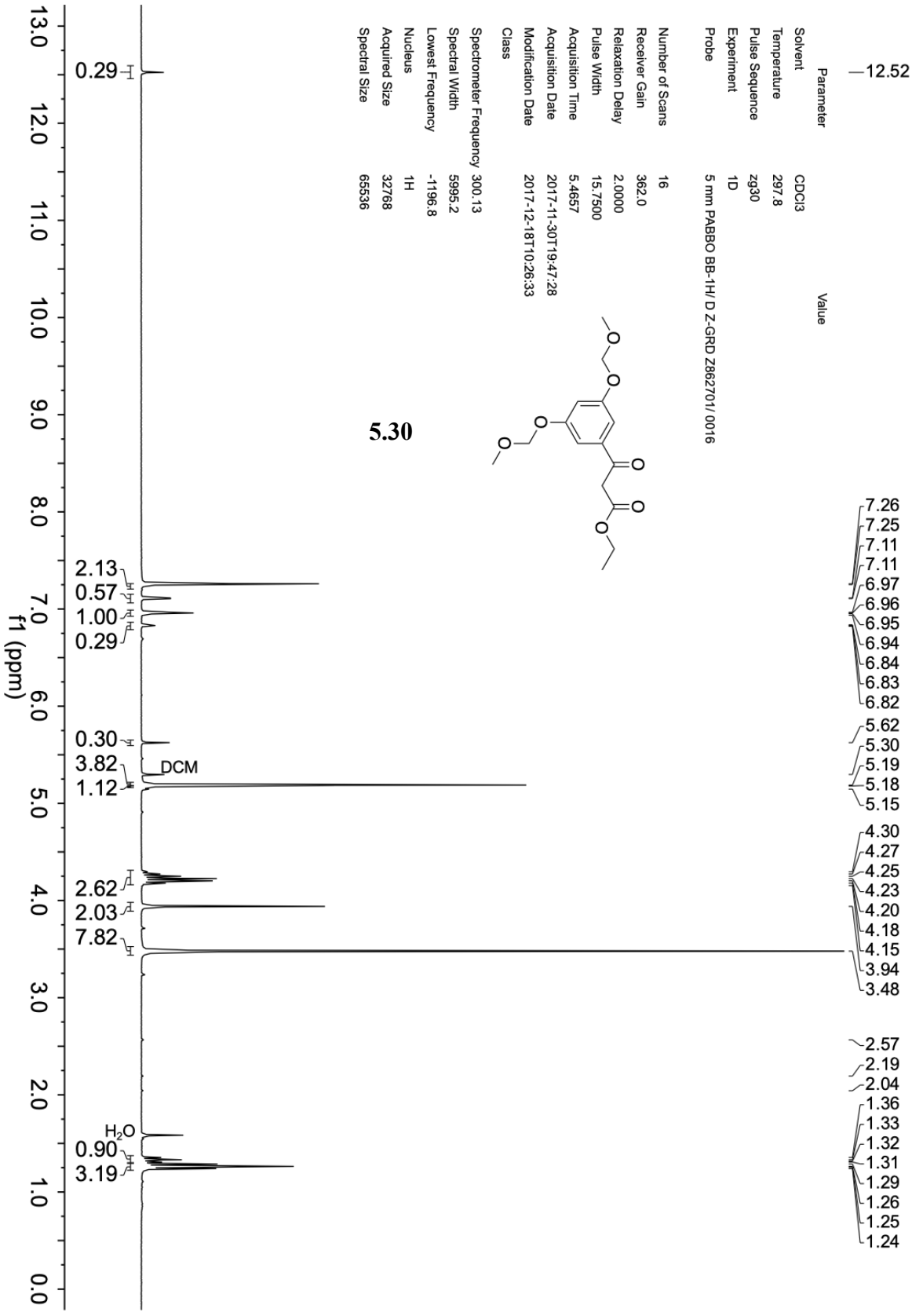
Parameter
Value
Solvent
CDCl3
Temperature
297.8
Pulse Sequence
zg30
Experiment
1D
Probe
5 mm PABBO BB-1H/ D Z-GRD Z862701/ 0016
Number of Scans
16
Receiver Gain
362.0
Relaxation Delay
2.0000
Pulse Width
15.7500
Acquisition Time
5.4657
Acquisition Date
2017-11-30T19:47:28
Modification Date
2017-12-18T10:26:33
Class
Spectrometer Frequency
300.13
Spectral Width
5995.2
Lowest Frequency
-1196.8
Nucleus
1H
Acquired Size
32768
Spectral Size
65536
5.30
12.52
7.26
7.25
7.11
7.11
6.97
6.96
6.95
6.94
6.84
6.83
6.82
5.62
5.30
5.19
5.18
5.15
4.30
4.27
4.25
4.23
4.20
4.18
4.15
3.94
3.48
2.57
2.19
2.04
1.36
1.33
1.32
1.31
1.29
1.26
1.25
1.24
0.29
2.13
0.57
1.00
0.29
0.30
3.82
1.12
2.62
2.03
7.82
H2O
0.90
3.19
DCM
f1 (ppm)

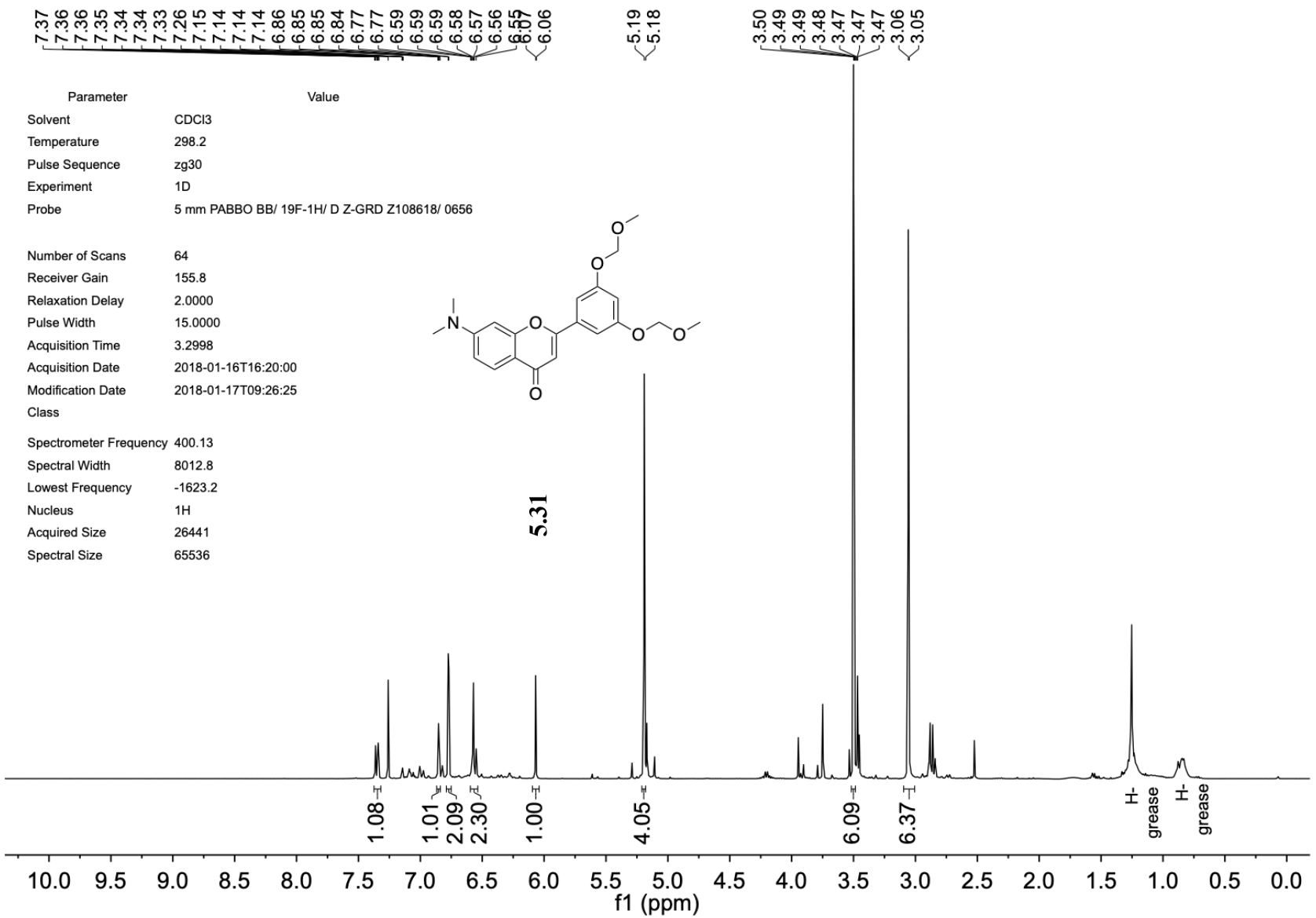
7.37 7.36 7.36 7.35 7.34 7.34 7.33 7.26 7.15 7.14 7.14 7.14 6.86 6.85 6.85 6.84 6.77 6.77 6.59 6.59 6.59 6.58 6.57 6.56 6.55 6.07 6.06
5.19 5.18
3.50 3.49 3.49 3.48 3.47 3.47 3.47 3.06 3.05
Parameter Value
Solvent CDCl3
Temperature 298.2
Pulse Sequence zg30
Experiment 1D
Probe 5 mm PABBO BB/ 19F-1H/ D Z-GRD Z108618/ 0656
Number of Scans 64
Receiver Gain 155.8
Relaxation Delay 2.0000
Pulse Width 15.0000
Acquisition Time 3.2998
Acquisition Date 2018-01-16T16:20:00
Modification Date 2018-01-17T09:26:25
Class
Spectrometer Frequency 400.13
Spectral Width 8012.8
Lowest Frequency -1623.2
Nucleus 1H
Acquired Size 26441
Spectral Size 65536
5.31
1.08 1.01 2.09 2.30 1.00 4.05 6.09 6.37
H-grease H-grease
10.0 9.5 9.0 8.5 8.0 7.5 7.0 6.5 6.0 5.5 5.0 4.5 4.0 3.5 3.0 2.5 2.0 1.5 1.0 0.5 0.0
f1 (ppm)

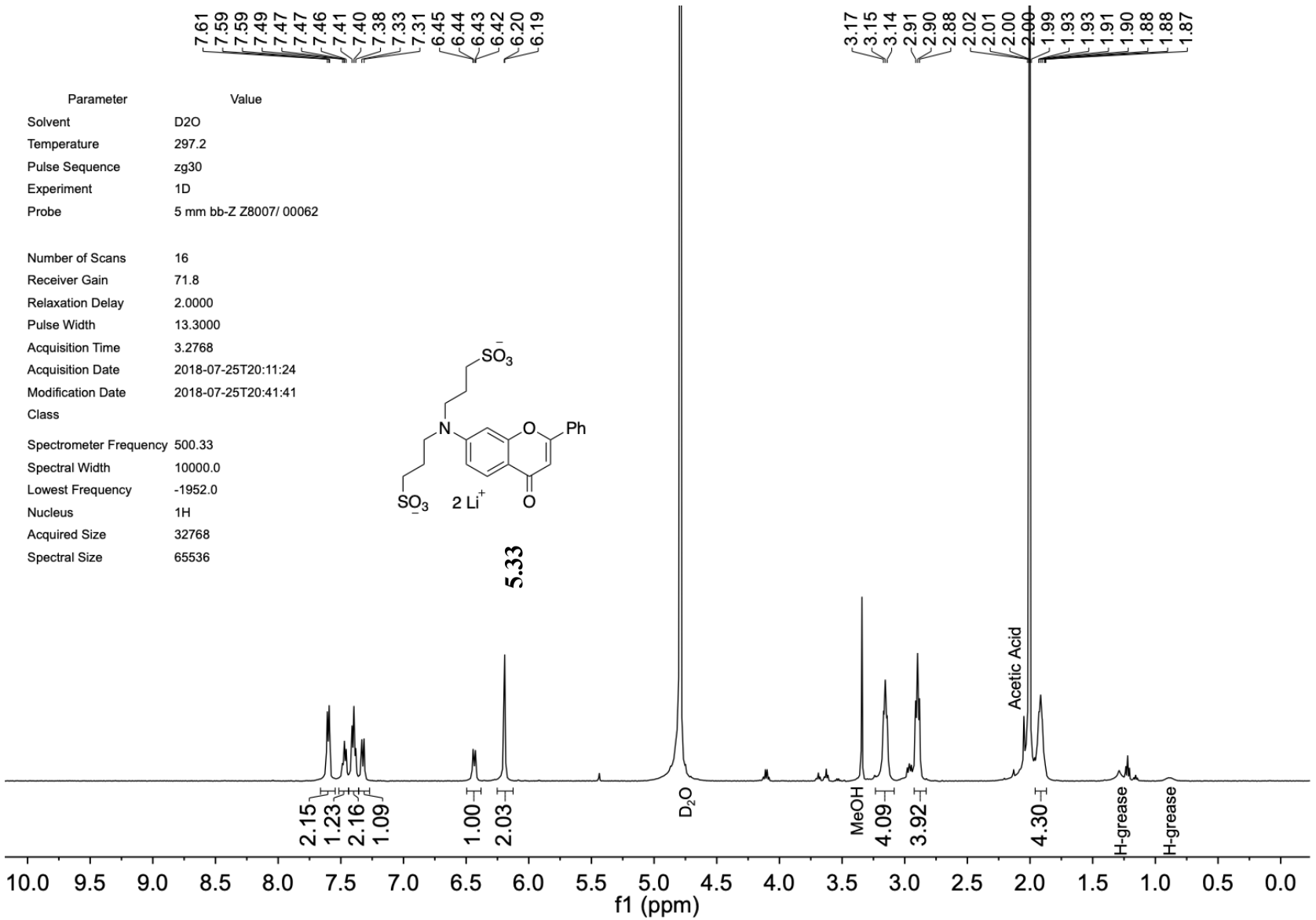
7.61 7.59 7.59 7.49 7.47 7.47 7.46 7.41 7.40 7.38 7.33 7.31 6.45 6.44 6.43 6.42 6.20 6.19
3.17 3.15 3.14 2.91 2.90 2.88 2.02 2.01 2.00 2.00 1.99 1.93 1.93 1.91 1.90 1.88 1.88 1.87
Parameter Value
Solvent D2O
Temperature 297.2
Pulse Sequence zg30
Experiment 1D
Probe 5 mm bb-Z Z8007/ 00062
Number of Scans 16
Receiver Gain 71.8
Relaxation Delay 2.0000
Pulse Width 13.3000
Acquisition Time 3.2768
Acquisition Date 2018-07-25T20:11:24
Modification Date 2018-07-25T20:41:41
Class
Spectrometer Frequency 500.33
Spectral Width 10000.0
Lowest Frequency -1952.0
Nucleus 1H
Acquired Size 32768
Spectral Size 65536
SO3
N
O
Ph
SO3 2 Li+ O
5.33
Acetic Acid
D2O
MeOH
H-grease
H-grease
2.15 1.23 2.16 1.09 1.00 2.03 4.09 3.92 4.30
10.0 9.5 9.0 8.5 8.0 7.5 7.0 6.5 6.0 5.5 5.0 4.5 4.0 3.5 3.0 2.5 2.0 1.5 1.0 0.5 0.0
f1 (ppm)

5.7.2 ^{11}B NMR spectrum

Parameter	Value
Solvent	Acetone
Temperature	296.7
Pulse Sequence	zg
Experiment	1D
Probe	5 mm bb-Z Z8007/ 00062
Number of Scans	2046
Receiver Gain	512.0
Relaxation Delay	0.0000
Pulse Width	8.0000
Acquisition Time	0.0559
Acquisition Date	2019-07-27T16:09:36
Modification Date	2019-07-27T16:46:18
Class	
Spectrometer Frequency	160.53
Spectral Width	64102.6
Lowest Frequency	-31966.8
Nucleus	11B
Acquired Size	3584
Spectral Size	8192

-5.84

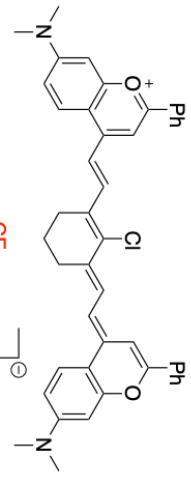

5.2

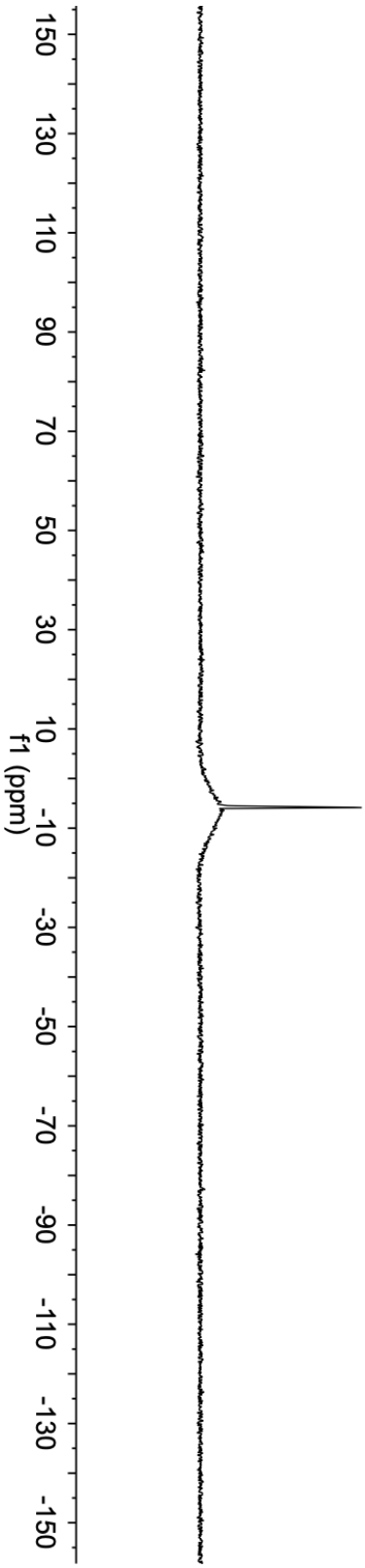

5.7.3 ^{13}C NMR Spectra

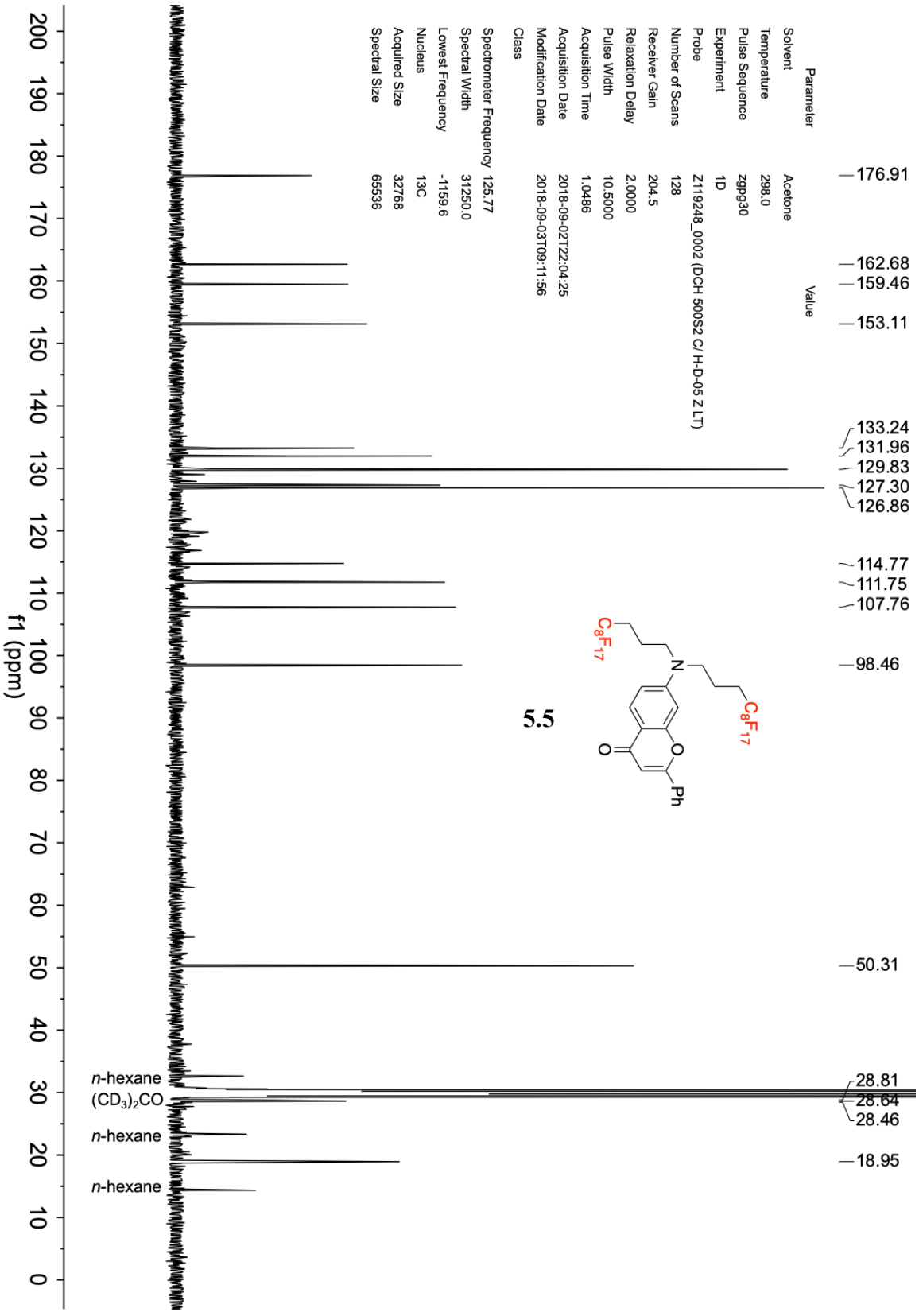

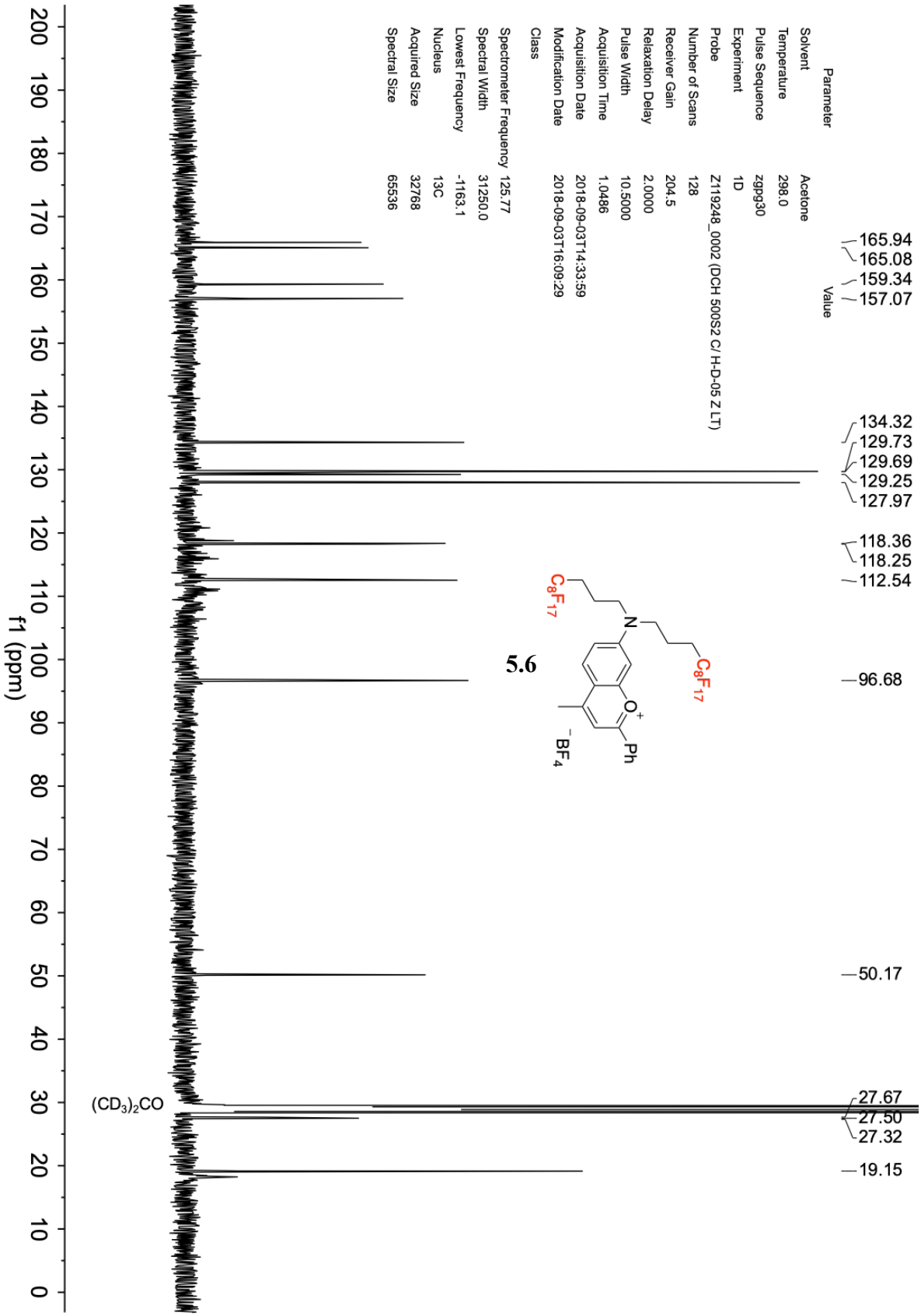
Parameter
Value
Solvent
Acetone
Temperature
298.0
Pulse Sequence
zgpg30
Experiment
1D
Probe
Z119248_0002 (DCH 500S2 C/ H-D-05 Z LT)
Number of Scans
128
Receiver Gain
204.5
Relaxation Delay
2.0000
Pulse Width
10.5000
Acquisition Time
1.0486
Acquisition Date
2018-09-03T14:33:59
Modification Date
2018-09-03T16:09:29
Class
Spectrometer Frequency
125.77
Spectral Width
31250.0
Lowest Frequency
-1163.1
Nucleus
13C
Acquired Size
32768
Spectral Size
65536
165.94
165.08
159.34
157.07
134.32
129.73
129.69
129.25
127.97
118.36
118.25
112.54
96.68
50.17
27.67
27.50
27.32
19.15
(CD3)2CO
f1 (ppm)
5.6
C8F17
N
C8F17
O+
Ph
BF4−

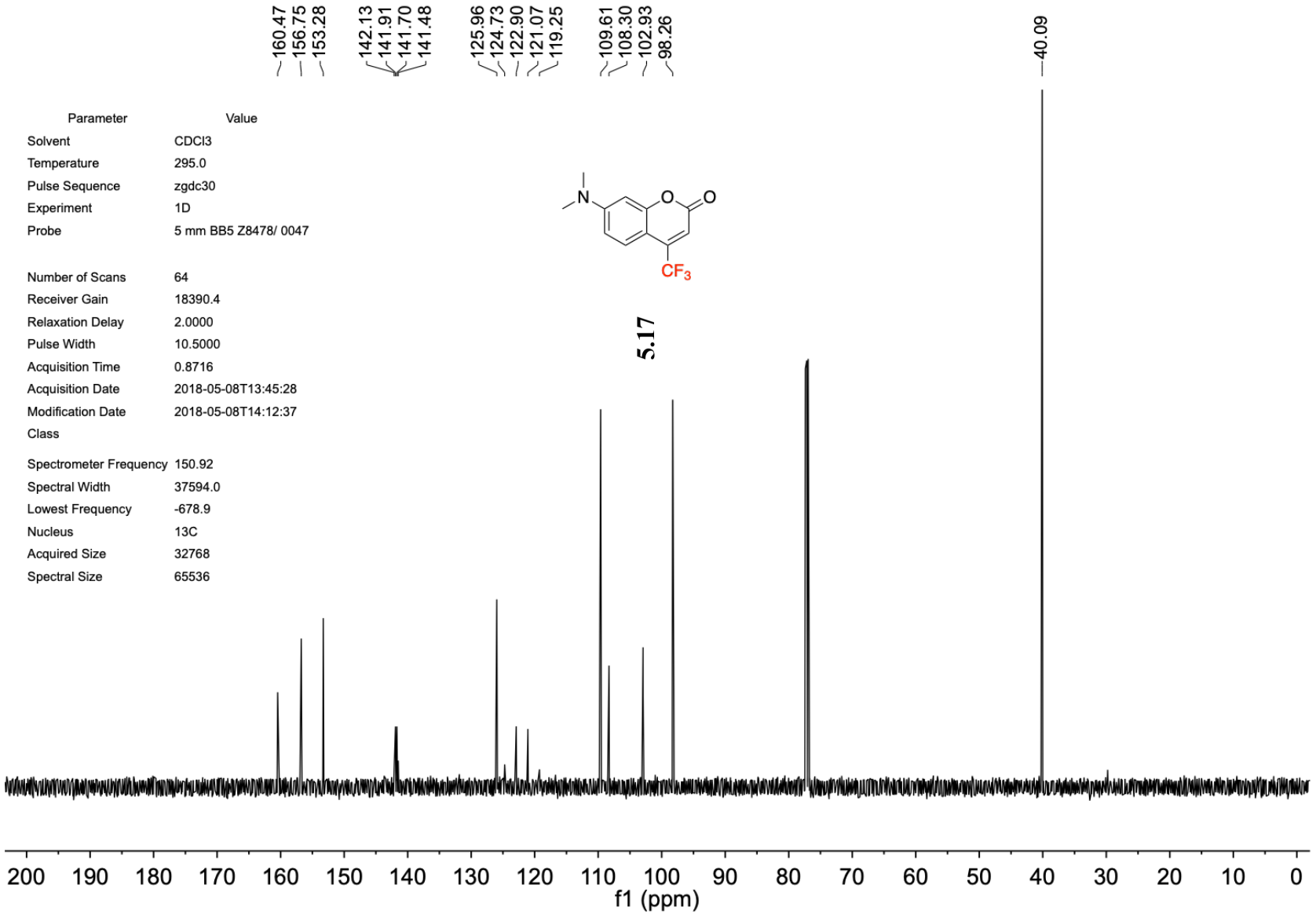
160.47
156.75
153.28
142.13
141.91
141.70
141.48
125.96
124.73
122.90
121.07
119.25
109.61
108.30
102.93
98.26
40.09
Parameter Value
Solvent CDCl3
Temperature 295.0
Pulse Sequence zgdc30
Experiment 1D
Probe 5 mm BB5 Z8478/ 0047
Number of Scans 64
Receiver Gain 18390.4
Relaxation Delay 2.0000
Pulse Width 10.5000
Acquisition Time 0.8716
Acquisition Date 2018-05-08T13:45:28
Modification Date 2018-05-08T14:12:37
Class
Spectrometer Frequency 150.92
Spectral Width 37594.0
Lowest Frequency -678.9
Nucleus 13C
Acquired Size 32768
Spectral Size 65536
N
O
O
CF3
5.17
200 190 180 170 160 150 140 130 120 110 100 90 80 70 60 50 40 30 20 10 0
f1 (ppm)

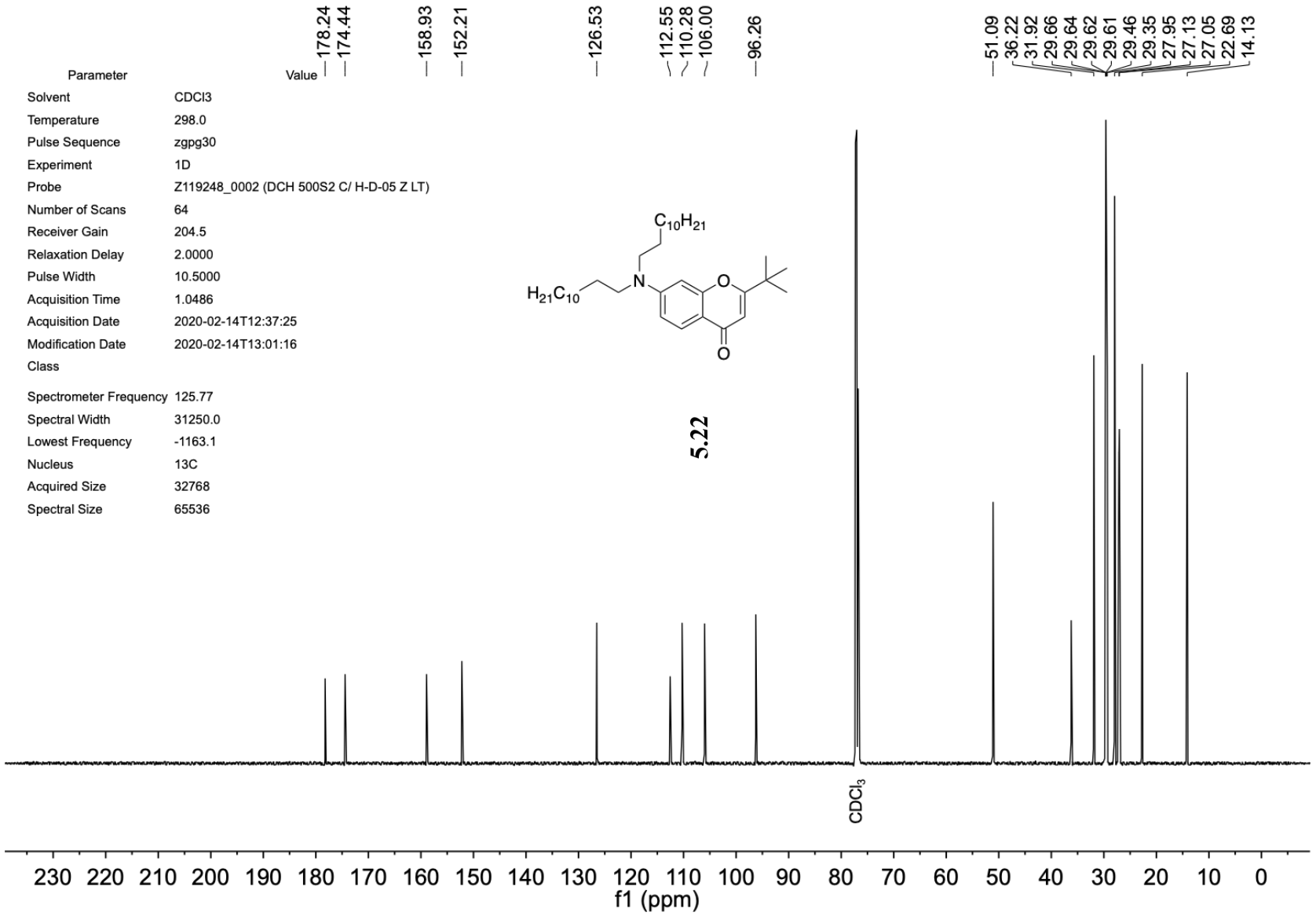
178.24
174.44
158.93
152.21
126.53
112.55
110.28
106.00
96.26
51.09
36.22
31.92
29.66
29.64
29.62
29.61
29.46
29.35
27.95
27.13
27.05
22.69
14.13
Parameter
Value
Solvent CDCl3
Temperature 298.0
Pulse Sequence zgpg30
Experiment 1D
Probe Z119248_0002 (DCH 500S2 C/ H-D-05 Z LT)
Number of Scans 64
Receiver Gain 204.5
Relaxation Delay 2.0000
Pulse Width 10.5000
Acquisition Time 1.0486
Acquisition Date 2020-02-14T12:37:25
Modification Date 2020-02-14T13:01:16
Class
Spectrometer Frequency 125.77
Spectral Width 31250.0
Lowest Frequency -1163.1
Nucleus 13C
Acquired Size 32768
Spectral Size 65536
$C_{10}H_{21}$
$H_{21}C_{10}$
N
O
O
5.22
$CDCl_3$
230 220 210 200 190 180 170 160 150 140 130 120 110 100 90 80 70 60 50 40 30 20 10 0
f1 (ppm)

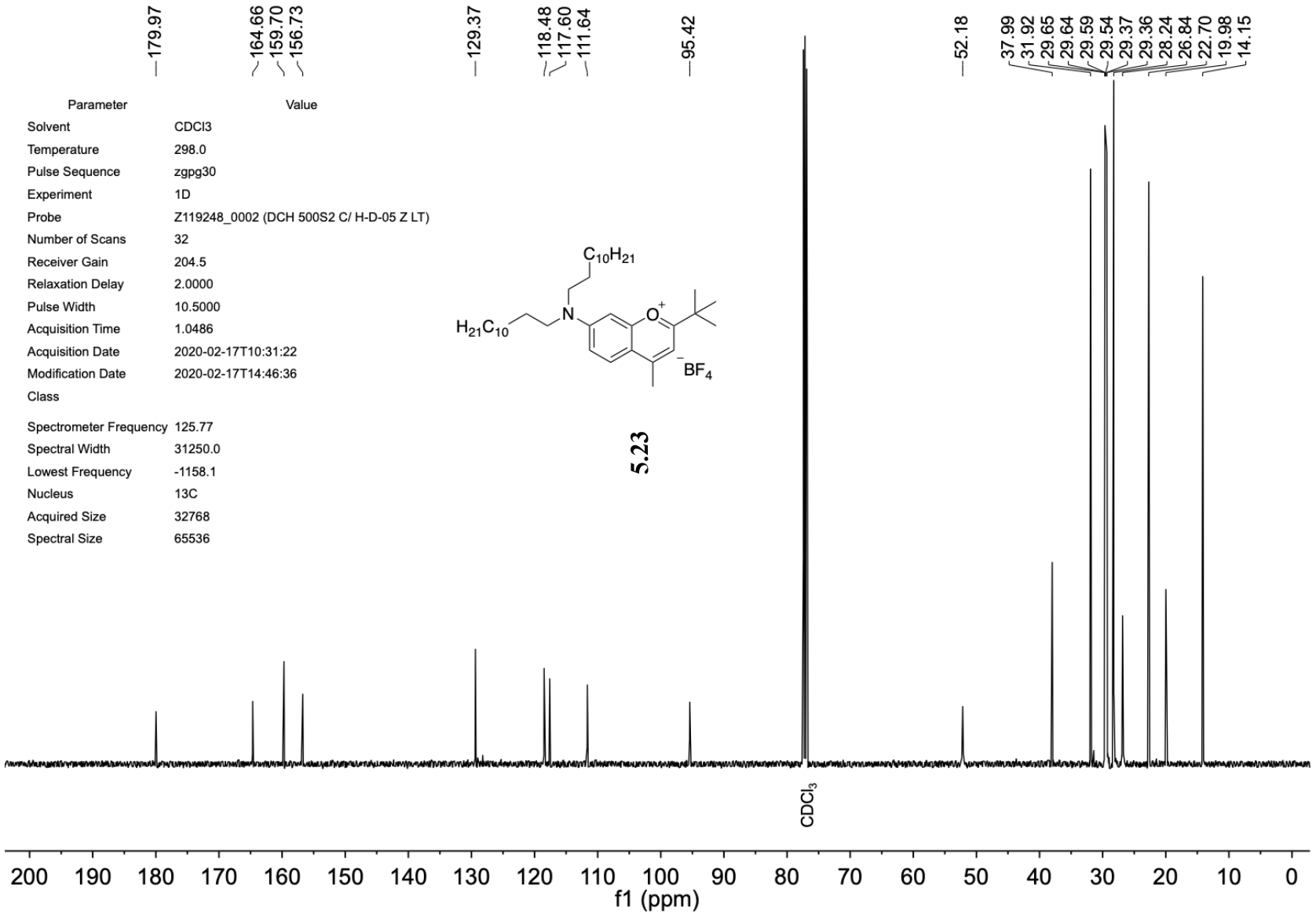
179.97
164.66
159.70
156.73
129.37
118.48
117.60
111.64
95.42
52.18
37.99
31.92
29.65
29.64
29.59
29.54
29.37
29.36
28.24
26.84
22.70
19.98
14.15
Parameter Value
Solvent CDCl3
Temperature 298.0
Pulse Sequence zgpg30
Experiment 1D
Probe Z119248_0002 (DCH 500S2 C/ H-D-05 Z LT)
Number of Scans 32
Receiver Gain 204.5
Relaxation Delay 2.0000
Pulse Width 10.5000
Acquisition Time 1.0486
Acquisition Date 2020-02-17T10:31:22
Modification Date 2020-02-17T14:46:36
Class
Spectrometer Frequency 125.77
Spectral Width 31250.0
Lowest Frequency -1158.1
Nucleus 13C
Acquired Size 32768
Spectral Size 65536
C10H21
H21C10
N
O+
BF4
5.23
CDCl3
200 190 180 170 160 150 140 130 120 110 100 90 80 70 60 50 40 30 20 10 0
f1 (ppm)

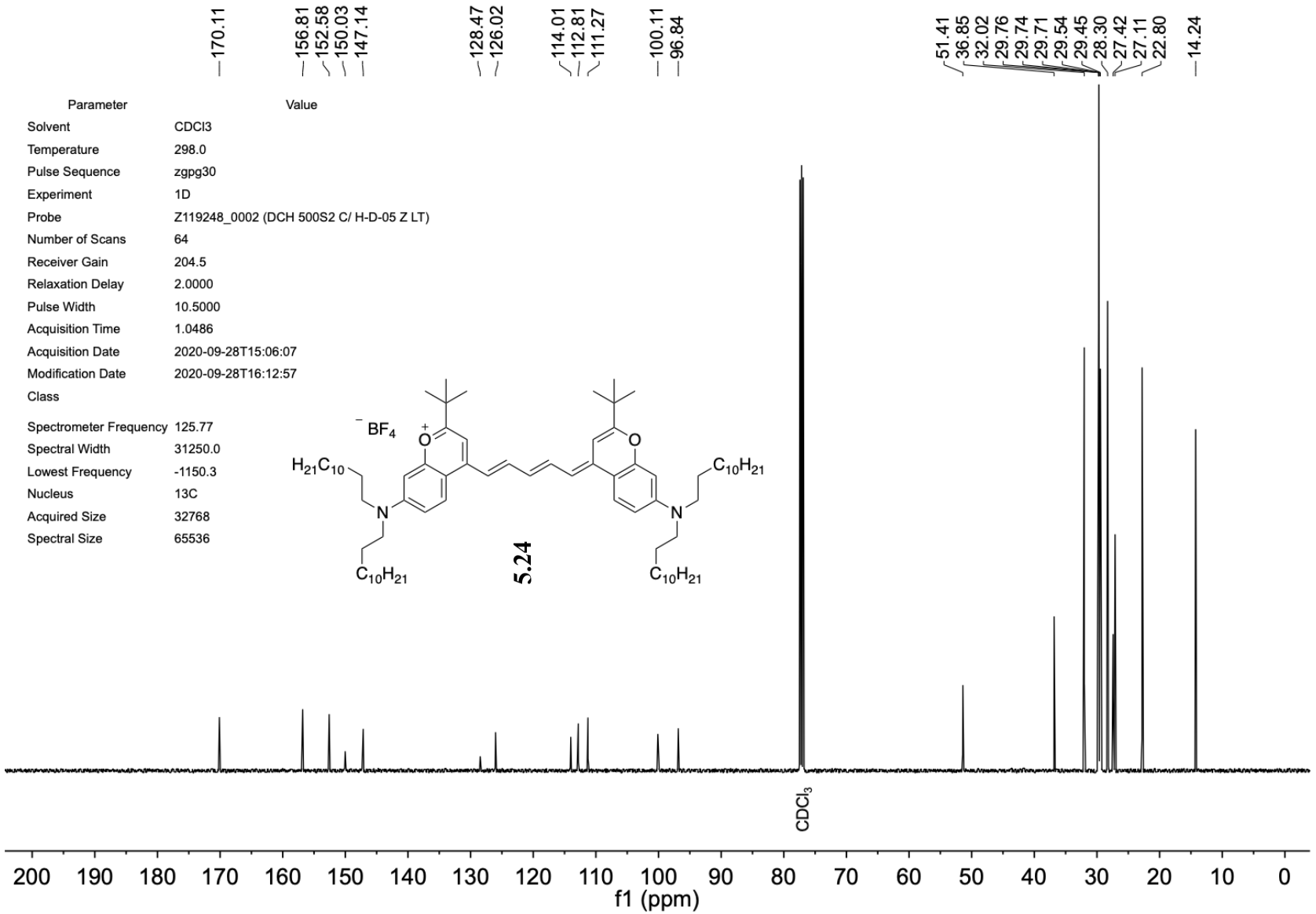
170.11
156.81
152.58
150.03
147.14
128.47
126.02
114.01
112.81
111.27
100.11
96.84
51.41
36.85
32.02
29.76
29.74
29.71
29.54
29.45
28.30
27.42
27.11
22.80
14.24
Parameter Value
Solvent CDCl3
Temperature 298.0
Pulse Sequence zgpg30
Experiment 1D
Probe Z119248_0002 (DCH 500S2 C/ H-D-05 Z LT)
Number of Scans 64
Receiver Gain 204.5
Relaxation Delay 2.0000
Pulse Width 10.5000
Acquisition Time 1.0486
Acquisition Date 2020-09-28T15:06:07
Modification Date 2020-09-28T16:12:57
Class
Spectrometer Frequency 125.77
Spectral Width 31250.0
Lowest Frequency -1150.3
Nucleus 13C
Acquired Size 32768
Spectral Size 65536
BF4
H21C10
C10H21
C10H21
C10H21
5.24
CDCl3
200 190 180 170 160 150 140 130 120 110 100 90 80 70 60 50 40 30 20 10 0
f1 (ppm)

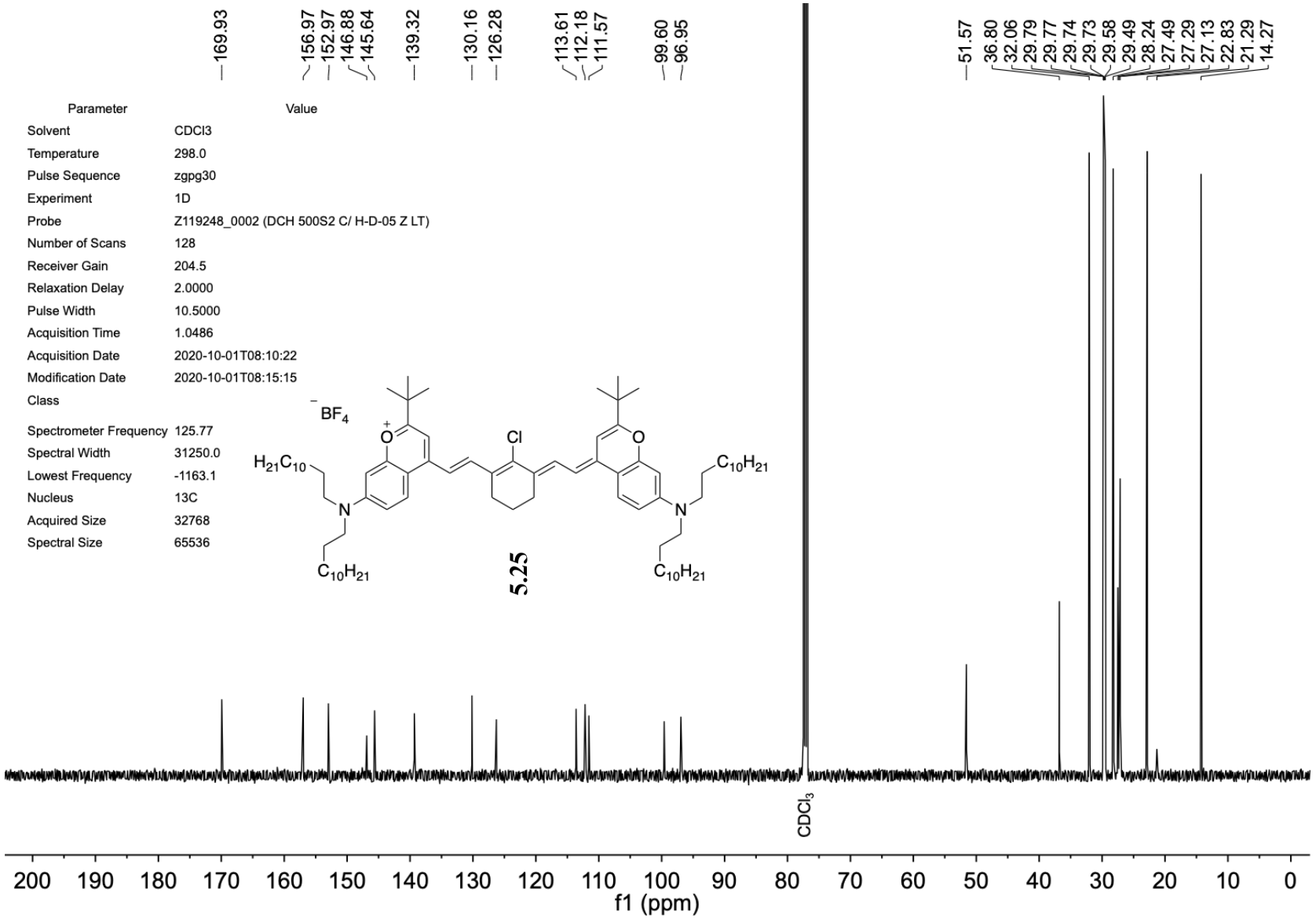
169.93
156.97
152.97
146.88
145.64
139.32
130.16
126.28
113.61
112.18
111.57
99.60
96.95
51.57
36.80
32.06
29.79
29.77
29.74
29.73
29.58
29.49
28.24
27.49
27.29
27.13
22.83
21.29
14.27
Parameter Value
Solvent CDCl3
Temperature 298.0
Pulse Sequence zgpg30
Experiment 1D
Probe Z119248_0002 (DCH 500S2 C/ H-D-05 Z LT)
Number of Scans 128
Receiver Gain 204.5
Relaxation Delay 2.0000
Pulse Width 10.5000
Acquisition Time 1.0486
Acquisition Date 2020-10-01T08:10:22
Modification Date 2020-10-01T08:15:15
Class
Spectrometer Frequency 125.77
Spectral Width 31250.0
Lowest Frequency -1163.1
Nucleus 13C
Acquired Size 32768
Spectral Size 65536
BF4
Cl
O
N
H21C10
C10H21
5.25
CDCl3
200 190 180 170 160 150 140 130 120 110 100 90 80 70 60 50 40 30 20 10 0
f1 (ppm)

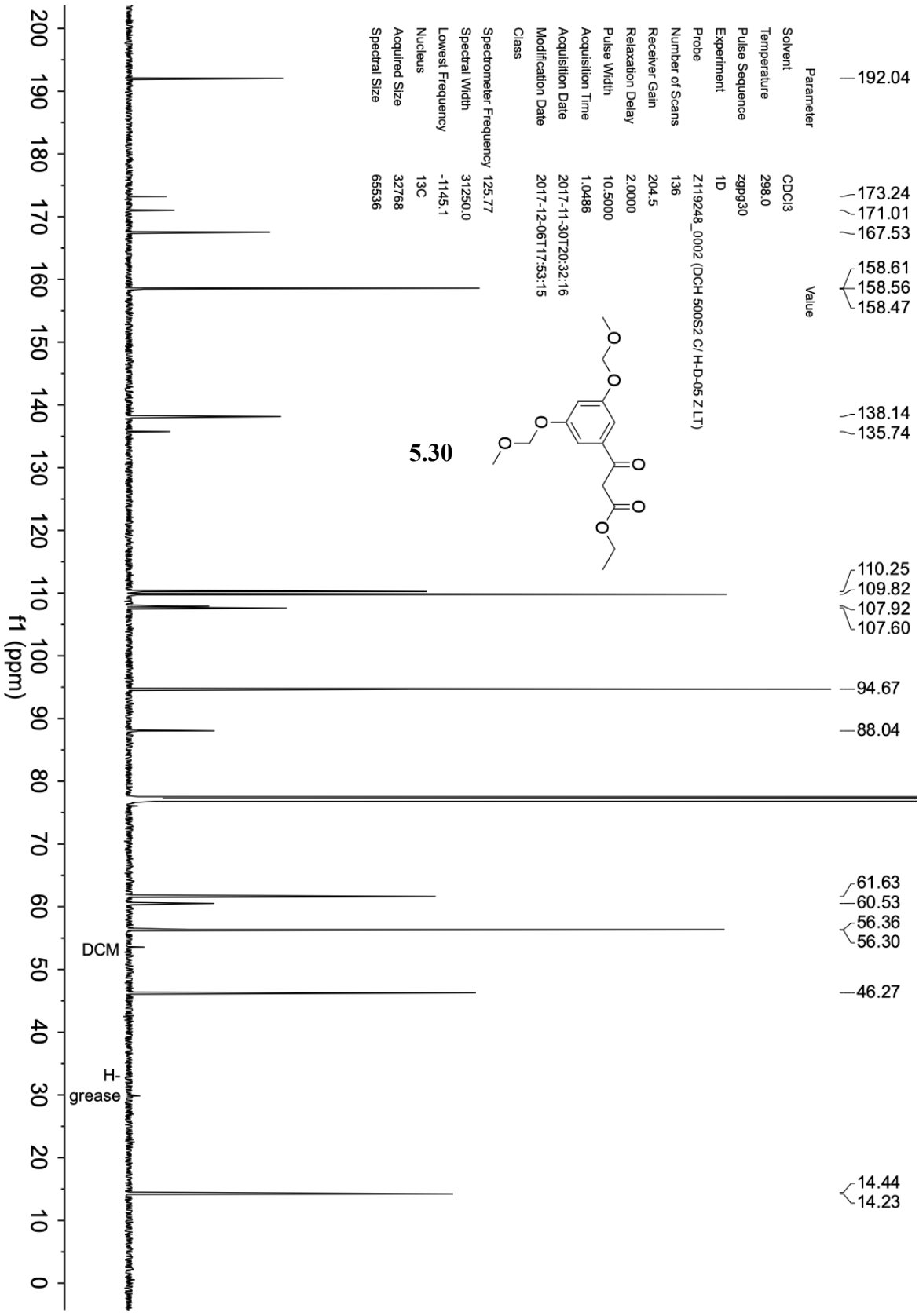
Parameter Value
Solvent CDCl3
Temperature 298.0
Pulse Sequence zgpg30
Experiment 1D
Probe Z119248_0002 (DCH 500S2 C/ H-D-05 Z LT)
Number of Scans 136
Receiver Gain 204.5
Relaxation Delay 2.0000
Pulse Width 10.5000
Acquisition Time 1.0486
Acquisition Date 2017-11-30T20:32:16
Modification Date 2017-12-06T17:53:15
Class
Spectrometer Frequency 125.77
Spectral Width 31250.0
Lowest Frequency -1145.1
Nucleus 13C
Acquired Size 32768
Spectral Size 65536
5.30
192.04
173.24
171.01
167.53
158.61
158.56
158.47
138.14
135.74
110.25
109.82
107.92
107.60
94.67
88.04
61.63
60.53
56.36
56.30
46.27
14.44
14.23
DCM
H-grease
f1 (ppm)

5.7.4 ^{19}F NMR Spectra

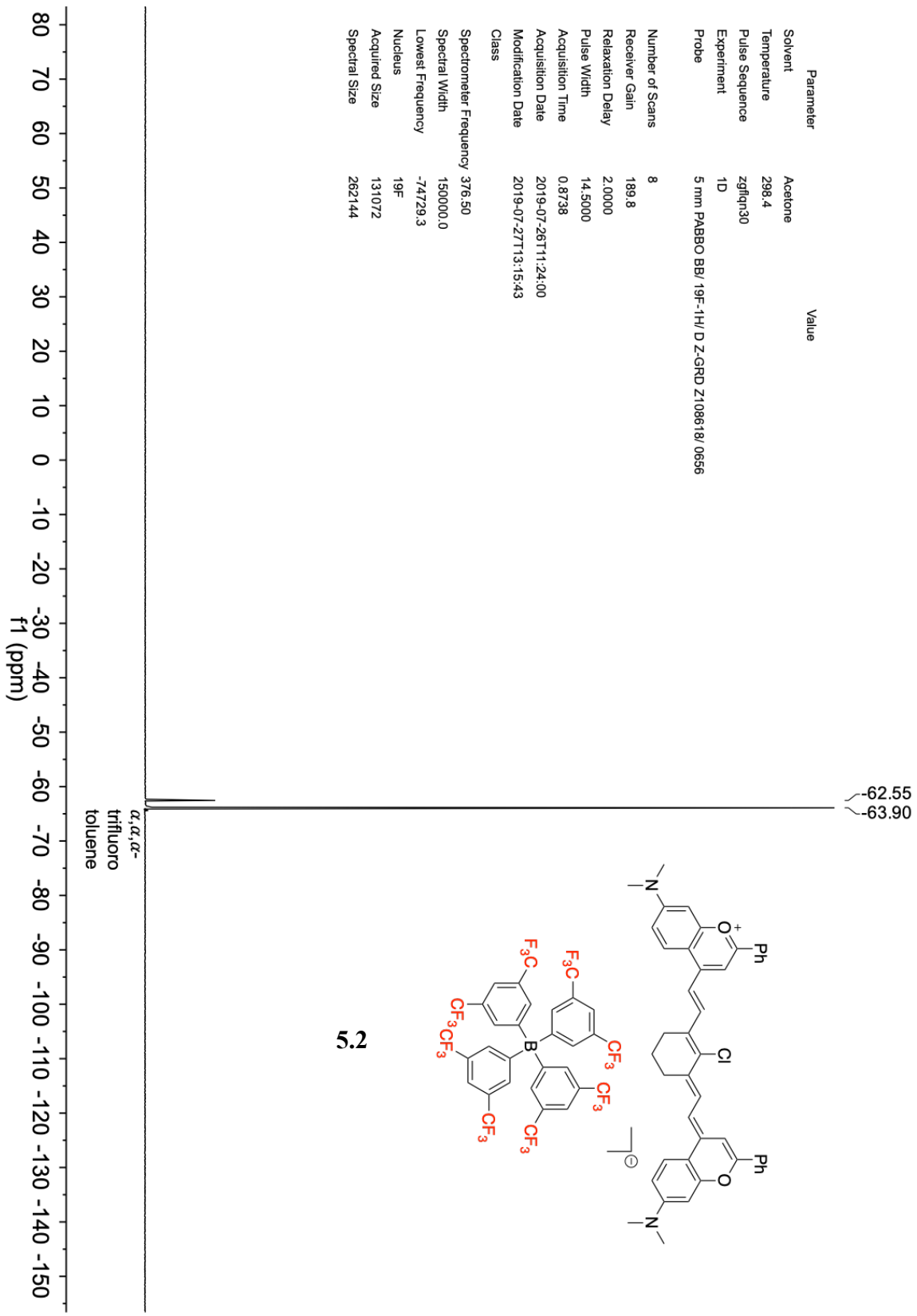

5.2

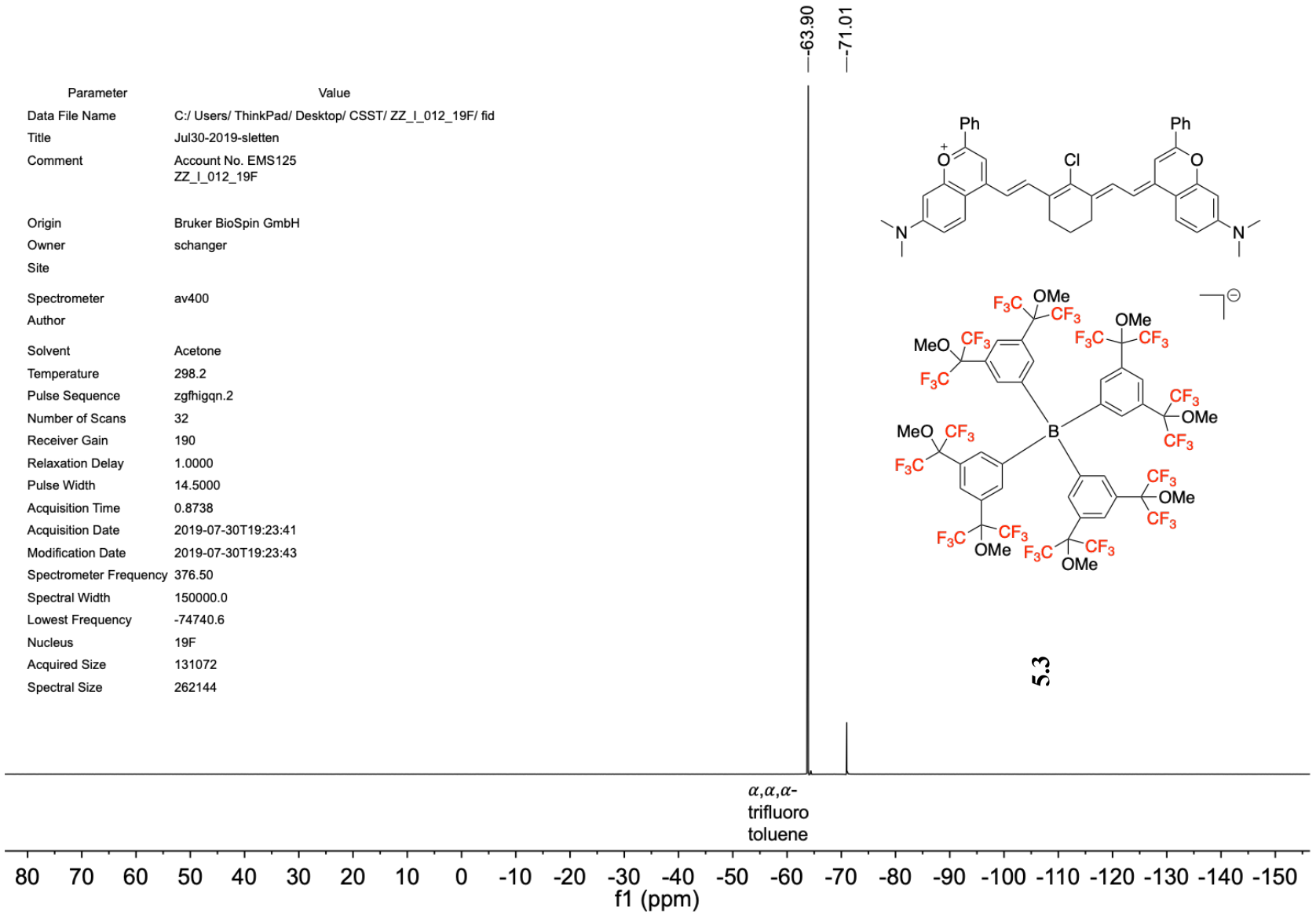
-63.90
-71.01
Parameter
Value
Data File Name
C:/ Users/ ThinkPad/ Desktop/ CSST/ ZZ_I_012_19F/ fid
Title
Jul30-2019-sletten
Comment
Account No. EMS125
ZZ_I_012_19F
Origin
Bruker BioSpin GmbH
Owner
schanger
Site
Spectrometer
av400
Author
Solvent
Acetone
Temperature
298.2
Pulse Sequence
zgfhigqn.2
Number of Scans
32
Receiver Gain
190
Relaxation Delay
1.0000
Pulse Width
14.5000
Acquisition Time
0.8738
Acquisition Date
2019-07-30T19:23:41
Modification Date
2019-07-30T19:23:43
Spectrometer Frequency
376.50
Spectral Width
150000.0
Lowest Frequency
-74740.6
Nucleus
19F
Acquired Size
131072
Spectral Size
262144
Ph
Ph
Cl
O
O
N
N
B
OMe
MeO
CF3
F3C
5.3
α,α,α-
trifluoro
toluene
80 70 60 50 40 30 20 10 0 -10 -20 -30 -40 -50 -60 -70 -80 -90 -100 -110 -120 -130 -140 -150
f1 (ppm)

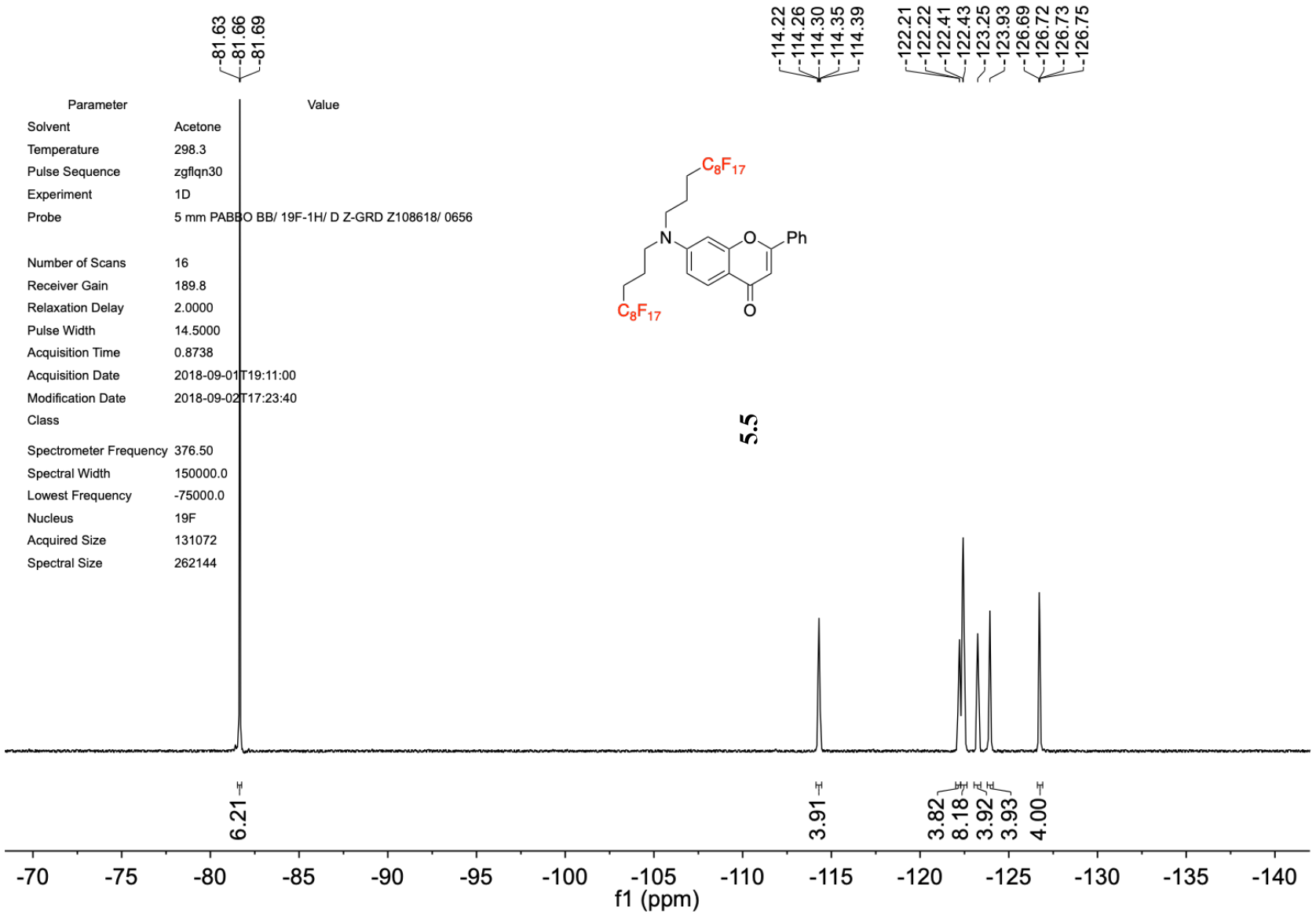
-81.63
-81.66
-81.69
-114.22
-114.26
-114.30
-114.35
-114.39
-122.21
-122.22
-122.41
-122.43
-123.25
-123.93
-126.69
-126.72
-126.73
-126.75
Parameter
Value
Solvent
Acetone
Temperature
298.3
Pulse Sequence
zgflqn30
Experiment
1D
Probe
5 mm PABBO BB/ 19F-1H/ D Z-GRD Z108618/ 0656
Number of Scans
16
Receiver Gain
189.8
Relaxation Delay
2.0000
Pulse Width
14.5000
Acquisition Time
0.8738
Acquisition Date
2018-09-01T19:11:00
Modification Date
2018-09-02T17:23:40
Class
Spectrometer Frequency
376.50
Spectral Width
150000.0
Lowest Frequency
-75000.0
Nucleus
19F
Acquired Size
131072
Spectral Size
262144
C8F17
N
O
Ph
C8F17
O
5.5
6.21
3.91
3.82
8.18
3.92
3.93
4.00
-70
-75
-80
-85
-90
-95
-100
-105
-110
-115
-120
-125
-130
-135
-140
f1 (ppm)

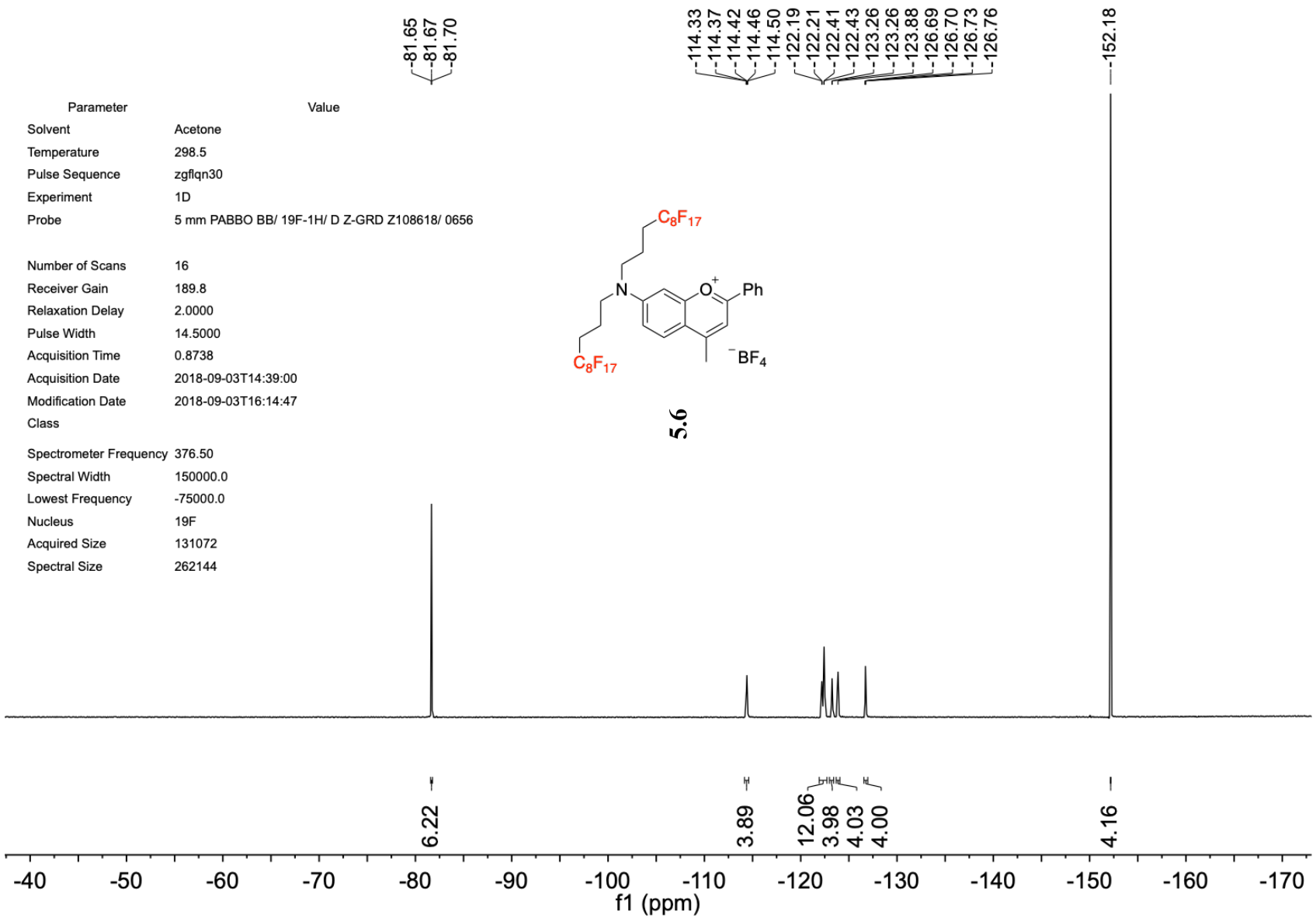
-81.65
-81.67
-81.70
-114.33
-114.37
-114.42
-114.46
-114.50
-122.19
-122.21
-122.41
-122.43
-123.26
-123.26
-123.88
-126.69
-126.70
-126.73
-126.76
-152.18
Parameter Value
Solvent Acetone
Temperature 298.5
Pulse Sequence zgflqn30
Experiment 1D
Probe 5 mm PABBO BB/ 19F-1H/ D Z-GRD Z108618/ 0656
Number of Scans 16
Receiver Gain 189.8
Relaxation Delay 2.0000
Pulse Width 14.5000
Acquisition Time 0.8738
Acquisition Date 2018-09-03T14:39:00
Modification Date 2018-09-03T16:14:47
Class
Spectrometer Frequency 376.50
Spectral Width 150000.0
Lowest Frequency -75000.0
Nucleus 19F
Acquired Size 131072
Spectral Size 262144
C8F17
N
O+
Ph
BF4
C8F17
5.6
6.22
3.89
12.06
3.98
4.03
4.00
4.16
-40
-50
-60
-70
-80
-90
-100
-110
-120
-130
-140
-150
-160
-170
f1 (ppm)

Parameter	Value
Solvent	CDCl3
Temperature	298.1
Pulse Sequence	zgflqn30
Experiment	1D
Probe	5 mm PABBO BB/ 19F-1H/ D Z-GRD Z108618/ 0656
Number of Scans	16
Receiver Gain	189.8
Relaxation Delay	2.0000
Pulse Width	14.5000
Acquisition Time	0.8738
Acquisition Date	2018-04-24T18:20:00
Modification Date	2018-04-24T18:29:37
Class	
Spectrometer Frequency	376.50
Spectral Width	150000.0
Lowest Frequency	-75000.0
Nucleus	19F
Acquired Size	131072
Spectral Size	262144

5.16

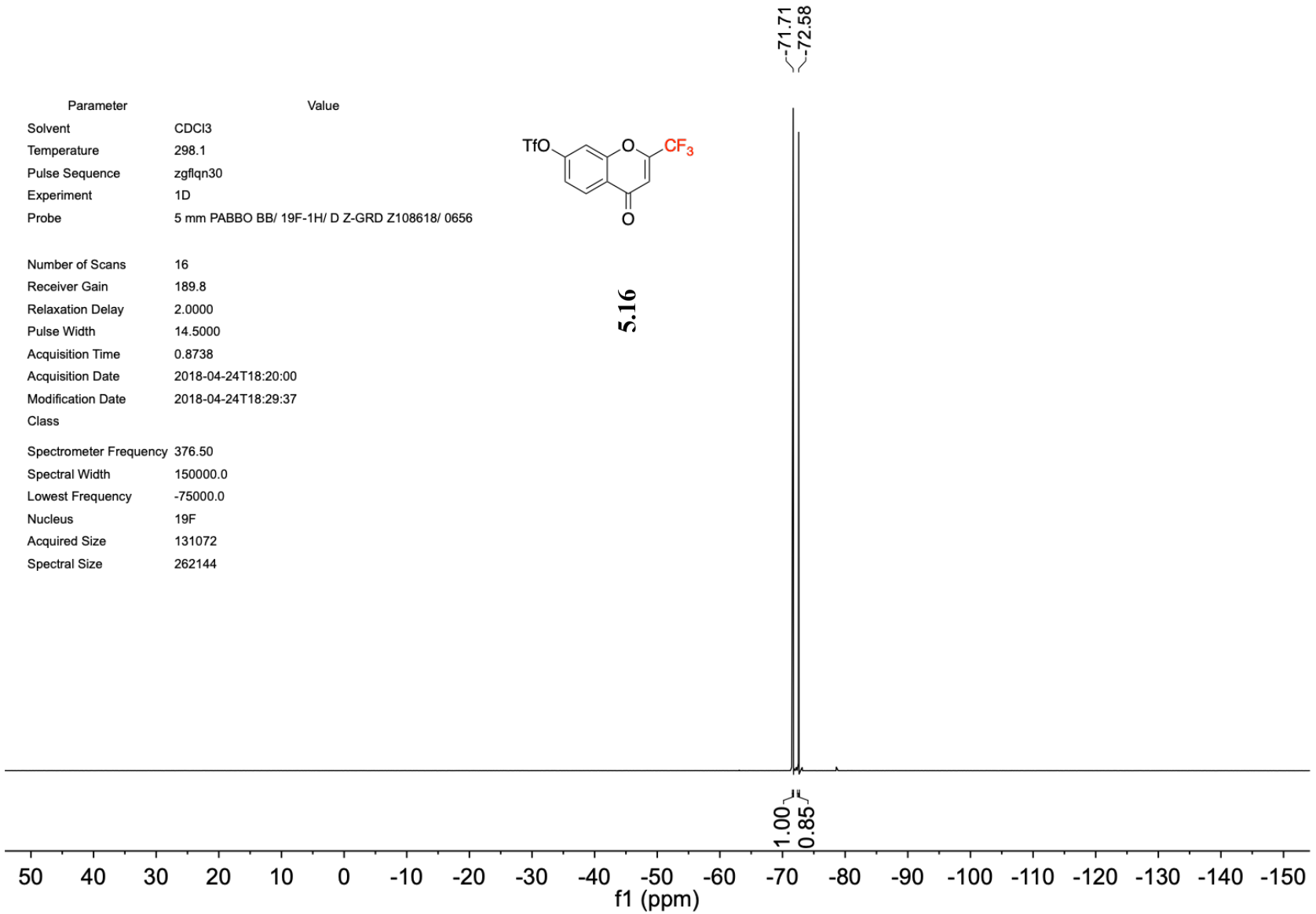

Parameter	Value
Solvent	Acetone
Temperature	298.5
Pulse Sequence	zgflqn30
Experiment	1D
Probe	5 mm PABBO BB/ 19F-1H/ D Z-GRD Z108618/ 0656
Number of Scans	16
Receiver Gain	189.8
Relaxation Delay	2.0000
Pulse Width	14.5000
Acquisition Time	0.8738
Acquisition Date	2018-04-19T22:30:00
Modification Date	2018-04-20T09:29:10
Class	
Spectrometer Frequency	376.50
Spectral Width	150000.0
Lowest Frequency	-75000.0
Nucleus	19F
Acquired Size	131072
Spectral Size	262144

5.17

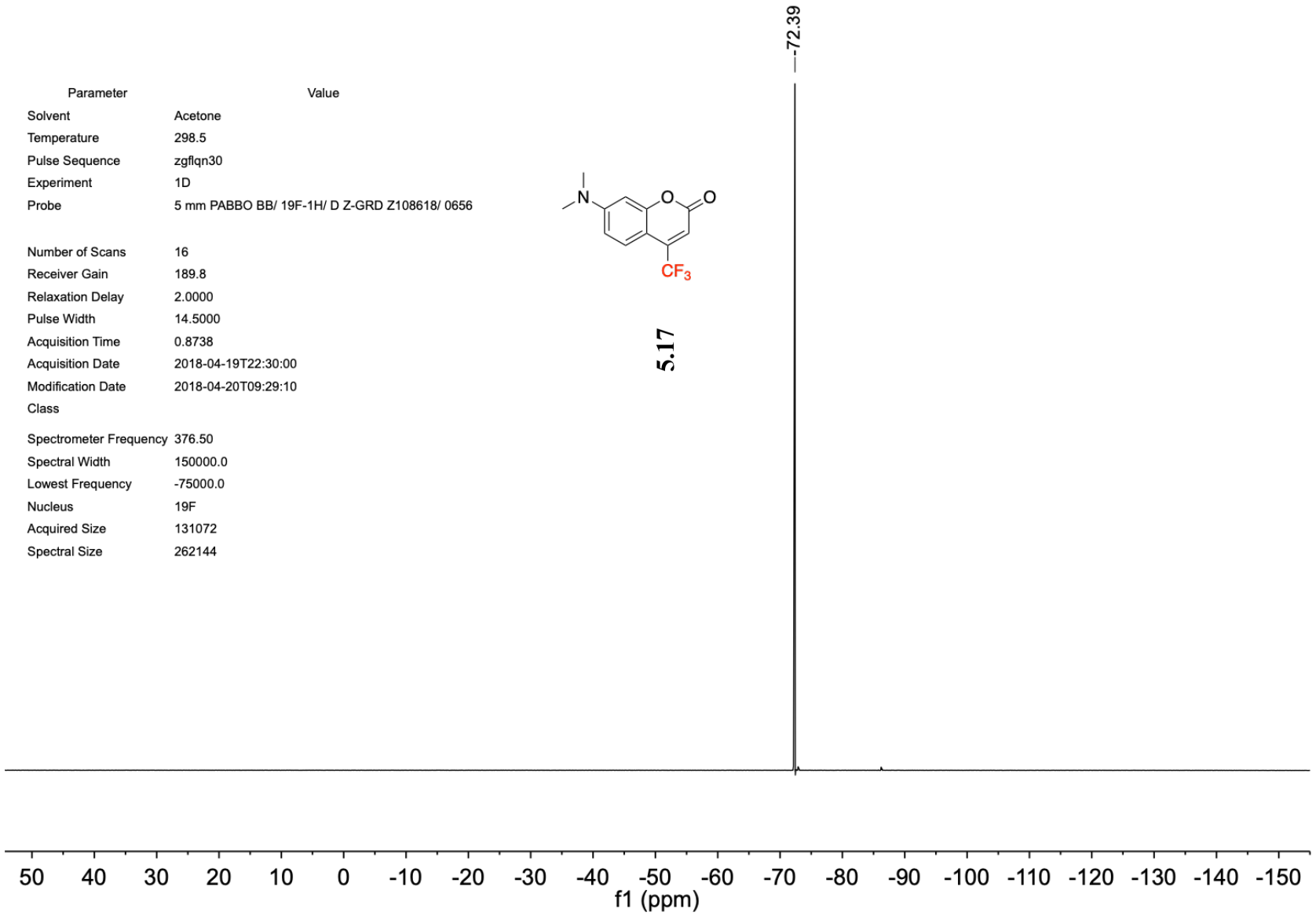

5.7.5 Absorbance Spectrum

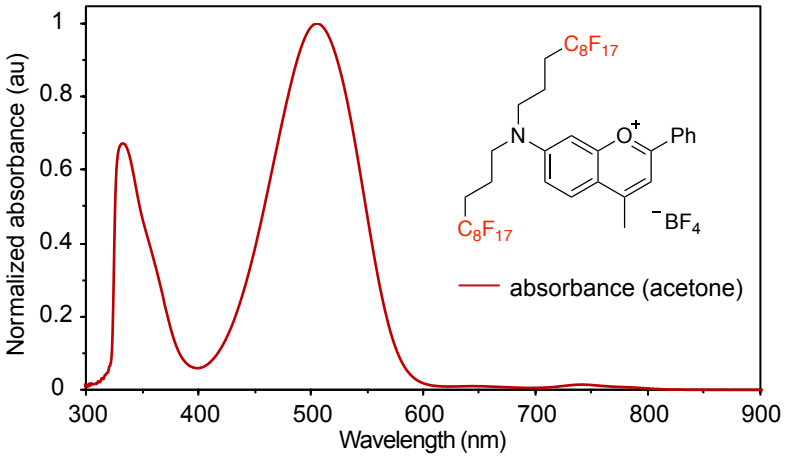

5.8 References and Notes

[1] Lee, Y. and Lai, Y. Synthesis, characterization, and biological evaluation of anti-her2 indocyanine green- encapsulated PEG-coated PLGA nanoparticles for targeted phototherapy of breast cancer cells. *PLoS ONE.* **2016**, 11, 89-98.

[2] Kirchherr, A. K.; Briel, A.; Mäder, K. Stabilization of Indocyanine Green by Encapsulation within Micellar Systems. *Mol. Pharm.* **2009**, *6*, 480–491.

[3] Bricks, J. L.; Slominskii, Y. L.; Panas, I. D.; Demchenko, A. P. Fluorescent J-Aggregates of Cyanine Dyes: Basic Research and Applications Review. *Methods Appl. Fluoresc.* **2017**, *6* , 012001.

[4] Getmanenko, Y. A.; Allen, T. G.; Kim, H.; Hales, J. M.; Sandhu, B.; Fonari, M. S.; Suponitsky, K. Y.; Zhang, Y.; Khrustalev, V. N.; Matichak, J. D.; et al. Linear and Third-Order Nonlinear Optical Properties of Chalcogenopyrylium-Terminated Heptamethine Dyes with Rigid, Bulky Substituents. *Adv. Funct. Mater.* **2018**, *28*, 1–12.

[5] Hales, J. M.; Barlow, S.; Kim, H.; Mukhopadhyay, S.; Bredas, J. L.; Perry, J. W.; Marder, S. R. Design of Organic Chromophores for All-Optical Signal Processing Applications. *Chem. Mater.* **2014**, *26*, 549–560.

[6] Harper, K. C.; Bess, E. N.; Sigman, M. S. Multidimensional Steric Parameters in the Analysis of Asymmetric Catalytic Reactions. *Nat. Chem.* **2012**, *4* (5), 366–374.

[7] Reisch, A.; Didier, P.; Richert, L.; Oncul, S.; Arntz, Y.; Mély, Y.; Klymchenko, A. S. Collective Fluorescence Switching of Counterion-Assembled Dyes in Polymer Nanoparticles. *Nat. Commun.* **2014**, *5*, 4089.

[8] Shulov, I.; Oncul, S.; Reisch, A.; Arntz, Y.; Collot, M.; Mely, Y.; Klymchenko, A. S. Fluorinated Counterion-Enhanced Emission of Rhodamine Aggregates: Ultrabright Nanoparticles for Bioimaging and Light -Harvesting. *Nanoscale* **2015**, *7*, 18198–18210.

[9] Melnychuk, N.; Klymchenko, A. S. DNA-Functionalized Dye-Loaded Polymeric Nanoparticles: Ultrabright FRET Platform for Amplified Detection of Nucleic Acids. *J. Am. Chem. Soc.* **2018**, *140*, 10856–10865.

[10] Andreiuk, B.; Reisch, A.; Bernhardt, E.; Klymchenko, A. S. Fighting Aggregation-Caused Quenching and Leakage of Dyes in Fluorescent Polymer Nanoparticles: Universal Role of Counterion. *Chem. Asian J.* **2019**, *14*, 836–846.

[11] Shulov, I.; Arntz, Y.; Mély, Y.; Pivovarenko, V. G.; Klymchenko, A. S. Non-Coordinating Anions Assemble Cyanine Amphiphiles into Ultra-Small Fluorescent Nanoparticles. *Chem. Commun.* **2016**, *52*, 7962–7965.

[12] Andreiuk, B.; Reisch, A.; Lindecker, M.; Follain, G.; Peyriéras, N.; Goetz, J. G.; Klymchenko, A. S. Fluorescent Polymer Nanoparticles for Cell Barcoding In Vitro and In Vivo. *Small* **2017**, *13*, 1–13.

[13] Kilin, V. N.; Anton, H.; Anton, N.; Steed, E.; Vermot, J.; Vandamme, T. F.; Mely, Y.; Klymchenko, A. S. Counterion-Enhanced Cyanine Dye Loading into Lipid Nano-Droplets for Single-Particle Tracking in Zebrafish. *Biomaterials* **2014**, *35*, 4950–4957.

[14] Gayton, J.; Autry, S.; Fortenberry, R.; Hammer, N.; Delcamp, J. Counter Anion Effect on the Photophysical Properties of Emissive Indolizine-Cyanine Dyes in Solution and Solid State. *Molecules* **2018**, *23*, 3051.

[15] Counterion exchange was also attempted with Lithium tetrakis(pentafluorophenyl)borate, but challenges with purification prevented acquisition of the spectroscopically pure salt.

[16] Bouit, P. A.; Aronica, C.; Toupet, L.; Guennic, B. Le; Andraud, C.; Maury, O. Continuous Symmetry Breaking Induced by Ion Pairing Effect in Heptamethine Cyanine Dyes: Beyond the Cyanine Limit. *J. Am. Chem. Soc.* **2010**, *132*, 4328–4335.

[17] Pascal, S.; Chi, S.-H.; Perry, J. W.; Andraud, C.; Maury, O. Impact of Ion-Pairing Effects on Linear and Nonlinear Photophysical Properties of Polymethine Dyes. *ChemPhysChem* **2020**, *21*, 2536–2542.

[18] Miller, M. A.; Sletten, E. M. Perfluorocarbons in Chemical Biology. *ChemBioChem* **2020**, cbic.202000297.

[19] Riess, J. G. Oxygen Carriers ("Blood Substitutes") Raison d'Etre, Chemistry, and Some Physiology. *Chem. Rev.* **2001**, *101*, 2797–2920.

[20] Janjic, J. M.; Ahrens, E. T. Fluorine-Containing Nanoemulsions for MRI Cell Tracking. *Wiley Interdiscip. Rev. Nanomedicine Nanobiotechnology* **2009**, *1*, 492–501.

[21] Tirotta, I.; Dichiarante, V.; Pigliacelli, C.; Cavallo, G.; Terraneo, G.; Bombelli, F. B.; Metrangolo, P.; Resnati, G. 19F Magnetic Resonance Imaging (MRI): From Design of Materials to Clinical Applications. *Chem. Rev.* **2015**, *115*, 1106–1129.

[22] Kislukhin, A. A.; Xu, H.; Adams, S. R.; Narsinh, K. H.; Tsien, R. Y.; Ahrens, E. T. Paramagnetic Fluorinated Nanoemulsions for Sensitive Cellular Fluorine-19 Magnetic Resonance Imaging. *Nat. Mater.* **2016**, *15*, 662–668.

[23] Rapoport, N.; Nam, K. H.; Gupta, R.; Gao, Z.; Mohan, P.; Payne, A.; Todd, N.; Liu, X.; Kim, T.; Shea, J.; et al. Ultrasound-Mediated Tumor Imaging and Nanotherapy Using Drug Loaded, Block Copolymer Stabilized Perfluorocarbon Nanoemulsions. *J. Control. Release* **2011**, *153*, 4–15.

[24] Díaz-López, R.; Tsapis, N.; Fattal, E. Liquid Perfluorocarbons as Contrast Agents for Ultrasonography and 19F-MRI. *Pharm. Res.* **2010**, *27*, 1–16.

[25] Tran, T. D.; Caruthers, S. D.; Hughes, M.; Marsh, J. N.; Cyrus, T.; Winter, P. M.; Neubauer, A. M.; Wickline, S. A.; Lanza, G. M. Clinical Applications of Perfluorocarbon Nanoparticles for Molecular Imaging and Targeted Therapeutics. *Int. J. Nanomedicine* **2007**, *2*, 515–526.

[26] Lim, Y. T.; Noh, Y. W.; Kwon, J. N.; Chung, B. H. Multifunctional Perfluorocarbon Nanoemulsions for 19F-Based Magnetic Resonance and near-Infrared Optical Imaging of Dendritic Cells. *Chem. Commun.* **2009**, No. 45, 6952–6954.

[27] Lim, Y. T.; Noh, Y. W.; Cho, J. H.; Han, J. H.; Choi, B. S.; Kwon, J.; Hong, K. S.; Gokarna, A.; Cho, Y. H.; Chung, B. H. Multiplexed Imaging of Therapeutic Cells with Multispectrally Encoded Magnetofluorescent Nanocomposite Emulsions. *J. Am. Chem. Soc.* **2009**, *131*, 17145–17154.

[28] Balducci, A.; Wen, Y.; Zhang, Y.; Helfer, B. M.; Hitchens, T. K.; Meng, W. S.; Wesa, A. K.; Janjic, J. M. A Novel Probe for the Non-Invasive Detection of Tumor-Associated Inflammation. *Oncoimmunology* **2013**, *2*, e23034.

[29] Bae, P. K.; Jung, J.; Chung, B. H. Highly Enhanced Optical Properties of Indocyanine Green/Perfluorocarbon Nanoemulsions for Efficient Lymph Node Mapping Using near-Infrared and Magnetic Resonance Imaging. *Nano Converg.* **2014**, *1*, 6.

[30] Cruz, L. J.; Que, I.; Aswendt, M.; Chan, A.; Hoehn, M.; Löwik, C. Targeted Nanoparticles for the Non-Invasive Detection of Traumatic Brain Injury by Optical Imaging and Fluorine Magnetic Resonance Imaging. *Nano Res.* **2016**, *9*, 1276–1289.

[31] Day, R. A.; Estabrook, D. A.; Logan, J. K.; Sletten, E. M. Fluorous Photosensitizers Enhance Photodynamic Therapy with Perfluorocarbon Nanoemulsions. *Chem. Commun.* **2017**, *53*, 13043–13046.

[32] Miller, M. A.; Sletten, E. M. A General Approach to Biocompatible Branched Fluorous Tags for Increased Solubility in Perfluorocarbon Solvents. *Org. Lett.* **2018**, *20*, 6850–6854.

[33] Sletten, E. M.; Swager, T. M. Fluorofluorophores: Fluorescent Fluorous Chemical Tools Spanning the Visible Spectrum. *J. Am. Chem. Soc.* **2015**, *136*, 13574–13577.

[34] Miller, M. A.; Day, R. A.; Estabrook, D. A.; Sletten, E. M. A Reduction-Sensitive Fluorous Fluorogenic Coumarin. *Synlett* **2020**, *31*, 450–454.

[35] Lim, I.; Vian, A.; van de Wouw, H.; Day, R. A.; Gomez, C.; Liu, Y.; Rheingold, A. L.; Campas, O.; Sletten, E. M. Fluorous Soluble Cyanine Dyes for Visualizing Perfluorocarbons in Living Systems. *J. Am. Chem. Soc.* **2020**.

[36] Estabrook, D. A.; Ennis, A. F.; Day, R. A.; Sletten, E. M. Controlling Nanoemulsion Surface Chemistry with Poly(2-Oxazoline) Amphiphiles. *Chem. Sci.* **2019**, *10* , 3994–4003.

[37] Day, R. A.; Estabrook, D. A.; Wu, C.; Chapman, J. O.; Togle, A. J.; Sletten, E. M. Systematic Study of Perfluorocarbon Nanoemulsions Stabilized by Polymer Amphiphiles. *ACS Appl. Mater. Interfaces* **2020**, *12*, 38887–38898.

[38] Thimsen, E.; Sadtler, B.; Berezin, M. Y. Shortwave-Infrared (SWIR) Emitters for Biological Imaging : A Review of Challenges and Opportunities. *Nanophotonics* **2017**, *6*, 1043–1054.

[39] Kiss, L. E.; Kövesdi, I.; Rábai, J. An Improved Design of Fluorophilic Molecules: Prediction of the Ln P Fluorous Partition Coefficient, Fluorophilicity, Using 3D QSAR Descriptors and Neural Networks. *J. Fluor. Chem.* **2001**, *108*, 95–109.

[40] Miller, M. A.; Sletten, E. M. A General Approach to Biocompatible Branched Fluorous Tags for Increased Solubility in Perfluorocarbon Solvents. *Org. Lett.* **2018**, *20*, 6850–6854.

[41] van den Broeke, J.; Deelman, B.; van Koten, G. Tetrakis{3,5-Bis(Perfluorohexyl)Phenyl}borate: A Highly Fluorous Anion. *Tetrahedron Lett.* **2001**, *42*, 8085–8087.

[42] Ghosh, S. K.; Ojeda, A. S.; Guerrero-Leal, J.; Bhuvanesh, N.; Gladysz, J. A. New Media for Classical Coordination Chemistry: Phase Transfer of Werner and Related Polycations into Highly Nonpolar Fluorous Solvents. *Inorg. Chem.* **2013**, *52*, 9369–9378.

[43] The reproducibility of the counterion exchange with **5.13** and subsequent solubility in PFOB warrants further study.

[44] The exponential increase in signal at shorter wavelengths is due to Rayleigh scattering of the emulsions.

[45] J. Bolós, S. Gubert, L. Anglada, J. M. Planas, C. Burgarolas, J. M. Castelló, A. Sacristán, J. A. Ortiz, *J. Med. Chem.* **1996**, *39*, 2962–2970.

[46] J. Izquierdo, A. Jain, S. Abdulkadir, G. Schiltz, *Synthesis* **2019**, *51*, 1342–1352.

[47] Zhijian, S.; Xiaohua, T.; Huawen, N.; Weiguo, C. Fenxi Huaxue **2005**, *33*, 1452–1454.

[48] Shynkar, V. V.; Klymchenko, A. S.; Kunzelmann, C.; Duportail, G.; Muller, C. D.; Demchenko, A. P.; Freyssinet, J. M.; Mely, Y. Fluorescent Biomembrane Probe for Ratiometric Detection of Apoptosis. *J. Am. Chem. Soc.* **2007**, *12*, 2187–2193.

[49] Eggeling, C.; Ringemann, C.; Medda, R.; Schwarzmann, G.; Sandhoff, K.; Polyakova, S.; Belov, V. N.; Hein, B.; von Middendorff, C.; Schönle, A.; et al. Direct Observation of the Nanoscale Dynamics of Membrane Lipids in a Living Cell. *Nature* **2009**, *457*, 1159–1162.

[50] Kucherak, O. A.; Oncul, S.; Darwich, Z.; Yushchenko, D. A.; Arntz, Y.; Didier, P.; Mély, Y.; Klymchenko, A. S. Switchable Nile Red-Based Probe for Cholesterol and Lipid Order at the Outer Leaflet of Biomembranes. *J. Am. Chem. Soc.* **2010**, *132*, 4907–4916.

[51] Sezgin, E.; Schneider, F.; Galiani, S.; Urbančič, I.; Waithe, D.; Lagerholm, B. C.; Eggeling, C. Measuring Nanoscale Diffusion Dynamics in Cellular Membranes with Super-Resolution STED–FCS. *Nat. Protoc.* **2019**, *14*, 1054–1083.

[52] Colom, A.; Derivery, E.; Soleimanpour, S.; Tomba, C.; Molin, M. D.; Sakai, N.; González-Gaitán, M.; Matile, S.; Roux, A. A Fluorescent Membrane Tension Probe. *Nat. Chem.* **2018**, *10*, 1118–1125.

[53] Straková, K.; López-Andarias, J.; Jiménez-Rojo, N.; Chambers, J. E.; Marciniak, S. J.; Riezman, H.; Sakai, N.; Matile, S. HaloFlippers: A General Tool for the Fluorescence Imaging of Precisely Localized Membrane Tension Changes in Living Cells. *ACS Cent. Sci.* **2020**, *6*, 1376–1385.

[54] Miller, E. W.; Lin, J. Y.; Frady, E. P.; Steinbach, P. A.; Kristan, W. B.; Tsien, R. Y. Optically Monitoring Voltage in Neurons by Photoinduced Electron Transfer through Molecular Wires. *Proc. Natl. Acad. Sci. U. S. A.* **2012**, *109*, 2114–2119.

[55] Collot, M.; Fam, T. K.; Ashokkumar, P.; Faklaris, O.; Galli, T.; Danglot, L.; Klymchenko, A. S. Ultrabright and Fluorogenic Probes for Multicolor Imaging and Tracking of Lipid Droplets in Cells and Tissues. *J. Am. Chem. Soc.* **2018**, *140*, 5401–5411.

[56] Lkeda, T.; Seo, M.; Lnoue, I.; Katayama, S.; Matsunaga, T.; Hara, A.; Komoda, T.; Tabuchi, M. Direct and Simple Fluorescence Detection Method for Oxidized Lipoproteins. *Anal. Chem.* **2010**, *82*, 1128–1132.

[57] Klymchenko, A. S. Solvatochromic and Fluorogenic Dyes as Environment-Sensitive Probes: Design and Biological Applications. *Accounts of Chemical Research*. **2017**, *50*, 366–375.

[58] Weston, A. W.; Suter, C. M. 3,5-dihydroxybenzoic acid. *Org. Synth.* **1941**, *21*, 27.

[59] White, B. M.; Zhao, Y.; Kawashima, T. E.; Branchaud, B. P.; Pluth, M. D.; Jasti, R. Expanding the Chemical Space of Biocompatible Fluorophores: Nanohoops in Cells. *ACS Cent. Sci.* **2018**, *4,* 1173–1178.

[60] Baek, K. H.; Karki, R.; Lee, E.-S.; Na, Y.; Kwon, Y. Synthesis and Investigation of Dihydroxychalcones as Calpain and Cathepsin Inhibitors. *Bioorg. Chem.* **2013**, *51*, 24–30.

[61] J. A Bexrud, P. Eisenberger, D. C. Leitch, P. R. Payne, *J. Am. Chem. Soc.* **2009**, *131*, 2116.

[62] Lei, Z.; Sun, C.; Pei, P.; Wang, S.; Li, D.; Zhang, X.; Zhang, F. Stable, Wavelength-Tunable Fluorescent Dyes in the NIR-II Region for In Vivo High-Contrast Bioimaging and Multiplexed Biosensing. *Angew. Chemie Int. Ed.* **2019**, *58*, 8166–8171.

[63] Schindelin, J.; Arganda-Carreras, I.; Frise, E.; Kaynig, V.; Longair, M.; Pietzsch, T.; Preibisch, S.; Rueden, C.; Saalfeld, S.; Schmid, B.; et al. Fiji: An Open-Source Platform for Biological-Image Analysis. *Nat. Methods* **2012**, *9*, 676–682.

[64] Rueden, C. T.; Schindelin, J.; Hiner, M. C.; DeZonia, B. E.; Walter, A. E.; Arena, E. T.; Eliceiri, K. W. ImageJ2: ImageJ for the next Generation of Scientific Image Data. *BMC Bioinformatics* **2017**, *18*, 529.

CHAPTER SIX

Polymethine Dye J-Aggregates Stabilized in Hollow Mesoporous Silica Nanoparticles for Shortwave Infrared Imaging

Material in Chapter Six is adapted from: Wei Chen,# Chi-An Cheng,# Emily D. Cosco,#, Shyam Ramakrishnan, Jakob G. P. Lingg, Oliver T. Bruns,* Jeffrey I. Zink,* and Ellen M. Sletten* Shortwave Infrared Imaging with J-Aggregates Stabilized in Hollow Mesoporous Silica Nanoparticles. *J. Am. Chem. Soc.* **2019**, *141*, 12475–12480. DOI: 10.1021/jacs.9b05195

6.1 Abstract

Tissue is translucent to shortwave infrared (SWIR, 1,000–1,300 nm) light, rendering optical imaging superior in this region. However, the widespread use of optical SWIR imaging has been limited, in part, by the lack of bright, biocompatible contrast agents that absorb and emit light above 1,000 nm. J-Aggregation offers a means to transform stable, near-infrared (NIR, 700–1,000 nm) fluorophores into red-shifted SWIR contrast agents. Here we demonstrate that J-aggregates of NIR fluorophore IR-140 can be stabilized inside hollow mesoporous silica nanoparticles (HMSNs) to result in biocompatible nanomaterials that absorb and emit SWIR light. The J-aggregates inside PEGylated HMSNs are stable for multiple weeks in buffer and enable high resolution imaging *in vivo* with 980 nm excitation.

6.2 Introduction

In the preceding chapters (Ch. 2–5), all optimization of polymethine fluorophores for contrast agents in shortwave infrared imaging was focused on tuning the properties of the monomer dye. These goals included red-shifting absorption and emission wavelength maxima, (Ch. 2–3) matching absorption wavelengths to desired laser wavelengths (Ch. 3), increasing fluorescence quantum yields and brightness (Ch. 4), and optimizing the solubility and delivery of the monomer dye (Ch. 5). The preceding studies were fruitful in improving the quality of SWIR images that could be obtained in living mice, in both speed and number of orthogonal channels. One of the next goals is to enable video-rate multiplexed imaging with SWIR absorption wavelengths longer than 1,064 nm. Longer excitation wavelengths will not only will enable an increased number of orthogonal channels, but also will facilitate more thorough study of the effects of excitation wavelengths on image quality (resolution, penetration depth, contrast, and sensitivity). There have only been a few studies which have begun to address some of these questions[1–2] which appears to have a more subtle effect, as opposed to the more widely studied impact of detection window.[3–5] Finally, as longer wavelengths of detection in the shortwave infrared offer improved contrast and resolution (Figure 6.1A), improved image quality could be achieved if bright fluorophores with longer peak emission wavelengths are obtained.

With the existing structure–photophysical property relationships on the flavylium scaffold performed in the Sletten Group[1, 6–7] it became clear that more drastic changes than simple functional group substitution would be needed to red shift absorption wavelengths beyond 1,100 nm. Methods, such as utilizing heavier atoms, for example, sulfur[8] and silicon[9] in polymethine scaffolds are promising, but also often come with a large decrease in Φ_F due to heavy atom effects, in addition to the effects of energy gap laws.[10] Further, lengthening the polymethine chain

beyond 7-methine units with simple methine backbones often results in loss of symmetric electron delocalization and/or chemical stability.[11] Alternately, J-aggregation is a red-shifting method that is quite attractive to us to explore for NIR and SWIR chromophores. J-Aggregation is the slip-stacked alignment of chromophores that leads to constructive coupling of the excited state transition dipoles (Figure 6.1B).[12–16] The photophysical consequences of J-aggregation are bathochromically shifted absorption and emission spectra, narrow absorption and emission bands with small Stokes shifts, enhanced absorbance coefficients (ε), and shortened fluorescence lifetimes which can result in enhanced quantum yields (Φ_F) and cycling rates. Many J-aggregate characteristics are beneficial qualities for *in vivo* imaging: red-shifted absorption and emission spectra will enable significant depth penetration during both excitation and image acquisition,[17–20] narrow bands can facilitate multiplexed imaging, and increased ε will result in bright materials. We envisioned that J-aggregation could be a powerful method to obtain more red-shifted photophysics using NIR and SWIR dyes, without the typical challenges, including brightness, electronic symmetry, and chemical stability, that are associated with red-shifting polymethine monomer absorption wavelengths.

Beginning our investigation into polymethine dye J-aggregates which could be utilized for SWIR imaging experiments, we surprised to find that, at the time, there were not any reported SWIR dyes with J-aggregation properties.[21] Further, much remains to be learned about the structural features of dye monomers which can induce or dictate the packing structures and dynamics involved in J-aggregation.[22–24] Thus, we decided to focus on, IR-140 (**6.1**), a commercially available heptamethine dye with $\lambda_{max,abs}$ = 826 nm and $\lambda_{max,em}$ = 875 nm (in DMSO). In 2016, Wang and Weiss reported that introduction of IR-140 to glutathione-coated quantum dots results in J-aggregate formation with two aggregates observed: J1, ($\lambda_{max,abs}$ = 965 nm, nonemissive)

and J2 ($\lambda_{max,abs}$ = 1040 nm, $\lambda_{max,em}$ = 1047 nm).[25] Additionally, IR-140 has been applied as a photo-polymerization initiator,[26–27] fluorescent payload,[28] component of plasmonic arrays[29–30] and as a Raman[31] and two-photon[32] imaging agent.

Despite the significant photophysical advantages J-aggregates can have over the monomer, there are few reports of employing J-aggregates for *in vivo* imaging due to the difficulty in obtaining and stabilizing the necessary chromophore alignment in complex settings.[33] Thus, to realize SWIR-emissive J-aggregates which would be stable in environments such as *in vivo*, we aimed to encapsulate the dyes inside of a hard nanomaterial. Nanostructures can sequester and protect payloads, rendering nanomaterials a promising approach toward stabilizing J-aggregates *in vivo*. In 2016, Zheng and co-workers performed image-guided surgery with porphyrin lipids that formed J-aggregates upon self-assembly into nanovesicles.[34] The following year, Xu and co-workers prepared pyrrolopyrrole cyanine J-aggregate-containing polymer micelles, which could be visualized after subcutaneous injection.[35] More recently, in 2018, Fan and co-workers reported a squaraine J-aggregate, stabilized in polymeric micelles, for SWIR image-guided photothermal therapy.[36] Finally, in 2019, Zhang and coworkers obtained J-aggregates of the SWIR polymethine dye FD-1080 inside micelles composed of dipalmitoylphosphatidylcholine (DMPC), and performed SWIR imaging upon excitation with 1,064 nm light. Each of these reports utilizes self-assembled organic nanomaterials,[37] which are prone to disassembly when diluted in the presence of hydrophobic biomolecules, leading to destabilization of the J-aggregate.[38]

Here, we employ robust, biocompatible, hollow mesoporous silica nanoparticles to stabilize and protect SWIR-emissive J- aggregates of IR-140 for *in vivo* imaging (Figure 6.1C,D). We envisioned that IR-140 J-aggregates could be formed on the negatively charged pores and inner surface of hollow mesoporous silica nanoparticles (HMSNs), similar to the aggregation

behavior on the surface of quantum dots with a negative surface charge.[25] Further, once the aggregates were assembled inside the particles, the hydrophobic nature of IR-140 would make them unlikely to disassemble in aqueous environments.

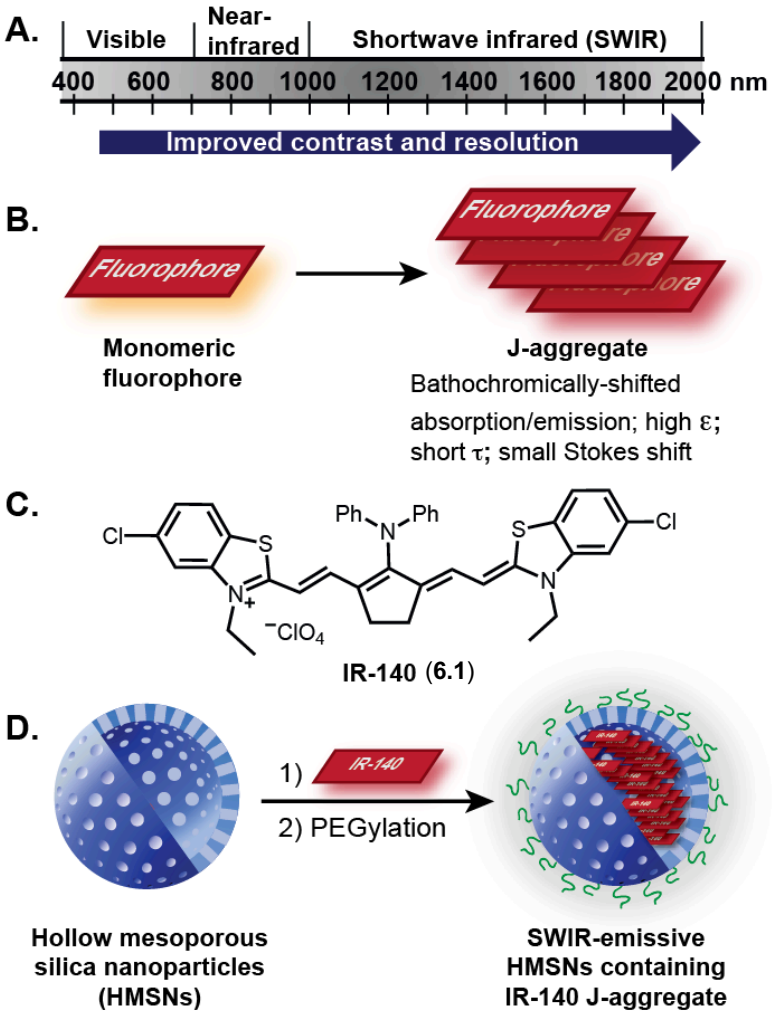

Figure 6.1 SWIR, J-aggregate and HMSN concepts. A) Regions of the electromagnetic spectrum employed for optical imaging. For further details on contrast and resolution within regions of the SWIR, see references [3–5, 19–20]. B) J-Aggregation and characteristic photophysical properties. C) IR-140 (**6.1**). D) Work reported herein: the stabilization of IR-140 J-aggregates in hollow mesoporous silica nanoparticles (HMSNs) to result in biocompatible SWIR-emissive contrast agents.

Hollow mesoporous silica nanoparticles (HMSNs) have 2−4 nm pores that open into a large, 10−200 nm cavity, allowing these nanostructures to carry significant cargo.[39–40] The

surfaces of the HMSNs can be modified to alter the biodistribution of the nanoparticles.[41–42] Consequently, there are numerous reports of HMSNs as the core scaffold of multifunctional materials.[39,42] Included in these studies are the loading or conjugation of visible[43–46] and near-infrared[39,47] fluorophores and administering the resulting nanomaterials for imaging. However, the controlled assembly of J-aggregates in HMSNs had yet to be demonstrated.

6.3 Results and Discussion

6.3.1 Preparation of IR-140 Loaded HMSNs

We prepared HMSNs[1] by synthesizing a mesoporous silica coating on a Stöber sphere core that was subsequently removed via etching with sodium carbonate (Scheme 6.1, Figure 6.2). The HMSNs were treated with varying amounts of IR-140 in different solvents (Figure 6.3A). J-Aggregate formation was assayed by UV/vis/NIR spectroscopy evaluating loss of monomeric IR-140 at 826 nm and formation of the J-aggregates at 965 nm (J1) and 1040 nm (J2). Upon optimization, we found that SWIR J-aggregates could be obtained when IR-140 dissolved in dimethyl sulfoxide (DMSO) was combined with HMSNs and washed. The washing procedure proved essential for obtaining the desired J2 aggregate formation (Figures 6.3B), with gentle PBS washes without sonication yielding the largest amount of the desired J2 aggregate (Figure 6.3B, dark blue line). When these optimized conditions were repeated on Stöber spheres that did not have pores or an inner surface for IR-140 to associate with, only a small J-band was observed (Figure 6.3B, gray line).

[1] All synthesis and loading experiments by Wei Chen and Chi-An Cheng

Scheme 6.1 Synthesis of hollow mesoporous silica nanoparticles (HMSNs).

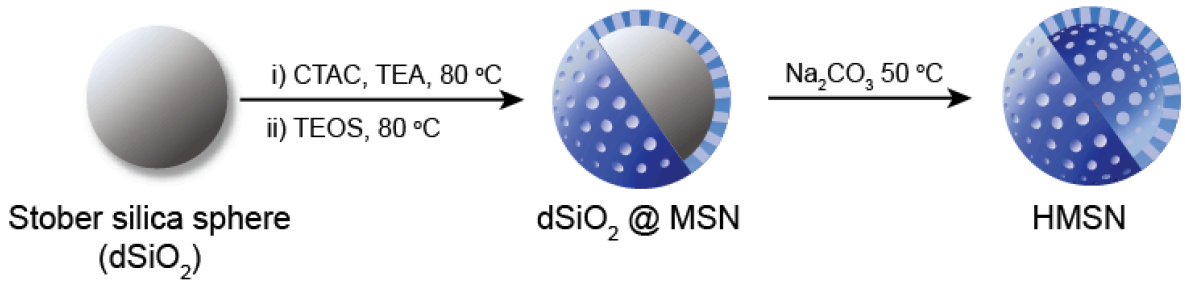

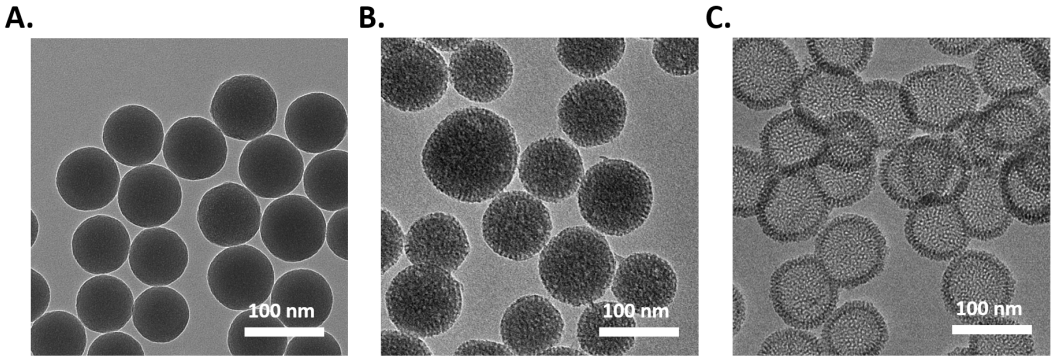

Figure 6.2 TEM images of (A) Stöber silica spheres, (B) $dSiO_2$@MSNs, and (C) HMSNs. The nanoparticles were dispersed in ethanol at a concentration of 0.1 mg/mL.

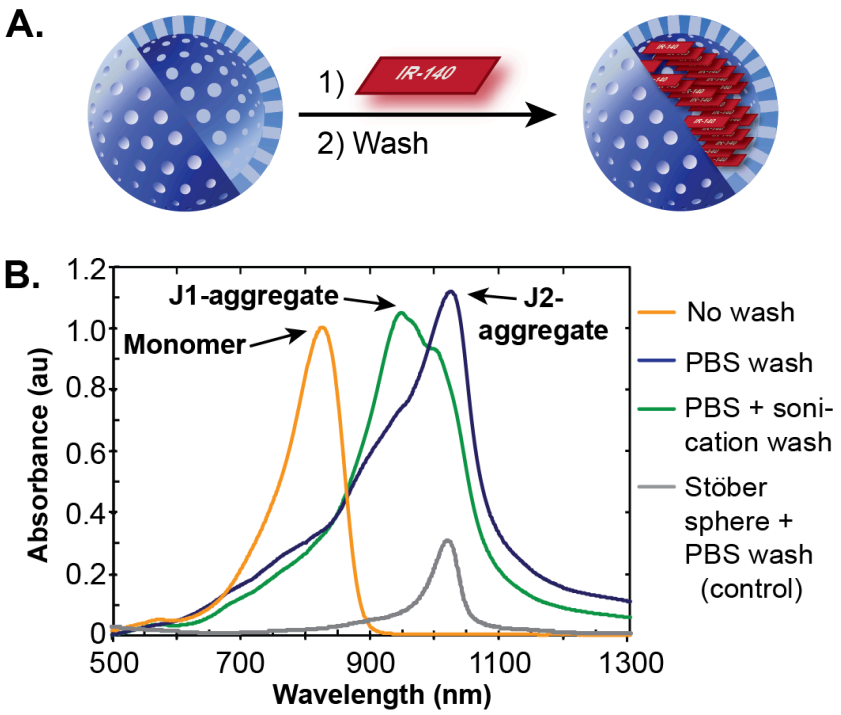

Figure 6.3 Loading and photophysics of IR-140 in HMSNs. A) Schematic of loading IR-140 into HMSNs. B) Washing conditions facilitate J-aggregation. 10 mg/mL HMSNs were combined with 10 mM IR-140 in DMSO and washed with PBS with (green) and without (dark blue) sonication. Prewash spectrum, diluted 1:350 is shown in orange. Loading control for solid, nonporous Stöber spheres is shown in gray.

The HMSNs were further characterized through transmission electron microscopy (TEM), which showed ~85 nm particles with a distinct cavity and pores (Figure 6.4A). While the pores are clearly visible in the TEM of the empty HMSNs, they are darkened after treatment with IR-140 (Figure 6.4B), suggesting the presence of IR-140.

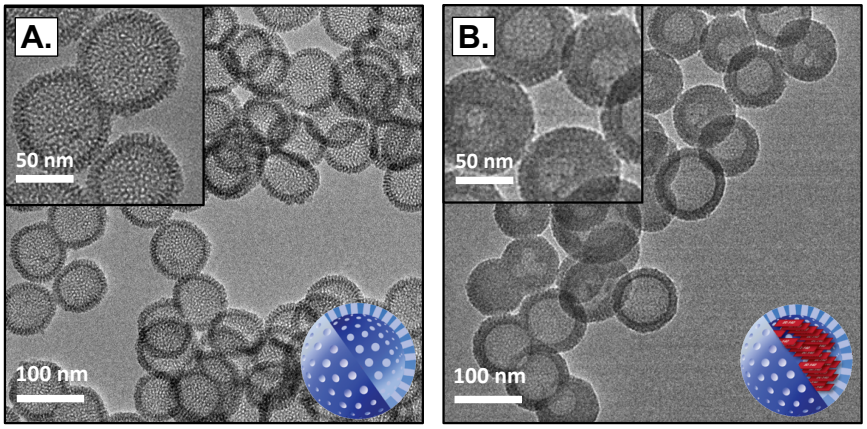

Figure 6.4 TEM images of HMSNs with (B) and without (A) IR-140 treatment.

6.3.2 Preparation of IR-140 Loaded HMSNs-PEG

After confirming that the HMSNs could facilitate J-aggregation of IR-140, we modified the surface with poly-(ethylene glycol) (PEG) such that they could be suspended in aqueous media. This was accomplished by loading HMSNs that had undergone surface silanization with (3-aminopropyl)- triethoxysilane (APTS) prior to Stöber sphere and surfactant removal (Scheme 6.2). This procedure resulted in HMSNs that were positively charged on the outside but still contained a negatively charged interior to associate with the cationic IR-140.[48] The introduction of IR-140 into the HMSNs-APTS proceeded similarly to the HMSNs, yielding analogous loading of IR-140 and a higher ratio of J2:J1 (Figure 6.5). After loading, a 23 kDa PEG-carboxylate was conjugated to the amines present on the outer surface of the HMSNs-APTS using carbodiimide chemistry (Scheme 6.2).

Scheme 6.2 Synthesis of IR-140-loaded HMSN-PEG. A) Overall synthesis starting from Stöber spheres. B) Detailed schematic of conjugation of PEG to the surface of HMSN-APTS. Note that we believe the APTS modification is only on the outer surface due to the Stöber silica sphere blocking the inner surface and the CTAC surfactant blocking the pores.[49–50]

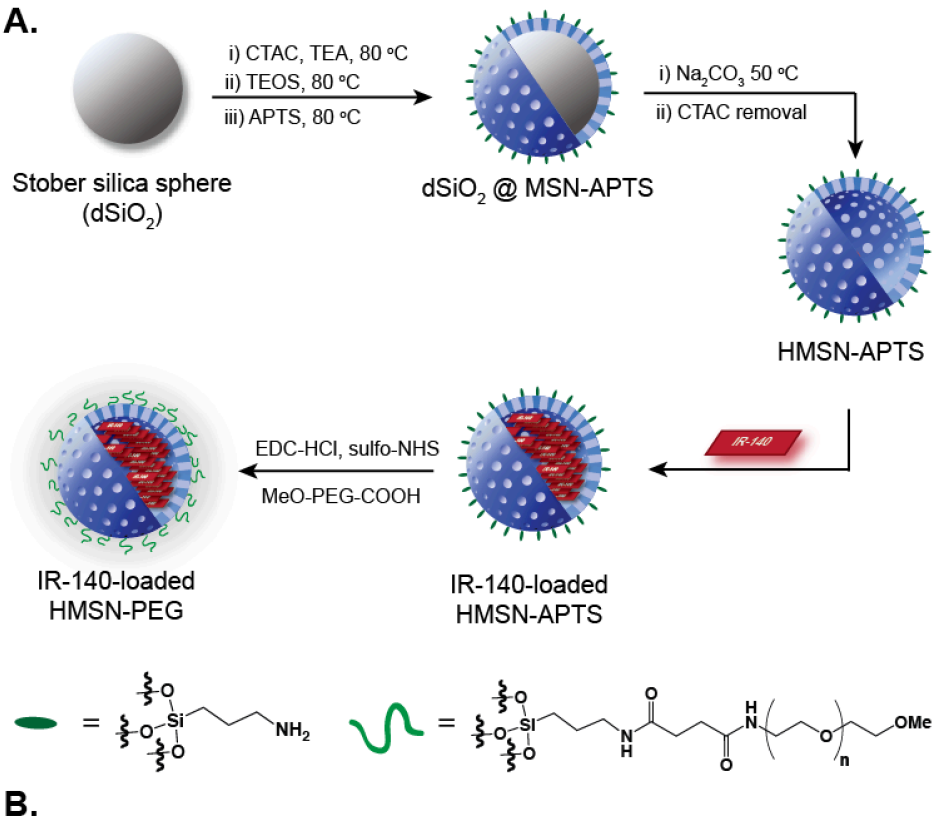

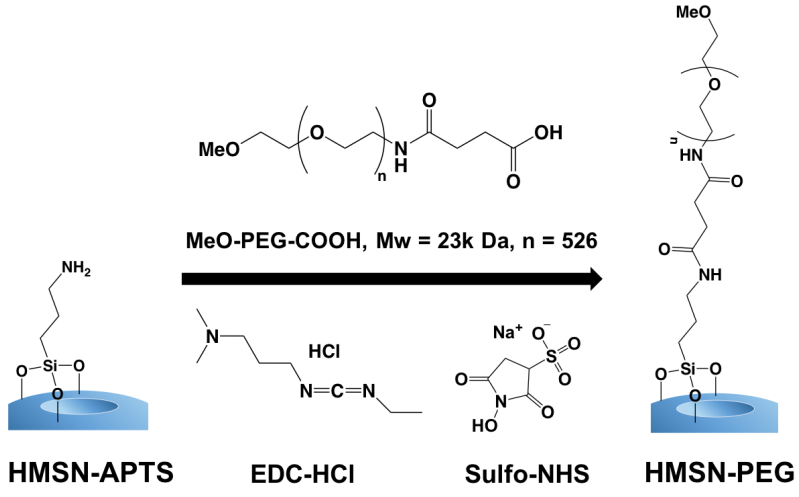

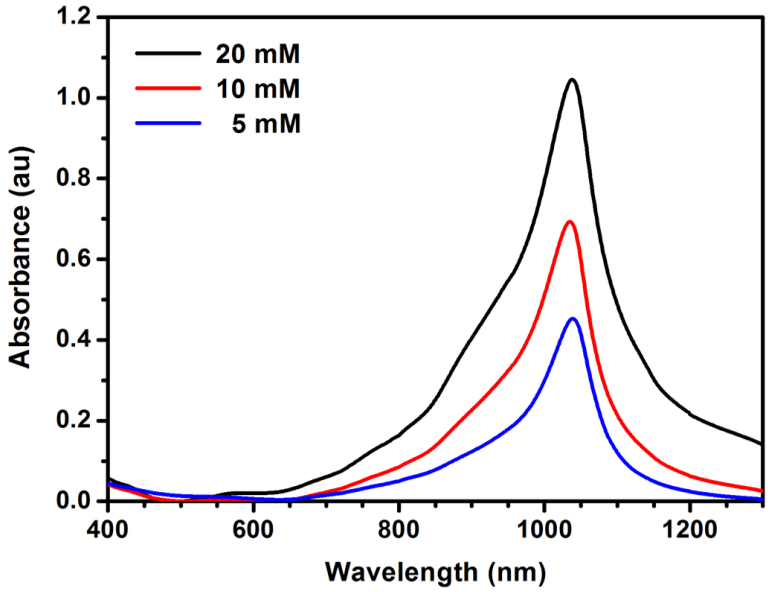

Figure 6.5 UV/Vis/NIR spectra of HMSNs-APTS containing IR-140 for dye loading concentrations of 20 mM (black), 10 mM (red), or 5 mM (blue) in PBS, after washing the particles with PBS (5 x 1 mL). The loading concentration of HMSNs-APTS was 10 mg/mL. The absorbance spectra were measured with 10 mm quartz cuvettes at 0.25 mg nanoparticles/mL.

6.3.3 Photophysical and Stability Characterization of IR-140 J-Aggregates

We evaluated the photophysical properties of the PEGylated HMSNs (HMSNs-PEG) containing IR-140 in comparison to IR-140 in solution as the monomer and J-aggregate (Figure 6.6A). Monomeric IR-140 has been well-characterized[51–52]; however, the solution J-aggregate of IR-140 had previously not been reported.[53] After screening numerous conditions (Figure 6.7), we found that 35% DMSO/0.9% NaCl in water afforded formation of the desired SWIR J-aggregate with a $\lambda_{max,abs}$ = 1042 nm, $\lambda_{max,em}$ = 1043 nm, ε = 3.9 × 105 M^{-1} cm^{-1}, and Φ_F = 0.01% (Table 6.1 Section 6.6.1–6.6.2). The IR-140-containing HMSNs-PEG had similar spectral properties with a $\lambda_{max,abs}$ = 1038 nm, $\lambda_{max,em}$ = 1047 nm, although the absorbance was considerably broader, which we attribute to the presence of other nonemissive aggregate states. When solutions of IR-140 in DMSO, IR-140 in 35% DMSO/0.9% NaCl in water, and IR-140 loaded HMSNs-PEG in PBS were excited with a 980 nm laser, the wavelength to be used for imaging experiments, the

IR-140 J-aggregate in solution and in the particles were similarly emissive, while the monomer was not excited by 980 nm light (Figures 6.6B and 6.8).[54] Thus, J- aggregation is essential for SWIR imaging with low energy excitation.

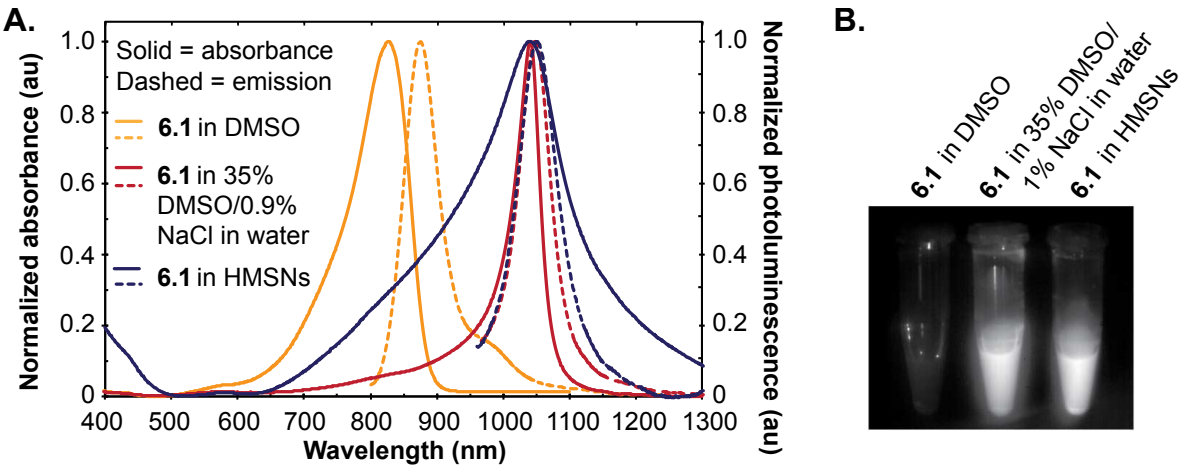

Figure 6.6 Photophysics of IR-140 species. A) Normalized absorption and emission of IR-140 J-aggregate in HMSNs-PEG (blue), J-aggregate in solution (red), and monomer (yellow). B) Emission (1000−1700 nm) of IR-140 monomer (left), J-aggregate in solution (middle) and J-aggregate in HMSNs-PEG (right) upon 980 nm excitation.

Table 6.1 Photophysical characterization of **6.1**.

Species	$\lambda_{max,abs}$ (nm)	ε ($M^{-1}cm^{-1}$)	$\lambda_{max,em}$ (nm)	Φ (%)
6.1 monomer[a]	826	$1.7 \pm 0.1 \times 10^5$	875	20[c]
6.1 J-aggregate[b]	1042	$3.9 \pm 0.4 \times 10^5$	1043	0.012 ± 0.007

[a] in DMSO; [b] in 35% DMSO/0.9% NaCl in water [c] Ref. [52]

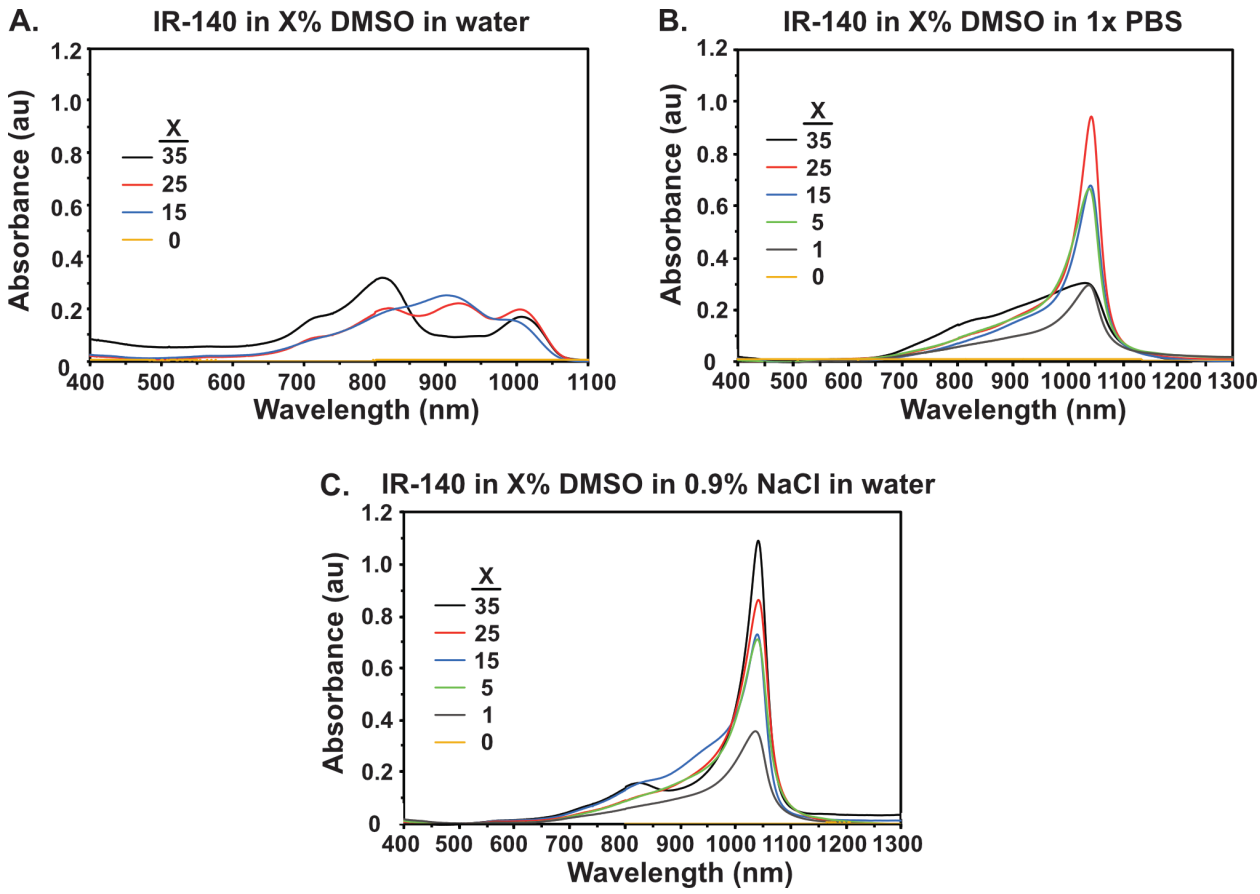

Figure 6.7 UV/Vis/NIR characterization of IR-140 J-aggregate formation in solution at 0.01 mg/mL in (A) DMSO/water (B) DMSO/1xPBS and (C) DMSO/0.9% NaCl in water.

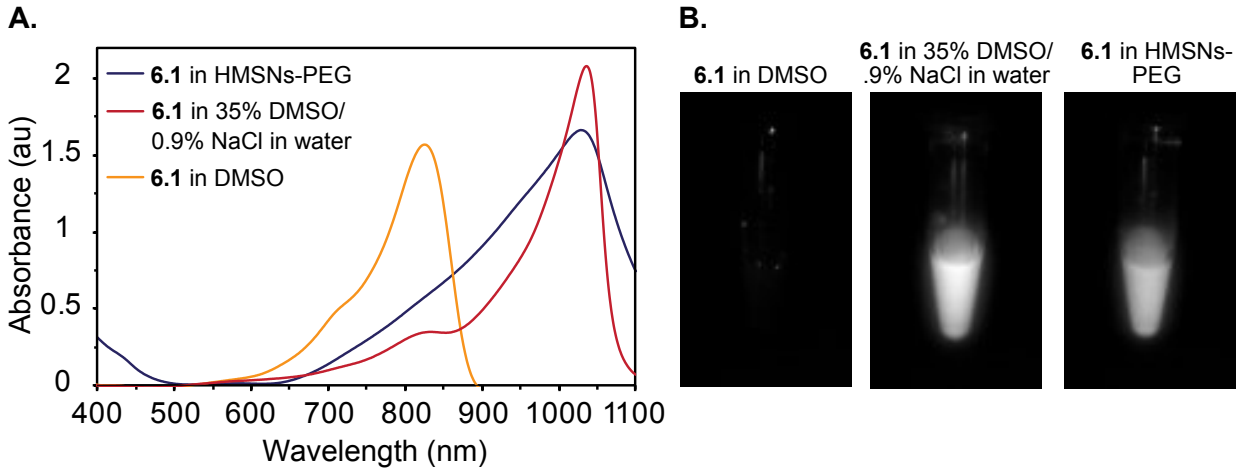

Figure 6.8 Absorbance and emission of monomer and J-aggregate states of IR-140 under 980 nm excitation. A) Absorbance traces of samples (10 mm path length) used in vial images in (B) and in Figure 6.6B, baseline corrected to 521 nm. B) Images of IR-140 monomer in DMSO (left), IR-140 J-aggregate in solution (center) and J-aggregate in HMSNs-PEG (right) under 980 nm

irradiation (99 ± 3 $mWcm^{-1}$). All Eppendorf tubes are placed in the same location, such that laser intensity across all samples is identical. Displayed images were background subtracted, averaged over 10 frames and the contrast was set to identical values for comparison.

Next, we analyzed the role of the HMSNs in stabilizing IR-140 J-aggregates. Over 2 weeks in PBS at room temperature, we observed only a ~10% decrease in absorbance from the IR-140 loaded HMSNs-PEG and no evidence that the packing of the IR-140 within the nanoparticles was changing (Figure 6.9A, blue; Figure 6.10). Comparatively, only ~8% of the J-aggregate in solution remained after 1 day (Figures 6.9A, red; Figure 6.10). Not only do the HMSNs stabilize the assembly of the J-aggregate, but they also enhance the photostability. The fluorescence of solutions containing IR-140 J-aggregate in 35% DMSO/0.9% NaCl in water and HMSNs-PEG containing IR-140 J- aggregate in PBS were continually irradiated with a 980 nm laser (97 $mWcm^{-2}$) and the fluorescence intensity was measured with an InGaAs camera. The photostability of monomeric IR-140 in DMSO was also evaluated via excitation at 785 nm (97 $mWcm^{-2}$). As shown in Figure 6.9B, the J-aggregates within the HMSNs-PEG are 4-fold more stable than the J-aggregates in solution and ~60-fold more stable than the monomer (Table 6.2, Section 6.6.3). This result is consistent with the use of silica shells to overcome the poor photostability that is characteristic of J-aggregates by limiting the amount of reactive oxygen species that can access the aggregate.[55] Photobleaching experiments in deoxygenated solvents support that the HMSNs protect the IR-140 J-aggregate from reactive oxygen species (Figure 6.11). The photobleaching rate of the solution IR-140 aggregate is substantially attenuated by the removal of oxygen, (~7x) while the photobleaching of the HMSNs IR-140 is improved by only ~2x. These data indicate that the IR-140 loaded inside the HMSNs are less affected by the presence of oxygen, which may be due to a shielding of reactive oxygen species by the dense silica shells, as suggested previously.[55] Taken

together, our data show that the HMSNs are critical for stabilizing J-aggregates to degradation by light and solution.

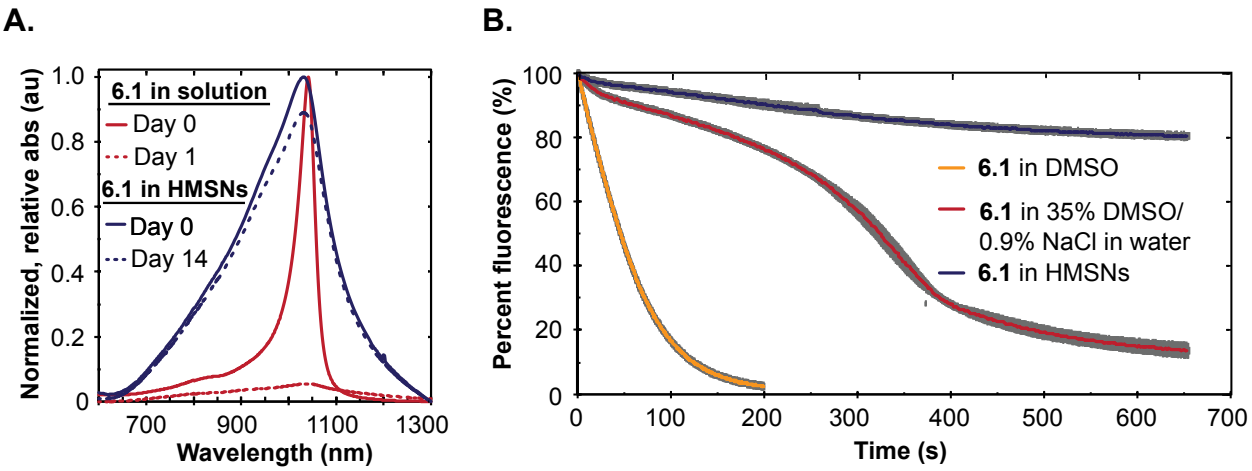

Figure 6.9 Stability of IR-140 species to solution and light. A) Normalized relative absorption of IR-140 J-aggregate in 35% DMSO/0.9% NaCl in water (red) and in HMSNs-PEG in PBS (blue) on day zero (solid) and day 1 or 14 (dotted). B) Photostability under laser irradiation (97 $mWcm^{-2}$) at 980 nm for IR-140 J-aggregate in HMSNs-PEG (blue) and IR-140 J-aggregate in 35% DMSO/0.9% NaCl in water (red), and at 785 nm for monomer in DMSO (yellow).

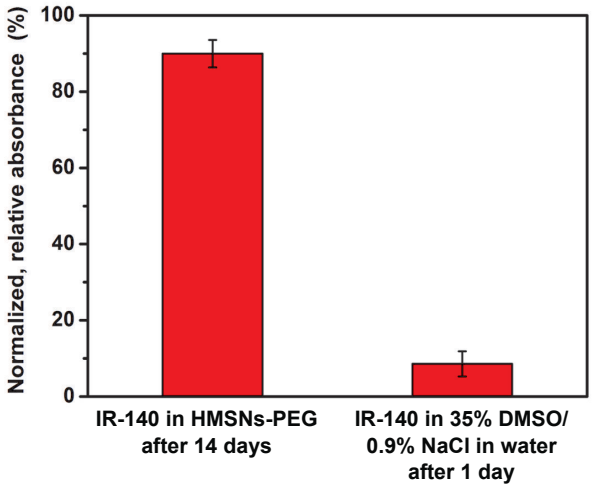

Figure 6.10. Stability of J-aggregates over time, displayed as the normalized, relative absorbance remaining for IR-140 in HMSNs-PEG after 14 days, and IR-140 in solution after 1 day. IR-140 loaded HMSNs-PEG were dispersed in PBS (0.25 mg/mL), and IR-140 J-aggregate was composed of 0.01 mg/mL IR-140 in 35% DMSO/0.9% NaCl in water. Error represents the standard deviation of three replicates.

Table 6.2 Photobleaching rates.

Species	λ_{ex} (nm)	k_{raw} (s^{-1}) x 10^3	k_{rel} (s^{-1}) x 10^3	Relative stability
6.1 monomer	785	19.54 ± 0.04	19 ± 1	1
6.1 J-aggregate	980	1.276 ± 0.008	1.28 ± 0.05	15 ± 1
6.1 in HMSNs-PEG	980	0.317 ± 0.002	0.32 ± 0.01	62 ± 5

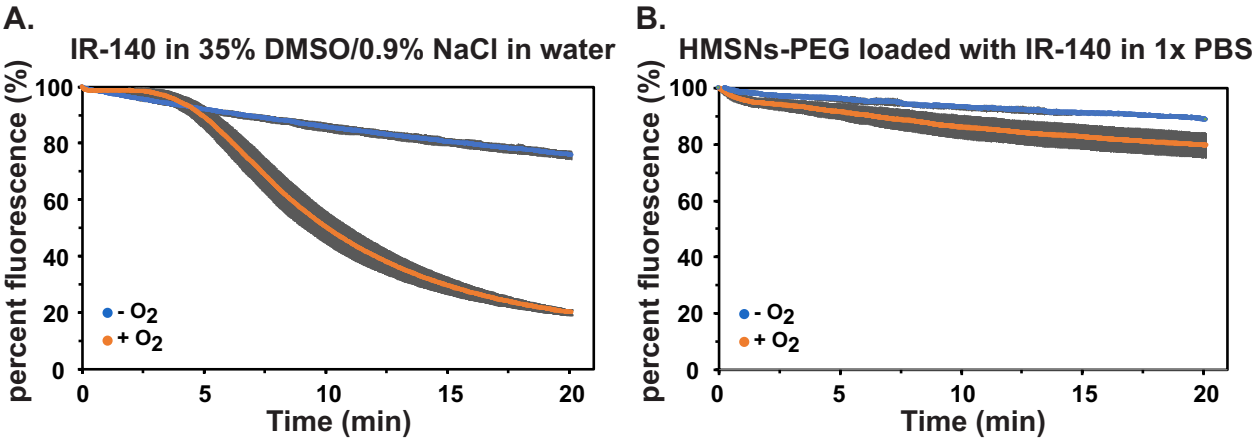

Figure 6.11 Photostability of J-aggregates in the presence and absence of oxygen. A) Raw data of IR-140 J-aggregate in 35 % DMSO/0.9% NaCl at 0.01 mg/mL under 980 nm irradiation with 79 mW cm^{-2} power density. The relative rates of oxygenated to deoxygenated photobleaching is 7.1 to 1. B) Raw data of HMSNs-PEG loaded with IR-140 at 1.0 mg/mL in 1x PBS under 980 nm irradiation with 101 mW cm^{-2} power density. The relative rates of oxygenated to deoxygenated photobleaching is 1.9 to 1. Error bars (grey) represent the standard deviation of three replicate experiments in (A) and (B) oxygenated and two replicate experiments in (B) deoxygenated. Deoxygenated samples were prepared by purging with N_2 for 30–60 min; oxygenated samples were not purged with N_2.

6.3.4 Cytotoxicity Studies and in vivo SWIR Imaging

Finally, with bright SWIR-emissive nanoparticles prepared and characterized, we evaluated their biocompatibility and *in vivo* imaging performance. *In vitro* studies showed no cytotoxicity of the IR-140 loaded HMSNs-PEG over 6 hours at concentrations up to 200 μg/mL (Figure 6.12). These data are consistent with other studies regarding mesoporous silica, which is generally considered nontoxic to animals.[56] We performed *in vivo* imaging experiments using

the IR-140 loaded HMSNs-PEG with excitation at 980 nm and collection from 1,000−1,700 nm. The SWIR-emissive HMSNs-PEG were intravenously injected into nude mice and the mice were immediately imaged (Figure 6.13). The HMSNs-PEG rapidly clear from the bloodstream and intense signal can be seen in the lungs, liver, and spleen. Fifty minutes after injection, the signal intensity within these organs remained constant (Figure 6.14).

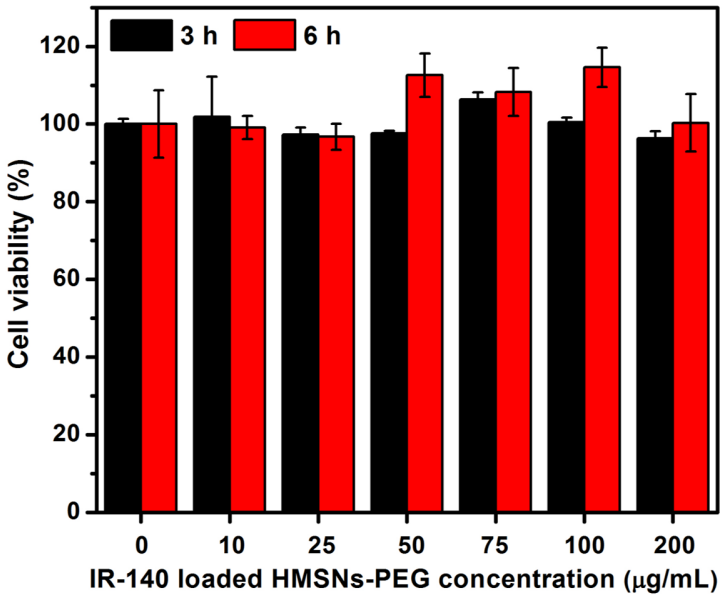

Figure 6.12[2] Cytotoxicity study of IR-140 loaded HMSNs-PEG examined by a CCK-8 assay. HeLa cells were incubated in 200 μL fresh Dulbecco's Modified Eagle Medium (DMEM) containing 0, 2, 5, 10, 15, 20, and 40 μg of IR-140 loaded HMSNs-PEG (*i.e.* 0, 10, 25, 50, 75, 100, and 200 μg/mL) for 3 (black) or 6 (red) hours at 37 °C. The viable cells in each condition was determined by the absorbance at 450 nm and 650 nm (as a reference). The DMEM (100 μL) mixed with CCK-8 reagent (10 μL) served as a background. Error bars represent the standard deviation of three replicate experiments.

[2] Cytotoxicity studies by Chi-An Cheng

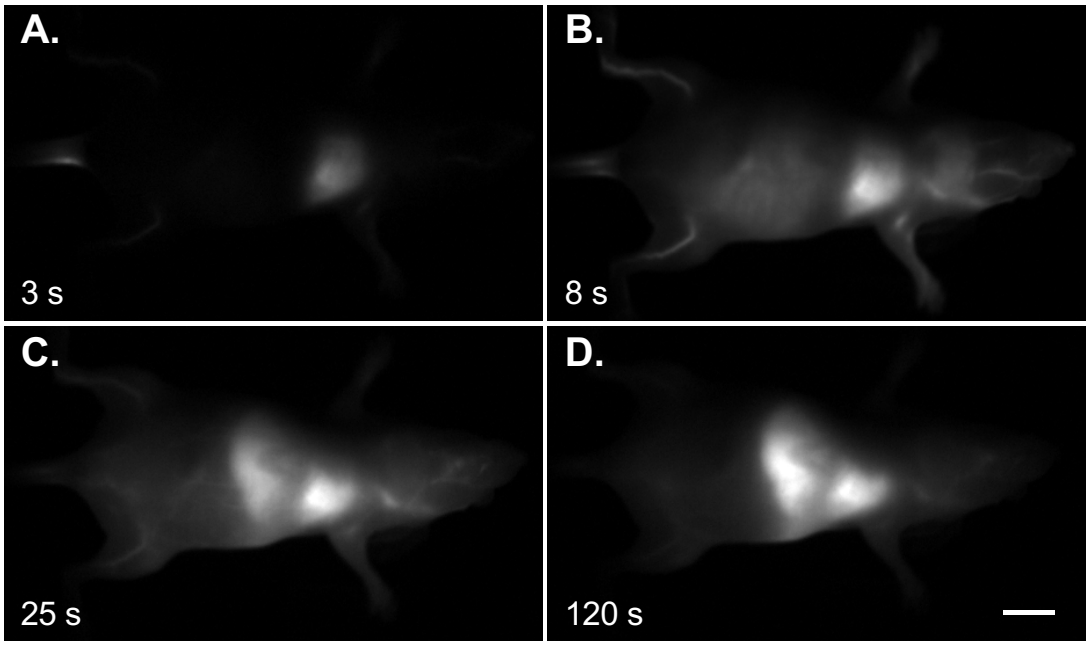

Figure 6.13 Whole-mouse imaging at 16 fps (980 nm, 91 mW cm^{-2} excitation; 1,000−1,700 nm collection) upon i.v. delivery of IR-140 HMSNs-PEG. Background subtracted stills were averaged over 5 frames at 3 s (A), 8 s (B), 25 s (C), and 120 s (D) post-injection. Scale bar represents 1 cm. Data are representative of two replicate experiments.

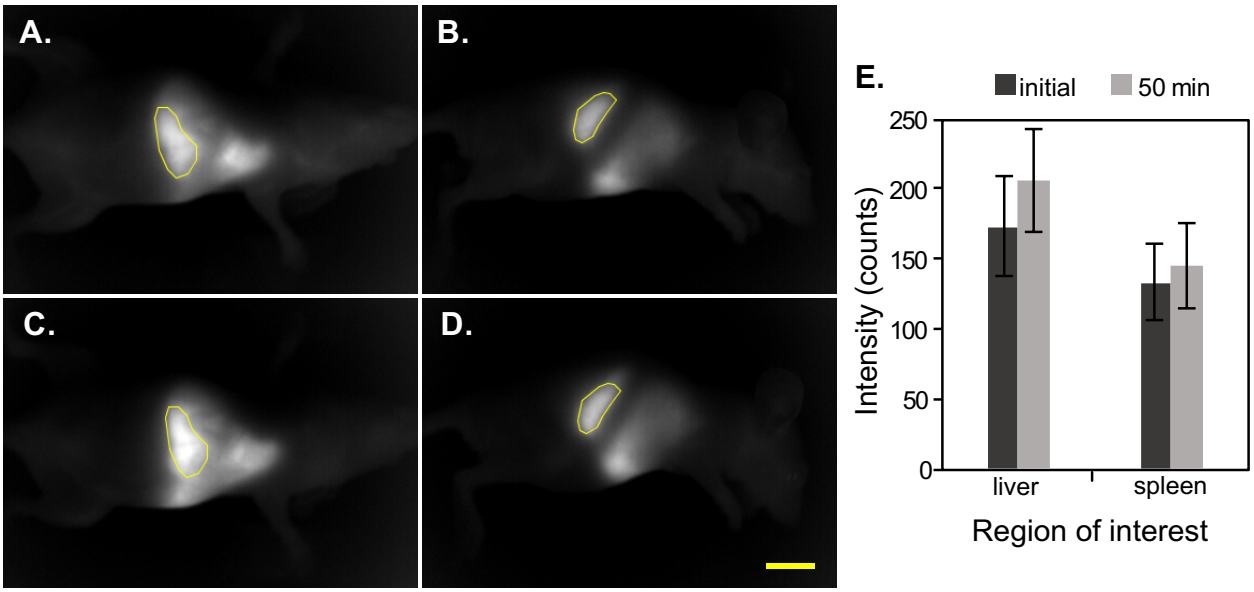

Figure 6.14 Images from the front (A/C) and left side (B/D) of a nude mouse directly after vascular clearance (~2 min post injection) (A/B), and after 50 min (C/D), showing uptake of IR-140 loaded HMSNs-PEG in the liver and spleen. Images were acquired with 60 ms exposure time at 16.65 fps with 980 nm ex. (91 ± 3 mW cm^{-2}) and 1,000–1,700 nm detection. Displayed images were background subtracted, averaged over 5 frames, outliers were removed, and the

contrast was set to identical values for comparison. Regions of interest were defined (denoted by yellow circles) and applied to quantify the intensity in the liver (A/C) and spleen (B/D) over time. Scale bar represents 1 cm. E) Quantification of signal for liver and spleen showing no significant change in signal over 50 minutes. Error bars represent the standard deviation over the regions of interest. Data are representative of two replicate experiments.

6.4 Conclusion

In summary, we have presented J-aggregation as an approach to prepare biocompatible, SWIR contrast agents and demonstrated this concept by stabilizing J-aggregates of the NIR fluorophore IR-140 inside HMSNs. The bathochromically shifted absorption and emission and small Stokes shifts of the IR-140 J-aggregate allow imaging with 980 nm excitation and 1,000−1,700 nm acquisition, providing high resolution *in vivo* images. The modularity of the HMSNs will enable facile exchange of the imaging agent as well as the addition of targeting agents and/or therapeutics, poising these materials to become SWIR theranostics.[57] While we did not observe an enhanced Φ_F with the IR-140 J-aggregate, likely due to disorder or intermolecular vibrations,[58–59] work is ongoing to access a SWIR J-aggregate that exhibits the superradience phenomena predicted by Kasha.[60] Further understanding of the molecular structure parameters which govern J-aggregation and resulting photophysical properties will enable J-aggregation in longer wavelength absorbing scaffolds and lead to materials which could be used for imaging experiments upon longer excitation wavelengths in the SWIR. Collectively, the use of J-aggregates stabilized in HMSNs as SWIR imaging agents has the potential to overcome the stability, toxicity, and brightness challenges of contrast agents for this compelling region of the electromagnetic spectrum.

6.5 Experimental Procedures

6.5.1 General Experimental Procedures

Materials IR-140 (95%), cetyltrimethylammonium chloride (CTAC, 25 wt% in water), cetyltrimethylammonium bromide (CTAB, 99+%), tetraethyl orthosilicate (TEOS, 98%), (3-aminopropyl)triethoxysilane (APTS, 99%), ammonium nitrate (NH_4NO_3, 98+%), triethanolamine (TEA, 99+%), 2-(*N*-morpholino)ethanesulfonic acid hydrate (MES hydrate, 99.5+%), and phosphate buffer saline (X10) were purchased from Sigma-Aldrich. Sodium carbonate anhydrous (99.5+%) was purchased from EMD Millipore. Alpha-methoxy-omega-carboxylic acid poly(ethylene glycol) (MeO-PEG-COOH, Mw = 23,000 Da) was purchased from Iris Biotech GmbH. Ethanol (200 proof) was purchased from Decon Laboratories, Inc. 1-Ethyl-3-(-3-dimethylaminopropyl) carbodiimide hydrochloride (EDC-HCl, 99+%), and *N*-hydroxysulfosuccinimide sodium salt (sulfo-NHS, 99+%) were purchased from CovaChem. Dimethyl sulfoxide (DMSO, 99.9+%), sodium hydroxide (NaOH, 97+%), and ammonium hydroxide (NH_4OH) purchased from Fisher Scientific. Dulbecco's modified Eagle's medium (DMEM) with high glucose, fetal bovine serum (FBS), antibiotics (10,000 U/mL penicillin, 10,000 μg/mL streptomycin, and 29.2 mg/mL L-glutamine), trypsin-ethylenediaminetetraacetic acid (trypsin-EDTA) (0.05 %), and Dulbecco's phosphate-buffered saline (DPBS) were purchased from Gibco. Cell counting kit-8 (CCK-8) was purchased from Dojindo Molecular Technologies, Inc. All chemicals were used without further purification.

Instrumentation Bath sonication was performed using a Branson 3800 ultrasonic cleaner or an Elma S15 Elmasonic. Masses for analytical measurements were taken on a Sartorius MSE6.6S-000-DM or MSA6.6S-000-DM Cubis Micro Balance. Absorbance spectra were collected on a JASCO V-770 UV/Vis/NIR spectrophotometer with a 2000 nm/min scan rate after blanking with

the appropriate solvent, on a Cary 5000 UV-Vis-NIR spectrophotometer or on a Shimadzu UV-1800 UV-Visible Scanning Spectrophotometer. Photoluminescence spectra were obtained on a Horiba Instruments PTI QuantaMaster Series fluorometer. Quartz cuvettes (10 mm, 3 mm and 2 mm) were used for absorbance and photoluminescence measurements. The dynamic light scattering (DLS) measurements were performed on a ZETAPALS instrument with a 660 nm red diode laser (Brookhaven Instruments Corporation). Zeta potential value was measured on a Malvern Zetasizer Nano at room temperature. Nitrogen adsorption/desorption isotherms were acquired at 77 K on a Autosorb-iQ, Quantachrome Instruments. Transmission electron microscopy was performed on a Tecnai T12 instrument with an operating voltage of 120 kV. Animal imaging was performed on custom instrumentation described below.

Abbreviations (3-Aminopropyl)triethoxysilane (APTS), Brunauer-Emmett-Teller (BET), Barrett-Joyner-Halenda (BJH), Cell counting kit-8 (CCK-8), Cetyltrimethylammonium bromide (CTAB), Cetyltrimethylammonium chloride (CTAC), Dichloroethane (DCE), Dichloromethane (DCM), dynamic light scattering (DLS), Dulbecco's modified Eagle's medium (DMEM), Dimethylsulfoxide (DMSO), Dulbecco's phosphate-buffered saline (DPBS), 1-Ethyl-3-(-3-dimethylaminopropyl) carbodiimide hydrochloride (EDC-HCl), Fetal bovine serum (FBS), frames per second (fps), hollow mesoporous silica nanoparticles (HMSNs), PEGylated HMSNs (HMSNs-PEG), Alpha-methoxy-omega-carboxylic acid poly(ethylene glycol) (MeO-PEG-COOH), 2-(*N*-morpholino)ethanesulfonic acid (MES), Sodium Chloride (NaCl), Sodium hydroxide (NaOH), Ammonium nitrate (NH_4NO_3), Ammonium hydroxide (NH_4OH), Near-infrared (NIR), Phosphate buffer saline (PBS), Poly(ethylene glycol) (PEG), *N*-hydroxysulfosuccinimide sodium salt (sulfo-NHS), Shortwave infrared (SWIR), Triethanolamine (TEA), transmission electron microscope (TEM), Tetraethyl orthosilicate (TEOS), Trypsin-ethylenediaminetetraacetic acid (trypsin-EDTA)

Cell culture procedures HeLa cells, a cervical cancer cell line, were cultured in T-75 flasks (Corning) with vented caps in a high glucose Dulbecco's modified Eagle's medium (DMEM) supplemented with 10 % fetal bovine serum (FBS), and 1 % antibiotics (100 U/mL penicillin and 100 μg/mL streptomycin) in a humidity-controlled incubator at 37 °C with 5% CO_2. The HeLa culture media were daily changed and the cells were harvested by trypsinization with 0.05% trypsin-ethylenediaminetetraacetic acid (EDTA) for passaging every 2–3 days.

Animal procedures Animal experiments were conducted in accordance with the approved institutional protocols of Helmholtz Zentrum München. Non-invasive whole mouse imaging was performed on two six-week old female CD-1 nude mice (22.4 g, 19.1 g), purchased from Charles River Laboratories. Mice were anesthetized with an i.p. injection of a ketamine/xylazine mixture. Tail vein injections were performed with a catheter assembled from a 30 ga needle connected through plastic tubing to a second 30 ga needle with syringe prefilled with isotonic saline solution. The bevel of the needle was then inserted into the tail vein and secured using tissue adhesive.

SWIR imaging apparatus For whole mouse imaging, we used a custom-built setup. A 35 W 980 nm laser (Lumics LU0980D350-D30AN) was coupled in a fiber (600 μm core, Thorlabs BF46LS01) The output from the fiber was fixed in an excitation cube and reflected off of a mirror (Thorlabs BBE1-E03), and passed through a positive achromat (Thorlabs AC254-050-B), 1000 nm shortpass filter (Thorlabs FESH 1000), and an engineered diffuser (Thorlabs ED1-S20-MD) to provide uniform illumination over the working area. The excitation flux at the object was adjusted to be close to 100 mW cm^{-2} with an error of ± 3% (power density used is defined separately in each experiment). The working area was covered by a heating mat coated with blackout fabric (Thorlabs BK5). A 4-inch square first-surface silver mirror (Edmund Optics, 84448) was used to direct the emitted light through a custom filter set (Thorlabs NF980-41, 3x

FELH1000, 2x FGL1000) to an Allied Vision Goldeye G-032 Cool TEC2 camera with sensor set point at -30 °C, equipped with a C-mount camera lens (Navitar, SWIR-35). The assembly was partially enclosed to avoid excess light while enabling manipulation of the field of view during operation. The image acquisition toolbox of MATLAB programming environment is used in combination with a custom MATLAB script to preview and collect the required image data. The prepared MATLAB script allows users to access basic functionalities of the image acquisition device by establishing a packet jitter free data streaming link between the desktop computer and the acquisition device.

6.5.2 Experimental Procedures[3]

Synthesis of Stöber silica spheres Stöber silica spheres were synthesized by a sol-gel reaction in basic solution as reported previously.[39]

Synthesis of hollow mesoporous silica nanoparticles (HMSNs) The synthesis of hollow mesoporous silica nanoparticles (HMSNs) was carried out by using Stöber silica spheres as the hard templates which were later removed by selective etching in a basic solution. First, CTAC (2 g, 25 wt% in water solution) and TEA (20 mg) were dissolved in D.I. water (20 mL) in a 100 mL round-bottom flask with vigorous stirring at 80 °C. The reaction mixture was stirred for 5 min followed by the addition of 10 mL of Stöber silica sphere solution prepared as described above, and stirred for 20 min. To coat mesoporous silica on the surface of Stöber silica spheres, TEOS (150 μL) was added dropwise to the solution with vigorous stirring. The nanoparticles were designated as $dSiO_2$@MSNs (Scheme 6.1). After 1 h, the solution was cooled to 50 °C and sodium carbonate (1.89 g) dissolved in D.I. water (3 mL) was added to selectively etch the Stöber silica

[3] All synthesis and loading by Wei Chen and Chi-An Cheng

sphere template in the mesoporous silica shell. The etching process was carried out at 50 °C for 2 h. Afterwards, the solution containing HMSNs were centrifuged (7830 rpm, 7197 g, 15 min) and washed with ethanol 3 times (3 x 50 mL) to remove the unreacted impurities. To remove the CTAC surfactant templates, HMSNs were dispersed in 50 mL of ethanol containing NH_4NO_3 (1 g). The solution was brought to 60 °C with vigorous stirring. After 1 h, the solution was cooled to room temperature, centrifuged (7830 rpm, 7197 g, 15 min), and washed once with ethanol (50 mL). The surfactant removal process was repeated two more times. Finally, surfactant free HMSNs were washed with D.I. water (2 x 50 mL) and ethanol (2 x 50 mL), respectively and stored in 10 mL of absolute ethanol for further use.

Synthesis of APTS functionalized HMSNs (HMSNs-APTS) APTS functionalized HMSNs (HMSNs-APTS) were synthesized by procedures similar to those of HMSNs. First, CTAC (2 g, 25 wt% in water solution) and TEA (20 mg) were dissolved in D.I. water (20 mL) in a 100 mL round-bottom flask with vigorous stirring at 80 °C. The reaction solution was stirred for 5 min followed by the addition of 10 mL of Stöber silica sphere solution prepared as described above. After stirring for 20 min, TEOS (150 μL) was added dropwise to the solution with vigorous stirring. After 1 h, a mixture of APTS (40 μL) and ethanol (120 μL) was added to the solution followed by stirring for another 1 h at 80 °C to conjugate APTS on the surface of HMSNs. The Stöber silica sphere etching and surfactant removal processes were the same as described in the synthesis of HMSNs section. The resulting nanoparticles were dispersed in ethanol and designated as HMSNs-APTS.

Loading of IR-140 in HMSNs, HMSNs-APTS, or $dSiO_2$@MSNs HMSNs, HMSNs-APTS, or $dSiO_2$@MSNs (2 mg) dispersed in ethanol were centrifuged (14000 rpm, 16873 g, 15 min) and washed with DMSO (3 x 1 mL) before IR-140 loading. HMSNs or HMSNs-APTS were then

dispersed in 200 μL of a DMSO solution containing 5, 10, or 20 mM IR-140 by sonication in a bath sonicator for 10 min. For $dSiO_2$@MSNs, the nanoparticles were dispersed in 200 μL of a DMSO solution containing 5, or 20 mM IR-140 by sonication in a bath sonicator for 10 min. After stirring the solution for 20 h to make IR-140 diffuse into the pores and cavity of HMSNs, HMSNs-APTS, or $dSiO_2$@MSNs, the solution containing the particles was centrifuged (14000 rpm, 16873 g, 15 min) and the supernatant was kept for loading capacity calculations. Then, IR-140 loaded HMSNs were washed with three different methods: (a) washed with PBS (1 mL) using a water bath sonication, (b) gently washed with PBS (1 mL) by using plastic transfer pipettes, and (c) washed with water (1 mL) by using plastic transfer pipettes, respectively, to remove free DMSO and DMSO loaded in the pores. IR-140 loaded HMSNs-APTS, or IR-140 loaded $dSiO_2$@MSNs were washed only by method (b). Afterwards, IR-140 loaded nanoparticles were centrifuged (8000 rpm, 5510 g, 3 min) to remove the supernatant. The washing steps were repeated 5 times. Finally, IR-140 loaded HMSNs, HMSNs-APTS, or $dSiO_2$@MSNs were re-dispersed in PBS (1 mL) solution by sonication.

PEG conjugation on the surface of IR-140 loaded HMSNs-APTS (HMSNs-PEG preparation)

To increase the colloidal stability, PEG was conjugated on the surface of IR-140 loaded HMSNs-APTS via amide bond formation. After IR-140 was loaded in HMSNs-APTS, the nanoparticles were gently washed with PBS (5 x 1 mL), D.I. water (2 x 1 mL), and MES buffer solution (pH = 6.0, 10 mM) (1 x 1 mL), respectively. Finally, IR-140 loaded HMSNs-APTS (2 mg) were dispersed in MES buffer (1 mL) by sonication. Alpha-methoxy-omega-carboxylic acid poly(ethylene glycol) (MeO-PEG-COOH, CAS No. 92450-99-2) (10 mg) was dissolved in MES buffer (200 μL) followed by the addition of EDC-HCl (5 mg) and sulfo-NHS (2.5 mg) pre-dissolved in MES buffer (300 μL). The solution was stirred for 30 min. Then, the MES buffer

solution containing the activated MeO-PEG-COOH (500 μL) was added to 1 mL of 2 mg/mL IR-140 loaded HMSNs-APTS MES solution. The solution was further mixed and stirred for 20 h to conjugate PEG on the surface of IR-140 loaded HMSNs-APTS. Then, IR-140 loaded HMSNs-PEG were centrifuged (10000 rpm, 8609 g, 10 min) and washed with D.I. water (2 x 1 mL) and PBS (1 x 1 mL) to remove the excess MeO-PEG-COOH, EDC-HCl, sulfo-NHS, and MES buffer solution. Finally, IR-140 loaded HMSNs-PEG were dispersed in PBS buffer (1 mL) solution for UV/Vis/NIR or photoluminescence measurements.

6.5.3 Figure Experimental Procedures

Figure 6.2 Stöber silica spheres, $dSiO_2$@MSNs, or HMSNs were dispersed in ethanol at a concentration of 0.1 mg/mL. The suspension (5 μL) of the nanoparticles was dropped onto the carbon-coated copper grid and dried at room temperature. Transmission electron microscopy was measured on a Tecnai T12 instrument with an operating voltage of 120 kV.

Figure 6.3B Refer to Section 6.5.2 "Loading of IR-140 in HMSNs, HMSNs-APTS, or $dSiO_2$@MSNs". 10 mM IR-140 was used as the loading solution. Then, IR-140 loaded HMSNs were washed by methods (a), (b), or (c) to compare the extent of IR-140 aggregate by using the above washing methods. The washing steps were repeated 5 times and finally IR-140 loaded HMSNs were re-dispersed in 1 mL of PBS solution by sonication.

Stöber silica spheres dispersed in ethanol were centrifuged (14000 rpm, 15 min) and washed with DMSO 3 times before IR-140 loading. Afterwards, Stöber silica spheres were dispersed in 200 μL of DMSO solution containing 10 mM IR-140 by sonication in a bath sonicator for 10 min. Then, the solution was stirred for 20 h. After the IR-140 loading, the solution containing the particles was centrifuged (14000 rpm, 15 min) to get IR-140 loaded Stöber silica spheres. Then, IR-140

loaded Stöber silica spheres were washed with 1 mL of PBS by gently washing with plastic transfer pipettes to remove free DMSO. After each washing step, IR-140-loaded Stöber silica spheres were centrifuged (8000 rpm, 3 min) to remove the supernatant. The washing steps were repeated 5 times and finally IR-140-loaded Stöber silica spheres were re-dispersed in PBS solution (1 mL) by sonication. The absorbance spectra of IR-140 loaded HMSNs or IR-140 loaded Stöber silica spheres were measured with 10 mm quartz cuvettes at a concentration of 0.25 mg nanoparticles/mL PBS on a Cary 5000 UV-Vis-NIR spectrophotometer at room temperature. Absorbance traces were corrected for the non-linearity between gratings. For the prewash spectrum, after the IR-140 (10 mM) loading, the particles solution (10 mg/mL) was diluted 1:350 with DMSO for measurement. The absorbance spectrum of the prewash sample was measured with 3 mm quartz cuvettes on a JASCO V-770 UV/Vis/NIR spectrophotometer at room temperature.

Figure 6.4 HMSNs and IR-140 loaded HMSNs were dispersed in ethanol and D.I. water, respectively at a concentration of 0.1 mg/mL. The suspension (5 μL) of the nanoparticles was dropped onto the carbon-coated copper grid and dried at room temperature. Transmission electron microscopy was measured on a Tecnai T12 instrument with an operating voltage of 120 kV.

Figure 6.5 HMSNs-APTS (2 mg) dispersed in ethanol were centrifuged (14000 rpm, 16873 g, 15 min) and washed with DMSO (3 x 1 mL) before IR-140 loading. Afterwards, HMSNs-APTS was dispersed in 200 μL of DMSO solution containing 5, 10, or 20 mM IR-140 by sonication in a bath sonicator for 10 min. Then, the solution was stirred for 20 h to let IR-140 diffuse into the pores and cavity of HMSNs-APTS. After the IR-140 loading, the solution containing the particles was centrifuged (14000 rpm, 16873 g, 15 min) to get IR-140 loaded HMSNs-APTS. Then, IR-140 loaded HMSNs-APTS were washed with PBS (1 mL) by gently washing with plastic transfer pipettes to remove free DMSO and DMSO loaded in the pores. After each washing step, IR-140

loaded HMSNs-APTS were centrifuged (8000 rpm, 5510 g, 3 min) to remove the supernatant. The washing steps were repeated 5 times and finally IR-140 loaded HMSNs-APTS were re-dispersed PBS (1 mL) by sonication. The absorbance spectra of IR-140 loaded HMSNs-APTS were measured with 10 mm quartz cuvettes at a concentration of 0.25 mg nanoparticles/mL PBS on a Cary 5000 UV/Vis/NIR Spectrophotometer at room temperature. Absorbance traces were corrected for the non-linearity between gratings.

Figure 6.6A All absorbance and emission traces were baseline corrected and normalized. Absorbance traces were acquired on a JASCO V-770 UV/Vis/NIR spectrophotometer. The slit widths used in fluorescence spectra were 5.76 mm for excitation and 11.52 mm for emission. The step size was 1.0 nm, integration time 0.1 s, and traces were acquired after an automatic detector background subtraction.

IR-140 monomer was dissolved in DMSO and diluted to an O.D. of ~ 0.7 for absorbance and less than 0.1 for fluorescence spectroscopy (ex. 785 nm) in a 1 cm path length cuvette. The monomer absorption trace was corrected for the non-linearity between gratings before baseline subtraction and normalization.

The IR-140 J-aggregate in 35% DMSO/0.9% NaCl was prepared by dissolving 0.02 mg of IR-140 in 350 μL DMSO, vortexing briefly, adding 650 μL 0.9% aqueous NaCl, and shaking briskly. The solution becomes warm and immediately loses the blue color. Absorbance and emission traces of the J-aggregate in solution were obtained with a 2 mm path length cuvette. For the fluorescence trace, a 10 mm path length was used on the excitation side and a 2 mm path length on the emission side. A reabsorption correction was performed on the emission trace analogous to that described in Section 6.6.1.

The IR-140 loaded HMSNs-PEG were prepared as described in the synthetic procedures, section VI. The absorbance was collected without dilution in a 10 mm cuvette. The fluorescence spectrum was obtained by diluting the sample to an O.D. of less than 0.1 in a 3 mm path length square quartz cuvette, and exciting at 885 nm with a shortpass filter (Thorlabs, FES0900).

Figure 6.6B Samples consisted of IR-140 monomer: 0.01 mg/mL IR-140 in DMSO (left); IR-140 J-aggregate in solution: 0.01 mg/mL IR-140 in 35% DMSO/0.9% NaCl in water (center); IR-140 HSMNs-PEG: 1 mg/mL in PBS (right). Vials were excited with 980 nm light (with Thorlabs FESH1000) with an average power density of 99 ± 3 $mWcm^{-2}$. Power densities over the three samples were not identical due to varying distance from the excitation cube. See Figure S12 for images with consistent distances from the excitation cube. Collection was from 1000–1700 nm (1000 nm LP, Edmund Optics 84-776). The custom lens system consists of a 4f configuration with a f=750.0mm lens (Thorlabs LB1247-C) and two f=200.0mm lenses (Thorlabs LB1199-C). For ergonomic reasons a 2'' protected silver-coated elliptical mirror (PFE20-P01) mounted to a kinematic mount (Thorlabs KCB2EC/M) was used. Images were acquired at 35 ms exposure time, 16.65 fps. Displayed image was background subtracted and averaged over 6 frames.

Figure 6.7 Samples were prepared as by dissolving 0.02 mg IR-140 in DMSO, and then adding to the appropriate aqueous phase (either MilliQ water, 1x PBS, or 0.9% NaCl in water) and shaking vigorously. The appropriate volumes of DMSO and aqueous phase were used to sum to 2.0 mL for each listed percentage. For the 0% DMSO traces, IR-140 is at its solubility limit, after sonicating 0.02 mg IR-140 in 1.0 mL of the appropriate solvent for 4 hours. Absorbance traces were measured in a 3.0 mm cuvette with blanking to the appropriate solvent mixture on a JASCO V-770 UV-Vis-NIR spectrophotometer.

Figure 6.8 Samples were prepared and excitation and acquisition was performed as described in Figure 6.6B. Absorbance traces were acquired on a Shimadzu UV-1800 UV-Visible Scanning Spectrophotometer.

Figure 6.9A Stability of IR-140 in HMSNs-PEG over time. IR-140 loaded HMSNs-PEG were dispersed in PBS at 0.25 mg/mL. The absorbance spectra were taken in a 3 mm path length cuvette immediately (day 0) and after 14 days (day 14) on a JASCO V-770 UV/Vis/NIR spectrophotometer. The absorbance was normalized, relative to spectrum (1). Results of the triplicate experiment are presented in Figure 6.10.

Stability of IR-140 in solution over time. IR-140 J-aggregate was prepared in DMSO as described in Figure 6.6A. The aggregate absorbance in a 2 mm path length cuvette was obtained immediately (day 0) and after 17 h storage in the dark (day 1) on a JASCO V-770 UV/Vis/NIR spectrophotometer. The absorbance was normalized, relative to spectrum at day 0. Results are reproduced in triplicate in Figure 6.10.

Figure 6.9B Three solutions were prepared: (a) 1 mg/mL solution of HMSNs-PEG containing IR-140 (b) 0.01 mg/mL IR-140 in 35% DMSO/0.9% NaCl solution, and (c) 0.01 mg/mL IR-140 in DMSO. Each solution (400 μL) was irradiated with 97 ± 3 mW cm^{-2} of 980 nm (a and b) and 785 nm (c) light and their emission was monitored by a SWIR camera. Acquisition settings were 2 fps and (a) 25 ms, (b) 15 ms, and (c) 0.3 ms. Excitation and emission settings were identical to Figure 6.6B. Error represents the standard deviation of three measurements.

Figure 6.10 IR-140 loaded HMSNs-PEG were dispersed in PBS (0.25 mg/mL). The absorbance spectra were taken in a 3 mm path length cuvette immediately (day 0) and after 14 days storage in the dark. IR-140 J-aggregate in solution was prepared by dissolving 0.02 mg IR-140 in 700 μL DMSO, and subsequently adding 1.3 mL 0.9% NaCl and briskly shaking. The aggregate

absorbance in a 2 mm path length cuvette was obtained immediately and after 24 h storage in the dark.

Figure 6.11

(A) Deoxygenated IR-140 solution J-aggregates were prepared by adding DMSO (1.4 mL) to IR-140 (0.04 mg) in a purged dram vial, followed by 0.9% NaCl solution in water (2.6 mL) and shaking. Solvents were deoxygenated by purging with N_2 for at least one hour. Oxygenated IR-140 solution J-aggregates were prepared analogously, but with solvents which had been exposed to air. Solutions (4 mL), sealed with septa, were irradiated for 20 min. The optical parameters for experiment in (A) consisted of the following: a 4-inch square first-surface silver mirror (Edmund Optics, 84448) was used to direct the emitted light through a custom filter set (Edmund optics #84-776, TL) to an Allied Vision Goldeye G-032 Cool TEC2 camera at -20 °C, equipped with a C-mount camera lens (Navitar, SWIR-35). Excitation light was passed through a positive achromat (Thorlabs AC254-050-B), 1000 nm shortpass filter (Thorlabs FESH 1100), and an engineered diffuser (Thorlabs ED1-S20-MD) to provide uniform illumination over the working area. Exposure time used was 100 ms, with 2 fps.

(B) Deoxygenated solutions of IR-140 containing HMSNs-PEG were purged with N_2 for at least 30 min, while oxygenated were left open to air. Both sample types (1 mg/L, 0.40 mL), sealed with septa, were irradiated for 20 minutes. The optical parameters for experiment in (B) consisted of the following: a 4-inch square first-surface silver mirror (Edmund Optics, 84448) was used to direct the emitted light through a custom filter set (Edmund optics #84-776, 3x FELH1000,) to an Allied Vision Goldeye G-032 Cool TEC2 camera at -20 °C, equipped with a C-mount camera lens (Navitar, SWIR-35). Excitation light was passed through a positive achromat (Thorlabs AC254-050-B), 1000 nm shortpass filter (Thorlabs FESH 1000), and an engineered

diffuser (Thorlabs ED1-S20-MD) to provide uniform illumination over the working area. Exposure time used was 200 ms, with 2 fps.

Data were analyzed analogous to that discussed in Section 6.6.3, however only the relative rates between oxygenated and deoxygenated experiments were calculated and evaluated.

Figure 6.12 The viabilities of HeLa cells after the treatment of IR-140 loaded HMSNs-PEG were examined by using a cell counting kit-8 (CCK-8) assay. The cells were seeded in 96-well plates at a density of 5 x 10^3 cells per well in 200 μL DMEM supplemented with 10% FBS and 1% antibiotics in a humidity-controlled incubator at 37 °C for 24 h attachment. After the attachment, the medium was removed and the cells were incubated in 200 μL fresh DMEM containing 0, 2, 5, 10, 15, 20, and 40 μg of IR-140 loaded HMSNs-PEG (*i.e.* 0, 10, 25, 50, 75, 100, and 200 μg/mL) for 3 or 6 h in an incubator at 37 °C. After incubation, the medium was removed and the treated cells were washed with DPBS 1 time (200 μL). To measure the cell viability, 100 μL of DMEM and 10 μL of CCK-8 cellular cytotoxicity reagent were added to each well. Then, the plates were put in the incubator for 2 h at 37 °C. To measure the number of the viable cells in each condition, a plate reader (Tecan M1000) was used to measure the absorbance at 450 nm and 650 nm (as a reference). The DMEM (100 μL) mixed with CCK-8 reagent (10 μL) served as a background control.

Figure 6.13–6.14 The IR-140 HMSNs-PEG in PBS were sonicated (Elma S15 Elmasonic) for 30 mins prior to injection and filtered through a 40 μm nylon filter. 200 μL of the IR-140 HMSNs-PEG in PBS were injected via the tail vein and immediately imaged. The excitation flux (980 nm) had an average power density of 91 ± 3 mW cm^{-2} over the field of view. Images were acquired at 60 ms exposure time and 16.65 fps, in 8-bit format. Displayed images were background subtracted

with an average of 10-frames from the pre-injection time points, outliers were removed, and the stills were averaged over 5 frames.

6.6 Notes Related to Chapter Six

6.6.1 Absorption Coefficients

Absorption coefficients were calculated according to the Beer-Lambert law,

$$A = \varepsilon l c \qquad \text{(Eq. 6.1)}$$

where A represents absorbance (unitless), ε the absorption coefficient ($M^{-1}cm^{-1}$), l the path length (cm), and c the concentration (M). Masses were determined on a microbalance and diluted using Hamilton microsyringes to concentrations within the linear range of the UV/Vis/NIR spectrophotometer. Four concentrations were obtained for each experiment and the reported error represents the standard deviation of three measurements.

The monomer absorption coefficient was straightforward as only one species is present in solution. These data were collected using a 10 mm quartz cuvette in DMSO. The raw data was corrected for non-linearity between gratings, and baseline corrected to 478 nm. The absorption coefficient at all relevant wavelengths is displayed below in Figure 6.15. The absorption coefficient at $\lambda_{max,abs}$ = 826 nm was 1.7 ± 0.1 x 10^5 $M^{-1}cm^{-1}$.

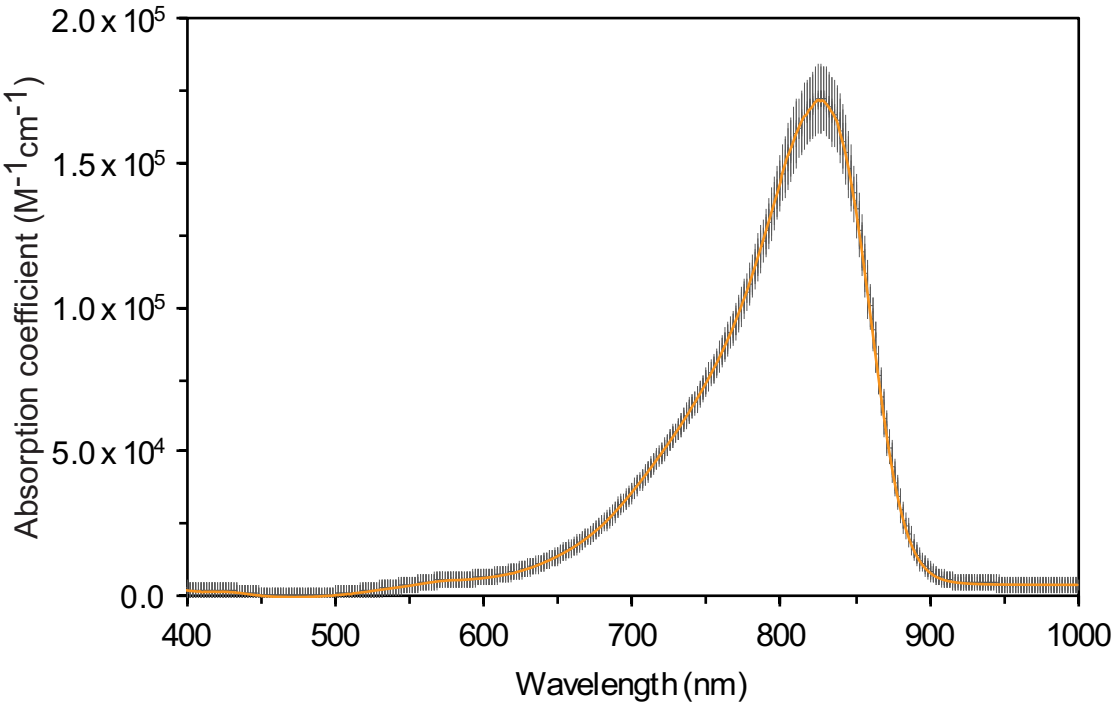

Figure 6.15 Absorption coefficient of IR-140 monomer in DMSO.

The J-aggregate absorption coefficient is more complex due to the requirement of high concentrations for selective formation of the J-aggregate over the monomer. As a result, to use higher concentrations, yet stay in the linear range of the spectrometer, these data were collected using a 3 mm cuvette. The raw data were baseline corrected to 449 nm and are included below in Figure 6.16. The uncorrected absorption coefficient (ε_{raw}) at $\lambda_{max,abs}$ = 1043 nm was 3.3 ± 0.3 x 10^5 $M^{-1}cm^{-1}$.

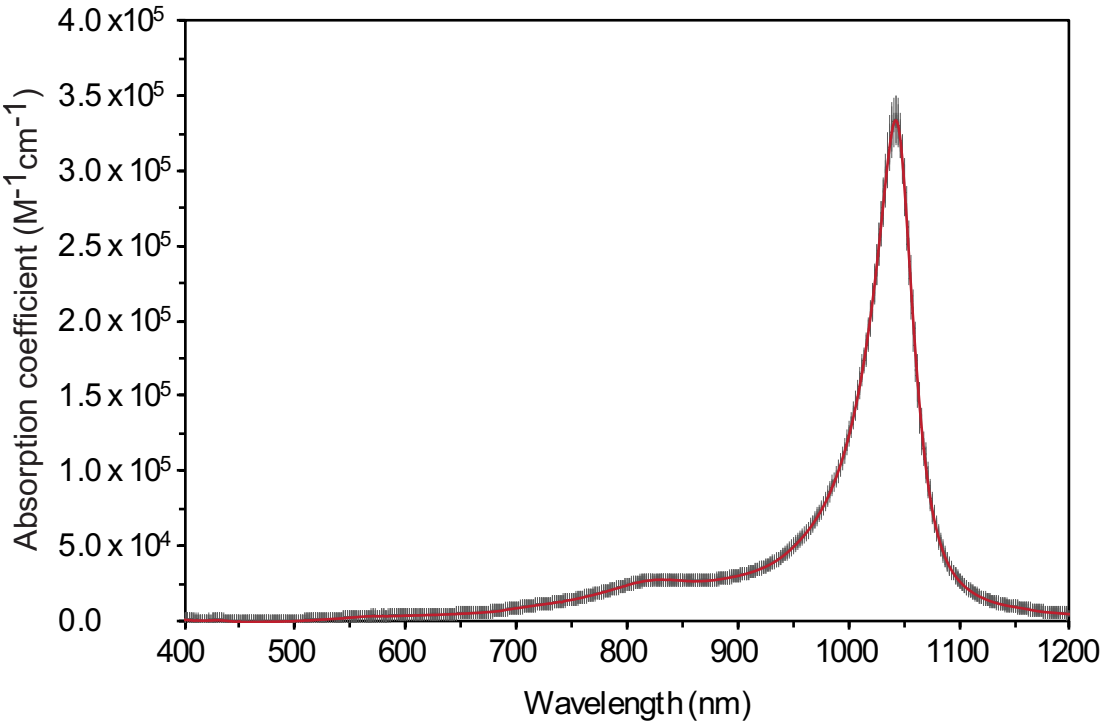

Figure 6.16 Uncorrected absorption coefficient of IR-140 J-aggregate in 35% DMSO/0.9% NaCl in water.

Despite the higher concentrations, some monomer remained in solution. The uncorrected data can be corrected for the remaining monomer in solution using the absorption coefficient of the monomer at its $\lambda_{max,abs}$ and making the assumption that the absorption coefficient of the monomer does not change significantly between 100% DMSO and 35% DMSO/0.9% NaCl in water. We used the equation:

$$\alpha_m + a_j = 1 \qquad \text{(Eq. 6.2)}$$

where α_m represents the mole fraction of monomer and α_j the mole fraction of J-aggregate. The value α_m for each absorbance trace was obtained using the Beer-Lambert law from the absorption coefficient of the monomer and the known concentration of total dye. The value a_j was then used as a multiplicative factor to correct the concentration of J-aggregate in solution. The absorption coefficient was then recalculated with the corrected concentration values. The corrected absorption

coefficient at $\lambda_{max,abs}$ = 1043 nm was 3.9 ± 0.4 x 10^5 $M^{-1}cm^{-1}$. Error was taken as the standard deviation of the three replicates. The corrected absorption coefficient is displayed below in Figure 6.17.

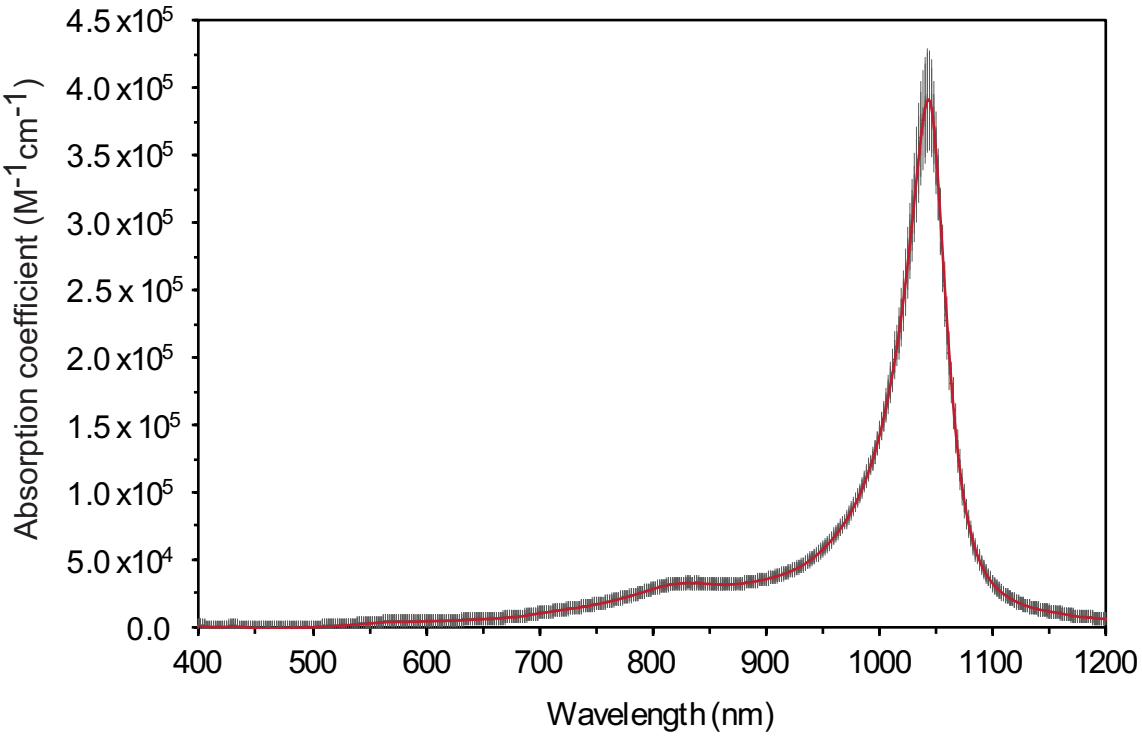

Figure 6.17 Corrected absorption coefficient of IR-140 J-aggregate in 35% DMSO/0.9% NaCl in water.

6.6.2 Quantum Yield

The photoluminescence quantum yield (Φ_F) of a molecule or material is defined as follows,

$$\Phi_F = \frac{P_E}{P_A} \qquad \text{(Eq. 6.3)}$$

where P_E and P_A are the number of photons absorbed and emitted, respectively. To determine the quantum yield, we either use a relative method with a known standard in the same region of the electromagnetic spectrum, or an absolute method, in which the number of photons absorbed and emitted are measured independently. Here, due to the limits of our petite integrating sphere (Horiba

KSPHERE-Petite with InGaAs detector Horiba Edison DSS IGA 020L), we use a relative method, with IR-26 as the known standard.

The quantum yield was measured at three different excitation wavelengths, 885 nm, 900 nm, and 915 nm and the results were averaged to obtain the value reported.

To compare an unknown to a reference with a known quantum yield, the following relationship was used:

$$\Phi_{F,x} = \Phi_{F,r}(m_x/m_f)(\eta_x{}^2/\eta_r{}^2) \qquad \text{(Eq. 6.4)}$$

Where *m* represents the slope of the line (y = *m*x + b) obtained from graphing integrated fluorescence intensity versus optical density across a series of samples, η is the refractive index of the solvent, and the subscripts *x* and *r* represent values of the unknown and reference, respectively. The ($\Phi_{F,r}$) of IR-26 was taken to be 0.05 ± 0.03%, as we have previously measured [61], and which agrees with several recent measurements.[52,62]

To obtain a plot of integrated fluorescence intensity versus absorbance for the reference and unknown, five solutions and a solvent blank were prepared and their absorbance and emission spectra were acquired. IR-26 was diluted in DCE to concentrations with optical densities less than 0.1 to minimize effects of reabsorption. The baseline corrected (to 1,500 nm) fluorescence traces were integrated from 950–1,500 nm, and the raw integrals were corrected by subtracting the integral over an identical range from fluorescence traces of the blank solvent (Figure 6.18A). The methods employed here were validated with comparison of IR-26 to IR-1061, giving a $\Phi_F$value of 0.3 ± 0.2 %, which is in agreement with our prior absolute quantum yield measurement,[61] but with lower precision due to the uncertainty in IR-26 absolute Φ_F.

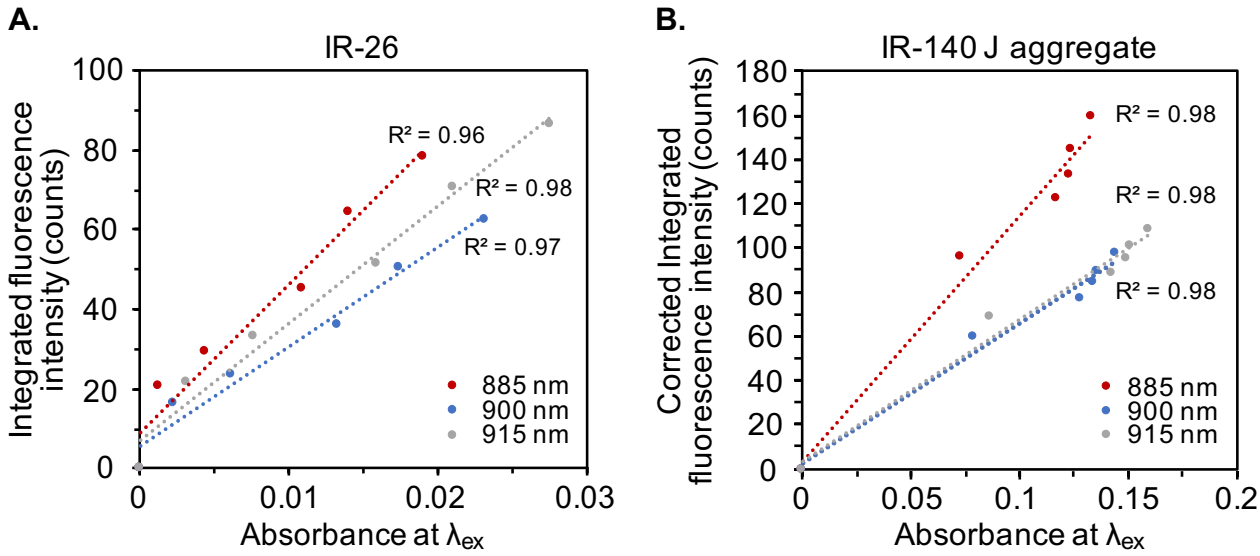

Figure 6.18 Solvent corrected integrated fluorescence intensity versus absorbance plots for A) IR-26 and B) IR-140 J-aggregate, also corrected for reabsorption.

The IR-140 J-aggregate was prepared as described in Figure 6.6A, in 35% DMSO/0.9% NaCl in water. Due to the necessity of using concentrated samples for IR-140 to remain in the J2 aggregate state, high concentrations of IR-140 J-aggregate were used for quantum yield measurements (the OD with a 2 mm path length at the relevant excitation wavelengths ranged from 0.07–0.16). The baseline corrected (to 1,400 nm) fluorescence traces of the optically dense IR-140 J-aggregate samples were corrected for reabsorption by the relationship,

$$I(\lambda) = I_o(\lambda)[-\ln(10^{-OD(\lambda)})/(1-10^{-OD(\lambda)})] \qquad \text{(Eq. 6.5)}$$

where $I(\lambda)$ and $I_o(\lambda)$ are the corrected and experimental fluorescence intensities at each wavelength, and $OD(\lambda)$ is the optical density of the sample at the corresponding wavelength. The corrected fluorescence traces were then integrated from 965– 1,400 nm, and the raw integrals were corrected by subtracting the integral over an identical range from fluorescence traces of the blank solvent.

The integrated fluorescence intensities were then plotted against the baseline corrected absorbance values at the relevant wavelength, and the slope and error in slope were obtained (R^2 > 0.95 for all traces) (Figure 6.18B).

The refractive index for DCE was taken as 1.440[10], while that of the 35% DMSO/0.9% NaCl solution in water was approximated as a binary mixture of 35% DMSO in water and taken to be 1.383.[63] Both values were designated to have a precision to ± 0.001.

The average quantum yield value (over 885 nm, 900 nm, and 915 nm excitations) was calculated to be 0.012 ± 0.007. Errors were propagated from the error in IR-26 Φ_F (± 0.03)[61], slope of the integrated fluorescence intensity versus optical density plot (unique for each trace, but ranged from 7–10% of the slope value), and refractive indices (± 0.001).

For quantum yield measurements, fluorescence traces were acquired with ex. 885 nm, 900 nm, and 915 nm with a 950 nm shortpass filter (Thorlabs FESH0950) and collection from 950–1400 nm for IR-140 J-aggregate and 950–1,500 for IR-26. The slits were 5.76 mm for excitation and 11.52 mm for emission. The step size used was 1.0 nm, integration time 0.1 s, and traces were acquired after an automatic detector background subtraction, and with the default excitation correction. All absorbance and fluorescence traces were taken in a 10 mm x 2 mm path length cuvette. For absorbance traces, the 2 mm path length was used, while emission traces were acquired with 10 mm at the excitation side and 2 mm on the emission side, with emission detection occurring at 90° from excitation.

6.6.3 Photobleaching Rates

All photobleaching data were fit to a mono-exponential decay and the rate constants were obtained from the first order reaction equation:

$$\ln[A] = -kt + \ln[A]_o \qquad \text{(Eq. 6.6)}$$

where A and A_o represent the emission collected at time t and the initial emission collected, respectively. All R^2 values were > 0.96. Error bars represent the standard deviation of three measurements. If a change in slope occurred in the ln[A] values (*i.e.* in the IR-140 J-aggregate bleaching in 35% DMSO/0.9% NaCl in water solution), the rate was taken as the initial rate and the lines were fit only to the linear region (Figure 6.19). This analysis conservatively estimates the photobleaching rate of the solution phase aggregate as slower than it appeared in subsequent time points (see Figure 6.9B).

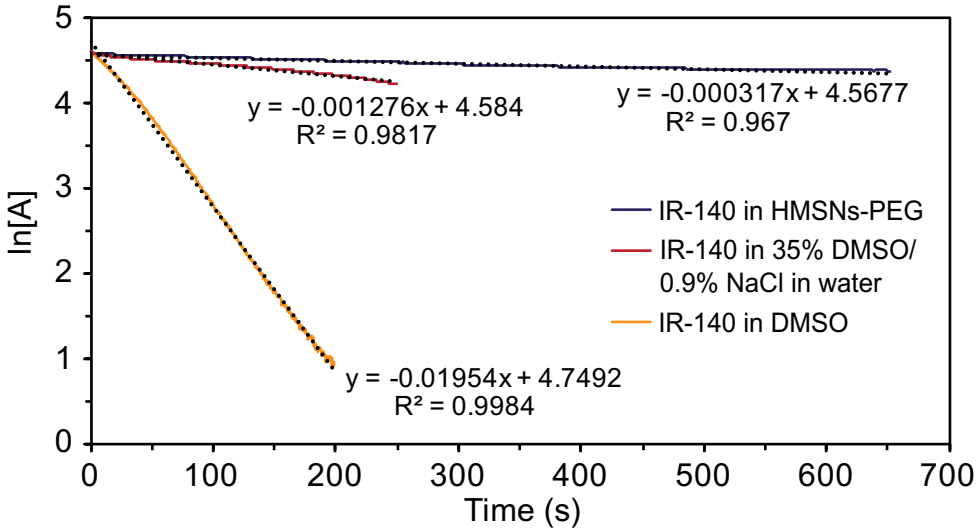

Figure 6.19 Photobleaching data plotted as the ln[A] vs time and the corresponding linear fits.

To compare photobleaching rates between samples irradiated at distinct wavelengths, it is necessary to consider the relative number of photons absorbed by each species. This requires corrections for (1) the difference in photon energy between the two wavelengths, and (2) the difference in photons absorbed by the two samples.

To account for photons of different energy, we go back to the common unit of number of photons per second per surface unit *Np,* ($cm^{-2}s^{-1}$). This value can be obtained by first calculating energy of a photon *Ep,* (J) at the wavelength of irradiation:

$$E_p = \frac{hc}{\lambda} \qquad \text{(Eq. 6.7)}$$

where *h* is Planck's constant, and *c* the speed of light. The *Np* can then be found from the irradiance *I* (Wcm^{-2}) and *Ep* by the following equation:

$$N_p = \frac{I}{E_p} \qquad \text{(Eq. 6.8)}$$

The *Np* for 980 nm and 785 nm light is 4.8×10^{17} and 3.8×10^{17} $cm^{-2}s^{-1}$, respectively.

To account for the difference in photons absorbed, we use the absorption coefficients at the wavelength of irradiation, λ_{ex}. For the IR-140 J-aggregate, the corrected absorption value was used. The absorption coefficient of IR-140 in HMSNs-PEG was taken to be that of the J-aggregate in solution. The relative values of $N_p \times \varepsilon$ can then be compared to obtain a ratio, *X* for each wavelength,

$$X_{785} = (N_{p,785} \times \varepsilon_m)/(N_{p,980} \times \varepsilon_j) \qquad \text{(Eq. 6.9)}$$

$$X_{980} = (N_{p,980} \times \varepsilon_j)/(N_{p,980} \times \varepsilon_j) \qquad \text{(Eq. 6.10)}$$

where ε_m and ε_j represent the aborbance coefficient of the monomer and J-aggregate, respectively, at their appropriate excitation wavelength, λ_{ex}. The ratio X_{785} was calculated to be 0.998, providing a correction factor for the relative number of photons absorbed per second in the 785 nm experiment compared to the 980 nm experiments, while the ratio X_{980} is 1.000. These values can be related to the relative rate, k_{rel} by the equation:

$$k_{rel} = \frac{k_{raw}}{X} \qquad \text{(Eq. 6.11)}$$

The relative rates with intermediate values used in the calculations are listed below in Table 6.3.

Table 6.3 Photobleaching rates and values used in calculations and corrections.

Sample	**λ_{ex} (nm)**	**Fluence ($mWcm^{-2}$)**	**k_{raw} (s^{-1}) x 10^3**	**ε at λ_i ($M^{-1}cm^{-1}$) x 10^{-5}**	**N_p**	**k_{rel} (s^{-1}) x 10^3**	**Relative stability**
6.1 monomer	785	97 ± 3	19.54 ± .04	1.18 ± 0.07	3.83 x10^{17}	19 ± 1	1
6.1 J-aggregate	980	97 ± 3	1.276 ± 0.008	0.95 ± 0.04	4.79 x 10^{17}	1.28 ± 0.05	15 ± 1
6.1 in HMSNs-PEG	980	97 ± 3	0.317 ± 0.002	0.95 ± 0.04	4.79 x 10^{17}	0.32 ± 0.01	62 ± 5

6.7 References and Notes

[1] Cosco, E. D.; Spearman, A. L.; Ramakrishnan, S.; Lingg, J. G. P.; Saccomano, M.; Pengshung, M.; Arús, B. A.; Wong, K. C. Y.; Glasl, S.; Ntziachristos, V.; et al. Shortwave Infrared Polymethine Fluorophores Matched to Excitation Lasers Enable Non-Invasive, Multicolour in Vivo Imaging in Real Time. *Nat. Chem.* **2020**, *12*, 1123–1130.

[2] Sun, C.; Li, B.; Zhao, M.; Wang, S.; Lei, Z.; Lu, L.; Zhang, H.; Feng, L.; Dou, C.; Yin, D.; et al. J -Aggregates of Cyanine Dye for NIR-II in Vivo Dynamic Vascular Imaging beyond 1500 nm. *J. Am. Chem. Soc.* **2019**, *141*, 19221–19225.

[3] Carr, J. A.; Aellen, M.; Franke, D.; So, P. T. C.; Bruns, O. T.; Bawendi, M. G. Absorption by Water Increases Fluorescence Image Contrast of Biological Tissue in the Shortwave Infrared. *Proc. Natl. Acad. Sci.* **2018**, *115*, 9080–9085.

[4] Hong, G.; Diao, S.; Chang, J.; Antaris, A. L.; Chen, C.; Zhang, B.; Zhao, S.; Atochin, D. N.; Huang, P. L.; Andreasson, K. I.; et al. Through-Skull Fluorescence Imaging of the Brain in a New near-Infrared Window. *Nat. Photonics* **2014**, *8*, 723–730.

[5] Diao, S.; Blackburn, J. L.; Hong, G.; Antaris, A. L.; Chang, J.; Wu, J. Z.; Zhang, B.; Cheng, K.; Kuo, C. J.; Dai, H. Fluorescence Imaging In Vivo at Wavelengths beyond 1500 nm. *Angew. Chemie Int. Ed.* **2015**, *54*, 14758–14762.

[6] Pengshung, M.; Li, J.; Mukadum, F.; Lopez, S. A.; Sletten, E. M. Photophysical Tuning of Shortwave Infrared Flavylium Heptamethine Dyes via Substituent Placement. *Org. Lett.* **2020**, *22*, 6150–6154.

[7] Cosco, E. D.; D. Arús, B. A.; Spearman, A. L.; Atallah, T. L.; Leland, O. S.; Caram, J. R.; Bischof, T. S.; Bruns, O. T.; Sletten. E. M. *Manuscript submitted.*

[8] A) Ding, B.; Xiao, Y.; Zhou, H.; Zhang, X.; Qu, C.; Xu, F.; Deng, Z.; Cheng, Z.; Hong, X. Polymethine Thiopyrylium Fluorophores with Absorption beyond 1000 Nm for Biological Imaging in the Second Near-Infrared Subwindow. *J. Med. Chem.* **2019**, *62*, 2049–2059. B) Wang, S.; Fan, Y.; Li, D.; Sun, C.; Lei, Z.; Lu, L.; Wang, T.; Zhang, F. Anti-Quenching NIR-II Molecular Fluorophores for in Vivo High-Contrast Imaging and PH Sensing. *Nat. Commun.* **2019**, *10*, 1058.

[9] Pengshung, M.; Neal, P.; Atallah, T. L.; Kwon, J.; Caram, J. R.; Lopez, S. A.; Sletten, E. M. Silicon Incorporation in Polymethine Dyes. *Chem. Commun.* **2020**, *56*, 6110–6113.

[10] Englman, R.; Jortner, J. The energy gap law for radiationless transitions in large molecules. *Mol. Phys.* **1970**, *18*, 145–164.

[11] Tolbert, L. M.; Zhao, X. Beyond the Cyanine Limit: Peierls Distortion and Symmetry Collapse in a Polymethine Dye. *J. Am. Chem. Soc.* **1997**, *119*, 3253–3258.

[12] Wuerthner, F.; Kaiser, T. E.; Saha-Moeller, C. R. J- aggregates: From serendipitous discovery to supramolecular engineering of functional dye materials. *Angew. Chem., Int. Ed.* **2011**, *50*, 3376−3410.

[13] J-aggregates; Kobayashi, T., Ed.; World Scientific: Singapore, 1996.

[14] Jelley, E. E. Spectral absorption and fluorescence of dyes in the molecular state. *Nature* **1936**, *138*, 1009−1010.

[15] Scheibe, G. Uber die veranderlichkeit der absorptionsspektren in losungen und die nebenvalenzen als ihre ursache. *Angew. Chem.* **1937**, *50*, 212−219.

[16] Hestand, N. J.; Spano, F. C. Molecular aggregate photophysics beyond the Kasah Model: Novel design principles for organic materials. *Acc. Chem. Res.* **2017**, *50*, 341−350.

[17] Thimsen, E.; Sadtler, B.; Berezin, M. Y. Shortwave-Infrared (SWIR) Emitters for Biological Imaging : A Review of Challenges and Opportunities. *Nanophotonics* **2017**, *6*, 1043–1054.

[18] Bashkatov, A. N.; Genina, E. A.; Kochubey, V. I.; Tuchin, V. V. Optical properties of human skin, subcutaneous and mucous tissues in the wavelength range from 400 to 2000 nm. *J. Phys. D: Appl. Phys.* **2005**, *38*, 2543−2555.

[19] Lim, Y. T.; Kim, S.; Nakayama, A.; Stott, N. E.; Bawendi, M. G.; Frangioni, J. V. Selection of quantum dot wavelengths for biomedical assays and imaging. *Mol. Imaging* **2003**, 2,50−64.

[20] Won, N.; Jeong, S.; Kim, K.; Kwag, J.; Park, J.; Kim, S. G.; Kim, S. Imaging depths of near-infrared quantum dots in first and second optical windows. *Mol. Imaging* **2012**, 11, 338−352.

[21] Shortly after the publication of this work, Sun *et al*. published the J-aggregation of a SWIR light absorbing dye for imaging (Ref. 2).

[22] Deshmukh, A. P.; Koppel, D.; Chuang, C.; Cadena, D. M.; Cao, J.; Caram, J. R. Design Principles for Two-Dimensional Molecular Aggregates Using Kasha's Model: Tunable Photophysics in Near and Short-Wave Infrared. *J. Phys. Chem. C* **2019**, *123*, 18702–18710.

[23] Deshmukh, A. P.; Bailey, A. D.; Forte, L. S.; Shen, X.; Geue, N.; Sletten, E. M.; Caram, J. R. Thermodynamic Control over Molecular Aggregate Assembly Enables Tunable Excitonic Properties across the Visible and Near-Infrared. *J. Phys. Chem. Lett.* **2020**, *11*, 8026–8033.

[24] Bricker, W. P.; Banal, J. L.; Stone, M. B.; Bathe, M. Molecular Model of J-Aggregated Pseudoisocyanine Fibers. *J. Chem. Phys.* **2018**, *149*, 024905.

[25] Wang, C.; Weiss, E. A. Sub-nanosecond resonance energy transfer in the near-infrared within self-assembled conjugates of PbS quantum dots and cyanine dye J-aggregates. *J. Am. Chem. Soc.* **2016**, *138*, 9557−9564.

[26] Soppera, O.; Turck, C.; Lougnot, D. J. Fabrication of microoptical devices by self-guiding photopolymerization in the near IR. *Opt. Lett.* **2009**, *34*, 461−463.

[27] Bonardi, A. H.; Dumur, F.; Grant, T. M.; Noirbent, G.; Gigmes, D.; Lessard, B. H.; Fouassier, J.-P.; Lalevee, J. Higher performance near-infrared (NIR) photoinitiating systems operating under low light intensity and in the presence of oxygen. *Macromolecules* **2018**, *51*, 1314−1324.

[28] Leung, K. C. F.; Nguyen, T. D.; Stoddart, J. F.; Zink, J. I. Supramolecular nanovalves controlled by proton abstraction and competitive binding. *Chem. Mater.* **2006**, *18*, 5919−5928.

[29] Zhou, W.; Dridi, M.; Suh, J. Y.; Kim, C. H.; Co, D. T.; Wasielewski, M. R.; Schatz, G. C.; Odom, T. W. Lasing action in strongly coupled plasmonic nanocavity arrays. *Nat. Nanotechnol.* **2013**, *8*, 506−511.

[30] Yang, A.; Hoang, T. B.; Dridi, M.; Deeb, C.; Mikkelsen, M. H.; Schatz, G. C.; Odom, T. W. Real-time tunable lasing from plasmonic nanocavity arrays. *Nat. Commun.* **2015**, *6*, 6939.

[31] Oseledchyk, A.; Andreou, C.; Wall, M. A.; Kircher, M. F. Folate-targeted surface-enhanced resonance Raman scattering nanop- robe ratiometry for detection of microscopic ovarian cancer. *ACS Nano* **2017**, *11*, 1488−1497.

[32] Berezin, M. Y.; Zhan, C.; Lee, H.; Joo, C.; Akers, W. J.; Yazdanfar, S.; Achilefu, S. Two-photon optical properties of near- infrared dyes at 1.55 μm excitation. *J. Phys. Chem. B* **2011**, *115*, 11530−11535.

[33] Bricks, J. L.; Slominskii, Y. L.; Panas, I. D.; Demchenko, A. P. Fluorescent J-aggregates of cyanine dyes: basic research and applications review. *Methods Appl. Fluoresc.* **2018**, *6*, 012001.

[34] Shakiba, M.; Ng, K. K.; Huynh, E.; Chan, H.; Charron, D. M.; Chen, J.; Muhanna, N.; Foster, F. S.; Wilson, B. C.; Zheng, G. Stable J-aggregation enabled dual photoacoustic and fluorescence nano- particles for intraoperative cancer imaging. *Nanoscale* **2016**, *8*, 12618−12625.

[35] Yang, C.; Wang, X.; Wang, M.; Xu, K.; Xu, C. Robust colloidal nanoparticles of pyrrolopyrrole cyanine J-aggregates with bring near- infrared fluorescence in aqueous

media: From spectral tailoring to bioimaging applications. *Chem. - Eur. J.* **2017**, *23*, 4310−4319.

[36] Sun, P.; Wu, Q.; Sun, X.; Miao, H.; Deng, W.; Zhang, W.; Fan, Q.; Huang, W. J-aggregate squaraine nanoparticles with bright NIR-II fluorescence for imaging guided photothermal therapy. *Chem. Commun.* **2018**, *54*, 13395−13398.

[37] Two other J-aggregates have been employed in vivo for photothermal therapy and photoacoustic imaging. (a) Song, X.; Gong, H.; Liu, T.; Cheng, L.; Wang, C.; Sun, X.; Liang, C.; Liu, Z. J- aggregates of organic dye molecules complexed with iron oxide nanoparticles for imaging-guided photothermal therapy under 915 nm light. *Small* **2014**, *10*, 4362−4370. (b) Dumani, D. S.; Brecht, H.-P.; Ivanov, V.; Deschner, R.; Harris, J. T.; Homan, K. A.; Cook, J. R.; Emelianov, S. Y.; Ermilov, S. A. Co-registered photoacoustic and fluorescent imaging of a switchable nanoprobe based on J-aggregates of indocyanine green." *Proc. SPIE 10494, Photons Plus Ultrasound: Imaging and Sensing* **2018**.

[38] Kim, S.; Shi, Y.; Kim, J. Y.; Park, K.; Cheng, J. X. Overcoming the barriers in micellar drug delivery: Loading efficiency, in vivo stability, and micelle-cell interaction. *Expert Opin. Drug Delivery* **2010**, *7*, 49−62.

[39] Chen, F.; Hong, H.; Shi, S.; Goel, S.; Valdovinos, H. F.; Hernandez, R.; Theuer, C. P.; Barnhart, T. E.; Cai, W. Engineering of hollow mesoporous silica nanoparticles for remarkably enhanced tumor active targeting efficacy. *Sci. Rep.* **2014**, *4*, 5080.

[40] Guardado- Alvarez, T. M.; Chen, W.; Norton, A. E.; Russell, M. M.; Connick, W. B.; Zink, J. I. Analyte-responsive gated hollow mesoporous silica nanoparticles exhibiting inverse functionality and an AND logic response. *Nanoscale 2016*, *8*, 18296−18300

[41] He, Q.; Zhang, Z.; Gao, F.; Li, Y.; Shi, J. In vivo biodistribution and urinary excretion of mesoporous silica nano- particles: Effects of particle size and PEGylation. *Small* **2011**, *7*, 271−280.

[42] Liu, J.; Luo, Z.; Zhang, J.; Luo, T.; Zhou, J.; Zhao, X.; Cai, K. Hollow mesoporous silica nanoparticles facilitated drug delivery via cascade pH stimuli in tumor microenvironment for tumor therapy. *Biomaterials* **2016**, *83*,51−65.

[43] Singh, R. K.; Kim, T. H.; Mahapatra, C.; Patel, K. D.; Kim, H. W. Preparation of self-activated fluorescence mesoporous silica hollow nanoellipsoids for theranostics. *Langmuir* **2015**, *31*, 11344−11352.

[44] Yang, S.; Chen, D.; Li, N.; Xu, Q.; Li, H.; Gu, F.; Xie, J.; Lu, J. Hollow mesoporous silica nanocarriers with multifunctional capping agents for in vivo cancer imaging and therapy. *Small* **2016**, *12*, 360−370.

[45] Huang, C. C.; Huang, W.; Yeh, C. S. Shell-by-shell synthesis of multi-shelled mesoporous silica nanospheres for optical imaging and drug delivery. *Biomaterials* **2011**, *32*, 556−564.

[46] Fan, Z.; Li, D.; Yu, X.; Zhang, Y.; Cai, Y.; Jin, J.; Yu, J. AIE luminogen- functionalized hollow mesoporous silica nanospheres for drug delivery and cell imaging. *Chem. - Eur. J.* **2016**, *22*, 3681−3685.

[47] Hong, S.; Kim, H.; Choi, Y. Indocyanine green-loaded hollow mesoporous silica nanoparticles as an activatable theranostic agent. *Nanotechnology* **2017**, *28*, 185102.

[48] Chen, W.; Tsai, P. H.; Hung, Y.; Chiou, S. H.; Mou, C. Y. Nonviral cell labeling and differentiation agent for induced pluripotent stem cells based on mesoporous silica nanoparticles. *ACS Nano* **2013**, *7*, 8423−8440.

[49] Zhang, Y.; Ang, C.Y.; Li, M.; Tan, S.Y.; Qu, Q.; Luo, Z.; Zhao, Y. *ACS Appl. Mater. Interfaces* **2015**, *7*, 18179–18187.

[50] Chen, W.; Cheng, C.A.; Zink, J.I. "Spatial, Temporal, and Dose Control of Drug Delivery using Noninvasive Magnetic Stimulation." *ACS Nano* **2019**, 13, 1292–1308.

[51] Rurack, K.; Spieles, M. Fluorescence quantum yields of a series of red and near-infrared dyes emitting at 600−1000 nm. *Anal. Chem.* **2011**, *83*, 1232−1242.

[52] Hatami, S.; Würth, C.; Kaiser, M.; Leubner, S.; Gabriel, S.; Bahrig, L.; Lesnyak, V.; Pauli, J.; Gaponik, N.; Eychmüller, A.; Resch-Genger, U. Absolute photoluminescence quantum yields of IR-26 and IR-emissive Cd1-xHgxTe and PbS quantum dots- method and material-inherent challenges. *Nanoscale* **2015**, *7*, 133−143.

[53] A sulfonated variant of the IR-140 chromophore has been characterized to J-aggregate in solution. See: (a) Berlephsch, H. V.; Bottcher, C. Cryo-transmission electron microscopy reveals meso- scopic H- and J-aggregates of near infrared cyanine dyes. *J. Photochem. Photobiol., A.* **2010**, *214*,16−21. (b) Ref. [22].

[54] NIR fluorophores have emission that extends into the SWIR. (a) Carr, J. A.; Franke, D.; Caram, J. R.; Perkinson, C. F.; Saif, M.; Askoxylakis, V.; Datta, M.; Fukumura, D.; Jain, R. K.; Bawendi, M. G.; Bruns, O. T. Shortwave infrared fluorescence imaging with the clinically-approved near-infrared dye indocyanine green. *Proc. Natl. Acad. Sci. U. S. A.* **2018**, *115*, 4465−4470. (b) Starosolski, Z.; Bhavane, R.; Ghaghada, K. B.; Vasudevan, S. A.; Kaay, A.; Annapragada, A. Indocyanine green fluorescence in second near- infrared (NIR-II) window. *PLoS One* **2017**, *12*, e0187563. (c) Zhu, S.; Hu, Z.; Tian, R.; Yung, B. C.; Yang, Q.; Zhao, S.; Kiesewetter, D. O.; Niu, G.; Sun, H.; Antaris, A. L.; Chen, X. Repurposing cyanine NIR-I dyes accelerates clinical translation of near-infrared-II (NIR-II) bioimaging. *Adv. Mater.* **2018**, *30*, 1802546.

[55] Qiao, Y.; Polzer, F.; Kirmse, H.; Kirstein, S.; Rabe, J. P. Nanohybrids from Nanotubular J-Aggregates and Transparent Silica Nanoshells. *Chem. Commun.* **2015**, *51*, 11980–11982.

[56] Chen, W.; Glackin, C. A.; Horwitz, M. A.; Zink, J. I. Nanomachines and other caps on mesoporous silica nanoparticles for drug delivery. *Acc. Chem. Res*. **2019**, *52*, 1531−1542.

[57] Zhao, N.; Yan, L.; Zhao, X.; Chen, X.; Li, A.; Zheng, D.; Zhou, X.; Dai, X.; Xu, F. J. Versatile types of organic/ inorganic nanohybrids: From strategic design to biomedical applications. *Chem. Rev.* **2019**, *119*, 1666−1762.

[58] Brixner, T.; Hildner, R.; Kohler, J.; Lambert, C.; Wurthner, F. Exciton transport in molecular aggregates− From natural antennas to synthetic chromophore systems. *Adv. Energy Mater.* **2017**, *7*, 1700236.

[59] Doria, S.; Sinclair, T. S.; Klein, N. F.; Bennett, D. I. G.; Chuang, C.; Freyria, F. S.; Steiner, C. P.; Foggi, P.; Nelson, K. A.; Cao, J.; Aspuru-Guzik, A.; Lloyd, S.; Caram, J. R.; Bawendi, M. G. Photochemical control of exciton superradiance in light-harvesting nanotubes. *ACS Nano* **2018**, *12*, 4556−4564.

[60] Kasha, M.; Rawls, H. R.; El-Bayoumi, M. A. The exciton model in molecular spectroscopy. *Pure Appl. Chem.* **1965**, *11*, 371−392.

[61] Cosco, E. D.; Caram, J. R.; Bruns, O. T.; Franke, D.; Day, R. A.; Farr, E. P.; Bawendi, M. G.; Sletten, E. M. Flavylium polymethine fluorophores for near- and shortwave infrared imaging. *Angew. Chem., Int. Ed.* **2017**, *56*, 13126−13129.

[62] Semonin, O. E.; Johnson, J. C.; Luther, J. M.; Midgett, A. G.; Nozik, A. J.; Beard, M. C. *J. Phys. Chem. Lett.* **2010**, *1*, 2445–2450.

[63] LeBel, R. G.; Goring, D. A. I. *J. Chem. Eng. Data* **1962**, *7*, 100–101.

CHAPTER SEVEN

Photophysical Properties of Indocyanine Green in the Shortwave Infrared Region

Work in this chapter is incorporated into a manuscript in preparation for publication with authors Emily D. Cosco, Irene Lim and Ellen M. Sletten*

7.1 Abstract

With the growing development of new contrast agents for optical imaging using near-infrared and shortwave infrared (SWIR) wavelengths, it is essential to have consistent benchmarks for emitters in these regions. Indocyanine green (ICG), a ubiquitous and FDA approved organic dye and optical imaging agent, is commonly employed as a standard for photophysical properties and biological performance for imaging experiments. Yet, its reported photophysical properties across organic and aqueous solvents vary greatly in the literature, which hinders its ability to be used as a consistent benchmark. Here, we measure photophysical properties in organic and aqueous solvents using InGaAs detection (~950–1700 nm), providing particular relevance for SWIR measurements and imaging.

7.2 Introduction

Indocyanine green (ICG) is a near-infrared (NIR, 700–1,000 nm) polymethine dye widely used as a contrast agent for optical imaging.[1] ICG has been FDA approved for ~60 years and is used pre-clinically and clinically in NIR optical imaging applications, including for angiography[2], lymphatic[3–6], biliary[7–8] and intestinal[9] functional imaging, dental

imaging,[10] and oncological image guided surgery.[11–13] Additionally, there is increasing interest in the use of fluorescence intraoperatively.[14–17] In 2018, it was reported that ICG has a long wavelength emission tail which extends past the NIR region.[18–19] This property has provided further attention to its use as an imaging agent in the shortwave infrared (SWIR, 1,000–2000 nm) region. Optical detection in the SWIR region of the electromagnetic spectrum offers increased contrast, resolution, and penetrative properties, compared to detection in the visible (VIS, 350–700 nm) and NIR regions. ICG has proven to be a successful SWIR contrast agent upon 785 or 808 nm excitation in single channel experiments for vasculature[20–21] and dental[22] imaging, and alongside dyes with more red-shifted absorption properties in multichannel experiments.[23–24] Notably, the SWIR emission of ICG was recently exploited in multispectral image-guided surgery in humans.[25]

Due to ICG's advantageous photophysical properties in biological media, such as blood and serum, high aqueous solubility, commercial accessibility, validated biological safety and fast hepatic clearance, ICG is both a promising contrast agent for the translation of SWIR imaging applications to clinical needs, and a natural benchmark for the development of improved and complementary optical tools for the SWIR. Indeed, ICG is commonly employed as a comparison for emitters and imaging applications in both the NIR[26] and the SWIR[24, 27–35]. However, the reported photophysical properties of ICG vary greatly in the literature, resulting in variable and inconsistent comparisons. Further, most previous photophysical measurements were performed on silicon detectors, which lose sensitivity at the NIR and SWIR wavelengths (~850–1,100 nm) relevant to the emissive properties of ICG.[36] Photophysical measurements in the literature are provided for reference and comparison in Section 7.7.1 (Table 7.3), where it is evident that many reported values for ICG are in contradiction. There are also few systematic photophysical studies

in which both absorptive properties and emissive properties are measured and compared in multiple solvents and biologically relevant media.[37–39]

Here, we measure absorptive and emissive photophysical properties, including absorption and emission spectra, absorption coefficients (ε), fluorescence quantum yields (Φ_F), and photostability for ICG in parallel across five media to enable consistent comparison. These data include measurements in the biological media fetal bovine serum (FBS) and whole blood, and use InGaAs detection for emissive properties, ensuring collection of the full emission spectra of ICG. We evaluate brightness values relevant to SWIR imaging experiments and corroborate the photophysical measurements using SWIR imaging. We aim for these data to be useful in understanding the photophysical behavior of ICG in changing environments and for the establishment of ICG as a comparative benchmark for diverse NIR and SWIR emitters and imaging applications, alike.

7.3 Results and Discussion

The solvents in which we chose to evaluate ICG photophysical properties are ethanol (EtOH), for an organic solvent reference, and the aqueous media: water, FBS, and whole blood (sourced as sheep's blood due to available quantity and safety). Additionally, we evaluated the photophysical properties of ICG when encapsulated in phospholipid-poly(ethylene)glycol micelles, a common delivery vehicle used for *in vivo* experiments. We chose to omit phosphate buffered saline (PBS), or other solutions with high ionic strengths, such as isotonic saline, as we and others[19] found that these solvents only minimally solubilize ICG as a monomer species. The purity of the ICG sample we used for measurements was verified using ^{1}H NMR (Section 7.8: Figures 7.6–7.7). The maximal absorption wavelengths ($\lambda_{max,abs}$), maximal emission wavelengths

($\lambda_{max,em}$), ε, Φ_F and brightness values calculated from these experimental measurements are listed in Table 7.1. Absorption and emission traces obtained in each of these solvents are displayed in Figure 7.1.

Table 7.1 Photophysics of ICG in various media.

Solvent	$\lambda_{max,abs}$ (nm)	ε ($M^{-1}cm^{-1}$)	$\lambda_{max,em}$ (nm)	Φ_F (%)	Brightness[f] × 10^4 ($M^{-1}cm^{-1}$)	SWIR emission, α[g] (%)	SWIR Brightness[h] × 10^4 ($M^{-1}cm^{-1}$)
EtOH	787	223,000 ± 6,000	815	14 ± 1	310 ± 20	1.44	4.5 ± 0.3
Water	779	156,000 ± 6,000	805	2.9 ± 0.2	45 ± 4	0.71	0.32 ± 0.03
FBS[a]	798	162,000 ± 3,000	811	12.0 ± 0.9	190 ± 20	1.43	2.8 ± 0.2
Micelles[b]	796	180,000 ± 8,000[d]	821	5.1 ± 0.3	92 ± 7	0.99	0.91 ± 0.07
Whole blood[c]	788	n.r.[e]	815	13 ± 1	n.r.	5.15	n.r.

[a] FBS = Fetal bovine serum. [b] 18:0 PEG2000 PE micelles dispersed in water. [c] defibrillated sheep blood. [d] an apparent absorption coefficient is used, as described in the experimental procedures. [e] high scattering prevented absorption coefficient measurements in this medium. [f] Brightness = ε × Φ_F.[g] SWIR emission (α); α= emission between 1,000–1,350 nm / total emission × 100. [h] SWIR Brightness = brightness × (α/100).

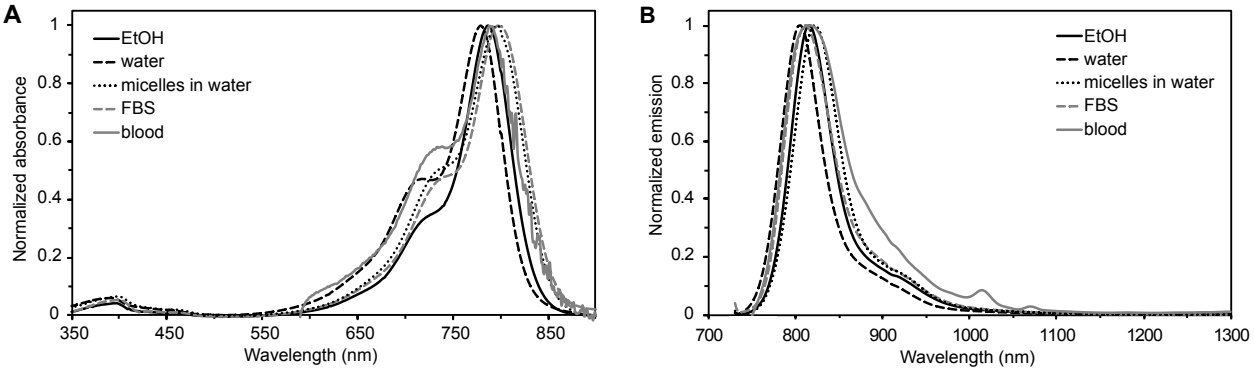

Figure 7.1 Absorption (A) and emission (B) (excitation: 710 nm) of ICG in various media. See Figure 7.2 for correction of the emission trace in blood.

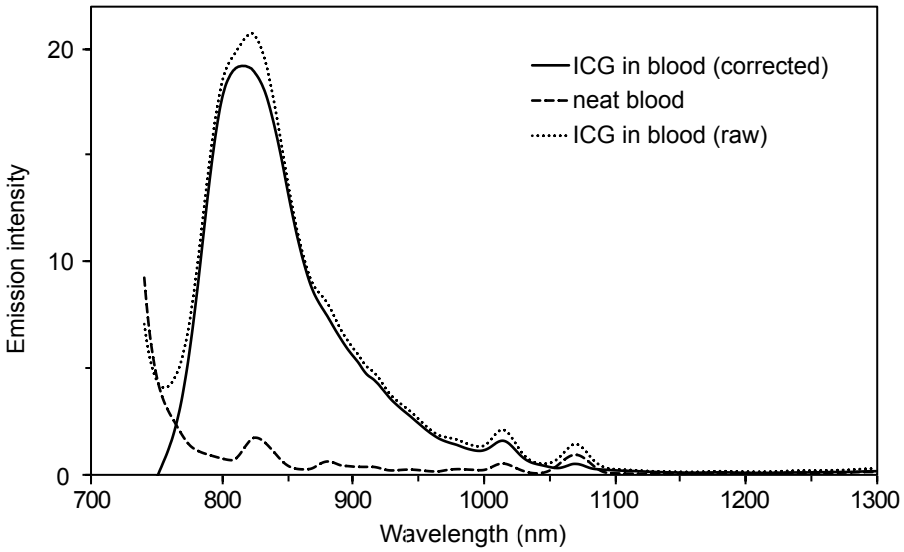

Figure 7.2 Correction for emission trace of ICG in blood (excitation wavelength = 710 nm).

Minor red shifts (9–19 nm) of the absorption peak are observed in FBS, micelles, and whole blood compared to water, similar to observations in prior studies. We find that the absorption coefficients are all larger than 10^5 $M^{-1}cm^{-1}$, with water at the lowest value at $\varepsilon = 1.56 \times 10^5$ $M^{-1}cm^{-1}$ (Figure 7.3). Similar ε values are observed in FBS and micelles in water, while ~1.4-fold improvement is observed in EtOH, with $\varepsilon = 2.23 \times 10^5$ $M^{-1}cm^{-1}$. Fluorescence quantum yield measurements also show the lowest values in water, with $\Phi_F = 2.9\%$. Micelles in water show minor improvements with $\Phi_F = 5.1\%$. In contrast, Φ_F in EtOH, FBS, and whole blood are all similar and considerably higher, between 12–14%. When combining the absorptive and emissive properties together, brightness values (brightness = $\varepsilon \times \Phi_F$) in water are the lowest at 4.5×10^5 $M^{-1}cm^{-1}$. The brightness compared to water is ~2-fold higher in micelles at 9.2×10^5 $M^{-1}cm^{-1}$, ~4-fold improved in FBS at 1.90×10^6 $M^{-1}cm^{-1}$, and ~79-fold higher in EtOH at 3.10×10^6 $M^{-1}cm^{-1}$. The total brightness in blood could not be evaluated photophysically due to high scattering coefficients preventing accurate absorption coefficient measurements. The SWIR brightness values (SWIR brightness = brightness × (α/100); = emission between 1,000–1,350 nm / total emission × 100)

followed a similar qualitative trend, yet benefit the micelles, FBS and EtOH by larger factors (~3–, ~9–, and ~14–fold, respectively), as these solvents have a larger fraction of total emission in the SWIR region compared to water. The emission ratio was calculated using the emission between 1,000–1,350 nm to approximate the SWIR region while avoiding interference from the doubling of the excitation wavelength at ~1,420 nm. This was deemed a good approximation as fluorescence beyond 1,350 nm was minimal in comparison to that of the shorter SWIR wavelengths.[18]

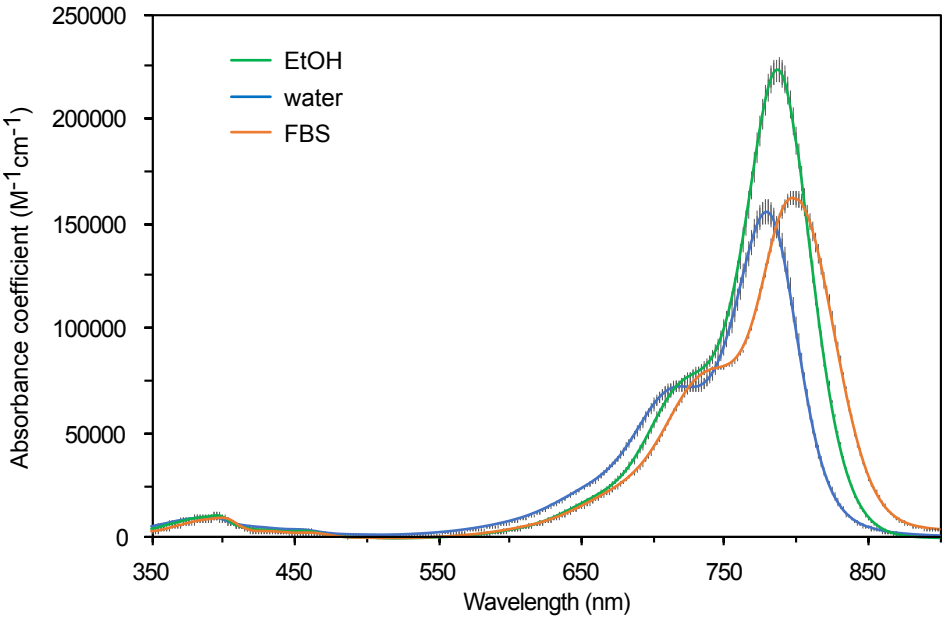

Figure 7.3 Absorption coefficient traces in ethanol (green), water (blue), and fetal bovine serum (FBS, orange).

Our measurements tend to agree with more recent literature values (see Section 7.7.1). In EtOH, the Φ_F value we measured (14%) corroborates the study by Rurack and Spieles[40], while the ε we measured is slightly higher than the reported value. As sources for error in ε tend to underestimate the true value, this difference could be reasonably explained by differences in purity due to the batches or sources of ICG. In water, the Φ_F we measured (2.9%) agrees with two

previous studies by Philip *et al.*[41] and Jin *et al.*[42], and is only slightly less than Hoshi *et al*.[43] The ε in water we measured was similar to the value reported by Carr *et al.*[18] The increased brightness of ICG in protein-containing media such as albumin solutions, serum, and blood is well-documented in many prior studies, due to binding with proteins present in these media. The photophysical values we measured in FBS were in good agreement with the study by Obnisbi *et. al.*[39] which reported a very similar ε and a slightly lower Φ_F value (9%) (error designation was not specified). Looking at measurements in similar media, Pauli *et al*.[44] found a slightly lower Φ_F value (8%) in bovine serum albumin (BSA). All previous Φ_F measurements in plasma[37–38] and human serum albumin (HSA)[41]**Error! Bookmark not defined.** were significantly lower, but two of these studies[37–38] used relative methods to DMSO at 13%[45] (more recent studies have characterized the Φ_F of ICG in DMSO by the absolute method to be between 22–26%.[43, 46]) Taken together, our photophysical measurements align with the recent values measured in different solvents in several studies. Moreover, the measurements presented in this article are obtained by the same methods, providing systematic photophysical measurements of ICG that are calibrated to each other. In addition, our values take into account the 1–5% of the emission which is in the SWIR, something few previous studies have done.[18]

For *in vivo* imaging applications, the photophysical measurements in blood or encapsulated in a delivery vehicle are the most relevant. These experiments can be challenging due to the high opacity, scattering, and absorption in blood, as well as variation in blood source and quality, which are potential causes for disparity between measurements. The sole literature report value for Φ_F of ICG in whole blood was reported in 1978 to be ~1.2%.[47] This is ~10-fold lower than the value we measured (13%), however the reference value for the relative measurement is unclear. Nonetheless, in the same study, the Φ_F value reported in water was also ~10-fold lower than the

value we measured here, indicating that the relative improvement between water and blood agrees with the values we obtained. The value we measured in blood is close to the Φ_F in FBS, and is much higher than that measured in water, indicating that the emissive behavior in FBS likely approximates that of blood. Finally, the modest increase in quantum yield and brightness for ICG in micelles (~2–3 fold) compared to pure water is in line with previous findings in which ICG brightness increased upon encapsulation in a variety of structurally different micelles.[42, 48–50]

Photostability is a key characteristic for imaging agents, and becomes particularly relevant when imaging is performed over a long temporal period or high-powered light irradiation is employed. Thus, photostability is a commonly compared property used to evaluate performance between chromophores. We examined the photostability of ICG in the selected solvents by irradiating samples of equal concentrations (5 mM) in capillary tubes with 785 nm excitation (119 mW cm^{-2}) and collecting the emission intensity over time (Table 7.2, Figures 7.4–7.5). ICG displayed the lowest photostability in water and the highest photostability in EtOH (improved by ~16-fold compared to water). Surprisingly, encapsulation in the PEG-lipid micelles did not offer an improvement in photostability compared to neat water. This observation is in contrast to findings by others, in which nanoparticle encapsulation, for example in poly(lactic-*co*-glycolic acid) polymer nanoparticles,[51] lipid-coated superparamagnetic iron oxide nanoparticles,[52] mesoporous silica nanoparticles[53], and calcium phosphate nanoparticles,[54] have increased photostability compared to free ICG. The larger size and in some cases hard composition of these nanoparticles may offer more shielding from the aqueous environment than the micelles observed here. In contrast, dissolution in whole blood and FBS improved the photostability of ICG compared to that in water by ~2-fold and ~4-fold, respectively. The high photostability of ICG in organic solvent compared to water is in agreement with previous observations,[55] although in the

same study, human plasma was found to result in even higher photostability than the organic solvents methanol and DMSO. These results support that photostability measurements of ICG in water will likely show faster photobleaching than would occur *in vivo*.

Table 7.2. Photobleaching rates of ICG in various media[1]

Solvent	Photobleaching rate $k_{raw} \times 10^3$ (s^{-1})	Relative photostability
EtOH	0.98 ± 0.09	16 ± 1
Water	15.5 ± 0.2	1
FBS[a]	3.85 ± 0.05	4.03 ± 0.06
Micelles[b]	14.2 ± 0.4	1.09 ± 0.03
Whole blood[c]	8.4 ± 0.3	1.84 ± 0.06

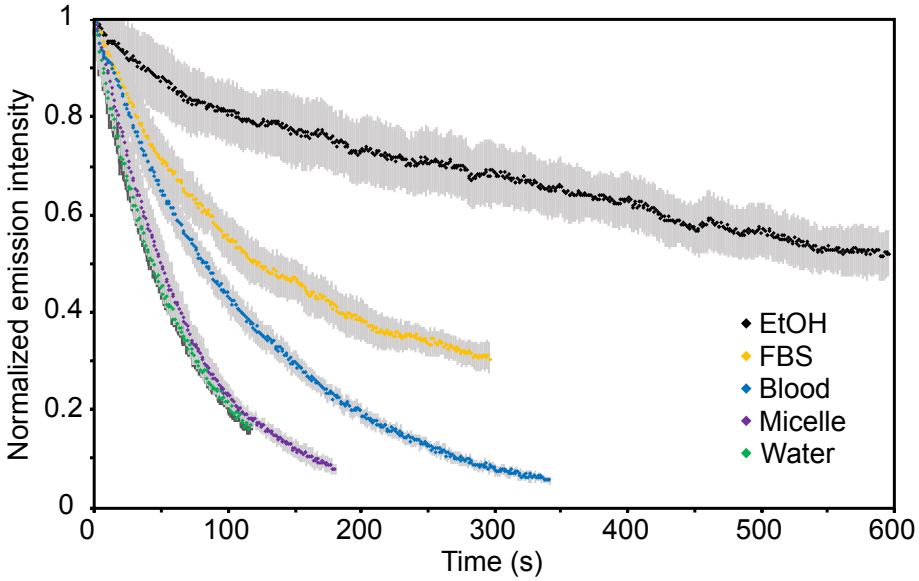

Figure 7.4 Photostability of ICG in different solvents. Samples were irradiated with 785 nm (119 mW cm^{-2}) light and their emission (LP 1,100 nm) was measured on a SWIR detector. Intensity is graphed as the percent initial emission. Error is displayed as the standard deviation of the triplicate measurement.

[1] Photostability and brightness experiments with Irene Lim

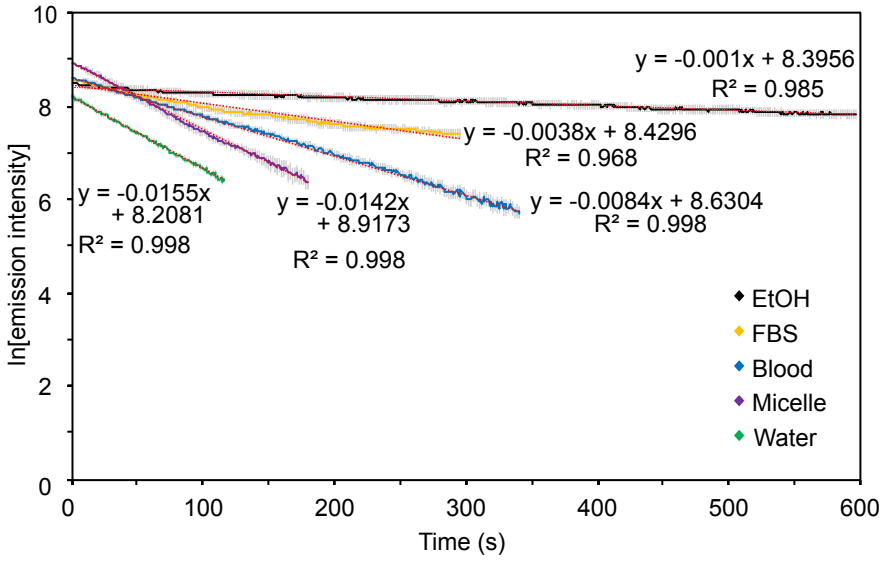

Figure 7.5 Photobleaching data plotted as the ln[emission intensity] vs. time and the corresponding linear fits.

Finally, we observed the SWIR emission of ICG in a SWIR imaging configuration and compared the brightness between the selected solvents. ICG was placed in capillary tubes at equal concentrations (5 mM) in the relevant solvents (Figure 7.6A), irradiated with 785 nm light (63 mW cm^{-2}) and the emission was observed with an InGaAs detector. Due to the small variation in laser irradiation over the area where tubes were imaged, we first measured the signal obtained from imaging with each tube positioned at all five locations in the capillary holder (Figure 7.7). From these images, we calculated the standard deviation between positions for each solvent, and applied these error values to the subsequent measurements. Next, we measured brightness values of the capillary tubes using 1,000 nm, 1,100 nm, and 1,300 nm longpass filtering (Figure 7.6B–D). Compared to water, the emission intensity in micelles, FBS, blood, and EtOH was higher by ~3-fold, ~10-fold, ~13-fold, and ~16-fold, respectively, using 1,000 nm longpass filtering. These ratios are similar to those obtained looking at the calculated SWIR brightness numbers in Table 7.1 for micelles, FBS, and EtOH. In blood, we observe slightly higher SWIR emission compared to FBS. This observation aligns well with the similar quantum yield measurements in blood and

FBS (Table 7.1). Additionally, although we were unable to obtain a calculated SWIR brightness number for ICG in blood (due to high scattering in absorption measurements), the comparative brightness measurement allows us to infer that the absorption coefficient value of ICG in blood must be similar, or slightly higher than that of FBS. Further, it allows us to arrive at an estimated value for SWIR brightness, ~4 x 10^4 using the relative performance of ICG in blood compared to water. Moving to longer wavelengths of detection, the overall emission intensity decreases drastically (Figure 7.6E). The SWIR emission from ICG decreases by ~5 fold using detection with 1,100 nm longpass filtering and by ~70-fold using detection with 1,300 nm longpass filtering, compared to detection with 1,000 nm longpass filtering. Yet, the relative brightness between solvents remains relatively similar in each of these detection windows, indicating that the different solvent environments have minimal effects on the shape of the emission tail.

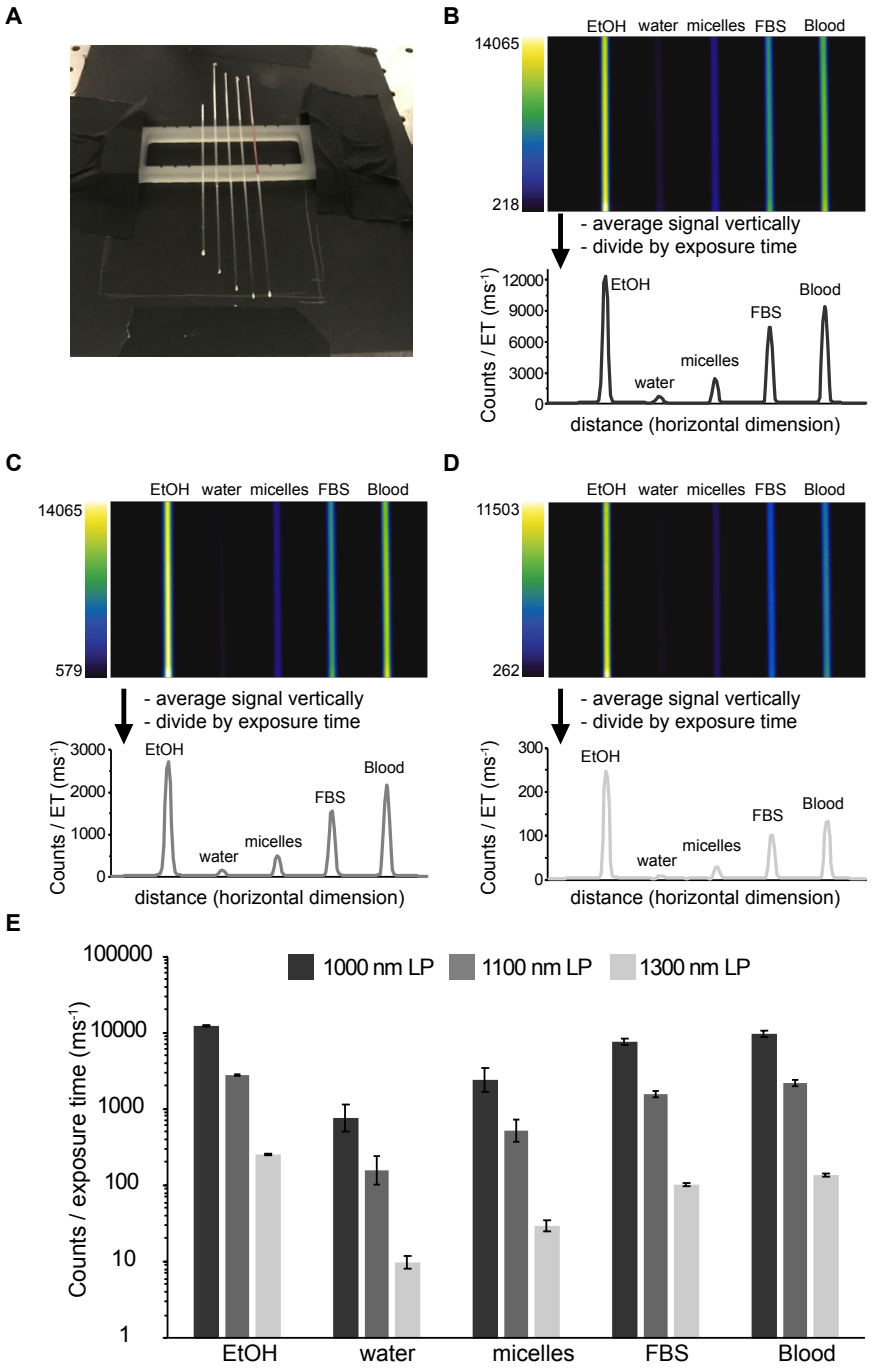

Figure 7.6 SWIR Brightness comparison of ICG emission in various solvents. A) Visible photograph of capillary tubes and holder used in imaging experiment. B–D) Images of capillary tubes and graphical profiles of emission intensity using 785 nm irradiation (63 mW cm^{-2}) with 1,000 nm (B, 1 ms ET), 1,100 nm (C, 5 ms ET), and 1,300 nm (D, 40 ms ET) longpass filtering. All emission intensities displayed in the graphs were corrected for exposure time differences. E) Quantification of emission intensity compared between solvents and longpass filter wavelengths. Error is estimated from a separate experiment (see Figure 7.7), which quantifies variation in emission intensity (as the standard deviation) due to positioning of the capillary tube in relation to the laser irradiation profile.

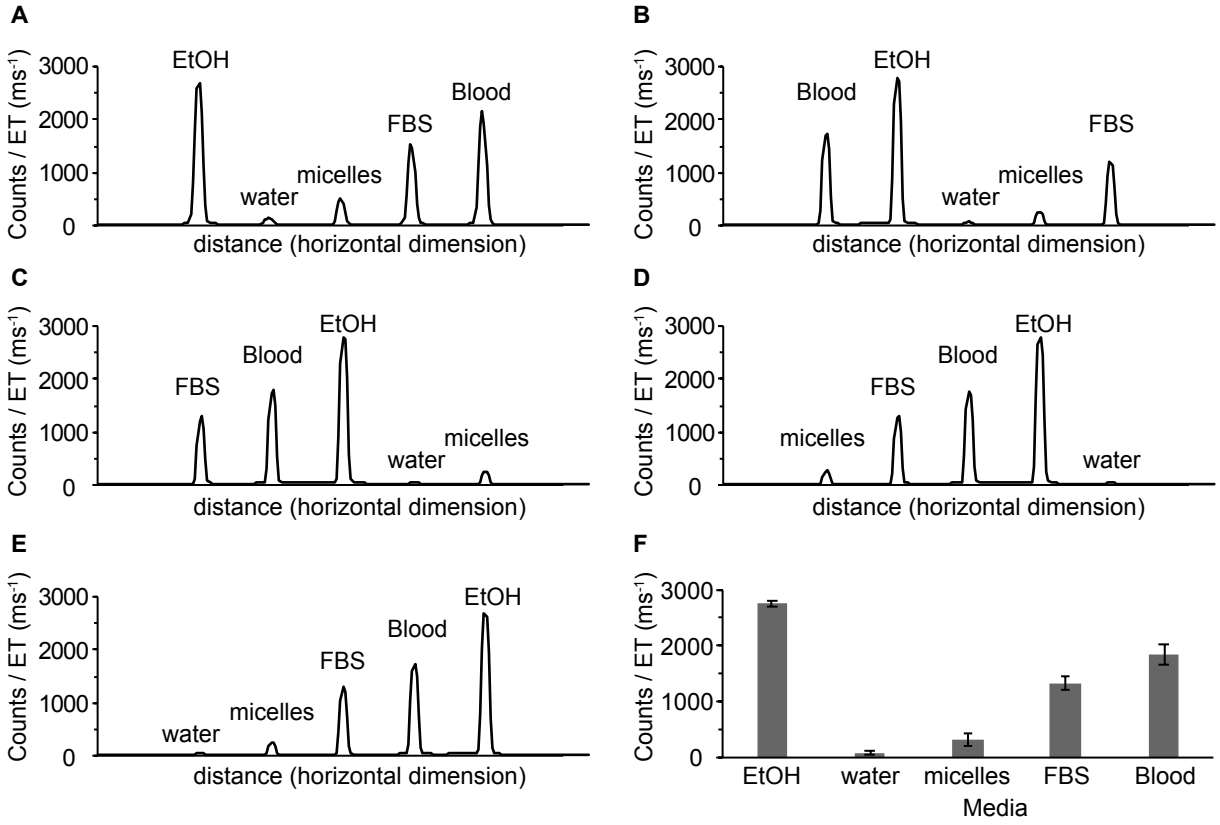

Figure 7.7 Brightness of capillaries containing equal concentrations (5 mM) of ICG in several solvents, positioned over five imaging locations (A–E) and compiled (F). Capillaries were excited with an average laser irradiation of 63 mW cm^{-2} and collected with 1,100 nm longpass filtering and an exposure time of 5 ms. Error in (F) is the standard deviation of the five measurements.

7.4 Conclusion

From the reported measurements, we find that solubilization in ethanol leads to the brightest solutions of ICG, and water significantly lowers brightness. Additionally, photobleaching occurs slowest in ethanol and fastest in water. A micellar formulation enhances the photophysical properties slightly from those measured in water. Moving to the biologically relevant media, we found that the photophysical behavior of ICG in whole blood and FBS is very similar and significantly brighter and more photostable than water. These differences in brightness are accentuated even more when only looking at SWIR wavelengths, where solutions in blood and FBS show between ~13 to ~16-fold higher emission than solutions in water, highlighting the

necessity of performing comparative SWIR experiments in these media. With simpler storage conditions, easier handling and decreased scattering in FBS compared to blood, this medium could be an ideal alternative to blood for benchmarking studies for brightness and photostability. When aiming for a comparison which will represent biological performance, comparisons to ICG in water should be avoided as aqueous media severely underestimate the ε, Φ_F, and photostability values that are present in biological media.

7.5 Experimental Procedures

7.5.1 Materials

Indocyanine Green (ICG) was purchased from Acros Organics (IR-125, laser grade). Ethanol (EtOH) (200 Proof) was purchased from Decon Labs. MilliQ water was dispensed from a MilliQ water purification system. Fetal bovine serum (FBS) was purchased from Genesee Scientific (Lot no. P078430) and was not heat inactivated. Defibrinated Sheep Blood was purchased from Thermo Scientific (Remel sheep blood defibrinated, Ref. R54012, Lot 883930 and Lot 142514). The lipid 18:0 PEG2000 PE was purchased from Avanti Polar Lipids. All materials were used as received without further purification.

7.5.2 Micelle fabrication

ICG (0.6 mg, 0.77 μmol) was massed (Sartorius MSE6.6S-000-DM Cubis Micro Balance) and dissolved in 3.0 mL MeOH. A volume of 2.75 mL of the ICG solution was then added to 44.1 mg of 18:0 PEG2000 PE (as a powder). Of this solution, 0.5 mL aliquots were taken into separate vials and evaporated on a rotary evaporator. To each vial, deionized water (5 mL) was added and the solution was sonicated in a bath sonicator for 1 minute.

7.5.3 Photophysical Measurements

Absorption Measurements Absorption spectra were acquired on a JASCO V-770 UV-VIS/NIR spectrophotometer with a 2000 nm/min scan rate after blanking with the appropriate solvent in quartz cuvettes (10 mm for measurements in EtOH, water, FBS, and micelles in water, 0.2 mm for measurements in whole blood).

Absorption coefficient measurements Absorption coefficients were measured using serial dilutions with Hamilton syringes in volumetric glassware and are taken as the average ± standard deviation of 3 replicate measurements. See Figure 7.3 for the reported traces and Table 7.1 for the reported values. The apparent absorption coefficient measurement for ICG in phospholipid-PEG micelles was obtained by taking micelle solutions and measuring absorption spectra. The micelle solutions were then lyophilized, re-dissolved in EtOH and their absorption spectra were acquired. From the absorption spectra in EtOH, the concentration of each original micelle solution could be obtained using the ε value in EtOH and Beer's law ($A = \varepsilon lc$) Thus, knowing the absorbance (A), path length (l), and, concentration (c) of the micelle solution, an apparent absorption value (ε) was calculated. The apparent absorption coefficient value was reported as the average and standard deviation of 5 measurements.

Emission measurements Photoluminescence spectra were obtained on a Horiba Instruments PTI QuantaMaster Series fluorometer with InGaAs detector Horiba Edison DSS IGA 020L in quartz cuvettes (10 mm for measurements in EtOH, water, and micelles in water, 2 mm for measurements in FBS, and 0.2 mm for measurements in whole blood) with a 90º angle between excitation and detection. The whole blood samples in a 0.2 mm cuvette were positioned at a 45º angle to both the excitation and detection directions for front-facing collection in order to minimize scattering and reabsorption by the blood. The reported emission trace of ICG in whole blood was corrected by

subtraction of the trace obtained using neat blood with identical acquisition conditions (Figure 7.2).

Quantum yield measurements Absolute quantum yield measurements were taken in a Horiba KSPHERE-Petite integrating sphere on the Horiba Instruments fluorometer and are reported as the average ± standard deviation of 3 replicate measurements. For quantum yield measurements, samples were excited with 710 nm and collected between 730–1375 nm. Slit widths were 15 nm excitation/emission with 1 nm step size and 0.1 s integration time. The excitation light was collected between 680–740 nm. The spectra were corrected for excitation with the default correction file using a bias of -1.047, and emission, using a NIR correction file calibrated to quanta. Integrals were obtained for each of the traces, between 740–1375 for the dye emission and between 680–740 nm for the excitation light. Measurements in EtOH, water, micelles, and FBS were obtained in 10 mm x 10 mm quartz cuvettes. Measurement in blood was obtained in a 10 mm x 2 mm quartz cuvette. Optical densities of all samples were below 0.1 au to minimize effects of reabsorption. See Table 7.1 for the reported quantum yield values.

7.5.4 SWIR Imaging apparatus

An InGaAs Camera (Allied Vision Goldeye G-032 Cool TEC2) camera was fitted with a C-mount camera lens (Kowa LM35HC-SW) and variable emission filters as defined in each experiment and mounted vertically above an imaging workspace. The camera used a sensor temperature set point of -30 °C. The "785" laser (LUMICS, LU0785DLU250-S70AN03, specified to an error of ± 10 nm) output was coupled cube via a 600 μm core fiber-optic bundle (Lumics, LU_LWL0600_0720_220D1A1). The output from the fiber was fixed in an excitation cube (Thorlabs KCB1E), reflected off of a mirror (Thorlabs BBE1-E03), and passed through a positive

achromat (Thorlabs AC254-050-AB-ML), 2x 1,000 nm shortpass filters (Edmund Optics #64-337) and an engineered diffuser (Thorlabs ED1-S20-MD) to provide uniform illumination over the working area. The excitation flux was measured over the area of interest with a digital optical power and energy meter (Thorlabs PM100D, specified to an error of ± 3%) and the values over the imaging area were averaged to reach the reported number. The assembly was partially enclosed to avoid excess light while enabling manipulation of the field of view during operation. Camera and lasers were externally controlled and synchronized by delivering trigger pulses of 5V Transistor-Transistor Logic to the laser drivers and camera using a programmable trigger controller with pulses generated with an Atmel Atmega328 micro-controller unit and programmed using Arduino Nano Rev 3 MCU (A000005) in the Arduino integrated development environment (IDE). Acquired imaging data is then transferred to the PC via a Gigabit Ethernet interface. For image acquisition, the toolbox of MATLAB programming environment was used in combination with a MATLAB script (CCDA V3, https://gitlab.com/brunslab/ccda) to preview and collect the required image data in 14-bit depth. Images were processed using the FIJI distribution of ImageJ.

7.5.5 Photobleaching Experiments

Solutions of ICG in each media were prepared and diluted to 5 mM by serial dilutions using micropipettes. Solutions were drawn up into capillary tubes (Corning, 100 μL) and placed in a capillary holder for alignment. Images were acquired of three capillary tube samples using 1,100 nm LP filtering (2x 1,000 nm and 1x 1,100 nm LP filters were used: FELH 1000 (Thorlabs), #84-766 (Edmund Optics), #84-768 (Edmund Optics)). Solutions were irradiated with the 785 nm laser (119 $mWcm^{-2}$) and images were collected at 1 fps with variable exposure times depending on the brightness of the sample (EtOH = 2 ms, water = 20 ms, micelles = 10 ms, FBS = 3 ms, blood = 2

ms). Images were background corrected, and a roi was drawn over each tube. The normalized average intensity and standard deviation of the three trials are plotted in Figure 7.4. All photobleaching data were fit to a mono-exponential decay (Figure 7.5) and the rate constants were obtained from the first order reaction equation:

$$\ln[A] = -kt + \ln [A]_o \qquad \text{(Eq. 7.1)}$$

where A and A_o represent the emission collected at time t and the initial emission collected, respectively. All R^2 values were > 0.96. The photobleaching rates (k_{raw}) are reported in Table 7.2. Relative photostability values were obtained by taking the ratio of the k_{raw} in water over the k_{raw} in the relevant solvent.

7.5.6 Brightness experiments

Solutions of ICG in each media were prepared and diluted to 5 mM by serial dilutions using micropipettes. Solutions were drawn up into capillary tubes (Corning, 100 μL) and placed in a capillary holder for alignment. Solutions were irradiated with the 785 nm laser (63 $mWcm^{-2}$) and images were collected with either 1,000 nm filtering (3x 1,000 nm LP filters were used: FELH 1000 (Thorlabs), 2x #84-766 (Edmund Optics)), 1,100 nm filtering (2x 1,000 nm and 1x 1,100 nm LP filters were used: FELH 1000 (Thorlabs), #84-766 (Edmund Optics), #84-768 (Edmund Optics)), or 1,300 nm filtering (2x 1,000 nm and 1x 1,300 nm LP filters were used: FELH 1000 (Thorlabs), #84-766 (Edmund Optics), #88-668 (Edmund Optics)). Frame rates and exposure times were variable depending on the brightness of the samples in the optical configuration (1,000 LP = 1 ms; 1,100 LP = 5 ms; 1,300 LP = 40 ms). Images were background subtracted, Z-averaged over 100 frames, rotated 90º clockwise, and cropped. The contrast was set in the 14-bit image and the minimum and maximum intensity values were recorded and are displayed in the legend next

to each image (Figure 7.6B–D) before converting the file to 8-bit for display. The look-up table LUT CET-L16[58] was used for display. The profiles were obtained by analyzing the plot profile over a rectangular area (averaging signal in the Y-dimension to display a single curve). The column graph (Figure 7.6E) was constructed using the highest value over each capillary tube and the error as measured in control experiments (Figure 7.7).

7.5.7 Abbreviations

BSA, bovine serum albumin; DLS, dynamic light scattering; DMSO, dimethylsulfoxide; EtOH, ethanol; FBS, fetal bovine serum; fps, frames per second; HSA, human serum albumin; ICG, indocyanine green; IDE, integrated development environment; LP, longpass; MeOH, methanol; MeOD, methanol-d_4; NIR, near-infrared; PBS, phosphate buffered saline; PEG, poly(ethylene glycol); SOP, standard operating procedure; UV, ultra violet; VIS, visible.

7.7 Notes Related to Chapter Seven

7.1.1 Photophysical Properties of ICG from the Literature

Table 7.3 Reported photophysical measurements for ICG. Alternate shading is used to visually delineate between changes in solvents.

Ref.	Year	Solvent	$\lambda_{max,abs}$ (nm)	ε ($M^{-1}cm^{-1}$)	$\lambda_{max,em}$ (nm)	Φ_F (%)
[40]	2011	EtOH	787	194,000 ± 6,000	818	13.2 ± 0.8
[59]	1994	EtOH	786	194,400	n.r.	5 ± 1
[60]	2002	EtOH	780	130,000	830	n.r.
[61]	2015	MeOH	785	204,000	822	7.8
[62]	2014	MeOH	785	n.r.	814	7.2
[37]	1996	MeOH	785	248,000	822	4.1 ± 0.6
[41]	1996	MeOH	782	n.r.	n.r.	4.3 ± 0.5
[59]	1994	MeOH	782	195,300	n.r.	4.0 ± 0.8

[47]	1978	MeOH	n.r.	n.r.	820	8 ± 2
[43]	2020	DMSO	n.r	n.r.	n.r.	26.2 ±
[46]	2012	DMSO	n.r.	n.r.	n.r.	22.8 ± 0.7
[47]	1978	DMSO	n.r.	n.r.	835	12 ± 2
[45]	1977	DMSO	795	n.r.	835	13
[43]	2020	Water	n.r.	n.r.	n.r.	3.7
[18]	2018	Water	n.r.	150,000	n.r.	0.9
[42]	2016	Water	779	n.r.	805	2.4 ± 0.2
[41]	1996	Water	780	n.r.	n.r.	2.7 ± 0.5
[37]	1996	Water	779	175,000	810	1.2 ± 0.2
[59]	1994	Water	779	n.r.	n.r.	1.0 ± 0.2
[47]	1978	Water	n.r.	n.r.	820	0.28 ± 0.06
[63]	2010	70:30 EtOH:water	n.r.	n.r.	n.r.	8.4 ± 0.1
[64]	2019	PBS	779	111,060	807	1.7
[46]	2012	PBS	n.r.	n.r.	n.r.	2.7 ± 0.2
[63]	2010	PBS	780	n.r.	n.r.	2.7 ± 0.1
[44]	2010	PBS	780	n.r.	810	4
[39]	2005	PBS	779	110,000	806	1
[38]	2000	PBS	780	115,000	812	1.2
[37]	1996	PBS	780	115,000	812	1.3 ± 0.2
[39]	2005	FBS	800	166,000	811	9
[38]	2000	bovine plasma	803	215,000	830	3.2
[37]	1996	plasma	803	215,000	829	~4 ± 1
[41]	1996	HSA[a]	800	n.r.	n.r.	4.0 ± 0.5
[44]	2010	BSA[b]	807	n.r.	822	8
[47]	1978	whole blood	n.r.	n.r.	830	1.2 ± 0.2

[a]HSA was prepared at 50 g/dm^3 in Hydrion pH 7.4 buffer. [b]BSA was prepared as 5 mass% (w/v) BSA in PBS.

7.7.2 Treatment of Photobleaching data

As all photobleaching experiments were performed with the same laser wavelength and irradiation, and the absorption maxima of ICG changes only slightly in the solvents studied, photobleaching rates are reported as raw rates without any corrections for wavelength, power density, or the number of absorbed photons. The raw rates most closely represent the effects one would observe in an imaging experiment, yet cannot directly compare molecular reactivity in different solvents as each solvent has a different absorption coefficient.

7.8 Spectra Related to Chapter Seven

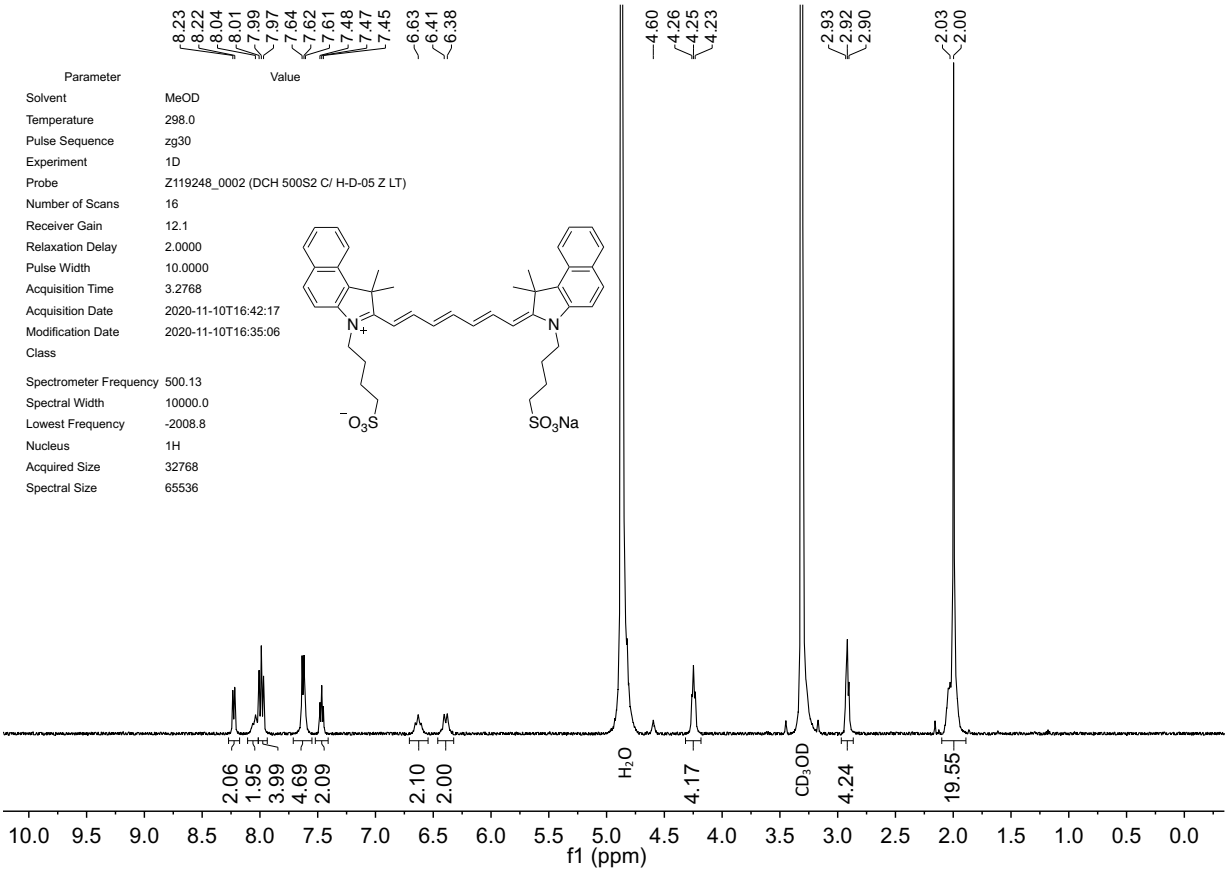

Figure 7.8. ^{1}H NMR spectrum of ICG in MeOD. Spectrum is in agreement with the literature.[65]

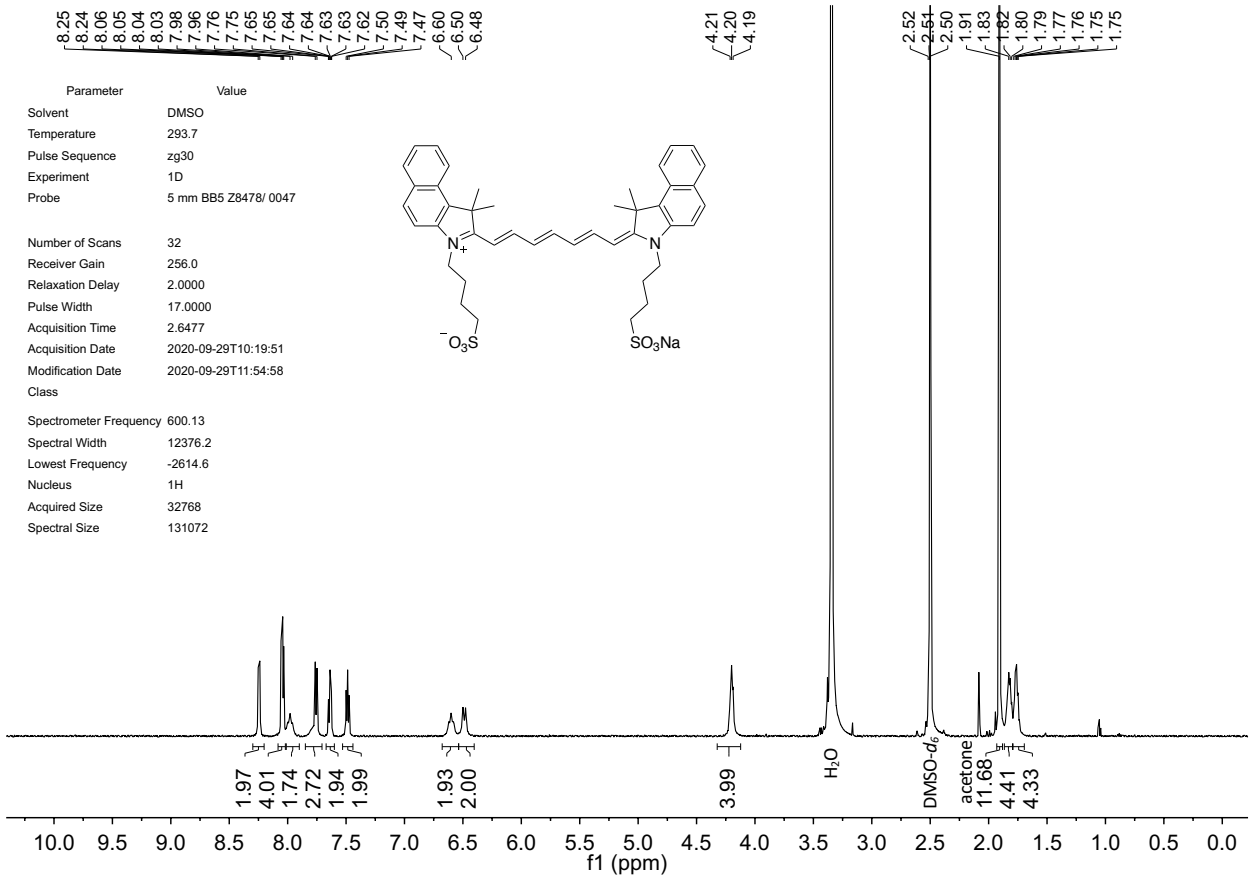

Figure 7.9. ^{1}H NMR spectrum of ICG in DMSO-d_6.

7.9 References

[1] Marshall, M. V; Rasmussen, J. C.; Tan, I.; Aldrich, M. B.; Adams, K. E.; Wang, X.; Fife, C. E.; Maus, E. A.; Smith, L. A.; Sevick-Muraca, E. M. Near-Infrared Fluorescence Imaging in Humans with Indocyanine Green: A Review and Update. *Open Surg. Oncol. J.* **2010**, *2*, 12–25.

[2] Tozzi, M.; Boni, L.; Soldini, G.; Franchin, M.; Piffaretti, G. Vascular Fluorescence Imaging Control for Complex Renal Artery Aneurysm Repair Using Laparoscopic Nephrectomy and Autotransplantation. *Case Rep. Transplant.* **2014**, *2014*, 563408.

[3] Rasmussen, J. C.; Tan, I.; Marshall, M. V; Fife, C. E.; Sevick-, E. M. Lymphatic Imaging in Humans with Near-Infrared Fluorescence. *Curr Opin Biotechnol* **2009**, *20*, 74–82.

[4] Kwon, S.; Sevick-Muraca, E. M. Functional Lymphatic Imaging in Tumor-Bearing Mice. *J. Immunol. Methods* **2010**, *360*, 167–172.

[5] Rasmussen, J. C.; Fife, C. E.; Sevick-Muraca, E. M. Near-Infrared Fluorescence Lymphatic Imaging in Lymphangiomatosis. *Lymphat. Res. Biol.* **2015**, *13*, 195–201.

[6] Cousins, A.; Thompson, S. K.; Wedding, A. B.; Thierry, B. Clinical Relevance of Novel Imaging Technologies for Sentinel Lymph Node Identification and Staging. *Biotechnol. Adv.* **2014**, *32*, 269–279.

[7] De Gasperi, A.; Mazza, E.; Prosperi, M. Indocyanine Green Kinetics to Assess Liver Function: Ready for a Clinical Dynamic Assessment in Major Liver Surgery? *World J. Hepatol.* **2016**, *8*, 355–367.

[8] Schwarz, C.; Plass, I.; Fitschek, F.; Punzengruber, A.; Mittlböck, M.; Kampf, S.; Asenbaum, U.; Starlinger, P.; Stremitzer, S.; Bodingbauer, M.; et al. The Value of Indocyanine Green Clearance Assessment to Predict Postoperative Liver Dysfunction in Patients Undergoing Liver Resection. *Sci. Rep.* **2019**, *9*, 1–7.

[9] Kwon, S.; Sevick-Muraca, E. M. Non-Invasive, Dynamic Imaging of Murine Intestinal Motility. *Neurogastroenterol Motil.* **2011**, *23*, 881-e344.

[10] Li, Z.; Yao, S.; Xu, J.; Wu, Y.; Li, C.; He, Z. Endoscopic Near-Infrared Dental Imaging with Indocyanine Green: A Pilot Study. *Ann. N. Y. Acad. Sci.* **2018**, *1421*, 88–96.

[11] Velde, E. A.; Veerman, T.; Subramaniam, V.; Ruers, T.; te Velde, E. A.; Veerman, T.; Subramaniam, V.; Ruers, T. The Use of Fluorescent Dyes and Probes in Surgical Oncology. *Eur. J. Surg. Oncol.* **2010**, *36*, 6–15.

[12] Polom, K.; Murawa, Dawid, M.; Young-soo, R.; Nowaczyk, P.; Hunerbein, M.; Murawa, P. Current Trends and Emerging Future of Indocyanine Green Usage in Surgery and Oncology. *Cancer* **2011**, *117*, 4812–4822.

[13] Schaafsma, B. E.; Mieog, J. S. D.; Hutteman, M.; van der Vorst, J. R.; Kuppen, P. J. K.; Löwik, C. W. G. M.; Frangioni, J. V; van de Velde, C. J. H.; Vahrmeijer, A. L. The Clinical Use of Indocyanine Green as a Near-Infrared Fluorescent Contrast Agent for Image-Guided Oncologic Surgery. *J. Surg. Oncol.* **2011**, *104*, 323–332.

[14] Daskalaki, D.; Fernandes, E.; Wang, X.; Bianco, F. M.; Elli, E. F.; Ayloo, S.; Masrur, M.; Milone, L.; Giulianotti, P. C. Indocyanine Green (ICG) Fluorescent Cholangiography During Robotic Cholecystectomy. *Surg. Innov.* **2014**, *21*, 615–621.

[15] Koch, M.; Ntziachristos, V. Advancing Surgical Vision with Fluorescence Imaging. *Annu. Rev. Med.* **2016**, *67*, 153–164.

[16] Yim, J. J.; Tholen, M.; Klaassen, A.; Sorger, J.; Bogyo, M. Optimization of a Protease Activated Probe for Optical Surgical Navigation. *Mol. Pharm.* **2017**, *15*, 750–758.

[17] Gioux, S.; Choi, H. S.; Frangioni, J. V. Image-Guided Surgery Using Invisible near-Infrared Light: Fundamentals of Clinical Translation. *Mol. Imaging* **2010**, *9*, 237–255.

[18] Carr, J. A.; Franke, D.; Caram, J. R.; Perkinson, C. F.; Saif, M.; Askoxylakis, V.; Datta, M.; Fukumura, D.; Jain, R. K.; Bawendi, M. G.; et al. Shortwave Infrared Fluorescence Imaging with the Clinically Approved Near-Infrared Dye Indocyanine Green. *Proc. Natl. Acad. Sci.* **2018**, *115*, 4465–4470.

[19] Starosolski, Z.; Bhavane, R.; Ghaghada, K. B.; Vasudevan, S. A.; Kaay, A.; Annapragada, A. Indocyanine Green Fluorescence in Second Near-Infrared (NIR-II) Window. *PLoS One* **2017**, *12*, e0187563.

[20] Yu, X.; Feng, Z.; Cai, Z.; Jiang, M.; Xue, D.; Zhu, L.; Zhang, Y.; Liu, J.; Que, B.; Yang, W.; et al. Deciphering of Cerebrovasculatures via ICG-Assisted NIR-II Fluorescence Microscopy. *J. Mater. Chem. B* **2019**, *7*, 6623–6629.

[21] Cai, Z.; Zhu, L.; Wang, M.; Roe, A. W.; Xi, W.; Qian, J. NIR-II Fluorescence Microscopic Imaging of Cortical Vasculature in Non-Human Primates. *Theranostics* **2020**, *10*, 4265–4276.

[22] Li, Z.; Zaid, W.; Hartzler, T.; Ramos, A.; Osborn, M. L.; Li, Y.; Yao, S.; Xu, J. Indocyanine Green–Assisted Dental Imaging in the First and Second near-Infrared Windows as Compared with X-Ray Imaging. *Ann. N. Y. Acad. Sci.* **2019**, *1448*, 42–51.

[23] Cosco, E. D.; Spearman, A. L.; Ramakrishnan, S.; Lingg, J. G. P.; Saccomano, M.; Pengshung, M.; Arús, B. A.; Wong, K. C. Y.; Glasl, S.; Ntziachristos, V.; et al. Shortwave Infrared Polymethine Fluorophores Matched to Excitation Lasers Enable Non-Invasive, Multicolour in Vivo Imaging in Real Time. *Nat. Chem.* **2020**, *12*, 1123–1130.

[24] Cosco, E. D.; Arús, B. A.; Spearman, A. L.; Atallah, T. L.; Leland, O. S.; Caram, J. R.; Bischof, T. S.; Bruns, O. T.; Sletten. E. M. Bright chromenylium polymethine dyes enable fast, four-color in vivo imaging with shortwave infrared detection. M*anuscript submitted.*

[25] Hu, Z.; Fang, C.; Li, B.; Zhang, Z.; Cao, C.; Cai, M.; Su, S.; Sun, X.; Shi, X.; Li, C.; et al. First-in-Human Liver-Tumour Surgery Guided by Multispectral Fluorescence Imaging in the Visible and near-Infrared-I/II Windows. *Nat. Biomed. Eng.* **2020**, *4*, 259–271.

[26] Patel, N. J.; Manivannan, E.; Joshi, P.; Ohulchanskyy, T. J.; Nani, R. R.; Schnermann, M. J.; Pandey, R. K. Impact of Substituents in Tumor Uptake and Fluorescence Imaging Ability of Near-Infrared Cyanine-like Dyes. *Photochem. Photobiol.* **2015**, *91*, 1219–1230.

[27] Wang, S.; Fan, Y.; Li, D.; Sun, C.; Lei, Z.; Lu, L.; Wang, T.; Zhang, F. Anti-Quenching NIR-II Molecular Fluorophores for in Vivo High-Contrast Imaging and PH Sensing. *Nat. Commun.* **2019**, *10*, 1058.

[28] Zhu, S.; Hu, Z.; Tian, R.; Yung, B. C.; Yang, Q.; Zhao, S.; Kiesewetter, D. O.; Niu, G.; Sun, H.; Antaris, A. L.; et al. Repurposing Cyanine NIR-I Dyes Accelerates Clinical Translation of Near-Infrared-II (NIR-II) Bioimaging. *Adv. Mater.* **2018**, *30*, 1802546.

[29] Lei, Z.; Sun, C.; Pei, P.; Wang, S.; Li, D.; Zhang, X.; Zhang, F. Stable, Wavelength-Tunable Fluorescent Dyes in the NIR-II Region for In Vivo High-Contrast Bioimaging and Multiplexed Biosensing. *Angew. Chemie Int. Ed.* **2019**, *58*, 8166–8171.

[30] Li, B.; Zhao, M.; Feng, L.; Dou, C.; Ding, S.; Zhou, G.; Lu, L.; Zhang, H.; Chen, F.; Li, X.; et al. Organic NIR-II Molecule with Long Blood Half-Life for in Vivo Dynamic Vascular Imaging. *Nat. Commun.* **2020**, *11*, 3102.

[31] Byrd, B. K.; Folaron, M. R.; Leonor, J. P.; Strawbridge, R. R.; Cao, X.; Bruza, P.; Davis, S. C. Characterizing Short-Wave Infrared Fluorescence of Conventional Near-Infrared Fluorophores. *J. Biomed. Opt.* **2019**, *24*, 1.

[32] Shi, Y.; Yuan, W.; Liu, Q.; Kong, M.; Li, Z.; Feng, W.; Hu, K.; Li, F. Development of Polyene-Bridged Hybrid Rhodamine Fluorophores for High-Resolution NIR-II Imaging. *ACS Mater. Lett.* **2019**, *1*, 418–424.

[33] Ding, B.; Xiao, Y.; Zhou, H.; Zhang, X.; Qu, C.; Xu, F.; Deng, Z.; Cheng, Z.; Hong, X. Polymethine Thiopyrylium Fluorophores with Absorption beyond 1000 nm for Biological Imaging in the Second Near-Infrared Subwindow. *J. Med. Chem.* **2019**, *62*, 2049–2059.

[34] Feng, Z.; Yu, X.; Jiang, M.; Zhu, L.; Zhang, Y.; Yang, W.; Xi, W.; Li, G.; Qian, J. Excretable IR-820 for in Vivo NIR-II Fluorescence Cerebrovascular Imaging and Photothermal Therapy of Subcutaneous Tumor. *Theranostics* **2019**, *9*, 5706–5719.

[35] Tian, R.; Ma, H.; Zhu, S.; Lau, J.; Ma, R.; Liu, Y.; Lin, L.; Chandra, S.; Wang, S.; Zhu, X.; et al. Multiplexed NIR-II Probes for Lymph Node-Invaded Cancer Detection and Imaging-Guided Surgery. *Adv. Mater.* **2020**, *32*, 1–10.

[36] Mangold, K.; Shaw, J. A.; Vollmer, M. The Physics of Near-Infrared Photography. *Eur. J. Phys.* **2013**, *34*, S51–S71.

[37] Licha, K.; Riefke, B.; Semmler, W. Synthesis and Characterization of Cyanine Dyes as Contrast Agents for Near-Infrared Imaging. *Proc. SPIE* **1996**, *2927*, 192–198.

[38] Licha, K.; Riefke, B.; Ntziachristos, V.; Becker, A.; Chance, B.; Semmler, W. Hydrophilic Cyanine Dyes as Contrast Agents for Near-Infrared Tumor Imaging: Synthesis, Photophysical Properties and Spectroscopic In Vivo Characterization¶. *Photochem. Photobiol.* **2000**, *72*, 392.

[39] Obnisbi, S.; Lomnes, S. J.; Laurence, R. G.; Gogbasbian, A.; Mariant, G.; Frangioni, J. V. Organic Alternatives to Quantum Dots for Intraoperative Near-Infrared Fluorescent Sentinel Lymph Node Mapping. *Mol. Imaging* **2005**, *4*, 172–181.

[40] Rurack, K.; Spieles, M. Fluorescence Quantum Yields of a Series of Red and Near-Infrared Dyes Emitting at 600−1000 nm. *Anal. Chem.* **2011**, *83*, 1232–1242.

[41] Philip, R.; Penzkofer, A.; Baumler, W.; Szeimies, R. M.; Abels, C. Absorption and Fluorescence Spectroscopic Investigation of Indocyanine Green. *J. Photochem. Photobiol., A* **1996**, *96*, 137–148.u

[42] Jin, T.; Tsuboi, S.; Komatsuzaki, A.; Imamura, Y.; Muranaka, Y.; Sakata, T.; Yasuda, H. Enhancement of Aqueous Stability and Fluorescence Brightness of Indocyanine Green Using Small Calix[4]Arene Micelles for near-Infrared Fluorescence Imaging. *Medchemcomm* **2016**, *7*, 623–631.

[43] Hoshi, R.; Suzuki, K.; Hasebe, N.; Yoshihara, T.; Tobita, S. Absolute Quantum Yield Measurements of Near-Infrared Emission with Correction for Solvent Absorption. *Anal. Chem.* **2020**, *92*, 607–611.

[44] Pauli, J.; Brehm, R.; Spieles, M.; Kaiser, W. A.; Hilger, I.; Resch-Genger, U. Novel Fluorophores as Building Blocks for Optical Probes for in Vivo near Infrared Fluorescence (NIRF) Imaging. *J. Fluoresc.* **2010**, *20*, 681–693.

[45] Benson, R. C.; Kues, H. A. Absorption and Fluorescence Properties of Cyanine Dyes. *J. Chem. Eng. Data* **1977**, *22*, 379–383.

[46] Würth, C.; Pauli, J.; Lochmann, C.; Spieles, M.; Resch-Genger, U. Integrating Sphere Setup for the Traceable Measurement of Absolute Photoluminescence Quantum Yields in the Near Infrared. *Anal. Chem.* **2012**, *84*, 1345–1352.

[47] Benson, R. C.; Kues, H. a. Fluorescence Properties of Indocyanine Green as Related to Angiography. *Phys. Med. Biol.* **1978**, *23*, 159–163.

[48] Kirchherr, A. K.; Briel, A.; Mäder, K. Stabilization of Indocyanine Green by Encapsulation within Micellar Systems. *Mol. Pharm.* **2009**, *6*, 480–491.

[49] Kim, T. H.; Chen, Y.; Mount, C. W.; Gombotz, W. R.; Li, X.; Pun, S. H. Evaluation of Temperature-Sensitive, Indocyanine Green-Encapsulating Micelles for Noninvasive near-Infrared Tumor Imaging. *Pharm. Res.* **2010**, *27*, 1900–1913.

[50] Meyer, J.; Cunea, A.; Sonntag-Bensch, D.; Welker, P.; Licha, K.; Holz, F. G.; Schmitz-Valckenberg, S. In Vivo Imaging of a New Indocyanine Green Micelle Formulation in an Animal Model of Laser-Induced Choroidal Neovascularization. *Investig. Ophthalmol. Vis. Sci.* **2014**, *55*, 6204–6212.

[51] Saxena, V.; Sadoqi, M.; Shao, J. Enhanced Photo-Stability, Thermal-Stability and Aqueous-Stability of Indocyanine Green in Polymeric Nanoparticulate Systems. *J. Photochem. Photobiol., B* **2004**, *74*, 29–38.

[52] Ma, Y.; Tong, S.; Bao, G.; Gao, C.; Dai, Z. Indocyanine Green Loaded SPIO Nanoparticles with Phospholipid-PEG Coating for Dual-Modal Imaging and Photothermal Therapy. *Biomaterials* **2013**, *34*, 7706–7714.

[53] Sharma, P.; Bengtsson, N. E.; Walter, G. A.; Sohn, H. B.; Zhou, G.; Iwakuma, N.; Zeng, H.; Grobmyer, S. R.; Scott, E. W.; Moudgil, B. M. Gadolinium-Doped Silica Nanoparticles Encapsulating Indocyanine Green for near Infrared and Magnetic Resonance Imaging. *Small* **2012**, *8*, 2856–2868.

[54] Altinoğlu, E. I.; Russin, T. J.; Kaiser, J. M.; Barth, B. M.; Eklund, P. C.; Kester, M.; Adair, J. H. Near-Infrared Emitting Fluorophore-Doped Calcium Phosphate Nanoparticles for in Vivo Imaging of Human Breast Cancer. *ACS Nano* **2008**, *2*, 2075–2084.

[55] Holzer, W.; Mauerer, M.; Penzkofer, A.; Szeimies, R.-M.; Abels, C.; Landthaler, M.; Bäumler, W. Photostability and Thermal Stability of Indocyanine Green. *J. Photochem. Photobiol., B* **1998**, *47*, 155–164.

[56] Schindelin, J.; Arganda-Carreras, I.; Frise, E.; Kaynig, V.; Longair, M.; Pietzsch, T.; Preibisch, S.; Rueden, C.; Saalfeld, S.; Schmid, B.; et al. Fiji: An Open-Source Platform for Biological-Image Analysis. *Nat. Methods* **2012**, *9*, 676–682.

[57] Rueden, C. T.; Schindelin, J.; Hiner, M. C.; DeZonia, B. E.; Walter, A. E.; Arena, E. T.; Eliceiri, K. W. ImageJ2: ImageJ for the next Generation of Scientific Image Data. *BMC Bioinformatics* **2017**, *18*, 529.

[58] Kovesi, P. Good Colour Maps: How to Design Them. arXiv:1509.03700 [cs.GR] 2015.

[59] Soper, S. A.; Mattingly, Q. L. Steady-State and Picosecond Laser Fluorescence Studies of Nonradiative Pathways in Tricarbocyanine Dyes: Implications to the Design of Near-IR Fluorochromes with High Fluorescence Efficiencies. *J. Am. Chem. Soc.* **1994**, *116*, 3744–3752.

[60] Kassab, K. Photophysical and Photosensitizing Properties of Selected Cyanines. *J. Photochem. Photobiol., B* **2002**, *68*, 15–22.

[61] Nani, R. R.; Shaum, J. B.; Gorka, A. P.; Schnermann, M. J. Electrophile-Integrating Smiles Rearrangement Provides Previously Inaccessible C4'-O-Alkyl Heptamethine Cyanine Fluorophores. *Org. Lett.* **2015**, *17*, 302–305.

[62] Okoh, O. A.; Bisby, R. H.; Lawrence, C. L.; Rolph, C. E.; Smith, R. B. Promising Near-Infrared Non-Targeted Probes: Benzothiazole Heptamethine Cyanine Dyes. *J. Sulfur Chem.* **2014**, *35*, 42–56..

[63] Russin, T. J.; Altmoğlu, E. Ï.; Adair, J. H.; Eklund, P. C. Measuring the Fluorescent Quantum Efficiency of Indocyanine Green Encapsulated in Nanocomposite Particulates. *J. Phys. Condens. Matter* **2010**, *22*, 334217.

[64] Thavornpradit, S.; Usama, S. M.; Park, G. K.; Shrestha, J. P.; Nomura, S.; Baek, Y.; Choi, H. S.; Burgess, K. QuatCy: A Heptamethine Cyanine Modification with Improved Characteristics. *Theranostics* **2019**, *9*, 2856–2867.

[65] Rüttger, F.; Mindt, S.; Golz, C.; Alcarazo, M.; John, M. Isomerization and Dimerization of Indocyanine Green and a Related Heptamethine Dye. *European J. Org. Chem.* **2019**, *2019*, 4791–4796.